

Magnetic Compression of Compact Tori

Experiment and Simulation

A Thesis Submitted to the
College of Graduate and Postdoctoral Studies
in Partial Fulfillment of the Requirements
for the degree of Doctor of Philosophy
in the Department of Physics and Engineering Physics
University of Saskatchewan
Saskatoon
Canada
By
Carl Dunlea

Permission to use

In presenting this thesis in partial fulfillment of the requirements for a Postgraduate degree from the University of Saskatchewan, I agree that the Libraries of this University may make it freely available for inspection. I further agree that permission for copying of this thesis in any manner, in whole or in part, for scholarly purposes may be granted by the professor or professors who supervised my thesis work or, in their absence, by the Head of the Department or the Dean of the College in which my thesis work was done. It is understood that any copying or publication or use of this thesis or parts thereof for financial gain shall not be allowed without my written permission. It is also understood that due recognition shall be given to me and to the University of Saskatchewan in any scholarly use which may be made of any material in my thesis. Requests for permission to copy or to make other use of material in this thesis in whole or part should be addressed to:

Head of the Department of Physics and Engineering Physics, Room 163, 116 Science Place,
University of Saskatchewan, Saskatoon, Saskatchewan, Canada S7N 5E2,

or:

Dean, College of Graduate and Postdoctoral Studies, University of Saskatchewan, 116 Thorvaldson Building, 110 Science Place Saskatoon, Saskatchewan, Canada S7N 5C9.

Abstract

The magnetic compression experiment at General Fusion was a repetitive non-destructive test to study plasma physics applicable to magnetic target fusion compression. A compact torus (CT) is formed with a co-axial gun into a containment region with an hour-glass shaped inner flux conserver, and an insulating outer wall. External coil currents keep the CT off the outer wall (radial levitation) and then rapidly compress it inwards. The optimal external coil configuration greatly improved both the levitated CT lifetime and the recurrence rate of shots with good compressional flux conservation. As confirmed by spectrometer data, the improved levitation field profile reduced plasma impurity levels by suppressing the interaction between plasma and the insulating outer wall during the formation process. Significant increases in magnetic field, electron density, and ion temperature were routinely observed at magnetic compression in the final external coil configuration tested, despite the prevalence of an instability, thought to be an external kink mode, at compression. Matching the decay rate of the levitation currents to that of the CT currents resulted in a reduced level of MHD activity associated with unintentional compression by the levitation field, and a higher probability of long-lived CTs. The DELiTE (Differential Equations on Linear Triangular Elements) framework was developed for spatial discretisation of partial differential equations on an unstructured triangular grid in axisymmetric geometry. The framework is based on discrete differential operators in matrix form, which are derived using linear finite elements and mimic some of the properties of their continuous counterparts. A single-fluid two-temperature MHD model is implemented in this framework. The inherent properties of the operators are used in the code to ensure global conservation of energy, particle count, toroidal flux, and angular momentum. The development of the discrete forms of the equations solved is presented. The code was applied to study the magnetic compression experiment. The numerical models developed to simulate CT formation, levitation, and magnetic compression are reported. A model for anisotropic thermal diffusion has been formulated and implemented to the code. A method for determining the q profile of the CT was established - simulated CT q profiles indicate that the magnetic compression experiment could be improved by modifying the q profile to regimes with increased stability against kink modes. Comparisons between simulated and experimental diagnostics are presented. A model of plasma/neutral fluid interaction was developed and included in the framework. The source rates of species momentum and energy due to ionization and recombination were derived using a simple method that enables determination of the volumetric rate of thermal energy transfer from electrons to photons and neutral particles due to radiative recombination, which has been neglected in other studies. The implementation of the model has enabled clarification of the mechanisms behind the increases in CT electron density that are routinely observed on the SPECTOR plasma injector well after CT formation. This understanding helps account for the exceptionally significant increase in electron temperature, and markedly reduced electron density, observed during the electrode edge biasing experiment conducted on SPECTOR. It is thought that edge fueling impediment, a consequence of a biasing-induced transport barrier, is largely responsible for the observed modifications to temperature and density.

Acknowledgments

I would like to thank my thesis supervisors Professors Akira Hirose and Chijin Xiao, especially for guidance and assistance with the CHI (Co-axial Helicity Injection) on the STOR-M tokamak over the second year of the PhD program. That was a great introduction to tokamak hardware and operation, and to laboratory work. Thanks to Dave McColl for his advice on various high power circuit modifications. A description of the CHI experiment is presented in [1]. Thanks to Professor Xiao in particular for helping arrange formalities over the final stages of the program, to Professor Andrei Smolyakov for the initial contact that led to this research work, and to my academic committee for general support and advice with the thesis formatting. Thanks to Debbie and Marj for always being friendly and willing to offer practical advice. The couple of winters I spent in Saskatoon would not have been as enjoyable without various wonderful people who I was lucky to meet there, especially Yanli, Winston, Lili, and Joel. At General Fusion (GF), many people were supportive and helped with the development of the work presented here. In particular, Wade Zawalski, Stephen Howard, and Kelly Epp were involved with the experiment and I learned a lot from them. Stephen helped guide the development of an equilibrium solver to model magnetic compression, and was very helpful with the experiment and with data analysis. Many of the improvements and developments that are presented here were achieved towards the end of the experimental phase of the project. After the experiment was decommissioned, Ivan Khalzov, in his spare time, supported the development of the brand new code framework that is described in detail in part two of this thesis; I am extremely grateful for his guidance. The work Stephen and I did on the equilibrium solver during a large part of 2015 is not presented here, but some lessons were learned from it and applied to the MHD code. Thanks to Meritt Reynolds and Charlson Kim at GF for discussions and insight, and to Masayoshi Nagata for useful feedback. Thanks also to Blake Rablah, Curtis Gutjahr and James Wilkie for assistance and advice relating to circuits, diagnostics, and hardware during the experiment (particularly towards the end), to Alex Mossman, Peter O’ Shea, Mike Donaldson, Michael Delage, and Michel Laberge for general support at various times, and to many of the great people at GF for being friendly and assisting with different aspects of the project. Thanks to the University of Saskatchewan ICT Research Computing Facility for advice and computing time. I would like to acknowledge the funding provided in part by General Fusion Inc., Mitacs, University of Saskatchewan, and NSERC. Thanks to my parents and family for their continual encouragement. Finally, I would like to thank my lovely Yanli for her support and patience throughout this process.

Contents

| | |
|--|-------------|
| Permission to use | i |
| Abstract | ii |
| Acknowledgments | iii |
| Table of contents | iv |
| List of tables | xi |
| List of figures | xii |
| List of symbols | xvii |
| List of abbreviations | xx |
| 1 Introduction | 1 |
| 1.1 Background - plasma and nuclear fusion | 1 |
| 1.2 General Fusion - overview | 5 |
| 1.3 Magnetic geometry of compact tori | 7 |
| 1.4 Scaling laws for magnetic compression | 10 |
| 1.5 Prior magnetic compression experiments | 15 |
| 1.5.1 S-1 spheromak | 16 |
| 1.5.2 ATC tokamak | 19 |
| 1.5.3 Ultra Low q device | 20 |
| 1.5.4 Merging-compression formation of tokamak plasmas | 24 |
| 1.5.5 Magnetic compression of FRCs | 24 |
| 1.6 Thesis outline | 24 |

PART 1: EXPERIMENT 28

| | |
|---|-----------|
| 2 Experiment overview | 29 |
| 2.1 Machine operation principles | 30 |
| 2.2 Diagnostics | 34 |
| 2.2.1 Magnetic field measurements - B probes | 35 |
| 2.2.2 Current measurements - Rogowski coils | 38 |
| 2.2.3 Density measurements - interferometry | 38 |
| 2.2.4 Temperature measurements - ion-Doppler spectroscopy | 42 |
| 2.2.5 Optical diagnostics | 44 |
| 3 Magnetic Levitation | 45 |
| 3.1 6-coil configuration, ceramic outer insulating wall | 46 |
| 3.2 6 coil configuration, quartz outer insulating wall | 51 |
| 3.3 CT rotation and toroidal MHD modes | 53 |
| 3.4 25-turn coil | 55 |
| 3.4.1 Coil design parameters | 55 |
| 3.4.2 Coil manufacture | 57 |
| 3.4.3 Levitated CT performance with the 25-turn coil | 58 |
| 3.5 Semi-permeable shell | 63 |
| 3.5.1 Stainless-steel shell test | 64 |
| 3.5.2 Effective skin depth for thin shells | 66 |
| 3.6 11-coil configuration, quartz outer insulating wall | 68 |
| 3.6.1 Levitation field decay rate | 70 |
| 3.6.2 Additional tests on the 11-coil configuration | 72 |
| 3.7 Using side-probe data to find CT outboard separatrix radius over time | 74 |
| 3.7.1 Levitation only shots with 70 mΩ cables | 76 |
| 3.7.2 Levitation only shots with 2.5 mΩ cables | 78 |
| 3.8 Comparison of total spectral power measurements and levitated CT lifetimes for various configurations | 81 |
| 3.9 Summary | 83 |
| 4 Magnetic Compression | 89 |
| 4.1 Overview of results | 90 |
| 4.2 Compressional instability | 99 |
| 4.3 Comparison of compression parameters between configurations | 101 |
| 4.4 Experimentally measured CT outboard separatrix radius for compression shots | 102 |
| 4.5 Scintillator data | 103 |

| | | |
|-----|---------|-----|
| 4.6 | Summary | 104 |
|-----|---------|-----|

PART 2: SIMULATIONS 106

| | | |
|----------|--|------------|
| 5 | Core code development and MHD model | 107 |
| 5.1 | Conservation schemes | 108 |
| 5.2 | Finite element method overview | 109 |
| 5.3 | Key notations and node-to-element mapping | 112 |
| 5.4 | Differential operators | 115 |
| 5.4.1 | First order node-to-element differential operators | 115 |
| 5.4.2 | First order element-to-node differential operators | 119 |
| 5.4.3 | Second order node-to-node differential operators | 121 |
| 5.4.3.1 | Alternative derivation of the second order node-to-node differential operators | 122 |
| 5.4.4 | First order node-to-node differential operators | 124 |
| 5.4.4.1 | Alternative derivations of the first order node-to-node differential operators | 127 |
| 5.5 | Axisymmetric two-temperature MHD model | 129 |
| 5.5.1 | Expression for $\dot{\psi}$ | 130 |
| 5.5.2 | Expressions for \dot{f} | 131 |
| 5.5.3 | Continuous form of MHD model equations and demonstration of conservation properties | 134 |
| 5.6 | Discrete form of MHD equations and conservation properties | 139 |
| 5.6.1 | Discretised MHD model | 139 |
| 5.6.2 | Conservation properties | 143 |
| 5.6.2.1 | Particle count conservation | 143 |
| 5.6.2.2 | Toroidal flux conservation | 143 |
| 5.6.2.3 | Angular momentum conservation | 144 |
| 5.6.2.4 | Energy conservation | 146 |
| 5.6.3 | Maintenance of energy and momentum conservation with artificial density diffusion | 150 |
| 5.7 | Summary | 153 |
| 6 | Models for CT formation, levitation and magnetic compression, and implementation of simulated diagnostics | 154 |
| 6.1 | Boundary conditions | 155 |
| 6.1.1 | Boundary conditions for density | 155 |
| 6.1.2 | Boundary conditions for velocity | 155 |

| | | |
|----------|--|------------|
| 6.1.3 | Boundary conditions for temperature | 156 |
| 6.1.4 | Boundary conditions for ψ | 156 |
| 6.1.5 | Boundary conditions for f | 158 |
| 6.2 | Vacuum field in insulating region | 160 |
| 6.3 | External sources of toroidal flux | 163 |
| 6.3.1 | External sources of toroidal flux for formation simulations | 163 |
| 6.3.1.1 | Time-dependent formation profile | 167 |
| 6.3.2 | External sources of toroidal flux for simulations starting with a Grad-Shafranov equilibrium | 170 |
| 6.4 | Toroidal flux conservation with insulating region | 173 |
| 6.4.1 | Formation simulations | 173 |
| 6.4.2 | Simulations starting with a Grad-Shafranov equilibrium | 174 |
| 6.4.3 | Illustration of toroidal flux conservation | 175 |
| 6.5 | Simulated diagnostics | 176 |
| 6.5.1 | Simulated diagnostics corresponding to experimental measurements . | 176 |
| 6.5.2 | Additional simulated diagnostics | 177 |
| 6.5.2.1 | q profile | 177 |
| 6.5.2.2 | Evaluation of CT volume and volume-averaged β | 179 |
| 6.6 | Summary | 179 |
| 7 | Simulation input parameters and results | 181 |
| 7.1 | Simulation input parameters | 182 |
| 7.2 | Simulated plasma-wall interaction | 186 |
| 7.2.1 | Effect of increasing levitation field soak-in | 186 |
| 7.2.2 | Effect of levitation field profile (11-coil <i>cf.</i> 6-coil configuration) | 189 |
| 7.3 | Evolution of the various fields, simulation 2353 | 190 |
| 7.4 | Evolution of fields when \mathbf{I}_{comp} changes polarity, simulation 2287 | 206 |
| 7.5 | Simulated diagnostics, and comparison with experimental results | 209 |
| 7.5.1 | Non-compression shots/simulations | 210 |
| 7.5.2 | Compression shots/simulations | 213 |
| 7.5.2.1 | Shots 39475, 39738, and 39510 | 213 |
| 7.5.2.2 | Shot 39735 | 216 |
| 7.5.2.3 | Simulation of compressional flux loss | 217 |
| 7.5.3 | Results from additional simulated diagnostics | 218 |
| 7.5.3.1 | Simulated diagnostics for $\psi_{CT}(t)$, $T_{max}(t)$, $r_s(t)$, $r_{axis}(t)$, $V_{CT}(t)$, and $\beta(t)$ | 219 |
| 7.5.3.2 | Simulated internal magnetic field | 221 |
| 7.5.3.3 | Simulated q profile | 223 |

| | | |
|----------------------------|---|------------|
| 7.5.3.4 | Adiabatic compression scalings | 225 |
| 7.5.3.5 | System energy components | 228 |
| 7.6 | Summary | 230 |
| 8 | Model for interaction between plasma and neutral fluids | 233 |
| 8.1 | Model overview | 235 |
| 8.2 | Scattering collision terms | 236 |
| 8.3 | Reactive collision terms | 238 |
| 8.3.1 | Ionization and recombination | 239 |
| 8.3.1.1 | Mass Conservation | 239 |
| 8.3.1.2 | Momentum Conservation | 242 |
| 8.3.1.3 | Energy Conservation | 244 |
| 8.3.2 | Charge exchange | 248 |
| 8.3.2.1 | 0 th moment of the charge exchange collision operator | 248 |
| 8.3.2.2 | 1 st moment of the charge exchange collision operator | 249 |
| 8.3.2.3 | 2 nd moment of the charge exchange collision operator | 250 |
| 8.4 | 3-fluid MHD equations | 251 |
| 8.4.1 | Mass conservation | 252 |
| 8.4.2 | Momentum conservation | 253 |
| 8.4.3 | Energy conservation | 253 |
| 8.5 | 2-fluid MHD equations | 254 |
| 8.6 | Conservation properties with inclusion of neutral fluid | 256 |
| 8.7 | Neutral fluid thermal diffusion | 257 |
| 8.8 | Simple model for charge exchange reactions | 258 |
| 8.9 | Simulation results with neutral fluid | 259 |
| 8.9.1 | Effect of inclusion of the Q_e^{rec} term | 263 |
| 8.9.2 | Neutral fluid interaction in SPECTOR geometry | 265 |
| 8.10 | Summary | 269 |
| PART 3: CONCLUSIONS | 271 | |
| 9 | Concluding remarks | 272 |
| BIBLIOGRAPHY | 280 | |
| PART 4: APPENDICES | 290 | |
| A | Plasma kinetic theory, MHD equations, and equilibrium models | 291 |

| | | |
|----------------|---|-----|
| A.1 | Distribution functions and the Boltzmann equation | 292 |
| A.2 | Moments of the distribution function | 294 |
| A.3 | Moments of the collision operator | 297 |
| A.4 | Braginskii equations from moments of the Boltzmann equation | 299 |
| A.4.1 | 0th moment (mass continuity equation) | 300 |
| A.4.2 | 1st moment (momentum equation) | 300 |
| A.4.3 | 2nd moment (energy equation) | 302 |
| A.5 | Chapman-Enskog closures | 305 |
| A.5.1 | Closures for a neutral gas | 305 |
| A.5.2 | Closures for an unmagnetized collisional plasma | 307 |
| A.5.3 | Closures for a magnetized plasma | 310 |
| A.6 | Single fluid magnetohydrodynamic equations | 311 |
| A.6.1 | 0th moment (mass continuity equation) | 312 |
| A.6.2 | 1st moment (momentum equation) | 312 |
| A.6.3 | Ohm's law | 315 |
| A.6.4 | 2nd moment (energy equation) | 316 |
| A.7 | Equilibrium models | 317 |
| A.7.1 | Grad-Shafranov equation | 317 |
| A.7.2 | Grad-Shafranov equation for case with linear $\lambda(\psi)$ profile | 320 |
| A.8 | Summary | 323 |
| B | Formulation of discretized MHD equations for energy conservation | 325 |
| B.1 | Overview | 325 |
| B.2 | Kinetic Energy | 327 |
| B.3 | Thermal Energy | 330 |
| B.3.1 | Viscous heating | 331 |
| B.3.1.1 | Discretisation of $\dot{U}_{Th\pi}$ | 333 |
| B.3.2 | Final expression for discretised form of \dot{U}_{Th} | 338 |
| B.4 | Magnetic energy | 339 |
| B.4.1 | Discretisation of $\dot{U}_{M\theta}$ | 339 |
| B.4.2 | Discretisation of $\dot{U}_{M\phi}$ | 341 |
| B.4.3 | Final expression for discretised form of \dot{U}_M | 346 |
| B.5 | Assembly of discretised momentum equation | 346 |
| B.6 | Summary | 348 |
| C | General code setup | 350 |
| C.1 | Computational grid | 350 |

| | | |
|------------|--|-----|
| C.2 | Timestepping methods | 353 |
| C.2.1 | Timestep correction and data preservation | 353 |
| C.3 | General discussion of diffusion coefficients | 355 |
| C.3.1 | Thermal diffusion | 355 |
| C.3.2 | Viscous diffusion | 356 |
| C.3.3 | Resistive diffusion | 358 |
| C.3.4 | Density diffusion | 358 |
| C.4 | Numerical solution of the Grad-Shafranov equation | 358 |
| C.5 | Code verification and validation | 363 |
| C.5.1 | Convergence studies (verification) | 363 |
| C.5.2 | Equilibrium solution comparison with Corsica solution (validation) . | 364 |
| C.6 | Summary | 367 |
| D | First results from plasma edge biasing on SPECTOR | 369 |
| D.1 | Introduction | 369 |
| D.2 | Experiment setup | 371 |
| D.3 | Circuit analysis | 373 |
| D.4 | Main results | 378 |
| D.5 | Summary | 381 |

List of Tables

| | | |
|-------|---|-----|
| 1.4.1 | Parameter scalings for adiabatic compression | 12 |
| 1.5.1 | Parameter compression scalings on ATC device | 20 |
| 2.1.1 | Sequence of machine operation | 31 |
| 2.2.1 | r, ϕ coordinates of magnetic probes (original configuration) | 35 |
| 3.2.1 | r, ϕ coordinates of magnetic probes (intermediate configuration) | 51 |
| 3.4.1 | 25-turn coil parameters | 55 |
| 5.3.1 | Notations for matrices of various dimensions | 113 |
| 7.1.1 | Selection of code input parameters for simulation 2353 | 182 |
| 8.3.1 | Coefficients for calculating ionization rate parameters | 240 |
| 8.9.1 | Neutral-relevant code input parameters for simulation 2353 | 259 |

List of Figures

| | | |
|-------|---|----|
| 1.1.1 | Fourth state of matter (image credit: http://www.grinp.com/plasma/physics.html) | 1 |
| 1.1.2 | Depiction of plasma properties and Rosette nebula | 1 |
| 1.1.3 | The Sun and schematic of D-T fusion reaction | 2 |
| 1.1.4 | MCF and ICF fusion | 3 |
| 1.2.1 | Current GF reactor concept (image credit: General Fusion) | 5 |
| 1.2.2 | GF plasma injectors | 6 |
| 1.3.1 | Tokamak and spheromak magnetic field profiles | 9 |
| 1.4.1 | CT Ψ contours for magnetic compression geometry, with geometric definitions | 11 |
| 1.5.1 | Schematics of S-1 device (image credit [22, 23]) | 16 |
| 1.5.2 | S-1 device; evolution of fluxes and q_{axis} (image credit: modified from [26]) | 17 |
| 1.5.3 | Poloidal cross-section of ATC device (image credit: [28]) | 19 |
| 1.5.4 | q profiles (ULQ device) (image credit: modified from [32]) | 21 |
| 2.1.1 | Machine schematic | 30 |
| 2.1.2 | ψ contours from MHD simulation, with CT formation and compression | 31 |
| 2.1.3 | Levitation and compression circuit | 33 |
| 2.1.4 | Total levitation and compression currents | 33 |
| 2.2.1 | Machine headplate schematic | 34 |
| 2.2.2 | Chalice schematic | 35 |
| 2.2.3 | Rogowski coil schematic | 38 |
| 2.2.4 | Michelson interferometer schematic | 39 |
| 3.1.1 | 6-coil configuration schematic and FEMM solution for levitation field | 46 |
| 3.1.2 | B_θ for shot 29205, six coils, ceramic insulating wall | 47 |
| 3.1.3 | B_ϕ and T_i for shot 29205, six coils, ceramic insulating wall | 49 |
| 3.1.4 | B_θ and n_e for shot 26366, six coils, ceramic insulating wall | 50 |
| 3.2.1 | B_ϕ and B_θ for shot 32930, six coils, quartz insulating wall | 51 |
| 3.2.2 | Optical intensity measurements for shot 32930, six coils, quartz insulating wall | 52 |
| 3.3.1 | B_θ fluctuations with toroidal mode $n = 2$ | 53 |
| 3.4.1 | LT-SPICE model schematic for the 25-turn coil | 56 |

| | | |
|--------|---|----|
| 3.4.2 | Circuit model outputs for 25-turn coil - no series resistance | 56 |
| 3.4.3 | FEMM output for the 25-turn coil | 57 |
| 3.4.4 | 25-turn coil on machine | 58 |
| 3.4.5 | Circuit model outputs for 25 turn coil - 1Ω series resistance | 59 |
| 3.4.6 | Performance improvement with series resistance (25-turn coil) | 59 |
| 3.4.7 | Improved performance with the 25-turn coil at high flux settings | 60 |
| 3.4.8 | B_θ and B_ϕ for shot 33622, 25-turn coil, quartz insulating wall | 60 |
| 3.4.9 | FEMM model, 25-turn coil moved up 25 mm, 10 kA at 1250 Hz | 61 |
| 3.4.10 | Percentage current rise for various levitation circuit configurations | 62 |
| 3.5.1 | B_θ for CT with the stainless steel flux-conserver | 65 |
| 3.5.2 | Electro-magnetic shielding in a thin conducting shell | 67 |
| 3.6.1 | 11-coil configuration | 69 |
| 3.6.2 | B_θ and B_ϕ for levitated CTs (11-coil configuration) | 70 |
| 3.6.3 | n_e , optical intensity, and T_i for levitated CTs (11-coil configuration) | 71 |
| 3.6.4 | B_θ , T_i , B_z and optical data with sustained I_{shaft} | 73 |
| 3.7.1 | FEMM models for finding $r_s(\phi, t)$ | 75 |
| 3.7.2 | Experimental data and functional fit to FEMM data (70 m Ω cables) | 76 |
| 3.7.3 | Time-sequence of $r_s(\phi, t)$ for shot 39650 (70 m Ω cables) | 77 |
| 3.7.4 | $r_s(\phi, t)$ for shot 39650 (70 m Ω cables) | 78 |
| 3.7.5 | Experimental data and functional fit to FEMM data (2.5 m Ω cables) | 78 |
| 3.7.6 | Time-sequence of $r_s(\phi, t)$ for shot 29205 (2.5 m Ω cables) | 79 |
| 3.7.7 | $r_s(\phi, t)$ for shots 29205 and 39573 (2.5 m Ω cables) | 80 |
| 3.8.1 | Spectrometer data | 81 |
| 3.8.2 | Comparison, across configurations, of CT lifetimes and effect of lithium gettering. | 82 |
| 3.9.1 | B_θ for six configurations | 84 |
| 4.1.1 | B_θ and $I_{lev} + I_{comp}$ for shot 28426 (6-coil configuration) | 90 |
| 4.1.2 | B_θ and I_{comp} for shot 28426 (6-coil configuration) | 91 |
| 4.1.3 | B_θ and I_{comp} for shot 39735 (11-coil configuration) | 93 |
| 4.1.4 | B_ϕ and n_e traces for shot 39735 (11-coil configuration) | 94 |
| 4.1.5 | Optical intensity measurements for shot 39735 (11-coil configuration) | 95 |
| 4.1.6 | B_θ for shot 39475 (11-coil configuration) | 95 |
| 4.1.7 | B_ϕ and n_e for shot 39475 (11-coil configuration) | 96 |
| 4.1.8 | Optical intensity and T_i measurements for shot 39475 (11-coil configuration) | 96 |
| 4.1.9 | n_e , T_i and optical intensity measurements for shot 39510, T_i for shot 38160 (11-coil configuration) | 97 |
| 4.1.10 | B_θ and B_ϕ for shot 28422 (6-coil configuration), $t_{comp} = 90\ \mu\text{s}$ | 98 |

| | | |
|--------|--|-----|
| 4.2.1 | Asymmetric current diversion | 99 |
| 4.2.2 | f contours at magnetic compression, simulation 1968 | 100 |
| 4.3.1 | Comparison of compression parameters | 101 |
| 4.4.1 | Measured CT separatrix radius for compression shot 39738 | 102 |
| 4.5.1 | Scintillator data for shot 39857 | 103 |
| 4.5.2 | n_e and optical data for shot 39857 | 104 |
| 5.2.1 | Linear basis function depiction for triangular elements | 111 |
| 5.4.1 | Node-to-element differential operator mechanism | 115 |
| 5.4.2 | Linear basis function depiction for triangular elements (top view (1)) | 118 |
| 5.4.3 | Element-to-node differential operator mechanism | 119 |
| 5.4.4 | Node-to-node second order differential operator mechanism | 121 |
| 5.4.5 | Node-to-node differential operator mechanism | 124 |
| 5.4.6 | Linear basis function depiction for triangular elements (top view (2)) | 128 |
| 5.6.1 | Illustration of particle, toroidal flux, and angular momentum conservation | 145 |
| 5.6.2 | System energy evolution for an MHD simulation starting with a Grad-Shafranov equilibrium | 149 |
| 6.1.1 | Normalised levitation and compression current signals | 157 |
| 6.2.1 | Computational mesh with insulating region, 6-coil configuration | 160 |
| 6.3.1 | Geometric profile for formation flux input and $\Phi_{form}(t)$ scaling | 166 |
| 6.3.2 | Geometry definitions and measured vs. simulated $I_{form}(t)$ | 169 |
| 6.3.3 | Comparison of measured and simulated B_ϕ (Grad-Shafranov equilibrium) | 171 |
| 6.4.1 | Illustration of simulated toroidal flux conservation | 176 |
| 7.2.1 | Poloidal flux contours for 6-coil configuration, effect of t_{lev} | 186 |
| 7.2.2 | f contours for 6-coil configuration, effect of t_{lev} | 188 |
| 7.2.3 | ψ and f contours for 11-coil configurations ($t_{lev} = 60 \mu\text{s}$) | 189 |
| 7.3.1 | Poloidal flux contours | 191 |
| 7.3.2 | Poloidal flux contours (confinement region) | 193 |
| 7.3.3 | Lines of poloidal current (f contours) | 194 |
| 7.3.4 | Lines of poloidal current (f contours), CT confinement region | 196 |
| 7.3.5 | Electron density profiles | 197 |
| 7.3.6 | Electron temperature profiles | 198 |
| 7.3.7 | Ion temperature profiles | 200 |
| 7.3.8 | Toroidal current density profiles | 202 |
| 7.3.9 | Poloidal current density profiles | 203 |
| 7.3.10 | Profiles of various velocity components | 205 |

| | | |
|--------|--|-----|
| 7.4.1 | ψ and f contours, and J_ϕ profiles, for a simulation with compression current reversal | 207 |
| 7.4.2 | (sequence continued) ψ and f contours, and T_e and J_θ profiles, for a simulation with compression current reversal | 208 |
| 7.5.1 | Comparison of measured and simulated B_θ (levitation - eleven coils) | 210 |
| 7.5.2 | Comparison of measured and simulated B_ϕ (levitation - eleven coils) | 211 |
| 7.5.3 | Comparison of experimentally measured and simulated CT separatrix radius | 212 |
| 7.5.4 | Comparison of measured and simulated n_e and T_i (levitation only) | 212 |
| 7.5.5 | Comparison of measured and simulated B_θ (compression - eleven coils) | 213 |
| 7.5.6 | Comparison of measured and simulated n_e and T_i (compression shots) | 214 |
| 7.5.7 | T_i contours, simulation 2351 | 215 |
| 7.5.8 | Comparison of measured and simulated r_s with magnetic compression | 215 |
| 7.5.9 | Comparison of measured and simulated poloidal and toroidal magnetic field at magnetic probe locations ($V_{comp} = 18$ kV, 11-coil configuration) | 216 |
| 7.5.10 | Comparison of measured and simulated n_e (compression shot 39735) | 217 |
| 7.5.11 | Measured $cf.$ simulated B_θ (compression - 6 coils, with flux loss) | 217 |
| 7.5.12 | Selection of additional simulated diagnostics for simulation 2353 | 219 |
| 7.5.13 | Internal CT B_z and B_ϕ profiles from simulation 2353 | 221 |
| 7.5.14 | q profile, simulation 2353 | 223 |
| 7.5.15 | q profile, simulation 2287 | 224 |
| 7.5.16 | Compression scalings, simulation 2287 | 226 |
| 7.5.17 | System energy evolution for simulation 2353 | 228 |
| 8.6.1 | Illustration of energy and particle conservation for MHD simulation with neutral fluid | 256 |
| 8.9.1 | Neutral fluid dynamics at bubble-in (1) | 260 |
| 8.9.2 | Neutral fluid dynamics at bubble-in (2) | 262 |
| 8.9.3 | Neutral fluid dynamics at bubble-in (3) | 263 |
| 8.9.4 | Effect of inclusion of the Q_e^{rec} term as an energy source for the neutral fluid | 264 |
| 8.9.5 | Poloidal flux contours and profiles of electron and neutral fluid densities in SPECTOR geometry | 266 |
| 8.9.6 | Profiles of electron density and temperature in SPECTOR geometry | 267 |
| 8.9.7 | Effect of neutral fluid dynamics in SPECTOR geometry | 267 |
| A.7.1 | Linear $\lambda(\psi)$ profile | 321 |
| C.1.1 | Mesh repairs | 351 |
| C.1.2 | Variable-resolution meshes | 352 |
| C.4.1 | Grad-Shafranov equilibrium solution example | 362 |

| | | |
|-------|--|-----|
| C.5.1 | Example convergence studies with varying h_e (triangular element size [m]) | 363 |
| C.5.2 | Corsica grid with triangulation | 364 |
| C.5.3 | Equilibrium solution comparison | 366 |
| D.2.1 | Biassing probe assembly | 372 |
| D.3.1 | Biassing probe circuit diagram | 373 |
| D.3.2 | Measured bias probe voltage and current (a), and poloidal field (b) for shot 26400, which had $V_{bc0} = 700$ V (3 mF capacitor) | 374 |
| D.3.3 | Biassing probe circuit diagram, including plasma voltage source, with current flow schematics | 375 |
| D.3.4 | Calculated / measured probe voltages, edge plasma resistance and bias currents for shot 26400 | 377 |
| D.4.1 | 3 mF capacitor: total CT lifetimes <i>cf.</i> V_{bc0} (bias capacitor voltage setting) | 378 |
| D.4.2 | 100 μ F capacitor: CT lifetimes <i>cf.</i> V_{bc0} | 379 |
| D.4.3 | 100 μ F capacitor: electron temperature and density profiles at 300 μ s, for $V_{bc0} \sim 2$ kV | 379 |
| D.4.4 | 100 μ F capacitor: (a) H_α intensity, (b) electron density (FIR interferometer) | 380 |

List of Symbols

| | |
|-----------------|---|
| α | subscripts $\alpha = i, e, n$ denote ion, electron and neutral particles/fluids |
| β | subscripts $\beta = r, \phi, z$ denote radial, toroidal and axial vector components |
| γ | adiabatic gas constant |
| Γ | boundary of system volume or boundary of computational domain |
| ϵ_0 | vacuum permittivity (8.85×10^{-12} [F/m]) |
| ζ | density diffusion coefficient [m ² /s] |
| η' | resistivity [Ω -m] |
| η | resistive diffusion coefficient [m ² /s] |
| θ | subscript, poloidal vector component |
| κ | thermal conductivity [$(\text{m}\cdot\text{s})^{-1}$] |
| λ_{mfp} | mean free path [m] |
| μ_0 | vacuum permeability ($4\pi \times 10^{-7}$ [H/m]) |
| μ | dynamic viscosity [kg m ⁻¹ s ⁻¹] |
| ν | viscous diffusion coefficient [m ² /s] |
| π | viscosity tensor [J/m ³] |
| ρ | mass density [kg/m ³] |
| ρ_c | charge density [C/m ³] |
| τ_{ii} | ion-ion collision time [s] |
| τ_{ie} | electron-ion collision time [s] |
| ϕ | toroidal flux [Wb] |
| χ | thermal diffusion coefficient [m ² /s] |
| Ψ | poloidal flux [Wb] |

| | |
|---------------|--|
| ψ | poloidal flux per radian [Wb/radian] |
| ω | angular speed [s^{-1}] |
| ω_c | cyclotron frequency [radians/s] |
| B | magnetic field [T] |
| $d\Gamma$ | elemental area [m^2] |
| dS | elemental area [m^2] |
| dV | elemental volume [m^3] |
| $d\mathbf{V}$ | elemental volume in velocity space [$\text{m}^3 \text{ s}^{-3}$] |
| e | electron charge [C] |
| E | electric field [V/m] |
| h | Planck's constant (6.63×10^{-34} [J-s]) |
| I_{comp} | compression coil current signal measured for a particular shot [kA] |
| I_{form} | formation current signal measured for a particular shot [kA] |
| I_{lev} | levitation coil current signal measured for a particular shot [kA] |
| I_{main} | main coil current setting for a particular shot [A] |
| I_{shaft} | shaft current signal measured for a particular shot [kA] |
| J | current density [A/m^2] |
| m | particle mass [kg] |
| n | number density [m^{-3}] |
| p | pressure [Pa] |
| q | particle charge [C] (or safety factor) |
| q | heat flux density [$\text{J m}^{-2} \text{ s}^{-1}$] |
| Q_{ie} | volumetric rate of ion-electron heat exchange [$\text{J m}^{-3} \text{ s}^{-1}$] |
| R | collisional friction force density [N/m^3] |
| T | temperature [J] or [eV] |
| t_{comp} | delay between firing formation capacitor banks and compression capacitor banks [μs] |
| $ t_{lev} $ | delay between firing levitation capacitor banks and formation capacitor banks [μs] |

| | |
|---------------------------|---|
| t_{gas} | delay between firing gas puff valves and formation capacitor banks [μ s] |
| U_K | kinetic energy [J] |
| $\dot{U}_{K\pi}$ | rate of decrease of U_K due to viscous dissipation [J/s] |
| U_{Th} | thermal energy [J] |
| $\dot{U}_{Th\pi}$ | rate of increase of U_{Th} due to viscosity [J/s] |
| $\dot{U}_{Thideal}$ | resistivity-independent rate of change of U_{Th} [J/s] |
| $\dot{U}_{Th\theta\eta}$ | rate of increase of U_{Th} due to ohmic heating associated with poloidal currents [J/s] |
| $\dot{U}_{Th\phi\eta}$ | rate of increase of U_{Th} due to ohmic heating associated with toroidal currents [J/s] |
| U_M | magnetic energy [J] |
| $U_{M\theta}$ | magnetic energy associated with poloidal field [J] |
| $U_{M\phi}$ | magnetic energy associated with toroidal field [J] |
| $\dot{U}_{M\theta ideal}$ | resistivity-independent rate of change of $U_{M\theta}$ [J/s] |
| $\dot{U}_{M\phi ideal}$ | resistivity-independent rate of change of $U_{M\phi}$ [J/s] |
| $\dot{U}_{M\theta\eta}$ | rate of decrease of $U_{M\theta}$ due to resistive decay of poloidal magnetic field [J/s] |
| $\dot{U}_{M\phi\eta}$ | rate of decrease of $U_{M\phi}$ due to resistive decay of toroidal magnetic field [J/s] |
| \mathbf{v} | fluid velocity [m/s] |
| \mathbf{V} | particle velocity [m/s] |
| V_{comp} | voltage to which compression capacitor banks are charged for a particular shot [kV] |
| V_{form} | voltage to which formation capacitor banks are charged for a particular shot [kV] |
| V_{gun} | voltage signal measured between machine electrodes [kV] |
| V_{lev} | voltage to which levitation capacitor banks are charged for a particular shot [kV] |
| V_{th} | particle thermal speed [m/s] |
| Z_{eff} | volume averaged ion charge |
| * | matrix multiplication |
| \circ | element-wise matrix multiplication |
| \oslash | element-wise matrix division |

List of Abbreviations

| | |
|---------|--|
| ATC | Adiabatic Toroidal Compressor |
| CT | Compact Torus |
| CHI | Coaxial Helicity Injection |
| DAQ | Data AcQuisition |
| DELiTE | Differential Equations on Linear Triangular Elements |
| FEMM | Finite Element Method Magnetics |
| FIR | Far Infra Red |
| FRC | Field Reversed Configuration |
| GF | General Fusion Inc. |
| H-mode | High Confinement Mode |
| ICF | Inertial Confinement Fusion |
| LCFS | Last Closed Flux Surface |
| MCF | Magnetic Confinement Fusion |
| MHD | Magneto Hydro Dynamics |
| MRT | Magnetised Ring Test |
| MTF | Magnetic Target Fusion |
| PCS | Plasma Compression, Small |
| PI3 | Plasma Injector 3 |
| SMRT | Super Magnetised Ring Test |
| SPECTOR | Spherical Compact Toroid |
| TS | Thomson Scattering |
| ULQ | Ultra Low Q |

Chapter 1

Introduction

1.1 Background - plasma and nuclear fusion

Plasma is a collection of ions, electrons and neutral particles that exhibits long range collective behaviour due to the electromagnetic forces between the charged particles.

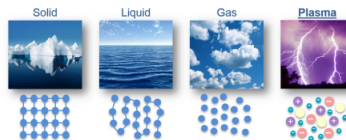
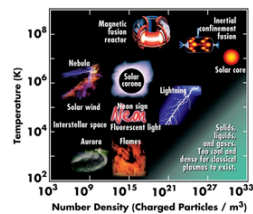


Figure 1.1.1: Fourth state of matter (image credit: <http://www.grinp.com/plasma/physics.html>)

When a solid, such as ice (see figure 1.1.1), is continuously heated, it changes phase to become a liquid, then a gas, and then a plasma. Plasma is known as the fourth state of matter - most of the visible universe is in the plasma state.



(a) Plasma Properties (Image credit: Contemporary Physics Education Project)

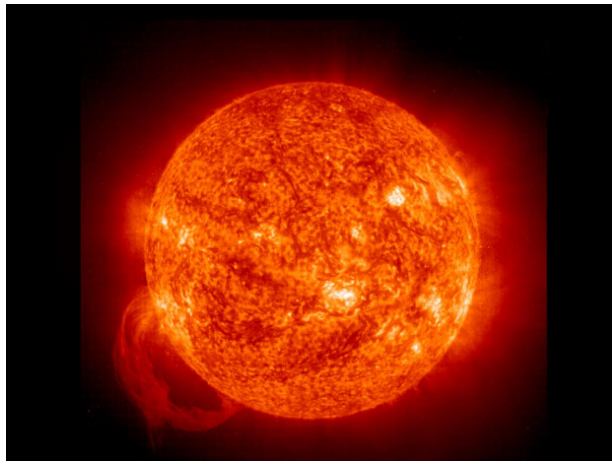


(b) Rosette nebula
(Image credit: <http://cs.astronomy.com/asy/m/nebulae/466016.aspx>)

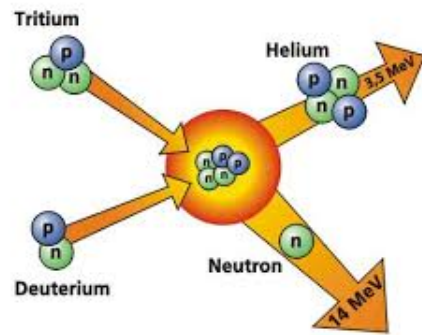
Figure 1.1.2: Depiction of plasma properties and Rosette nebula

Figure 1.1.2(a) indicates the number densities and temperatures of various plasmas - for comparison, note that the number density of air is $\sim 10^{25} \text{ m}^{-3}$. Terrestrial plasmas include the aurora, lightning, flames, and the plasmas found in neon and fluorescent light tubes. Solar nebulae (e.g., figure 1.1.2(b)), where stars are formed, are predominantly composed of very tenuous plasmas, while the extreme density of plasmas characteristic of inertial confinement fusion devices approaches that of the solar core.

When two positively charged ions are forced so close together that the mutually attractive nuclear force overcomes the mutually repulsive Coulomb force, nuclear fusion will occur - the ions fuse together in a process that releases energy.



(a) Sun - Image credit: <https://www.nationalgeographic.com>



(b) D-T fusion - Image credit: <http://www.fz-juelich.de>

Figure 1.1.3: The Sun and schematic of D-T fusion reaction

Fusion powers the stars - in solar plasmas (figure 1.1.3(a)), the ions are forced close together by immense gravitational forces. Stars are powered by fusion of hydrogen and its isotopes for most of their lives, and, if they are hot enough, fuse helium and then heavier elements as the hydrogen and then the helium supplies are exhausted.

Unlike nuclear fission, fusion is not associated with long-term radioactivity, and the fuel source for the most easily attainable forms of fusion are abundant on earth. The fusion reaction which requires one of the lowest temperatures to initiate is the deuterium-tritium (D-T) reaction ($D + T \rightarrow He^4 (3.5 \text{ MeV}) + n (14.1 \text{ MeV})$), depicted in figure 1.1.3(b). Deuterium and tritium are isotopes of hydrogen. Deuterium can be extracted from sea-water and tritium can be obtained from neutron activation of lithium-6. For the D-T reaction, when the ions are heated to $\sim 10 \text{ keV} = \sim 10^8 \text{ Kelvin}$, they have enough energy to overcome the Coulomb barrier and fuse, releasing a high energy neutron which escapes the plasma. In this type of *neutronic* (i.e., neutron-producing reactions) fusion, the energetic neutron is used to heat an external water supply, producing steam which is harnessed to generate electricity with turbines in the usual way. The Lawson criterion (triple product form), given

by the product of the plasma number density, the energy confinement time and the plasma (ion) temperature, specifies the minimum value of that product required for fusion ignition (the condition where sufficient energy is produced by fusion reactions to self-sustain further reactions): $n\tau_E T_i \geq 3.1 \times 10^{21} \text{ keV-s-m}^{-3}$.

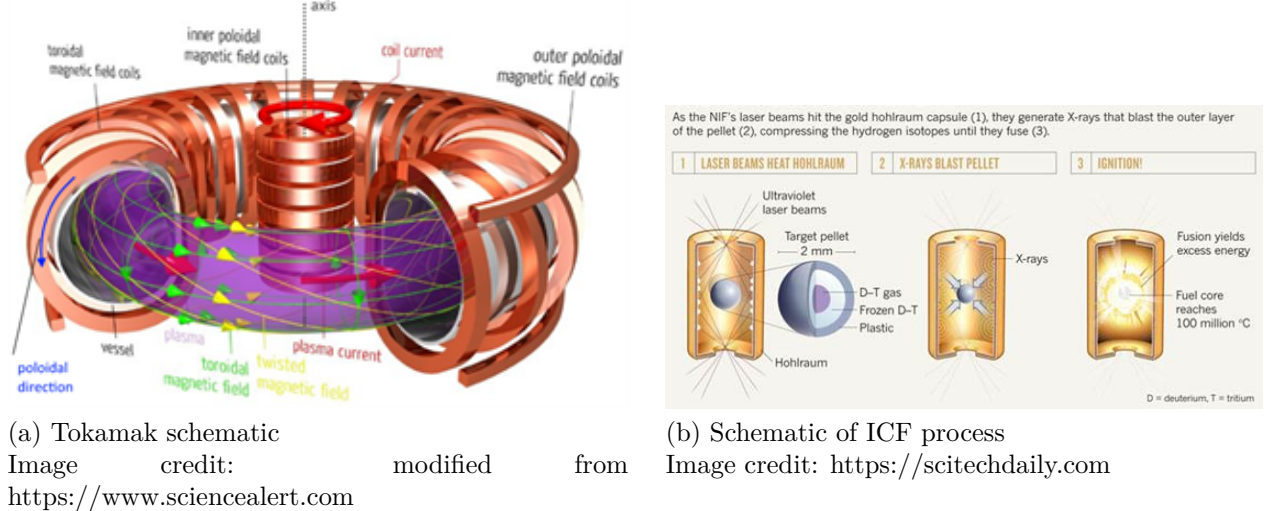


Figure 1.1.4: MCF and ICF fusion

The two most prevalent and well-researched potential methods towards achieving a fusion power generation industry are magnetic confinement fusion (MCF) and inertial confinement fusion (ICF). The tokamak depicted in figure 1.1.4(a) is based on magnetic confinement. Ions and electrons, the charged particles that constitute the bulk of the plasma, gyrate around and stream along magnetic field lines. A toroidal magnetic field is produced by poloidally-directed currents in the toroidal field coils that surround the vacuum vessel. Note that the poloidal and toroidal directions are indicated by the blue and green arrows respectively in figure 1.1.4(a). Neutral gas (*e.g.*, a mix of deuterium and tritium) is injected into the vacuum vessel and is broken down to form a plasma by the action of a toroidal electric field that is induced by transformer action as a result of the poloidal magnetic field due to toroidal currents in the inner poloidal field coils (the standard vertical ferromagnetic iron core shaft inside the inner poloidal coils, which concentrates the magnetic field within it, is not shown in the figure). The same toroidal electric field drives a toroidal plasma current - this current produces a poloidal magnetic field. The combination of the toroidal and poloidal magnetic fields result in a twisted magnetic field. The charged plasma particles gyrate around, and stream along these twisted helical field lines, resulting in confinement of the particles within the vacuum vessel.

The twisted helical field prevents the particle escape that would occur due to the combination of curvature, ∇B , and $\mathbf{E} \times \mathbf{B}$ particle drifts if the confinement was by toroidal field alone. Particle drift for species α (*i.e.*, ion or electron) due to magnetic field curvature, which

results in a field-perpendicular centrifugal force on the particle, is given by

$$\mathbf{V}_{\alpha c} = \frac{V_{\alpha\parallel}^2}{\omega_{c\alpha} B^3} \mathbf{B} \times (\mathbf{B} \cdot \nabla) \mathbf{B}$$

Here, $V_{\alpha\parallel}$ is the particle speed in the direction parallel to the magnetic field, $\omega_{c\alpha} = q_\alpha B / m_\alpha$ is the cyclotron frequency, where m_α is the particle mass and q_α is the particle charge. The ∇B drift is given by $\mathbf{V}_{\alpha \nabla B} = \frac{V_{\alpha\perp}^2}{2\omega_{c\alpha} B^2} \mathbf{B} \times \nabla B$. Here, $V_{\alpha\perp}$ is the particle speed in the direction perpendicular to the magnetic field. Note that ∇B , resulting from having closer spacing between the toroidal field coils at the inboard side of the machine, is directed horizontally towards the machine axis. With the assumption that the magnetic field is due to currents outside the volume of interest so that $\nabla \times \mathbf{B} = 0 \Rightarrow (\mathbf{B} \cdot \nabla) \mathbf{B} = B \nabla B$, the expression for the combined curvature and ∇B drifts is:

$$\mathbf{V}_{\alpha c} + \mathbf{V}_{\alpha \nabla B} = \frac{1}{\omega_{c\alpha} B^2} (V_{\alpha\parallel}^2 + \frac{1}{2} V_{\alpha\perp}^2) \mathbf{B} \times \nabla B$$

This combined drift is vertically directed and is in opposite directions for electrons and ions because of its dependence on the sign of q_α . Left unchecked, the combined drift leads to charge separation and a vertically directed electric field is established. This field would then result in $\mathbf{E} \times \mathbf{B}$ particle drifts in the horizontal direction. The $\mathbf{E} \times \mathbf{B}$ drifts are much faster than the combined curvature and ∇B drifts, so the particles would ultimately reach the outboard vessel walls due to the $\mathbf{E} \times \mathbf{B}$ drifts, which have been established by the action of the curvature and ∇B drifts. The superimposition of a poloidal magnetic field on the toroidal field prevents particle loss by this drift mechanism - electrons, which are much lighter and faster than ions, stream along the twisted helical field lines and neutralise the polarization that would arise, in the absence of poloidal field, due to the curvature and ∇B drifts.

In principle, in magnetic confinement devices, the confined plasma would be heated to fusion conditions by ohmic heating due to the plasma current, with possible supplementary heating by external sources such as ion or electron cyclotron resonance heating, neutral beam heating, Bernstein waves etc. Overall, magnetic confinement devices work by confining the plasma at low densities ($\sim 10^{20} [\text{m}^{-3}]$), and the long term goal is for continuous steady state operation.

Inertial confinement fusion devices are pulsed systems and use inertial forces to confine a plasma for very short durations, during which the plasma is heated very rapidly to fusion conditions. Typical densities are $\sim 10^{32} [\text{m}^{-3}]$, with confinement times of less than a nanosecond. A schematic of the inertial confinement process used at the National Ignition Facility (NIF) is illustrated in figure 1.1.4(b). X-rays generated by the action of powerful laser beams directed on the inner surfaces of the gold "hohlraum", cause the explosion of the outer plastic layer of a ~ 2 mm diameter capsule. The resultant implosion of the fuel

at the center of the capsule compresses and momentarily confines the fuel while heating it to plasma state and then to fusion conditions. In principle, the implosion must be precisely spherically-symmetric so as to avoid instabilities that would lead to confinement loss.

Magnetic target fusion (MTF) occupies the middle ground between the methods of magnetic and inertial confinement. Like ICF, it is a pulsed system, but with much longer confinement times (~ 1 ms). In principle, plasma with low density ($\sim 10^{20} [\text{m}^{-3}]$) and temperature (~ 100 eV) is magnetically confined, and then compressed, by the action of inertial forces on a movable external flux conserver, to fusion conditions, characterised by moderate density ($\sim 10^{23} [\text{m}^{-3}]$) and high temperature (~ 10 keV), such that the Lawson criterion is met. It is expected that the major obstacle to MCF, which is the long-term maintenance of an instability-free magnetically confined plasma, may be overcome by reducing the requirement to that of preserving stability for a short time. At the same time, it is hoped that the major obstacle to ICF - the difficulty in achieving an extremely rapid, nearly perfectly symmetric compression - can be surmounted by compressing the plasma, which is magnetically confined, over a much longer timescale - the aim is for inertial compression over $\sim 100 \mu\text{s}$ compared with ~ 200 ps in the ICF regime.

1.2 General Fusion - overview

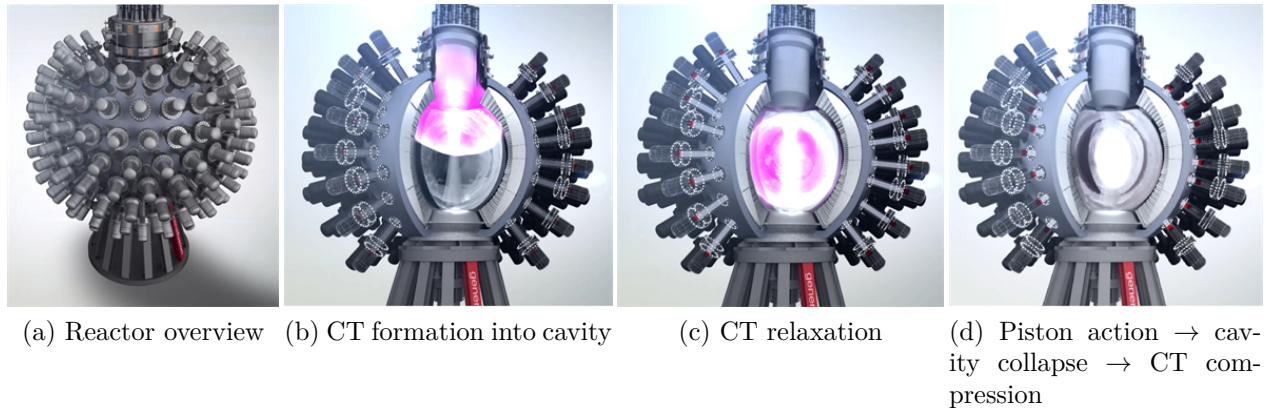


Figure 1.2.1: Current GF reactor concept (image credit: General Fusion)

General Fusion (GF), founded in 2002, is a private, investor-funded company. GF is developing a MTF power plant, based on the concept of compressing a compact torus (CT) plasma to fusion conditions by the action of external pistons on a liquid lead-lithium shell surrounding the CT[3]. The most recent design for the proposed prototype GF reactor, with outer radius ~ 10 m, is depicted in figure 1.2.1(a). A plasma injector, based on a magnetized

Marshall gun, sits on top of a hollow metal sphere that is partially filled with liquid metal (lead-lithium mixture). The sphere is surrounded by many pistons that are attached to its surface. Due to the action of jets inside the sphere, the liquid metal is rotating toroidally inside the hollow metal sphere. Centrifugal forces due to the toroidal rotation causes an approximately spherical vacuum cavity to open up inside the spherical shell of rotating liquid metal. As indicated in figure 1.2.1(b), the plasma injector forms a compact torus (CT) into the cavity. A central shaft, which carries vertically-directed current to provide additional CT-stabilising toroidal field can be seen in the figure. In this test-prototype design, the solid metal shaft would be damaged by the immense inboard pressures during compression, and would have to be replaced after each compression shot. Future designs may use liquid metal jets as a renewable shaft, or an alternative stabilisation method may be found - the ultimate goal is for a reactor design that can accomplish a compression shot every second. The CT is allowed to self-organise and stabilise - figure 1.2.1(c). The inner surface of the cavity in the liquid metal is the outer magnetic flux conservator for the CT. As depicted in figure 1.2.1(d), the pistons attached to the outer surface of the hollow sphere are triggered simultaneously, resulting in the addition to the sphere of more liquid metal that is directed with spherical symmetry radially inwards through a honeycomb-like mesh located at the inner surface of the hollow sphere. The additional liquid metal causes the cavity to collapse over $\sim 100 \mu\text{s}$. In principle, this causes the CT plasma to be heated to fusion conditions.

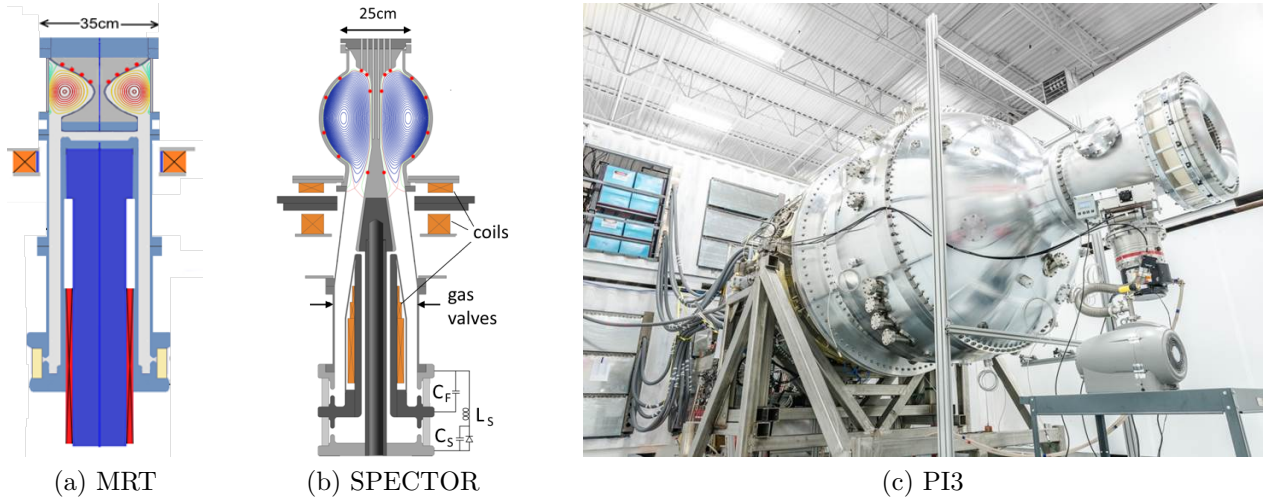


Figure 1.2.2: GF plasma injectors

Figure 1.2.2 shows three of the four most recent plasma injectors at GF. Not shown here, the "tokamak" machine was a short-term experiment based on the MRT (Magnetised Ring Test) design, but with a separate circuit, in addition to the principal formation circuit, to drive axial central shaft current, thereby producing CTs with additional stabilising toroidal field, and having an addition control mechanism for CT q profiles. It was found that main-

taining long-duration shaft current led to longer-lived, more stable CTs. That experiment paved the way for the SPECTOR (Spherical Compact Toroid) and PI3 (Plasma Injector 3) designs which also have separate shaft current circuits. All four injectors operate based on the principle of the magnetised Marshall gun [4, 5]. The operation is described in section 2.1 below. The MRT and SPECTOR machines are both $\sim 2\text{m}$ in height, while PI3 is $\sim 5\text{m}$ in length. The MRT machines were in operation until 2016, when it was replaced by SPECTOR, which is still operating. PI3 was built in 2017, and has been undergoing testing until now.

To study the plasma physics of compressed CTs, GF has conducted several PCS (Plasma Compression, Small) tests. In a PCS test, which takes place outdoors in a remote location, a CT is compressed by symmetrically collapsing the outer aluminum flux conserver with the use of chemical explosives. PCS tests are destructive, and therefore do not employ the full array of diagnostics used in CT formation and characterization experiments in the laboratory, and can only be executed every few months, the time needed to fabricate and commission a new injector. There have been sixteen PCS tests to date - PCS tests 1 \rightarrow 11 have been conducted with MRT machines, test 12 was on the "tokamak" machine, and tests 13 \rightarrow 16 have been on SPECTOR machines. The PCS program goal of significant compressional ion heating has not yet been achieved. Significant progress, in particular after the transition to the SPECTOR design, has been made in improving the stability of compressed CTs.

The magnetic compression experiment at GF was designed as a repetitive non-destructive test to study plasma physics applicable to MTF compression. Although not intended to compress a CT to the same degree as a PCS test, a principal goal of the magnetic compression experiment was to gain insights to the performance and stability of compressed CTs, and thereby advance the PCS program.

1.3 Magnetic geometry of compact tori

Spheromaks are self-organizing, force-free plasma configurations with comparable toroidal and poloidal magnetic fluxes that are self-sustained by internal currents. A spheromak is an example of a solution to MHD equilibrium. In equilibrium, the MHD equation of motion reduces to $\nabla p = \mathbf{J} \times \mathbf{B}$. Almost all laboratory plasmas have $\beta = 2\mu_0 p/B^2 \ll 1$, so it is a good approximation to set $\nabla p \sim 0$, so that $\mathbf{J} \parallel \mathbf{B}$ or, using Ampere's law, $\nabla \times \mathbf{B} \parallel \mathbf{B}$. Equivalently, we can write $\nabla \times \mathbf{B} = \lambda \mathbf{B}$. This is the equation of force-free equilibrium. Magnetic helicity is defined as $K = \int \mathbf{A} \cdot \mathbf{B} dV$, where \mathbf{A} is the vector potential and dV is an elemental volume. Examples of fields that contain helicity include those that contain

twisted, knotted, kinked or linked flux tubes, and force-free fields [6, 7, 8].

Magnetic helicity can be well described as follows [9]: If we approximate the magnetic field in a closed volume, with the boundary condition $\mathbf{B} \cdot \hat{\mathbf{n}} = 0$ (*i.e.*, perfectly conducting walls), by a collection of N closed flux tubes, the quantity

$$K = \sum_{i=1}^N \sum_{j=1}^N L_{ij} \phi_i \phi_j$$

describes the total mutual flux linkage contained in the volume. Here,

$$L_{12} = -\frac{1}{4\pi} \oint_1 \oint_2 \frac{d\mathbf{x}}{d\sigma} \cdot \frac{\mathbf{r}}{r^3} \times \frac{d\mathbf{y}}{d\tau} d\tau d\sigma$$

is the Gauss linking number (*cf.* mutual inductance for two closed conducting loops). The linking number quantifies the linking of two closed loops, which are labeled here as loops 1 and 2, parametrized by σ and τ respectively (points on loop 1 are labeled as $\mathbf{x}(\sigma)$, points on loop 2 are labeled as $\mathbf{y}(\tau)$), with $\mathbf{r} = \mathbf{y} - \mathbf{x}$. Letting $N \rightarrow \infty$ (so that $\phi_i \rightarrow 0$), then

$$K = -\frac{1}{4\pi} \int \int \mathbf{B}(\mathbf{x}) \cdot \left(\frac{\mathbf{r}}{r^3} \times \mathbf{B}(\mathbf{y}) \right) d^3x d^3y$$

Use of the Coulomb gauge ($\nabla \cdot \mathbf{A} = 0$) implies that $\mathbf{A}(\mathbf{x}) = -\frac{1}{4\pi} \int \frac{\mathbf{r}}{r^3} \times \mathbf{B}(\mathbf{y}) d^3y$, leading to the standard definition of helicity as $K = \int \mathbf{A} \cdot \mathbf{B} dV$.

Taylor [10] found that for any magnetized plasma with finite helicity, there is a unique minimum energy state, characterised by force free currents ($\mathbf{J} \parallel \mathbf{B}$) and a uniform inverse length λ . Spheromak magnetic configurations occupy a state of minimum energy subject to a given magnetic helicity; the minimum energy final state of the self-organizing process is defined by Woltjer-Taylor theory [10, 11]. It can be shown [9] that for all quasi-ideal MHD dynamics, that total magnetic helicity is conserved; plasmas reach a state of minimal energy equilibrium while maintaining a constant level of helicity. Magnetic helicity is conserved even in some processes that require finite plasma resistivity, such as magnetic reconnection. As shown in [10, 11], helicity is approximately conserved at low resistivity and exact helicity conservation is regained as $\eta' \rightarrow 0$ (not only at the limit $\eta' = 0$), where $\eta' [\Omega - m]$ is the plasma resistivity. The minimization of plasma energy subject to the constant helicity constraint can be done using the method of Lagrange multipliers and the force-free equation

$$\nabla \times \mathbf{B} = \lambda \mathbf{B} \tag{1.3.1}$$

with constant eigenvalue $\lambda [m^{-1}]$, is the result. With fixed λ and the boundary condition being that \mathbf{B} is parallel to the surface in a closed cylindrical volume, the lowest order solution to the force-free equation gives the magnetic field components of a spheromak in that geometry

[12].

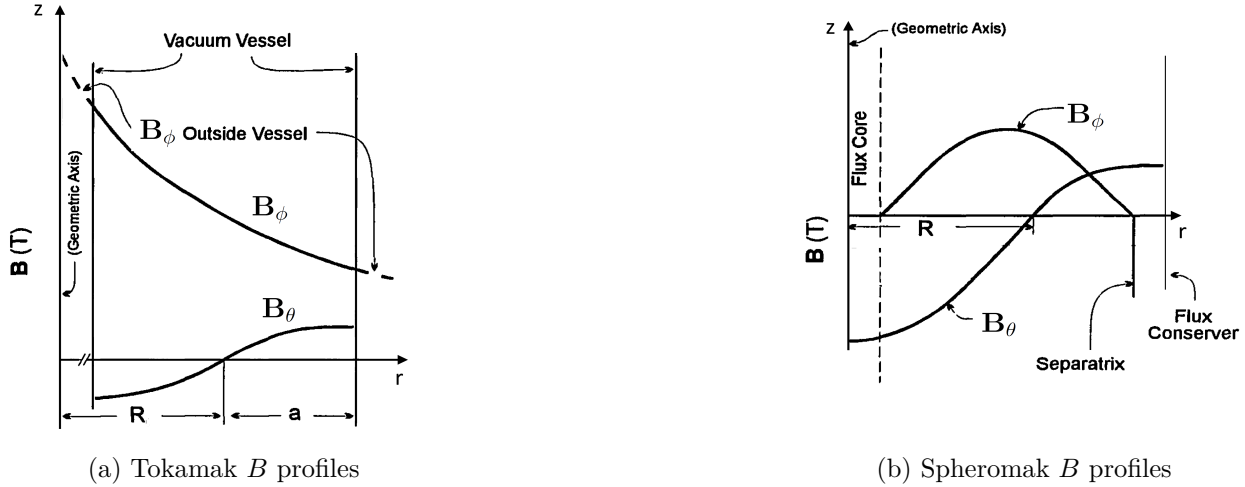


Figure 1.3.1: Tokamak and spheromak magnetic field profiles

Figure 1.3.1(a) indicates the profiles for the toroidal and poloidal components of the magnetic field for the case of a tokamak. Note that B_ϕ , the toroidal field, which is produced by currents in external coils (as depicted in figure 1.1.4(a)), is much larger than B_θ , the poloidal field, which is produced by internal plasma toroidal current, and that it increases towards the geometric axis where the external coils are closer together. By contrast, in a spheromak, the field components are of the same order (figure 1.3.1(b)), and both field components are due to internal plasma currents. In the flux core and outside the separatrix, B_θ is finite due to toroidal currents in the spheromak. On the other hand, just as there is no field outside a long solenoid whose ends have been joined to form a torus, $B_\phi = 0$ at the spheromak edge.

Injection of spheromaks with significant helicity-content into a tokamak plasma has been proposed as a means for current drive. In helicity injection current drive, helicity conserving magnetic relaxation processes incorporate helicity added to the system by dissipating any excess free energy, increasing parallel currents and keeping the plasma close to the Taylor state [13]. Helicity is injected by driving current on injector magnetic flux, Ψ_{main} . The helicity injection rate is given by $2V_{gun}\Psi_{main}$ [15, 16]. V_{gun} , the injection voltage, is the voltage across the helicity injection device electrodes, and Ψ_{main} is the injector bias flux. The spheromak's field reconnects (relaxes) to that of the tokamak to add helicity. It is because helicity is conserved even in the presence of turbulent tearing that current can be expected to be driven as a result of helicity injection [14]. A CHI (Co-axial Helicity Injection) device was devised to inject current to STOR-M. I worked with the CHI device on the STOR-M tokamak in the plasma physics laboratory at the University of Saskatchewan for about a year before starting on the magnetic compression project at General Fusion. Various circuit

modifications were made to the CHI circuits, including adding capacitor bank extensions, and experimenting with high current switch and triggering configurations. Spheromak injection into STOR-M usually resulted in disruption of the tokamak discharge. After modifying the CHI device to operate at increased power, it looked like tokamak current was increased by a few kiloamps just prior to disruption, but careful testing proved that the signals indicating a current drive were actually spurious, caused by inductive pickup. The CHI device was attached to a portable vacuum chamber, to characterise the CTs produced. Magnetic probes were constructed, using the principles outlined later in section 2.2.1, to measure poloidal and toroidal field near the CT edge. Langmuir probes were made and returned reasonable estimates for edge CT density and temperature. Further details of the helicity injection experiment are presented in [1].

1.4 Scaling laws for magnetic compression

If a magnetically confined plasma is compressed on a time-scale less than the resistive magnetic decay time of the plasma, the magnetic fluxes are conserved. In cylindrical coordinates with azimuthal symmetry, poloidal flux at the magnetic axis can be expressed, assuming that the plasma torus has a circular poloidal cross-section, as

$$\Psi_{axis} = \int_R^{R+a} \mathbf{B}_\theta \cdot d\mathbf{s} \sim 2\pi Ra \langle B_\theta \rangle \quad (1.4.1)$$

where $d\mathbf{s} = ds\hat{\mathbf{z}}$, and $ds = 2\pi r dr$ is an annular elemental area of radius r , with its center at $r = 0$, and with the same axial coordinate as the magnetic axis, a [m] and R [m] are the minor and major radii of the plasma torus, and $\langle B_\theta \rangle$ is the average poloidal field between $r = R$ and $r = R + a$. Note that $\psi = \frac{1}{2\pi}\Psi$ is the poloidal flux per radian. The axisymmetric MHD code that was developed in support of this work (part two of the thesis) evolves ψ , rather than Ψ , and the various other fields that are evolved are expressed in terms of ψ . Both Ψ and ψ will be referred to in the thesis.

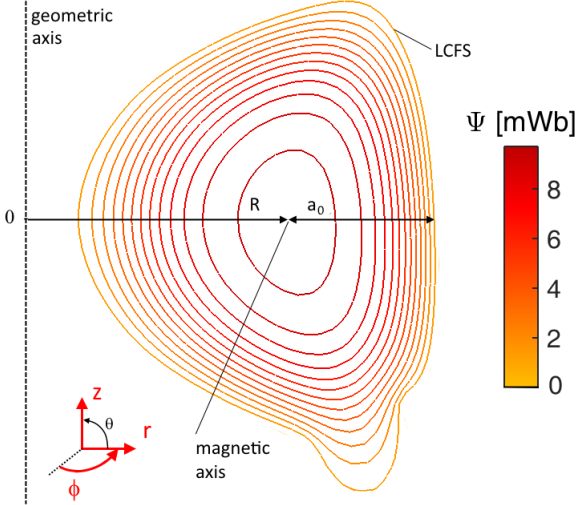


Figure 1.4.1: CT Ψ contours for magnetic compression geometry, with geometric definitions

For irregular axisymmetric toroidal geometries with non-circular poloidal cross-sections, as associated with the magnetic compression experiment, the relationship expressed in equation 1.4.1 also approximately holds, where, as indicated in figure 1.4.1, $a \rightarrow a_0 = a(\theta = 0)$ is the distance from the magnetic axis to the last closed poloidal flux surface (LCFS) at poloidal angle $\theta = 0$. The magnetic axis, LCFS, and scaling of Ψ are also indicated in the figure. Note that the poloidal field should be approximately perpendicular to the line denoted as a_0 in the figure for the relationship to hold. With poloidal flux conservation, equation 1.4.1 yields the compression scaling laws $\frac{B_{\theta 2}}{B_{\theta 1}} = \frac{a_1 R_1}{a_2 R_2}$, where the subscripts 2 and 1 indicate post-compression and pre-compression parameters respectively. Introducing the notation

$$\tilde{x} = \frac{x_2}{x_1}$$

the compression scaling for B_θ can be equivalently expressed as $\tilde{B}_\theta = \tilde{a}^{-1} \tilde{R}^{-1}$ or $B_\theta \rightarrow a^{-1} R^{-1}$, *i.e.*, the post compression poloidal field magnitude scales inversely with the product of the post compression minor and major radii. For simplicity, the subscript 2 will be dropped for the remainder of this section. Toroidal flux can be expressed to the first order as $\phi = \int \mathbf{B}_\phi \cdot d\mathbf{s}_\phi \sim S \langle B_\phi \rangle$, where S is the cross-sectional area of the plasma torus in the poloidal plane, and $\langle B_\phi \rangle$ is the average toroidal field in the cross-section, yielding the compression scaling for the toroidal field as $B_\phi \rightarrow S^{-1}$. An assumption of adiabatic compression implies that there is no energy lost due to loss of particles and their associated energy. If the compression time is short compared with the particle confinement time, the compression scaling for the particle number density is $n \rightarrow V^{-1}$, where V is the volume of the plasma torus. If the compression time is also short compared with the thermal confinement time, adiabaticity implies constant $p\rho^{-\gamma} = nT (nm_i)^{-\frac{5}{3}}$ so that, using the scaling for n , $T \rightarrow n^{\frac{2}{3}} \rightarrow V^{-\frac{2}{3}}$.

Here, $\gamma = \frac{c_p}{c_v}$ is the adiabatic gas constant, where $c_p [\text{J kg}^{-1}\text{K}^{-1}]$ is the specific heat capacity at constant pressure, and $c_v [\text{J kg}^{-1}\text{K}^{-1}]$ is the specific heat capacity at constant volume. $\gamma = \frac{N+2}{N}$, where N is the number of degrees of freedom of the bulk species. For a monatomic gas, $N = 3$, so that $\gamma = \frac{5}{3}$. For a given material, the availability of translational, rotational and intra-molecular exchanges characterise the value of N . Stokes theorem and the integral of Ampere's law in the poloidal plane yields $B_\theta L = \mu_0 I_p$, where L is the path length along the LCFS, so, using the scaling for B_θ , $I_p \rightarrow L a^{-1} R^{-1}$. Toroidal beta (standard beta) is the ratio of the plasma pressure to the toroidal field contribution to magnetic pressure: $\beta_\phi = \frac{p}{p_M} = \frac{2\mu_0 n T}{B_\phi^2}$. Using the scalings for n , T , and B_ϕ , this gives the scaling for toroidal beta as $\beta_\phi \rightarrow V^{-\frac{5}{3}} S^2$. In the same manner, the compression scaling for poloidal beta is found as $\beta_\theta \rightarrow V^{-\frac{5}{3}} a^2 R^2$. For geometries with circular poloidal-plane cross-sections, the volume of the plasma torus can be approximated as $V \sim 2\pi^2 R a^2$, the cross-sectional area is $S = \pi a^2$, and the LCFS path length is $L = 2\pi a$, so the scalings can be expressed in terms of a and R .

| parameter | B_θ | B_ϕ | n | T | I_p | β_ϕ | β_θ |
|--|-------------------|----------|-----------------|-------------------------------------|---------------------|------------------------------------|------------------------------------|
| scaling (general case) | $a_0^{-1} R^{-1}$ | S^{-1} | V^{-1} | $V^{-\frac{2}{3}}$ | $L a_0^{-1} R^{-1}$ | $V^{-\frac{5}{3}} S^2$ | $V^{-\frac{5}{3}} a_0^2 R^2$ |
| scaling (circular \times section) | $a^{-1} R^{-1}$ | a^{-2} | $a^{-2} R^{-1}$ | $a^{-\frac{4}{3}} R^{-\frac{2}{3}}$ | R^{-1} | $a^{\frac{2}{3}} R^{-\frac{5}{3}}$ | $a^{-\frac{4}{3}} R^{\frac{1}{3}}$ |

Table 1.4.1: Parameter scalings for adiabatic compression

The principal adiabatic compression scalings for toroidal geometry with circular and irregular poloidal cross-sections are collected in table 1.4.1. In chapter 7, the adiabatic compression scalings for the general case will be compared with MHD simulation results.

The compressional evolution of plasma temperature is determined by non-adiabatic as well as adiabatic processes. Adiabatic processes include the compressional work associated with the external magnetic field and the loss of electron energy due to ionization of neutral particles [17, 18] (note that electron thermal energy is converted to potential energy in the ionization process). Impurity radiation, radiative recombination losses in an optically thin plasma, losses associated with finite particle confinement times, and ohmic heating are examples of non-adiabatic processes [18]. Ohmic heating involves resistive heating by plasma currents, and can be viewed as the conversion of magnetic to thermal energy, part of which is lost from the system by heat diffusion. Classical ohmic heating power assumes that plasma resistivity is determined by the Spitzer formula:

$$\eta'[\Omega - m] = \frac{\pi Z_{eff} e^2 \sqrt{m_e} \Lambda}{(4\pi\epsilon_0)^2 (T_e [\text{J}])^{1.5}} \quad (1.4.2)$$

Here, Z_{eff} is the effective (volume averaged) ion charge, e is the electron charge, m_e is the electron mass, $\Lambda \sim 10$ is the Coulomb logarithm, ϵ_0 is vacuum permittivity, and T_e is the ion temperature in Joules. However, anomalous resistivity can occur when the ratio of the electron fluid drift velocity to the thermal or Alfvén velocities is too high [18]. Both ratios are expected to decrease with adiabatic compression, so it seems unlikely, but remains unconfirmed, that anomalous resistivity will increase during compression [18, 19].

It is interesting how ohmic heating power density scales with adiabatic compression: ohmic heating power density is $P_\Omega = \eta' J_\phi^2$ [W/m³]. The Spitzer resistivity formula gives the compression scaling for resistivity: $\eta' \propto T_e^{-\frac{3}{2}} \Rightarrow \eta' \rightarrow V$. Toroidal current density is $J_\phi = I_p/S$. With the approximation $V \sim RS$, this implies that $\Rightarrow J_\phi \rightarrow L a_0^{-1} V^{-1}$, so that $P_\Omega \rightarrow L^2 a_0^{-2} V^{-1}$. Power density lost from the plasma due to line radiation is $P_{rad} \propto n_e n_{imp}$, where n_{imp} [m⁻³] is the impurity number density, so that the associated compression scaling is $P_{rad} \rightarrow V^{-2}$.

In cases with circular poloidal cross-section, where $P_\Omega \rightarrow V^{-1}$, the relation $P_{rad} \rightarrow (P_\Omega)^2$ implies that there may be no compressional heatings of electrons for a plasma where there is an initial balance between ohmic heating and radiative losses [18]. Mitigating this is the effect that increased n_e leads to an increased rate of ionization, so that the impurities can evolve to a less radiative charge state. The condition in which this effect allows ohmic compressional heating to be effective in radiation dominated plasmas is explored in [20]. In that work, it was shown that when the pre-compression electron temperature is greater than 25 eV in plasmas where oxygen is the dominant impurity, or greater than 20 eV when carbon is the dominant impurity, and if $n_e \tau_p \gtrsim 1 \times 10^{15}$ s/m³ (τ_p is the particle confinement time), then compression can raise electron temperature significantly even for radiation dominated plasmas. In [18], the compression of a low temperature spheromak was simulated with a time dependent power balance model. It was found that, since the input energy due to ohmic heating is much greater than the work done in compressing the ions and electrons, that the relationship between τ_p and the time over which compression is executed is not important as long as both are much shorter than the magnetic decay time. The importance of the effect of identical adiabatic compression scalings for toroidal current density and electron density, in cases with circular poloidal cross-section, was highlighted. This allows high temperature states to be achieved through the effect of increasing n_e leading to an increased ionization rate and less radiative impurity ions. An increased ionization rate leads to higher Z_{eff} , which in turn leads to a further increase in ohmic heating power, as $\eta' \propto Z_{eff}$. It was found that the most significant compressional electron temperature increases are for cases where the radiation power loss dominates the power loss caused by particle recycling [18].

Compression in minor radius, while keeping major radius constant, can be achieved by ramping up the toroidal field in a tokamak. In this compression scenario, $C > 1$, the geometric compression ratio, is defined as $C = \tilde{a}^{-1} = \frac{a_1}{a}$, or $a \rightarrow C^{-1}$. The vertical field due to toroidal currents in external poloidal field coils (see figure 1.1.4(a)) is also increased so as to maintain constant R . This type of compression was done on the TUMAN series of tokamaks [21]. In this scenario, with circular poloidal cross-section, poloidal beta increases as

$$\beta_\theta \rightarrow a^{-\frac{4}{3}} R^{\frac{1}{3}} \Rightarrow \frac{\beta_\theta}{\beta_{\theta 1}} = \left(\frac{a}{a_1} \right)^{-\frac{4}{3}} \left(\frac{R}{R_1} \right)^{\frac{1}{3}} = C^{+\frac{4}{3}}$$

while toroidal beta decreases as $\beta_\phi \rightarrow C^{-\frac{2}{3}}$. In a tokamak, where $B_\phi \gg B_\theta$, the magnetic energy in the plasma can be approximated as $U_M = \frac{1}{2\mu_0} \int B_\phi^2 dV$. The volume of integration doesn't change with compression, since the toroidal field is externally imposed, so that magnetic energy scales as $U_M \rightarrow S^{-2}$ (general-case scalings). The plasma thermal energy is $U_{Th} = \frac{1}{\gamma-1} \int p dV$, so that $U_{Th} \rightarrow nTV \rightarrow V^{-\frac{2}{3}}$. For constant major radius compression in cases with circular poloidal cross-section, the total magnetic energy of the machine ($U_M \rightarrow a^{-4}$) increases much faster than the thermal energy of the plasma ($U_{Th} \rightarrow a^{-\frac{4}{3}}$), so that this type of compression is very inefficient in terms of magnetic energy input to thermal energy gain.

Compression that maintains constant aspect ratio R/a , with circular poloidal cross-section, was designated as *Type A* compression in an early paper [19] which has been referenced in many subsequent papers dealing with magnetic compression. *Type A* compression is achieved by sharply ramping up external B_z , the vertical field due to toroidal currents in external poloidal field coils at the same time as external B_ϕ is increased. In this case, both R and a scale in proportion to C^{-1} . Since R is not constant, the $1/R$ scaling of B_ϕ has to be accounted for when estimating the total machine magnetic energy, which is again approximately $U_M = \frac{1}{2\mu_0} \int B_\phi^2 dV$. The pre-compression toroidal field is $B_{\phi 1}(R) = \frac{B_{\phi 11} R_1}{R}$, where $B_{\phi 11}$ is the pre-compression toroidal field at pre-compression major radius $R = R_1$. The post-compression toroidal field is $B_{\phi 2}(R) = \frac{B_{\phi 22} R_2}{R}$, where $B_{\phi 22}$ is the post-compression toroidal field at post-compression major radius $R = R_2$. This leads to a compression scaling for toroidal field at a fixed radius R : $\frac{B_{\phi 2}(R)}{B_{\phi 1}(R)} = \frac{B_{\phi 22} R_2}{B_{\phi 11} R_1} = \left(\frac{a}{a_1} \right)^{-2} \frac{R}{R_1} = C^2 C^{-1} = C$, so that $B_\phi(R) \rightarrow C$. The total machine magnetic energy adiabatic compression scaling for *Type A* compression is then $U_M \rightarrow C^2$. The expression for plasma thermal energy scaling remains as $U_{Th} \rightarrow a^{-\frac{4}{3}} R^{-\frac{2}{3}}$. For *Type A* compression, this is $U_{Th} \rightarrow C^2$, same as the scaling for magnetic energy. Thus, *Type A* compression is far more energy-efficient than the constant R method of compression. Toroidal and poloidal beta scale equally in proportion to C .

External toroidal field coil current is unmodified in *Type B* compression [19], which was also defined for the case with circular poloidal cross-section. Increasing external B_z pushes

the plasma inwards towards the machine axis, where the toroidal field is larger. In this compression scenario the geometric compression ratio is defined as $C = \frac{R_1}{R}$, or $R \rightarrow C^{-1}$. Minor radius scales as $a \rightarrow C^{-\frac{1}{2}}$, and toroidal beta increases more than poloidal beta at compression. The expression for scaling of toroidal field at a fixed radius R is the same as that for *Type A* compression: $\frac{B_{\phi22}(R)}{B_{\phi11}(R)} = \left(\frac{a}{a_1}\right)^{-2} \frac{R}{R_1}$. For *Type B* compression this leads to $B_{\phi}(R) \rightarrow \text{constant}$, so that the total machine magnetic energy scales with the magnetic energy associated with B_z , which is orders of magnitude less than the total machine magnetic energy, and is comparable to the thermal energy, which scales as $U_{Th} \rightarrow C^{\frac{4}{3}}$.

1.5 Prior magnetic compression experiments

The experiment on which this work is based represents the first time that magnetic compression has been attempted on plasmas produced by a magnetised Marshall gun. In the past, mostly in the 1970's and 1980's, there were several studies looking at magnetic compression of conventional tokamak plasmas. Magnetic compression of spheromaks was the focus of the S-1 experiment, and there have also been a few studies of magnetic compression of reversed field pinches (RFPs) and field reversed configurations (FRCs).

1.5.1 S-1 spheromak

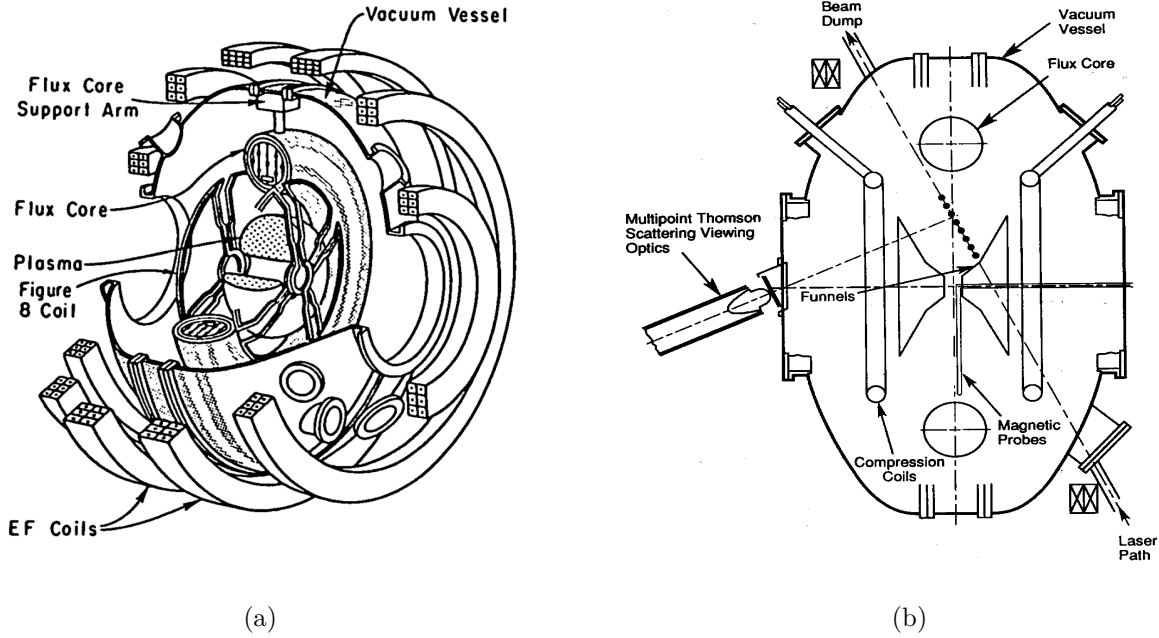


Figure 1.5.1: Schematics of S-1 device (image credit [22, 23])

The S-1 device ($R = 50$ cm, $a = 25$ cm, pre-compression) [22, 23] used a toroidally shaped flux core to generate spheromaks by inductive means. The flux core indicated in figures 1.5.1(a) and (b) contains both poloidal and toroidal windings. A quasi steady-state equilibrium axial magnetic field is produced by an additional two toroidal turns in the flux core and by toroidal currents in the external equilibrium field (EF) coils. To prevent outgassing, while maintaining rapid flux penetration, the flux core coils are covered with a very thin layer (<0.5 mm) of resistive inconel. Despite its complexity, inductive formation has the advantage, over the more conventional formation technique using magnetized Marshall guns ([4, 5], see also section 2.1 for the operating principles), that there are no large formation currents flowing between electrodes, thereby eliminating the source of impurities to the plasma that arises at the electrode surfaces.

Stabilization of the tilt instability (which can be envisaged by seeing the spheromak as a magnetic dipole directed against the background axial field) and shift instabilities, during formation and compression, was achieved on S-1 with the use of passive conducting stabilisers. The "figure 8" stabilizers used initially (see figure 1.5.1(a)), before the installation of the in-vessel magnetic compression coils, required that more than 10% of spheromak poloidal flux remained linked to the flux core [22, 24] for MHD stability. The funnel-shaped stabilisers used later removed the requirement for flux linking. These are depicted, along with the in-vessel

compression coils, in figure 1.5.1(b). Note that compression coils located inside the vacuum vessel were also part of the recent design proposal, presented in [25], for a spheromak magnetic compressor. Current with a rise time of 100 to 200 μ s was driven in the S-1 compression coils with a 1 MJ capacitor bank. The plasma-internal magnetic probe array and the sampling locations for the ten-point Thomson scattering system used to find electron temperature and density are indicated in figure 1.5.1(b).

Pre-compression S-1 spheromaks had toroidal plasma current $I_p \sim 200$ kA, corresponding to peak poloidal field $B_\theta \sim 0.15$ T. If a plasma is compressed self-similarly, so that the minor radius decreases in the same proportion as the major radius, toroidal and poloidal fluxes are expected to be conserved, so that the Taylor equilibrium state is maintained. A geometrical compression factor of $\frac{R_1}{R} \sim \frac{a_1}{a} \sim C \sim 1.6$ (recall that R_1 and a_1 denote the pre-compression major and minor radii, while R and a denote the post compression radii) was achieved on the S-1 device [23], leading the researchers to classify the regime as *Type A* compression (see section 1.4). The deviation of major radius compression scaling from that of minor radius compression scaling was found to be less than 10%. The availability of spheromak-internal temperature, density, and magnetic field point diagnostics allowed the researchers to produce shot-averaged poloidal flux contours over the compression cycle, and enabled determination of the compression scalings for density, temperature and magnetic field, and comparison with the predicted scalings.

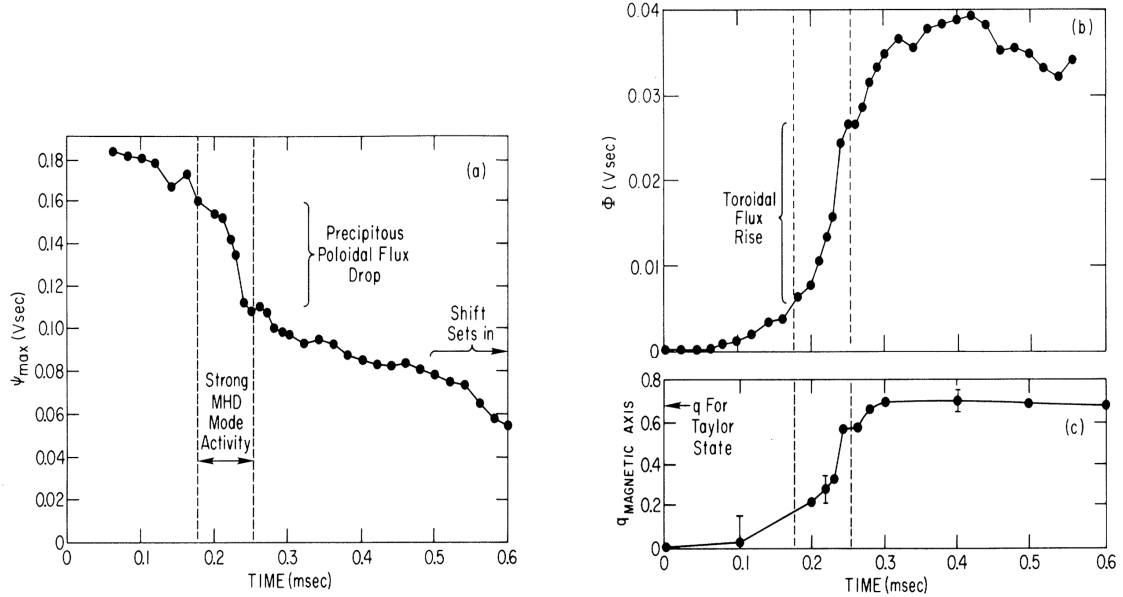


Figure 1.5.2: S-1 device; evolution of fluxes and q_{axis} (image credit: modified from [26])

Fine spatial resolution of the magnetic field measurements allowed for experimental confirmation of several aspects of basic theory. Figure 1.5.2 indicates the experimentally determined evolution of the poloidal and toroidal magnetic fluxes and of q at the magnetic axis.

The relaxation of the magnetic configuration towards the minimum energy (Taylor) state is characterised by the rapid conversion of poloidal to toroidal flux from 180 μs to 250 μs [10, 27, 26]. Good spatial resolution of field measurements also enabled experimental confirmation of the approximate conservation of the individual fluxes, and of the absence of flux conversion, during compression. The level of conservation of the fluxes was improved by increasing the compression field - this may have been related to the increased electron temperature (reduced resistivity) seen with more compression. The total spheromak magnetic energy was measured directly and shown to increase with compression. It was shown experimentally that the local electron beta remained constant during compression (*i.e.*, $n_{e0}T_{e0} \sim B_{\phi0}^2$, where the subscript 0 indicates peak values around the magnetic axis), and that the compression was non-adiabatic. Density scaled as $\frac{n_e}{n_{e1}} \propto C$, compared with the prediction of $\frac{n_e}{n_{e1}} \sim C^3$ for the case of particle conservation. Particle losses were also observed for uncompressed S-1 spheromaks, but τ_p , the particle confinement time, was found to decrease significantly with compression. This was thought to have been due partially to the effect of geometric shrinking, and largely due to some extra particle loss mechanism, that was attributed to the enhanced fluctuation level that was associated with increased drift velocities.

Electron current density ($J_\phi \sim I_p/\pi a^2$) was seen to increase significantly at compression, with approximately the predicted scaling of $\frac{J_\phi}{J_{\phi1}} \sim \frac{I_p}{I_{p1}} \left(\frac{a_1}{a}\right)^2 \sim C C^2 = C^3$. Ion temperatures were measured based on Doppler broadening of impurity line radiation. The contribution of Stark broadening to the observed temperature broadening was determined to be small for the observed transitions at the electron densities measured. Electron and ion temperatures were observed to increase at compression, but not with the adiabatic scaling of $\frac{T}{T_1} \sim C^2$. Peak T_e rose from ~ 40 eV to ~ 100 eV with compression, and ion temperatures of up to 500 eV were measured at compression. Prior to compression, T_i was generally greater than T_e by a factor of two to four, and was up to a factor of five greater than T_e at peak compression. In general, it was found that T_i correlated well with T_e , and T_i also correlated with the level of the fluctuations recorded in B . It was concluded that T_e increased at compression largely due to increased ohmic heating as I_p increased, and that ion temperature increases were largely due to anomalous non-collisional heating mechanisms (microinstabilities such as drift waves and ion cyclotron waves) that were excited by the large values of J_ϕ/n_e at compression. These microinstabilities were thought to be related to fluctuations observed in magnetic field measurements, which were enhanced at compression [23].

1.5.2 ATC tokamak

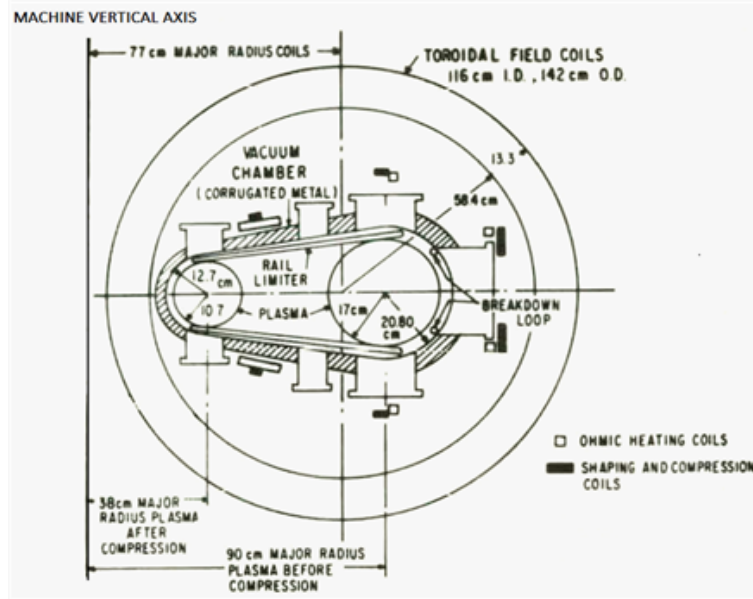


Figure 1.5.3: Poloidal cross-section of ATC device (image credit: [28])

The Adiabatic Toroidal Compressor (ATC) experiment ($R = 90$ cm, $a = 17$ cm, before compression), which was operated in the 1970's, employed *Type B* compression. As in standard tokamaks, the vacuum vessel is enclosed by the toroidal field coils, but in the ATC, molybdenum rail limiters guide the plasma inwards at compression, which is activated by increasing toroidal current in the compression coils depicted in figure 1.5.3 from 2 to 10 kA over 2 ms. To allow for rapid penetration of compression field, the vacuum vessel shell was quite electrically resistive, made from 0.7 mm thick stainless steel. The principal obstacle to successful compression was that radial field errors would cause the plasma column to shift vertically, leading to excessive interaction between the plasma and the rail limiters [29], and ultimately a disruptive instability. The radial field errors were thought to be due to the effect of eddy currents induced in the vacuum vessel. A solution allowing completion of the full compression cycle was found by imposing an optimised radial correction field, and installing passive stabiliser coils that opposed any remaining vertical shift [29]. A Thomson scattering (TS) system was used to obtain measurements of T_e and n_e at points inside the plasma column. TS electron densities were calibrated using microwave interferometry measurements - vertical interferometry chords were located at the pre-compression and post-compression major radii of 90 cm and 38 cm. Charge exchange spectroscopy was used to measure ion temperature.

Compression in a , R , B_ϕ , I_p , n_e , and T_i was observed with scalings consistent with predictions for *Type B* compression.

| parameter | Pre-compression | Post-compression |
|-----------------------|---------------------------------------|--------------------------|
| R | 90 cm | 38 cm |
| a | 17 cm | 10 cm |
| B_ϕ | 1.5 T | 4.6 T |
| I_p | 60 kA | 150 kA |
| T_i | 200 eV | 600 eV |
| T_e | 1 keV | 2 keV |
| $\langle n_e \rangle$ | $1 - 2 \times 10^{19} \text{ m}^{-3}$ | 10^{20} m^{-3} |

Table 1.5.1: Parameter compression scalings on ATC device

Variation of ATC parameters for typical compressed discharges are indicated in table 1.5.1. While T_i scaled as $T_i \rightarrow C^{\frac{4}{3}}$, where $C = 90/38 = 2.37$, T_e was found to scale in proportion to C , and the explanation given [29] was that $\tau_{Ei} > \tau_{comp} \sim \tau_{Ee}$, where τ_{Ei} and τ_{Ee} are the ion and electron energy confinement times, and $\tau_{comp} \sim 2 \text{ ms}$ is the time over which the compression field is increased to its maximum, so that T_e could not be expected to follow the adiabatic scaling law. Since, $T_e \rightarrow C$ in the ATC experiment, while n_e and B_θ scale with the *Type B* predictions, it could be expected that $\beta_{\theta e} = 2\mu_0 n_e T_e / B_\theta^2$ should remain constant at compression, and this was verified, at least in the case with relatively low 40 kA pre-compression plasma current.

The ATC compression mechanism is similar to the "radial magnetic pumping" scheme proposed in 1969 [30], in which it was suggested that a tokamak plasma would be maintained over several B_z compression cycles, and that ions could be heated further at each compression. However, each ATC discharge terminated in a disruption when the plasma column was pushed on to the inner limiter that protects the vacuum vessel. In [29], it was recommended that high frequency magnetic compression on ATC would be technically difficult, but that low frequency compression on a device, with dimensions increased to five to ten times those of ATC, might lead to fusion initiation.

1.5.3 Ultra Low q device

The scenario of attaining ohmic ignition of fusion through the combination of an ultra-low- q (ULQ) discharge and adiabatic magnetic compression was explored in [31]. The safety factor in the cylindrical approximation with $R \gg a$ is $q(r) = \frac{rB_\phi}{RB_\theta}$. With this definition, the current density can be expressed, using Ampere's law, as $J_\phi(r) = \frac{2B_\theta}{\mu_0 r} = \frac{2B_\phi}{\mu_0 q R}$. The ULQ regime explored on the REPUTE-1 device ($R = 82 \text{ cm}$, $a = 22 \text{ cm}$), has safety factor q less than one, which, compared with traditional tokamak regimes, enables higher toroidal current density for the same toroidal field, so that ohmic heating is increased, reducing the need for

supplementary heating. Application of minor radius magnetic compression leads to a further increase in ohmic heating.

Low q operation is also associated with high beta (*i.e.*, low toroidal field), which is advantageous for the design of compact, relatively low cost reactors [32]. The energy confinement time, which is key to meeting the Lawson criterion, is generally higher for high q - for ohmically heated plasmas the energy confinement time is found experimentally to scale as

$$\tau_E \sim 0.07 \bar{n}_e a R^2 q_{edge} \quad (1.5.1)$$

where \bar{n}_e is the average electron density in units of 10^{20} m^{-3} , and q_{edge} is the edge safety factor [33]. In general, tokamaks have high q and low beta, while reversed field pinches (RFPs) have low q and high beta.

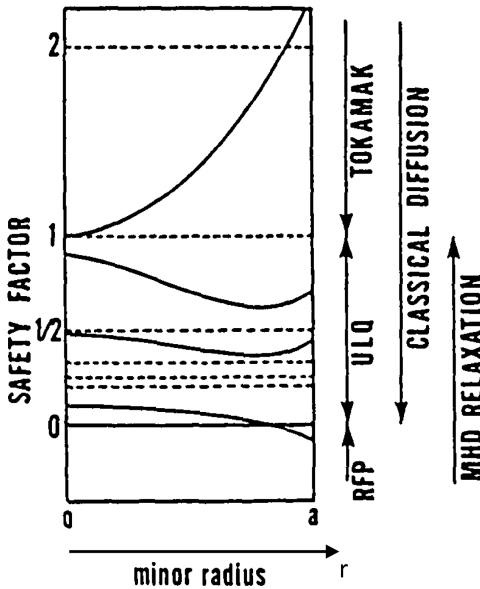


Figure 1.5.4: q profiles (ULQ device) (image credit: modified from [32])

Radial q profiles for various regimes are indicated in figure 1.5.4. The dissipative processes which determine the q profile of an equilibrium, independent of the initial state of the plasma, vary from regime to regime. As shown in [34], tokamaks and RFPs are on different dissipative branches. In general, two distinct dissipative processes can be identified - resistive magnetic field diffusion, which leads to $\frac{dq}{dr} > 0$ and peaked current density profiles in tokamaks, and MHD relaxation associated with m (poloidal mode number) = 1 kink activity [10, 35], which leads to $\frac{dq}{dr} < 0$ and flat current density profiles in RFPs [32]. The ULQ regime q profile is a result of competition between the two processes. When $q < 1$, such as in ULQ, spheromak, and RFP regimes, the $m=1$ helical kink mode is enhanced and stabilised through MHD relaxation [36]. MHD analysis indicated that, with sufficient magnetic shear and moderate magnetic Reynolds numbers, the ULQ regime was marginally stable against both ideal and

resistive modes [32]. Note that R_m , the magnetic Reynolds number, indicates the relative magnitude of the advective and diffusive contributions to the rate of change of magnetic field. The MHD equation for the rate of change of magnetic field is given by $\frac{\partial \mathbf{B}}{\partial t} = \nabla \times \mathbf{v} \times \mathbf{B} + \nabla \times (\eta \nabla \times \mathbf{B})$, yielding $R_m = \frac{vL}{\eta}$, where v is the plasma fluid velocity, L is the system's characteristic length scale, and η [m²/s] = $\frac{\eta' [\Omega \text{-m}]}{\mu_0}$ is the plasma resistive diffusion coefficient.

Power density balance in an ohmically heated fusion plasma is given by [31, 37]

$$\begin{aligned} P [\text{W/m}^3] &= \frac{du_{tot}}{dt} = P_\Omega + P_\alpha - P_L - P_B \\ &= \eta' J_\phi^2 + \frac{n^2}{4} Q_\alpha < \sigma V > - \frac{3nT}{\tau_E} - C_B n^2 \sqrt{T} \end{aligned}$$

where u_{tot} [J/m³] is the total plasma energy density, $\eta' [\Omega \text{-m}] \propto T_e^{-1.5}$ is the plasma resistivity, and P_Ω , P_α , P_L and P_B are the contributions to power density balance from ohmic heating, alpha particle heating, transport losses, and Bremsstrahlung radiative losses respectively. Q_α [J] is the (3.5 MeV) alpha particle energy for D-T fusion, $< \sigma V >$ [m³/s] is the fusion reaction rate, τ_E [s] is the energy confinement time, and $C_B \propto Z_{eff}$ is a coefficient that scales the losses associated with Bremsstrahlung losses. This model assumes that Bremsstrahlung radiative losses are much greater than losses due to impurity line radiation [37], which is a reasonable assumption at high temperatures when ions have been stripped of all their electrons. In addition, cyclotron radiative losses are neglected, without clear justification. Following the widespread observation that energy confinement time in magnetic confinement devices generally scales with density (equation 1.5.1), the assumption is made that $\tau_E = Kn$, where K is some constant. The expression for power density balance can then be re-expressed as

$$P = C_\Omega J_\phi^2 T^{-\frac{3}{2}} + C_\alpha n^2 T^{\frac{7}{2}} - C_L T - C_B n^2 T^{\frac{1}{2}} \quad (1.5.2)$$

where $C_\Omega = C_\Omega(Z_{eff})$, $C_\alpha = C_\alpha(Z_{imp}, Z_{eff})$, $C_L \propto \frac{1}{K}$, and $C_B \propto Z_{eff}$ are known approximations from empirical scalings [31, 37]. The steady-state equilibrium power balance condition is $P = 0$, and the stability of the power-balance equilibrium is determined by the signs of $\frac{\partial P}{\partial n}$ and $\frac{\partial P}{\partial T}$. For example, if $\frac{\partial P}{\partial T} < 0$, a perturbation to the equilibrium balance leading to a temperature increase would result in a loss of energy, while a temperature reduction would lead to an increase of energy. The ignition point of interest is the "thermal runaway" point, where a small perturbation in n or T moves the plasma into the regime where the alpha heating is dominant [31, 37]. The ignition saddle point values for T and n that satisfy $P = \frac{\partial P}{\partial n} = \frac{\partial P}{\partial T} = 0$ can be calculated. For example given inputs $\tau_E = 2.5$ s, $Z_{eff} = 1.5$, and $Z_{imp} = 8$ to enable assessment of C_Ω , C_α , C_L , and C_B , it is found that $T = 5.3$ keV and $n = 5 \times 10^{20}$ m⁻³ are required for ignition.

If magnetic compression, with increasing external toroidal field only, keeping R fixed, is carried out, an updated expression for the power density balance applies. The adiabatic compression scalings in table 1.4.1 can be used, with $a^{-1} \rightarrow C$, to modify equation 1.5.2:

$$P = C_\Omega C^2 J_{\phi 1}^2 T_1^{-\frac{3}{2}} + C_\alpha C^{\frac{26}{3}} n_1^2 T_1^{\frac{7}{2}} - C_L C^{\frac{4}{3}} T_1 - C_B C^{\frac{14}{3}} n_1^2 T_1^{\frac{1}{2}} \quad (1.5.3)$$

Again, parameters with subscript 1 denote pre-compression values. Adiabatic compression enhances the ohmic heating input ($P_\Omega \rightarrow C^2$) more than the transport losses ($P_L \rightarrow C^{\frac{4}{3}}$), and enhances the alpha particle heating ($P_\alpha \rightarrow C^{\frac{26}{3}}$) more than the Bremsstrahlung losses ($P_B \rightarrow C^{\frac{14}{3}}$), so that ohmic ignition can be achieved more easily at reduced τ_E and J_ϕ . Recalling that $\tau_E = Kn$, and noting that C_L is given as $C_L = \frac{0.048}{K} \left[\frac{\text{MW}}{\text{m}^3} \text{s keV}^{-1} \right]$ [31], equation 1.5.3, with $P = 0$, can be used to find an expression for the energy confinement time as

$$\tau_E = \frac{0.048 n_1 C^{\frac{10}{3}} T_1}{C_\Omega C^2 J_{\phi 1}^2 T_1^{-\frac{3}{2}} + C_\alpha C^{\frac{26}{3}} n_1^2 T_1^{\frac{7}{2}} - C_B C^{\frac{14}{3}} n_1^2 T_1^{\frac{1}{2}}} \quad (1.5.4)$$

With $T_1 = 600$ eV and $n_1 = 2 \times 10^{19} \text{ m}^{-3}$, the ignition parameters $T = 5.3$ keV and $n = 5 \times 10^{20} \text{ m}^{-3}$ can, in principle, be achieved with $C = 5$. These pre-compression values can be used in equation 1.5.4, to find the energy confinement time as $\tau_E = 0.15$ s, which is around 5% of the 2.5 s energy confinement time that would be required for ignition in the case without compression, as a result of the intensification of the ohmic and alpha particle heating power with adiabatic compression.

It was envisaged that the external B_ϕ would be maintained after compression, and that the compressed regime with an unprecedented level of ohmic heating would naturally expand in minor radius, as determined by the magnetic diffusion timescale of the plasma, attaining the more stable tokamak configuration. In [31], no particular emphasis was placed on assessing the stability of the low q plasma during compression. The main results of the magnetic compression experiment on REPUTE-1 were reported in [36, 38]. Post-compression transition to the tokamak regime was not reported, but q_a increased from around 0.3 to 0.65 at compression, before settling, post-compression at around 0.5. Reduction in minor radius at compression, and post-compression expansion into the increased toroidal field, was observed. A significant reduction of visible light emission was observed during magnetic compression, as a result of reduced plasma-wall interaction as the plasma column is pushed away from the vacuum vessel walls. The observed increase in plasma current after magnetic compression was attributed to reduced resistivity due to plasma-wall interaction reduction. The post-compression reduction in q_a was attributed to the increase in plasma current. As q_a variation led to rational surfaces at the edge, increased MHD activity was observed, and consequent plasma-wall interaction was seen to increase again, but to levels lower than those before compression.

1.5.4 Merging-compression formation of tokamak plasmas

Merging-compression is a spherical tokamak (ST) plasma formation method that involves the merging and magnetic reconnection of two plasma rings, followed by inward radial magnetic compression of the resultant single torus to form a spherical tokamak plasma configuration. The initial tori are formed inductively around coils internal to the vacuum vessel, and the compression coils are also internal, an approach with some similarities to that developed on the S-1 device. This ST plasma formation method has the advantage of eliminating the need for a traditional central solenoid - in an ST, space is limited in the central post and is inadequate for solenoids capable of inducing toroidal plasma currents in the MA range [39]. The merging phase leads to efficient transformation of magnetic to kinetic, then thermal energy (up to 15 MW of ion heating power was recorded on MAST), and also leads to a rapid increase of plasma current [39]. The merging compression ST formation method was first used on START [40, 41] in 1991, and then in MAST [42, 43], and is currently employed on the compact high field spherical tokamak ST40 at Tokamak Energy Ltd. [39].

1.5.5 Magnetic compression of FRCs

In the experiment described in [44], FRC (field reversed configuration) ion temperatures of up to 2 keV were achieved with magnetic compression. FRCs can be formed by merging two spheromaks with opposite helicity and are self-confined by almost purely poloidal fields. Helion Energy Inc. has compressed FRCs, attaining ion temperatures of around 5 keV; a set of independently triggered formation and acceleration coils are used to form and merge two oppositely directed supersonic FRCs [45].

1.6 Thesis outline

Part one of this work presents an overview of the magnetic compression experiment, the principal tests undertaken, and the main findings. A paper [46] based on the material in part one has been published in the arXiv electronic journal, and has been submitted to a peer-reviewed journal. Most of the results presented in the paper were obtained over the time after GF officially stopped the project and allowed me several weeks additional time to work alone with the machine and obtain data for the PhD thesis. In that period, various modifications to the external coil configuration were implemented, leading to significantly improved performance of levitated and magnetically compressed CTs. Useful discussions

and technical assistance from the co-authors was helpful in achieving the results obtained. In particular, Stephen Howard helped guide the development of the CT separatrix measurement technique. Experimental data included in the paper (and in this thesis) was written to file using GF IGOR-PRO data analysis software and processed using a MATLAB code that I wrote for data analysis and presentation. Four conference posters [47, 48, 49, 50] have been presented, partially based on the experimental results.

Chapter 2 is a brief description of the key features of the magnetic compression experiment. The machine and its working principles, and main operational and plasma diagnostics are presented.

In chapter 3, the principal external coil configurations explored to hold plasma off the insulating wall surrounding the CT containment region by the action of a levitation field formed by toroidal currents in external coils are described. Interaction between plasma and the insulating wall during the CT formation process was a major obstacle to progress with the experiment, as it led to plasma impurities and radiative cooling. The main results from the various configurations tested are presented, and modifications to the experiment that lead to improved performance of levitated CTs are described.

The principal observations and findings relating to CT behaviour at magnetic compression constitute chapter 4. Once again, various configurations were experimented with, and progress was made towards successful compression in the most recent configuration, leading to regular achievement of significant increases in CT magnetic field, density, and ion temperature at compression. The signs of an MHD instability that was prevalent at compression are described, along with a possible mechanism behind the observations.

Part two of the thesis, and appendices A, B and C, focus on the development of the new DELiTE (Differential Equations on Linear Triangular Elements) framework that was developed for spatial discretisation of partial differential equations on a triangular grid in axisymmetric geometry. Two papers [51, 52], based on the material presented in part two have been submitted to arXiv and to peer-reviewed journals. Ivan Khalzov, the co-author on these papers, helped guide the development of the conservative finite element code framework. With his guidance, I modified his original isothermal version of the MHD code to include a model for energy evolution while conserving net system energy. My contribution also included implementation of various simulated diagnostics including the q profile solver, development of models for CT formation, levitation and compression, implementation of the resulting sets of equations to code, running the simulations, and performing code verification and validation checks. I developed and implemented, with some advice from Dr. Khalzov, a model for interaction between plasma and neutral fluids, and models for maintenance of toroidal

flux conservation with the inclusion of a partially electrically insulating computational domain. I implemented the methods for data saving and plotting, and timestep adjustment. Three conference posters [48, 49, 50], partially based on the material in part two, have been presented.

Chapter 5 presents the development of discrete differential operators in matrix form, which are derived using linear finite elements to mimic some of the properties of their continuous counterparts, and constitute the core of the framework. A single-fluid two-temperature MHD model is implemented in the framework in order to study the magnetic compression experiment. Note that the continuous set of equations that describe the MHD model and various forms of the Grad-Shafranov equation that describe MHD equilibrium in the axisymmetric case, are derived in appendix A. The full set of continuous equations that describe the axisymmetric MHD model are presented in chapter 5, and various conservation properties of the system are demonstrated. As demonstrated in appendix B, the discrete differential operators and the discrete forms of the mass and energy conservation equations are used to derive a discrete form of the momentum equation which, as a consequence of the inherent properties of the operators, ensures that total energy of the system described by the complete set of discretised MHD equations is conserved with appropriate boundary conditions. In chapter 5, it is demonstrated how global conservation of energy, particle count, toroidal flux, and angular momentum for the discrete system of equations is ensured due to operator properties.

The various methods constructed to simulate CT formation into a levitation field, and magnetic compression, are described in chapter 6. The boundary conditions applied to the various fields are discussed, and the techniques established to couple the vacuum field solution in insulating regions to the full MHD solutions in the remainder of the domain are presented. The coupling of the solutions leads to a more physical representation of the processes involved in the interaction between plasma and the insulating wall during CT formation; special care is taken to maintain toroidal flux conservation. The development and implementation of a range of simulated diagnostics that have experimental counterparts, as well as additional simulated diagnostics including evaluation of CT q profile, and other CT-internal simulated measurements, are reported.

Chapter 7 introduces some of the primary code inputs. Simulation results, including time-evolution of the various fields solved for, and comparisons between experimentally-obtained and simulated diagnostics are presented. The experiment lacked adequate CT-internal plasma diagnostics for evaluation of how closely the adiabatic compression scalings were followed, but the scalings are assessed from simulations for which the available experimental diagnostics closely match their simulated counterparts.

The development and implementation to code of the discrete forms of the equations that

describe interaction between plasma and neutral fluids, when ionization, recombination, and charge exchange processes are included in the model, is outlined in chapter 8. Simulation and experimental results indicating interaction between plasma and neutral fluids are compared.

Main conclusions, and suggestions for further improvements to the experiment and its simulation are presented in chapter 9.

As mentioned above, appendix A consists of a derivation of the MHD equations, using principles of basic kinetic theory, which are solved for in the code. This lays the groundwork for chapter 8, in which expressions for the terms in the coupled sets of plasma fluid and neutral fluid equations, that pertain to reactive collisions, are developed. Derivations of various equilibrium models are also presented in appendix A.

A discrete form of the MHD equations which ensures (with appropriate boundary conditions) total energy conservation, is derived in appendix B. Appendix C describes general code aspects, such as the computational grid, timestepping methods, a description of the numerical solution for the Grad-Shafranov equation, a general discussion of diffusion coefficients and their implementation, and outcomes of code validation and verification.

A description of an edge-biasing experiment conducted on the SPECTOR plasma injector, and initial results, are presented in appendix D. A paper [53] based on the material presented in appendix D has been submitted to the arXiv electronic journal, and to a peer-reviewed journal. The results obtained in that work were obtained over a period of two weeks. I was allowed to try the biasing experiment on SPECTOR at GF and based the report for the University comprehensive exam on the work. My contribution to the material in the paper was the design and construction of the electrode assembly and biasing circuit, and all data and circuit analysis. Discussions and technical assistance from the GF team was helpful in accomplishing the results. The insertion of a disc-shaped molybdenum electrode, biased at up to +100V, into the edge of the CT, resulted in up to 1 kA radial current being drawn. Electron temperature, as measured with a Thomson-scattering diagnostic, was found to increase by a factor of up to 2.4 in the optimal configuration. H_α intensity was observed to decrease, and CT lifetimes increased by a factor of up to 2.3. A significant reduction in electron density was observed; this is thought to be due to the effect of a transport barrier, established by edge biasing, impeding CT fueling, where the fueling source is neutral gas that remains concentrated around the machine gas valves after CT formation, an effect that was verified by simulations that are presented in chapter 8. Particularly because of the issues encountered with plasma impurities in the magnetic compression experiment, special care was taken to choose a plasma-compatible materials for the biasing electrode assembly.

PART 1: EXPERIMENT

Chapter 2

Experiment overview

The SMRT (Super Magnetised Ring Test) magnetic compression experiment, which was operated at General Fusion from 2013 to 2016, was designed as a repetitive non-destructive test to study plasma physics applicable to magnetic target fusion compression. SMRT was identical to the MRT machines (section 1.2), with the exception that the aluminum flux conserver surrounding the CT confinement region was replaced with an insulating outer wall. Also, in the SMRT design, currents in external coils surrounding the containment region produce a magnetic field which applies a radial force on the plasma that "levitates" it off the outer wall during CT formation and relaxation, and then rapidly compresses it inwards. GF had hoped to be able to produce and magnetically compress levitated CTs with the same characteristics as the non-levitated CTs produced in standard MRT machines. With extensive lab-based diagnostics, this would give insight to the behavior of CTs that were compressed in the PCS experiments (section 1.2). By 2016, GF had shifted the focus of the PCS experiments to producing and explosively compressing spherical tokamak plasmas which had far better performance than their spheromaks. Partly because of the investment that would be required in order to redesign an experiment that would magnetically compress spherical tokamaks, and partly because of the problems with impurities and possibly other factors associated with the existing magnetic compression design, GF decided to move resources to other projects that are part of their scientific objectives.

This chapter begins with an overview of the magnetic compression device, with a description of the operating principles in section 2.1. The principal experimental diagnostics used are presented, along with details of their functionality, in section 2.2.

2.1 Machine operation principles

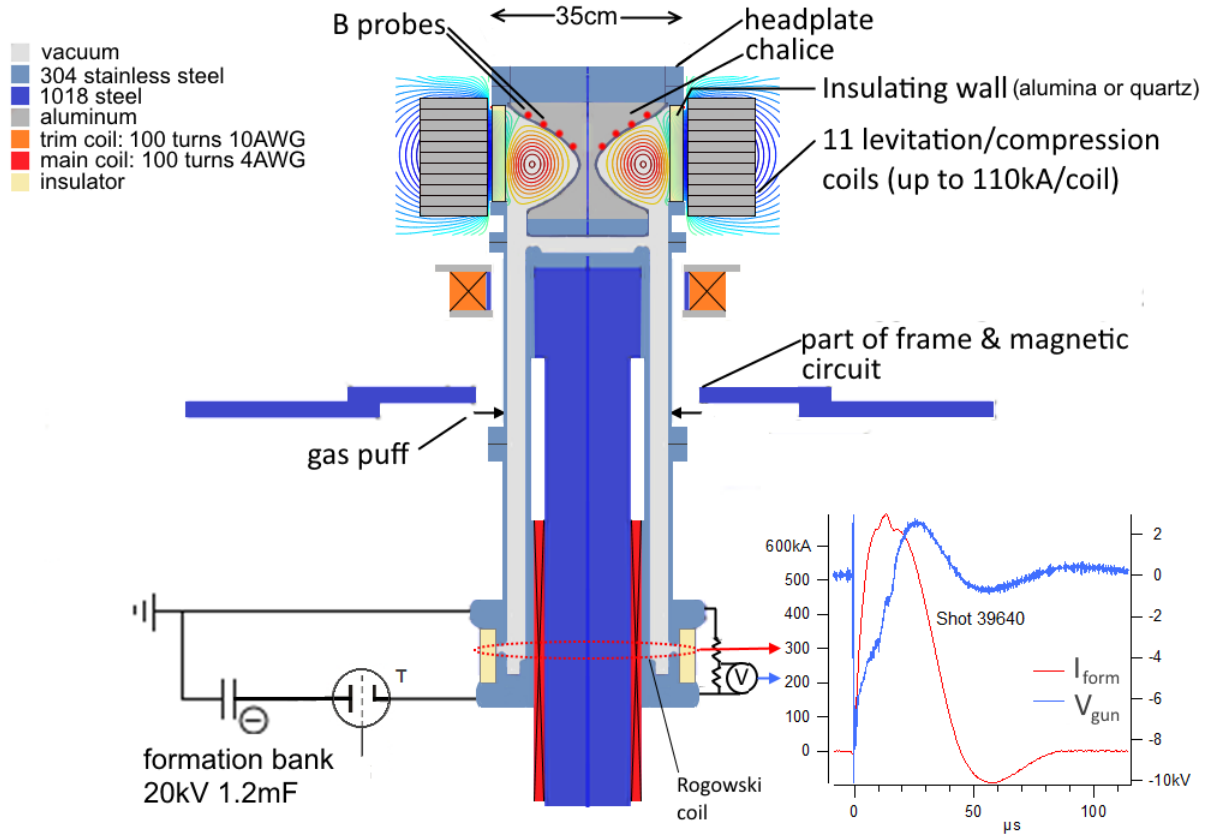


Figure 2.1.1: Machine schematic

Figure 2.1.1 shows a schematic of the magnetic compression device, with spheromak and levitation ψ contours from an equilibrium model superimposed. Measurements of formation current ($I_{\text{form}}(t)$), and voltage across the formation electrodes ($V_{\text{gun}}(t)$) are also indicated. Note that the principal materials used in the machine construction, and some key components, are indicated by the color-key at the top left of the figure. The sequence of machine operation is as follows:

| | | |
|-------|--|---|
| (i) | $t \sim -3 \text{ s}$ | Main coil is energised with steady state ($\sim 4\text{s}$ duration) current (I_{main}) |
| (ii) | $t = t_{\text{gas}} \sim -400 \mu\text{s}$ | Gas is injected into vacuum |
| (iii) | $t = t_{\text{lev}} \sim -400 \mu\text{s} \rightarrow -40 \mu\text{s}$ | Levitation banks, charged to voltage V_{lev} , are fired |
| (iv) | $t = 0\text{s}$ | Formation banks, charged to voltage V_{form} , are fired |
| (v) | $t = t_{\text{comp}} \sim 40 \mu\text{s} \rightarrow 150 \mu\text{s}$ | Compression banks, charged to voltage V_{comp} , are fired |

Table 2.1.1: Sequence of machine operation

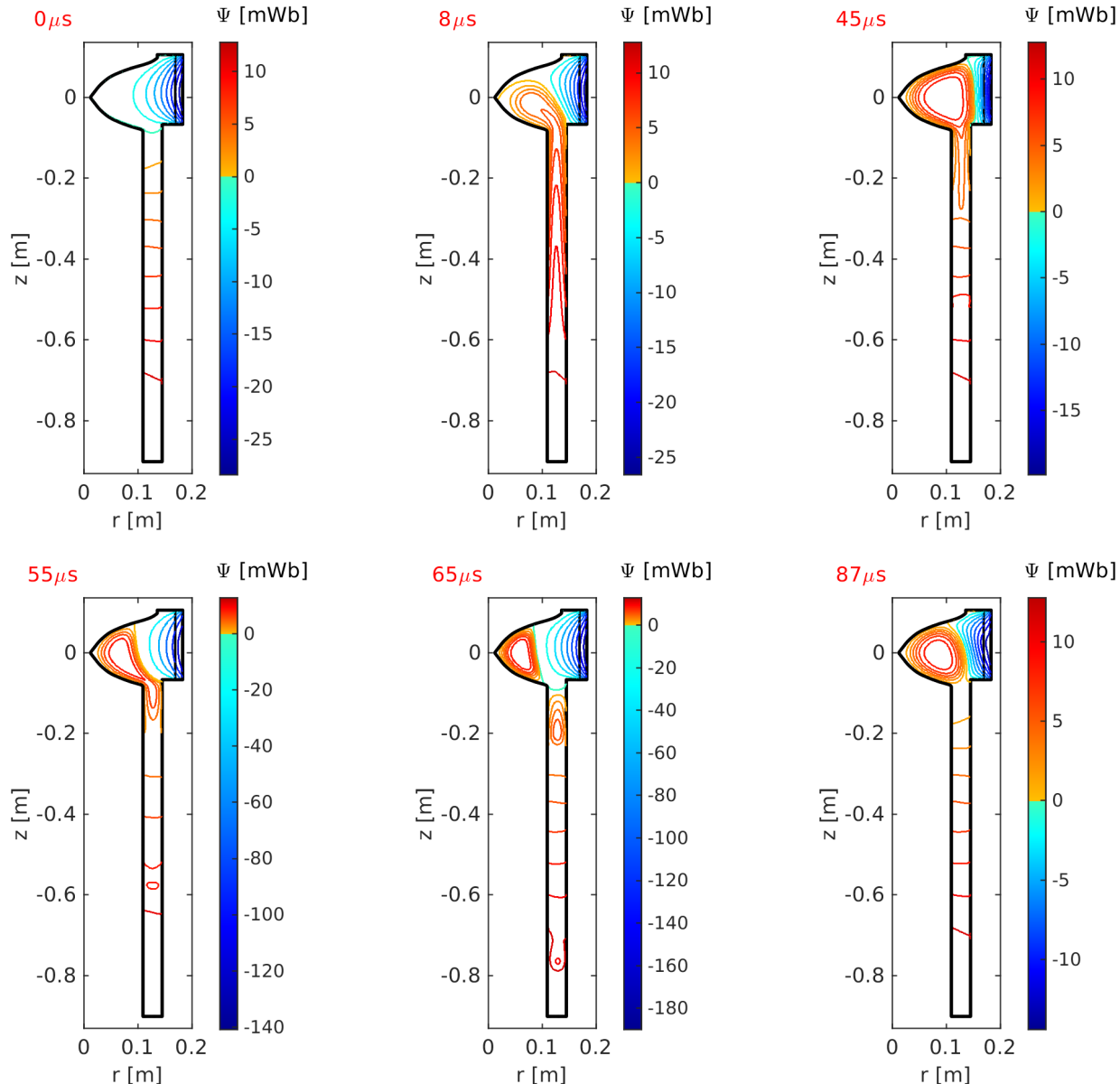


Figure 2.1.2: ψ contours from MHD simulation, with CT formation and compression

To better illustrate the sequence of operation, ψ contours from an MHD simulation (see

part two of the thesis) of the magnetic compression experiment are shown in figure 2.1.2. Note that ψ contours represent poloidal field lines, and that the vertical black line at the top-right of the figures at $r \sim 17$ cm represents the inner radius of the insulating wall. Vacuum field only is solved for to the right of the line, and the plasma dynamics are solved for in the remaining solution domain to the left of the line. The inner radius of the stack of eleven levitation/compression coils (which are not depicted here) is located at the outer edge of the solution domain, at $r \sim 18$ cm. Simulation times are notated in red at the top left of the figures. Note that the colorbar scaling changes over time; $\max(\psi)$ decreases slowly over time as the CT decays, while $\min(\psi)$ increases as the levitation current in the external coils decays, and then drops off rapidly as the compression current in the external coils is increased, starting at $t_{comp} = 45 \mu\text{s}$ in this simulation. At time $t = 0$, the stuffing field ($\psi > 0$) due to currents in the main coil fills the vacuum below the containment region, and has soaked well into all materials around the gun, while the levitation field fills the containment region. Simulated CT formation is initiated with the addition of toroidal flux below the gas puff valves located at $z = -0.43$ m; initial intra-electrode radial formation current is assumed to flow at the z -coordinate of the valves. As described in detail in chapter 6, toroidal flux addition is scaled over time in proportion to $\int_0^t V_{gun}(t') dt'$. Open field lines that are resistively pinned to the electrodes, and partially frozen into the conducting plasma, have been advected by the $\mathbf{J}_r \times \mathbf{B}_\phi$ force into the containment region by $t = 8 \mu\text{s}$ (\mathbf{J}_r is the radial formation current density across the plasma between the electrodes, and \mathbf{B}_ϕ is the toroidal field due to the axial formation current in the electrodes). By $45 \mu\text{s}$, open field lines have reconnected at the entrance to the containment region to form closed CT flux surfaces. The presence of a pressure gradient directed towards the CT center allows formation of a toroidal diamagnetic current which in turn helps sustain the CT poloidal field. At these early times, open field lines remain in place surrounding the CT. Compression starts at $45 \mu\text{s}$ and peak compression is at $65 \mu\text{s}$. The CT expands again between $65 \mu\text{s}$ and $87 \mu\text{s}$ as the compression current in the external levitation/compression coils reduces. Note that at $55 \mu\text{s}$, magnetic compression causes closed CT poloidal field lines that extend down the gun to be pinched off at the gun entrance, where they reconnect to form a second smaller CT. Field lines that remain open surrounding the main CT are then also reconnectively pinched off, forming additional closed field lines around the main CT, while the newly reconnected open field lines below the main CT act like a slingshot that advects the smaller CT down the gun, as can be seen at $65 \mu\text{s}$.

A pulse-width modulation system was used for current control in the main coil circuit. The working gas was typically He, H₂, or D₂, with valve plenum pressure ~ 30 psi (gauge), and optimal vacuum pressure $\sim 1 \times 10^{-8}$ Torr. The formation capacitor bank (240 kJ bank consisting of $24 \times 50 \mu\text{F}$, 20 kV capacitors in parallel) drives up to 1 MA of

current, with a half period of $50\ \mu\text{s}$ (see figure 2.1.1). The original configuration had six levitation/compression coils, with each coil having its own levitation and compression circuit. The $120\ \text{kJ}$ levitation bank consisted of $2 \times 50\ \mu\text{F}$, $20\ \text{kV}$ capacitors in parallel for each coil, and there were four of these capacitors in parallel for each coil for the $240\ \text{kJ}$ compression bank.

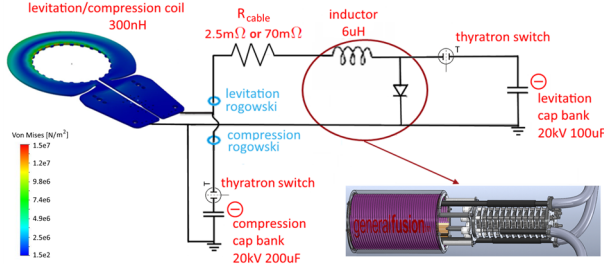


Figure 2.1.3: Levitation and compression circuit

Figure 2.1.3 illustrates the circuit for one of the single-turn levitation and compression coils. Each coil (or coil-pair in the case of the configuration with eleven coils) had a separate identical circuit. Unlike the crowbarred levitation currents, the compression currents are allowed to ring with the capacitor discharge.

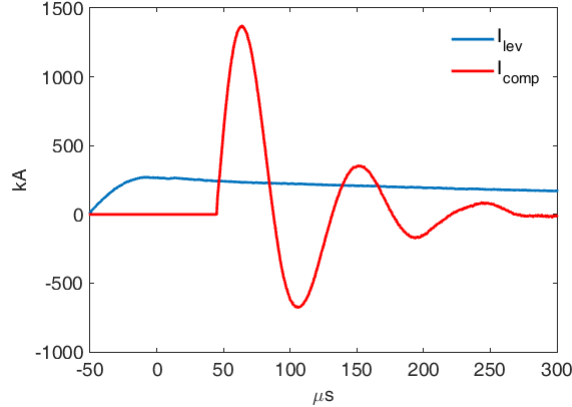


Figure 2.1.4: Total levitation and compression currents

Levitation and compression current profiles are shown in figure 2.1.4, for a case with $V_{lev} = 12\ \text{kV}$, $V_{comp} = 18\ \text{kV}$, $t_{lev} = -50\ \mu\text{s}$, and $t_{comp} = 45\ \mu\text{s}$. Note that the currents indicated are divided (approximately equally) between the coils. With $2.5\ \text{m}\Omega$ resistance cables (denoted as R_{cable} in figure 2.1.3) in place between the holding inductors and coils, the crowbarred levitation current drops to zero at around $3\ \text{ms}$.

2.2 Diagnostics

The experiment used a variety of measurements to characterise machine operation and diagnose plasma behaviour. In this section an overview of the measurements employed will be given, followed by brief descriptions of the operating principles for each diagnostic in sections 2.2.1 to 2.2.5.

Formation, levitation and compression currents were measured using Rogowski coils, while formation voltage was measured with a voltage divider arrangement. The locations of the current and voltage measurement devices are indicated in figures 2.1.1 and 2.1.3.

Plasma diagnostics included magnetic field measurements at magnetic probes embedded in the chalice (the inner flux conserver depicted in figure 2.1.1), and interferometers to record line averaged electron density. Ion temperature was estimated using an ion Doppler diagnostic. Visible light emission is recorded by two survey spectrometers which have variable exposure durations, and by six fiber-coupled photodiodes that record time-histories of total optical emission.

The absence of magnetic field, and spatially resolved density and temperature measurements internal to the CT, means that there is a high level of uncertainty about internal plasma dynamics. Internal plasma diagnostics are only useful if the degree of plasma perturbation due to the diagnostic is tolerable. Relative to more conventional magnetically confined plasmas, the small size and high density of the CTs studied in this project impose a lower tolerance on what can acceptably be inserted into the plasma. Non-invasive diagnostics, that can provide spatially resolved information, include Thomson scattering for electron density and temperature, and polarimetry for magnetic field measurements. Although Thomson scattering is employed on other projects at GF, it was never implemented on the magnetic compression experiment. A polarimetry diagnostic is under development, but again, was not used on this experiment.

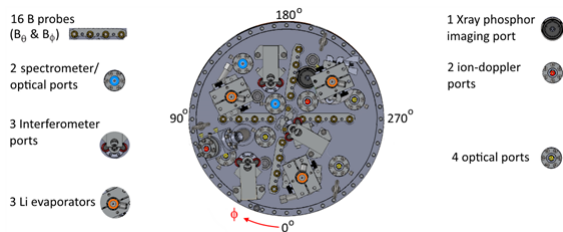


Figure 2.2.1: Machine headplate schematic

Figure 2.2.1 shows the schematic of the machine headplate indicating main diagnostics and lithium gettering ports.

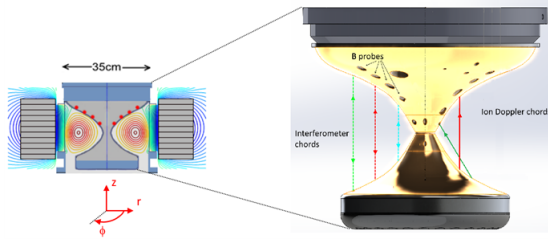


Figure 2.2.2: Chalice schematic

Figure 2.2.2 depicts the tungsten-coated aluminum chalice which is the inner flux-conserver, indicating the locations of some of magnetic probe ports and the lines-of-sight for the ion-Doppler and interferometer diagnostics. For ease of depiction, the ion-Doppler/interferometer chords are shown to be located on the same poloidal plane. Line-averaged electron density was obtained along chords at $r = 35$ mm, $r = 65$ mm and $r = 95$ mm using dual 1310 nm and 1550 nm He-Ne laser interferometers. Dual wavelength interferometers were used to enable compensation for errors due to machine vibration during a shot. Each beam is split in two - one of the split beams travels through the plasma and is reflected off a retroreflector in the base of the chalice and then passes through the plasma a second time before being transmitted away from the injector by optic fiber and merging with the other split beam (which has travelled an equivalent path but with the distance traveled by the first beam through the plasma being replaced by an equal distance through air), for interference analysis leading to line-averaged n_e . An indication of ion temperature, along the vertical chord at $r = 45$ mm and the diagonal chord with its upper point at $r \sim 20$ mm, was found from Doppler broadening of line radiation from singly ionized helium.

Each of the sixteen magnetic probes was located at the closed end of a thin-walled stainless steel tube embedded in axially directed holes in the chalice. The r, ϕ coordinates of the magnetic probes, where $r = 0$ is defined as being at the machine axis, are:

| | | | | | | | | | | | | | | | | |
|---------------|----|-----|----|-----|----|-----|----|-----|----|-----|----|-----|-----|-----|-----|-----|
| r [mm] | 26 | 26 | 39 | 39 | 52 | 52 | 64 | 64 | 77 | 77 | 90 | 90 | 103 | 103 | 116 | 116 |
| ϕ [deg.] | 90 | 270 | 10 | 190 | 90 | 270 | 10 | 190 | 90 | 270 | 10 | 190 | 90 | 270 | 10 | 190 |

Table 2.2.1: r, ϕ coordinates of magnetic probes (original configuration)

2.2.1 Magnetic field measurements - B probes

A standard magnetic probe is one way to measure magnetic field. The voltage signal induced in a coil of wire due to a changing field can be integrated to give the field magnitude over time. Faraday's law of induction is: $\nabla \times \mathbf{E} = -\dot{\mathbf{B}}$. Integrating over the area of the probe's coil, using Stoke's theorem ($\int \nabla \times \mathbf{a} \cdot d\mathbf{S} = \int \mathbf{a} \cdot d\mathbf{l}$), and noting that $V = \int \mathbf{E} \cdot d\mathbf{l}$, a formula

for the voltage induced in a single loop of wire with loop-area A is arrived at: $V = -A\dot{B}$. Here, it's assumed that the magnetic field is uniform within the loop. Only the component of the magnetic field that is perpendicular to the plane of the loop contributes to the induced voltage. For a coil with N turns,

$$B(t) = -\frac{1}{NA} \int_0^t V(t') dt' \quad (2.2.1)$$

The measured voltage signal can be time-integrated using an RC integrator, or can be integrated numerically. Numerical integration has the advantage of not attenuating the incoming signal. The voltage signal is proportional to \dot{B} , N and A , so for a given (estimated) value of \dot{B} , the product NA must be sufficiently large that the voltage signal can be picked up by the data acquisition (DAQ) system and also not be dominated by background noise. On the other hand keeping the probe as small as possible is good so that the perturbation of the plasma due to the presence of the probe is minimised. Equation 2.2.1 can be rearranged as

$$NA \sim \frac{V_{min}\tau_{est}}{B_{est}}$$

to give an estimate for the minimum required value of NA . Here, V_{min} is the minimum induced probe voltage that will allow an adequate signal to noise ratio while meeting the minimum DAQ sensitivity, and B_{est} and τ_{est} are estimates for the field magnitude that will be measured, and its characteristic rise time.

Another criterion that must be considered when designing a magnetic probe is the probe response time, *i.e.*, the minimum time period over which changes in the magnetic field can be captured by the probe. This minimum time period is given by $\tau_{LR} = \frac{L}{R}$ where L is the coil inductance, and R is the resistance of the combined coil and coil-to-DAQ system circuit. The coil inductance can be calculated from one of the two following standard formulae: If $w = \frac{h_c}{r_c} < 1$, where r_c is the radius of the circular coil turns, and h_c is the height of the coil (for a coil with non-overlapping turns which are stacked one on top of the other, $h_c = N d_w$, where d_w is the diameter of the coil wire), then for an air-cored coil

$$L = \frac{\mu_0 N^2 \pi r_c^2}{h_c} \left(1 - \frac{8w}{3\pi} + \frac{w^2}{2} - \frac{w^4}{4} + \mathcal{O}w^6 \right) [\text{H}]$$

If $w > 1$, then

$$L = \mu_0 N^2 \pi r_c^2 [\text{H}]$$

In either case, the number of turns should be minimised, in order to reduce L and maintain good high frequency response, while still having the product NA sufficient for adequate signal strength. Additional considerations include that the coil winding must be protected from

heat, and that the diffusion time of the magnetic field through the heat shielding material must be small enough that the probe can pick up the required information. The B probe coils used on the magnetic compression experiment each had ten turns of 34 AWG magnet wire ($0.86 \Omega/m$), with cross-sectional area 0.02 mm^2 . Each of the probes located at the coordinates indicated in table 2.2.1 had two ten-turn windings, which were individually oriented so as to measure poloidal and toroidal field components. The coils were wound on Delrin forms which were inserted in hollow thin-walled stainless steel tubes with one closed end. The outer surfaces of the closed ends of the tubes, and the inner surface of the chalice, were tungsten coated. Tungsten coating of plasma facing surfaces reduces the level of sputtering of impurity ions into the plasma, which in turn reduces the level of plasma cooling due to line radiation. Each tube was inserted in vertical holes through the chalice, as depicted in figure 2.2.2, with the closed end of the tubes flush with the chalice walls. The skin diffusion time for the magnetic field through the closed ends of the tubes can be estimated as $\tau_{diff} \sim \frac{t^2 \mu}{\eta'}$, where $t = 0.5 \text{ mm}$ is the tube wall thickness, $\mu = \mu_0 \mu_r$ is the material permeability (relative permeability $\mu_r \sim 1$ for stainless steel, so $\mu = \mu_0$), and $\eta' [\Omega - \text{m}]$ is the material resistivity ($\sim 1.16 \times 10^{-6} \Omega - \text{m}$ for stainless steel), so that $\tau_{diff} \sim 0.3 \mu\text{s}$. With a coil design such that $\tau_{LR} < \tau_{diff}$, this implies that changes in field magnitude over times $t \gtrsim 0.3 \mu\text{s}$ are captured.

The usual practice is to calibrate magnetic probes using a known field so that a calibration factor can be found for converting the integrated voltage signal to a field amplitude. From equation 2.2.1, the calibration factor is $1/NA$. N may be known accurately but A can only be approximated, particularly for coils with more than a single layer of windings.

Particular care was taken to reduce, as much as possible, the noise pickup on the electrical signals. The magnet wire coil feedthroughs were arranged in twisted pairs as far as the machine headplate. From there, shielded cables transmitted the signals a short distance to electrically shielded boxes, where the electrical signals are electronically integrated, using a passive low-pass filter type integrator, and the integrated signals were converted to optical signals. Standard optic cables transmitted these signals a distance of several meters to an electrically shielded area, where they were converted back to electrical signals, digitised (*i.e.*, converted to digital data suitable for computer processing), and stored for analysis.

2.2.2 Current measurements - Rogowski coils

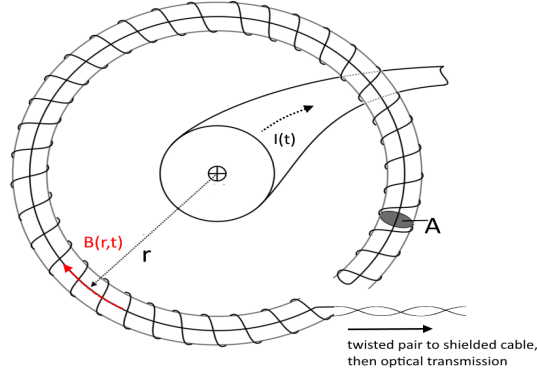


Figure 2.2.3: Rogowski coil schematic

The principles behind magnetic probe operation also apply to Rogowski coils, which are used to measure time varying currents. Figure 2.2.3 is a schematic of a Rogowski coil. N turns of wire, with each turn having cross-sectional area A , are wrapped around an internal torus-shaped form. The wire is returned along the toroidal path inside the poloidal windings, so that there is no net toroidal turn. Using Stoke's theorem, Ampere's law defines the magnetic field produced by a current as $B(r, t) = \frac{\mu_0 I(t)}{2\pi r}$, where r is the distance from the current path in the direction perpendicular to the current flow. In combination with equation 2.2.1, this implies that the amplitude of a time varying current can be determined from the time-integral of the measured induced voltage in a coil as

$$I(t) = -\frac{2\pi r}{NA\mu_0} \int_0^t V(t') dt' \quad (2.2.2)$$

A Rogowski coil, encircling the cables that connected each levitation/compression coil to its associated levitation inductor and capacitor bank, was used to measure the levitation current for each of the levitation/compression coils. Similarly, Rogowski coils were used to record the compression current for each of the levitation/compression coils. As depicted in figure 2.1.1, a single Rogowski coil encircling the lower machine insulator was used to record formation current.

2.2.3 Density measurements - interferometry

Line averaged electron density can be measured through determination of the phase shift of an electromagnetic wave traversing the plasma. The amount of phase shift caused by crossing

through the plasma depends on the line-averaged refractive index of the plasma which, in turn, depends on the line averaged electron density. A standard interferometric technique is based on splitting a laser beam into two beams which are directed along two paths of equal length, with a segment of one of the paths being through the plasma. The beams are then merged and the relative phase shift is assessed.

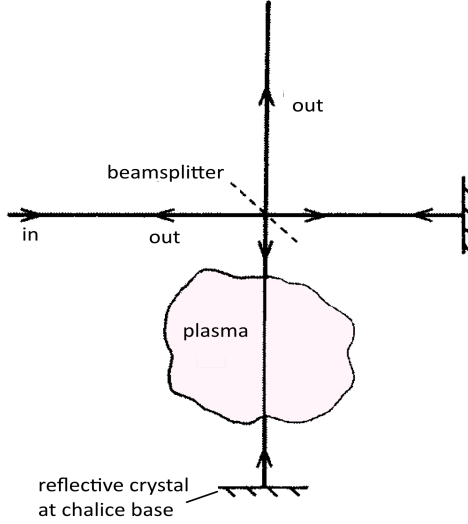


Figure 2.2.4: Michelson interferometer schematic

The schematic is indicated in figure 2.2.4 for the case of a Michelson-type interferometer, which was used in the magnetic compression experiment - note that the plasma-traversing beam crosses through the plasma twice. Retroreflectors positioned at the base of the chalice (figure 2.2.2) reflect the beam back up through the plasma. The reference beam is directed along a path of equal length in ambient air.

After traversing their respective paths, the electric fields associated with the beams are $Ee^{i\omega t}$ and $Ee^{i(\omega t+\phi)}$, with phase difference ϕ between them, and the total electric field of the merged beams is $E_t = Ee^{i\omega t}(1 + e^{i\phi})$. The merged beam power is proportional to $|E_t|^2$. Using basic trigonometric identities, it can be shown that $|E_t|^2 = 2E^2(1 + \cos(\phi))$, so that the phase shift can be found by measuring the merged beam power.

Geometric optics defines that the phase lag applied to a wave due to travelling a distance L in a medium of refractive index $N = \frac{c}{v_{phase}} = \frac{ck}{\omega}$ is

$$\phi = \int_0^L N \frac{\omega}{c} dl = \int_0^L k dl$$

Here, $c = 3 \times 10^8$ m/s is the speed of light in a vacuum, v_{phase} [m/s] is the phase speed of the wave, k [m^{-1}] = $\frac{2\pi}{\lambda}$ is the wavenumber, where λ [m] is the wavelength, and ω [radian/s] = kv_{phase} is the angular frequency of the wave. The wavenumber k for the reference beam is

$k = k_0 = \frac{\omega}{c}$. The plasma-traversing beam also has wavenumber $k = k_0$ for the plasma-external segment of its path, and $k = k_{plasma}$ for the segment through the plasma. Hence, after merging, the phase difference between the two beams will be

$$\Delta\phi = \int_0^{L_p} (k_{plasma} - k_0) dl \quad (2.2.3)$$

where L_p is the length of the path through the plasma. In order to find an expression relating the phase difference to electron density, the dispersion relation describing how the wavenumber depends on the wave frequency must be defined. Systems of linear differential equations can be studied using Fourier analysis - if any one quantity in the equations varies sinusoidally with a particular frequency, then all other quantities in the equations must vary at the same frequency [54]. The plasma fluid equations are not linear, so there is nonlinear coupling between frequencies. The equations can be linearised if the perturbation amplitudes are considered to be small relative to the steady state quantities, *i.e.*, $\tilde{x} \ll x$ for all quantities x and perturbations \tilde{x} . The process of linearisation involves the first order expansion of the equations, where second and higher order terms are neglected. All oscillating quantities are represented with exponential notation, for example the plasma number density is represented as $n = n_0 + \tilde{n}$, where $\tilde{n} \sim e^{i(\mathbf{k} \cdot \mathbf{r} - \omega t)}$. Gradients and time derivatives of perturbed quantities can be represented as $\nabla \rightarrow i\mathbf{k}$ and $\frac{\partial}{\partial t} \rightarrow -i\omega$.

Taking the curl of Faraday's law, and using Ampere's law gives

$$\begin{aligned} \nabla \times \nabla \times \mathbf{E} &= -\nabla \times \dot{\mathbf{B}} \\ \Rightarrow -\nabla^2 \mathbf{E} + \nabla(\nabla \cdot \mathbf{E}) &= -\frac{\partial}{\partial t}(\nabla \times \mathbf{B}) \\ &= -\frac{\partial}{\partial t}(\mu_0 \mathbf{J} + \mu_0 \epsilon_0 \dot{\mathbf{E}}) \end{aligned} \quad (2.2.4)$$

From Gauss's law, $\nabla \cdot \mathbf{E} = \frac{\rho_c}{\epsilon_0}$, where ρ_c [Coulomb/m³] is the charge density. In a vacuum, $\rho_c = 0$ and $\mathbf{J} = \mathbf{0}$, so the vacuum wave equation is $\nabla^2 \tilde{\mathbf{E}} = \frac{1}{c^2} \frac{\partial^2 \tilde{\mathbf{E}}}{\partial t^2}$, where the relation $c^2 = \frac{1}{\mu_0 \epsilon_0}$ has been used. The perturbation to the electric field scales as $\tilde{\mathbf{E}} \sim e^{i(\mathbf{k} \cdot \mathbf{r} - \omega t)}$, so that dispersion relation for electromagnetic waves in a vacuum can be expressed as

$$\omega^2 = c^2 k^2$$

In a plasma, quasineutrality holds over distances greater than the Debye length, so $\nabla \cdot \mathbf{E} = \frac{\rho_c}{\epsilon_0} = 0$. Hence, in terms of the field perturbations,

$$\nabla^2 \tilde{\mathbf{E}} = \frac{\partial}{\partial t} \left(\mu_0 \tilde{\mathbf{J}} + \frac{1}{c^2} \dot{\tilde{\mathbf{E}}} \right) \quad (2.2.5)$$

In plasma, $\tilde{\mathbf{J}} \neq \mathbf{0}$ so an expression for $\tilde{\mathbf{J}}$ must be found in order to find the dispersion relation. The electron momentum equation in an unmagnetised cold plasma is $m_e n_e (\dot{\mathbf{v}}_e + (\mathbf{v}_e \cdot \nabla) \mathbf{v}_e) = -e n_e \mathbf{E}$, where \mathbf{v}_e is the electron fluid velocity. This can be linearised about an equilibrium with $\mathbf{v}_{e0} = \mathbf{0}$, leading to $i\omega m_e \tilde{\mathbf{v}}_e = e \tilde{\mathbf{E}}$. Over the short timescales associated with high frequency phenomena, the ions can be considered to be fixed in space, so that $\tilde{\mathbf{J}} = -n_0 e \tilde{\mathbf{v}}_e$. Combination of these last two expressions leads to $\tilde{\mathbf{J}} = \frac{i n_0 e^2 \tilde{\mathbf{E}}}{\omega m_e}$, so that, referring to equation 2.2.5, $\frac{\partial}{\partial t} (\mu_0 \tilde{\mathbf{J}}) \rightarrow \mu_0 \frac{n_0 e^2 \tilde{\mathbf{E}}}{m_e} = \frac{\omega_{pe}^2}{c^2} \tilde{\mathbf{E}}$, where $\omega_{pe} = \sqrt{\frac{e^2 n_e}{\epsilon_0 m_e}}$ is the electron plasma frequency. Thus, the dispersion relation for high frequency waves in an unmagnetised plasma is

$$\omega^2 = c^2 k_{plasma}^2 + \omega_{pe}^2 \quad (2.2.6)$$

This dispersion relation also holds for magnetized plasmas in which $\omega_{ce} \gg \omega$, where $\omega_{ce} = \frac{eB}{m_e}$ is the electron cyclotron frequency [54]. Note that if the wave frequency ω is less than the plasma frequency, then k and N are imaginary and the wave is evanescent. For wave propagation, $\omega > \omega_{pe} \Rightarrow n_e < \frac{\omega^2 \epsilon_0 m_e}{e^2}$. The wave can propagate through the plasma only if the plasma density n_e is less than some critical density:

$$n_c = \frac{\omega^2 \epsilon_0 m_e}{e^2} \quad (2.2.7)$$

Equation 2.2.6 implies that the beam wavenumber for the path segment through the plasma can be expressed as $k_{plasma} = \frac{1}{c} \sqrt{\omega^2 - \omega_{pe}^2}$. Hence, with $k_0 = \frac{\omega}{c}$, the phase difference (equation 2.2.3) can be re-expressed as

$$\Delta\phi = \int_0^{L_p} \left(\frac{\omega}{c} \left(1 - \left(\frac{\omega_{pe}}{\omega} \right)^2 \right)^{\frac{1}{2}} - \frac{\omega}{c} \right) dl$$

In the limit $\omega \gg \omega_{pe}$, $\left(1 - \left(\frac{\omega_{pe}}{\omega} \right)^2 \right)^{\frac{1}{2}} \approx 1 - \frac{1}{2} \left(\frac{\omega_{pe}}{\omega} \right)^2$, so this can be reduced to

$$\Delta\phi = -\frac{1}{2} \frac{\omega}{c} \int_0^{L_p} \left(\frac{\omega_{pe}}{\omega} \right)^2 dl$$

Using the definitions for the plasma frequency and the critical density, this implies that

$$\Delta\phi = -\frac{\omega}{2c n_c} \int_0^{L_p} n_e dl$$

Therefore, the line averaged electron density $\frac{1}{L_p} \int_0^{L_p} n_e dl$ can be assessed through determination of the phase shift, which is a function of the power of the merged beams.

2.2.4 Temperature measurements - ion-Doppler spectroscopy

When bound electrons in atoms or partially ionized ions undergo transitions from upper to lower discrete energy levels (*i.e.*, quantum states), photons are emitted. The photon energy is given by $E_p = E_i - E_j = h\nu = \frac{hc}{\lambda}$, where E_i is the energy of the upper level which the electron originally occupied, and E_j is the energy of the lower level which the electron occupies after the transition, $h = 6.63 \times 10^{-34}$ [J-s] is Planck's constant, c is the speed of light, while λ [m] and ν [s⁻¹] are the wavelength and frequency respectively of the radiation associated with the photon. When the radiation emitted by a group of particles is measured, radiation at frequencies/wavelengths corresponding to dominant transitions appear as relatively bright spectral lines in an otherwise uniform and continuous radiation spectrum. When prior knowledge of the dominant transitions for different types of particles is available, spectral lines can be used to identify the particles whose radiation spectrum is being measured. Due to various spectral line broadening mechanisms, in particular natural broadening, pressure broadening, and Doppler broadening, the radiation emitted as a result of transition between any two particular energy levels is spread over a range of frequencies.

Natural broadening arises because, as a consequence of the uncertainty principle, the quantum states of an atom or ion have a small spread in energy [55]. The lifetime of the atom or ion in a particular state k is finite due to spontaneous transitions to lower quantum states. The effective spread in energy is given by $\Delta E \approx \frac{h}{2\pi\tau_k}$, where the lifetime in state k is given by $\tau_k = \frac{2}{\sum_j A_{kj}}$, where A_{kj} [s⁻¹] is the probability per unit time for spontaneous transition from state k to state j . The corresponding broadening of the range of wavelengths for radiation emitted due to transitions from state k is given by $\Delta\lambda = \frac{hc}{\Delta E} \approx 2\pi c\tau_k$ [55].

Density broadening (also known as pressure or collisional broadening) arises from the influence of nearby particles on the emitting atom or ion. The collisional approach to calculating density broadening considers that collisions between the atom (or ion) and electrons cause broadening by interrupting the emission of the wave train. An uncertainty in the frequency of the emission is introduced, analogous to the uncertainty in the upper quantum state energy level that leads to natural broadening [56]. The quasistatic approach to calculating density broadening looks at the effect of the electric fields due to nearby particles, which perturb the atomic energy levels in the emitting atom or ion. Shifts in quantum state energy levels are known as Stark shifts, so this mechanism is known as Stark broadening [55]. The measurements of line widths of Stark-broadened lines can be used to determine ion densities in plasmas where density is high enough that Stark broadening is the dominant broadening effect.

Due to the Doppler effect, if a moving object emits a wave with a frequency ν_0 in its own reference frame, the frequency measured in the frame of a stationary observer is modified

by the effect of the object's motion. If the object is moving at velocity V towards or away from the observer, where V is positive if the object is moving towards the observer, or negative if moving away, then the observed frequency is given by $\nu = \nu_0(1 + \frac{V}{c})$. In a plasma, individual ions (and atoms) have a distribution of thermal speeds, towards and away from the point of observation, and the net effect is a spread in observed wavelengths and frequencies, *i.e.*, broadening of the observed spectral line. When thermal motion causes a particle to move towards the observer, the emitted radiation will be shifted to a higher frequency. Likewise, when the emitter moves away, the frequency will be lowered. If $F(V_L)$ is the particle distribution function for the velocity component along the line of sight between the particles and the point of observation, (*i.e.*, $F(V_L) dV_L$ is the fraction of particles with velocity between V_L and $V_L + dV_L$ along the line of sight), then the corresponding frequency distribution is $F(\nu) d\nu = F\left(\left(\frac{\nu}{\nu_0} - 1\right) c\right) \frac{dV_L}{d\nu} d\nu$. If the distribution for the velocity component along the line of sight is given by a Maxwellian:

$$F(V_L) dV_L = \sqrt{\frac{m_i}{2\pi T_i}} \exp\left(\frac{-m_i V_L^2}{2T_i}\right) dV_L$$

where m_i and T_i are the mass and temperature (in Joules) of the atom or ion, then the corresponding frequency distribution is

$$F(\nu) d\nu = \frac{c}{\nu_0} \sqrt{\frac{m_i}{2\pi T_i}} \exp\left(\frac{-m_i c^2 (\nu - \nu_0)^2}{2T_i \nu_0^2}\right) d\nu$$

which is a Gaussian profile (*i.e.*, of the form $g(x) = a \exp\left(\frac{-(x-b)^2}{2\sigma^2}\right)$, where b is the expected (mean) value, and σ is the standard deviation), with variance $\sigma^2 = \frac{T_i \nu_0^2}{m_i c^2} = \frac{V_{thi}^2 \nu_0^2}{2c^2}$, where $V_{thi} = \sqrt{\frac{2T_i}{m_i}}$ is the ion thermal speed. The full-width-half-maximum for a Gaussian profile $g(x)$ is given by $g_{FWHM} = 2\sigma\sqrt{2\ln(2)}$, so for frequency broadening due to the ion Doppler effect, the full-width-half-maximum is $\nu_{FWHM} \sim 1.7 \frac{\nu_0}{c} V_{thi}$. When Doppler broadening is the dominant broadening mechanism, as is the case for many applications, determination of ν_{FWHM} enables an estimation of the ion temperature along the line of sight of the diagnostic. Doppler broadening can be measured for either the majority ion species, or any prevalent impurity ion. For hydrogen plasmas, where the first ionisation energy is 13.6 eV, Doppler broadening of the hydrogen line is only useful for diagnosing cooler edge plasma. Therefore, measurement of the temperature of impurity ions with higher ionization energies is more practical in many cases. When the thermal equilibration time between the majority ions and the impurity ion is short, as is often the case for plasmas with moderate density [55], this measurement gives a good estimate of the majority ion temperature. In the magnetic compression experiment, where working gas was generally helium, the ion-Doppler diagnostic was focused on the He II line at 468.5nm.

While Doppler broadening of the observed spectral line leads to a frequency distribution with a Gaussian profile, natural broadening and density broadening result in frequency distributions with a Lorentzian profiles. Generally, temperature (*i.e.*, Doppler) and density broadening are the dominant broadening mechanisms - natural broadening is rarely observed directly, except in nebular environments. The combination of temperature broadening and density broadening leads to a Voigt profile for the frequency distribution. This is the convolution of Gaussian and Lorentzian profiles, and has no simple analytic form. Ion-Doppler measurements over magnetic compression, presented in chapter 4 were carefully analysed to assess the relative contributions of temperature and density broadening to the observed broadening of the He II line. In some cases, by assessing the quality of the fits of photon count against photon frequency profiles to Lorentzian and Gaussian profiles, line broadening that at first glance seemed to indicate a particularly significant temperature increase at compression, was deemed to be due to density broadening. With reference to data presented in [57, 58], an error in the temperature measurement (He II line at 468.5 nm) due to density broadening has been evaluated as ~ 17 eV for a density of $1.6 \times 10^{22} \text{ m}^{-3}$, and the error falls off in proportion to $n_e^{0.83}$. Density along the ion-Doppler chords is not directly evaluated, but from this information, along with observations of the variation of line averaged density with radius, sensible estimates to the contribution of density broadening to the indicated temperature increases can be evaluated on a shot-to-shot basis.

2.2.5 Optical diagnostics

The intensity of optical emission along vertical chords at the locations of the optical ports indicated in figure 2.2.1 was recorded over time. Optic fibres carry the signals to an electrically screened area where they are converted to electrical signals using photodiodes, then the electrical signals are digitised and stored for analysis.

Chapter 3

Magnetic Levitation

This chapter includes a description, with experimental results, of the main configurations tested to form a CT into a levitation field, which applies a radial force on the plasma that "levitates" it off the outer insulating wall. Configurations are presented in the chronological order in which they were tested. The original configuration, comprising six coils around a ceramic insulating tube, is the focus of section 3.1. Section 3.2 presents results from the configuration with six coils around a quartz insulating tube that had increased internal radius. Section 3.3 discusses the fluctuations that were routinely observed on poloidal field signals associated with CTs produced in standard MRT machines, but were absent for magnetically levitated CTs. This discrepancy led to the theory that mode-locking might be impeding coherent CT toroidal rotation, and was a consideration that led to the design of the 25-turn levitation coil configuration that is the focus of section 3.4. Along with improved toroidal symmetry of the levitation field, the 25-turn coil had a modified poloidal field profile, and closed the gaps located above and below the stack of six discrete coils in the original 6-coil configuration. This led to reduced plasma-wall interaction during CT formation, and significantly improved levitated CT performance. Section 3.5 outlines the semi-permeable shell concept, and the experiment that was conducted to test if it was the action of the levitation field itself, rather than plasma impurity considerations, that was responsible for the absence of fluctuations on levitated CT poloidal field signals, and for the relatively poor performance of levitated CTs compared with CTs produced in MRT machines. Shortly after that test, the magnetic compression experiment was scheduled to be decommissioned. Section 3.6 focuses on levitated CT performance in the final configuration tested during the extra time allocated to me to get data for this thesis. That configuration, comprising eleven coils around the quartz insulating tube had a levitation field profile similar to that of the multi-turn coil, and also led to significantly improved levitated CT performance. The strategy of matching the decay rates of levitation current and CT currents was developed in that configuration, and led to an understanding of the compressional instability that is discussed

in chapter 4. The method developed to experimentally measure the outboard equatorial CT separatrix is described in section 3.7. A comparison of total spectral power and levitated CT lifetime for the principal configurations tested is presented in section 3.8. This chapter concludes with a summary in section 3.9.

3.1 6-coil configuration, ceramic outer insulating wall



Figure 3.1.1: 6-coil configuration schematic and FEMM solution for levitation field

Figure 3.1.1(a) indicates, for the original configuration with six coils, the coils, chalice, stainless steel extension, and aluminum return current bars that carry axial current outside the insulating wall. The inner radii of the original ceramic (alumina - Al_2O_3) wall and the quartz (silica - SiO_2) wall that was tested later are shown in figure 3.1.1(b). This is an output plot from the open-source FEMM (Finite Element Method Magnetics) program [59], with 30 kA per levitation coil and an input current frequency of 800 Hz. Contours of ψ_{lev} , poloidal levitation flux, are shown, with the plot colour-scaling being proportional to $|B|$. FEMM models alternating currents as sinusoidal waveforms in time, so we chose $|t_{lev}| = 300 \mu\text{s}$ to be the quarter-period, giving a frequency of 800 Hz. In the 6-coil configuration, it was found that CT lifetimes could be increased by $\sim 10\%$ by firing the levitation capacitors at $t_{lev} \sim -300 \mu\text{s}$, well before firing the formation capacitors. This allows the levitation field to soak into the stainless steel above and below the wall, resulting in line-tying (field-pinning); magnetic field that is allowed to soak into the steel can only be displaced on the resistive timescale of the metal, which is longer than the time it takes for the CT to bubble-in to the containment region. Note that the principal materials used in the construction of the magnetic compression machine are indicated in figure 2.1.1. As confirmed by MHD simulations (see section 7.2), this line-tying effect is thought to have reduced plasma-wall interaction and CT impurity inventory by making it a little harder for magnetised plasma entering the confinement region

to push aside the levitation field. As described in section 6.1, FEMM models were used to produce boundary conditions for ψ , pertaining to the peak values of toroidal currents in the main, levitation, and compression coils at the relevant frequencies, for MHD and equilibrium simulations. For MHD simulations, boundary conditions for $\psi_{lev}(\mathbf{r}, t)$ and $\psi_{comp}(\mathbf{r}, t)$ are scaled over time according to the experimentally measured waveforms for $I_{lev}(t)$ and $I_{comp}(t)$.

The 7.5 cm high stainless steel extension indicated in figure 3.1.1(a) was an addition to the original configuration that also helped reduce the problem of plasma-wall interaction - in the original design without the extension, the ceramic insulating outer wall extended down an additional 7.5 cm. With the original levitation field profile from six coils, and without the extension, CTs were short-lived, up to $\sim 100 \mu\text{s}$ as determined from the poloidal B-probes embedded in the aluminum inner flux conserver at $r = 52 \text{ mm}$ (see figures 2.1.1, 2.2.1, and 2.2.2), compared with over $300 \mu\text{s}$ on MRT injectors with an aluminum outer flux conserver. CT lifetime was increased, up to $\sim 170 \mu\text{s}$, with the addition of the steel extension. The extension mitigated the problems of sputtering of steel at the lower alumina/steel interface, and of plasma interaction with the insulating wall during the formation process.

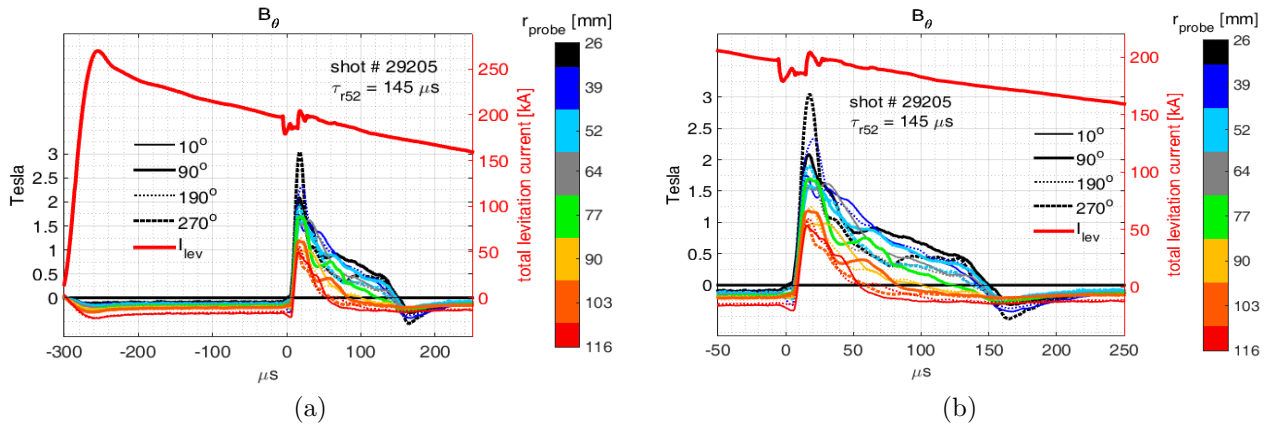


Figure 3.1.2: B_θ for shot 29205, six coils, ceramic insulating wall

Figures 3.1.2(a) and (b) (close-up view) shows $B_\theta(r, t)$, the poloidal field traces measured at the magnetic probes located in the chalice wall, for shot 29205. With optimisation of the machine settings (V_{form} , V_{lev} , I_{main} , t_{lev} and t_{gas} - see table 2.1.1) for longest lived CTs, this was a typical shot in the configuration with six coils and a ceramic (alumina) outer insulating wall, with the steel extension in place. As indicated in table 2.2.1, there are sixteen probes located in the chalice - eight of these are located at four different radii ($r = 39, 64, 90$, and 116 mm) at toroidal angle $\phi = 10^\circ$ and $\phi = 190^\circ$, and there are an additional eight probes at ($r = 26, 52, 77$, and 103 mm) at $\phi = 90^\circ$ and $\phi = 270^\circ$. Magnetic probe signals are colored by the r-coordinates of the probe locations, with toroidal coordinates of the probe locations

denoted by linestyle, as denoted in the plot legends. Note that B_θ is the field component parallel to the chalice surface in the poloidal plane. Total levitation current, measured with Rogowski coils, is also indicated (thick red lines, right axes). CT lifetime is gauged using the τ_{r52} metric (indicated in figures 3.1.2(a) and (b)), which is the time at which the average of the poloidal field measured at the two probes at $r = 52$ mm crosses zero.

For shot 29205, $t_{lev} = -300 \mu\text{s}$, so with a current rise time of $\sim 40 \mu\text{s}$ in the levitation coils, the poloidal levitation field measured at the probes reaches its maximum negative value at $t \sim -260 \mu\text{s}$, when the total levitation current is around 260 kA (~ 43 kA per coil). After its peak, the poloidal levitation field decays at the same rate as the levitation current. Formation capacitors are fired at $t = 0 \mu\text{s}$ and, referring to figure 2.1.2, it takes $\sim 10 - 20 \mu\text{s}$ for the gun (stuffing) flux to be advected up to the probe locations. The total levitation current has dropped to around 200 kA by the time the magnetised plasma bubbles into the confinement region. Until this time ($\sim 10 \mu\text{s}$), the poloidal field measured at the probes is purely the levitation field. When the magnetised plasma bubbles into the confinement region, it displaces the levitation field, and the polarity of the measured field reverses - the stuffing field has opposite polarity to the levitation field, *i.e.*, the toroidal currents in the main solenoidal coil and the levitation coils are in opposite directions. Over the next several tens of μs , during and after reconnection of poloidal field to form closed flux surfaces, the CT undergoes Taylor relaxation during which part of the poloidal flux is converted to toroidal flux. The CT shrinks and is displaced inwards by the relatively constant levitation field as the CT currents and fields decay resistively. Starting at the outer probes and progressing inwards towards the inner probes, the CT field measured at the probes is replaced by the levitation field. After $\sim 150 \mu\text{s}$, the poloidal field measured at all the B probes is the levitation field once again. Note that, when levitation field is being measured at the probes, that $|B_\theta|$ is larger at the outer probes, due to the $1/(r_{coil} - r_{probe})$ scaling of levitation field with levitation current in the external coils. On the other hand, when CT field is being measured at the probes, B_θ is larger at the inner probes, due to the $1/r_{probe}^2$ scaling of CT field with CT flux - poloidal field lines are bunched together progressively more at smaller radii.

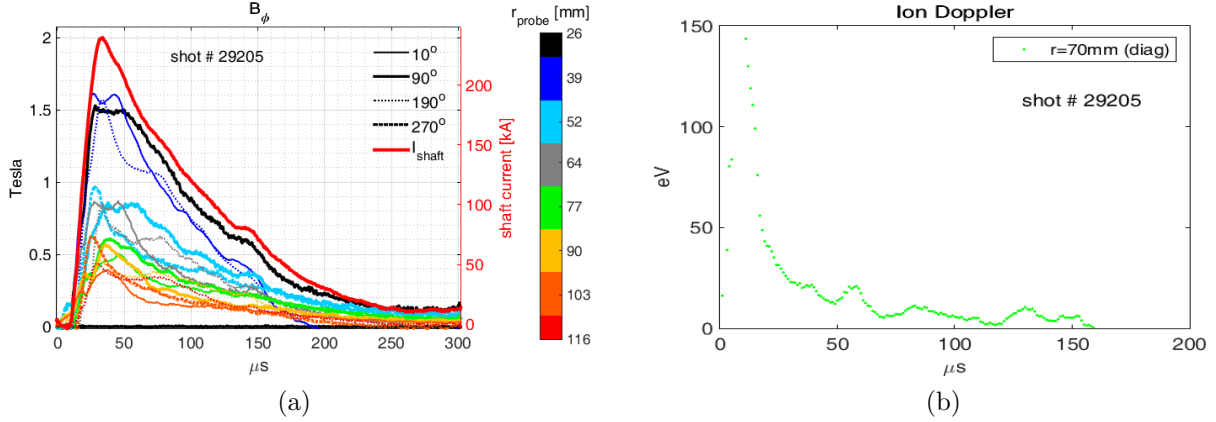


Figure 3.1.3: B_ϕ and T_i for shot 29205, six coils, ceramic insulating wall

Figure 3.1.3(a) shows the toroidal field, $B_\phi(r, t)$, measured at the chalice probes, for shot 29205. The toroidal field is due to poloidal shaft current in the aluminum chalice, and not due to poloidal CT current - recall that the field outside a toroidal solenoid is zero - in this analogy the plasma's poloidal current constitutes the solenoid's current. Shaft current is induced to flow in the metal surrounding the CT confinement area as the system tries to conserve the toroidal flux introduced at CT formation, and continues to decay resistively for several tens of microseconds after the CT currents have resistively decayed. I_{shaft} (thick red traces in figure 3.1.3(a), right axis) is calculated from $B_\phi(r, t)$ using Ampere's law. As the CT shrinks due to resistive decay of CT currents, compounded by mild magnetic compression due to being pushed on by the relatively constant levitation field, which decays much more slowly than the CT currents, increasing proportions of poloidal shaft current can divert from the initial paths in the aluminum bars shown in figure 3.1.1(a), and flow through the ambient plasma surrounding the CT. This will be clarified in section 4.2. Shaft current increases when it flows along the reduced inductance path through the ambient plasma. There is evidence in 3.1.3(a) of mild magnetic compression by the levitation field starting at around 130 μs on shot 29205. This is evident from the overall rise in shaft current at 130 μs , and from the increase in B_ϕ at the probes, particularly at the inner probes located at $(r, \phi) = (26 \text{ mm}, 90^\circ)$, $(39 \text{ mm}, 10^\circ)$, and $(52 \text{ mm}, 90^\circ)$. As outlined in section 3.6.1, this unintentional compression event was eliminated in the 11-coil configuration with the implementation of a levitation circuit modification.

Figure 3.1.3(b) shows an ion Doppler measurement for the same shot. Only the ion Doppler diagnostic looking along the green colored diagonal chord with its lower point $r = 70$ mm, indicated in figure 2.2.2, was functioning for this shot. A peak ion temperature measurement in that region, of around 150 eV, is recorded at around 15 μs , when plasma enters the confinement region. Viscous heating is the predominant ion heating mechanism during CT formation, as ions are rapidly advected up the gun into the confinement region.

Further ion acceleration occurs at early times around the confinement region entrance as open field lines reconnect to form closed flux surfaces. The jets associated with this reconnection process leads to additional ion viscous heating. The subsequent ion cooling due to thermal transport to the vessel walls has an offset due to collisional heat exchange with electrons that are being heated ohmically. The slight increase in ion temperature seen here at $\sim 130 \mu\text{s}$ is likely due to compressional heating associated with (unintentional) magnetic compression of the CT by the levitation field at around the same time. Interferometer electron density measurements are not available for shot 29205, so the error in measured ion temperature associated with density broadening can not be assessed for this shot. This error will be discussed in section 3.6.1 when presenting electron density and ion temperature measurements for shots for which both diagnostics are available.

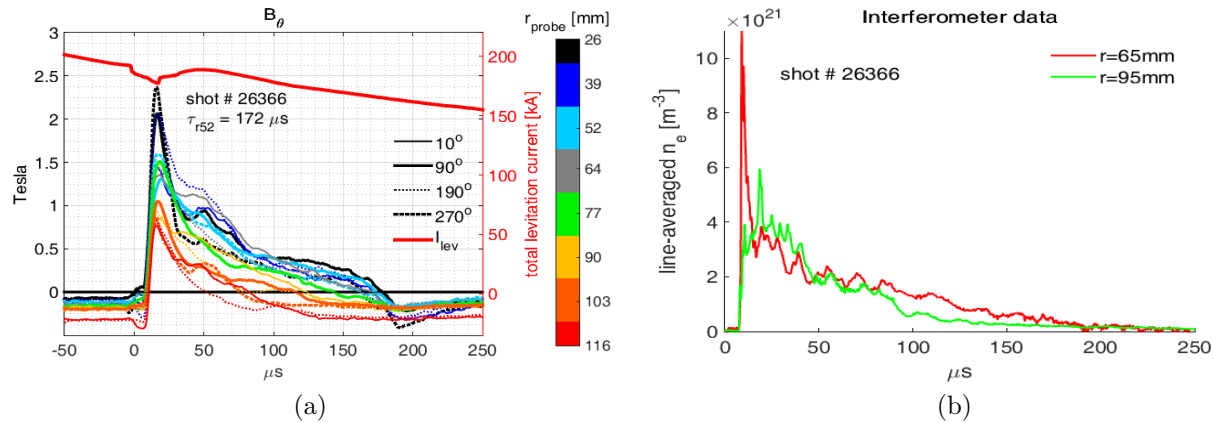


Figure 3.1.4: B_θ and n_e for shot 26366, six coils, ceramic insulating wall

Figure 3.1.4(a) shows the measured poloidal field for shot 26366, which, with $\tau_{r52} = 170 \mu\text{s}$, was the longest-lived shot taken in the 6-coil configuration with the ceramic outer insulating wall. Repeatability of long lived shots was poor, until the implementation of the levitation circuit modification described in section 3.6.1. Figure 3.1.4(b) indicates the line averaged density recorded for this shot. There are initial spikes in density at $\sim 15 \mu\text{s}$, when plasma enters the confinement region at high speed and is compressed against the upper chalice walls. MHD simulations indicate that closed CT flux surfaces have formed by around $30 \mu\text{s}$. The CT decays resistively and shrinks over time as it is pushed inwards by the relatively constant levitation field. The inward movement of the CT magnetic axis, around which density is expected to be concentrated, may explain the fact that the line-averaged density along the inner chord at $r = 65 \text{ mm}$ approaches and sometime surpasses (as it does in this shot) the density at $r = 95 \text{ mm}$. The innermost interferometer chord at $r = 35 \text{ mm}$ was generally not operational.

3.2 6 coil configuration, quartz outer insulating wall

An insulating wall with increased internal radius was tested (original alumina tube with $r_{in} = 144$ mm was replaced with a quartz tube with $r_{in} = 170$ mm). The resistive part of $\dot{\psi}$ is $\dot{\psi}_\eta = \eta \Delta^* \psi$ (see section 5.5.1), where Δ^* is the elliptic Laplacian-type operator used in the Grad-Shafranov equation, and η [m²/s] is the magnetic diffusivity, so CT lifetime should scale with l^2 , where l is some characteristic length scale associated with the CT. The radius of the inboard wall of the chalice at $z = 0$ is $r_w \sim 20$ mm. The minor CT radius for a given r_{in} would be approximately $a \sim \frac{r_{in} - r_w}{2}$, so assuming that $l \sim a$, we have $\frac{l_{quartz}^2}{l_{ceramic}^2} \sim 1.5$.

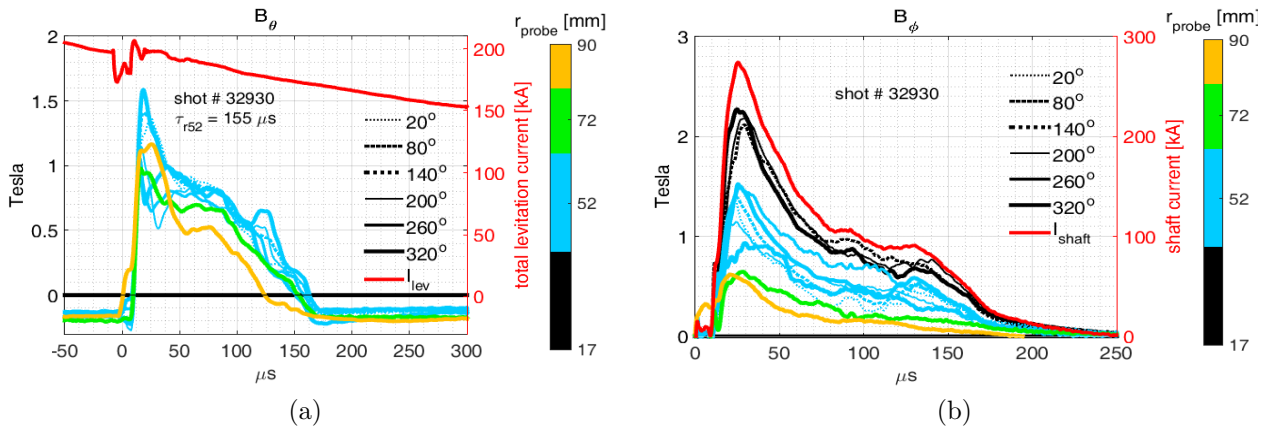


Figure 3.2.1: B_ϕ and B_θ for shot 32930, six coils, quartz insulating wall

From this rough estimate, an increase from ~ 170 μ s to ~ 260 μ s would be expected with the transition to a larger radius insulating tube, if the tube material was not changed. Figure 3.2.1(a) indicates how, contrary to expectations, CT lifetime decreased noticeably (~ 170 μ s to ~ 150 μ s) with the transition, so that in terms of CT lifetime, quartz was almost *twice* as bad as ceramic - shot 32930 produced one of the longest-lived CTs in the configuration with six coils around the quartz wall. The quartz wall led to more plasma impurities, and consequent further radiative cooling, and therefore an increased rate of resistive decay. Note that, for the configuration with six coils and the quartz wall, the chalice was replaced with a different model, which had the same geometric shape, but had fewer probes at different locations, which are indicated in the following table:

| | | | | | | | | | | |
|---------------|----|-----|-----|----|----|-----|-----|-----|-----|-----|
| r [mm] | 17 | 17 | 17 | 52 | 52 | 52 | 52 | 52 | 72 | 90 |
| ϕ [deg.] | 80 | 200 | 320 | 20 | 80 | 140 | 200 | 260 | 320 | 320 |

Table 3.2.1: r, ϕ coordinates of magnetic probes (intermediate configuration)

With six probes located toroidally every 60° at $r = 52$ mm, the updated chalice design was intended to give more information on MHD activity associated with toroidal modes. The primary motivation for the re-design was for implementation on other GF plasma injectors, which routinely indicated magnetic fluctuations with toroidal mode number $n = 2$ on the measured B_θ signals, as determined by examining the B_θ signals from probes located at the same radius 180° apart toroidally. Six probes toroidally spaced at the same radius could, in principle, enable identification of modes up to $n = 5$. The two inner probes on the original chalice at $r = 26$ mm were replaced with three probes at $r = 17$ mm. This change was implemented because it was considered that during the PCS experiments, the CT may be compressed to radii smaller than 26 mm, in which case the new inboard probes would give additional information. It turned out that the poloidal field measurements at the three inner probes was never trustworthy, so these measurements are not shown in figure 3.2.1(a). t_{lev} was set to $-300 \mu\text{s}$ for shot 32930. Looking at the rise of B_θ at the probe at $(r, \phi) = (52 \text{ mm}, 320^\circ)$ at $t \sim 120 \mu\text{s}$, there is evidence of mild (unintentional) magnetic compression associated with the mismatch between the decay rates of CT and external levitation currents.

Figure 3.2.1(b) shows the measured toroidal field, and the crowbarred shaft current, for shot 39230. Unlike the poloidal field measurements at the $r = 17$ mm probes, toroidal field measurements at those probes were acceptable. Again, the rise in I_{shaft} at $t \sim 120 \mu\text{s}$, provides evidence of mild, unintended, magnetic compression.

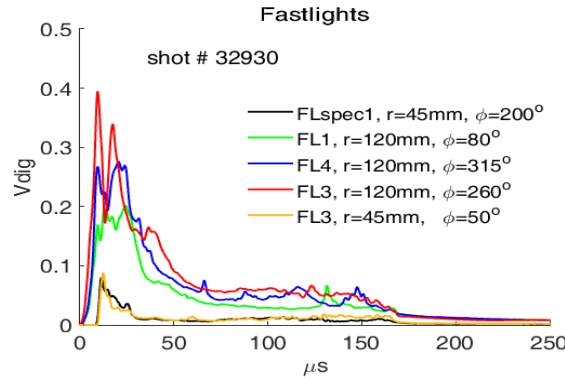


Figure 3.2.2: Optical intensity measurements for shot 32930, six coils, quartz insulating wall

Figure 3.2.2 indicates, for the same shot, the light intensity, presented in units of voltage induced in the photodiodes, measured along the vertical chords at the optical port locations for this configuration. The ports located at $r = 120$ mm have a view down the gun barrel, so the plasma breakdown is observed. Toroidal symmetry of the signal magnitude indicates an even breakdown. While the level of symmetry varies from shot to shot, repeated shots with asymmetric optical signals early in time can be an indication of a some electrode imperfection that would require correction. Optical intensity increases in regions of increased density

where line radiation intensity, which scales as n_e^2/Z_{eff} , is high. Bremsstrahlung radiation can also contribute to optical radiation emission, but is generally negligible compared with optical emission due to line radiation at the temperatures associated with this experiment. Optical intensity at the inner chords at $r = 45$ mm rises from zero later than at the outer 120 mm chords due to a delay in the plasma reaching the inner regions after it enters the CT containment area. Light intensity remains lower at the inner chords partly because the optical emission there is from the CT only, with no source from down the gun, where intra-electrode currents may continue to flow for extended times, and also due to the extended lengths of the parts of the outer chords that pass through the CT.

3.3 CT rotation and toroidal MHD modes

Before introducing the next configuration used to study levitated CTs, it is worth discussing some details relating to the lack of observation, during the magnetic compression experiment, of magnetic fluctuations with toroidal mode number $n = 2$, that were routinely observed on the measured poloidal field signals of CTs produced with standard MRT machines. The toroidal mode number is obtained by phase analysis of signals from probes located at different toroidal angles.

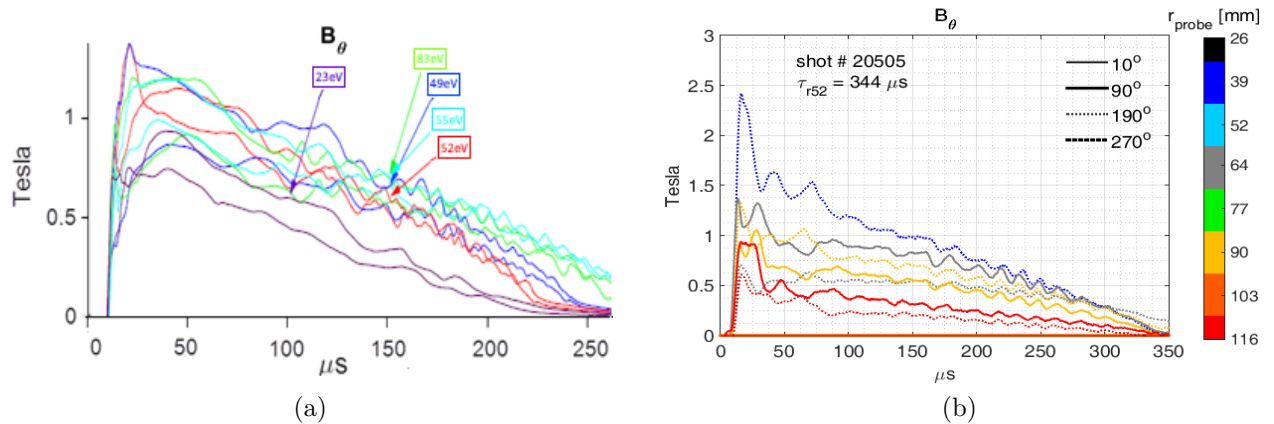


Figure 3.3.1: B_θ fluctuations with toroidal mode $n = 2$

Figure 3.3.1(a) shows B_θ traces at a single probe from a selection of shots taken with MRT-type injectors, from 2013, around the time when titanium gettering was first used on GF injectors. The burgundy traces are from two shots prior to titanium gettering, and do not have the $n = 2$ fluctuations exhibited by the shots after gettering. Electron temperature, as measured using Thomson-scattering, indicates that electron temperature increased by a factor of between two and four as a result of gettering. Ions and electrons cool and recombine if they

reach the walls of the vacuum vessel. Gettering materials such as titanium and lithium act as a reservoir that absorbs these cold particles and reduces the rate at which they are "recycled" back into the plasma [60]. Figure 3.3.1(b) shows B_θ traces, also with $n = 2$ fluctuations, from the best shot taken on the magnetic compression experiment during the period when the insulating outer wall was replaced with an aluminum flux conserver. This configuration was implemented in order to confirm (which it did) that the initial poor performance of levitated CTs (with six coils and before the stainless steel extension shown in figure 3.1.1(a)) was not due to an inherent machine defect (*e.g.*, gas injection, electrode conditioning etc.) and was indeed due the unknowns associated with CT formation into a levitation field. Note that only some of the magnetic probes were functioning for this shot. Since the probes at $r = 52$ mm were also not working, the lifetime parameter τ_{r52} is estimated for shot 20505 by interpolation using the field traces at $r = 39$ and $r = 64$ mm.

These $n = 2$ fluctuations are evidence of coherent CT toroidal rotation, and were absent on shots taken on the magnetic compression device with the outer insulating wall and levitation coils in place. There was concern that rotation could be impeded by mode-locking caused by toroidal asymmetry in the levitation field, introduced by the gaps in toroidal levitation current associated with single-turn coils. A set of six new coils (coil outline is depicted in figure 2.1.3), which reduced the field error, was manufactured. Analysis with the MAGNET code, an add-on to the Solidworks program, indicated that field asymmetry would be improved significantly, by a factor of ~ 10 , with the new coils. Also, a 25-turn, high inductance ($160 \mu\text{H}$) coil was experimented with - this reduced the original field error by a factor of ~ 100 - see section 3.4. It turned out that levitation field asymmetry associated with the original single-turn coils was not likely a problematic issue at the level of performance achieved. At the settings for low-flux CTs, no improvement in CT lifetime or symmetry was seen with either the new set of discrete coils or the 25-turn coil, and there was no additional evidence of CT rotation, or that a mode-locking issue had been alleviated. X-ray phosphor videos indicated the likelihood of, but couldn't confirm CT rotation. In retrospect, ion Doppler or Mach probe diagnostics would ideally have been used to systematically check for rotation. The $n = 2$ fluctuations observed on B_θ signals with standard MRT machines may be connected with internal reconnection events that occurred upon exceeding a threshold in CT temperature that was not attained on the magnetic compression experiment due to radiative cooling associated with impurities from the insulating wall. As described in section 3.5.1, $n = 2$ fluctuations were also observed when the levitation field was allowed to soak through a relatively resistive stainless steel outer flux conserver. In that case, the levitation field is present but the impurity cooling problem is alleviated. Coherent CT rotation was confirmed later in the experiment; $n = 1$ fluctuations regularly appeared on the B_θ traces when CT toroidal field was increased with the use of 80 kA crowbarred formation current. This exper-

iment presented in section 3.6.2.

3.4 25-turn coil

A 25-turn single-conductor levitation coil was built to test if levitated CT performance could be improved by:

1. Reducing the field errors associated with the 6-coil configuration
2. Reducing plasma-wall interaction during the formation process

To test the first hypothesis, the coils was designed with a single length of conductor (insulated AWG-4 copper wire). To test the second hypothesis, the coil was made with a height that filled the gaps that were present above and below the 6-coil stack, outboard of the insulating wall. Filling the gaps resulted in a large concentration of poloidal flux and resultant magnetic pressure at the top and bottom of the coil - this proved not to be an issue with sufficient clamping force.

3.4.1 Coil design parameters

| 25-turn coil parameters | | | | | | | |
|-------------------------|------------------------|-------------|--|--|-----------|---------------------|--|
| d[m] | d (inc. insul.)[m] | # turns | coil height [m] | internal diameter [m] | R' [mΩ/m] | L (length wire) [m] | |
| 0.005189 | 0.0096 | 25 | 0.24 | 0.386 | 0.815 | 30.31636911 | |
| R [mΩ] | L_calc (air-core) [μH] | L_FEMM [μH] | rise time [μs] (from SPICE using L_FEMM) | I_max at 15kV [kA] (from SPICE using L_FEMM) | | | |
| 24.70784 | 220 | 116 | 180 | 16 | | | |

Table 3.4.1: 25-turn coil parameters

Table 3.4.1 shows the parameters that were chosen for the 25-turn coil. A lower bound on the coil inductance was imposed by the number of turns required to cover the entire height of the quartz wall. The upper bound on inductance was set by the maximum desired current rise time, and the minimum desired levitation field, which depends on the coil current, which is constrained by the available capacitor voltage and capacitance. The value of 220 μ H for the inductance of the air-cored coil with these parameters were obtained using inductance

calculators[61, 62], which take the coil-wire's insulation thickness into account. This value was confirmed by an actual measurement when the coil was made. FEMM was used to calculate the value of $116 \mu\text{H}$ for the inductance with the aluminum chalice present inside the coil.

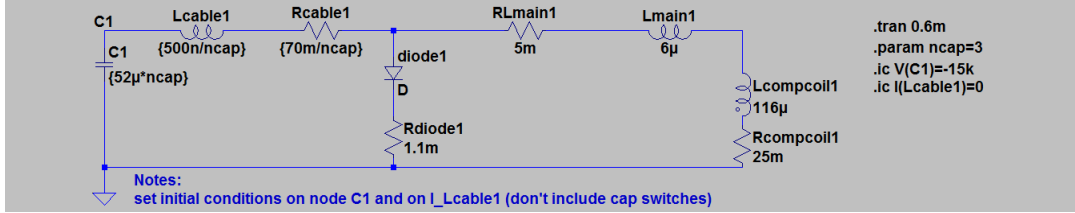


Figure 3.4.1: LT-SPICE model schematic for the 25-turn coil

Figure 3.4.1 shows the LT-SPICE model used to simulate the coil currents and rise times. The main (holding) $6 \mu\text{H}$ inductor, and diode (stack) in the model, are depicted at the bottom-right of figure 2.1.3.

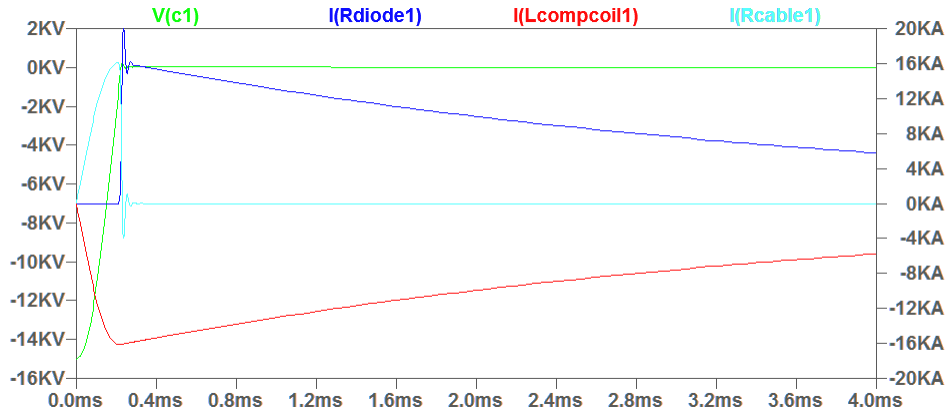


Figure 3.4.2: Circuit model outputs for 25-turn coil - no series resistance

Figure 3.4.2 shows the traces of $V_{capacitor}$, I_{diode} , I_{coil} , and I_{cable} at $V_{lev} = 15 \text{ kV}$ obtained from the model. Note that the main inductor-driven crowbarred current continues to flow in the diode stack $I(Rdiode1)$ and coil $I(Lcompcoil1)$ after the capacitor voltage, and the current in $Rcable1$, change polarity and drop to zero (refer to figure 3.4.1). The current in the coil ($\sim 15 \text{ kA}$ with $V_{lev} = 15 \text{ kV}$) at $t = t_{rise} = \sim 180 \mu\text{s}$ was used in FEMM along to evaluate the resultant levitation field, with t_{rise} (the time it takes for the levitation current in the coil to attain its maximum value) determining the frequency input to FEMM to be $f = \frac{1}{4(t_{rise})} = \sim 1.4 \text{ kHz}$.

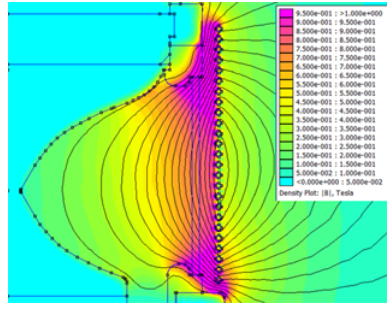


Figure 3.4.3: FEMM output for the 25-turn coil

The FEMM output for the 25-turn coil is shown in figure 3.4.3. Compared with levitation field profile for the 6-coil configuration, depicted in figure 3.1.1(b), it can be seen that the field profile with the 25-turn coil should fix the problem associated with the gaps above and below the 6-coil stack. Levitation field can easily be displaced through those gaps as magnetised plasma enters the pot at high speed - ions are the free to impact the wall and sputter high Z impurities into the plasma, resulting in performance degradation due to radiative cooling. It seems reasonable that, on the 6-coil setup, a levitation field that is strong enough to keep the CT off the insulating wall above and below the coil stack may be too strong to allow successful plasma entry to the pot. When the levitation field is too strong, the entry to the CT containment region can be partially blocked, especially when line tying effects impede entry further when the field is allowed to soak well into the steel outboard of the entry to the containment region. As shown in section 7.2.2, the MHD simulation code that we developed confirms that a field profile like that associated with the 25-turn coil reduces plasma-wall interaction during the formation process. The major drawback with the 25-turn coil was that it wouldn't allow fast compression because of its extended current-rise time. $t_{rise} \sim 180 \mu\text{s}$ cf. $\sim 20 \mu\text{s}$ for the discrete coils in the compression circuit; in any case it would probably break if placed under the high $\mathbf{J} \times \mathbf{B}$ forces associated with large compression currents.

3.4.2 Coil manufacture

To make the coil, a 30 m length AWG-4 wire was wound on a dense foam cylindrical core that had been machined to size (and wrapped in Mylar sheet for subsequent removal of the coil), and the winding was wrapped in eight layers of heavy fiberglass cloth. That assembly was then placed in a mould that was made by gluing the base of a hollow cardboard tube (~ 42 cm inner diameter, designed for making concrete pillars) to a thick cardboard base. The top of the tube was sealed off with plastic sheeting and a moderate vacuum (~ 0.5 psi) was established in the assembly by attaching a plastic tube (1 cm inner diameter) leading from the vacuum pump to a sealed feedthrough made at the bottom of the cardboard tube. Another sealed

feedthrough was made at the top of the cardboard tube through which activated epoxy resin was pumped at up to 30 psi. This arrangement had the desired result of reducing the number and size of structurally-detrimental air bubbles in the fiberglass as it set. Upon setting, the coil was removed from its mould for finishing.

3.4.3 Levitated CT performance with the 25-turn coil

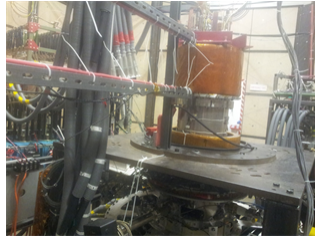


Figure 3.4.4: 25-turn coil on machine

Figure 3.4.4 shows the 25-turn coil on the machine with a 2 m long feedthrough intended to reduce field error. In the 6-coil configuration, the longest-lived CTs were achieved at generally low settings for V_{form} , I_{main} , and V_{lev} (note that for optimal CT performance, these machine settings scale with one another), resulting in low-flux CTs. For example, V_{form} and I_{main} would typically have been 12 kV and 45 A, compared with 16 kV and 70 A for best performance on MRT machines. Note that $V_{form} = 16$ kV correspond to a peak formation current of $I_{form} \sim 700$ kA, while $I_{main} = 70$ A corresponds to a gun flux of around 12 mWb. Increasing these parameters on the magnetic compression injector in the 6-coil configuration led to increased impurity levels and degraded lifetime further. Initial testing on the 25 turn coil configuration was done at typical optimal low flux settings of $V_{form} \sim 12$ kV, $V_{lev} \sim 12$ kV, and $I_{main} \sim 45$ A. At these setting, there was no real improvement in CT lifetime, or any indication that the CTs produced was behaving any differently than previously. This indicated that the improved toroidal symmetry of the field produced with the coil did not benefit CT performance. However, one of the advantages of the single continuous coil winding is that it facilitated the addition of resistance to the circuit. The decay time constant of the crowbarred levitation current is determined by $\tau_{decay} \sim L/R$, and can be reduced by adding resistance to the circuit in series with the cable between the coil and the main inductor. Note that the cable resistance is included in the resistance denoted as $RLmain1$ in the LT-SPICE model depicted in figure 3.4.1.

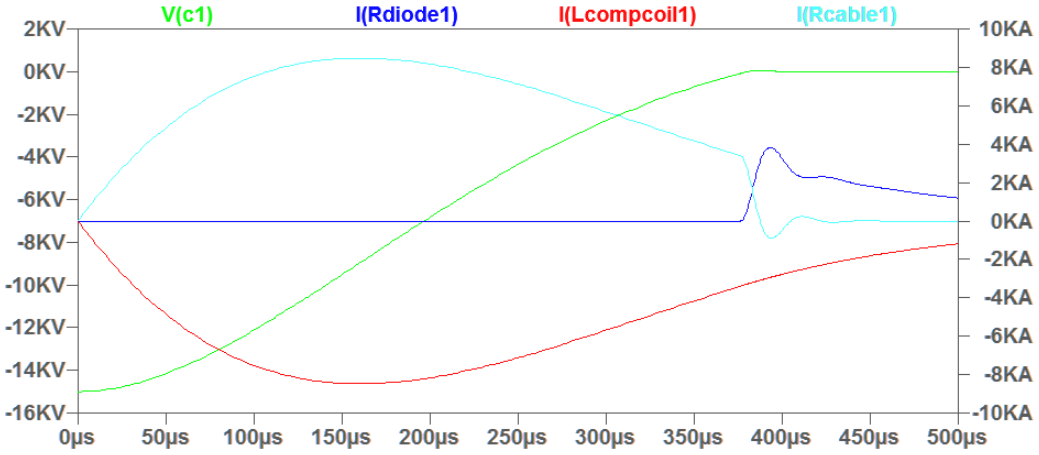


Figure 3.4.5: Circuit model outputs for 25 turn coil - 1Ω series resistance

As shown in figure 3.4.5, with 1Ω resistance in series, the current in the coil decays to zero from its peak at $\sim 160\mu\text{s}$ to $< 2\text{kA}$ over $\sim 300\mu\text{s}$, which is around the total time over which the CTs decay completely after bubble in. With the original circuit design, the levitation field would decay very slowly relative to the CT (see figure 2.1.4), so the CT is being effectively compressed by the levitation field. In fact, as discussed later in section 3.6.1, due to this effect, the asymmetry or instability that was apparent during practically every instance of magnetic compression was also evident in most levitation-only shots. By matching the levitation field decay time to that of the CT, the CT is allowed to retain the size that it would have if it was being held in place and stabilised by eddy currents induced in an outboard flux-conserver instead of an outboard levitation field. This will be discussed further, and it will be shown in section 3.7 that CTs retained more volume when the levitation field decay time was optimised.

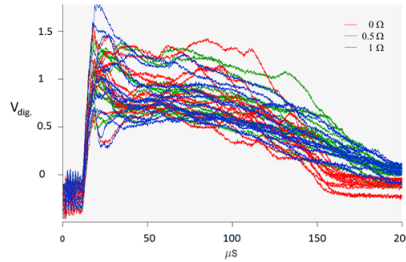


Figure 3.4.6: Performance improvement with series resistance (25-turn coil)

When resistance was added to the circuit, CT lifetimes in the 25-turn coil configuration increased by up to 20%, as indicated in figure 3.4.6, which shows traces of measured B_θ at a single magnetic probe at $r = 52\text{ mm}$ for shots with different series resistances (one trace per shot). It can be seen how, with the addition of series resistance, the B_θ signals also indicate a smoother decay that is consistent with a reduction in fluctuations that are associated with MHD activity due to unintentional magnetic compression.

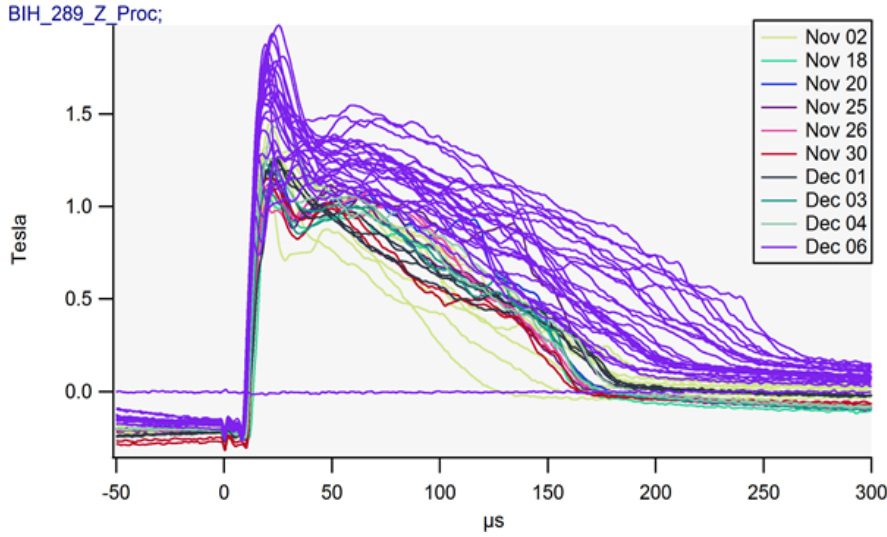


Figure 3.4.7: Improved performance with the 25-turn coil at high flux settings

When the coil was tested at higher formation settings such as $V_{form} = 16$ kV, $V_{lev} = 16$ kV, and $I_{main} \sim 60$ A, CT lifetimes improved dramatically. Figure 3.4.7 shows the performance improvement with the 25-turn coil at the higher formation settings. Traces are of measured B_θ at a single magnetic probe at $r = 52$ mm, for a selection of shots (one signal per shot). The traces from the shots taken with the 25-turn coil in place at the higher formation settings (on December 6th 2015) are in dark purple. The remaining traces in figure 3.4.7 are from shots taken in the 6-coil configuration with the quartz wall, at low-flux settings (recall that higher formation settings led to performance degradation in the 6-coil configurations).

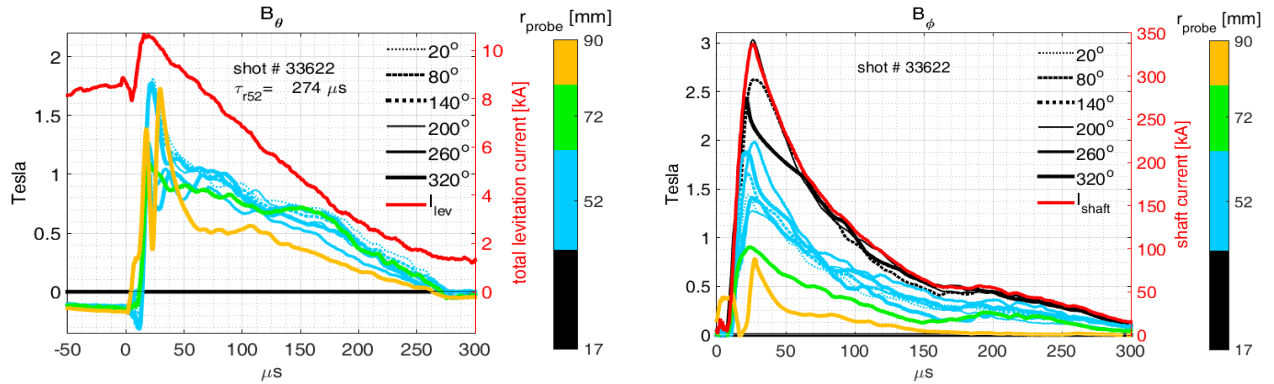


Figure 3.4.8: B_θ and B_ϕ for shot 33622, 25-turn coil, quartz insulating wall

Figures 3.4.8(a) and (b) show traces of measured B_θ and B_ϕ at the chalice magnetic probes for shot 33622 in the 25-turn configuration. As indicated in figure 3.4.8(a) (right axis), with 1Ω series-resistance in the levitation circuit, the coil current peak is ~ 10 kA and decays at around the same rate as the CT currents. The single levitation capacitor was fired at $t_{lev} = -150$ μs, which is the rise time of the levitation current for this configuration. Comparing

figures 3.2.1(a) and 3.4.8(a), it can be seen that the CT lifetime increased substantially, by almost 80% from $\tau_{r52} = 155 \mu\text{s}$ to $\tau_{r52} = 274 \mu\text{s}$. It can also be seen how, for the 25-turn coil configuration, the levitation current increases by a much greater proportion when the plasma enters the confinement region at around 15 μs . As discussed below, this is due to the increased inductance of the levitation coil in the 25-turn coil configuration.

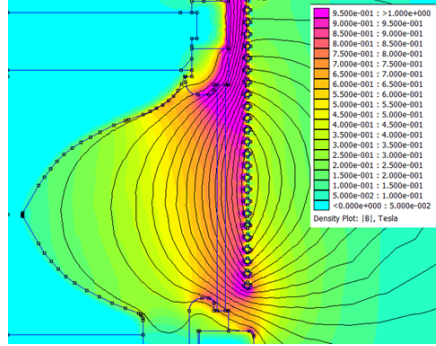


Figure 3.4.9: FEMM model, 25-turn coil moved up 25 mm, 10 kA at 1250 Hz

The 25-turn coil was tested after being shifted up 25 mm – from FEMM (see figure 3.4.9), the field at the top of the quartz wall is unchanged while the field at the bottom was then comparable to that with the standard six coils at 30 kA/coil. On the same day (approximately the same machine conditions), 40 shots with the coil down, then another 40 with it shifted up 25 mm, were taken. Over 10 of the shots with the coil down had lifetimes $>150 \mu\text{s}$, compared with just one shot with the coil up. This indicated that having a coil outboard of the bottom of the quartz wall was partly responsible for the improved performance. Due to machine geometry constraints, a similar test with the coil moved down could not be done.

There was some discussion about the cause of the benefit seen with the 25-turn coil. One candidate for the improvement was the increase in the ratio, between the coil inductance and the main circuit holding inductor, that was associated with the 25-turn coil. When magnetised conducting plasma enters the pot (confinement region) it reduces the inductance of the part of the levitation circuit that includes the levitation/compression coil and the material that the coil encompasses. The levitation current increases when the coil inductance is reduced when plasma enters the pot. If the percentage rise of the levitation current is maximised, it means that levitation current prior to plasma entry to the pot can be minimised. This reduction in levitation field reduces the likelihood that the levitation field will be strong enough to partially block plasma entry to the pot, while still allowing the field that is present when the plasma does enter to be strong enough to levitate the plasma away from the insulating wall.

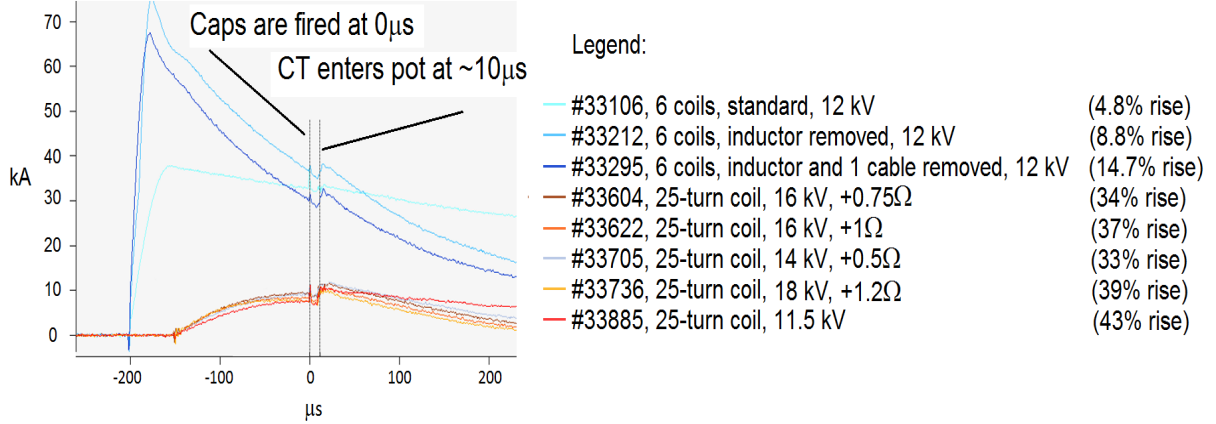


Figure 3.4.10: Percentage current rise for various levitation circuit configurations

The currents indicated in figure 3.4.10 are for one of the six coils (blue traces), and for the 25-turn coil (red → orange traces). Comparing the data from shots 33016 and 33885, the percentage rise in levitation current when plasma enters the pot is up to nine times higher with the multiturn coil. For the discrete coils, $L_{coil}/L_{main} = 600 \text{ nH}/6 \mu\text{H} = 0.1$. For the multiturn coil, $L_{coil}/L_{main} = 116 \mu\text{H}/6 \mu\text{H} \sim 20$. The two darker blue traces in figure 3.4.10 are from shots 33212 and 33295, taken when the main inductors were removed from the levitation circuit, which has the effect of increasing the peak levitation current at the same V_{lev} , and increasing the decay rate of levitation current as $\tau_{LR} \sim L/R$ is reduced. This configuration was experimented with on 6-coil configuration, but no benefit to CT lifetime was observed. Shot 33295 was taken after also removing one of the two $5 \text{ m}\Omega$, 500 nH coaxial cables that connect the main inductor to the coil for each of the six levitation coil circuits. Note that levitation capacitors were prefired $200 \mu\text{s}$ before formation for the shots indicated here with the 6-coil setup (blue traces), in order to achieve the line-tying benefit that is discussed in section 3.1. On the 25-turn configuration coil (red → orange traces), the levitation capacitors were prefired as late as it is possible to (at $|t_{lev}| \sim t_{rise} \sim 150 \mu\text{s}$ before formation) while maintaining maximum field at the time of plasma entry to the CT confinement region. As discussed in section 3.6, the line-tying strategy was not useful when the field profile was optimised to reduce plasma-wall interaction.

The 25-turn coil proved to be beneficial because it reduced plasma-wall interaction at high formation settings. At low formation settings, without addition levitation circuit series resistance, CT lifetimes showed no improvement over those seen with the 6-coil configuration. This indicates that neither improved toroidal symmetry of the field produced, nor the increase of the ratio between the coil inductance and the main circuit holding inductor, were wholly responsible for the improvement seen, although they may have enhanced performance at the settings for high-flux CT production. That the inductance ratio increase was not wholly responsible for the improvement is further confirmed by the fact that no benefit was seen

when the main inductors were removed from the levitation circuit on the 6-coil setup, and supported again by the performance improvement observed with the 11-coil configuration (which had a levitation field profile similar to that of the 25-turn configuration) at high formation settings with approximately the same coil inductance, see section 3.6. The benefit seen with series resistance in the 25-turn coil levitation circuit was a completely separate effect that was obtained by optimizing the decay rate of levitation current to match the decay rate of CT currents.

3.5 Semi-permeable shell

One of the proposals for a configuration that would allow repetitive magnetic compression while retaining the possibly stabilising benefits of a metal wall, eliminating the need for a levitation field and the problems associated with plasma impurity contamination due to the insulating outer wall, was the semi-permeable shell system. This would involve a thin-walled metal tube (shell) in place of the insulating wall. A thin inconel shell with a thickness of ~ 0.5 mm was the most likely candidate for success. Inconel was chosen because of its relatively high resistivity and good structural properties. The classical skin depth formula is

$$\delta_{skin} = \sqrt{2\eta' / (\mu_0 \omega)} \quad (3.5.1)$$

The angular frequency of the compression field can be calculated by approximating the compression waveform as a sine wave. The rise time of the compression current is around $20\ \mu\text{s} \Rightarrow \omega \sim 2\pi / (4 \times 20 \times 10^{-6}) \sim 7.8 \times 10^4 \text{ rad/s}$. Using the values $\eta'_{inconel} = 1.03 \times 10^{-6} [\Omega - \text{m}]$ and vacuum permeability $\mu_0 = 4\pi \times 10^{-7} [\text{H/m}]$, this gives $\delta_{skin} \sim 5 \text{ mm}$. In principle the amplitude of a field would be attenuated by a factor of $1/e \sim 0.37$ by a conductor with thickness δ_{skin} , so the semi-permeable shell concept initially seemed feasible.

An analysis was undertaken using FEMM to help calculate the heating of the inconel shell. The compression current waveform was Fourier decomposed using MATLAB and its component frequencies and amplitudes were successively input to FEMM in a loop via a LUA script. For each FEMM analysis based on a single amplitude and frequency, the current density in the shell was calculated to find the corresponding temperature rise in the shell using the shell-material's resistivity and specific heat capacity, and the duration of the compression current. The temperature increments due to each Fourier harmonic were then added to find the final estimated maximum temperature. Using this process, and also the more straightforward method using FEMM with a single frequency and amplitude based on the approximation of the compression waveform as a sine wave, it was found that the central region of the inconel shell's cross-section would reach a temperature of $\sim 900^\circ\text{C}$ after just one

shot (melting point of inconel is 1400°C), although that estimate didn't account for thermal diffusion. The maximum pressure due to $\mathbf{J} \times \mathbf{B}$ forces at magnetic compression on the shell was calculated to be 30 MPa, based on FEMM outputs. With inconel as the semi-permeable shell material, the concept appeared worth a try - compressional heating of the shell was deemed acceptable, and it was envisaged that the thin shell could be structurally supported against compressional forces by welding a hundred or so steel pins (diameter ~ 2 mm, length ~ 1 cm) pointing radially outwards from the outer tube surface and embedding it in an epoxy tube.

A similar analysis was used to assess the feasibility of using a 30 μm (porous) coating of tungsten on the existing alumina (Al_2O_3) wall. The classical skin-depth for porous tungsten with an estimated resistivity of $\eta' = \eta'_W/2 = 1.1 \times 10^{-7} [\Omega - \text{m}]$, (η'_W is the resistivity of pure tungsten) at $\omega = 8.16 \times 10^4$ rad/s, is $\delta_{\text{skin}} = 1.6$ mm. The method outlined above indicated that the field would be attenuated by just 17%, but that part of the porous coating would reach a peak temperature of $\sim 18000^\circ\text{C}$ (melting point of pure tungsten is 6800°C). Another major issue was that the bonding strength of the coating to the alumina was unknown, and the coating would have to withstand huge pressure forces. Maximum pressure on the shell was calculated to be 20 MPa. Overall, the concept of using a thin coating of tungsten on an alumina shell appeared out of reach due to excessive heating and material bonding issues.

The same procedure indicated that a 30 μm coating of lithium would melt and be probably be ionized over a single magnetic compression shot. A peak temperature of $\sim 12000^\circ\text{C}$ at compression would be attained (melting point of lithium is 180°C), and 780 kJ of energy per mole of lithium would be imparted - the 1st and 2nd ionization energies of lithium are 520 and 7300 kJ/mol. This raised the concern that plasma contamination with lithium impurities might be an issue when lithium was used as a gettering agent during magnetic compression. Time-resolved spectroscopic analysis could have helped to clarify this, but was not available during the experiment.

3.5.1 Stainless-steel shell test

A test with a stainless steel outer flux conserver was conducted largely with the goal of observing the effect of allowing levitation field to interact with a CT that was supported with a conducting wall. This investigation was largely driven by concern over the absence, as discussed in section 3.3, of the $n = 2$ fluctuations, commonly observed with MRT injector-produced CTs, on levitated CT B_θ signals. With a stainless shell with wall thickness 3.8 mm, wrapped in three layers of 1.5 mm diameter copper wire, replacing the insulating wall, the maximum CT lifetime was only $\sim 150 \mu\text{s}$ even after around 600 cleaning shots *cf.* $\sim 200 \mu\text{s}$

with the aluminum shell (standard MRT machine) after around 600 cleaning shots. Compared with the aluminum flux conserver, the resistivity of the stainless steel flux conserver is increased by a factor of ten, leading to more magnetic field soakage, and consequent impurity sputtering, radiative cooling, and reduced CT lifetimes. After lithium coating, lifetime increased to $\sim 250 \mu\text{s}$ with hydrogen plasmas, and $\sim 200 \mu\text{s}$ with helium plasmas.

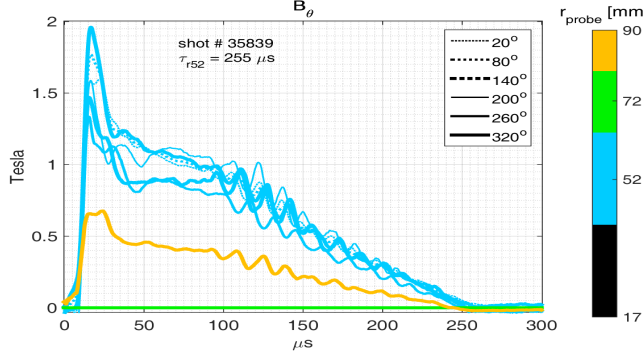


Figure 3.5.1: B_θ for CT with the stainless steel flux-conserver

With hydrogen, CTs often exhibited $n = 2$ fluctuations on the B_θ signals, as indicated in figure 3.5.1. Note that not all of the magnetic probes were functioning - the signals relevant to the probes at $r = 17 \text{ mm}$ and $r = 77 \text{ mm}$ have been zeroed out in figure 3.5.1. Removing the copper wire resulted in a reduction of CT lifetime to $\lesssim 160 \mu\text{s}$ for hydrogen and $\lesssim 190 \mu\text{s}$ for helium, both without apparent $n = 2$ activity. Placing the 25-turn coil around the bare steel shell resulted, with a short delay ($|t_{lev}|$) between firing of levitation and formation capacitors, and low B_{lev} , in CT lifetimes of $\sim 210 \mu\text{s}$ with hydrogen, $\sim 250 \mu\text{s}$ with helium, with $n = 2$ behaviour being observed in both cases. With $|t_{lev}| > 300 \mu\text{s}$, and low B_{lev} , the CT life was maximized, $\sim 270 \mu\text{s}$ with He, with occasional weak $n = 2$. With high B_{lev} , especially at long $|t_{lev}|$, the CT lifetimes were less consistent, with behaviour that is characteristic of unintentional low-level compression - note that these tests were done without series resistance in place in the levitation circuit. With high B_{lev} , $n = 2$ fluctuations were present only with short $|t_{lev}|$.

This set of results confirms that a high, relatively constant levitation field is detrimental to CT performance - as shown in sections 3.4.3 and 3.6.1, performance is better when the levitation field decays at the same rate as ψ_{CT} . The fact that CT lifetimes with the steel shell were lower than the CT typical lifetimes observed an aluminum outer flux-conserving shell, but were increased when the 25-turn coil was placed around the steel shell suggests that stainless steel is not a good material with regard to impurities and that levitation field can reduce impurity levels by keeping the CT off the wall. The improvement seen with the levitation field was enhanced by increasing $|t_{lev}|$ through the effect of line-tying, as outlined in section 3.1. When the levitation field was increased, the unintentional low-level compression is

more effective and starts earlier in time resulting in diminished performance. With long $|t_{lev}|$ and high B_{lev} , the effect of blocking the entry of magnetized plasma to the CT containment region also become problematic, especially because the levitation field is being tied in the entire resistive shell.

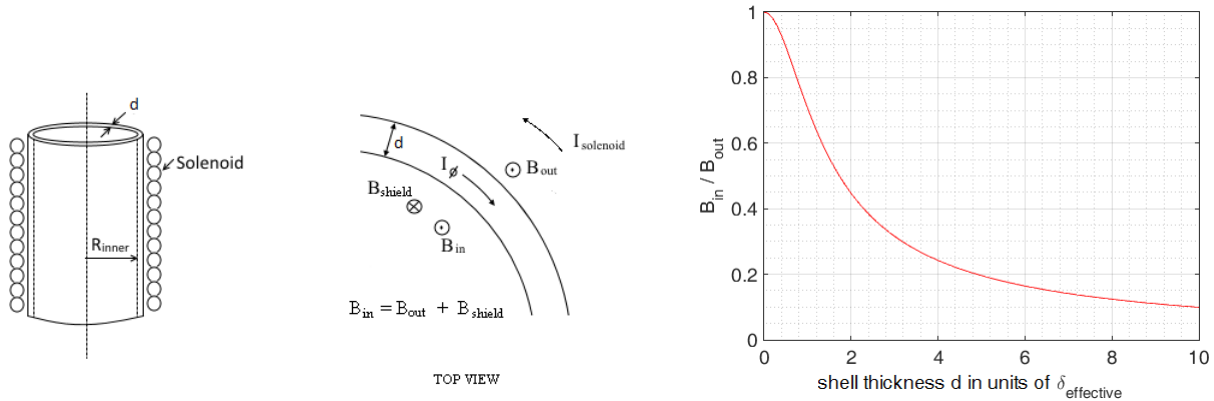
It has been confirmed that $n = 2$ fluctuations are a sign of internal MHD activity associated with increased electron temperature, as discussed in section 3.3. It was thought that this correlation, and the absence of the fluctuations on levitated CTs, was a sign that levitated CTs were colder than flux-conserved CTs, and the problems encountered with plasma wall interaction in the levitation configurations made that scenario more likely. However, the longest-lived CTs produced with the 25-turn configuration endured for up to 10% longer than, and may therefore be assumed to be hotter than the CTs produced in the configuration with the stainless steel flux conserver. It may be that the levitation field acts to damp out helically propagating magnetic fluctuations at the outboard CT edge and that internal MHD activity is relatively unchanged. The $n = 1$ magnetic fluctuations (see section 3.6.2), observed when 80 kA additional crowbarred shaft current was applied to the machine in the eleven coil configuration, partially confirmed coherent toroidal rotation of levitated CTs, and may have been a result of more vigorous MHD activity that remained apparent despite damping.

3.5.2 Effective skin depth for thin shells

As outlined in section 3.5, the concept of using an inconel semi-permeable shell configuration seemed feasible. However, towards the end of the series of tests with the stainless steel shell, it was realised that when $d \sim \delta_{skin}$ (d is the shell thickness and δ_{skin} is the classical skin depth - equation 3.5.1), the interior of a shell with inner radius R_{in} is effectively screened from an externally applied field if:

$$d > \delta_{eff} = \frac{\delta_{skin}^2}{R_{in}} \quad (3.5.2)$$

This relationship [63, 64], which effectively scuppered the semi-permeable shell concept, can be derived as follows:



(a) Schematic of thin conducting shell with external solenoid

(b) Shielding of external B_{out} versus d in units of δ_{eff}

Figure 3.5.2: Electro-magnetic shielding in a thin conducting shell

With reference to figure 3.5.2(a), when current flows in a solenoid surrounding an electrically conducting shell, the field inside the shell is $B_{in} = B_{out} + B_{shield}$, where B_{out} is the field applied external to the shell, and B_{shield} (with orientation opposite to that of B_{out}) is the field produced by the current driven by the electric field induced along the shell circumference. The induced electric field is found using Faraday's law, taking the integral over the area enclosed by the shell, and using Stokes' theorem:

$$E_\phi = -\frac{R_{in}}{2} \dot{B}_{in} \quad (3.5.3)$$

Assuming the time dependence $B_{in} \sim B_{in0} e^{-i\omega t}$, this leads to: $E_\phi = \frac{i}{2} \omega R_{in} B_{in}$. By Ohm's law, $\mathbf{J} = \sigma \mathbf{E}$, so that the current per unit shell height is $I_\phi = \frac{i}{2} \omega \sigma R_{in} B_{in} d$. Here, σ [S/m] = $\frac{1}{\eta'}$ is the electrical conductivity of the shell material in Siemens/meter. Ampere's law defines the relation between I_ϕ and B_{shield} : $\nabla \times \mathbf{B} = \mu_0 \mathbf{J} \Rightarrow \int \mathbf{B}_{shield} \cdot d\mathbf{l} = \mu_0 I_\phi \Rightarrow$

$$B_{shield} = \frac{i}{2} \mu_0 \omega \sigma R_{in} B_{in} d$$

Here, Stokes theorem has been used again, and the integral was taken over a rectangular cross-sectional area of unit shell height in a plane of constant azimuthal angle. In terms of conductivity, $\delta_{skin}^2 = 2/(\mu_0 \omega \sigma)$, so that

$$B_{shield} = i R_{in} B_{in} d / \delta_{skin}^2$$

Since $B_{in} = B_{out} + B_{shield}$, $\frac{B_{in}}{B_{out}} = 1 + \frac{B_{shield}}{B_{out}} = 1 + \frac{B_{shield}}{B_{in}} \frac{B_{in}}{B_{out}} = 1 + \frac{i R_{in} d}{\delta_{skin}^2} \frac{B_{in}}{B_{out}} \Rightarrow \frac{B_{in}}{B_{out}} \left(1 - \frac{i R_{in} d}{\delta_{skin}^2} \right) = 1$. Substituting $b = \frac{R_{in} d}{\delta_{skin}^2}$, this leads to

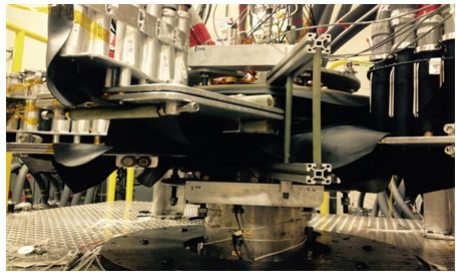
$$\begin{aligned}
\left| \frac{B_{in}}{B_{out}} \right| &= \left| \frac{1}{1 - ib} \right| = \left| \frac{1 + ib}{1 + b^2} \right| = \sqrt{\left(\frac{1}{1 + b^2} \right)^2 + \left(\frac{b}{1 + b^2} \right)^2} = \frac{1}{1 + b^2} \sqrt{1 + b^2} \\
&= \frac{1}{\sqrt{1 + \left(\frac{R_{in}d}{\delta_{skin}^2} \right)^2}} = \frac{1}{\sqrt{1 + (d/\delta_{eff})^2}}
\end{aligned}$$

where $\delta_{eff} = \frac{\delta_{skin}^2}{R_{in}}$. Figure 3.5.2(b) is a plot of $\left| \frac{B_{in}}{B_{out}} \right|$ against shell thickness d in units of δ_{eff} , the effective skin depth. This plot holds for any material at any field frequency when $d \sim \delta_{skin}$. For $R_{in} = 169$ mm (the inner radius of the quartz wall for the magnetic compression experiment), and $\delta_{skin} = 4.5$ mm (classical skin depth for high resistivity inconel, $\sigma \sim 1 \times 10^6$ S/m, at 12.5 kHz, the frequency of the magnetic compression fields), $\delta_{eff} = 0.12$ mm. From figure 3.5.2(b), it can be seen that field strength inside the shell would be attenuated by $\sim 25\%$ for $d \sim 0.1$ mm, and attenuated by 80% for $d \sim 0.5$ mm.

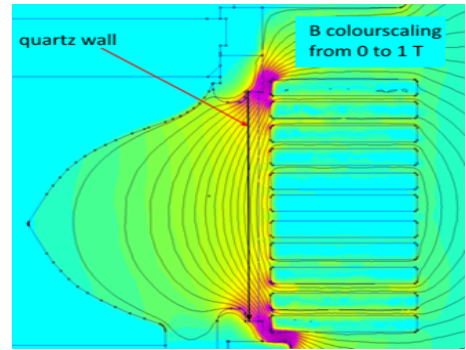
This information seemed to make the semi-permeable shell concept impossible, as the minimum shell thickness considered to be structurally adequate (with additional reinforcement from horizontal steel pins on the outer wall of the shell that would be embedded in an external fiberglass form) was around 0.5 mm, and the corresponding 80% attenuation of compression field would be unacceptable.

3.6 11-coil configuration, quartz outer insulating wall

The 11-coil configuration was tested after GF had decided to stop the magnetic compression experiment in February 2016, after the last few months of testing with a stainless steel flux conserver. I was given a few additional weeks (three, extended to seven) to try and get additional data for the PhD. The 11-coil configuration consisted of five coil pairs and one single coil, and approximately reproduced the levitation field profile of the 25-turn coil, allowing for formation and compression of higher-flux CTs with correspondingly increased lifetimes (CT lifetime scales with ψ_{CT}). Each coil-pair was assembled using one of the original coils and one of the newer coils that were designed to increase toroidal symmetry in the levitation/compression field. The remaining newer coil was included on its own, positioned 3rd from the bottom of the 11-coil stack, to further increase the field at the bottom of the wall. In contrast to the 25-turn coil configuration, magnetic compression was possible with the 11-coil setup. As shown in chapter 4, magnetic compression performance was greatly improved over that with the 6-coil configuration, due to the modified compression (and/or levitation) field profile.



(a) 11 coils on machine



(b) FEMM model - 11 coils

Figure 3.6.1: 11-coil configuration

Figure 3.6.1(a) shows the 11-coil stack installed on the machine - the single coil is on the right. Each coil/coil-pair is connected to its own levitation circuit via the two outer co-axial cables in the cable connecting bracket attached to the coil/coil-pair. One of the six brackets can be seen in the upper left foreground. Each of the inner four co-axial cables in each bracket links individually to a single $52 \mu\text{F}$, 20 kV compression capacitor and thyratron switch. Figure 3.6.1(b) shows a FEMM output plot for the 11-coil setup with 16 kA per coil and a frequency of 4 kHz, corresponding to the experimentally determined optimal delay of $|t_{lev}| = 50 \mu\text{s}$ between the firing of the levitation and formation capacitor banks. The 11-coil configuration was an entirely new build, with new parts that had to be baked and vacuum conditioned before testing. Baking involved wrapping the machine in insulating material and maintaining it under vacuum at around 150°C for three to four days to remove water. An inner flux conserving "chalice" with magnetic probe locations listed in table 2.2.1 was used, and a new quartz wall was installed. A different material (alumina or boron-nitride) would have been far better for CT performance, but there wasn't time to wait an additional few weeks to manufacture an insulating tube from a more plasma-compatible material. After baking the assembly, the first CT with a lifetime of greater than 150 μs was achieved within four days of cleaning shots, compared with over thirty days for the same milestone on the configuration with six coils around the quartz insulating wall. This may have been largely due to the improved levitation field profile, but also may be because, with limited time available, care was taken to pre-bake the chalice and quartz tube at 200°C for two days in a low pressure oven, and to avoid contact of the parts with (water-containing) air during installation on the machine.

3.6.1 Levitation field decay rate

The strategy of adding resistance to the levitation circuits, to match the decay rates of external levitation and CT currents, as initially tested on the 25-turn coil, was used again on the 11-coil configuration.

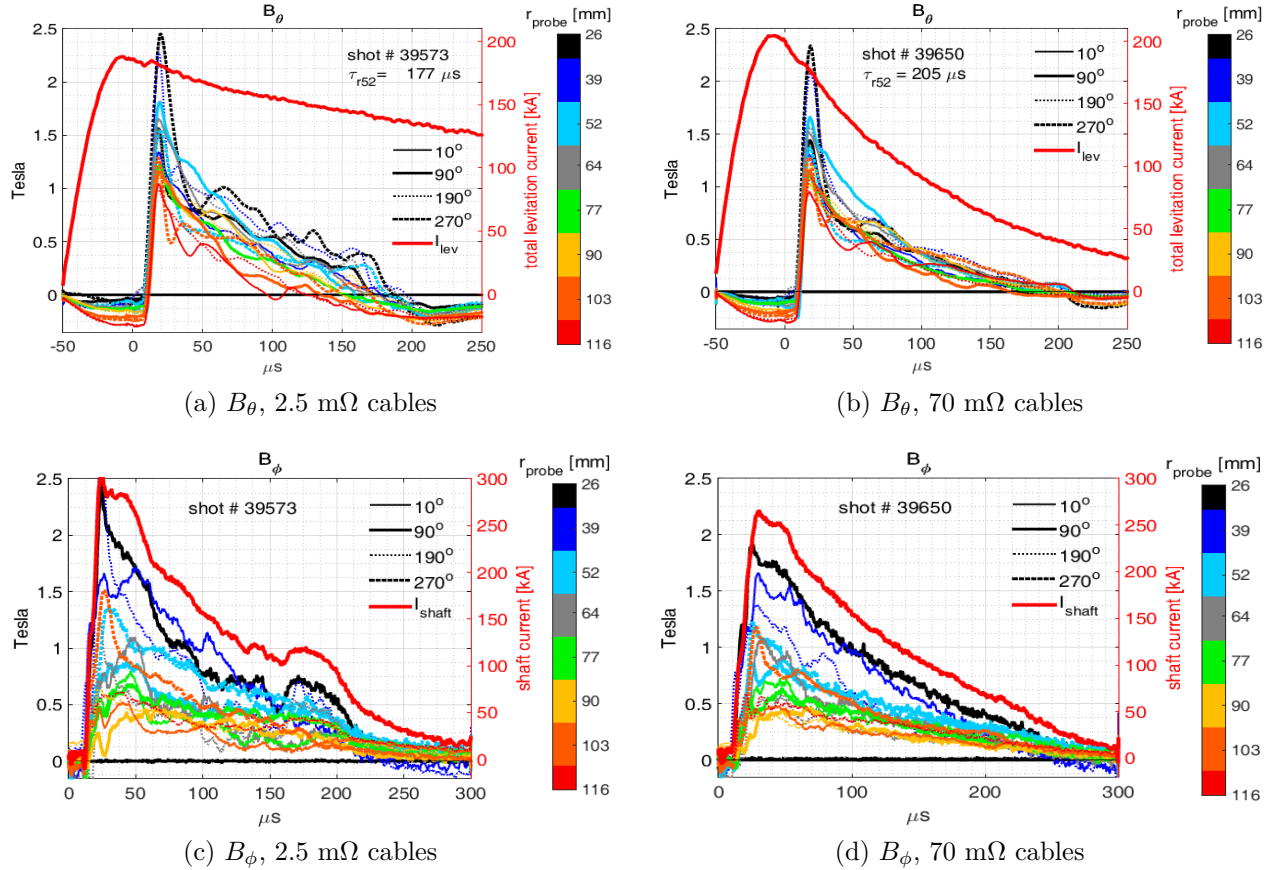


Figure 3.6.2: B_θ and B_ϕ for levitated CTs (11-coil configuration)

Figure 3.6.2 shows B_θ and B_ϕ for two shots with different cable resistances for the 11-coil configuration. These two shots were both at $V_{form} = 16$ kV - additional settings for shot 39573 included $V_{lev} = 13.8$ kV and $I_{main} = 73$ A (corresponding to ~ 12 mWb gun flux), and for shot 39650, $V_{lev} = 16$ kV and $I_{main} = 70$ A. To achieve the same levitation current with the additional cable resistance, V_{lev} was increased for shot 39650. It can be seen how the decay rate of I_{lev} approximately matches that of the CT toroidal current (as determined by positive B_θ) with a 70 mΩ cable replacing the original pair of 5 mΩ cables in parallel (*i.e.*, total 2.5 mΩ) between the main holding inductor and coil in each levitation circuit. A much higher rate of "good" shots, smoother decays of B_θ and B_ϕ (less apparent MHD activity), and a lifetime increase generally of around 15 – 20%, was observed with the 70 mΩ cables in place. There is evidence of mild magnetic compression starting at around 150 μs

on shot 39573 (figure 3.6.2(c)), even though the compression capacitors were not fired. In this shot, this is particularly evident from the rise B_ϕ (especially at the (26 mm, 90°) and (52 mm, 190°) probes) and from the overall rise in shaft current at 150 μ s - see discussion in section 3.1. The CT is decaying far faster than the levitation field with the low resistance cables in place, so that it is being compressed more and more as ψ_{CT} decreases.

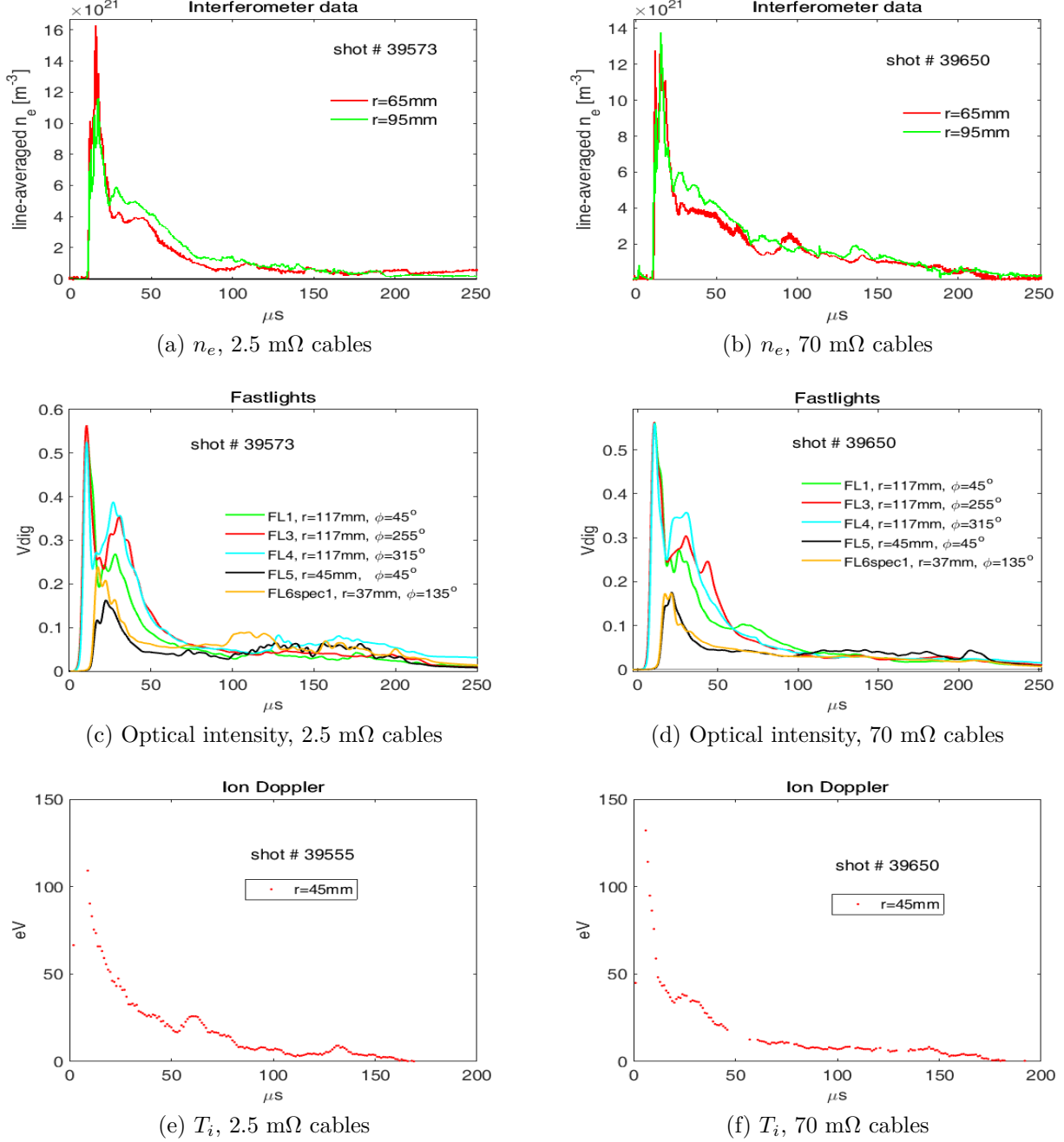


Figure 3.6.3: n_e , optical intensity, and T_i for levitated CTs (11-coil configuration)

Figures 3.6.3(a) and (b) compare the line averaged density measurements for shots 39573 and 39650. Corresponding to the longer CT lifetime and larger CT size associated with shot

39650, the density falls more gradually compared with the density decay rate for shot 39573. MHD activity may lead to enhanced particle loss. In general, shots with implementation of decay rate matching exhibited less evidence of strong internal MHD activity. Associated with this, as can be seen by comparing figures 3.6.3(c) and (d), optical intensity measurements are relatively fluctuation free in shot 39650, especially around 150 μ s when the CT in shot 39573 is extinguished. Optical intensity increases in regions of increased density, where line radiation intensity, which scales as n_e^2/Z_{eff} , is high. Ion Doppler data was not well resolved for shot 39573, and only the diagnostic looking along the vertical chord at $r = 45$ mm (see figure 2.2.2) was working for shot 39650. Shot 39555 was similar to shot 39573 and was also taken in the configuration with low resistance cables. Figures 3.6.3(e) and (f) indicate how fluctuations in measured ion temperature are more apparent with the low resistance cables in place. In both cases, the maximum ion temperature is at ~ 10 μ s when plasma enters the CT confinement region, due to high velocities achieved by the plasma through the action of formation forces, which leads to high levels of ion viscous heating. With reference to data presented in [57, 58], an error in the temperature measurement (He II line at 468.5nm) due to density broadening has been evaluated as ~ 17 eV for a density of 1.6×10^{22} m $^{-3}$, and the error falls off in proportion to $n_e^{0.83}$. Density along the ion-Doppler chords is not directly evaluated, but from this information, along with observations of the variation of line averaged density with radius, the error in the T_i measurement along the $r = 45$ mm chord for shot 39650 can be roughly estimated as being ~ 12 eV at 20 μ s and ~ 2 eV at 100 μ s .

3.6.2 Additional tests on the 11-coil configuration

- Around ten coil configurations, including configurations with passive and open-circuited coils (up to four configurations per day) were tested. Recall that the experiment with eleven coils was conducted in a quite a rush over a few weeks after the experiment had been scheduled for decommissioning. There was no obviously outstandingly beneficial configuration apart from the setup with all coils on with 70 m Ω cables. It would have been worth testing with the single coil located near the bottom of the stack moved towards the top of the stack, to see if increased levitation field at the top of the wall was more beneficial than increased field at the bottom, but again there wasn't time to do this.

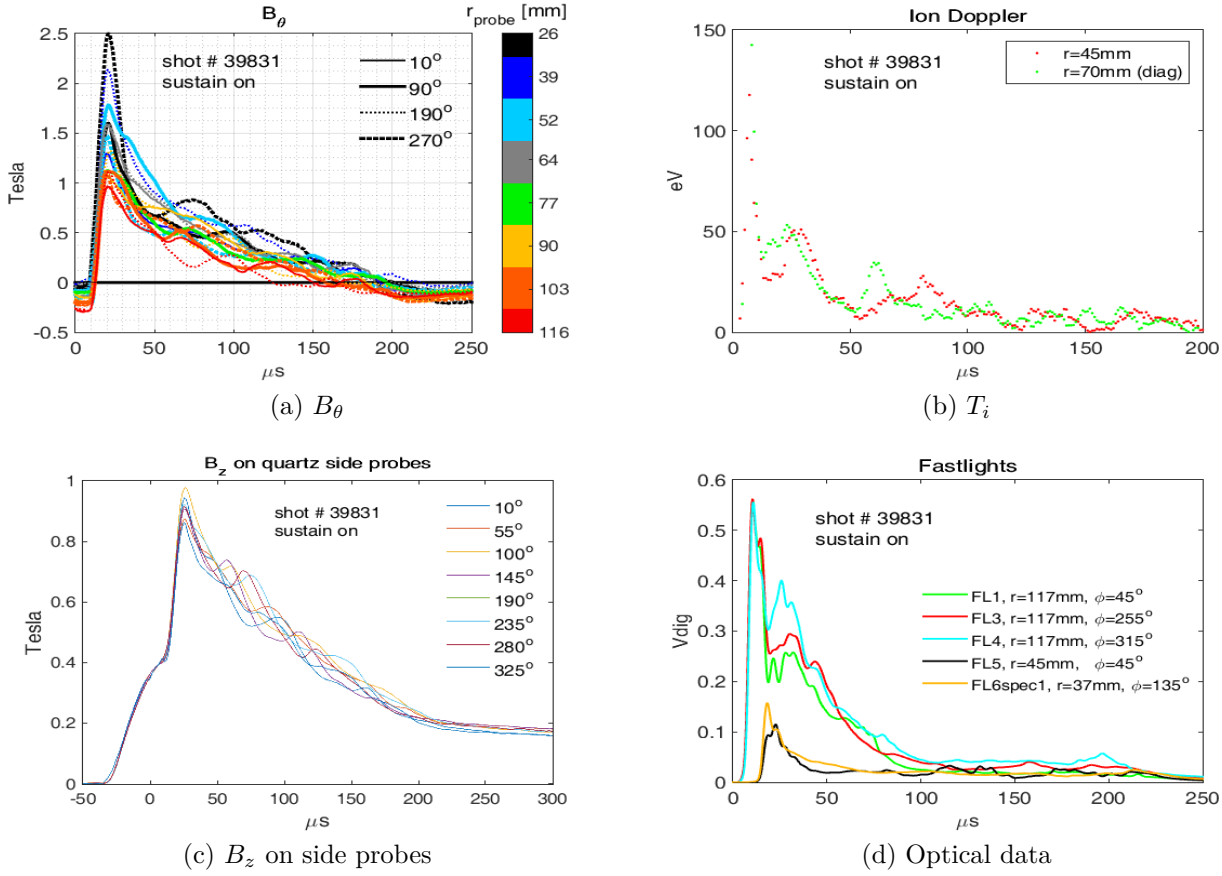


Figure 3.6.4: B_θ , T_i , B_z and optical data with sustained I_{shaft}

- A few shots were taken with up to 80 kA sustained shaft current. This involved connecting one of the levitation circuits, including its two capacitors and main holding inductor, in parallel with the formation banks across the formation electrodes. In that configuration, the lower coil-pair was left open-circuited. Sustainment at far higher currents significantly extends CT lifetimes in standard MRT machines. It wasn't possible to try and add more capacitors because no more levitation circuits could be borrowed without degrading levitation to unacceptable levels. In fact, the reduction in levitation current had to be compensated for by replacing the 70 m Ω cables in two of the five remaining the levitation circuits with 2.5 m Ω cables. There wasn't time in the available period to set up new circuits. Oscillations with toroidal mode number $n = 1$ were observed on the B_θ signals on some shots with 80 kA sustained current. The fluctuations recorded on measured B_θ , T_i , B_z and optical signals for shot 39831 are indicated in figure 3.6.4, where the B_z signals were recorded at probes located on the outside of the quartz wall, as described below in section 3.7. In general, fluctuations in these signals are enhanced with the unintentional magnetic compression scenario associated with lower resistance cables in place in the levitation circuits, but seem to be further enhanced in this case. This suggests enhanced MHD activity with additional

shaft current, which may be related to the effect of the compressional instability in the presence of increased CT toroidal field. It would have been interesting to observe the effect of sustained I_{shaft} with 70 mΩ cables in place on all the levitation circuits. The $n = 1$ mode on B_θ signals confirmed, for the first time on this experiment, coherent CT rotation and the existence of closed flux surfaces. Apart from that, there were no other noticeable effects associated with the additional driven shaft current.

3.7 Using side-probe data to find CT outboard separatrix radius over time

A set of eight magnetic probes with windings to measure B_r , B_ϕ , and B_z , were attached to the outside of the insulating wall at $\phi = 10^\circ$, 55° , 100° , 145° , 190° , 235° , 280° , and 325° . The probes were installed at $z = 0$ mm (*i.e.*, the chalice waist) on the earlier configuration with six coils around the ceramic (alumina) wall (with stainless steel extension in place), and again at $z = 6$ mm on the configuration with eleven coils around the quartz wall. The probes measured the levitation field which is compressed when the plasma enters the pot. A bigger CT will displace a greater proportion of the levitation flux, so that $B_\theta(\phi, t) = B_\theta(r_s(\phi, t))$, where $B_\theta(\phi, t)$ is the poloidal field measured at the side probe, and $r_s(\phi, t)$ is the radius of the CT's separatrix at the z -coordinate of the probe. By definition of the separatrix, $\psi_{CT}(\phi, t) + \psi_{lev}(\phi, t) = 0$ at $r_s(\phi, t)$, where ψ_{CT} and ψ_{lev} are the contributions to ψ that arise due to CT currents and external coil currents respectively. We expect that $\psi_{lev}(\phi, t) \approx \psi_{lev}(t)$, with any deviation from toroidal symmetry being due either to coil misalignment, or asymmetry associated with discrete coils. However, the CT poloidal flux, and therefore r_s , can vary with toroidal angle, depending on MHD activity in the CT. The r component of the experimentally measured field at the probes proved to be negligible, so we made the approximation $B_z \approx B_\theta$. We used a set of FEMM models to estimate the value of B_z that would be measured at the probes for varying r_s .

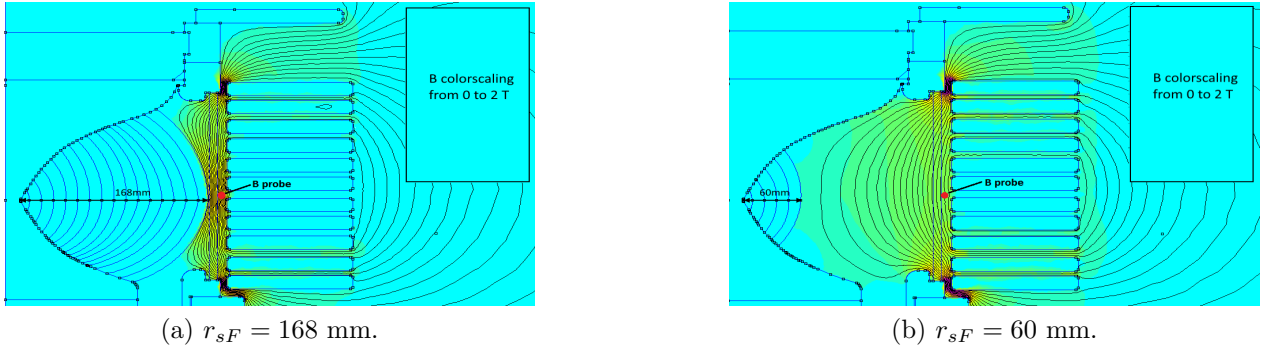


Figure 3.7.1: FEMM models for finding $r_s(\phi, t)$

Figure 3.7.1 shows two of the seventeen FEMM models used to find r_s for the 11-coil configuration. A material with artificially high conductivity ($\sigma = 10^{12}$ S/m) was assigned to the areas representing the nested "plasmas" in FEMM. The seventeen models are identical except that, starting with the model with $r_{sF} = 168$ mm (note $r_{quartz} = 170$ mm), the outermost of the set of nested shells representing "plasma" material is removed for each successive model. Figure 3.7.1(a) shows the FEMM solution (contours of ψ , coloured by $|B|$) for the model with $r_{sF} = 168$ mm, and figure 3.7.1(b) shows the solution for the case with $r_{sF} = 60$ mm, where r_{sF} is the radius, at the same z coordinate as the probes, of the outermost layer of "plasma material" in the FEMM model.

With the levitation coil currents in the models determined from experimental measurements, and the coil current frequencies set to a high value (~ 1 MHz), FEMM was run for each model. The high conductivity of the material representing plasma, and the high current frequency, ensure minimal penetration of levitation field into the "plasma" region, so that the true separatrix radius is modelled. A LUA script was written so that each of the models can be loaded successively and run automatically through FEMM, and the required data for each solution can be written to file for processing. The required data consists, for each model, of r_{sF} and $B_{zF}(r_{sF})$, where $B_{zF}(r_{sF})$ is the FEMM solution for B_z at the probe location $((r, z) = (177 \text{ mm}, 6 \text{ mm})$ for the 11-coil configuration) for a given r_{sF} . The process was repeated for another set of FEMM models based on the 6-coil configuration with the reduced insulator inner radius ($r_{ceramic} = 144$ mm), with the probe location being $(r, z) = (161 \text{ mm}, 0 \text{ mm})$.

3.7.1 Levitation only shots with 70 mΩ cables

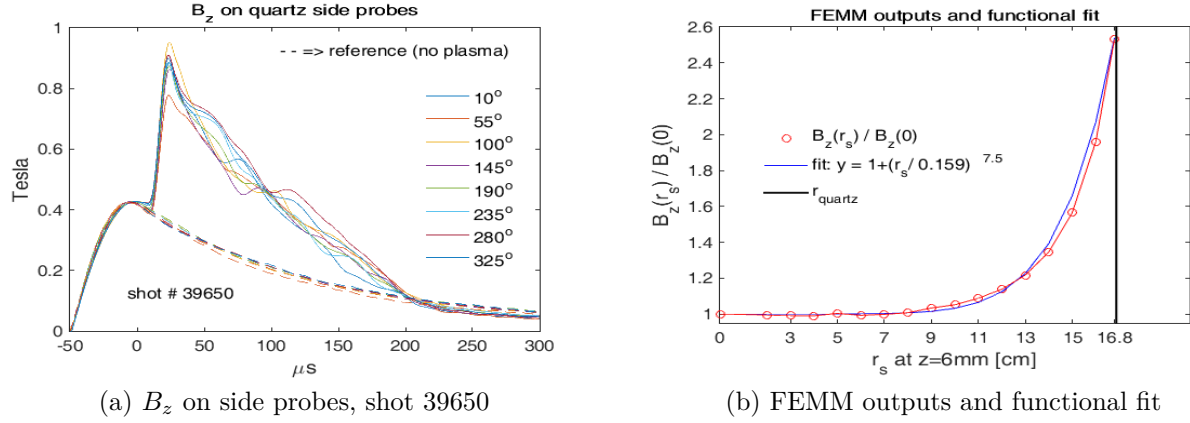


Figure 3.7.2: Experimental data and functional fit to FEMM data (70 mΩ cables)

Figure 3.7.2(a) shows the $B_z(\phi, t)$ signals measured at the eight probes for shot 39650, along with $B_{zref}(\phi, t)$, the reference signals which are the averages of the $B_{zref}(\phi, t)$ signals from three levitation-only shots taken without charging or firing the formation banks. The $B_z(\phi, t)$ and $B_{zref}(\phi, t)$ signals were calibrated using $B_{zF}(0)$ (*i.e.*, no superconducting "plasma" material in the FEMM model) to determine the peak field amplitude at $\sim 0 \mu s$ (before CT entry in the case of $B_z(\phi, t)$). Shot 39650 was taken in the 11-coil configuration with 70 mΩ cables in place between each main levitation inductor and coil-pair/coil, with $|t_{lev}| = 50 \mu s$. Figure 3.7.2(b) shows $B_{zF}(r_s) / B_{zF}(0)$ plotted against r_s using data from the set of FEMM models for the 11-coil configuration. A function of the form $y = 1 + (r_s / 0.159)^{7.5}$ was found to be a good fit to the data. Using the data from each of the eight probes, this functional fit is inverted to find $r_s(\phi, t)$ at each of the toroidal angles associated with the probes. At each probe, we have recorded $B_{zref}(\phi, t)$, and $B_z(\phi, t)$, so $r_s(\phi, t)$ can be found using the formula

$$r_s(\phi, t) = 0.159 (B_z(\phi, t) / B_{zref}(\phi, t) - 1)^{\frac{1}{7.5}} \quad (3.7.1)$$

Note that $r_s(\phi, t)$ becomes complex-valued if $B_{zref}(\phi, t) > B_z(\phi, t)$ - care has to be taken to ensure that probe signals are properly calibrated, and signals from any probes that have unusual responses must be ignored, in order for the method to work. Note also that for $r_s \lesssim 9$ cm, the slope of the function fit in 3.7.2(b) is too flat to be successfully inverted with good accuracy.

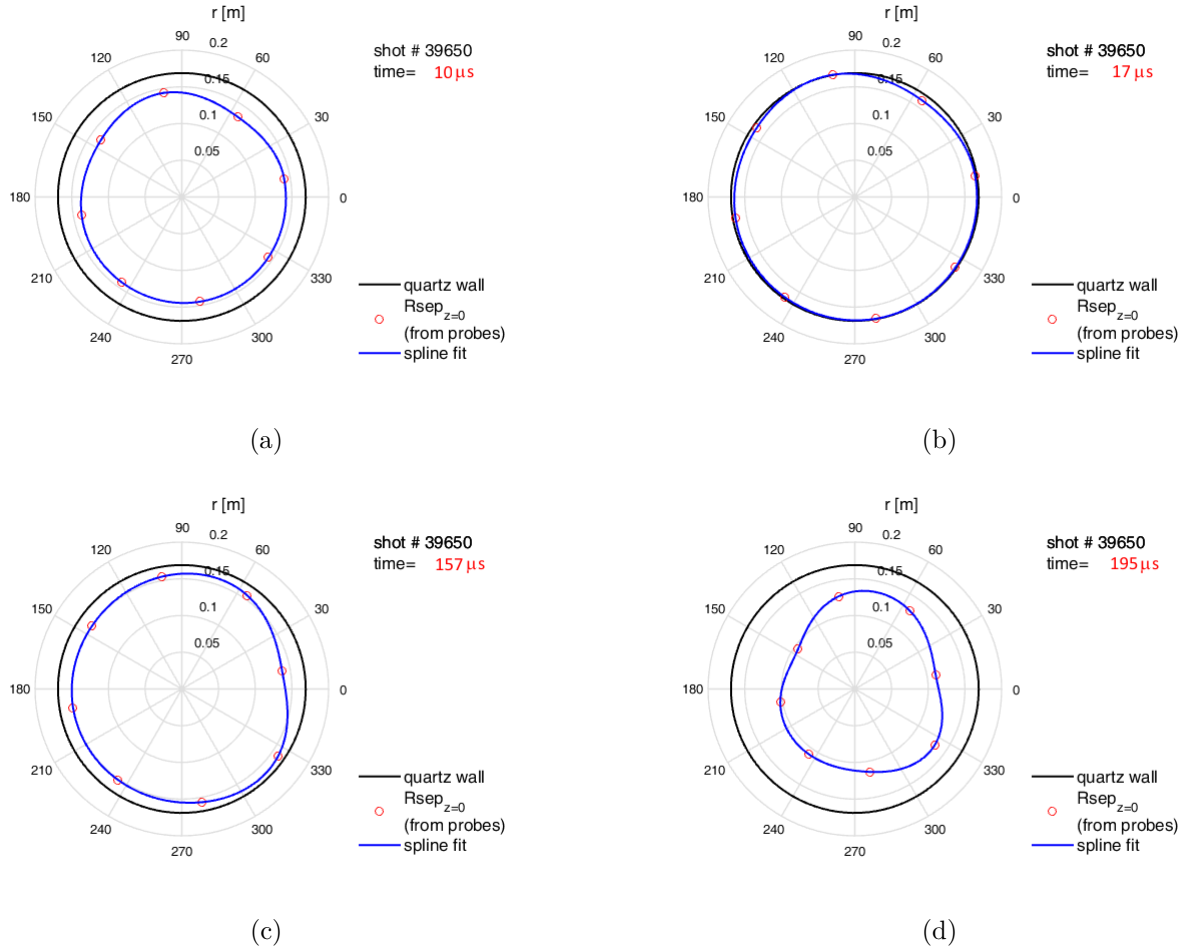


Figure 3.7.3: Time-sequence of $r_s(\phi, t)$ for shot 39650 (70 m Ω cables)

Figure 3.7.3 shows images from a video that is the output of a MATLAB code that finds $r_s(\phi, t)$ based on $B_z(\phi, t)$ recorded at the side probes during shot 39650, and the functional fit in equation 3.7.1 that was obtained using the FEMM models. It can be seen that the plasma enters the confinement region at $t = 10\ \mu\text{s}$, and that at $t = 17\ \mu\text{s}$ the CT fills the space right up to the inner radius of the quartz wall, at $z = 6\ \text{mm}$ (z coordinate of the side probes). It remains at around this size and then starts to shrink at around $157\ \mu\text{s}$. At this time it looks like it is being pushed in more at around $\phi = 10^\circ$. At $195\ \mu\text{s}$, there are signs of an $n = 3$ mode - the CT is being pushed in more at around $\phi = 10^\circ$ and 150° , and is reacting by starting to bulge outwards at $\phi = 80^\circ, 210^\circ$ and 330° . The CT is gone shortly after $195\ \mu\text{s}$.

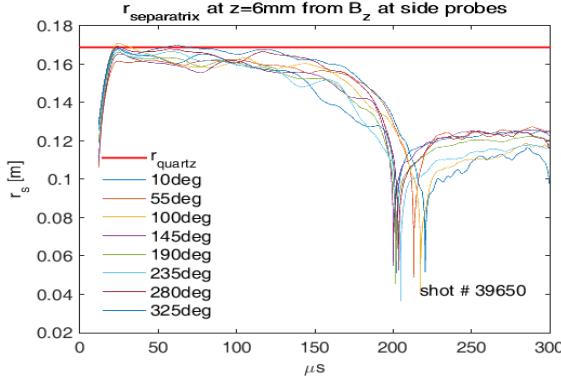


Figure 3.7.4: $r_s(\phi, t)$ for shot 39650 (70 mΩ cables)

Figure 3.7.4 is a plot of the modelled $r_s(\phi, t)$ against time for shot 39650. As also indicated in figure 3.7.3(c), the CT starts to shrink in from the inner radius of the wall at around 150 μs. As mentioned, the evaluation for $r_s(\phi, t)$ is not valid when $B_{zref}(\phi, t) > B_z(\phi, t)$. It can be seen in figure 3.7.2(a) that (due to inaccuracies in probe responses etc.) $B_{zref}(\phi, t) > B_z(\phi, t)$ after around 200 μs.

3.7.2 Levitation only shots with 2.5 mΩ cables

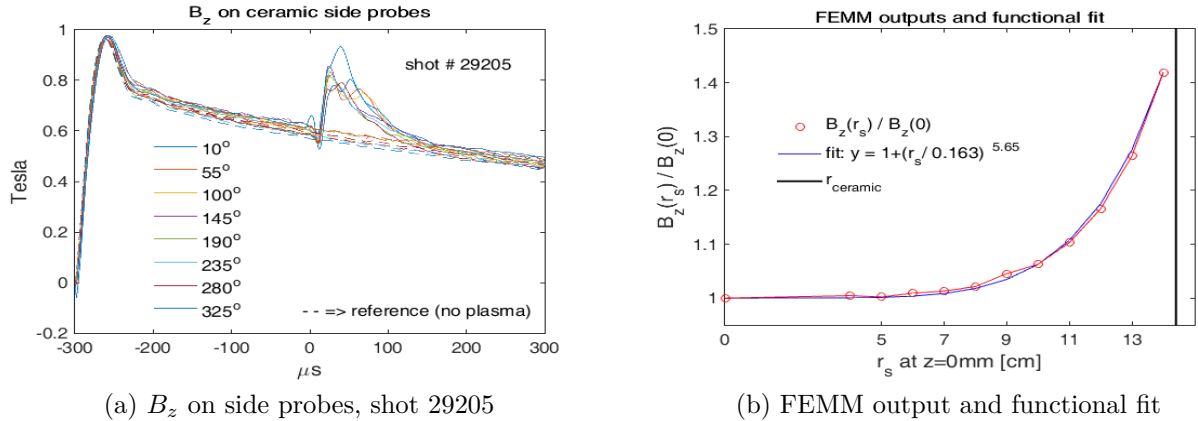


Figure 3.7.5: Experimental data and functional fit to FEMM data (2.5 mΩ cables)

Figure 3.7.5(a) shows the $B_\theta(\phi, t)$ and $B_{zref}(\phi, t)$ signals for shot 29205. Shot 29205 was taken in the configuration with six coils surrounding the shortened alumina insulating wall, with 2×5 mΩ cables in parallel between the main levitation inductors and the coils, and with $|t_{lev}| = 300$ μs to allow for enhanced field line pinning and reduced plasma-wall interaction in the 6-coil configuration. Figure 3.7.5(b) shows $B_z(r_{sF})/B_z(0)$ plotted against r_{sF} for the 6-coil configuration. A function of the form $y = 1 + (r_s/0.163)^{5.65}$ was found to be a good

fit to the FEMM data and the procedure followed to get $r_s(\phi, t)$ from the experiment data is as described above.

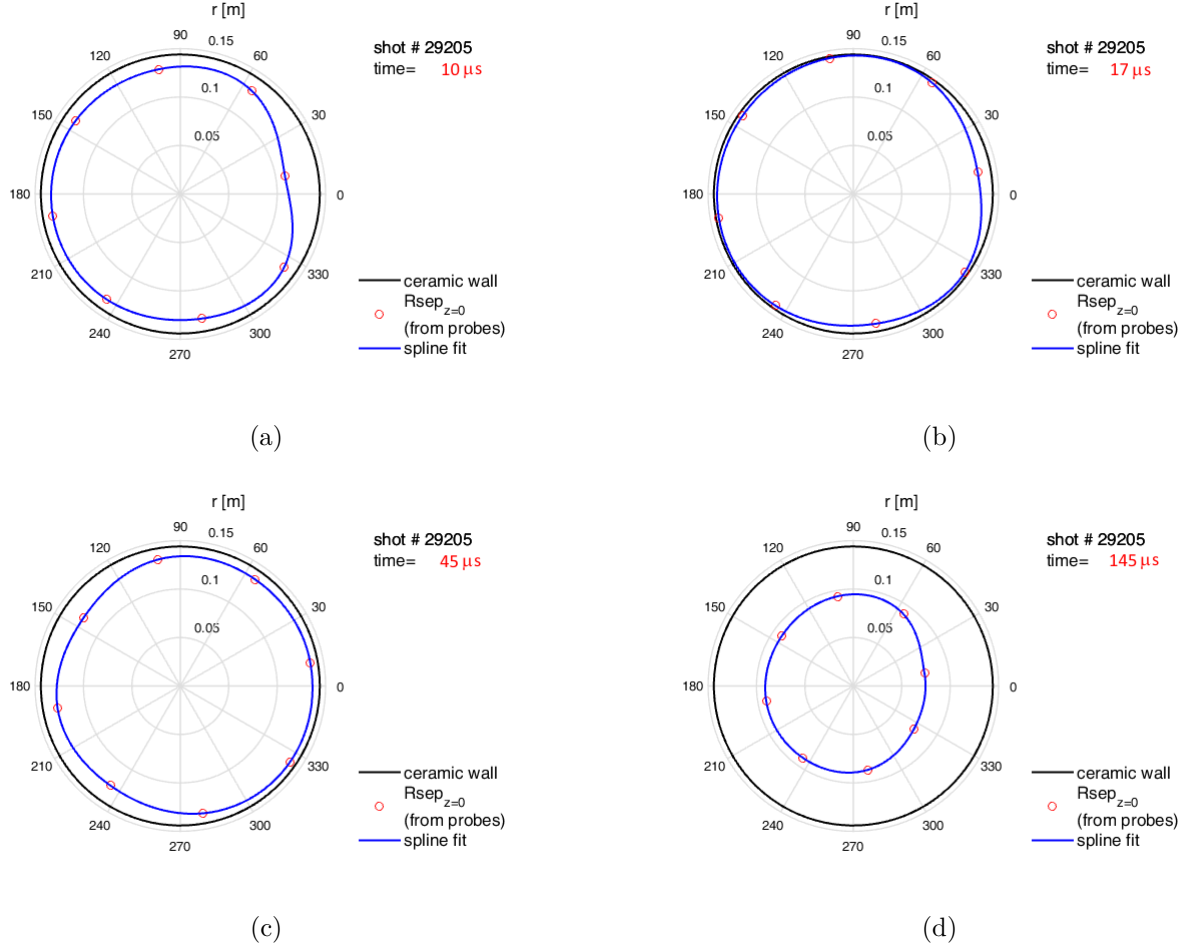
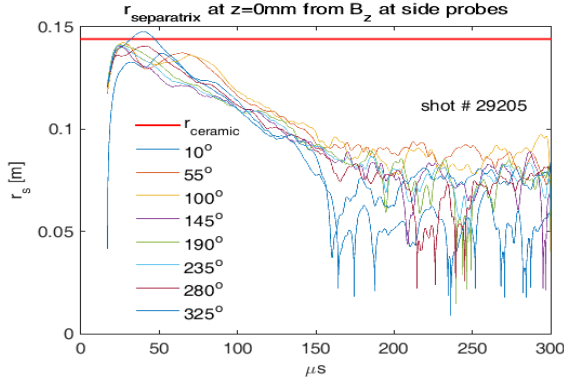
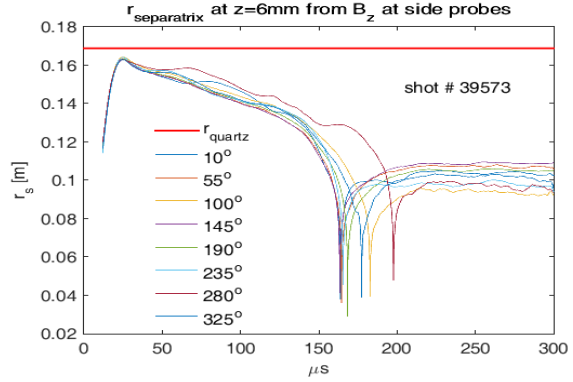


Figure 3.7.6: Time-sequence of $r_s(\phi, t)$ for shot 29205 (2.5 mΩ cables)

Figure 3.7.6 shows images at four times, indicating $r_s(\phi, t)$ based on the FEMM model outputs. As in figure 3.7.3, it can be seen that the plasma enters the confinement region at $t = 10 \mu\text{s}$, and that at $t = 17 \mu\text{s}$ the CT fills the space right up to the inner radius of the insulating wall. With the low resistance cables, for a shot on the 6-coils with ceramic wall configuration, the levitation field is constantly compressing the CT. It can be seen (figure 3.7.6(c)) how the CT has already started to shrink at $45 \mu\text{s}$, whereas the CT retains its maximum volume up until around $157 \mu\text{s}$ when the levitation field decay rate is optimized (figure 3.7.3(c)). The CT continues to be pushed inwards rapidly and is extinguished shortly after $145 \mu\text{s}$.



(a) $r_s(\phi, t)$ for shot 29205 (2.5 mΩ cables)



(b) $r_s(\phi, t)$ for shot 39573 (2.5 mΩ cables)

Figure 3.7.7: $r_s(\phi, t)$ for shots 29205 and 39573 (2.5 mΩ cables)

Figure 3.7.7(a) is a plot of the modelled $r_s(\phi, t)$ for the same shot. As also indicated in figure 3.7.6(c), the CT starts to shrink in from the inner radius of the wall at around 50 μs. Calculated r_s is not valid after around 150 μs, when $B_z(\phi, t) \leq B_{zref}(\phi, t)$ (see figure 3.7.5(a)). Figure 3.7.7(b) is a plot of the modelled $r_s(\phi, t)$ for shot 39573, which also had the original levitation circuits with 2×5 mΩ cables in parallel between the main levitation inductors and the coils, but was taken on the 11-coil configuration, and therefore the functional fit indicated in figure 3.7.2(b) was used to extract $r_s(\phi, t)$. The CT in shot 39573 ($V_{form} = 16$ kV), lives longer than that in shot 29205 ($V_{form} = 12$ kV). However, the CTs in shots 29205 and 39573 are similar in that they both shrink rapidly in comparison with shot 39650 (figure 3.7.4), in which the decay-rate matching strategy was used.

3.8 Comparison of total spectral power measurements and levitated CT lifetimes for various configurations

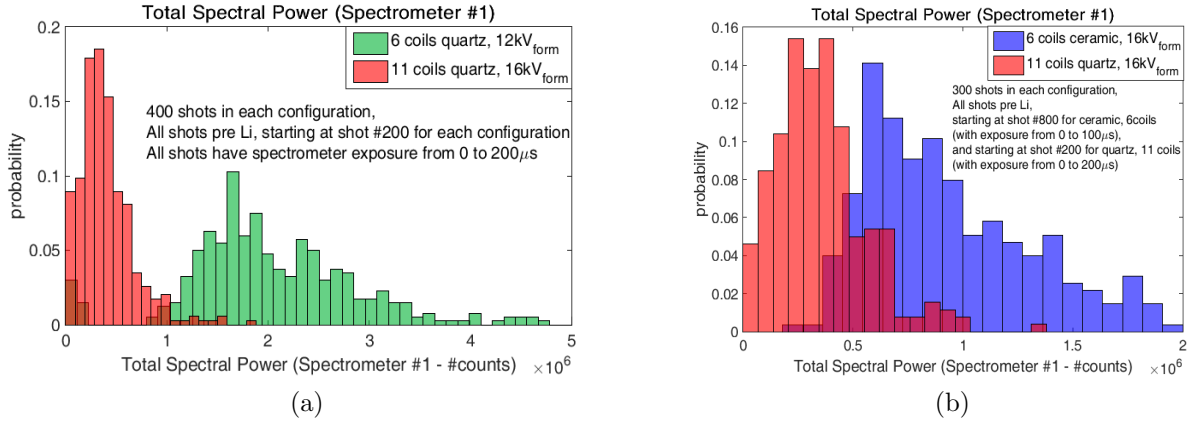


Figure 3.8.1: Spectrometer data

Figure 3.8.1(a) shows normalised histograms comparing total spectral power recorded with spectrometer #1 for shots with the quartz wall in place, for the 6-coil and 11-coil configurations. Data from 400 pre-lithium shots for each configuration, all with spectrometer exposure from 0 to 200 μ s, is included. Each shot in the selection was taken after at least 200 post-baking cleaning shots in the relevant configuration. Having the same spectrometer exposure time and the same number of cleaning shots prior to the shots being selected for comparison in each configuration is important for a valid comparison. The validity of the data was verified by comparing the total spectral power recorded with the measured intensity of plasma optical emission at around the same location as the spectrometer, and finding a good correlation. The locations of spectrometer and optical ports on the machine headplate are indicated in figure 2.2.1. Spectrometer #1 is the inner of the two spectrometers, and both spectrometers had vertical lines of sight. Even at increased formation voltage, total spectral power is around four times lower with eleven coils. This is particularly unusual because on a given configuration, it's expected that higher formation current (*i.e.*, V_{form}) leads to increased ablation of electrode material and consequently increased impurity levels and total spectral power.

Due to variations in spectrometer exposure settings throughout the experiment, the available data does not allow for direct comparison of recorded spectral power between the ceramic and quartz wall on the 6-coil configuration. As discussed previously, CT lifetimes decreased

significantly with the transition from the ceramic to quartz wall, so it is expected the spectral power would be far higher with the quartz wall. Figure 3.8.1(b) shows data comparing total spectral power recorded with spectrometer #1 for the 6-coil (ceramic wall) and 11-coil (quartz wall) configurations. Spectrometer exposure was 0 to 100 μ s for the selection of shots taken in the 6-coil configuration, and 0 to 200 μ s for those taken in the 11-coil configuration. Naturally, spectral power increases with increase exposure time. There were four times as many prior cleaning shots, which tend to reduce impurity and spectral power levels, for the configuration with the ceramic wall and six coils. Despite the different exposure times and number of cleaning shots, and despite the quartz wall, total spectral power is several times lower with the 11-coil configuration. Comparing the spectral powers for shots in the 6-coil configuration with the quartz wall (figure 3.8.1(a)) and ceramic wall (figure 3.8.1(b)), it can be seen how the spectral power is indeed significantly higher in the case with the quartz wall, even though the shots with the ceramic wall were taken at higher formation voltage. There were, however, four times as many prior cleaning shots, and spectrometer exposure was reduced, for the configuration with the ceramic wall, so this last comparison is not conclusive.

It is thought that the 11-coil setup reduced impurities and the associated energy losses due to line radiation because it reduced the level of interaction between plasma and the outer insulating wall during the bubble-in process. The data presented in figure 3.8.1 confirms that the benefit from the reduction of plasma-insulating wall interaction appears more significant than any impurity increase caused by either the transition from the ceramic to the quartz wall, or plasma-electrode interaction (*i.e.*, increased V_{form}).

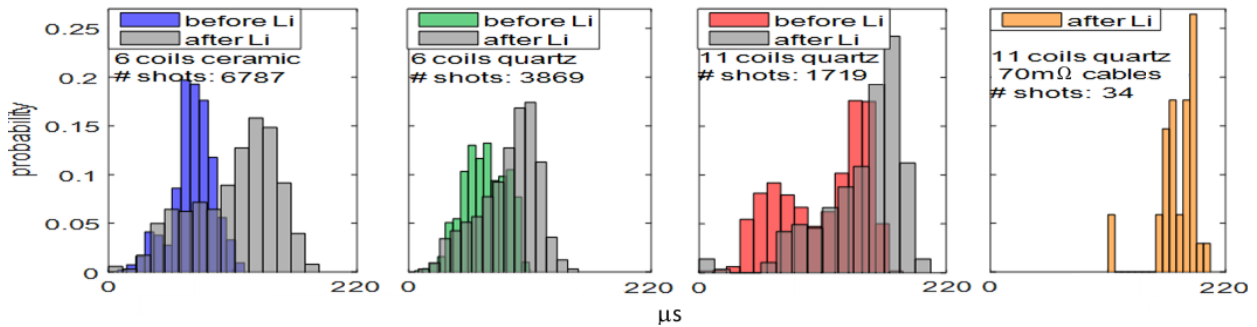


Figure 3.8.2: Comparison, across configurations, of CT lifetimes and effect of lithium gettering.

As indicated in the normalised histograms in figure 3.8.2, pre-lithium CT lifetimes were longer with the ceramic wall, despite the smaller volume. Lithium gettering was very effective on the ceramic wall ($\sim 70\%$ lifetime increase), but not so effective on quartz ($\sim 30\%$ lifetime increase). Lifetime increased significantly with the 11-coil configuration. The "double-Gaussian" shape of the (before Li) distribution for eleven coils may be due to the $\sim 35\%$ of shots taken in that configuration in suboptimal machine-parameter space (*i.e.* values of

V_{form} , V_{lev} , I_{main} , and t_{gas}) that were rapidly explored in the last days of the experiment in new configurations such as without levitation inductors, with additional crowbarred sustain current, and with passive or open-circuited levitation/compression coils. Note that of the 10,000+ shots from which data is taken for this levitated CT lifetime comparison, and the ~40,000 shots taken in total over the three year duration of the experiment, only 34 shots in the best of the configurations tested - eleven coils with $70\text{ m}\Omega$ cables - are shown because the 11-coil configuration was explored rapidly in the days before the experiment was decommissioned. It can be seen that the repeatability of good shots was significantly improved in that configuration.

3.9 Summary

The principal obstacle to the progress of the magnetic compression experiment was the problem associated with radiative cooling that arose due to interaction at CT formation between plasma entering the containment region and the insulating outer wall that was required in the design to allow operation of the compression field. In the original six-coil configurations, plasma being rapidly advected into the containment region during the formation process was able to displace the levitation field into the large gaps above the coil stack, and come into contact with the insulating wall. This issue was only identified during the experiment with the 25-turn coil configuration, shortly before the experiment was scheduled for decommissioning, and was only partly resolved with the eleven coil configuration over the last few weeks of extended operation.

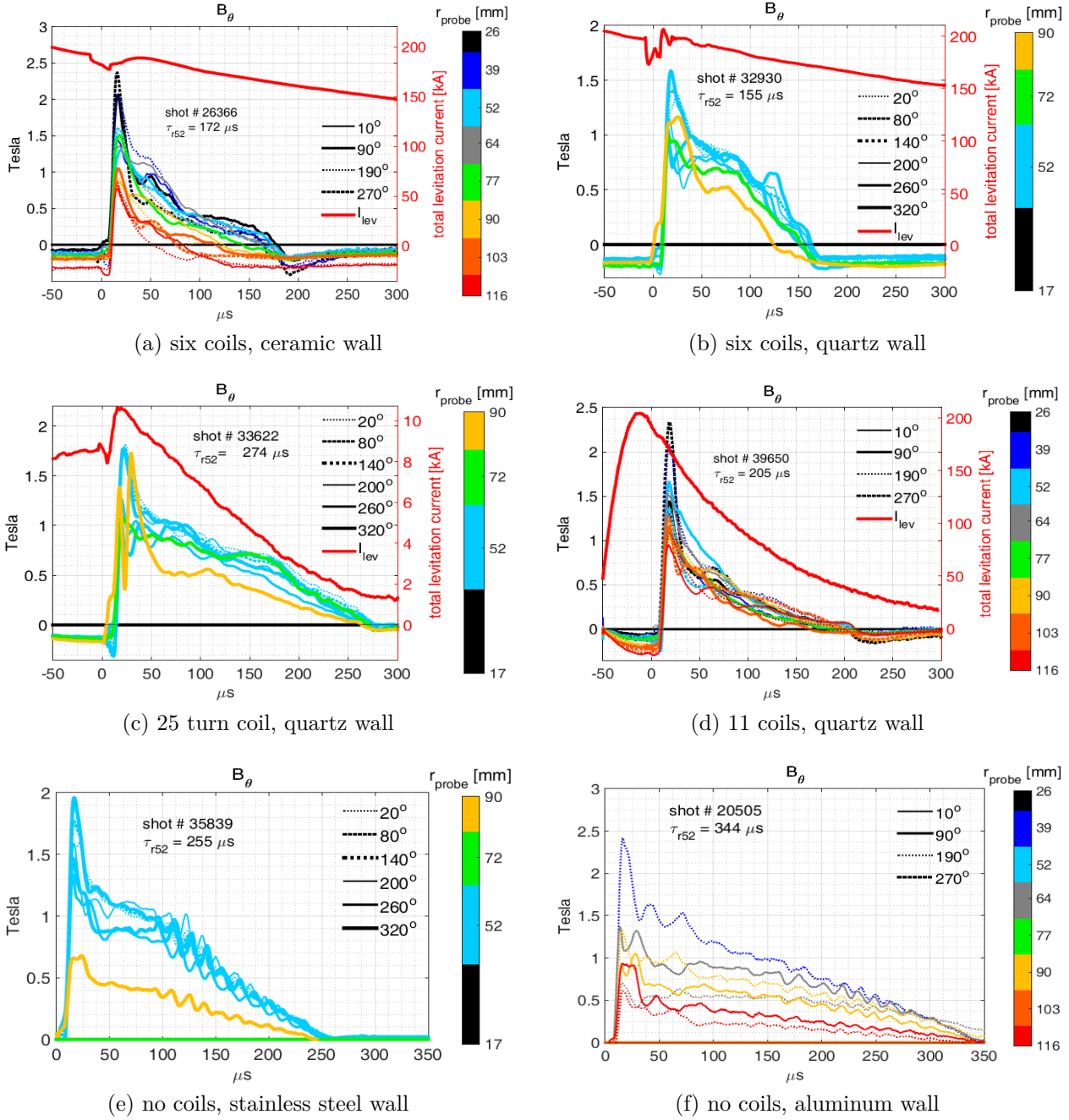


Figure 3.9.1: B_θ for six configurations

Figure 3.9.1 shows poloidal field traces for the six principal configurations tested. Comparing figures 3.9.1(a) and (b), and noting, as outlined in section 3.2, that a 50% increase in CT lifetime was expected with the switch to the larger internal radius insulating tube, it can be seen how quartz was significantly worse than ceramic as a plasma-facing material. For these two shots, $|t_{\text{lev}}|$ was $300 \mu\text{s}$ - as mentioned in section 3.1, and confirmed by MHD simulations (see section 7.2.1), the strategy of allowing the levitation field more time to soak into the steel above and below the insulating wall led to a reduced level of plasma-wall interaction

and slightly increased CT lifetimes in the 6-coil configurations.

Apparently, plasma/material interaction during formation was reduced with the modified levitation field profiles of the 25-turn coil and eleven-coil configurations, in which current carrying coils extended along the entirety of the outer surface of the insulating wall. Spectrometer data and observations of CT lifetime confirm that the improved design led to reduced levels of plasma impurities and radiative cooling. Consistent with this explanation for the improvement, at the same initial CT poloidal flux, as determined by the voltage on the formation capacitors and the current in the main coil, CT lifetimes were around the same for the six-coil, 25-turn coil, and eleven-coil configurations. However the 25-turn coil and eleven-coil configurations allowed for the successful formation of higher flux, physically larger, CTs - formation voltage could be increased from 12 kV to 16 kV and main coil current could be increased from 45A to 70A, corresponding to an increase in Ψ_{gun} from around 8 mWb to 12 mWb. In contrast, the benefit of increased initial CT flux was outweighed by the performance degradation due to increased wall interaction in the six coil setup. With CT lifetimes of up to 274 μ s, the longest-lived levitated CTs were produced with the 25-turn coil configuration (figure 3.9.1(c)), despite the presence of the quartz wall. This was almost double the maximum $\sim 150 \mu$ s lifetimes seen with six coils around the quartz wall, but still less than the $\sim 340 \mu$ s lifetimes observed without levitation with an aluminum flux conserver (figure 3.9.1(f)). The eleven coil configuration, with a field profile similar to that of the 25-turn coil setup, also enabled the production of relatively high-flux CTs with correspondingly increased lifetimes (figure 3.9.1(d)). Levitation circuit modification to match the decay rates of the levitation and plasma currents led to more stable, larger, longer lived plasmas, and a greatly increased rate of good shots, by avoiding unintentional magnetic compression during CT levitation. This strategy was implemented with the 25-turn coil and eleven-coil configurations. The experimental technique developed to measure the CT outboard separatrix confirmed that optimisation of levitation field damping led to CTs that remained physically larger over extended times. In general, the recurrence rate of good shots in the 25-turn coil configuration was poor compared with that in the 11-coil configuration. However, it remains unclear why the longest-lived CTs produced with the 25-turn configuration outlived those produced in the 11-coil configuration. One possible explanation is that the toroidal symmetry of the levitation field played a role at high formation settings. A second explanation may be the effect of the exceptionally thick lithium coating that was applied during the test with the 25-turn coil configuration.

A third possible explanation is that the ratio of the coil inductance to the levitation circuit holding inductance was increased from $L_{coil}/L_{main} = 600 \text{ nH}/6 \mu\text{H} = 0.1$ for the 11-coil configuration to $L_{coil}/L_{main} = 116 \mu\text{H}/6 \mu\text{H} \sim 20$ for the 25-turn coil. When conductive plasma enters the pot (confinement region) it reduces the inductance of the part of the

levitation circuit that includes the levitation/compression coil and the material that the coil encompasses. The levitation current increases when the inductance is reduced as plasma enters the pot. If the percentage rise of the levitation current is increased, by increasing the ratio L_{coil}/L_{main} , it means that levitation current prior to plasma bubble-in can be minimised. This reduction in I_{lev} reduces the likelihood that the levitation field will be strong enough to partially block plasma entry to the pot, while still allowing the field that is present, when the plasma does enter, to be strong enough to levitate the plasma away from the insulating wall. Comparing figures 3.9.1(c) and (d), it can be seen how the levitation current increases significantly at bubble-in for the 25-turn coil only. FEMM models indicate that the levitation fluxes found to be optimal at moderately high formation settings for the 25-turn and 11-coil configurations were approximately the same prior to plasma entry to the containment region. It may be that the increased levitation flux at CT entry in the 25-turn configuration was more efficient at keeping plasma off the wall. The optimal settings for $|t_{lev}|$ in the two configurations were limited by t_{rise} , the rise time of the levitation current for the particular configuration. While the strategy of increasing $|t_{lev}|$ to allow the levitation field more time to soak into the steel above and below the insulating wall led to slightly increased CT lifetimes on the 6-coil configurations, it was found that $|t_{lev}|$ should be reduced to as low a value as possible on the 25-turn coil and 11-coil configurations for best performance. Reducing $|t_{lev}|$ reduces the likelihood that the levitation field will impede, through the line tying effect, plasma entry to the containment region at formation. The benefit of slightly reducing plasma-wall interaction by *increasing* $|t_{lev}|$, and the line-tying effect, outweighed the detrimental effect of pot-entry blocking in the 6-coil configuration only. With the high inductance 25-turn coil, optimal $|t_{lev}|$ was equal to $t_{rise} \sim 150 \mu\text{s}$, while for the 11-coil configuration, optimal $|t_{lev}|$ was set to $t_{rise} \sim 50 \mu\text{s}$. It may be that allowing the level of levitation flux that was present in the containment region upon plasma entry in the 25-turn configuration to soak into the steel above and below the wall, even for 50 μs in the 11-coil configuration, degraded performance by impeding plasma entry to the containment region. The requirement for increased $|t_{lev}|$, and consequent pot-entry blocking may have been the cause of the poor repeatability of good shots in the 25-turn configuration. Future designs should optimise between the ideals of minimal coil inductances while maximising the coil to levitation circuit inductance ratios.

The 25-turn coil extended farther above and below the insulating wall than the stack of eleven coils - a fourth possible explanation for the (occasional) improved performance of the 25-turn coil over the 11-coil configuration is that the increased levitation field, relative to that for the 11-coil configuration, at the top and bottom of the insulating wall, played a key role. At low formation settings, without addition levitation circuit series resistance, levitated CT lifetimes in the 25-turn configuration were comparable to those in both the 11-coil and 6-coil configurations. It is clear that the feature shared by the 25-turn and

11-coil configurations, of closing the gaps that remained above and below the coil stack in the 6-coil configurations, was responsible for enabling the formation of high flux CTs with correspondingly increased lifetimes, and that the unconfirmed mechanism that enabled (occasional) even better performance in the 25-turn configuration was also effective only at high formation settings.

Compared with the aluminum flux conserver, a stainless steel wall led to more impurities and shorter CT lifetimes (figures 3.9.1(e) and (f)), likely due to more CT field-diffusion into the material, leading to enhanced sputtering. Toroidal $n = 2$ magnetic perturbations were observed on CTs produced with both stainless steel and aluminum outer flux conservers, and remained even when a moderate levitation field was allowed to soak through the stainless steel wall, but were absent in all configurations tested in which a CT was held off an outer insulating wall by a levitation field. It is known that $n = 2$ fluctuations are a sign of internal MHD activity associated with increased electron temperature. However, the longest-lived CTs produced with the 25-turn coil configuration endured for up to 10% longer than, and may therefore be reasonably assumed to be hotter than the CTs produced with the stainless steel outer flux conserver. It is possible that the levitation field acts to damp out helically propagating magnetic fluctuations at the outboard CT edge and that internal MHD activity is relatively unchanged. The $n = 1$ magnetic fluctuations observed when 80 kA additional crowbarred shaft current was applied to the machine in the eleven-coil configuration confirmed coherent toroidal CT rotation, and may have been a result of more vigorous MHD activity that remained apparent despite damping.

As presented in [65], the e-folding time characterising the decay rate of spheromak magnetic field is:

$$\tau_{mag} = \frac{1}{2Z_{eff}} R^2 T_{e0} \sqrt{T_{eE}} \quad (3.9.1)$$

where R [m] is an estimate for the outer CT separatrix (~ 0.15 m for the magnetic compression experiment), T_{e0} [keV] is the peak electron temperature and T_{eE} [keV] is the edge electron temperature (expected to be < 10 eV). The fact that the best levitated CT lifetimes were $\sim 20\%$ less than lifetimes seen on the machine when the insulating outer wall was replaced with the standard MRT aluminum flux conserver may be accounted for by the higher impurity-associated Z_{eff} of levitated CTs. It is clear that the switch from the alumina wall to the quartz wall led to an increased impurity level. The 11-coil configuration reduced the impurity problem but a further reduction in impurities and Z_{eff} would have been achieved in a configuration with eleven coils on an alumina insulating wall. It seems clear that CT lifetimes comparable with those achieved with the aluminum flux conserver could be attained in such a configuration. An obvious further improvement would be to implement an even more compatible plasma facing material. It is well known that boron nitride (BN) is a good material for minimising impurity levels in cases when an insulating material comes in contact

with plasma, and is often used as an insulating component on probes that are inserted into a plasma. Compared with alumina, boron has lower Z than aluminum, and nitrogen is less reactive than oxygen, and is thus less likely to combine with other impurities to form high Z molecules that would lead to further radiative cooling. While standard hot-pressed BN, which has a hexagonal crystal structure, contains up to 5% oxygen and other impurities, pyrolytic boron nitride (PBN), which has a diamond-like crystal structure, is an extremely pure (>99.999%) form of BN that is manufactured using a chemical vapor deposition (CVD) process. Due to the manufacturing process, PBN is generally available only in thin sheets or thin-walled tubes. An eleven coil configuration including a PBN tube with 2 mm wall thickness located with a close fit inside an alumina tube would be a natural next step toward improving levitated CT performance. The alumina tube would be able to support vacuum and should ideally have an inner radius at least equal to that of the quartz tube which it would replace. It may be, as discussed, that the 25-turn coil had some additional advantages over the eleven-coil configuration, that could be reproduced in a new build.

A redesign of the experiment involving levitation and compression coils located inside the vacuum vessel, as was implemented on the S-1 magnetic compression [23], device would involve a lot of work but would avoid the problem of impurity contamination associated with the external insulating wall. The design of vacuum-tight power transmission to the internal coils would be a challenge. It would be worth attempting a minor change with a new insulating wall material on the eleven coil configuration, and assess the results, before attempting such a major modification.

Chapter 4

Magnetic Compression

The focus of this chapter is on the results obtained when CTs were magnetically compressed. Section 4.1 presents an overview of the principal observations from representative compression shots taken in the main configurations that were introduced in chapter 3. It will be shown that, particularly with the eleven coil configuration, significant increases in magnetic field, density, and ion temperature were routinely observed at compression. Various metrics for magnetic compression performance were developed and are presented here. The compressional instability that was observed on most compression shots is discussed in section 4.2. A comparison of compressional performance between configurations is presented in section 4.3. The cause of the high frequency fluctuations observed on the field measurements for many compression shots taken in the six coil configuration is discussed. The method developed to experimentally evaluate the CT outboard equatorial separatrix, described in chapter 3, is applied to a compressed shot, and indicates a significant geometric compression factor of around two. Indications, from scintillator data, of fusion neutron production during CT formation, is presented in section 4.5. The chapter concludes with a summary in section 4.6.

4.1 Overview of results

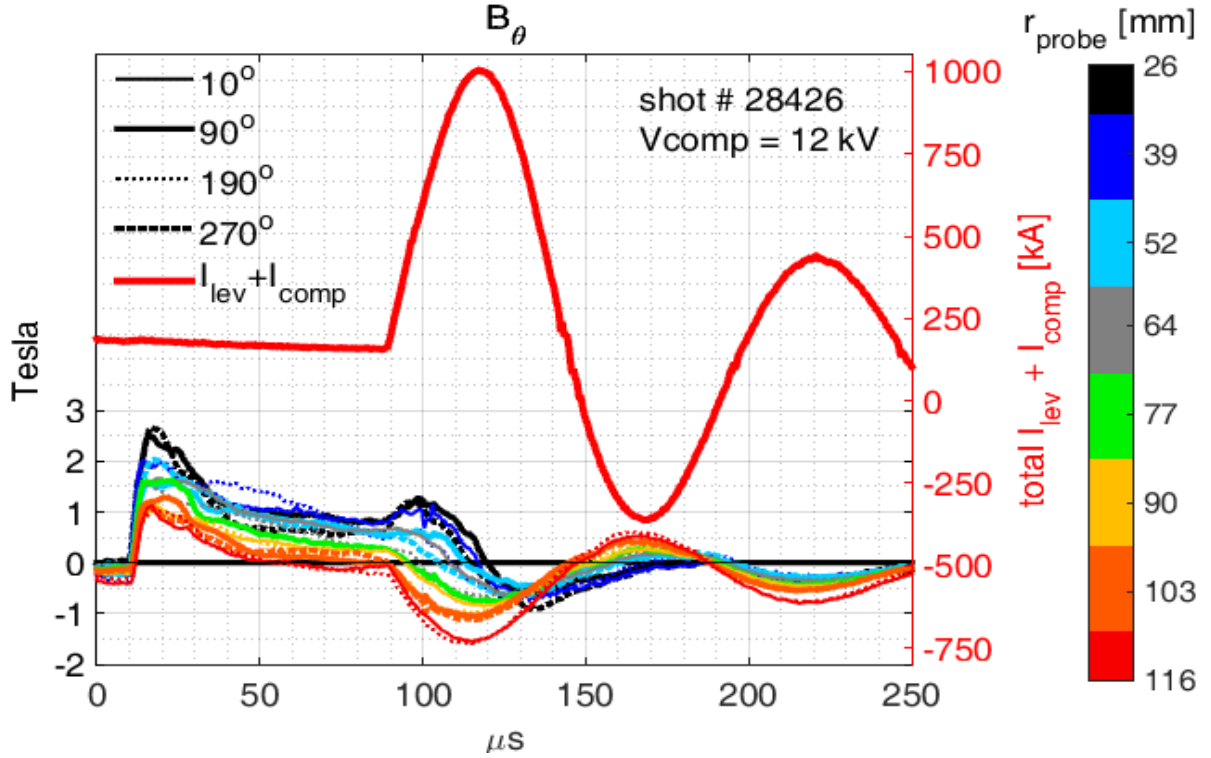


Figure 4.1.1: B_θ and $I_{lev} + I_{comp}$ for shot 28426 (6-coil configuration)

Figure 4.1.1 shows B_θ traces and total levitation plus compression current (right axis) for shot 28426, which was taken in the 6-coil configuration, with $V_{comp} = 12$ kV and $t_{comp} = 90$ μ s. Shot 28426 is a representative compression shot for the 6-coil configuration. The levitation capacitors were fired at $t_{lev} = -300$ μ s (the original low resistance 2.5 m Ω cables were in place), and by the time the plasma has entered the confinement region at around 15 μ s, the total levitation current (divided approximately equally between the six coils) has dropped to ~ 200 kA. By $t = t_{comp} = 90$ μ s, the total levitation current has dropped further, to around 150 kA. At this time, the compression capacitors are fired, and the total compression current rises over $t_{rise} \sim 25$ μ s to its peak, for $V_{comp} = 12$ kV, of around 850 kA, so that the total combined levitation and compression current is around 1 MA at the time peak compression, around 115 μ s. In this shot, the CT is compressed inwards beyond the probes at $r = 77$ mm, so B_θ at the probes located at $r \geq 77$ mm (*i.e.*, green, light orange, dark orange, and red traces) is a measurement of the compression field after ~ 90 μ s, while, in general, the CT poloidal field is measured at $r < 77$ mm, until ~ 120 μ s. Note that the combined levitation and compression current changes polarity at around 150 μ s and again at ~ 190 μ s, because the compression current is allowed to ring with the capacitor discharge.

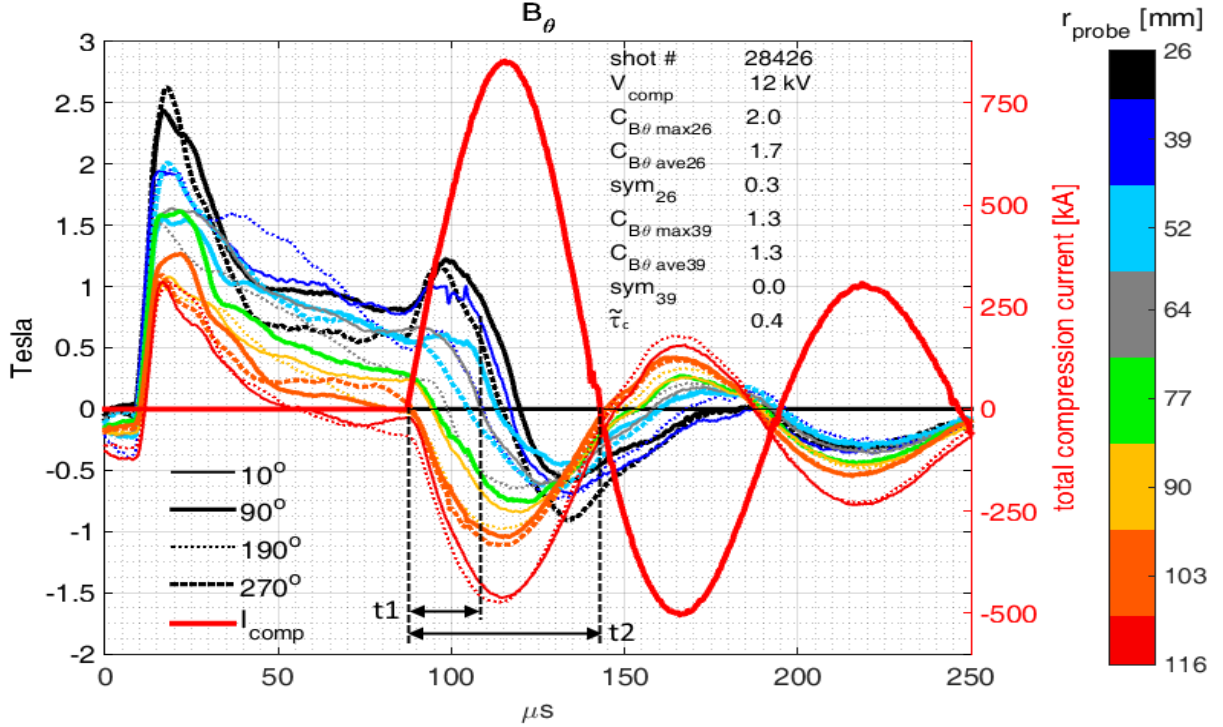


Figure 4.1.2: B_θ and I_{comp} for shot 28426 (6-coil configuration)

The B_θ traces for shot 28426 are produced again in figure 4.1.2, where, for clarity, the compression current, this time without the superimposed levitation current, is also shown. Experimental data at GF is usually analysed and visualised using IGOR-PRO software, but for the magnetic levitation and compression data, some MATLAB scripts were written so that data from individual shots could be visualised quickly without waiting one to two minutes for the IGOR program to load the data for each shot. In figure 4.1.2, some of the Matlab-calculated parameters that were considered good indications of the quality of the compression shot are displayed. $C_{B\theta\text{max}}(r)$ and $C_{B\theta\text{ave}}(r)$ are the maximum and average of the two poloidal magnetic compression ratios, obtained at the two probes located at radius r mm, 180° apart toroidally, e.g., $C_{B\theta\text{max}26} = \max(C_{B\theta_{90^\circ r26}}, C_{B\theta_{270^\circ r26}})$, where, for example, $C_{B\theta_{270^\circ r26}} = B_{\theta CT\text{peak}}/B_{\theta CT\text{pre}}$, where $B_{\theta CT\text{peak}}$ and $B_{\theta CT\text{pre}}$ are the values of B_θ , measured with the probe at $r = 26$ mm, $\phi = 270^\circ$, at the peak of compression and just before compression respectively. The values of $C_{B\theta\text{max}26} = 1.7$ and $C_{B\theta\text{ave}26} = 1.3$ obtained for this shot are quite low, for the reasons discussed below. Note that when $|B_{\theta CT\text{pre}}| < |B_{\theta lev\text{pre}}|$, where $|B_{\theta lev\text{pre}}|$ (note $B_{\theta lev\text{pre}} < 0$) is the absolute value of the poloidal levitation field that would be measured at the probe just before compression if no CT was present, a "levitation offset" should be included when calculating these compression ratios. In those cases, the compression ratio would be $C_{B\theta} = (B_{\theta CT\text{peak}} - B_{\theta lev\text{peak}})/(B_{\theta CT\text{pre}} - B_{\theta lev\text{pre}})$, where $B_{\theta lev\text{peak}}$ is the poloidal levitation field that would be measured at the probe at peak compression if

no CT was present. However, these cases (anyway, only one shot which is being ignored) are not interesting because there's not much left to compress if $|B_{\theta CTpre}| < |B_{\theta levpre}|$. This is especially true for shots with the decay rate of the levitation field matching the CT's decay rate, when $|B_{\theta levpre}|$ is very low - for example $B_{\theta levpre} \sim -0.01$ T for shot 39735 (figure 4.1.3), while $B_{CTpre} \sim 0.3$ T.

Parameters sym_r give an indication of the toroidal asymmetry of the magnetic compression at the probes located at radius r mm. Shots with sym_r close to zero have toroidally symmetric compression at radius r mm. With parameters $sym_{26} = 0.3$, and $sym_{39} = 0$, shot 28426 had quite symmetric compression at $r = 26$ mm, and very symmetric compression at $r = 39$ mm. Asymmetry of the magnetic field at compression was typical for both the 6-coil and 11-coil configurations, with only a slight improvement with the 11-coil configuration - this shot has exceptionally symmetric compression of poloidal field.

The parameter $\tilde{\tau}_c$ indicates the level of compressional flux conservation, and is calculated as $\tilde{\tau}_c = t1/t2$, where $t1$ and $t2$ are indicated in figure 4.1.2. $t2 \sim 50\ \mu\text{s}$ is the half-period of the compression current, and $t1$ is the time from t_{comp} to the average of the times when B_θ at the two $r = 26$ mm probes fall to their pre-compression values (at $t = t_{comp}$). If the CT doesn't lose flux during compression, due to, for example, enhanced resistive flux loss, or some instability that disrupts flux surfaces, the measured B_θ at the inner probes rises and falls approximately in proportion to the compression current, and $t1 \sim t2$. Shots for which flux is not lost due to any mechanism besides the usual resistive loss are characterised by $\tilde{\tau}_c \sim 1$. This characterisation method assumes that the CT is not being compressed to a radius less than 26 mm. If that did happen, the indication of B_θ increase at 26 mm should disappear early ($\tilde{\tau}_c \ll 1$), and then there would be no data whatsoever available to assess the compression beyond 26 mm. If the CT is being compressed beyond 26 mm, and stays stable, it may expand back to $r > 26$ mm after the peak in compression field, but there are no examples of that occurrence in the data.

Shots taken in the 6-coil configuration generally became "unstable", and lose poloidal flux, during magnetic compression - the low value of parameter $\tilde{\tau}_c$ of around 0.4 for shot 28426 is typical for shots taken in the 6-coil configuration. Compression ratios are low for shots that don't conserve their poloidal flux during compression, so the low value of $C_{B\theta ave26}=1.7$ for shot 28426 is also typical for shots taken in the 6-coil configuration. The proportion of poloidal flux conserving shots with high magnetic compression ratios increased dramatically with the transition to the 11-coil configuration, as indicated later in section 4.3.

If the CT remains stable during compression, it expands to its pre-compression state (apart from resistive flux losses and thermal losses) between $t \sim t_{comp} + 25\ \mu\text{s}$ and $t \sim t_{comp} + 50\ \mu\text{s}$. When the compression current changes direction at $t \sim t_{comp} + 50\ \mu\text{s}$, the CT poloidal field reconnects with the compression field, and a new CT with polarity opposite to

that of the previous CT is induced in the containment region, compressed, and then allowed to expand. The process repeats itself at each change in polarity of the compression current until either the plasma loses too much heat, or the compression current is sufficiently damped. As shown in chapter 7, MHD simulations model this effect while closely reproducing experimental measurements for B_θ , line-averaged n_e , and T_i (from the ion-Doppler diagnostic), and X-ray-phosphor imaging indicates the compressional heating of up to three distinct plasmoids on many compression shots. Note also that, as shown in section 7.5.2.3, MHD simulations support the idea that loss of CT poloidal flux at compression leads to the collapse in poloidal field that is characterised by having parameter $\tilde{\tau}_c$ less than one.

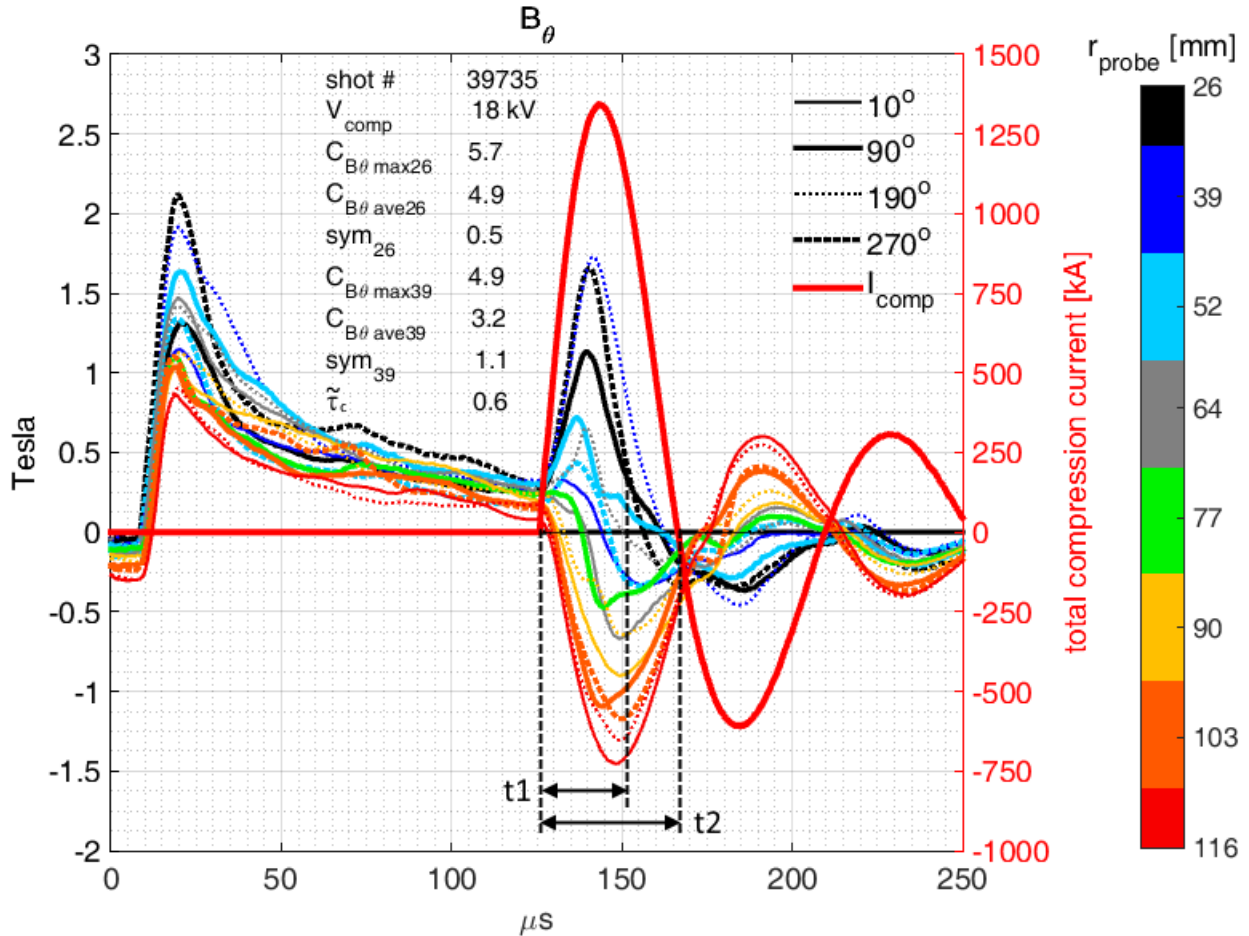


Figure 4.1.3: B_θ and I_{comp} for shot 39735 (11-coil configuration)

Figure 4.1.3 shows B_θ traces and total compression current (without levitation current) for shot 39735, in the 11-coil configuration. This is one of the few shots that were compressed late in time, at $\sim 130 \mu\text{s}$. The voltage on the compression capacitors was close to their maximum setting, at 18 kV, resulting in $\sim 1.3 \text{ MA}$ of total compression current. The values of $C_{B\theta \text{ max}26} = 5.7$ and $C_{B\theta \text{ ave}26} = 4.9$ obtained for this shot are particularly high, partly because the CT was compressed late when most of its poloidal flux had resistively decayed

away. Shot 39735, has parameter $\tilde{\tau}_c = 0.6$, $sym_{26} = 0.5$ and $sym_{39} = 1.1$, which classify it as a shot with quite asymmetric compression (especially, as indicated by sym_{39} , in the poloidal plane defined by $\phi = 10^\circ - -190^\circ$), that lost a significant proportion of its flux.

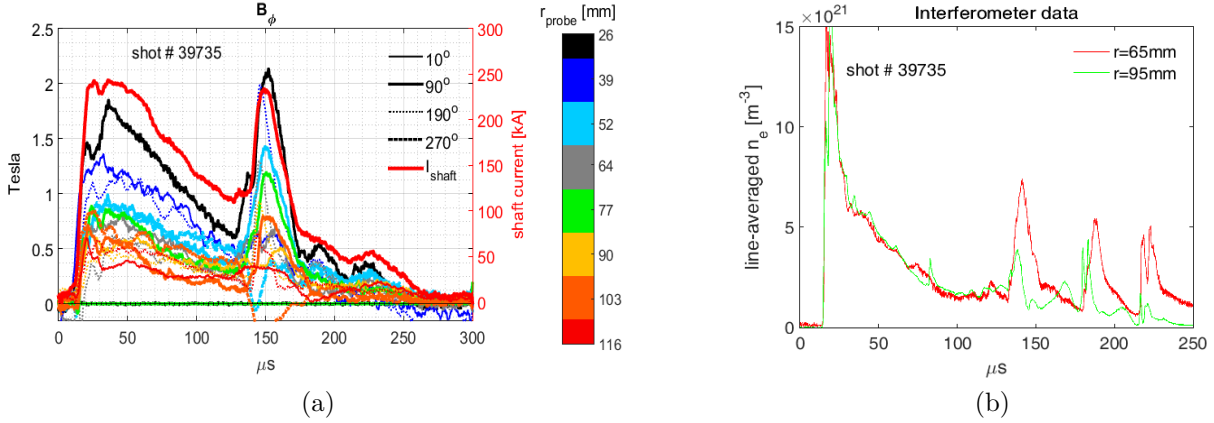


Figure 4.1.4: B_ϕ and n_e traces for shot 39735 (11-coil configuration)

Figure 4.1.4 shows measured toroidal field and line-averaged electron density for shot 39735. As discussed in sections 3.1 and 4.2, B_ϕ rises at compression as shaft current increases when it is able to divert from the aluminum bars outside the insulating wall to a lower inductance path through ambient plasma outside the CT. For the 1st, 2nd and 3rd compressions, this is particularly evident from the rise of the $r = 26$ mm probe signal. An obvious exception is during the 1st compression at $\sim 150\text{ }\mu\text{s}$, when the toroidal field at $\phi = 270^\circ$ drops off - this is an indication of the compressional instability that is discussed later in section 4.2. The measured electron densities shown in figure 4.1.4(b) are line-averaged quantities obtained with He-Ne laser interferometers looking down the vertical chords at $r = 65\text{ mm}$ and $r = 95\text{ mm}$ that are indicated in figure 2.2.2. The three distinct density peaks correspond to the three CT compressions. Line-averaged electron density at $r = 65\text{ mm}$ increased by a factor of around five at the main compression cycle. From the time difference between the peaks at compression of the two n_e signals, the electron density front at the main compression is found to move inwards at $\sim 10\text{ km/s}$.

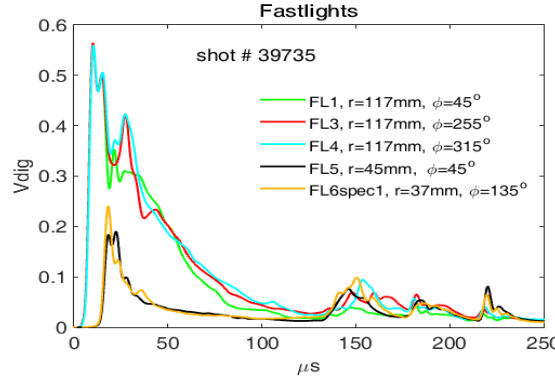


Figure 4.1.5: Optical intensity measurements for shot 39735 (11-coil configuration)

Figure 4.1.5 shows measured optical intensity for shot 39735. Plasma breakdown is indicated as being toroidally symmetric. Light intensity increases at each of the three compressions when density and associated line radiation intensity increases. At $t_{comp} = 130 \mu\text{s}$, intensity at $r = 117 \text{ mm}$, $\phi = 45^\circ$ (green trace) does not rise to the same level as at the other 117 mm chords, indicating toroidally asymmetric compression. Ion-Doppler data is not available for this shot.

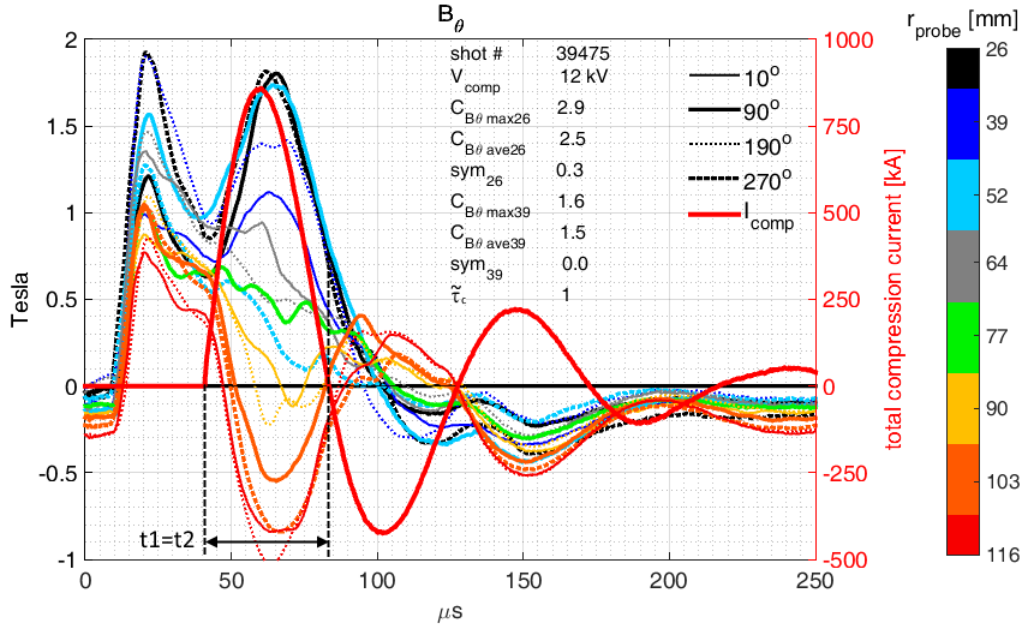


Figure 4.1.6: B_θ for shot 39475 (11-coil configuration)

Figure 4.1.6 shows the measured B_θ for shot 39475. This shot had the more usual choice of $t_{comp} = 45 \mu\text{s}$ at a moderate formation voltage of 12 kV. The magnetic compression ratios calculated are also moderate, at $C_{B\theta \text{ max}26} = 2.9$ and $C_{B\theta \text{ ave}26} = 2.5$. With the calculated parameters $\tilde{\tau}_c = 1$, $sym_{26} = 0.3$ and $sym_{39} = 0$, this shot conserved poloidal flux at compression, and the compression was symmetric. As indicated in section 4.3, flux conserving shots were

common only in the 11-coil configuration. Note that $B_{\theta 270^\circ r26} > B_{\theta 90^\circ r26}$, $B_{\theta 270^\circ r52} < B_{\theta 90^\circ r52}$, $B_{\theta 190^\circ r39} \gg B_{\theta 10^\circ r39}$, while $B_{\theta 190^\circ r64} \sim B_{\theta 10^\circ r64}$, from formation until the start of compression, just as in shot 39735 (figure 4.1.3) - it's likely that magnetic probe calibrations are largely responsible for this.

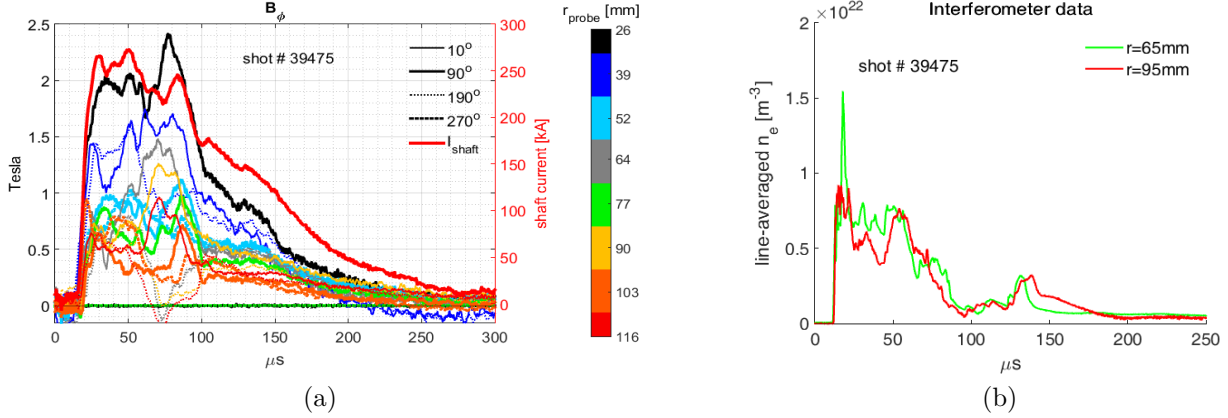


Figure 4.1.7: B_ϕ and n_e for shot 39475 (11-coil configuration)

Figure 4.1.7 shows the measured B_ϕ and line-averaged electron density traces for shot 39475. While not as distinct as for shot 39735 (figure 4.1.4(b)), there are again three density peaks corresponding to the three compressions. The B_ϕ signals for this shot are an excellent exemplification of the instability that was observed on most compression shots. It can be seen how B_ϕ at all four probes at 190° drops during compression, while the field at the other toroidal angles rises. The angle at which the signal drops varies, apparently randomly, from shot to shot, but shots were generally quite consistent in displaying this behaviour.

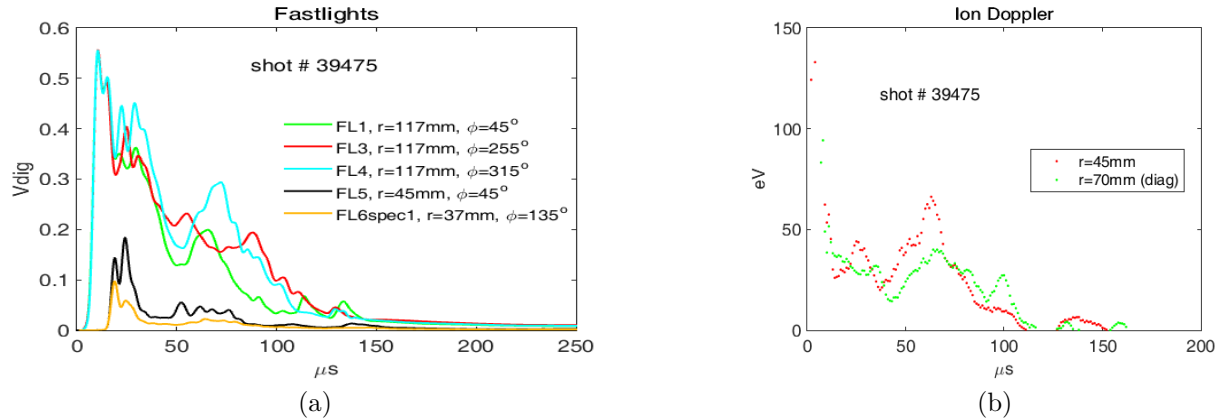


Figure 4.1.8: Optical intensity and T_i measurements for shot 39475 (11-coil configuration)

Figure 4.1.8(a) shows measured optical intensity for shot 39475. Plasma breakdown is again indicated as being toroidally symmetric. The light intensity increases at compression

when density and associated line radiation intensity increases. At $t_{comp} = 45 \mu\text{s}$, intensity at $r = 117 \text{ mm}$, $\phi = 255^\circ$ (red trace) does not rise to the same level as at the other 117 mm chords, indicating toroidally asymmetric compression. Compared with data for shot 39735 (figure 4.1.5), it can be seen how the factors by which optical intensity increases at compression are relatively minor for this shot, especially at the inner chords at $r = 37 \text{ mm}$ and $r = 45 \text{ mm}$. This is likely related to the reduced value of V_{comp} for this shot. Figure 4.1.8(b) shows the ion-Doppler temperature measurement for shot 39475, where the diagnostic was focused along the two chords indicated in figure 2.2.2. At moderate $V_{comp} = 12 \text{ kV}$, the ion temperature increase at compression is still significant, indicated as rising from around 20 eV to 70 eV at the $r = 45 \text{ mm}$ chord.

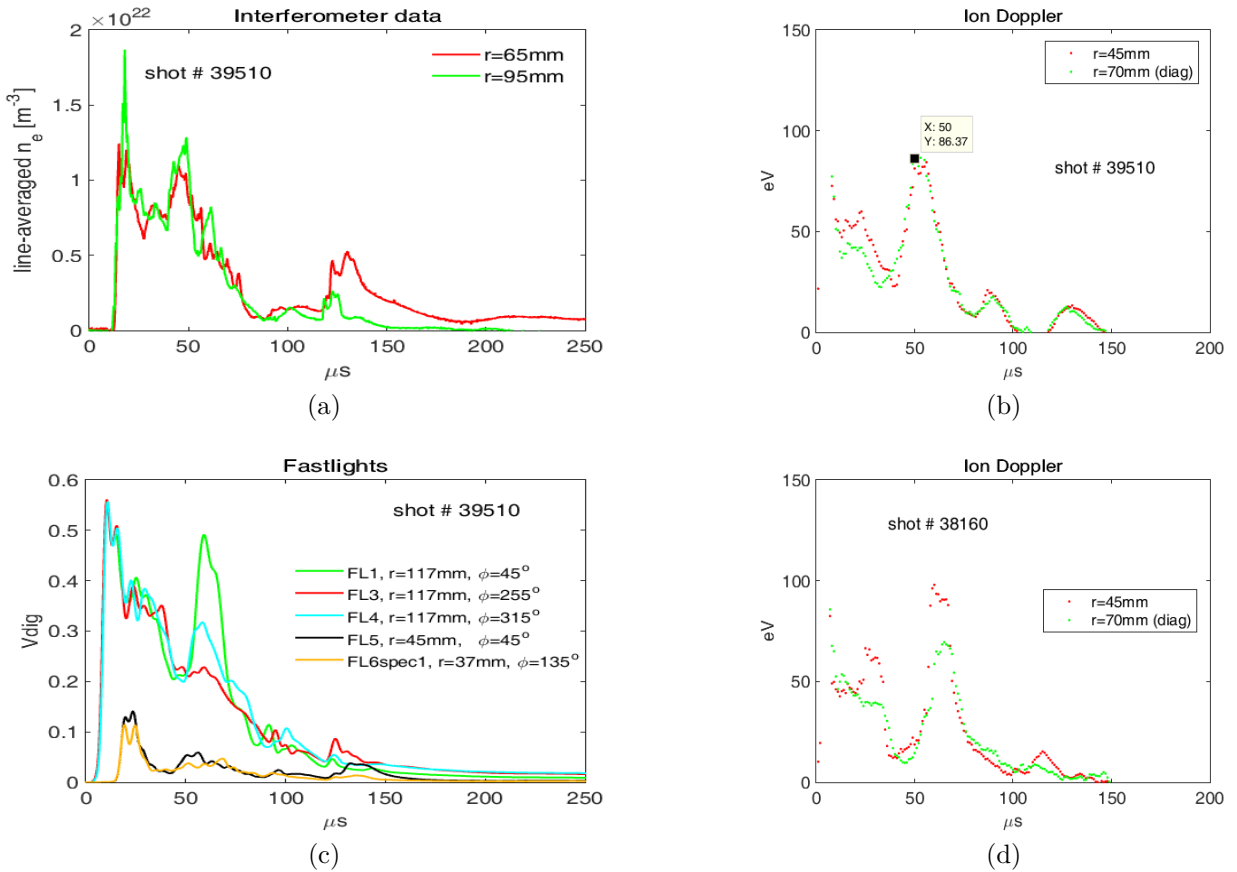


Figure 4.1.9: n_e , T_i and optical intensity measurements for shot 39510, T_i for shot 38160 (11-coil configuration)

Figures 4.1.9(a) and (b) show the density and ion-Doppler temperature measurements for shot 39510, which was also a flux conserving shot, but with $t_{comp} = 40 \mu\text{s}$, and increased compressional energy, with $V_{comp} = 18 \text{ kV}$. With increased compressional energy, the indicated increases in both density and ion temperature are more significant than in shot 39475. For this shot, an increase in ion temperature by a factor of around four, from $\sim 25 \text{ eV}$ to ~ 100

eV, is measured in the region of the ion Doppler chords. A maximum error in the temperature measurement (He II line at 468.5nm) due to density broadening has been evaluated as ~ 12 eV for density levels associated with shot 39510 at peak compression [57, 58]. Figure 4.1.9(c) shows measured optical intensity for shot 39510. Plasma breakdown is indicated as being toroidally symmetric, but this diagnostic indicates that compression may have been quite asymmetric. The light intensity increases at compression when density and associated line radiation intensity increases, particularly at $r = 117$ mm, $\phi = 45^\circ$ (green trace). Figure 4.1.9(d) shows the ion-Doppler measurement for shot 38160, which had $t_{comp} = 45$ μ s and $V_{comp} = 14$ kV. The density measurement for shot 38160, which indicated typical density values, was not considered to be trustworthy - extreme increases in optical emission at the time of compression indicated that the density may have been underestimated. Although the ion temperature rise at compression looks significant for this shot, careful analysis indicated that, around peak compression, Lorentzian profiles are better fits than Gaussian profiles to plots of photon count against photon frequency, indicating the likelihood that density broadening rather than temperature broadening was the dominant broadening mechanism for shot 38160 (see discussion in section 2.2.4). Gaussian profiles were better fits to the data for shots 39475 and 39510, so it is believed that the ion-Doppler measurements for those shots are true indications of temperature rise at compression. Note that ion-Doppler temperature increases at compression were significant on the 11-coil configuration only.

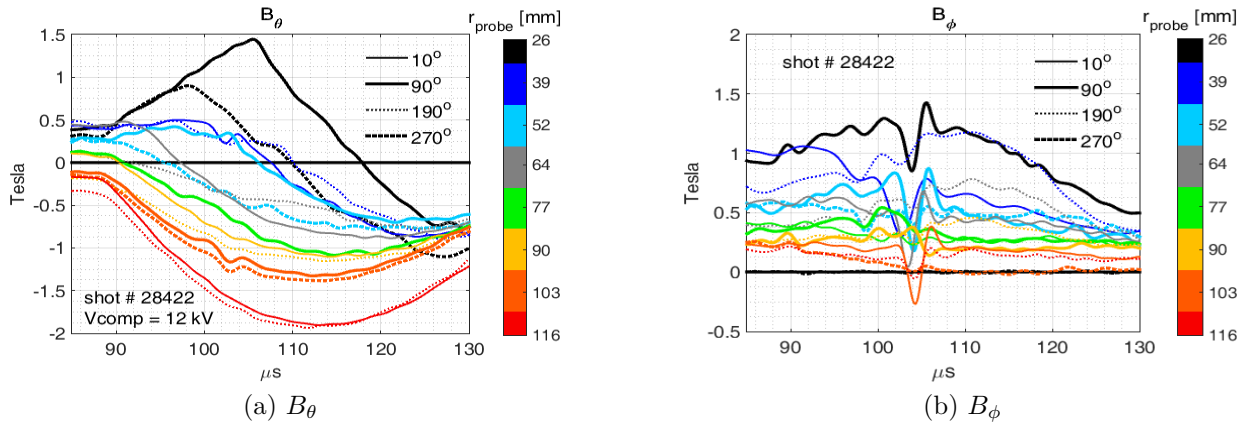


Figure 4.1.10: B_θ and B_ϕ for shot 28422 (6-coil configuration), $t_{comp} = 90$ μ s

Many compression shots on the 6-coils-ceramic build, some on the 6-coils-quartz build, but apparently none on the 11-coils configuration, have high frequency B_ϕ spikes - fluctuations up to one Tesla, with half-periods of ~ 3 μ s, see, for example, figure 4.1.10. These events are evident primarily on the B_ϕ probes but are often evident on the B_θ probes too. The fact that the insulation on the last build with eleven coils was more robust to account for the proximity of the top and bottom coil-pairs to the steel vessel, points to the likelihood that

a coil-to-coil or coil-to-aluminum-bar electrical short was involved in the events on earlier configurations. Confirming this, the few shots for which there is a clear indication of a coil short on the X-ray-phosphor images do display this type of behaviour on their B_ϕ traces. An external poloidal arc would induce a B_ϕ fluctuation, and if there was a toroidal component to the arc, then also a fluctuation in B_θ . On the other hand, we expect the plasma to adjust itself to preserve its pressure-balanced structure, so toroidal magnetic perturbations should result in poloidal ones too.

4.2 Compressional instability

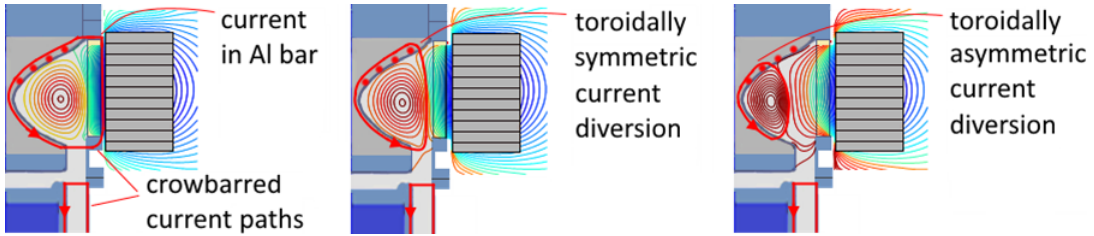


Figure 4.2.1: Asymmetric current diversion

Figure 4.2.1 shows a possible explanation for the compressional instability that was routinely observed. After the $50\ \mu\text{s}$ formation capacitor-driven pulse, toroidal-flux conserving crowbarred current continues to flow, primarily along two separate paths as indicated. In addition, it is likely that there is a third current path, consisting of the merger of the two paths indicated here. Referring to the upper path, initially most of the outboard part of this current is in the aluminum bars depicted in figure 3.1.1(a). Shaft current, and B_ϕ at probes, rise at compression as the current path shifts symmetrically to a lower inductance path (central subfigure); now the outboard part of the current loop travels through the ambient plasma outboard of the CT. The asymmetric current diversion depicted in the right subfigure will be discussed after outlining how the symmetric shifting current path mechanism is reproduced in MHD simulations:

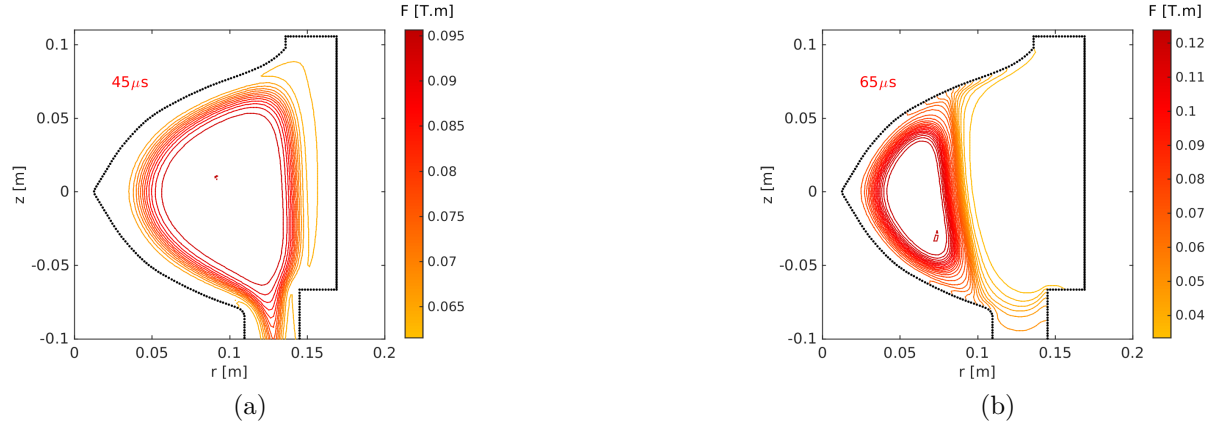


Figure 4.2.2: f contours at magnetic compression, simulation 1968

Figure 4.2.2 shows contours of f at $45\mu\text{s}$ just prior to magnetic compression, and at $65\mu\text{s}$, at peak magnetic compression. Contours of $f = rB_\phi$ represent paths of poloidal current. Closely spaced contours indicate regions of high gradients of f , which in turn are regions of high currents. The MHD equations implemented to the code are formulated such that the code has various conservation properties (see section 5.6.2), including conservation of toroidal flux. It can be seen in figure 4.2.2(b) how the imposition of toroidal flux conservation leads to the induction, at magnetic compression, of poloidal currents flowing from wall-to-wall through the ambient plasma just external to the outboard boundary of the CT.

If some mechanism causes the CT to be compressed more at a particular toroidal angle (an effect which the axisymmetric MHD code cannot reproduce), the inductance of the current path at that angle will be reduced further and more current will flow there (right subfigure in figure 4.2.1), enhancing the instability. This is analogous to the mechanisms behind external kink and toroidal sausage type instabilities. As the current path moves inwards past the probes at a particular toroidal angle, B_ϕ at the probes will change polarity at that toroidal angle, as is observed on most compression shots (*e.g.*, figures 4.1.4(a) and 4.1.7(a)). As the CT decompresses as I_{comp} decreases, the current path returns towards its pre-compression path. It is noteworthy that although the magnetically compressed CTs generally exhibit this instability, there is a noticeable correlation in that the compression shots that have a high value of $\tilde{\tau}_c$ (*i.e.*, apparent flux conservation during compression) seem to exhibit the clearest manifestation of the instability, through the behaviour of the B_ϕ signals - shot 39475 (figure 4.1.7(a)) is a good example of this. As mentioned earlier, even levitated, but non-compressed shots, exhibited this behaviour to some degree (*e.g.*, figure 3.6.2(c)), in cases where the levitation currents were not optimised to decay at near the rate of the CT currents.

4.3 Comparison of compression parameters between configurations

The impedances (effective resistance to alternating current, due to combined effects of ohmic resistance and reactance) of the coils arrays are slightly different for the 6-coil and 11-coil configurations, leading to a few percent variation in peak compression current at the same V_{comp} . At $V_{comp} = 18$ kV, measured peak I_{comp} was ~ 200 kA per coil in the 6-coil configuration, compared with ~ 210 kA per coil-pair (and ~ 210 kA in the single coil 3rd from the bottom of the stack) in the 11-coil configuration. At the same V_{comp} , compressional flux, as estimated from FEMM model outputs, is around 1.7 times higher in the 6-coil configuration, relative to the 11-coil configuration, due to the large gaps (see figure 3.1.1(b) *cf.* figure 3.6.1(b)), above and below the coil stack, that ease entry of compressional flux into the containment region for the 6-coil configuration.

In general, as external compressional flux is increased, the level of CT flux conservation at compression is reduced, while, for the same level of flux conservation, magnetic compression ratios are increased. A fair comparison of compression performance metrics across builds can be obtained by comparing the metrics for shots with the same level of external compressional flux. For around the same external compressional flux, we would ideally compare shots with $V_{comp} = 14$ kV in the 11-coil configuration against shots with $V_{comp} = 8.2$ kV (which were not taken) in the 6-coil configuration, but a reasonable comparison of compression parameter trending can be made looking at shots with $V_{comp} = 14$ kV for the 11-coil configuration, and $V_{comp} = 7$ kV $\rightarrow 9$ kV in the 6-coil configuration.

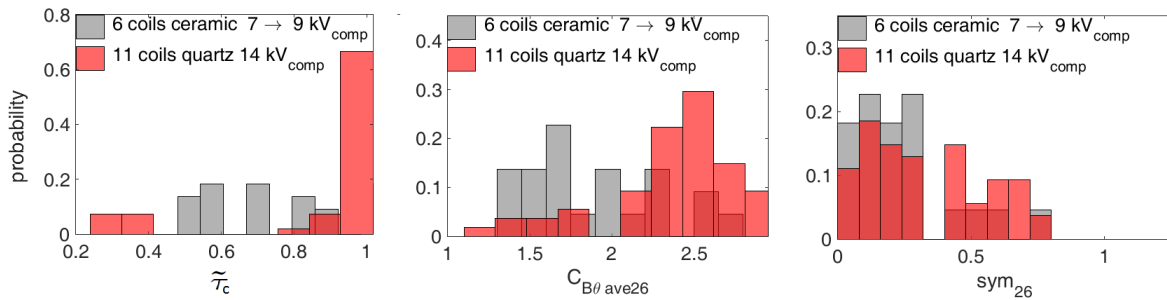


Figure 4.3.1: Comparison of compression parameters

Figure 4.3.1 shows normalised histograms of key compression parameters that were defined below figure 4.1.2. The recurrence rate of shots that conserved CT flux at compression was significantly improved in the 11-coil configuration. Around 70% of shots had good CT flux conservation (*i.e.*, $\tilde{\tau}_c \sim 1$) in the 11-coil configuration, while only $\sim 10\%$ of shots conserved $\sim 80\%$ of flux (*i.e.*, $\tilde{\tau}_c \sim 0.8$) in the 6-coil configuration. Poloidal magnetic compression ratios

(characterised by $C_{B\theta\text{ave}26}$) would be expected to be low when CT flux is lost, and it can be seen how the ratios are nearly doubled on average in the 11-coil configuration. Compression asymmetry (characterised by sym_{26}) remains poor in both configurations. While reduced plasma wall interaction at formation and consequent reduced impurity radiation cooling in the 11-coil configuration was certainly behind the huge improvement in lifetimes of levitated CTs (figures 3.8.2 and 3.9.1), it seems likely, but can't be confirmed without further experiment or 3D simulation, that a different mechanism was responsible for the orders of magnitude improvement in the rate of shots with good CT flux conservation at compression. Supporting this, shots taken in the 11-coil configuration with compression fired late when plasma has had time for significant diffusive cooling (*e.g.*, figure 4.1.3) generally conserved *more* flux than those fired early in time in the 6-coil configuration (*e.g.*, figure 4.1.2). The improvement is likely to be largely due to the compression field profile itself, which led to more uniform outboard compression, as opposed to largely equatorial outboard compression with the six coil configuration. Equatorially-focused outboard compression may have caused the CT to bulge outwards and upwards/downwards above and below the equator, leading to poloidal field reconnection, CT depressurisation and possible disruption as a consequence.

4.4 Experimentally measured CT outboard separatrix radius for compression shots

Using the method outlined in section 3.7, it is possible to determine the CT separatrix at the equator ($z \sim 0$ mm) for compression shots.

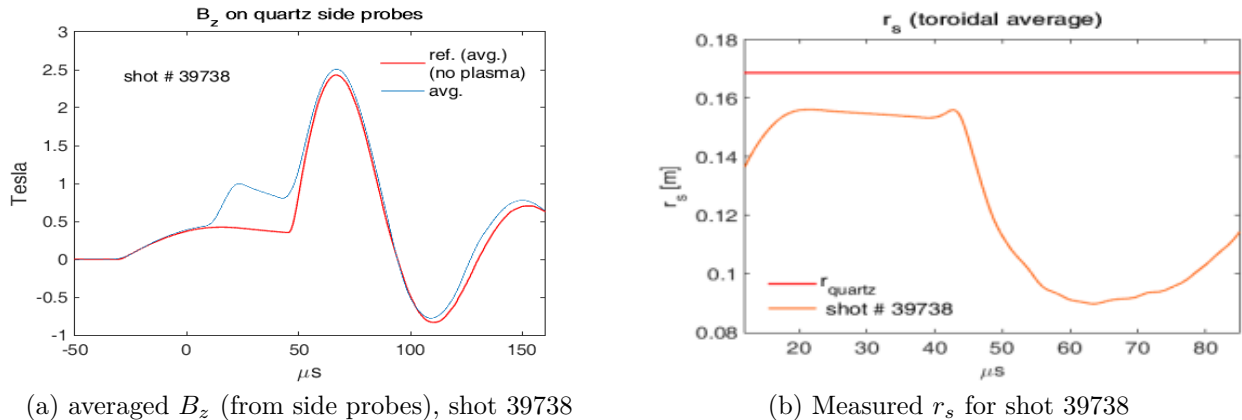


Figure 4.4.1: Measured CT separatrix radius for compression shot 39738

Figure 4.4.1(a) shows the averages of the eight $B_\theta(\phi, t)$ and $B_{z\text{ref}}(\phi, t)$ signals for shot 39738, which had $V_{\text{comp}} = 18$ kV, $|t_{\text{lev}}| = 30$ μs , $t_{\text{comp}} = 45$ μs , and was taken in the 11-coil

configuration with $70\text{ m}\Omega$ cables in place in the levitation circuits, so that the functional fit indicated in figure 3.7.2(b) was used to find $r_s(t)$, which is shown in figure 4.4.1(b). For compression shots, it is convenient to find the toroidally averaged r_s using toroidally averaged probe data. As seen in figure 4.4.1(a), at compression, the reference B_z is very close to B_z when the CT is present, so that errors in probe signal response can lead to instances when $B_{z\text{ref}}(\phi, t) > B_z(\phi, t)$, and consequent complex-valued $r_s(\phi, t)$ solutions (see section 3.7). Using the toroidally averaged signals reduces the likelihood of this error. For shot 39738, a radial compression factor, in terms of equatorial outboard CT separatrix, of $C_s = 1.7$ is indicated. Note that $r_s \sim 9\text{ cm}$ at peak compression. As outlined in section 3.7.1, when $r_s \lesssim 9\text{ cm}$, the slope of the functional fit in 3.7.2(b) is too flat to be successfully inverted with good accuracy. For this reason, C_s cannot be evaluated if the CT is compressed more than in shot 39378. An example of a shot in which compression is too strong for successful evaluation of C_s is shot 39735 (figure 4.1.3) which also has $V_{\text{comp}} = 18\text{ kV}$, but is compressed later ($t_{\text{comp}} = 130\text{ }\mu\text{s}$), when pre-compression CT flux has decayed to lower levels and therefore compression is more extreme.

4.5 Scintillator data

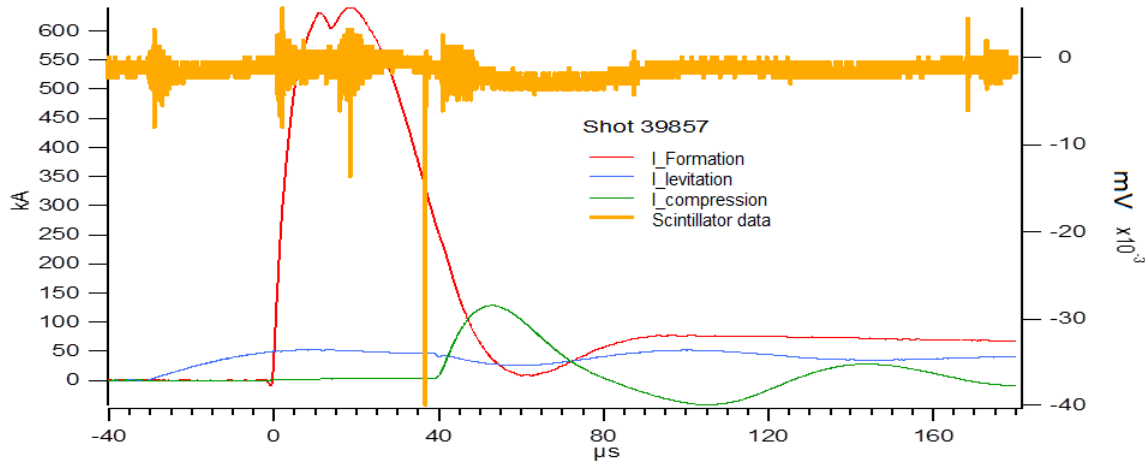


Figure 4.5.1: Scintillator data for shot 39857

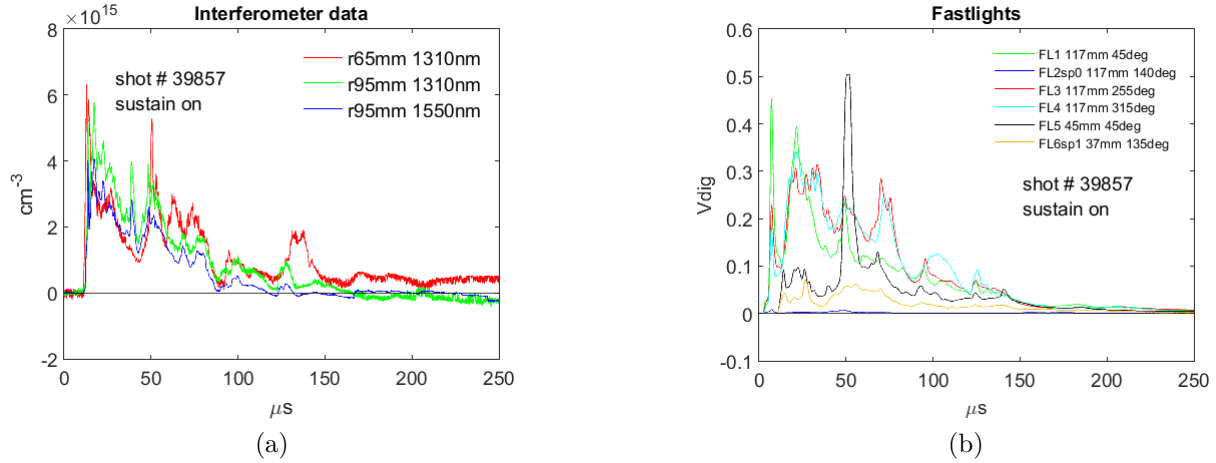


Figure 4.5.2: n_e and optical data for shot 39857

- Scintillator spikes were observed at the very beginning of magnetic compression on three of the twenty shots taken with deuterium on the last night of the period during which the 11-coil configuration was tested. The spikes coincide with the initial rises towards elevated peaks observed on the density and optical emission signals. Note scintillator data should be shifted 3 μ s forward in figure 4.5.1. Shot 39857 was one of the three shots on which this behaviour was observed.
- Scintillator spikes were seen on two of the twenty deuterium shots, at the time when plasma entered the CT containment region. This is most likely related to viscous heating of ions during CT formation.

4.6 Summary

The recurrence rate of shots in which the CT poloidal flux was conserved during magnetic compression is an indication of resilience against a disruption-inducing instability during compression, and was increased from around 10% to 70% with the transition to the levitation/compression field profile of the eleven-coil configuration. The improvement is likely to be largely due to the compression field profile itself, which led to more uniform outboard compression, as opposed to the largely equatorial outboard compression associated with the six coil configuration. The effect of having a reduced impurity concentration and increased CT plasma temperature prior to compression initiation, as a consequence of the improved levitation field profile, may also have played a role. Due to improved flux conservation at compression, magnetic compression ratios increased significantly with the eleven coil configuration. Magnetic compression usually did not exhibit good toroidal symmetry.

In the eleven coil configuration, poloidal field at the CT edge, at fixed $r = 26$ mm, increased by a factor of up to six at compression, while line averaged electron density at fixed $r = 65$ mm was observed to increase by 400%, with the electron density front moving inwards at up to 10 km/s. Ion Doppler measurements, at fixed $r = 45$ mm indicated ion temperature increases at magnetic compression by a factor of up to four. Increases in poloidal field, density, and ion temperature at compression were significant only in the eleven coil configuration. Experimentally measured CT outer equatorial separatrix indicated a radial compression factor of up to 1.7, which is close to the maximum compression factor that can be resolved by the diagnostic. It may be that larger compression factors, in terms of CT outer equatorial separatrix, which cannot be evaluated, were achieved with shots when compression was fired later in time. Ideally it would be good to have diagnostics to get information about internal CT characteristics. Internal magnetic probes would be difficult to implement without interference and plasma contamination and due to the small size of the CT containment region, but non-invasive diagnostics such as a Thomson scattering system to assess internal electron temperature and density profiles would be useful and practical.

Indications of an instability, thought to be an external kink, occurred very frequently during magnetic compression and during under-damped magnetic levitation. Levitation circuit modification to match the decay rates of the levitation and plasma currents led to more stable, longer lived plasmas, and a greatly increased rate of good shots, by avoiding unintentional magnetic compression during CT levitation. An obvious improvement to the experiment design would be to drive additional shaft current and raise the q profile to MHD stable regimes.

PART 2: SIMULATIONS

Chapter 5

Core code development and MHD model

This chapter is focused on the core aspects of the DELiTE (Differential Equations on Linear Triangular Elements) framework that was developed for spatial discretisation of partial differential equations on an unstructured triangular grid in axisymmetric geometry, and applied to study the magnetic compression experiment. The framework, which is implemented in MATLAB, is based on discrete differential operators in matrix form, which are derived using linear finite elements and mimic some of the properties of their continuous counterparts. A single-fluid two-temperature MHD code is implemented in this framework. The inherent properties of the operators are used to ensure global conservation of energy, particle count, toroidal flux, and angular momentum.

The concept of conservation schemes and the importance of conservation properties in numerical methods is the focus of section 5.1. An overview of the finite element method used is presented in section 5.2. Definitions of key notations used, and descriptions of mappings between elemental and nodal quantities, are presented in section 5.3. In section 5.4, the finite element method is applied to derive various first and second order derivative matrix operators that mimic some of the properties of their continuous counterparts.

In section 5.5, expressions for $\dot{\psi}$ and \dot{f} are developed. The particular form of the expression for \dot{f} leads, together with properties of the discrete operators, to conservation of toroidal flux for the discretised system. The continuous forms of the equations defining the axisymmetric two-temperature MHD model are presented and used to demonstrate various conservation properties that the discrete model will mimic.

Note that in appendix B, the derivative matrix operators, discrete forms of the mass and energy conservation equations, and the expressions for $\dot{\psi}$ and \dot{f} , are used to develop a discrete form of the momentum equation which, using the special properties of the differential operators, ensures that total energy of the system described by the complete set of discretised

MHD equations is conserved with appropriate boundary conditions. In section 5.6, the full set of discretised MHD equations is presented, along with the closure models, including the model for anisotropic thermal diffusion. Global conservation of mass, toroidal flux, angular momentum, and energy for the system of equations in discrete form is demonstrated. A summary in section 5.7 concludes the chapter.

5.1 Conservation schemes

Ideally, a numerical discretisation method should, as well as accurately representing the continuous form of the mathematical equations that describe a particular physical system, reproduce the physical properties of the system being modelled. In practice, such properties are often expressed as conservation laws, and their maintenance can be just as important as standard numerical method assessment gauges like convergence, stability, accuracy, and range of applicability. Numerical solutions that contradict basic physical principles by, for example, destroying mass or energy are inherently unreliable when applied to novel physical regimes. On the other hand, many numerical methods do not have strong conservation properties, or conserve only some naturally conserved quantities, but can still regularly produce informative results that have a resemblance to real-world observations. However, as more complicated physical systems are modelled, physically incorrect numerical solutions can go unnoticed. This is especially true in simulating complex physical models, such as fluid dynamics or magnetohydrodynamics (MHD), where the maintenance of conservation laws puts more constraints on numerical schemes and, thus, helps to avoid spurious solutions. It is best to deal with the physical fidelity of the model at the numerical method design level [79], and try to replicate, in the discretised form, as many of the conservation laws inherent to the original physical system as possible.

Numerical methods with discrete conservation properties are well known in computational fluid dynamics (for example, [79, 80, 81, 82]), and in computational MHD [83, 84, 85]. In this chapter, a novel numerical scheme for a two-dimensional (axisymmetric) compressible MHD system is presented. The scheme is based on a continuous Galerkin linear finite element method on an unstructured triangular mesh and by construction has global (for the whole domain) conservation of mass, energy, toroidal flux and angular momentum. A novelty of the code is that all discrete spatial differential operators are represented as matrices, and the discretized MHD equations are obtained by simply replacing the original continuous differentiations with the corresponding matrix operators.

Note that by global conservation of a quantity in our numerical method, we imply that there is a discretised analogue of the continuity equation for that quantity, and, when in-

tegrated over the volume, its fluxes are completely cancelled in the interior of the domain, even though the explicit form of these fluxes are not always given. As shown in [86] and [79], global conservation for a method with local support (*i.e.*, local stencil) also implies local conservation. To enable the development of a numerical formulation with the aforementioned conservation properties, the discrete differential operators must obey a property equivalent, for a scalar field $u(\mathbf{r})$ and a vector field $\mathbf{p}(\mathbf{r})$, to

$$\int u \nabla \cdot \mathbf{p} dV + \int \mathbf{p} \cdot \nabla u dV = \int u \mathbf{p} \cdot d\Gamma \quad (5.1.1)$$

so that the discrete forms of the differential product rule and divergence theorem are satisfied [87]. This is the essence of mimetic schemes, also known as support operator methods, to which this work is closely related [79, 88].

5.2 Finite element method overview

Physical laws are usually expressed in terms of partial differential equations, for which there is often no analytical solution. Various discretization methods solve for an approximation of the equations. In the finite element method, the solution domain is divided into finite element subdomains, and an approximate solution is developed over each element. The element-specific solutions are assembled to obtain the approximate overall domain solution. Continuous functions $u(\mathbf{r})$ are approximated by piecewise continuous functions $U(\mathbf{r})$ using a combination of basis functions, as

$$u(\mathbf{r}) \approx U(\mathbf{r}) = \sum_{n=1}^N U_n \phi_n(\mathbf{r}) \quad (5.2.1)$$

where $\phi_n(\mathbf{r})$ is the basis function associated with node n , and U_n constitute a set of N scalar coefficients. Each finite element is associated with a number of nodes, located at discrete points on the solution domain, at which the solution to $U(\mathbf{r})$ will be evaluated. The basis functions in the finite element method depend on the dimensionality of the problem, and the order of the approximation sought. A principle of the finite element method is to require the approximate solution $U(\mathbf{r})$ to satisfy the differential equation in a weighted-integral sense. For example, in one dimension, if the partial differential equation is $-\frac{\partial}{\partial x} \left(x \frac{\partial u(\mathbf{r})}{\partial x} \right) + u(\mathbf{r}) = 0$, the requirement for the approximate solution can be written as

$$\int_0^L w R dx = 0 \quad (5.2.2)$$

where the integral is over the solution domain spanning from $x = L$ to $x = 0$, w is a weight function, and the residual is $R = -\frac{\partial}{\partial x} \left(x \frac{\partial U(\mathbf{r})}{\partial x} \right) + U(\mathbf{r})$. A linearly independent equation is obtained for each independent function w - in this way, sufficient equations can be generated in order to solve for the unknowns coefficients U_n . The method of using the basis functions as weight functions is known as the Galerkin method. In the example here, the basis function must be twice differentiable because the partial differential equation is second order. To weaken the basis function continuity requirements, integration by parts is used to remove the second differentiation on $U(\mathbf{r})$ in equation 5.2.2, and apply it to w . This method reduces equation 5.2.2 to the so-called "weak formulation":

$$\int_0^L \left(\frac{\partial w}{\partial x} \left(x \frac{\partial U(\mathbf{r})}{\partial x} \right) + w U(\mathbf{r}) \right) dx - \left[w x \frac{\partial U(\mathbf{r})}{\partial x} \right]_0^L = 0 \quad (5.2.3)$$

In this work, we develop linear approximations to $U(\mathbf{r})$. To develop the finite element discretisation, we drew inspiration from material presented in [89], which in turn, is based on material in [90], in which a finite element method is used to solve Laplace and Poisson equations in two dimensions. The two-dimensional computational domain, with azimuthal symmetry in cylindrical coordinates, is represented by an unstructured triangular mesh. The freely-available mesh generator DISTMESH [91, 92, 93] was adapted to provide the computational grid - see appendix C.1 for details on the mesh generation. Nodes are located at triangle vertices. In the linear finite element method, any continuous function $u(\mathbf{r})$ is approximated as a piecewise continuous function $U(\mathbf{r})$ that is linear across each triangular element:

$$u(\mathbf{r}) \approx U(\mathbf{r}) = \sum_{e=1}^{N_e} U^e(\mathbf{r}) \quad (5.2.4)$$

where N_e is the number of elements, and $U^e(\mathbf{r})$ represents $U(\mathbf{r})$ within element e :

$$U^e(\mathbf{r}) = A^e + B^e r + C^e z \quad (5.2.5)$$

Here, A^e , B^e and C^e are constants that are specific to element e . These coefficients will be derived in section 5.4.1. Equivalent to equation 5.2.4, and analogous to equation 5.2.1 for the linear approximation method, $U(\mathbf{r})$ may be defined using a combination of basis functions as

$$u(\mathbf{r}) \approx U(\mathbf{r}) = \sum_{n=1}^{N_n} U_n \phi_n(\mathbf{r}) \quad (5.2.6)$$

where N_n is the number of nodes, U_n represents the values of $U(\mathbf{r})$ at node n , and $\phi_n(\mathbf{r}) \equiv \phi_n(r, z)$ is the basis function associated with node n .

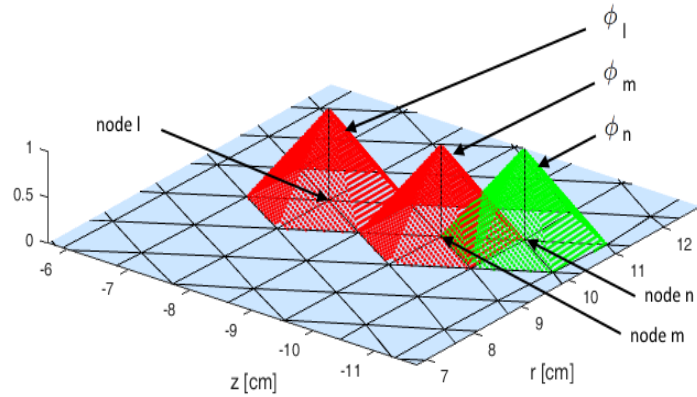


Figure 5.2.1: Linear basis function depiction for triangular elements

The linear basis functions have the forms of pyramids, as depicted in figure 5.2.1, which indicates a portion of a computation mesh, with depictions of the basis functions for example nodes l , m and n . Each node n is associated with a pyramid function ϕ_n , which has an elevation of one above the node, and falls linearly to zero at the immediately surrounding nodes. Each pyramid function ϕ_n has e_n sides, where e_n is the node-specific number of triangular elements surrounding node n . Note that the pyramid shapes associated with basis functions for nodes on the domain boundary have, in addition, one or more vertical sides at the boundaries. The remaining individual pyramid-side functions are defined by sections of planes that are tilted relative to the $r - z$ plane. Thus, each node is associated with e_n tilted planes. In total, there are K tilted planes defined in the solution domain, where $K = \sum_{n=1}^{N_n} e_n = 3N_e$. Each triangular element is associated with three tilted planes. The tilted planes are truncated to constitute pyramid sides by defining the functions representing the pyramid sides as

$$\psi_n^e(\mathbf{r}) = a_n^e + b_n^e r + c_n^e z \quad (5.2.7)$$

with the additional truncating property that $\psi_n^e(\mathbf{r}) = 0$ for all points located at \mathbf{r} which lie outside the triangular element associated with ψ_n^e . The notation ψ_n^e indicates that each pyramid side function is associated with a particular node n , and with a particular triangular element e . The coefficients a_n^e , b_n^e , and c_n^e are also associated with a particular node and element, and are such that $\psi_n^e = 1$ at its associated node n , and $\psi_n^e = 0$ at the other two nodes in the triangular element e . In summary, the basis functions $\phi_n(\mathbf{r})$, which define pyramid shapes with a peak elevation of one at node n , can be expressed as

$$\phi_n(\mathbf{r}) = \sum_{e_n} \psi_n^e(\mathbf{r}) \quad (5.2.8)$$

where the summation is over the pyramid side functions associated with node n , each of which is non-zero only over its associated triangular element. The basis functions have the property that $\phi_n(r_j, z_j) = \delta_{nj}$, where δ_{nj} is the Kronecker delta, and (r_j, z_j) are the coordinates of node j . Noting that the volume of a pyramid is given by

$$V_{\text{pyramid}} = sH/3 \quad (5.2.9)$$

where s is the pyramid base area and H is the pyramid height, this leads naturally, for any continuous function $U(\mathbf{r})$ (including the piecewise linear approximation), to the property

$$\int \phi_n(\mathbf{r}) U(\mathbf{r}) dr dz = (U_n + \mathcal{O}(h_e)) \int \phi_n(\mathbf{r}) dr dz \approx \frac{U_n s_n}{3} \quad (5.2.10)$$

where $U_n = U(r_n, z_n)$, s_n is the support area of node n (area of the base of the pyramid function defined by $\phi_n(\mathbf{r})$), pyramid height $H = 1$, and h_e is the typical element size. This identity is analogous to the integral property of the Dirac delta function. In deriving the property, it is assumed that the function $U(\mathbf{r})$ is sufficiently smooth that it is approximately constant (to order h_e) in the support area of node n . We neglect the term of order h_e because our numerical scheme has overall the first order accuracy, as defined by the use of linear basis functions.

Another important property of the basis functions is related to partition of unity - the sum of all the basis functions in the domain, at any point in the domain (*i.e.*, at non-nodal locations, as well as at nodal locations), is equal to one. This property also hold for the pyramid side functions, *i.e.*, $\sum_{n=1}^{N_n} \phi_n(\mathbf{r}) = \sum_{n=1}^{N_n} \psi_n(\mathbf{r}) = 1$.

5.3 Key notations and node-to-element mapping

In this chapter, the notation \underline{X} (or \underline{x}) will be used to denote vectors of dimensions $[N_n \times 1]$ that contain node-associated quantities, while $\underline{X}^e [N_e \times 1]$ denotes vectors of element-associated quantities. The notation $\underline{\underline{X}}^e$ will be used to denote matrices of dimensions $[N_e \times N_n]$ that operate on vectors of nodal quantities \underline{X} , to produce vectors of elemental quantities \underline{Y}^e , while $\underline{\underline{X}}_n [N_n \times N_e]$ operates on vectors of elemental quantities \underline{X}^e to produce vectors of nodal quantities \underline{Y} . The notations $\underline{\underline{X}}$ and $\widehat{\underline{\underline{X}}}$ will be used to denote square matrices with dimensions $[N_n \times N_n]$ and $[N_e \times N_e]$ respectively. Notations defining the various matrix dimensions are collected in table 5.3.1.

| | | # columns | | |
|--------|-------|-----------------------------|-----------------------------|-----------------------------|
| | | 1 | N_n | N_e |
| # rows | N_n | <u><u>X</u></u> | <u><u>X</u></u> | <u><u>X_n</u></u> |
| | N_e | <u><u>X^e</u></u> | <u><u>X^e</u></u> | <u><u>X̂</u></u> |

Table 5.3.1: Notations for matrices of various dimensions

We introduce node-to-element averaging as

$$\langle \underline{X} \rangle^e = \frac{1}{3} \underline{\underline{M}^e} * \underline{X} \quad (5.3.1)$$

Here, the connectivity matrix $\underline{\underline{M}^e}$ has dimensions $[N_e \times N_n]$. Each row of $\underline{\underline{M}^e}$ corresponds to a particular triangular element, and has only three non-zero entries. $\underline{\underline{M}^e}(e, n) = 1$ for the column indexes n corresponding to the indexes n of the nodes located at the vertices of the triangle with index e . The symbol $*$ represents regular matrix multiplication. The radial coordinates of element centroids are defined with $\underline{r}^e = (r_1^e, r_2^e, \dots r_{N_e}^e)^T = \langle \underline{r} \rangle^e$, where $\underline{r} = (r_1, r_2, \dots r_{N_n})^T$ contains the r coordinates of the nodes. The superscript T implies the transpose operation. Similarly, the axial centroid coordinates are defined as $\underline{z}^e = \langle \underline{z} \rangle^e$. The vector of nodal support areas \underline{s} , containing the areas of the bases of the pyramid functions associated with the nodes, is related to \underline{s}^e , the vector of elemental areas, as $\underline{s} = \underline{\underline{M}^e}^T * \underline{s}^e$.

Volume integrals over the computational domain can be approximated in two ways, corresponding to nodal or elemental representations of the integrand function

$$\int u(\mathbf{r}) dV \approx \underline{dV}^T * \underline{U} \quad \text{or} \quad \int u(\mathbf{r}) dV \approx \underline{dV}^{eT} * \underline{U}^e$$

where $\underline{dV} = \frac{2\pi}{3} \underline{s} \circ \underline{r}$ contains the volumes associated with each node, which are found by integrating the node-associated areas from 0 to 2π in the toroidal direction, and $\underline{dV}^e = 2\pi \underline{s}^e \circ \underline{r}^e$ contains the elemental volumes. The factor of three in the former expression arises because each elemental area is shared by three nodes. Note that these two approximations do not give identical results for vectors related by equation 5.3.1, unless the original integrand function is constant. The symbol \circ represents the Hadamard product, piecewise element-by element multiplication (*i.e.*, $(\underline{a} \circ \underline{b})_i = a_i b_i$), and the symbol \oslash represents Hadamard division, piecewise element-by element division (*i.e.*, $(\underline{a} \oslash \underline{b})_i = a_i / b_i$).

Defining $\underline{\underline{R}}$, $\underline{\underline{S}}$, $\widehat{\underline{\underline{R}}}$ and $\widehat{\underline{\underline{S}}}$ as the diagonal arrays constructed from \underline{r} , \underline{s} , \underline{r}^e , and \underline{s}^e , we define a volume-averaging operator

$$\underline{\underline{W}_n} = \underline{\underline{R}}^{-1} * \underline{\underline{S}}^{-1} * \underline{\underline{M}^e}^T * \widehat{\underline{\underline{S}}} * \widehat{\underline{\underline{R}}} \quad (5.3.2)$$

that is used to map element-based quantities to node-based quantities, as

$$\langle \underline{U}^e \rangle = \underline{\underline{W}_n} * \underline{U}^e \quad (5.3.3)$$

This operator satisfies the following identity:

$$\underline{dV}^T * \left(\underline{Q} \circ \left(\underline{\underline{W}_n} * \underline{U}^e \right) \right) = \underline{dV}^{eT} * \left(\underline{Q}^e \circ \underline{U}^e \right) \quad (5.3.4)$$

where \underline{U}^e and \underline{Q}^e are the discrete representations, defined at the element centroids, of the approximations to the continuous functions $u(\mathbf{r})$ and $q(\mathbf{r})$, and \underline{Q} is the discrete representation, defined at the nodes, of $q(\mathbf{r})$, and is related to \underline{Q}^e by equation 5.3.1. A proof of this identity follows:

$$\begin{aligned} \underline{dV}^T * \left(\underline{Q} \circ \left(\underline{\underline{W}_n} * \underline{U}^e \right) \right) &= \frac{2\pi}{3} (\underline{s} \circ \underline{r})^T * \left(\underline{Q} \circ \left(\underline{\underline{R}}^{-1} * \underline{\underline{S}}^{-1} * \underline{\underline{M}}^{eT} * \underline{\underline{S}} * \underline{\underline{R}} * \underline{U}^e \right) \right) \\ &= \frac{2\pi}{3} \underline{Q}^T * \left(\underline{\underline{M}}^{eT} * \underline{\underline{S}} * \underline{\underline{R}} * \underline{U}^e \right) \\ &= \frac{2\pi}{3} \left(\underline{\underline{S}} * \underline{\underline{R}} * \underline{U}^e \right)^T * \left(\underline{Q}^T * \underline{\underline{M}}^{eT} \right)^T \quad (\text{transpose}) \\ &= 2\pi \left(\underline{\underline{S}} * \underline{\underline{R}} * \underline{U}^e \right)^T * \left(\frac{1}{3} \underline{\underline{M}}^e * \underline{Q} \right) \\ &= \underline{dV}^{eT} * \left(\underline{Q}^e \circ \underline{U}^e \right) \quad (\text{use eqn. 5.3.1}) \end{aligned}$$

Note that the matrix transpose relation

$$(\mathbb{A} * \mathbb{B})^T = \mathbb{B}^T * \mathbb{A}^T \quad (5.3.5)$$

for matrices \mathbb{A} and \mathbb{B} , is used to transpose the scalar on the right side of the equation in the third last step of the derivation above. In the particular case with $\underline{Q} = \underline{1}$, the identity becomes

$$\underline{dV}^T * \left(\underline{\underline{W}_n} * \underline{U}^e \right) = \underline{dV}^{eT} * \underline{U}^e \quad (5.3.6)$$

5.4 Differential operators

5.4.1 First order node-to-element differential operators

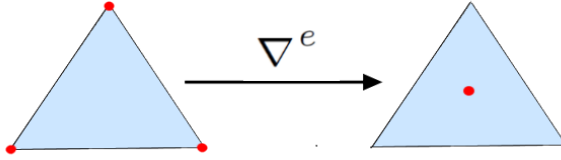


Figure 5.4.1: Node-to-element differential operator mechanism

The node-to-element derivative operator matrices are defined such that

$$\begin{aligned}\underline{U}'_r &= \underline{\underline{D}r^e} * \underline{U} \\ \underline{U}'_z &= \underline{\underline{D}z^e} * \underline{U}\end{aligned}$$

Referring for example to the radial derivative operator, application of $\underline{\underline{D}r^e}$, a matrix with dimensions $[N_e \times N_n]$, to the vector \underline{U} , returns $\underline{U}'_r [N_e \times 1]$, containing the values for the radial derivatives of $U(\mathbf{r})$ inside the triangular elements. The node-to-element gradient and divergence operations, for cylindrical coordinates with azimuthal symmetry are

$$\underline{\underline{\nabla^e}} \underline{U} = (\underline{\underline{D}r^e} * \underline{U}) \hat{\mathbf{r}} + (\underline{\underline{D}z^e} * \underline{U}) \hat{\mathbf{z}} \quad (5.4.1)$$

and

$$\underline{\underline{\nabla^e}} \cdot \underline{\mathbf{P}} = ((\underline{\underline{D}r^e} * (\underline{r} \circ \underline{P}_r)) + (\underline{\underline{D}z^e} * (\underline{r} \circ \underline{P}_z))) \otimes \underline{r}^e \quad (5.4.2)$$

where \underline{P}_r and \underline{P}_z are the nodal representations of the r and z components the continuous vector field $\mathbf{p}(\mathbf{r})$. A schematic of the node-to-element gradient operation mechanism is indicated in figure 5.4.1.

To derive the $\underline{\underline{D}r^e}$ and $\underline{\underline{D}z^e}$ operators we use the elemental representation of $U(\mathbf{r})$, equations 5.2.4 and 5.2.5. Equation 5.2.5 defines the values of the approximation $U(\mathbf{r})$ at the nodes as

$$U_\varepsilon = A^e + B^e r_\varepsilon + C^e z_\varepsilon \quad (5.4.3)$$

where $\varepsilon = i, j, k$ denotes the indexes of the nodes at the vertices of triangular element e .

In the following, the element-specific node indexes i, j, k will be replaced with the indexes 1, 2 and 3 for simplicity. From equation 5.2.5, the radial and axial first spatial derivatives of $U^e(\mathbf{r})$ are constants across the element e , and are given by $\frac{\partial U^e}{\partial r} = B^e$, and $\frac{\partial U^e}{\partial z} = C^e$. Expressions for B^e and C^e are found using equation 5.4.3:

$$U_1 - U_3 = B^e(r_1 - r_3) + C^e(z_1 - z_3)$$

$$U_2 - U_3 = B^e(r_2 - r_3) + C^e(z_2 - z_3)$$

$$\begin{aligned} \Rightarrow B^e &= \frac{\partial U^e}{\partial r} = \frac{U_1(z_2 - z_3) + U_2(z_3 - z_1) + U_3(z_1 - z_2)}{2s^e} \\ C^e &= \frac{\partial U^e}{\partial z} = \frac{U_1(r_2 - r_3) + U_2(r_3 - r_1) + U_3(r_1 - r_2)}{-2s^e} \end{aligned} \quad (5.4.4)$$

The triangle area s^e is introduced here, assuming that vertices are numbered counterclockwise, noting that $2s^e = |\mathbb{R}^e|$, where $|\mathbb{R}^e|$ is the determinant of array $\mathbb{R}^e = \begin{pmatrix} 1 & r_1 & z_1 \\ 1 & r_2 & z_2 \\ 1 & r_3 & z_3 \end{pmatrix}$, so that

$$2s^e = (r_1 - r_3)(z_2 - z_3) - (r_2 - r_3)(z_1 - z_3)$$

The element-specific spatial derivatives can also be expressed in terms of the coefficients in the element-specific pyramid-side functions ψ_1^e , ψ_2^e , and ψ_3^e . As noted earlier, each pyramid-side function is specific to a particular node, and to a particular element, and is defined as $\psi_n^e(\mathbf{r}) = a_n^e + b_n^e r + c_n^e z$, and has the property $\psi_n^e(r_j, z_j) = \delta_{nj}$. This yields, for each element e , the identity $\mathbb{R}^e * \mathbb{C}^e = \mathbb{I}$, or

$$\begin{pmatrix} 1 & r_1 & z_1 \\ 1 & r_2 & z_2 \\ 1 & r_3 & z_3 \end{pmatrix} * \begin{pmatrix} a_1^e & a_2^e & a_3^e \\ b_1^e & b_2^e & b_3^e \\ c_1^e & c_2^e & c_3^e \end{pmatrix} = \begin{pmatrix} 1 & 0 & 0 \\ 0 & 1 & 0 \\ 0 & 0 & 1 \end{pmatrix}$$

$$\Rightarrow \mathbb{C}^e = (\mathbb{R}^e)^{-1} = \frac{1}{2s^e} \begin{pmatrix} (r_2 z_3 - r_3 z_2) & (r_3 z_1 - r_1 z_3) & (r_1 z_2 - r_2 z_1) \\ (z_2 - z_3) & (z_3 - z_1) & (z_1 - z_2) \\ (r_3 - r_2) & (r_1 - r_3) & (r_2 - r_1) \end{pmatrix} \quad (5.4.5)$$

Comparing equations 5.4.4 with equation 5.4.5, it is evident that

$$\begin{aligned}\frac{\partial U^e}{\partial r} &= U_1 b_1^e + U_2 b_2^e + U_3 b_3^e = \begin{pmatrix} b_1^e & b_2^e & b_3^e \end{pmatrix} * \begin{pmatrix} U_1 \\ U_2 \\ U_3 \end{pmatrix} \\ \frac{\partial U^e}{\partial z} &= U_1 c_1^e + U_2 c_2^e + U_3 c_3^e = \begin{pmatrix} c_1^e & c_2^e & c_3^e \end{pmatrix} * \begin{pmatrix} U_1 \\ U_2 \\ U_3 \end{pmatrix}\end{aligned}\quad (5.4.6)$$

Given the values of the approximation for the piecewise linear function $U(\mathbf{r})$ on the triangle vertices, and the element-specific array \mathbb{C}^e evaluated using equation 5.4.5, equations 5.4.6 can be used to determine the values of the spatial derivatives of $U(\mathbf{r})$ at the interior of each element. $\underline{\underline{Dr}}^e$ and $\underline{\underline{Dz}}^e$ are initially defined as sparse all-zero arrays. Reverting to node-specific notation, where i, j, k are the indexes of the nodes at the vertices of element e , the values b_i^e, b_j^e and b_k^e are inserted in row e of $\underline{\underline{Dr}}^e$ with placements at the column indexes i, j, k . Similarly, the values c_i^e, c_j^e and c_k^e , for each element, are used to assemble $\underline{\underline{Dz}}^e$. The resulting derivative operators produce exact derivatives for nodal functions with linear dependence on r and z , and have first order accuracy (*i.e.*, $\mathcal{O}(h_e)$) when applied to nonlinear functions. The operators introduced in the following sections are all based on these node-to-element derivative operators, and so they all have the same accuracy.

Here, we will demonstrate a property of the node-to-element operators that will be used to demonstrate angular momentum conservation later in section 5.6.2.3. For any continuous scalar functions f and g , the identity (Stoke's theorem) holds that

$$\int (\nabla f \times \nabla g) \cdot d\mathbf{S} = \int \nabla \times (f \nabla g) \cdot d\mathbf{S} = \int f \nabla g \cdot d\mathbf{l} \quad (5.4.7)$$

With azimuthal symmetry, $\int (\nabla f \times \nabla g) \cdot d\mathbf{S} = \int (f'_z g'_r - f'_r g'_z) \hat{\phi} \cdot d\mathbf{S} = \int (f'_z g'_r - f'_r g'_z) ds_\phi$, where ds_ϕ is an elemental area in the poloidal $(r - z)$ plane. Hence, the discrete form of

$\int (\nabla f \times \nabla g) \cdot d\mathbf{S}$, using the node-to-element differential operators, is

$$\begin{aligned}
\left(\int (\nabla f \times \nabla g) \cdot d\mathbf{S} \right)_{disc.} &= \underline{s}^{eT} * \left(\left(\underline{Dz}^e * \underline{f} \right) \circ \left(\underline{Dr}^e * \underline{g} \right) - \left(\underline{Dr}^e * \underline{f} \right) \circ \left(\underline{Dz}^e * \underline{g} \right) \right) \\
&= \left(\underline{Dz}^e * \underline{f} \right)^T * \hat{\underline{S}} * \left(\underline{Dr}^e * \underline{g} \right) - \left(\underline{Dr}^e * \underline{f} \right)^T * \hat{\underline{S}} * \left(\underline{Dz}^e * \underline{g} \right) \\
&= \underline{f}^T * \underline{Dz}^{eT} * \hat{\underline{S}} * \underline{Dr}^e * \underline{g} - \underline{f}^T * \underline{Dr}^{eT} * \hat{\underline{S}} * \underline{Dz}^e * \underline{g} \\
&= \underline{f}^T * \left(\underline{Dz}^{eT} * \hat{\underline{S}} * \underline{Dr}^e - \underline{Dr}^{eT} * \hat{\underline{S}} * \underline{Dz}^e \right) * \underline{g} \\
&= \underline{f}^T * \left(\underline{B}^T - \underline{\underline{B}} \right) * \underline{g} \\
&= \underline{f}^T * \underline{\underline{A}} * \underline{g}
\end{aligned} \tag{5.4.8}$$

where $\underline{\underline{B}} = \underline{Dr}^{eT} * \hat{\underline{S}} * \underline{Dz}^e$. Setting $\underline{f} = \underline{\phi_m}$ and $\underline{g} = \underline{\phi_n}$, where $\underline{\phi_m}$ and $\underline{\phi_n}$ are the vectors defining the nodal values of basis functions ϕ_m and ϕ_n respectively (i.e., $\underline{\phi_m}(k) = \delta_{mk}$ and $\underline{\phi_n}(k) = \delta_{nk}$), equations 5.4.8 and 5.4.7 imply that

$$A_{mn} \equiv A(m, n) = \underline{\phi_m}^T * \underline{\underline{A}} * \underline{\phi_n} = \int \phi_m \nabla \phi_n \cdot d\mathbf{l} \tag{5.4.9}$$

We will show that each element of $\underline{\underline{A}}$ is zero at internal nodes, i.e., $(\underline{\underline{A}})_{int} = 0$. There are four cases to consider: (1) $m \neq n$ and nodes m and n are not adjacent, (2) $m = n$, (3) m and n are the indexes of adjacent internal nodes, and (4) m and n are the indexes of adjacent nodes located on the boundary of the computational domain. In case (1), A_{mn} is obviously zero. In case (2), $A_{mn} = \underline{\phi_m}^T * (\underline{\underline{B}}^T - \underline{\underline{B}}) * \underline{\phi_m} = \underline{\phi_m}^T * \underline{\underline{B}}^T * \underline{\phi_m} - \underline{\phi_m}^T * \underline{\underline{B}} * \underline{\phi_m}$. The first term scalar term here can be transposed, so that $A_{mn} = 0$ in case (2).

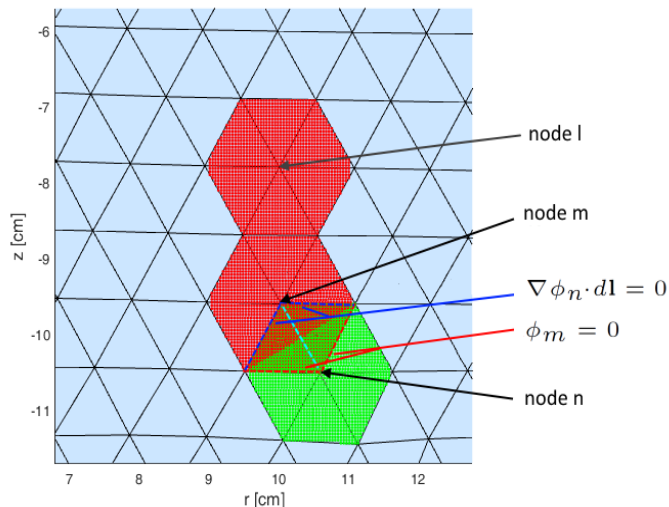


Figure 5.4.2: Linear basis function depiction for triangular elements (top view (1)).

Figure 5.4.2 is a top-view of figure 5.2.1. Note the dark blue dashed lines represent the

part of the boundary of basis function ϕ_n that overlaps with ϕ_m , and the red dashed lines represent the part of the boundary of ϕ_m that overlaps with ϕ_n . Referring to equation 5.4.9 and to figure 5.4.2, the only contribution to A_{mn} in case (3) is from the contour integral $\int \phi_m \nabla \phi_n \cdot d\mathbf{l}$ along the boundary (depicted with dark blue and red dashed lines) of the diamond-shape representing the overlapping area of the basis functions ϕ_m and ϕ_n . It can be seen that $\phi_m = 0$ along part of the contour, and $\nabla \phi_n \cdot d\mathbf{l} = 0$ along the remaining parts, so that $A_{mn} = 0$ in case (3). In case (4), when m and n are the indexes of adjacent nodes located on the boundary of the computational domain, the integral $\int \phi_m \nabla \phi_n \cdot d\mathbf{l}$ would be finite along the light blue dashed line connecting nodes m and n (in case (4), the light blue dashed line would represent part of the computational domain boundary). Therefore, A_{mn} is finite only when m and n are the indexes of adjacent nodes located on the boundary of the computational domain, leading to the identity

$$(\underline{\underline{Dz}}^{eT} * \widehat{\underline{\underline{S}}} * \underline{\underline{Dr}}^e - \underline{\underline{Dr}}^{eT} * \widehat{\underline{\underline{S}}} * \underline{\underline{Dz}}^e)_{int} = 0 \quad (5.4.10)$$

5.4.2 First order element-to-node differential operators

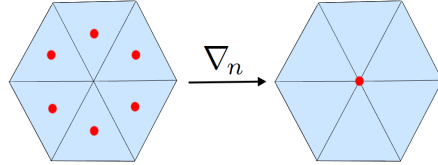


Figure 5.4.3: Element-to-node differential operator mechanism

The element-to-node derivative operator matrices are defined such that

$$\begin{aligned} \underline{U}'_r &= \underline{\underline{Dr}}_n * \underline{U}^e \\ \underline{U}'_z &= \underline{\underline{Dz}}_n * \underline{U}^e \end{aligned}$$

Referring for example to the radial derivative operator, application of the $\underline{\underline{Dr}}_n$ operator, which is a matrix with dimensions $[N_n \times N_e]$, to the vector $\underline{U}^e [N_e \times 1]$, which contains the values of $U(\mathbf{r})$ at the element centroids, returns $\underline{U}'_r [N_n \times 1]$, the values for the radial derivatives of $U(\mathbf{r})$ at the nodes. The element-to-node gradient and divergence operations, for cylindrical coordinates with azimuthal symmetry are

$$\underline{\underline{\nabla}}_n \underline{U}^e = (\underline{\underline{Dr}}_n * \underline{U}^e) \hat{\mathbf{r}} + (\underline{\underline{Dz}}_n * \underline{U}^e) \hat{\mathbf{z}} \quad (5.4.11)$$

and

$$\underline{\underline{\nabla}_n} \cdot \underline{\mathbf{P}}^e = \left(\left(\underline{\underline{D}r_n} * \left(\underline{r}^e \circ \underline{P}_r^e \right) \right) + \left(\underline{\underline{D}z_n} * \left(\underline{r}^e \circ \underline{P}_z^e \right) \right) \right) \otimes \underline{r} \quad (5.4.12)$$

A schematic of the element-to-node gradient operation mechanism is indicated in figure 5.4.3. The element-to-node differential operators are derived in relation to the node-to-element operators by requiring the discrete form of equation 5.1.1 to hold:

$$\underline{dV}^T * \left[\underline{\mathbf{P}} \cdot \left(\underline{\underline{\nabla}_n} \underline{U}^e \right) \right] + \underline{dV}^{eT} * \left[\underline{U}^e \circ \left(\underline{\underline{\nabla}}^e \cdot \underline{\mathbf{P}} \right) \right] = 0 \quad (5.4.13)$$

or

$$\underline{dV}^T * \left[\underline{U} \circ \left(\underline{\underline{\nabla}_n} \cdot \underline{\mathbf{P}}^e \right) \right] + \underline{dV}^{eT} * \left[\underline{\mathbf{P}}^e \cdot \left(\underline{\underline{\nabla}}^e \cdot \underline{U} \right) \right] = 0 \quad (5.4.14)$$

In this derivation, it is assumed that the boundary term $\int \mathbf{u}\mathbf{p} \cdot d\Gamma = 0$, *i.e.*, there is no flux of the continuous vector field $\mathbf{u}\mathbf{p}$ through the boundary. For arbitrary discrete nodal representations $\underline{\mathbf{P}}$ (equation 5.4.13) and \underline{U} (equation 5.4.14), a consequence of this assumption is that the element-to-node gradient operator produces valid results at the boundary nodes only if the original continuous function u is zero at the boundary (*i.e.*, $u|_\Gamma = 0$). Similarly, the element-to-node divergence operator produces valid results at the boundary nodes only if the original continuous function \mathbf{p} has no component perpendicular to the boundary (*i.e.*, $\mathbf{p}_\perp|_\Gamma = 0$). In the following, we will refer to these conditions as the natural boundary conditions. For the terms involving radial derivatives, equation 5.4.14 implies that

$$\begin{aligned} \underline{dV}^T * \left(\underline{U} \circ \left(\left(\underline{\underline{D}r_n} * \left(\underline{r}^e \circ \underline{P}_r^e \right) \right) \otimes \underline{r} \right) \right) &= -\underline{dV}^{eT} * \left(\underline{P}_r^e \circ \left(\underline{\underline{D}r}^e * \underline{U} \right) \right) \\ \Rightarrow \frac{2\pi}{3} \underline{s}^T * \left(\underline{U} \circ \left(\underline{\underline{D}r_n} * \left(\underline{r}^e \circ \underline{P}_r^e \right) \right) \right) &= -2\pi \underline{s}^{eT} * \left(\underline{r}^e \circ \underline{P}_r^e \circ \left(\underline{\underline{D}r}^e * \underline{U} \right) \right) \\ \Rightarrow \frac{1}{3} \underline{U}^T * \left(\underline{\underline{S}} * \left(\underline{\underline{D}r_n} * \left(\underline{r}^e \circ \underline{P}_r^e \right) \right) \right) &= -\left(\underline{r}^e \circ \underline{P}_r^e \right)^T * \left(\underline{\underline{S}} * \underline{\underline{D}r}^e * \underline{U} \right) \\ \Rightarrow \frac{1}{3} \underline{U}^T * \left(\underline{\underline{S}} * \left(\underline{\underline{D}r_n} * \left(\underline{r}^e \circ \underline{P}_r^e \right) \right) \right) &= -\underline{U}^T * \left(\underline{\underline{D}r}^{eT} * \underline{\underline{S}} * \left(\underline{r}^e \circ \underline{P}_r^e \right) \right) \quad (\text{transpose}) \end{aligned}$$

Hence, the element-to-node derivative operators are

$$\begin{aligned} \underline{\underline{D}r_n} &= -3\underline{\underline{S}}^{-1} * \left(\underline{\underline{D}r}^{eT} * \underline{\underline{S}} \right) \\ \underline{\underline{D}z_n} &= -3\underline{\underline{S}}^{-1} * \left(\underline{\underline{D}z}^{eT} * \underline{\underline{S}} \right) \end{aligned} \quad (5.4.15)$$

These definitions can alternatively be obtained using equation 5.4.13. Noting the particular case when $\underline{U} = \underline{1}$, then equation 5.4.14 leads to the identity

$$\underline{dV}^T * \left[\underline{\nabla}_n \cdot \underline{\mathbf{P}}^e \right] = 0 \quad (5.4.16)$$

5.4.3 Second order node-to-node differential operators

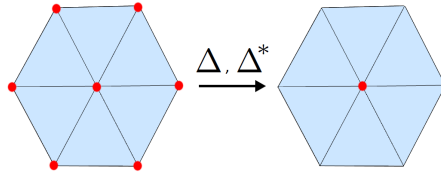


Figure 5.4.4: Node-to-node second order differential operator mechanism

Discrete forms of node-to-node second order differential operators, with dimensions $[N_n \times N_n]$, can be constructed using combinations of the first order node-to-element and element-to-node operators. For example, the discrete form of the Laplacian operator in cylindrical coordinates, with azimuthal symmetry, is

$$\underline{\underline{\Delta}} \underline{U} = \underline{\nabla}_n \cdot \underline{\nabla}^e \underline{U} = \left(\left(\underline{\underline{D}}r_n * \left(\underline{r}^e \circ \left(\underline{\underline{D}}r^e * \underline{U} \right) \right) \right) + \left(\underline{\underline{D}}z_n * \left(\underline{r}^e \circ \left(\underline{\underline{D}}z^e * \underline{U} \right) \right) \right) \right) \circ \underline{r} \quad (5.4.17)$$

Note that $\underline{\underline{\Delta}} \underline{U}$ may be expressed as $\underline{\nabla}_n \cdot \underline{\mathbf{P}}^e$, where $\underline{\mathbf{P}}^e = \underline{\nabla}^e \underline{U}$. Therefore, equation 5.4.16 implies that

$$\underline{dV}^T * \left[\underline{\underline{\Delta}} \underline{U} \right] = 0 \quad (5.4.18)$$

The condition $\mathbf{p}_\perp|_\Gamma = 0$, required for correct evaluation of $\underline{\nabla}_n \cdot \underline{\mathbf{P}}^e$ at the boundary nodes, is equivalent to having the normal component of the gradient of the continuous function u equal to zero at the boundary. Thus, the operation $\underline{\underline{\Delta}} * \underline{U}$ produces correct results at the boundary nodes only if the natural boundary condition is satisfied, which in this case is $(\nabla_\perp u)|_\Gamma = 0$.

The discrete form of the elliptic operator used in the Grad-Shafranov equation, in cylindrical coordinates with azimuthal symmetry is (see equation A.7.10)

$$\underline{\underline{\Delta}}^* \underline{U} = \underline{r}^2 \circ \left(\underline{\nabla}_n \cdot \left(\left(\underline{\nabla}^e \underline{U} \right) \circ \underline{r}^{e2} \right) \right) = \underline{r} \circ \left(\underline{\underline{D}}r_n * \left(\left(\underline{\underline{D}}r^e * \underline{U} \right) \circ \underline{r}^e \right) + \underline{\underline{D}}z_n * \left(\left(\underline{\underline{D}}z^e * \underline{U} \right) \circ \underline{r}^e \right) \right) \quad (5.4.19)$$

The $\underline{\underline{\Delta}}$ and $\underline{\underline{\Delta}}^*$ operator mechanisms are indicated in figure 5.4.4. Note that equation 5.4.16

implies that

$$\underline{dV}^T * \left[\left(\underline{\underline{\Delta}}^* \underline{U} \right) \otimes \underline{r}^2 \right] = 0 \quad (5.4.20)$$

Again, the operation $\underline{\underline{\Delta}}^* \underline{U}$ produces correct results at the boundary nodes only if the natural boundary condition is satisfied, which in this case is $((\nabla_{\perp} u) / r^2) |_{\Gamma} = 0$.

5.4.3.1 Alternative derivation of the second order node-to-node differential operators

It is illustrative to show how the second order node-to-node differential operators can be derived directly using the fundamental finite element methods, outlined in section 5.2, of constructing a weighted integral and obtaining the weak formulation expression. This method also leads to the definitions of the first order element-to-node differential operators, without employing the procedure, outlined in section 5.4.2, of invoking the discrete form of equation 5.1.1.

The Laplacian operator is defined as $\Delta u(\mathbf{r}) = \nabla \cdot \nabla u(\mathbf{r})$. With the Galerkin method, the basis functions $\phi_j(\mathbf{r})$, where $j = 1 : N_n$, are used as weighting functions. Defining

$$L(\mathbf{r}) = \Delta U(\mathbf{r}) = \nabla \cdot \nabla U(\mathbf{r})$$

where $U(\mathbf{r})$ and $L(\mathbf{r})$ are the piecewise linear approximations to the continuous function $u(\mathbf{r})$ and $\Delta u(\mathbf{r})$, the relevant weighted integral equality is

$$\begin{aligned} \int \phi_j(\mathbf{r}) L(\mathbf{r}) dr dz &= \int \phi_j(\mathbf{r}) \nabla \cdot \nabla U(\mathbf{r}) dr dz \\ &= \int \nabla \cdot (\phi_j \nabla U) dr dz - \int \nabla \phi_j \cdot \nabla U dr dz \quad (\text{integration by parts}) \\ &= \oint (\phi_j \nabla U) \cdot d\mathcal{L} - \int \nabla \phi_j \cdot \nabla U dr dz \quad (\text{using Green's theorem}) \end{aligned} \quad (5.4.21)$$

Here, Greens theorem is used to reduce the integral over area to an integral evaluated on the boundary \mathcal{L} . Note $d\mathcal{L} = \hat{\mathbf{n}} d\mathcal{L}$, where $\hat{\mathbf{n}}(\mathbf{r})$ is the unit outward normal to the boundary. If $(\nabla_{\perp} U(\mathbf{r})) |_{\Gamma} = 0$, *i.e.*, the component of ∇U perpendicular to the boundary, is zero at the boundary, then the boundary integral can be neglected. This will be discussed further below. Dropping the boundary term and applying the linear basis function expansion (equation

5.2.6) to $U(\mathbf{r})$, the resulting expression is

$$\int \phi_j L(\mathbf{r}) dr dz = - \sum_{i=1}^{N_n} U_n \int \nabla \phi_j \cdot \nabla \phi_n dr dz \quad (5.4.22)$$

Equation 5.2.10 is used to expand the left side of this equation as $L_j s_j/3$. On the right side, matrix $\underline{\underline{L}a}$ of size $N_n \times N_n$ is introduced as

$$\underline{\underline{L}a}(j, n) = - \int \nabla \phi_j \cdot \nabla \phi_n dr dz \quad (5.4.23)$$

Hence, equation 5.4.22 can be re-expressed in matrix form as

$$\begin{aligned} \frac{\underline{\underline{L}}(j) \underline{s}(j)}{3} &= \sum_{n=1}^{N_n} (\underline{\underline{L}a}(j, n) \underline{U}(n)) \\ \Rightarrow \underline{\underline{L}} &= \underline{\underline{\Delta}} * \underline{U} = 3 \underline{\underline{S}}^{-1} * \underline{\underline{L}a} * \underline{U} \\ \Rightarrow \underline{\underline{\Delta}} &= 3 \underline{\underline{S}}^{-1} * \underline{\underline{L}a} \end{aligned} \quad (5.4.24)$$

Expressing the pyramid functions in terms of the pyramid side functions according to equation 5.2.8, then referring to equations 5.4.23 and 5.4.24, $\underline{\underline{\Delta}}$ can be expressed as

$$\begin{aligned} \underline{\underline{\Delta}}(j, n) &= -\frac{3}{s_j} \int \left(\sum_{e_j} \frac{\partial \psi_j^e(\mathbf{r})}{\partial r} \sum_{e_n} \frac{\partial \psi_n^e(\mathbf{r})}{\partial r} + \sum_{e_j} \frac{\partial \psi_j^e(\mathbf{r})}{\partial z} \sum_{e_n} \frac{\partial \psi_n^e(\mathbf{r})}{\partial z} \right) dr dz \\ &= -\frac{3}{s_j} \int \left(\sum_{e_j \cap e_n} b_j^e b_n^e + \sum_{e_j \cap e_n} c_j^e c_n^e \right) dr dz \\ &= -\frac{3}{s_j} \left(\sum_{e_j \cap e_n} b_j^e b_n^e + \sum_{e_j \cap e_n} c_j^e c_n^e \right) s^e \end{aligned}$$

Here, $\sum_{e_j \cap e_n}$ implies summation over the set of elements surrounding node n that overlap with the elements surrounding node j (see the example in section 5.4.4.1 for clarification). Referring to equations 5.4.6, it can be seen how this implies that the discrete Laplacian operator, in matrix form, is

$$\underline{\underline{\Delta}} = - \left(3 \underline{\underline{S}}^{-1} \right) * \left(\underline{\underline{D}r}^{eT} * \underline{\underline{S}} * \underline{\underline{D}r}^e + \underline{\underline{D}z}^{eT} * \underline{\underline{S}} * \underline{\underline{D}z}^e \right) \quad (5.4.25)$$

With the definition $\underline{\underline{\Delta}} \underline{U} = \underline{\nabla}_n \cdot \underline{\nabla}^e \underline{U}$, this leads naturally to the definitions of the element-to-node operators (equation 5.4.15) - in this case, the properties of the element-to-node operators outlined in section 5.4.2 arise because the boundary term in equation 5.4.21 was dropped.

The method outlined in this section results again in the expression for the Laplacian and Δ^* operations in cylindrical coordinates, as defined by equations 5.4.17 and 5.4.19, where the operator properties 5.4.18 and 5.4.20 follow naturally.

5.4.4 First order node-to-node differential operators

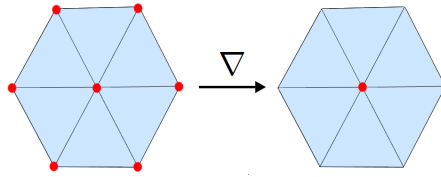


Figure 5.4.5: Node-to-node differential operator mechanism

The node-to-node derivative operator matrices $\underline{\underline{D}}r$ and $\underline{\underline{D}}z$, with dimensions $[N_n \times N_n]$, are used to evaluate, at the nodes, the radial and axial derivatives of any function $U(\mathbf{r})$ that is defined at the nodes, and are defined as

$$\begin{aligned}\underline{U}'_r &= \underline{\underline{D}}r * \underline{U} \\ \underline{U}'_z &= \underline{\underline{D}}z * \underline{U}\end{aligned}$$

The node-to-node gradient and divergence operations, for cylindrical coordinates with azimuthal symmetry are

$$\underline{\nabla} \cdot \underline{U} = (\underline{\underline{D}}r * \underline{U}) \hat{\mathbf{r}} + (\underline{\underline{D}}z * \underline{U}) \hat{\mathbf{z}} \quad (5.4.26)$$

and

$$\underline{\nabla} \cdot \underline{\mathbf{P}} = \left((\underline{\underline{D}}r * (r \circ \underline{P}_r)) + (\underline{\underline{D}}z * (r \circ \underline{P}_z)) \right) \otimes r \quad (5.4.27)$$

A schematic of the node-to-node gradient operation mechanism is illustrated in figure 5.4.5. Here, we will look at the derivation of $\underline{\underline{D}}r$, the derivation of $\underline{\underline{D}}z$ is analogous. The node-to-node operators can be expressed in terms of the node-to-element operators by considering the expansion of $U(\mathbf{r})$ in terms of the piecewise-linear functions $U^e(\mathbf{r})$ (equation 5.2.4):

$$U(\mathbf{r}) = \sum_e U^e(\mathbf{r})$$

This implies that

$$U'_r(\mathbf{r}) = \sum_e U_r^{e'}(\mathbf{r})$$

Applying the Galerkin method, we obtain

$$\int \phi_j(\mathbf{r}) U'_r(\mathbf{r}) dr dz = \int \phi_j(\mathbf{r}) \sum_e U_r^{e'}(\mathbf{r}) dr dz \quad (5.4.28)$$

where integral is taken over the support area of the basis function $\phi_j(\mathbf{r})$. Note that $U_r^{e'} = B^e$ (equation 5.2.5). Expanding the right side of equation 5.4.28 in terms of pyramid side functions according to equation 5.2.8, and using equation 5.2.10 to expand the left side, this implies that

$$\begin{aligned} \frac{U'_{rj} s_j}{3} &= \sum_{e_j} \int \psi_j^e(\mathbf{r}) B^e dr dz \\ &= \sum_{e_j} B^e \int \psi_j^e(\mathbf{r}) dr dz \\ &= \sum_{e_j} B^e \frac{s^e}{3} \end{aligned}$$

Therefore, in our method the derivative at a node is defined as the area-weighted average of the elemental derivatives in the support of that node. With use of connectivity matrix $\underline{\underline{M}}^e$, this definition can be written as:

$$\begin{aligned} \underline{\underline{U}}'_r &= \left(\underline{\underline{S}}^{-1} * \left(\underline{\underline{M}}^{eT} * \widehat{\underline{\underline{S}}} * \underline{\underline{D}}r^e \right) \right) * \underline{\underline{U}} \\ \Rightarrow \underline{\underline{D}}r &= \underline{\underline{S}}^{-1} * \left(\underline{\underline{M}}^{eT} * \widehat{\underline{\underline{S}}} * \underline{\underline{D}}r^e \right) \end{aligned} \quad (5.4.29)$$

The derivation of $\underline{\underline{D}}z$ follows from that of $\underline{\underline{D}}r$, with $\underline{\underline{D}}z = \left(\underline{\underline{S}}^{-1} * \left(\underline{\underline{M}}^{eT} * \widehat{\underline{\underline{S}}} * \underline{\underline{D}}z^e \right) \right)$.

Now we introduce some special properties of the node-to-node differential operators. $U'_r(\mathbf{r})$, the radial spatial derivative of the approximate solution $U(\mathbf{r})$, can alternatively be expressed, using the basis function expansion (equation 5.2.6), as

$$U'_r(\mathbf{r}) = \sum_{n=1}^{N_n} U_n \phi'_{rn}(\mathbf{r}) \quad (5.4.30)$$

Applying the Galerkin method, we obtain

$$\int \phi_j U'_r(\mathbf{r}) dr dz = \sum_{n=1}^{N_n} U_n \int \phi_j \phi'_{rn} dr dz \quad (5.4.31)$$

Again, from equation 5.2.10, the left side of this equation is $U'_{rj} s_j / 3$. On the right side,

matrix $\underline{\underline{Lr}}$ of size $N_n \times N_n$ is introduced as

$$\frac{1}{3} \underline{\underline{Lr}}(j, n) = \int \phi_j \phi'_{rn} dr dz \quad (5.4.32)$$

Hence, equation 5.4.31 can be re-expressed as

$$\underline{U}'_r(j) \underline{S}(j) = \sum_{n=1}^{N_n} (\underline{\underline{Lr}}(j, n) \underline{U}(n)) \quad (5.4.33)$$

or in matrix form: $\underline{S} * \underline{\underline{Dr}} * \underline{U} = \underline{\underline{Lr}} * \underline{U}$

$$\Rightarrow \underline{\underline{Dr}} = \underline{S}^{-1} * \underline{\underline{Lr}} \quad (5.4.34)$$

With integration by parts and Green's theorem, equation 5.4.32 implies that

$$\begin{aligned} \underline{\underline{Lr}}(j, n) &= 3 \int \phi_j \phi'_{rn} dr dz \\ &= 3 \int (-\phi'_{rj} \phi_n + (\phi_j \phi_n)'_r) dr dz \\ &= 3 \left(- \int \phi_n \phi'_{rj} dr dz + \oint \phi_j \phi_n dz \right) \end{aligned}$$

The boundary term vanishes at internal nodes, so that $\underline{\underline{Lr}}(j, n) = -\underline{\underline{Lr}}(n, j)$ at the internal nodes. This implies that all elements of the matrix $\underline{\underline{Lr}} + \underline{\underline{Lr}}^T$ are equal to zero, except for the elements corresponding to boundary nodes. Hence, using equation 5.4.34, and noting that the transpose of a diagonal matrix is the same matrix, we obtain

$$(\underline{\underline{S}} * \underline{\underline{Dr}} + \underline{\underline{Dr}}^T * \underline{\underline{S}})_{int} = 0 \quad (5.4.35)$$

where the subscript *int* denotes all elements of the matrix that correspond to interior (non-boundary) nodes. There is an analogous identity for the $\underline{\underline{Dz}}$ operator:

$$(\underline{\underline{S}} * \underline{\underline{Dz}} + \underline{\underline{Dz}}^T * \underline{\underline{S}})_{int} = 0 \quad (5.4.36)$$

As a consequence of these identities, the node-to-node differential operators have some important properties that mimic properties of the corresponding continuous operators. In

particular, the discrete expression for the volume integral in equation 5.1.1 is

$$\begin{aligned}
& \underline{dV}^T * \left[\underline{U} \circ (\underline{\nabla} \cdot \underline{\mathbf{P}}) + \underline{\mathbf{P}} \cdot (\underline{\nabla} \underline{U}) \right] \\
&= \underline{dV}^T * \left[\underline{U} \circ \left(\underline{Dr} * (\underline{r} \circ \underline{P}_r) + \underline{Dz} * (\underline{r} \circ \underline{P}_z) \right) \otimes \underline{r} + \underline{P}_r \circ \left(\underline{Dr} * \underline{U} \right) + \underline{P}_z \circ \left(\underline{Dz} * \underline{U} \right) \right] \\
&= \frac{2\pi}{3} \left[\underline{U}^T * \underline{S} * \left(\underline{Dr} * \underline{R} * \underline{P}_r + \underline{Dz} * \underline{R} * \underline{P}_z \right) + \underline{P}_r^T * \underline{S} * \underline{R} * \underline{Dr} * \underline{U} + \underline{P}_z^T * \underline{S} * \underline{R} * \underline{Dz} * \underline{U} \right] \\
&= \frac{2\pi}{3} \underline{U}^T * \left[\left(\underline{S} * \underline{Dr} + \underline{Dr}^T * \underline{S} \right) * \underline{R} * \underline{P}_r + \left(\underline{S} * \underline{Dz} + \underline{Dz}^T * \underline{S} \right) * \underline{R} * \underline{P}_z \right]
\end{aligned}$$

Note that in the last step, transpose operations on the scalar expressions have been performed. Hence, due to equations 5.4.35 and 5.4.36

$$\underline{dV}^T * \left[\left(\underline{U} \circ (\underline{\nabla} \cdot \underline{\mathbf{P}}) + (\underline{\nabla} \underline{U}) \cdot \underline{\mathbf{P}} \right) \right] = 0 \quad (\text{if } \underline{U}|_\Gamma = 0 \text{ or } \underline{\mathbf{P}}_\perp|_\Gamma = 0) \quad (5.4.37)$$

For the particular case of $\underline{U} = \underline{1}$, this implies that

$$\underline{dV}^T * \left[\underline{\nabla} \cdot \underline{\mathbf{P}} \right] = 0 \quad (\text{if } \underline{\mathbf{P}}_\perp|_\Gamma = 0) \quad (5.4.38)$$

5.4.4.1 Alternative derivations of the first order node-to-node differential operators

Note that while the expansion of $U(\mathbf{r})$ in terms of the piecewise-linear functions $U^e(\mathbf{r})$ (equation 5.2.4) was used to define the node-to-node operators, the basis function expansion (equation 5.2.6) was required to demonstrate the operator properties in equations 5.4.35 to 5.4.38. It is illustrative to note that the operators can be defined equivalently using the latter expansion. The procedure for deriving the radial node-to-node derivative operator is demonstrated as follows. After doing the expansion and applying the Galerkin method, the array of integrals $\underline{\underline{Lr}}$, defined in equation 5.4.32, can be expressed, after expressing the basis functions in terms of the pyramid side functions according to equation 5.2.8, as

$$\underline{\underline{Lr}}(j, n) = 3 \int \left(\sum_{e_j}^{e_n} \psi_j^e(\mathbf{r}) \sum_{e_n}^{e_n} \psi_{rn}^{e'}(\mathbf{r}) \right) dr dz$$

Here, $\sum_{e_j}^{e_n} \psi_{rn}^{e'}(\mathbf{r})$ implies summation of the radial derivatives of the pyramid side functions $\psi_n^e(\mathbf{r})$ that are non-zero over the triangular elements that have a vertex at node n . Similarly $\sum_{e_j}^{e_n} \psi_j^e(\mathbf{r})$ implies summation over the pyramid side functions ψ_j^e defined over the elements

immediately surrounding node j . Equation 5.2.7 defines that

$$\psi_{rn}^{e'}(\mathbf{r}) = b_n^e \quad (\text{if } (r, z) \text{ is in the triangular element associated with } \psi_n^e)$$

$$\psi_{rn}^{e'}(\mathbf{r}) = 0 \quad (\text{otherwise})$$

In either case, the constant can be taken outside the integral, and $\underline{Lr}(j, n)$ can be re-expressed as $\underline{Lr}(j, n) = 3 \sum_{e_j} \psi_{rn}^{e'}(\mathbf{r}) \sum_{e_j} \int \psi_j^e(\mathbf{r}) dr dz$. Using again the expression for the volume of a pyramid (equation 5.2.9), the remaining integral in $\underline{Lr}(j, n)$ is $\int \psi_j^e(\mathbf{r}) dr dz = \frac{s^e}{3}$, where s^e is the area of the triangular element associated with the pyramid side function ψ_j^e . Thus

$$\underline{Lr}(j, n) = \sum_{e_j \cap e_n} b_n^e s^e \quad (5.4.39)$$

where $\sum_{e_j \cap e_n}$ implies summation over the set of elements surrounding node n that overlap with the elements surrounding node j . This can be clarified with an example.

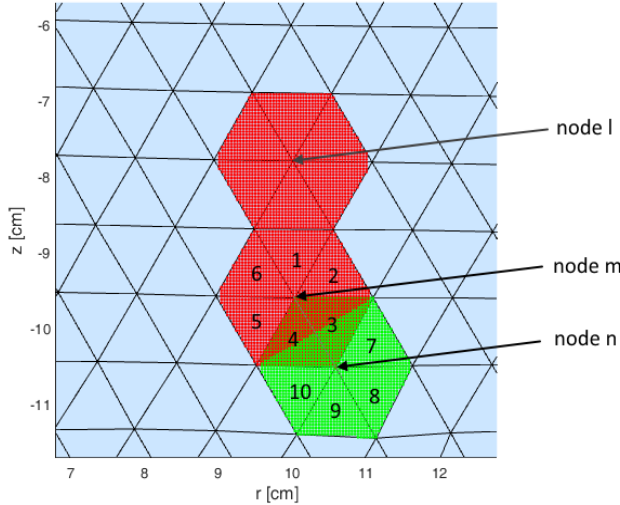


Figure 5.4.6: Linear basis function depiction for triangular elements (top view (2))

As shown in figure 5.4.6 above, which is a top view of figure 5.2.1, nodes n and m are adjacent, and are each surrounded by six triangular elements in this example. Only elements 3 and 4 are in the overlapping regions defined by bases of the pyramid functions ϕ_n and ϕ_m . Each element is associated with three pyramid-side functions and three sets of coefficients a_n^e , b_n^e , and c_n^e . In this example, $\underline{Lr}(n, m) = b_m^3 s^3 + b_m^4 s^4$, where, for example, b_m^3 is one of the three coefficients defining the pyramid-side function that is non-zero only over element 3, and that has an elevation of one at node m , while s^3 is the area of triangular element 3. Meanwhile, $\underline{Lr}(m, n) = b_n^3 s^3 + b_n^4 s^4$, $\underline{Lr}(m, m) = \sum_{i=1}^6 b_m^i s^i$, $\underline{Lr}(n, n) = \sum_{i=3}^4 b_n^i s^i + \sum_{i=7}^{10} b_n^i s^i$, and since node

l is not adjacent to node m nor to node n , $\underline{\underline{Lr}}(l, m) = \underline{\underline{Lr}}(m, l) = \underline{\underline{Lr}}(l, n) = \underline{\underline{Lr}}(n, l) = 0$. Having developed an analytical expression for $\underline{\underline{Lr}}$ in terms of the pyramid side functions, $\underline{\underline{Dr}}$ can be evaluated using equation 5.4.34. The procedure for deriving $\underline{\underline{Dz}}$ using the basis function expansion method is analogous.

The node-to-node differential operators can alternatively be defined directly in terms of the node-to-element differential operators simply by requiring the discrete form of equation 5.1.1 to hold. The identity implies that when the continuous functions \mathbf{p} and u are such that $\mathbf{p}_\perp|_\Gamma = 0$ or $u|_\Gamma = 0$, that $\int u \nabla \cdot \mathbf{p} dV = - \int \mathbf{p} \nabla u dV$. Thus, with the boundary conditions $\underline{U}|_\Gamma = 0$ or $\underline{\mathbf{P}}_\perp|_\Gamma = 0$:

$$\begin{aligned}
\underline{dV}^T * \left\{ \underline{U} \circ \left(\left(\underline{\underline{Dr}}_n * \left(\underline{r}^e \circ \underline{P}_r^e \right) \right) \otimes \underline{r} \right) \right\} &= - \underline{dV}^T * \left\{ \underline{P}_r \circ \left(\underline{\underline{Dr}} * \underline{U} \right) \right\} \\
\Rightarrow \underline{s}^T * \left(\underline{U} \circ \left(\underline{\underline{Dr}}_n * \left(\underline{r}^e \circ \underline{P}_r^e \right) \right) \right) &= - \underline{s}^T * \left(\underline{r} \circ \underline{P}_r \circ \left(\underline{\underline{Dr}} * \underline{U} \right) \right) \\
\Rightarrow \underline{U}^T * \left(\underline{\underline{S}} * \left(\underline{\underline{\underline{Dr}}}_n * \left(\frac{1}{3} \underline{\underline{M}}^e * \left(\underline{r} \circ \underline{P}_r \right) \right) \right) \right) &= - \left(\underline{r} \circ \underline{P}_r \right)^T * \left(\underline{\underline{S}} * \underline{\underline{Dr}} * \underline{U} \right) \\
\Rightarrow \left(\frac{1}{3} \underline{\underline{\underline{M}}^e} * \left(\underline{r} \circ \underline{P}_r \right) \right)^T * \left(\underline{\underline{\underline{Dr}}}_n^T * \underline{\underline{S}} * \underline{U} \right) &= - \left(\underline{r} \circ \underline{P}_r \right)^T * \left(\underline{\underline{S}} * \underline{\underline{Dr}} * \underline{U} \right) \quad (\text{transpose}) \\
\Rightarrow \left(\underline{r} \circ \underline{P}_r \right)^T * \left(\frac{1}{3} \underline{\underline{\underline{M}}^e}^T * \underline{\underline{\underline{Dr}}}_n^T * \underline{\underline{S}} * \underline{U} \right) &= - \left(\underline{r} \circ \underline{P}_r \right)^T * \left(\underline{\underline{S}} * \underline{\underline{Dr}} * \underline{U} \right) \\
\Rightarrow \underline{\underline{Dr}} &= - \frac{1}{3} \underline{\underline{\underline{S}}}^{-1} * \underline{\underline{\underline{M}}^e}^T * \underline{\underline{\underline{Dr}}}_n^T * \underline{\underline{S}} \\
&= \underline{\underline{\underline{S}}}^{-1} * \underline{\underline{\underline{M}}^e}^T * \underline{\underline{\underline{S}}} * \underline{\underline{\underline{Dr}}}^e \quad (\text{use eqn. 5.4.15})
\end{aligned}$$

Again, the procedure for deriving $\underline{\underline{Dz}}$ using the basis function expansion method is analogous. While this derivation method is short and simple, demonstration of the special operator properties requires, as outlined previously, the expansion of the derivatives of $U(\mathbf{r})$ in terms of the basis functions.

5.5 Axisymmetric two-temperature MHD model

A two-temperature plasma MHD model, in which the electrons and ions are allowed to have different temperatures, is a compromise between the single-fluid and two-fluid MHD models. It has the relative computational simplicity of the single-fluid model, but from the energy point of view it treats electrons and ions as two separate fluids, and allows implementation of different thermal diffusion coefficients for the electrons and ions. In the following, SI units will be used, but temperatures will be expressed in Joules unless otherwise indicated. As shown in appendix A, the MHD equations can be derived from basic kinetic theory. The Grad-Shafranov equation, derived in appendix A.7.1, describes MHD equilibrium in the case

with toroidal symmetry:

$$\Delta^* \psi = - \left(\mu_0 r^2 \frac{dp}{d\psi} + f \frac{df}{d\psi} \right)$$

Here, ψ is the poloidal flux per radian, and $f(\psi) = rB_\phi$. The numerical method implemented to code to solve the Grad-Shafranov equation, using the discrete form of the Δ^* operator (section 5.4.3), is presented in appendix C.4. In equilibrium, when \mathbf{J} is parallel to \mathbf{B} , the magnetic field topology is described by equation 1.3.1: $\nabla \times \mathbf{B} = \lambda \mathbf{B}$. As shown in appendix A.7.2, this implies that $\lambda = \lambda(\psi)$, with the consequence that general axisymmetric force free states must have λ constant on a flux surface. Unlike the Taylor state, in which fields satisfy $\nabla \times \mathbf{B} = \lambda \mathbf{B}$ with constant λ , λ can vary across flux surfaces in general axisymmetric force free states. A simple model assuming a linear dependence of λ on ψ [6, 78] is presented in appendix A.7.2, and is implemented as an option when solving the Grad-Shafranov equation. Example solutions are presented in appendices C.4 and C.5.2.

In addition to the continuous forms of the two-temperature MHD equations, from appendix summary A.8, we require expressions for $\dot{\psi}$ and \dot{f} to complete the axisymmetric model:

5.5.1 Expression for $\dot{\psi}$

Referring to Ampere's law, the reduced form of Ohm's law (equation A.6.12) implies that $\mathbf{E} + \mathbf{v} \times \mathbf{B} = \eta \nabla \times \mathbf{B}$, so that $E_\phi = \eta(\nabla \times \mathbf{B})_\phi - (\mathbf{v} \times \mathbf{B})_\phi$. Here $\eta [\text{m}^2/\text{s}] = \frac{\eta'}{\mu_0}$ is the magnetic diffusivity. The electric field is defined as $\mathbf{E} = -\nabla \Phi_E - \dot{\mathbf{A}}$, where \mathbf{A} is the magnetic vector potential defined by $\mathbf{B} = \nabla \times \mathbf{A}$, and Φ_E is the electric potential, so that:

$$-\nabla_\phi \Phi_E - \dot{\mathbf{A}}_\phi = \eta \left(\frac{\partial B_r}{\partial z} - \frac{\partial B_z}{\partial r} \right) \hat{\phi} - (v_z B_r - v_r B_z) \hat{\phi} \quad (5.5.1)$$

With toroidal symmetry, the first term goes to zero. Noting that $\psi = rA_\phi$ (equation A.7.2), and referring to equation A.7.18 for the definitions of the components of the axisymmetric magnetic field, we can re-express this as

$$\dot{\psi} = \eta \left(r \frac{\partial}{\partial r} \left(\frac{1}{r} \frac{\partial \psi}{\partial r} \right) + \frac{\partial^2 \psi}{\partial z^2} \right) - v_z \frac{\partial \psi}{\partial z} - v_r \frac{\partial \psi}{\partial r} = \eta \Delta^* \psi - (\mathbf{v} \cdot \nabla) \psi \quad (5.5.2)$$

$$\Rightarrow \dot{\psi} = \dot{\psi}_{ideal} + \dot{\psi}_\eta = -(\mathbf{v} \cdot \nabla) \psi + \eta \Delta^* \psi \quad (5.5.3)$$

Here, $\dot{\psi}_{ideal}$ is the part of $\dot{\psi}$ that would occur even in a perfectly conductor, for example in an ideal plasma, and $\dot{\psi}_\eta$ is the part of $\dot{\psi}$ that is due to diffusive effects associated with electrical

resistivity.

5.5.2 Expressions for \dot{f}

General case

Taking the curl of Ohm's law, we obtain: $\nabla \times \mathbf{E} = \nabla \times (\eta' \mathbf{J} - \mathbf{v} \times \mathbf{B})$. Using Faraday's law ($\nabla \times \mathbf{E} = -\dot{\mathbf{B}}$), and Ampere's law, this implies that

$$\dot{\mathbf{B}} = \nabla \times (\mathbf{v} \times \mathbf{B} - \eta' \mathbf{J}) = \nabla \times (\mathbf{v} \times \mathbf{B}) - \nabla \times (\eta \nabla \times \mathbf{B}) \quad (5.5.4)$$

To find $\dot{f} = r \dot{B}_\phi$, we want an expression for

$$\dot{f} = r \left((\nabla \times (\mathbf{v} \times \mathbf{B}))_\phi - (\nabla \times (\eta \nabla \times \mathbf{B}))_\phi \right) \quad (5.5.5)$$

As was done with $\dot{\psi}$, \dot{f} can be split into an ideal part and a resistive part:

$$\dot{f} = \dot{f}_{ideal} + \dot{f}_\eta = r (\nabla \times (\mathbf{v} \times \mathbf{B}))_\phi + r (-\nabla \times (\eta \nabla \times \mathbf{B}))_\phi \quad (5.5.6)$$

This can be alternatively expressed as a full divergence of terms. Along with inherent properties of the differential operators, the discrete form of the full-divergence expression will ensure conservation of toroidal flux. To derive the full divergence expression, it is convenient to expand \dot{f}_{ideal} and \dot{f}_η separately. The following relationships will be used to expand \dot{f}_{ideal} :

$$\begin{aligned} \nabla \left(\frac{v_\phi}{r} \right) &= \frac{1}{r} \nabla v_\phi + v_\phi \nabla \left(\frac{1}{r} \right) \\ \Rightarrow \nabla v_\phi &= r \nabla \omega + \omega \hat{\mathbf{r}} \end{aligned} \quad (5.5.7)$$

Here, $\omega = v_\phi/r$ is the plasma angular speed. Replacing v_ϕ in this expression with $\frac{f}{r}$:

$$\nabla \left(\frac{f}{r} \right) = r \nabla \left(\frac{f}{r^2} \right) + \left(\frac{f}{r^2} \right) \hat{\mathbf{r}} \quad (5.5.8)$$

$$\begin{aligned}
\dot{f}_{ideal} &= r(\nabla \times \mathbf{v} \times \mathbf{B})_\phi \\
&= r(\cancel{v(\nabla \cdot \mathbf{B})} - \mathbf{B}(\nabla \cdot \mathbf{v}) + (\mathbf{B} \cdot \nabla) \mathbf{v} - (\mathbf{v} \cdot \nabla) \mathbf{B})_\phi \\
&= r \left(-B_\phi \nabla \cdot \mathbf{v} + \mathbf{B} \cdot \nabla v_\phi + \frac{B_\phi v_r}{r} - \mathbf{v} \cdot \nabla B_\phi - \frac{v_\phi B_r}{r} \right) \\
&= r^2 \left(-\frac{f}{r^2} \nabla \cdot \mathbf{v} + \frac{1}{r} \mathbf{B} \cdot \nabla v_\phi + \frac{f}{r^3} v_r - \frac{1}{r} \mathbf{v} \cdot \nabla \left(\frac{f}{r} \right) - \frac{\omega B_r}{r} \right) \\
&= r^2 \left(-\frac{f}{r^2} \nabla \cdot \mathbf{v} + \frac{1}{r} \mathbf{B} \cdot (r \nabla \omega + \omega \hat{\mathbf{r}}) + \frac{f}{r^3} v_r \right. \\
&\quad \left. - \frac{1}{r} \mathbf{v} \cdot \left(r \nabla \left(\frac{f}{r^2} \right) + \left(\frac{f}{r^2} \right) \hat{\mathbf{r}} \right) - \frac{\omega B_r}{r} \right) \quad (\text{use eqns. 5.5.7, 5.5.8}) \\
&= r^2 \left(-\frac{f}{r^2} \nabla \cdot \mathbf{v} + \mathbf{B} \cdot \nabla \omega + \cancel{\frac{\omega B_r}{r}} + \cancel{\frac{f}{r^3} v_r} - \mathbf{v} \cdot \nabla \left(\frac{f}{r^2} \right) - \cancel{\frac{f}{r^3} v_r} \cancel{- \frac{\omega B_r}{r}} \right) \\
\Rightarrow \dot{f}_{ideal} &= r^2 \nabla \cdot \left(-\left(\frac{f}{r^2} \mathbf{v} \right) + \omega \mathbf{B} \right)
\end{aligned}$$

To expand \dot{f}_η , an additional relation needs to be established. Taking the curl of the poloidal component of the axisymmetric magnetic field defined in equation A.7.4 leads to

$$\begin{aligned}
\nabla \times \mathbf{B}_\theta &= \nabla \times (\nabla \psi \times \nabla \phi) \\
&= \nabla \psi (\cancel{\nabla \cdot \nabla \phi}) - \nabla \phi (\nabla \cdot \nabla \psi) + (\nabla \phi \cdot \nabla) \nabla \psi - (\nabla \psi \cdot \nabla) \nabla \phi \\
&= - \left(\nabla \cdot \nabla \psi - \frac{2}{r} \frac{\partial \psi}{\partial r} \right) \nabla \phi
\end{aligned}$$

Note that, using equation A.7.10, $\Delta^* \psi$ can be written as $\Delta^* \psi = r^2 \nabla \cdot \left(\frac{\nabla \psi}{r^2} \right) = \nabla \cdot \nabla \psi - \frac{2}{r} \frac{\partial \psi}{\partial r}$, leading to the relation

$$\nabla \times (\nabla \psi \times \nabla \phi) = -\Delta^* \psi \nabla \phi \quad (5.5.9)$$

for any function $\psi(r, z)$ defined in geometry with azimuthal symmetry. Since, with axisymmetry, the curl of a poloidal vector is toroidal, and vice-versa, we can write

$$\begin{aligned}
\dot{f}_\eta \hat{\phi} &= -r (\nabla \times (\eta \nabla \times \mathbf{B}))_\phi \hat{\phi} \\
&= -r \nabla \times (\eta \nabla \times \mathbf{B}_\phi) \\
&= -r \nabla \times \eta (\nabla f \times \nabla \phi) \\
&= -r (-\eta \Delta^* f \nabla \phi + \nabla \eta \times (\nabla f \times \nabla \phi)) \quad (\text{use eqn. 5.5.9}) \\
&= -r (-\eta \Delta^* f \nabla \phi + \nabla f (\nabla \eta \cdot \nabla \phi) - \nabla \phi (\nabla \eta \cdot \nabla f)) \\
&= r \left(\eta r^2 \nabla \cdot \left(\frac{\nabla f}{r^2} \right) + (\nabla \eta \cdot \nabla f) \right) \frac{\hat{\phi}}{r} \\
\Rightarrow \dot{f}_\eta &= r^2 \left(\eta \nabla \cdot \left(\frac{\nabla f}{r^2} \right) + \left(\nabla \eta \cdot \left(\frac{\nabla f}{r^2} \right) \right) \right) \\
&= r^2 \nabla \cdot \left(\frac{\eta}{r^2} \nabla f \right)
\end{aligned}$$

Hence,

$$\dot{f} = \dot{f}_{ideal} + \dot{f}_\eta = r^2 \nabla \cdot \left(- \left(\frac{f}{r^2} \mathbf{v} \right) + \omega \mathbf{B} + \frac{\eta}{r^2} \nabla f \right) \quad (5.5.10)$$

Isothermal case

The more general and useful case described above is that η has spatial dependence: $\eta = \eta(T_e(r, z))$. The isothermal version of the code (in which energy is not conserved) assumes constant temperature, with spatially constant η , so that

$$\dot{f}_{iso} = \dot{f}_{ideal} + \dot{f}_{\eta iso} = r (\nabla \times \mathbf{v} \times \mathbf{B})_\phi + r \eta (\nabla^2 \mathbf{B})_\phi \quad (5.5.11)$$

Here,

$$(\nabla^2 \mathbf{B})_\phi = \nabla^2 B_\phi - \frac{B_\phi}{r^2} = \frac{1}{r} \frac{\partial}{\partial r} \left(r \frac{\partial B_\phi}{\partial r} \right) + \frac{\partial^2 B_\phi}{\partial z^2} - \frac{B_\phi}{r^2} = \frac{\partial^2 B_\phi}{\partial r^2} + \frac{1}{r} \frac{\partial B_\phi}{\partial r} - \frac{B_\phi}{r^2} + \frac{\partial^2 B_\phi}{\partial z^2}$$

By the definition of the Δ^* operator (equation A.7.10),

$$\begin{aligned}
\Delta^* (r B_\phi) &= r \frac{\partial}{\partial r} \left(\frac{1}{r} \frac{\partial (r B_\phi)}{\partial r} \right) + \frac{\partial^2 (r B_\phi)}{\partial z^2} = r \frac{\partial}{\partial r} \left(\frac{1}{r} \left(r \frac{\partial B_\phi}{\partial r} + B_\phi \right) \right) + r \frac{\partial^2 B_\phi}{\partial z^2} \\
&= r \left(\frac{\partial^2 B_\phi}{\partial r^2} + \frac{1}{r} \frac{\partial B_\phi}{\partial r} - \frac{B_\phi}{r^2} + \frac{\partial^2 B_\phi}{\partial z^2} \right)
\end{aligned}$$

so that

$$\dot{f}_{\eta iso} = r\eta(\nabla^2\mathbf{B})_\phi = \eta\Delta^*(rB_\phi) = \eta\Delta^*f \quad (5.5.12)$$

5.5.3 Continuous form of MHD model equations and demonstration of conservation properties

Combining these expressions for $\dot{\psi}$ and \dot{f} (equations 5.5.3 and 5.5.10) with the continuous forms of the two-temperature MHD equations (from appendix summary A.8), the full set of equations describing the axisymmetric MHD model is:

$$\dot{n} = -\nabla \cdot (n\mathbf{v}) \quad (5.5.13)$$

$$\dot{\mathbf{v}} = -\mathbf{v} \cdot \nabla \mathbf{v} + \frac{1}{\rho} (-\nabla p - \nabla \cdot \bar{\boldsymbol{\pi}} + \mathbf{J} \times \mathbf{B}) \quad (5.5.14)$$

$$\dot{p}_i = -\mathbf{v} \cdot \nabla p_i - \gamma p_i \nabla \cdot \mathbf{v} + (\gamma - 1) (-\nabla \cdot \mathbf{q}_i + Q_{ie} - \bar{\boldsymbol{\pi}} : \nabla \mathbf{v}) \quad (5.5.15)$$

$$\dot{p}_e = -\mathbf{v} \cdot \nabla p_e - \gamma p_e \nabla \cdot \mathbf{v} + (\gamma - 1) (-\nabla \cdot \mathbf{q}_e - Q_{ie} + \eta' \mathbf{J}^2) \quad (5.5.16)$$

$$\dot{\psi} = -\mathbf{v} \cdot \nabla \psi + \eta \Delta^* \psi \quad (5.5.17)$$

$$\dot{f} = r^2 \nabla \cdot \left(-\left(\frac{f}{r^2} \mathbf{v} \right) + \omega \mathbf{B} + \frac{\eta}{r^2} \nabla f \right) \quad (5.5.18)$$

where $\omega = v_\phi/r$ is the plasma angular speed, and η [m²/s] = $\eta' [\Omega - m]/\mu_0$ is the plasma resistive diffusion coefficient. Note that n is the ion number density, so that the electron number density is $n_e = Z_{eff}n$, where Z_{eff} is the volume-averaged ion charge. We assume ideal gas laws for ions and electrons:

$$\begin{aligned} p_i &= nT_i \\ p_e &= Z_{eff}nT_e \end{aligned} \quad (5.5.19)$$

Total plasma fluid pressure is $p = p_i + p_e$. The boundary conditions and closure for this model (namely, definitions of thermal fluxes \mathbf{q}_i and \mathbf{q}_e , viscous stress tensor $\bar{\boldsymbol{\pi}}$ and ion-electron heat exchange rate Q_{ie}) will be discussed in section 5.6.1.

With axisymmetry, the magnetic field can be represented in divergence-free form accord-

ing to equation A.7.4:

$$\mathbf{B} = \nabla\psi \times \nabla\phi + f\nabla\phi \quad (5.5.20)$$

Referring to equation 5.5.9, the current density in this case is

$$\mathbf{J} = \frac{1}{\mu_0} \nabla \times \mathbf{B} = \frac{1}{\mu_0} (-\Delta^* \psi \nabla\phi + \nabla f \times \nabla\phi) \quad (5.5.21)$$

and the Lorentz force is

$$\mathbf{J} \times \mathbf{B} = -\frac{1}{\mu_0 r^2} \left(\Delta^* \psi \nabla\psi + f \nabla f \right) + \frac{\mathbf{B} \cdot \nabla f}{\mu_0 r} \hat{\phi} \quad (5.5.22)$$

The system described by equations 5.5.13 - 5.5.18 has a number of exact conservation laws expressed by corresponding continuity equations. The obvious one is conservation of particles, expressed by equation 5.5.13, with the boundary condition $\mathbf{v}_\perp|_\Gamma = 0$, corresponding to impermeable walls, where the subscript \perp implies the component perpendicular to the boundary. Another conserved quantity is toroidal flux, defined as

$$\Phi = \int B_\phi dr dz = \int \frac{f}{r} dr dz = \frac{1}{2\pi} \int \frac{f}{r^2} 2\pi r dr dz = \frac{1}{2\pi} \int \frac{f}{r^2} dV$$

Equation 5.5.18 implies that the rate of change of system toroidal flux is

$$\dot{\Phi} = \frac{1}{2\pi} \int \nabla \cdot \left(-\frac{f}{r^2} \mathbf{v} + \omega \mathbf{B} + \frac{\eta}{r^2} \nabla f \right) dV = \frac{1}{2\pi} \int \left(-\frac{f}{r^2} \mathbf{v} + \omega \mathbf{B} + \frac{\eta}{r^2} \nabla f \right) \cdot d\mathbf{T} \quad (5.5.23)$$

With appropriate boundary conditions, for example $\mathbf{v}|_\Gamma = \mathbf{0}$ and $(\nabla_\perp f)|_\Gamma = 0$, or $\mathbf{v}_\perp|_\Gamma = \mathbf{0}$ and $(B_{\theta\perp} v_\phi + \eta(\frac{\nabla_\perp f}{r}))|_\Gamma = 0$, toroidal flux is conserved. Note that the electric field at the system boundary is

$$\begin{aligned} \mathbf{E}|_\Gamma &= (-\mathbf{v} \times \mathbf{B} + \eta \nabla \times \mathbf{B})|_\Gamma \\ &= (-\mathbf{v}_\phi \times \mathbf{B}_\theta - \mathbf{v}_\theta \times \mathbf{B}_\phi - \mathbf{v}_\theta \times \mathbf{B}_\theta + \eta(-\Delta^* \psi \nabla\phi + \nabla f \times \nabla\phi))|_\Gamma \\ &= \left(-\mathbf{v}_\phi \times (\mathbf{B}_{\theta\parallel} + \mathbf{B}_{\theta\perp}) - B_\phi (\mathbf{v}_{\theta\perp} + \mathbf{v}_{\theta\parallel}) \times \hat{\phi} + (\mathbf{v} \cdot \nabla\psi) \nabla\phi + \eta \left(-\Delta^* \psi \nabla\phi + \frac{\nabla f}{r} \times \hat{\phi} \right) \right)|_\Gamma \end{aligned}$$

Here, the subscript \parallel implies the component parallel to the boundary. Hence, the poloidal component of the electric field parallel to the boundary is

$$E_{\theta\parallel}|_\Gamma = \left(B_{\theta\perp} v_\phi - B_\phi v_{\theta\perp} + \eta \frac{\nabla_\perp f}{r} \right)|_\Gamma \quad (5.5.24)$$

Therefore, either of the sets of boundary conditions listed above for toroidal flux conservation correspond to having the poloidal component of the electric field perpendicular to the bound-

ary, the condition, in the case of azimuthal symmetry, for perfectly electrically conducting walls.

Conservation of angular momentum is established after noting that in the axisymmetric case

$$(\mathbf{v} \cdot \nabla \mathbf{v})_\phi = v_r \frac{\partial v_\phi}{\partial r} + \frac{v_r v_\phi}{r} + v_z \frac{\partial v_\phi}{\partial z} = \frac{v_r}{r} \frac{\partial(r v_\phi)}{\partial r} + \frac{v_z}{r} \frac{\partial(r v_\phi)}{\partial z} = \frac{1}{r} \mathbf{v} \cdot \nabla(r v_\phi)$$

and that the ϕ coordinate of the divergence of the viscous stress tensor, which is transpose symmetric (see equation B.3.7), is

$$(\nabla \cdot \bar{\boldsymbol{\pi}})_\phi = \frac{1}{r} \frac{\partial}{\partial r} (r \pi_{r\phi}) + \frac{\partial}{\partial z} (\pi_{z\phi}) + \frac{\pi_{r\phi}}{r} = \frac{1}{r^2} \frac{\partial}{\partial r} (r^2 \pi_{r\phi}) + \frac{1}{r^2} \frac{\partial}{\partial z} (r^2 \pi_{z\phi}) = \frac{1}{r} \nabla \cdot (r \pi_{r\phi} \hat{\mathbf{r}} + r \pi_{z\phi} \hat{\mathbf{z}})$$

The continuity equation for angular momentum density is then

$$\begin{aligned} \frac{\partial}{\partial t} (\rho v_\phi r) &= m_i \dot{n} v_\phi r + \rho \dot{v}_\phi r \\ &= - \left[m_i v_\phi r \nabla \cdot (n \mathbf{v}) + \rho \mathbf{v} \cdot \nabla(r v_\phi) \right] - \nabla \cdot (r \pi_{r\phi} \hat{\mathbf{r}} + r \pi_{z\phi} \hat{\mathbf{z}}) + \frac{1}{\mu_0} \mathbf{B} \cdot \nabla f \quad (5.5.25) \\ &= - \nabla \cdot \left(\rho v_\phi r \mathbf{v} + r \pi_{r\phi} \hat{\mathbf{r}} + r \pi_{z\phi} \hat{\mathbf{z}} - \frac{f}{\mu_0} \mathbf{B} \right) \end{aligned}$$

Hence, the rate of change of total system angular momentum is

$$\dot{P}_\phi = \frac{\partial}{\partial t} \left(\int (\rho r v_\phi) dV \right) = - \int \left(\rho v_\phi r \mathbf{v} + r \pi_{r\phi} \hat{\mathbf{r}} + r \pi_{z\phi} \hat{\mathbf{z}} - \frac{f}{\mu_0} \mathbf{B} \right) \cdot d\mathbf{I}$$

With appropriate boundary conditions, total system angular momentum is conserved. One set of appropriate boundary conditions is as follows. The first term here vanishes with the boundary conditions for impermeable walls, $\mathbf{v}_\perp|_\Gamma = \mathbf{0}$. Referring to equation B.3.7, it can be seen that with the boundary condition $(\nabla_\perp \omega)|_\Gamma = 0$, the second and third terms vanish too. The boundary condition $(\nabla_\perp \omega)|_\Gamma = 0$ is physical only in unusual cases; for example, there may be no viscosity at the wall due to rotation of the wall. The last term is zero with the boundary condition $(\nabla_\parallel \psi)|_\Gamma = 0$ (i.e., $\psi|_\Gamma = C$ (constant)), corresponding to having the magnetic field parallel to the boundary.

The rate of change of the system's total energy is the sum of the rates of change of kinetic, thermal, and magnetic energies:

$$\dot{U}_{Total} = \dot{U}_K + \dot{U}_{Th} + \dot{U}_M = \int \frac{\partial}{\partial t} \left[\frac{1}{2} \rho v^2 + \frac{p}{\gamma - 1} + \frac{B^2}{2\mu_0} \right] dV$$

Using the vector identity

$$(\mathbf{A} \times \mathbf{B}) \cdot (\mathbf{C} \times \mathbf{D}) = (\mathbf{A} \cdot \mathbf{C})(\mathbf{B} \cdot \mathbf{D}) - (\mathbf{A} \cdot \mathbf{D})(\mathbf{B} \cdot \mathbf{C}) \quad (5.5.26)$$

$B^2 = (\nabla\psi \times \nabla\phi) \cdot (\nabla\psi \times \nabla\phi) = (\nabla\psi \cdot \nabla\psi)(\nabla\phi \cdot \nabla\phi) - (\nabla\psi \cdot \nabla\phi)(\nabla\phi \cdot \nabla\psi) + \left(\frac{f}{r}\right)^2$. With azimuthal symmetry, $\nabla\psi \cdot \nabla\phi = 0$, so that $B^2 = \left(\frac{\nabla\psi}{r}\right)^2 + \left(\frac{f}{r}\right)^2$.

$$\Rightarrow \dot{U}_{Total} = \dot{U}_K + \dot{U}_{Th} + \dot{U}_M = \int \left[\left(\frac{1}{2} \dot{\rho} v^2 + \rho \mathbf{v} \cdot \dot{\mathbf{v}} \right) + \frac{\dot{p}}{\gamma - 1} + \frac{1}{2\mu_0} \left(\frac{\partial}{\partial t} \left(\left(\frac{\nabla\psi}{r} \right)^2 + \left(\frac{f}{r} \right)^2 \right) \right) \right] dV \quad (5.5.27)$$

Using the continuous MHD equations, this may be evaluated as

$$\dot{U}_{Total} = \int \nabla \cdot (\Sigma_\beta (\mathbf{v}_\beta Y_\beta) + \mathbf{S} + \mathbf{q}) dV \quad (5.5.28)$$

Here, the subscript β refers to the spatial coordinates, Y_β are complicated expressions involving various physical parameters (η, γ, μ_0), and fields ρ, v_β, \dots etc., \mathbf{S} [W/m²] = $\mathbf{E} \times \mathbf{H}$ is the Poynting vector, and \mathbf{q} [W/m²] is the heat flux density vector. When the system is surrounded by solid walls, $\mathbf{v}_\perp|_\Gamma = \mathbf{0}$. Applying the divergence theorem,

$$\dot{U}_{Total} = \int (\mathbf{S} + \mathbf{q}) \cdot d\Gamma$$

Thus, system energy is conserved, apart from the fluxes of electromagnetic and thermal energy lost through the system boundary. If additional boundary conditions correspond to perfectly electrically conducting and thermally insulating walls, then there will be no energy fluxes out of the system, and total energy will be conserved. System energy conservation with appropriate boundary conditions can be proved for the continuous MHD equations as follows. Note that $-\mathbf{v} \cdot \nabla \mathbf{v} = -\nabla(v^2/2) + \mathbf{v} \times (\nabla \times \mathbf{v})$. Referring to equation 5.5.21, and using equation 5.5.26 again, note also that $J^2 = \frac{1}{\mu_0^2} \left(\left(\frac{\Delta^* \psi}{r} \right)^2 + \left(\frac{\nabla f}{r} \right)^2 \right)$. Expressing the total system energy as the sum of kinetic, thermal and magnetic energy, and referring to equations

5.5.13 - 5.5.18, the continuity equation for energy density is

$$\begin{aligned}
\dot{u}_{Total} &= \dot{u}_K + \dot{u}_{Th} + \dot{u}_M \\
&= \frac{\partial}{\partial t} \left(\frac{\rho \mathbf{v}^2}{2} + \frac{p}{\gamma - 1} + \frac{1}{2\mu_0 r^2} ((\nabla \psi)^2 + f^2) \right) \\
&= \frac{m_i \dot{n} \mathbf{v}^2}{2} + \rho \mathbf{v} \cdot \dot{\mathbf{v}} + \frac{\dot{p}}{\gamma - 1} + \frac{1}{\mu_0 r^2} (\nabla \psi \cdot (\nabla \dot{\psi}) + f \dot{f}) \\
&= - \left[\frac{m_i \mathbf{v}^2}{2} \nabla \cdot (n \mathbf{v}) + \rho \mathbf{v} \cdot \nabla \frac{\mathbf{v}^2}{2} \right] \\
&\quad - \left[\mathbf{v} \cdot \nabla p + \frac{\mathbf{v} \cdot \nabla p + \gamma p \nabla \cdot \mathbf{v}}{\gamma - 1} \right] \\
&\quad - \left[\frac{1}{\mu_0 r^2} \Delta^* \psi (\mathbf{v} \cdot \nabla \psi) + \frac{1}{\mu_0 r^2} \nabla \psi \cdot \nabla (\mathbf{v} \cdot \nabla \psi) \right] \\
&\quad - \left[\frac{1}{\mu_0 r^2} f (\mathbf{v} \cdot \nabla f) + \frac{1}{\mu_0} f \nabla \cdot \left(\frac{f}{r^2} \mathbf{v} \right) \right] \\
&\quad + \left[\frac{1}{\mu_0} \omega \mathbf{B} \cdot \nabla f + \frac{1}{\mu_0} f \nabla \cdot (\omega \mathbf{B}) \right] \\
&\quad + \left[\frac{\eta (\Delta^* \psi)^2}{\mu_0 r^2} + \frac{1}{\mu_0 r^2} \nabla \psi \cdot \nabla (\eta \Delta^* \psi) \right] \\
&\quad + \left[\frac{\eta (\nabla f)^2}{\mu_0 r^2} + \frac{f}{\mu_0} \nabla \cdot \left(\frac{\eta}{r^2} \nabla f \right) \right] \\
&\quad - \left[\nabla \cdot (\mathbf{q}_i + \mathbf{q}_e) \right] \\
&\quad - \left[\mathbf{v} \cdot (\nabla \cdot \bar{\boldsymbol{\pi}}) + \bar{\boldsymbol{\pi}} : \nabla \mathbf{v} \right] \\
&= - \nabla \cdot \left(\frac{m_i n \mathbf{v}^2}{2} \mathbf{v} + \frac{\gamma p}{\gamma - 1} \mathbf{v} + \frac{(\mathbf{v} \cdot \nabla \psi)}{\mu_0 r^2} \nabla \psi \right. \\
&\quad \left. + \frac{f^2}{\mu_0 r^2} \mathbf{v} - \frac{1}{\mu_0} \omega f \mathbf{B} - \frac{\eta \Delta^* \psi}{\mu_0 r^2} \nabla \psi - \frac{\eta f}{\mu_0 r^2} \nabla f + \mathbf{q}_i + \mathbf{q}_e + \bar{\boldsymbol{\pi}} \cdot \mathbf{v} \right) \tag{5.5.29}
\end{aligned}$$

Note that the five magnetic terms involving μ_0 in the final full-divergence expression constitute the Poynting flux. Taking the integral over the final expression for \dot{u}_{total} over the system volume, and applying Gauss's theorem, it can be seen how total system energy is conserved with appropriate boundary conditions, for example $\mathbf{v}|_{\Gamma} = \mathbf{0}$, $\mathbf{q}_{i\perp}|_{\Gamma} = \mathbf{q}_{e\perp}|_{\Gamma} = \mathbf{0}$, $(\nabla_{\perp} \psi)|_{\Gamma} = 0$ and $(\nabla_{\perp} f)|_{\Gamma} = 0$, or $\mathbf{v}_{\perp}|_{\Gamma} = \mathbf{0}$, $\mathbf{q}_{i\perp}|_{\Gamma} = \mathbf{q}_{e\perp}|_{\Gamma} = \mathbf{0}$, $(\nabla_{\perp} \psi)|_{\Gamma} = 0$ and $(B_{\theta\perp} v_{\phi} + \eta \left(\frac{\nabla_{\perp} f}{r} \right))|_{\Gamma} = 0$. Referring to equation 5.5.24, note that either of these sets of boundary conditions also eliminates energy loss associated with Poynting flux. Note that the terms $+\frac{(\mathbf{v} \cdot \nabla \psi)}{\mu_0 r^2} \nabla \psi$ and $-\frac{\eta \Delta^* \psi}{\mu_0 r^2} \nabla \psi$ in the final full-divergence expression in equation 5.5.29 constitute the part of the Poynting flux that arises due to the toroidal component of the electric field at the boundary. The boundary condition $(\nabla_{\perp} \psi)|_{\Gamma} = 0$ or $(\Delta^* \psi)|_{\Gamma} = 0$ is

required to eliminate this contribution. Referring to equation 5.5.17, it can be seen that the combination of boundary conditions $\mathbf{v}_\perp|_\Gamma = \mathbf{0}$ and $\psi|_\Gamma = 0$ automatically leads to the boundary condition $(\Delta^* \psi)|_\Gamma = 0$. Therefore, the boundary condition $(\nabla_\perp \psi)|_\Gamma = 0$ included above in the lists of requirements for maintenance of system energy conservation may be replaced with the requirement $\psi|_\Gamma = 0$.

5.6 Discrete form of MHD equations and conservation properties

In this section, the full set of discretised equations for a two-temperature MHD model is presented. The model has been constructed so as to preserve the global conservation laws inherent to the original continuous system of equations. Referring to the properties of the differential operators, it will be demonstrated how the conservation characteristics associated with the continuous form of the MHD equations (see section 5.5) are replicated by the discrete form. In order to preserve the conservation laws of the system in discrete form, the pairs of terms which constitute full divergences, denoted with square brackets in equations 5.5.25 and 5.5.29, have been discretised in compatible way, *i.e.*, the appropriate corresponding discrete operators are used in these terms, and with particular boundary conditions, the operator properties lead to the cancellation of each pair.

5.6.1 Discretised MHD model

The discretised equations for the axisymmetric MHD model, in a form that ensures conservation of total system energy, are presented in appendix summary B.6. The discrete form of the single fluid energy equation (equation B.6.2) is partitioned into parts pertaining to the ions and electrons, with the inclusion of discrete forms of the species thermal diffusion and heat exchange terms. With the inclusion of artificial density diffusion, the resulting set of discretised equations is:

$$\begin{aligned}
\dot{\underline{n}} &= -\underline{\nabla} \cdot (\underline{n} \circ \underline{\mathbf{v}}) + \underline{\nabla}_{\underline{n}} \cdot (\zeta \circ \underline{\nabla}^e \underline{n}) \\
\dot{\underline{v}_r} &= -\underbrace{\underline{\underline{D}} * \left(\frac{\underline{v}^2}{2}\right) - \underline{v}_z \circ (\underline{\underline{D}} * \underline{v}_r - \underline{\underline{D}} * \underline{v}_z) + \underline{v}_\phi \circ (\underline{\underline{D}} * (\underline{r} \circ \underline{v}_\phi)) \otimes \underline{r}}_{-(\mathbf{v} \cdot \nabla \mathbf{v})_r = (-\nabla(v^2/2) + \mathbf{v} \times (\nabla \times \mathbf{v}))_r} - \underbrace{(\underline{\underline{D}} * \underline{p}) \otimes \underline{\rho}}_{-\frac{1}{\rho}(\nabla p)_r} \\
&\quad - \underbrace{\underline{\Pi}_r \otimes \underline{\rho}}_{-\frac{1}{\rho}(\nabla \cdot \underline{\pi})_r} + \underbrace{(-(\underline{\underline{D}} * \underline{\psi}) \circ (\underline{\Delta}^* \underline{\psi}) - (\underline{f} \circ (\underline{\underline{D}} * \underline{f}))) \otimes (\mu_0 \underline{r}^2 \circ \underline{\rho}) + \underline{f}_{\zeta r} \otimes \underline{\rho}}_{\frac{1}{\rho}(\mathbf{J} \times \mathbf{B})_r} \\
\dot{\underline{v}_\phi} &= -\underline{\mathbf{v}} \cdot (\underline{\nabla} (\underline{r} \circ \underline{v}_\phi)) \otimes \underline{r} - \underbrace{\underline{\Pi}_\phi \otimes \underline{\rho}}_{-\frac{1}{\rho}(\nabla \cdot \underline{\pi})_\phi} + \underbrace{(\underline{\underline{W}}_n * (\underline{\mathbf{B}}_\theta^e \cdot (\underline{\nabla}^e \underline{f}))) \otimes (\mu_0 \underline{r} \circ \underline{\rho}) + \underline{f}_{\zeta \phi} \otimes \underline{\rho}}_{\frac{1}{\rho}(\mathbf{J} \times \mathbf{B})_\phi} \\
\dot{\underline{v}_z} &= -\underbrace{\underline{\underline{D}} * \left(\frac{\underline{v}^2}{2}\right) + \underline{v}_r \circ (\underline{\underline{D}} * \underline{v}_r - \underline{\underline{D}} * \underline{v}_z) + \underline{v}_\phi \circ (\underline{\underline{D}} * (\underline{r} \circ \underline{v}_\phi)) \otimes \underline{r}}_{-(\mathbf{v} \cdot \nabla \mathbf{v})_z = (-\nabla(v^2/2) + \mathbf{v} \times (\nabla \times \mathbf{v}))_z} - \underbrace{(\underline{\underline{D}} * \underline{p}) \otimes \underline{\rho}}_{-\frac{1}{\rho}(\nabla p)_z} \\
&\quad - \underbrace{\underline{\Pi}_z \otimes \underline{\rho}}_{-\frac{1}{\rho}(\nabla \cdot \underline{\pi})_z} + \underbrace{(-(\underline{\underline{D}} * \underline{\psi}) \circ (\underline{\Delta}^* \underline{\psi}) - \underline{f} \circ (\underline{\underline{D}} * \underline{f})) \otimes (\mu_0 \underline{r}^2 \circ \underline{\rho}) + \underline{f}_{\zeta z} \otimes \underline{\rho}}_{\frac{1}{\rho}(\mathbf{J} \times \mathbf{B})_z} \\
\dot{\underline{p}_i} &= -\underline{\mathbf{v}} \cdot (\underline{\nabla} \underline{p}_i) - \gamma \underline{p}_i \circ (\underline{\nabla} \cdot \underline{\mathbf{v}}) + (\gamma - 1) \left[-\underline{\nabla}_{\underline{n}} \cdot \underline{\mathbf{q}}_i^e + \underline{Q}_{ie} + \underbrace{\underline{Q}_\pi}_{-\underline{\pi} : \nabla \mathbf{v}} + \underline{Q}_\zeta \right] \\
\dot{\underline{p}_e} &= -\underline{\mathbf{v}} \cdot (\underline{\nabla} \underline{p}_e) - \gamma \underline{p}_e \circ (\underline{\nabla} \cdot \underline{\mathbf{v}}) + (\gamma - 1) \left[-\underline{\nabla}_{\underline{n}} \cdot \underline{\mathbf{q}}_e^e - \underline{Q}_{ie} \right. \\
&\quad \left. + \underbrace{(\eta/\mu_0) \circ ((\underline{\Delta}^* \underline{\psi}) \otimes \underline{r})^2}_{\eta' J_\phi^2} + \underbrace{\underline{\underline{W}}_n * ((\eta^e/\mu_0) \circ ((\underline{\nabla}^e \underline{f}) \otimes \underline{r}^e)^2)}_{\eta' J_\theta^2} \right] \\
\dot{\underline{\psi}} &= -\underline{\mathbf{v}} \cdot (\underline{\nabla} \underline{\psi}) + \underline{\eta} \circ (\underline{\Delta}^* \underline{\psi}) \\
\dot{\underline{f}} &= \underline{r}^2 \circ \left[-\underline{\nabla} \cdot (\underline{f} \circ \underline{\mathbf{v}} \otimes \underline{r}^2) + \underline{\nabla}_{\underline{n}} \cdot (\underline{\mathbf{B}}_\theta^e \circ \underline{\omega}^e) + \underline{\nabla}_{\underline{n}} \cdot (\underline{\eta}^e \circ (\underline{\nabla}^e \underline{f}) \otimes \underline{r}^{e2}) \right] \tag{5.6.1}
\end{aligned}$$

Here, $\underline{\eta}^e = \langle \underline{\eta} \rangle^e$, and $\underline{\omega}^e = \langle \underline{v}_\phi \otimes \underline{r} \rangle^e$ (equation 5.3.1). $\underline{\underline{W}}_n$ is the volume-averaging operator (equations 5.3.2 and 5.3.3), and $\underline{\mathbf{B}}_\theta^e = (-(\underline{\underline{D}} * \underline{\psi}) \hat{\mathbf{r}} + (\underline{\underline{D}} * \underline{\psi}) \hat{\mathbf{z}}) \otimes \underline{r}^e$. These discretised equations are written in a form which is a direct analogue of their continuous representations with inclusion of several extra terms. Namely, the continuity equation has an artificial density diffusion term, which is required for density smoothing and avoiding negative density regions. The density diffusion coefficient ζ [m^2/s] can be spatially held constant or can be increased where density gradients are high or density values approach zero. The components of force per volume vector $\underline{\mathbf{f}}_\zeta = (\underline{f}_{\zeta r}, \underline{f}_{\zeta \phi}, \underline{f}_{\zeta z})^T$ in the velocity equations and the heating term \underline{Q}_ζ in the ion pressure equation are included to cancel the effect of artificial

density diffusion on the total system momentum and energy.

To close the system of equations, we need to specify the forms of the viscous terms $\underline{\Pi}$ and Q_π , the species heat exchange term Q_{ie} , the resistive diffusion coefficient $\underline{\eta}$, and the heat flux density terms $\underline{\mathbf{q}}_i^e$ and $\underline{\mathbf{q}}_e^e$. As mentioned in appendix B, we have implemented, for simplicity, the unmagnetised version of the viscous stress tensor. The components of $\underline{\Pi}$ represent the discrete forms of the components of $\nabla \cdot \underline{\pi}$, and are defined by equation B.6.1:

$$\begin{aligned}\underline{\Pi}_r &= \left[-2\underline{\underline{D}r_n} * (\underline{\mu}^e \circ \underline{r}^e \circ (\underline{\underline{D}r^e} * \underline{v}_r)) - \underline{\underline{D}z_n} * (\underline{\mu}^e \circ \underline{r}^e \circ (\underline{\underline{D}r^e} * \underline{v}_z + \underline{\underline{D}z^e} * \underline{v}_r)) \right] \oslash \underline{r} \\ &\quad + \frac{2}{3} (\underline{\underline{D}r_n} * (\underline{\mu}^e \circ (\underline{\nabla^e} \cdot \underline{\mathbf{v}}))) + 2 \underline{\mu} \circ \underline{v}_r \oslash \underline{r}^2 \\ \underline{\Pi}_\phi &= - (\underline{\nabla_n} \cdot (\underline{\mu}^e \circ \underline{r}^{e2} \circ (\underline{\nabla^e} \underline{\omega}))) \oslash \underline{r} \\ \underline{\Pi}_z &= \left[-2\underline{\underline{D}z_n} * (\underline{\mu}^e \circ \underline{r}^e \circ (\underline{\underline{D}z^e} * \underline{v}_z)) - \underline{\underline{D}r_n} * (\underline{\mu}^e \circ \underline{r}^e \circ (\underline{\underline{D}r^e} * \underline{v}_z + \underline{\underline{D}z^e} * \underline{v}_r)) \right] \oslash \underline{r} \\ &\quad + \frac{2}{3} (\underline{\underline{D}z_n} * (\underline{\mu}^e \circ (\underline{\nabla^e} \cdot \underline{\mathbf{v}})))\end{aligned}\tag{5.6.2}$$

Here, $\underline{\mu}^e = < \underline{\mu} >^e$ (equation 5.3.1). The discrete form of $-\underline{\pi} : \nabla \mathbf{v}$, which appears in the expression for \dot{p}_i , is given by equation B.6.3:

$$\begin{aligned}Q_\pi &= \underline{\underline{W_n}} * \left[\underline{\mu}^e \circ \left\{ 2 (\underline{\underline{D}r^e} * \underline{v}_r)^2 + 2 (\underline{\underline{D}z^e} * \underline{v}_z)^2 + (\underline{r}^e \circ (\underline{\nabla^e} \underline{\omega}))^2 \right. \right. \\ &\quad \left. \left. + (\underline{\underline{D}r^e} * \underline{v}_z + \underline{\underline{D}z^e} * \underline{v}_r)^2 - \frac{2}{3} (\underline{\nabla^e} \cdot \underline{\mathbf{v}})^2 \right\} \right] + 2 \underline{\mu} \circ (\underline{v}_r \oslash \underline{r})^2\end{aligned}\tag{5.6.3}$$

The representations in equations 5.6.2 and 5.6.3 are consistent with the discrete form of energy conservation, as will be explicitly demonstrated in section 5.6.2.4. $\underline{\mu}^e [\text{kg m}^{-1}\text{s}^{-1}] = \underline{\rho}^e \circ \underline{\nu}^e$ specifies dynamic viscosity at element centroids, where $\underline{\nu}^e [\text{m}^2/\text{s}]$ specifies kinematic viscosity. As discussed in more detail in appendix C.3, a certain minimum level of artificial viscosity, which depends on the time-step, simulation type, and mesh resolution, is required for numerical stability. Simulations that involve CT formation and consequent extreme plasma acceleration and steep gradients in the velocity fields are run with dynamic viscosity set to constant $\mu = \rho_0 \nu_0$, for typical code input $\nu_0 \sim 700 [\text{m}^2/\text{s}]$, where $\rho_0 \sim 6 \times 10^{-6} [\text{kg/m}^3]$ is a typical representative mass density.

The resistive diffusion coefficient may be held spatially constant, or is based on the Spitzer formula

$$\underline{\eta} = \frac{m_e}{1.96 e^2 \mu_0} \oslash (Z_{eff} \underline{n} \circ \underline{\tau_{ei}}) = \left(418 Z_{eff} (\underline{T_e} [\text{eV}])^{-\frac{3}{2}} \right) [\text{m}^2/\text{s}]\tag{5.6.4}$$

where the electron-ion collision time (*cf.* equation A.5.7) is

$$\tau_{ei} = \left(\frac{6\sqrt{2}\pi^{1.5}\epsilon_0^2\sqrt{m_e}}{\Lambda e^4 Z_{eff}^2} \right) \left(\underline{T}_e [\text{J}] \right)^{\frac{3}{2}} \oslash \underline{n} = \left(3.45 \times 10^{10} \frac{\left(\underline{T}_e [\text{eV}] \right)^{\frac{3}{2}} \oslash \underline{n} [\text{m}^{-3}]}{Z_{eff}^2} \right) [\text{s}]$$

The heat exchange term \underline{Q}_{ie} (*cf.* equation A.8.7) gives the rate at which energy is imparted from the electrons to the ions due to collisions between ion and electron fluids:

$$\begin{aligned} \underline{Q}_{ie} &= 3(m_e/m_i) Z_{eff} \underline{n} \circ \left(\underline{T}_e [\text{J}] - \underline{T}_i [\text{J}] \right) \oslash \tau_{ei} \\ &= \left(7.6 \times 10^{-33} Z_{eff}^3 \left(\underline{T}_e [\text{eV}] - \underline{T}_i [\text{eV}] \right) \circ \left(\underline{T}_e [\text{eV}] \right)^{-\frac{3}{2}} \circ \left(\underline{n} [\text{m}^{-3}] \right)^2 / \mu_i \right) [\text{W/m}^3] \end{aligned} \quad (5.6.5)$$

Here, μ_i is the ion mass in units of proton mass.

Gyrorotation of plasma particles along magnetic field lines implies that cross-field thermal diffusion is impeded, while temperature equalizes quickly along the field lines. To include the effect of significantly enhanced thermal diffusion parallel to the magnetic field, we include anisotropy in the model for thermal diffusion. The species heat flux density can be expressed as (equation A.8.6)

$$\begin{aligned} \mathbf{q}_\alpha &= - \left(\kappa_{\parallel\alpha} \nabla_{\parallel} T_\alpha + \kappa_{\perp\alpha} \nabla_{\perp} T_\alpha \right) \\ &= - \left(\kappa_{\parallel\alpha} \nabla_{\parallel} T_\alpha - \kappa_{\perp\alpha} \nabla_{\parallel} T_\alpha + \kappa_{\alpha\perp} \nabla_{\parallel} T_\alpha + \kappa_{\perp\alpha} \nabla_{\perp} T_\alpha \right) \\ &= - \left(\left(\kappa_{\parallel\alpha} - \kappa_{\perp\alpha} \right) \nabla_{\parallel} T_\alpha + \kappa_{\perp\alpha} \nabla_{\perp} T_\alpha \right) \end{aligned}$$

where $\kappa_{\parallel\alpha}$ and $\kappa_{\perp\alpha}$ $[(\text{m}\cdot\text{s})^{-1}]$ are the thermal conductivities for species α , pertaining to thermal diffusion parallel and perpendicular to the magnetic field. With azimuthal symmetry, the toroidal component of $\nabla_{\parallel} T_\alpha$ can be dropped as it will not make a finite contribution to $\nabla \cdot \mathbf{q}_\alpha$, so that the discrete forms of \mathbf{q}_α may be expressed as

$$\underline{\mathbf{q}}_\alpha^e = - \left\{ \left(\kappa_{\parallel\alpha}^e - \kappa_{\perp\alpha}^e \right) \circ \left(\underline{\mathbf{B}}_\theta^e \circ \left(\underline{\mathbf{B}}_\theta^e \cdot \left(\underline{\underline{\nabla}}^e \underline{T}_\alpha \right) \right) \oslash \underline{B}^{e2} \right) + \kappa_{\perp\alpha}^e \circ \left(\underline{\underline{\nabla}}^e \underline{T}_\alpha \right) \right\} \quad (5.6.6)$$

Physically, the thermal conductivities vary with local conditions;

e.g., $\kappa_{\parallel\alpha}(\mathbf{r}, t) = n_\alpha(\mathbf{r}, t) \chi_{\parallel\alpha}(\mathbf{r}, t)$. As discussed in more detail in appendix C.3, simulations of the magnetic compression experiment were usually run with constant conductivities, of the order $\kappa_{\parallel\alpha} = n_0 \chi_{\parallel\alpha}$ and $\kappa_{\perp\alpha} = n_0 \chi_{\perp\alpha}$, where $n_0 \sim 1 \times 10^{21} [\text{m}^{-3}]$ is a typical representative number density, and the thermal diffusion coefficients are held constant, for example $\chi_{\parallel e} \sim 16000$, $\chi_{\parallel i} \sim 5000$, $\chi_{\perp e} \sim 240$ and $\chi_{\perp i} \sim 120 [\text{m}^2/\text{s}]$. The high parallel coefficients represent rapid equilibration of temperature along field lines, while the perpendicular coefficients are chosen to match the experimentally observed resistive decay rate of CT currents. Enhanced

thermal diffusion acts as a proxy for anomalous energy sink mechanisms, including radiative losses.

5.6.2 Conservation properties

Here, we demonstrate that the discretised system of equations 5.6.1 has the same global conservation laws as the original continuous system.

5.6.2.1 Particle count conservation

Integrating the discrete form of the continuity equation over volume, we obtain the rate of change of the total number of particles in the system:

$$\begin{aligned}\dot{N} &= \underline{dV}^T * \underline{\dot{n}} \\ &= \underline{dV}^T * \left\{ -\underline{\nabla} \cdot (\underline{n} \circ \underline{\mathbf{v}}) + \underline{\nabla}_{\underline{n}} \cdot (\underline{\zeta}^e \circ (\underline{\nabla}^e \underline{n})) \right\}\end{aligned}$$

With boundary conditions $\underline{\mathbf{v}}_{\perp}|_{\Gamma} = \mathbf{0}$, or $\underline{\mathbf{v}}|_{\Gamma} = \mathbf{0}$, identity 5.4.38 determines that the first term is zero. The second term is always zero, due to property 5.4.16. Hence, total particle count is conserved. Note that if no boundary conditions are explicitly applied to density, \underline{n} will automatically evolve to satisfy the natural boundary condition $(\underline{\zeta} \nabla_{\perp} \underline{n})|_{\Gamma} = 0$, as a consequence of the properties of the element-to-node divergence operation (section 5.4.2).

5.6.2.2 Toroidal flux conservation

Analogous to equation 5.5.23, the discrete expression for the rate of change of system toroidal flux follows from the discrete expression for \dot{f} in equation 5.6.1

$$\begin{aligned}\dot{\Phi} &= \frac{1}{2\pi} \underline{dV}^T * \left\{ \underline{\dot{f}} \otimes \underline{r}^2 \right\} \\ &= \frac{1}{2\pi} \underline{dV}^T * \left\{ -\underline{\nabla} \cdot (\underline{f} \circ \underline{\mathbf{v}} \otimes \underline{r}^2) + \underline{\nabla}_{\underline{n}} \cdot (\underline{\mathbf{B}}_{\theta}^e \circ \underline{\omega}^e) + \underline{\nabla}_{\underline{n}} \cdot (\underline{\eta}^e \circ (\underline{\nabla}^e \underline{f}) \otimes \underline{r}^{e2}) \right\}\end{aligned}$$

Once again, with boundary conditions $\underline{\mathbf{v}}_{\perp}|_{\Gamma} = \mathbf{0}$, identity 5.4.38 determines that the first term is zero. The second and third terms are zero, due to property 5.4.16. Hence, system toroidal flux is conserved. Note that in this case \underline{f} will automatically evolve to satisfy the natural boundary condition $(\underline{\mathbf{B}}_{\theta\perp} \underline{\omega} + \underline{\eta} (\nabla_{\perp} \underline{f}) / \underline{r}^2)|_{\Gamma} = 0$ if no boundary conditions are explicitly

imposed on \underline{f} . In combination with the boundary conditions $\underline{\mathbf{v}}_\perp|_\Gamma = \mathbf{0}$, this corresponds to having the poloidal component of the electric field perpendicular to the boundary, the condition, in the case of azimuthal symmetry, for a perfectly electrically conducting boundary (see equation 5.5.24).

Simulations that include CT formation and compression are run with the boundary conditions $\underline{v}_\beta|_\Gamma = 0$ applied explicitly to each velocity component, so that the automatically imposed boundary condition for f , corresponding to the physical case of a perfectly electrically conducting boundary, becomes $(\nabla_\perp f)|_\Gamma = 0$.

As described in section 6.4, when part of the computational boundary is modelled as an electrical insulator, special care must be taken to define the explicitly applied boundary condition for f along the insulator boundary, in order to maintain global toroidal flux conservation. In such cases, only the conducting boundary regions are allowed to retain the naturally imposed boundary conditions for f .

5.6.2.3 Angular momentum conservation

The rate of change of system angular momentum is

$$\dot{P}_\phi = \frac{\partial}{\partial t} \left(\int (\rho r v_\phi) dV \right) = m_i \int (r v_\phi \dot{n} + n r \dot{v}_\phi) dV$$

Here, it will be shown that system angular momentum is conserved for the discrete model when the terms corresponding to density diffusion in the discrete expressions for \dot{n} and \dot{v}_ϕ are neglected. In section 5.6.3, it will be shown that angular momentum conservation can be maintained even with the inclusion of these terms. In discrete form, the rate of change of angular momentum is

$$\begin{aligned} \dot{P}_\phi = m_i \underline{dV}^T * & \left\{ - \left(\underline{r} \circ \underline{v}_\phi \right) \circ \left(\underline{\underline{\nabla}} \cdot \left(\underline{n} \circ \underline{\mathbf{v}} \right) \right) \right. \\ & + \left(\underline{n} \circ \underline{r} \right) \circ \left\{ - \underline{\mathbf{v}} \cdot \left(\underline{\underline{\nabla}} \left(\underline{r} \circ \underline{v}_\phi \right) \right) \otimes \underline{r} - \underline{\underline{\Pi}}_\phi \otimes \underline{\rho} \right. \\ & \left. \left. + \underline{\underline{\mathbf{W}}}_n * \left(\underline{\mathbf{B}}_\theta^e \cdot \left(\underline{\underline{\nabla}}^e \underline{f} \right) \right) \otimes \left(\mu_0 \underline{r} \circ \underline{\rho} \right) \right\} \right\} \end{aligned} \quad (5.6.7)$$

The first two terms here can be simplified to

$-m_i \underline{dV}^T * \left\{ \left(\underline{r} \circ \underline{v}_\phi \right) \circ \left(\underline{\underline{\nabla}} \cdot \left(\underline{n} \circ \underline{\mathbf{v}} \right) \right) + \left(\underline{n} \circ \underline{\mathbf{v}} \right) \cdot \left(\underline{\underline{\nabla}} \left(\underline{r} \circ \underline{v}_\phi \right) \right) \right\}$. With boundary conditions $\underline{\mathbf{v}}_\perp|_\Gamma = \mathbf{0}$, this combination vanishes due to identity 5.4.37. With reference to the definition for $\underline{\underline{\Pi}}_\phi$ (equation 5.6.2), if no boundary conditions are explicitly applied to \underline{v}_ϕ , the properties of the element-to-node divergence operation will automatically impose the natural boundary

conditions $(\nabla_{\perp} \omega)|_{\Gamma} = 0$, and the third term in equation 5.6.7 will vanish due to identity 5.4.16. With reference to equation 5.3.6, the fourth term in equation 5.6.7 can be expressed as

$$\begin{aligned}
& \frac{1}{\mu_0} \underline{dV}^{eT} * \left\{ \underline{\mathbf{B}}_{\theta}^e \cdot (\underline{\nabla}^e \underline{f}) \right\} \\
&= \frac{2\pi}{\mu_0} (\underline{s}^e \circ \underline{r}^e)^T * \left\{ \left(-(\underline{Dz}^e * \underline{\psi}) \circ (\underline{Dr}^e * \underline{f}) + (\underline{Dr}^e * \underline{\psi}) \circ (\underline{Dz}^e * \underline{f}) \right) \otimes \underline{r}^e \right\} \\
&= \frac{2\pi}{\mu_0} \underline{s}^{eT} * \left\{ -(\underline{Dz}^e * \underline{\psi}) \circ (\underline{Dr}^e * \underline{f}) + (\underline{Dr}^e * \underline{\psi}) \circ (\underline{Dz}^e * \underline{f}) \right\} \\
&= \frac{2\pi}{\mu_0} \left(-(\underline{Dr}^e * \underline{f})^T * (\underline{\hat{S}} * (\underline{Dz}^e * \underline{\psi})) + (\underline{Dz}^e * \underline{f})^T * (\underline{\hat{S}} * (\underline{Dr}^e * \underline{\psi})) \right) \\
&\frac{2\pi}{\mu_0} \underline{f}^T * \left((-\underline{Dr}^{eT} * \underline{\hat{S}} * \underline{Dz}^e + \underline{Dz}^{eT} * \underline{\hat{S}} * \underline{Dr}^e) * \underline{\psi} \right)
\end{aligned}$$

and vanishes due to identity 5.4.10, when the boundary condition $\psi|_{\Gamma} = 0$ is applied. Thus for angular momentum conservation, no boundary conditions are applied on v_{ϕ} , and $\psi|_{\Gamma}$ must be set to zero.

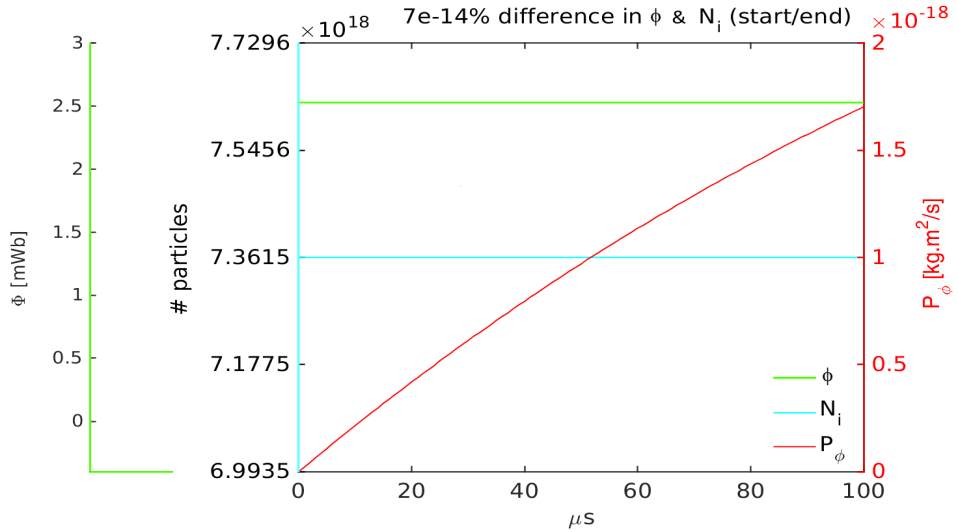


Figure 5.6.1: Illustration of particle, toroidal flux, and angular momentum conservation

Figure 5.6.1 shows how the total number of particles (*i.e.*, $\#$ ions, N_i), toroidal flux, and angular momentum, calculated as the integrals over the computational domain, is conserved to numerical precision for a 100 μ s simulation that started from a Grad-Shafranov equilibrium, with explicitly applied boundary conditions $v_r|_{\Gamma} = v_z|_{\Gamma} = 0$, and $\psi|_{\Gamma} = 0$.

5.6.2.4 Energy conservation

Analogous to the continuous expression 5.5.29, the discrete expression for total system energy is

$$\begin{aligned}
\dot{U}_{Total} &= \dot{U}_K + \dot{U}_{Th} + \dot{U}_M \\
&= \frac{\partial}{\partial t} \left(\underline{dV}^T * \left\{ \frac{\underline{\rho} \circ \underline{\mathbf{v}}^2}{2} + \frac{\underline{p}}{\gamma - 1} + \frac{1}{2\mu_0} \underline{f}^2 \otimes \underline{r}^2 \right\} + \underline{dV}^{eT} * \left\{ \frac{1}{2\mu_0} (\underline{\nabla}^e \underline{\psi})^2 \otimes \underline{r}^{e2} \right\} \right) \\
&= \underline{dV}^T * \left\{ \frac{m_i \dot{\underline{n}} \circ \underline{\mathbf{v}}^2}{2} + \underline{\rho} \circ \underline{\mathbf{v}} \cdot \dot{\underline{\mathbf{v}}} + \frac{\dot{\underline{p}}}{\gamma - 1} + \frac{1}{\mu_0} \underline{f} \circ \dot{\underline{f}} \otimes \underline{r}^2 \right\} \\
&\quad + \underline{dV}^{eT} * \left\{ \frac{1}{\mu_0} (\underline{\nabla}^e \underline{\psi}) \cdot (\underline{\nabla}^e \dot{\underline{\psi}}) \otimes \underline{r}^{e2} \right\} \\
&= - \left[\underline{dV}^T * \left\{ \frac{1}{2} \underline{v}^2 \circ (\underline{\nabla} \cdot (\underline{\rho} \circ \underline{\mathbf{v}})) + \frac{1}{2} (\underline{\rho} \circ \underline{\mathbf{v}}) \cdot (\underline{\nabla} \underline{v}^2) \right\} \right] \\
&\quad - \left[\underline{dV}^T * \left\{ \underline{\mathbf{v}} \cdot (\underline{\nabla} \underline{p}) + \frac{1}{\gamma - 1} (\underline{\mathbf{v}} \cdot (\underline{\nabla} \underline{p}) + \gamma \underline{p} \circ (\underline{\nabla} \cdot \underline{\mathbf{v}})) \right\} \right] \\
&\quad - \left[\frac{1}{\mu_0} \underline{dV}^T * \left\{ (\underline{\mathbf{v}} \cdot (\underline{\nabla} \underline{\psi})) \circ (\underline{\Delta}^* \underline{\psi}) \otimes \underline{r}^2 \right\} + \underline{dV}^{eT} * \left\{ (\underline{\nabla}^e \underline{\psi}) \cdot (\underline{\nabla}^e (\underline{\mathbf{v}} \cdot (\underline{\nabla} \underline{\psi}))) \otimes \underline{r}^{e2} \right\} \right] \\
&\quad - \left[\frac{1}{\mu_0} \underline{dV}^T * \left\{ (\underline{f} \circ \underline{\mathbf{v}} \otimes \underline{r}^2) \cdot (\underline{\nabla} \underline{f}) + \underline{f} \circ (\underline{\nabla} \cdot (\underline{f} \circ \underline{\mathbf{v}} \otimes \underline{r}^2)) \right\} \right] \\
&\quad + \left[\frac{1}{\mu_0} \underline{dV}^T * \left\{ \underline{\omega} \circ (\underline{W}_n * (\underline{\mathbf{B}}_\theta^e \cdot (\underline{\nabla}^e \underline{f}))) + \underline{f} \circ (\underline{\nabla}_n \cdot (\underline{\mathbf{B}}_\theta^e \circ \underline{\omega}^e)) \right\} \right] \\
&\quad + \left[\frac{1}{\mu_0} \underline{dV}^T * \left\{ \underline{\eta} \circ ((\underline{\Delta}^* \underline{\psi}) \otimes \underline{r})^2 \right\} + \underline{dV}^{eT} * \left\{ (\underline{\nabla}^e \underline{\psi}) \cdot (\underline{\nabla}^e (\underline{\eta} \circ (\underline{\Delta}^* \underline{\psi}))) \otimes \underline{r}^{e2} \right\} \right] \\
&\quad + \left[\frac{1}{\mu_0} \underline{dV}^T * \left\{ \underline{W}_n * ((\underline{\eta}^e \circ (\underline{\nabla}^e \underline{f}) \otimes \underline{r}^{e2}) \cdot (\underline{\nabla}^e \underline{f})) + \underline{f} \circ (\underline{\nabla}_n \cdot (\underline{\eta}^e \circ (\underline{\nabla}^e \underline{f}) \otimes \underline{r}^{e2})) \right\} \right] \\
&\quad - \left[\underline{dV}^T * \left\{ \underline{\nabla}_n \cdot (\underline{\mathbf{q}}_i^e + \underline{\mathbf{q}}_e^e) \right\} \right] \\
&\quad - \left[\underline{dV}^T * \left\{ \underline{\mathbf{v}} \cdot \underline{\mathbf{P}} - \underline{Q}_\pi \right\} \right] \tag{5.6.8}
\end{aligned}$$

Note that each set of square brackets has a counterpart in equation 5.5.29, the continuous form of \dot{U}_{Total} . The poloidal magnetic energy is expressed in terms of the element-centered gradient of $\underline{\psi}$, as required for consistency with the definition of the second order $\underline{\Delta}^*$ differential operator. Here, it will be shown how, using the various mimetic properties of the differential operators, that the terms in each set of square brackets cancel when appropriate boundary conditions are applied, leading to total system energy conservation.

The terms in the first set of square brackets here represents the contribution to \dot{U}_K due to advection, and vanish, with boundary conditions $\mathbf{v}_\perp|_\Gamma = \mathbf{0}$, due to equation 5.4.37 (where $\underline{\mathbf{P}} = \underline{\rho} \circ \underline{\mathbf{v}}$ and $\underline{U} = \underline{v}^2$). The terms in the second of square brackets represents the contribution

to \dot{U}_{Th} from compressional heating and, with the same boundary conditions, also vanish due to equation 5.4.37 (with $\underline{\mathbf{P}} = \underline{\mathbf{v}}$ and $\underline{U} = \underline{p}$).

The terms in the third, fourth and fifth sets of square brackets in equation 5.6.8 represent the contribution to \dot{U}_K that arises from the discrete forms of the components of $(\mathbf{J} \times \mathbf{B})$ in combination with the ideal (non-resistive) part of \dot{U}_M . Using identity 5.4.19 to expand the $\underline{\underline{\Delta}}^*$ operator, the terms in the third set of square brackets can be expressed as

$$-\frac{1}{\mu_0} \left[\underline{dV}^T * \left\{ \left(\underline{\mathbf{v}} \cdot (\underline{\underline{\nabla}} \underline{\psi}) \right) \circ (\underline{\nabla}_n \cdot ((\underline{\nabla}^e \underline{\psi}) \otimes \underline{r}^{e2})) \right\} + \underline{dV}^{eT} * \left\{ \left((\underline{\nabla}^e \underline{\psi}) \otimes \underline{r}^{e2} \right) \cdot (\underline{\underline{\nabla}}^e (\underline{\mathbf{v}} \cdot (\underline{\nabla} \underline{\psi}))) \right\} \right]$$

These terms cancel due to identity 5.4.14, where $\underline{\mathbf{P}}^e = ((\underline{\nabla}^e \underline{\psi}) \otimes \underline{r}^{e2})$ and $\underline{U} = \underline{\mathbf{v}} \cdot (\underline{\nabla} \underline{\psi})$.

With boundary condition $\mathbf{v} \perp|_{\Gamma} = \mathbf{0}$, the terms in the fourth set of square brackets cancel due to identity 5.4.37. Using equation 5.3.4, where $\underline{Q} = \underline{\omega} = \underline{v}_\phi \otimes \underline{r}$, the terms in the fifth set of square brackets can be expressed as

$$\frac{1}{\mu_0} \left[\underline{dV}^{eT} * \left\{ (\underline{\mathbf{B}}_\theta^e \circ \underline{\omega}^e) \cdot (\underline{\nabla}^e \underline{f}) \right\} + \underline{dV}^T * \left\{ \underline{f} \circ (\underline{\nabla}_n \cdot (\underline{\mathbf{B}}_\theta^e \circ \underline{\omega}^e)) \right\} \right]$$

This combination cancels due to identity 5.4.14, where $\underline{\mathbf{P}}^e = (\underline{\mathbf{B}}_\theta^e \circ \underline{\omega}^e)$ and $\underline{U} = \underline{f}$.

The terms in the sixth set of square brackets represent the rate of increase of thermal energy due to ohmic heating from toroidal currents (first term), in combination with the rate of decrease of magnetic energy associated with poloidal field, due to resistive decay of the toroidal currents (second term). As is true in the continuous case, these terms are balanced in the discrete case. Using identity 5.4.19, the combination may be expressed as

$$\frac{1}{\mu_0} \left[\underline{dV}^T * \left\{ (\underline{\eta} \circ (\underline{\underline{\Delta}}^* \underline{\psi})) \circ (\underline{\nabla}_n \cdot ((\underline{\nabla}^e \underline{\psi}) \otimes \underline{r}^{e2})) \right\} + \underline{dV}^{eT} * \left\{ ((\underline{\nabla}^e \underline{\psi}) \otimes \underline{r}^{e2}) \cdot (\underline{\underline{\nabla}}^e (\underline{\eta} \circ (\underline{\underline{\Delta}}^* \underline{\psi}))) \right\} \right]$$

and vanishes due to identity 5.4.14, where $\underline{\mathbf{P}}^e = ((\underline{\nabla}^e \underline{\psi}) \otimes \underline{r}^{e2})$ and $\underline{U} = \underline{\eta} \circ (\underline{\underline{\Delta}}^* \underline{\psi})$.

The terms in the seventh set of square brackets in equation 5.6.8 represent the rate of increase of thermal energy due to ohmic heating from poloidal currents (first term), in combination with the rate of decrease of magnetic energy associated with toroidal magnetic field, due to resistive decay of the poloidal currents (second term). Again, these terms cancel, which is physically representative. Referring to equation 5.3.6, the combination vanishes due to identity 5.4.14, where $\underline{\mathbf{P}}^e = (\underline{\eta}^e \circ (\underline{\nabla}^e \underline{f}) \otimes \underline{r}^{e2})$ and $\underline{U} = \underline{f}$.

With reference to the definitions of the discrete forms for the thermal flux $\underline{\nabla}_n \cdot \underline{\mathbf{q}}_\alpha^e$, where $\underline{\mathbf{q}}_\alpha^e$ is defined in equation 5.6.6, it can be seen how the terms in the eighth set of square brackets in equation 5.6.8 vanish due to equation 5.4.16. Boundary conditions that are explicitly applied to the pressure fields break computational-domain-energy conservation, and enable

thermal losses in accordance with the thermal conduction model and the values explicitly applied to n_0 , $(\chi_{\parallel\alpha})|_{\Gamma}$ and $(\chi_{\perp\alpha})|_{\Gamma}$, but thermal energy fluxes through the boundary may be systematically accounted for.

To deal with the viscosity related terms in the final set of square brackets in equation 5.6.8, the substitutions $\underline{\mathbf{P}}_1 = (\underline{v}_r \oslash \underline{r}) \hat{\mathbf{r}}$, $\underline{\mathbf{P}}_2 = (\underline{v}_z \oslash \underline{r}) \hat{\mathbf{z}}$ and $\underline{\mathbf{P}}_3 = (\underline{v}_z \oslash \underline{r}) \hat{\mathbf{r}} + (\underline{v}_r \oslash \underline{r}) \hat{\mathbf{z}}$ are made, and the expansion of terms, using equations 5.6.2, 5.6.3, and 5.3.6 is

$$\begin{aligned}
& \underline{dV}^T * \left\{ -\underline{\mathbf{v}} \cdot \underline{\mathbf{P}} + Q_{\pi} \right\} \\
&= 2 \left[\underline{dV}^T * \left\{ \underline{\mathbf{P}}_1 \cdot \left(\underline{\nabla}_n \left(\underline{\mu}^e \circ \underline{r}^{e2} \circ (\underline{\nabla}^e \cdot \underline{\mathbf{P}}_1) \right) \right) \right\} + \underline{dV}^{eT} * \left\{ \underline{\mu}^e \circ \underline{r}^{e2} \circ (\underline{\nabla}^e \cdot \underline{\mathbf{P}}_1)^2 \right\} \right] \\
&+ 2 \left[\underline{dV}^T * \left\{ \underline{\mathbf{P}}_2 \cdot \left(\underline{\nabla}_n \left(\underline{\mu}^e \circ \underline{r}^{e2} \circ (\underline{\nabla}^e \cdot \underline{\mathbf{P}}_2) \right) \right) \right\} + \underline{dV}^{eT} * \left\{ \underline{\mu}^e \circ \underline{r}^{e2} \circ (\underline{\nabla}^e \cdot \underline{\mathbf{P}}_2)^2 \right\} \right] \\
&+ \left[\underline{dV}^T * \left\{ \underline{\mathbf{P}}_3 \cdot \left(\underline{\nabla}_n \left(\underline{\mu}^e \circ \underline{r}^{e2} \circ (\underline{\nabla}^e \cdot \underline{\mathbf{P}}_3) \right) \right) \right\} + \underline{dV}^{eT} * \left\{ \underline{\mu}^e \circ \underline{r}^{e2} \circ (\underline{\nabla}^e \cdot \underline{\mathbf{P}}_3)^2 \right\} \right] \\
&- \frac{2}{3} \left[\underline{dV}^T * \left\{ \underline{\mathbf{v}} \cdot \left(\underline{\nabla}_n \left(\underline{\mu}^e \circ (\underline{\nabla}^e \cdot \underline{\mathbf{v}}) \right) \right) \right\} + \underline{dV}^{eT} * \left\{ \underline{\mu}^e \circ (\underline{\nabla}^e \cdot \underline{\mathbf{v}})^2 \right\} \right] \\
&+ \left[\underline{dV}^T * \left\{ \underline{\omega} \circ \left(\underline{\nabla}_n \cdot \left(\underline{\mu}^e \circ \underline{r}^{e2} \circ (\underline{\nabla}^e \underline{\omega}) \right) \right) \right\} + \underline{dV}^{eT} * \left\{ \underline{\mu}^e \circ \underline{r}^{e2} \circ (\underline{\nabla}^e \underline{\omega})^2 \right\} \right] \\
&- 2 \left[\underline{dV}^T * \left\{ \underline{\mu} \circ (\underline{v}_r \oslash \underline{r})^2 - \underline{\mu} \circ (\underline{v}_r \oslash \underline{r})^2 \right\} \right]
\end{aligned}$$

The terms in the first to fourth sets of square brackets here vanish due to equation 5.4.13, where, for example, for the first set of square brackets, $\underline{\mathbf{P}} = \underline{\mathbf{P}}_1$ and $\underline{U}^e = \underline{\mu}^e \circ \underline{r}^{e2} \circ (\underline{\nabla}^e \cdot \underline{\mathbf{P}}_1)$. The terms in the fifth set of square brackets vanish due to equation 5.4.14 where $\underline{U} = \underline{\omega}$ and $\underline{\mathbf{P}}^e = \underline{\mu}^e \circ \underline{r}^{e2} \circ (\underline{\nabla}^e \underline{\omega})$, and the terms in the final set obviously cancel. Thus, the volume-integrated rate of increase of thermal energy due to viscous heating is balanced by the volume-integrated rate of decrease of kinetic energy due to viscous dissipation, which is also a property of the physical system (see appendix B.3.1).

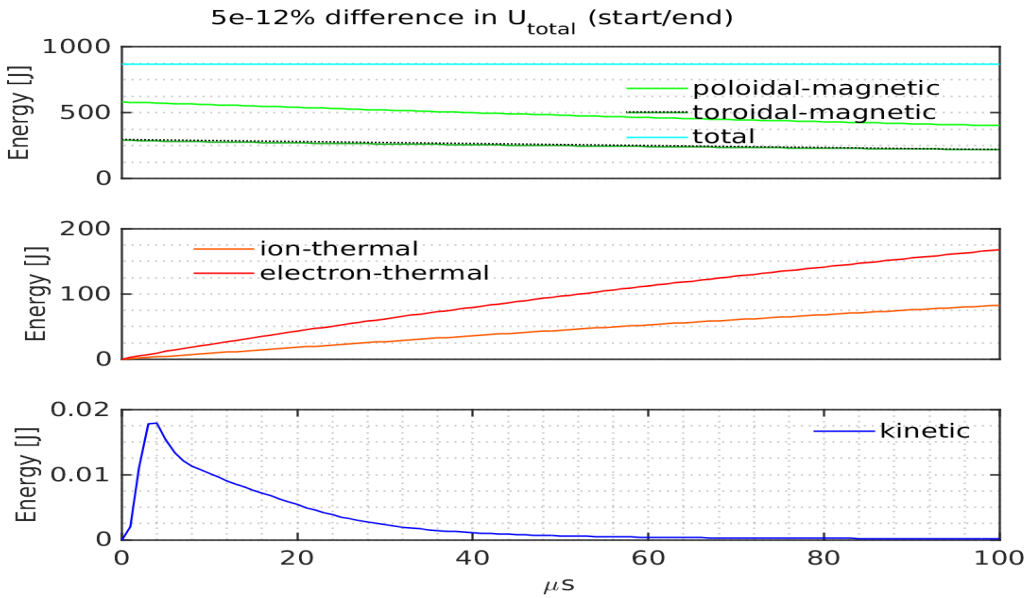


Figure 5.6.2: System energy evolution for an MHD simulation starting with a Grad-Shafranov equilibrium

Figure 5.6.2 shows the partition of energy, and how total energy is conserved approximately to machine precision for a $100\ \mu\text{s}$ simulation with moderate time-step and mesh resolution, using Runge-Kutta second order time-stepping, that started from a Grad-Shafranov equilibrium. It can be seen that the magnetic energy is largely due to poloidal field in this case, and that the decrease in magnetic energy due to resistive decay of plasma currents is approximately canceled (with some offset due to changes in kinetic energy) by the increase thermal energy. The simulation started with cold plasma. Thermal energy is imparted directly to the electron fluid by ohmic heating and is collisionally transferred from the electrons to the ions (term Q_{ie} in equations 5.5.15 and 5.5.16). In summary, as the plasma currents decay resistively, the magnetic energy decreases, while the thermal energy increases by the same amount due to ohmic heating. For simulations starting with a Grad-Shafranov equilibrium, as in this case, the plasma is in equilibrium and kinetic energy is practically negligible. The only explicitly applied boundary conditions are $v_r|_\Gamma = v_z|_\Gamma = 0$, and $\psi|_\Gamma = 0$. In contrast, simulations presented in chapter 7 that include CT formation and magnetic levitation and magnetic compression, are run with explicitly applied boundary conditions for ψ that are determined by experiment. This enables inward electromagnetic energy fueling and outward electromagnetic losses (Poynting flux). In those simulations, boundary conditions are explicitly applied to the pressure fields to enable thermal losses in accordance with the thermal conduction model, and boundary conditions for f are explicitly applied to the parts of the domain boundary that represent insulating regions.

5.6.3 Maintenance of energy and momentum conservation with artificial density diffusion

As mentioned earlier, the components of force per volume vector $\underline{f}_\zeta = (\underline{f}_{\zeta r}, \underline{f}_{\zeta \phi}, \underline{f}_{\zeta z})^T$ in the velocity equations, and the heating term \underline{Q}_ζ in the ion pressure equation (equation 5.6.1) are included to cancel the effect of artificial density diffusion on the total system momentum and energy. There are two models for the correction terms. The first model is straightforward and maintains conservation of energy and angular momentum when density diffusion is included in the mass continuity equation. It is evaluated simply by treating the density diffusion as a particle source and assessing the local (*i.e.*, nodal) correction terms as the local effects of the source on momentum and energy. However this model can lead locally to negative ion pressure if the density gradients are extreme, so it is not suitable for inclusion in simulations of CT formation and compression. The model works satisfactorily for other simulation types, for example the resistive decay of a magnetised plasma described by an equilibrium model. The second model is more complicated - it maintains conservation of volume integrated energy and can not cause negative ion pressure, but angular momentum conservation is not maintained. Both models for the correction terms compensate for additional r and z directed momentum introduced due to density diffusion - for the first model the compensation is local, while for the second model the compensation is in the volume integrated sense. The simulations presented in chapter 7 use the second model.

The correction terms for the first model are derived as follows. For convenience, we use the notation $\underline{\zeta}_n = \underline{\nabla}_n \cdot (\underline{\zeta} \circ \underline{\nabla}^e n)$. Referring to equation 5.6.1, note that $\dot{\underline{n}}|_\zeta = \underline{\zeta}_n$, $\dot{\underline{v}}_\beta|_\zeta = \underline{f}_{\zeta \beta} \oslash \underline{\rho}$, and $\dot{\underline{p}}_i|_\zeta = \underline{Q}_\zeta$ are the parts $\dot{\underline{n}}$, $\dot{\underline{v}}_\beta$, and $\dot{\underline{p}}_i$ respectively that are associated with density diffusion. The local rate of change of the β component (where, here, $\beta = r, z$) of momentum per unit volume due to the local particle source/sink terms arising due to density diffusion is set to zero by design, resulting in

$$\begin{aligned} \left(\frac{\partial}{\partial t} (m_i \underline{n} \circ \underline{v}_\beta) \right)_\zeta &= m_i \left(\dot{\underline{n}} \circ \underline{f}_{\zeta \beta} \oslash \underline{\rho} + \underline{\zeta}_n \circ \underline{v}_\beta \right) = 0 \\ \Rightarrow \underline{f}_{\zeta \beta} &= -m_i \underline{v}_\beta \circ \underline{\zeta}_n \end{aligned}$$

Naturally, for $\beta = \phi$, this expression for $\underline{f}_{\zeta \beta}$ also locally cancels additional angular momentum per unit volume introduced by density diffusion. The rate of change of energy per unit volume

due to local particle source/sink terms associated with density diffusion is also set to zero:

$$\begin{aligned} \left(\frac{\partial}{\partial t} \left(\frac{1}{2} m_i \underline{n} \circ \underline{v}^2 + \frac{1}{\gamma-1} \underline{p}_i \right) \right)_\zeta &= \frac{1}{2} m_i \underline{\zeta_n} \circ \underline{v}^2 + \sum_\beta (m_i \underline{n} \circ \underline{v}_\beta \circ \underline{f}_{\zeta\beta} \otimes \underline{\rho}) + \underline{Q}_\zeta = 0 \\ \Rightarrow \underline{Q}_\zeta &= \frac{1}{2} m_i \underline{v}^2 \circ \underline{\zeta_n} \end{aligned}$$

Hence, the contributions to \dot{U}_K and \dot{U}_{Th} arising from the artificial density diffusion and relevant correction terms cancel by design as:

$$(\dot{U}_K + \dot{U}_{Th})_\zeta = \underline{dV}^T * \left\{ m_i \left(\frac{1}{2} - 1 + \frac{1}{2} \right) \underline{v}^2 \circ \underline{\zeta_n} \right\} = 0$$

However, note that if density gradients are extreme, $\underline{\zeta_n}$ and hence \underline{Q}_ζ will have some very large negative values, so that \underline{p}_i can become negative.

For the second model of correction terms, $\underline{Q}_\zeta = 0$, and a suitable choice of $\underline{f}_{\zeta\beta}$ that ensures maintenance, in a volume integrated sense, of conservation of total energy, is

$$\underline{f}_{\zeta\beta} = \frac{1}{2} m_i \zeta \left[\underline{W_n} * \left((\underline{\nabla^e} \underline{n}) \cdot (\underline{\nabla^e} \underline{v}_\beta) \right) + \underline{\nabla_n} \cdot \left(\underline{v}_\beta^e \circ (\underline{\nabla^e} \underline{n}) \right) - \underline{v}_\beta \circ (\underline{\Delta} \underline{n}) \right] \quad (5.6.9)$$

Note that while this term also cancels modifications to the r and z directed momentum resulting from density diffusion, modification to angular momentum is not compensated for. This method requires that ζ is spatially constant so that, in this case $\underline{\zeta_n} = \zeta \underline{\Delta} \underline{n}$. Expressions for $\underline{f}_{\zeta\beta}$ that also conserve angular momentum can be derived if ζ is made to be spatially dependent, but this additional complication has been omitted for now.

Using expression in equation 5.6.9 for $\underline{f}_{\zeta\beta}$, the total contribution to the volume integral of the β component of momentum per unit volume (where $\beta = r, z$) from terms associated

with density diffusion is

$$\begin{aligned}
\dot{P}_\beta|_\zeta &= \underline{dV}^T * \left\{ \left(\frac{\partial}{\partial t} \left(m_i \underline{n} \circ \underline{v}_\beta \right) \right)_\zeta \right\} \\
&= \underline{dV}^T * \left\{ m_i \underline{\zeta_n} \circ \underline{v}_\beta + \underline{f}_{\zeta\beta} \right\} \\
&= \underline{dV}^T * \left\{ m_i \zeta \left(\underline{\Delta} \underline{n} \right) \circ \underline{v}_\beta + \frac{1}{2} m_i \zeta \left[\underline{\underline{W}_n} * \left(\left(\underline{\nabla^e} \underline{n} \right) \cdot \left(\underline{\nabla^e} \underline{v}_\beta \right) \right) \right. \right. \\
&\quad \left. \left. + \underline{\nabla_n} \cdot \left(\underline{v}_\beta^e \circ \left(\underline{\nabla^e} \underline{n} \right) \right) - \underline{v}_\beta \circ \left(\underline{\Delta} \underline{n} \right) \right] \right\} \\
&= \frac{1}{2} m_i \zeta \underline{dV}^T * \left\{ \underline{\underline{W}_n} * \left(\left(\underline{\nabla^e} \underline{n} \right) \cdot \left(\underline{\nabla^e} \underline{v}_\beta \right) \right) + \underline{v}_\beta \circ \left(\underline{\Delta} \underline{n} \right) \right\} \\
&= \frac{1}{2} m_i \zeta \left[\underline{dV}^{eT} * \left\{ \left(\underline{\nabla^e} \underline{n} \right) \cdot \left(\underline{\nabla^e} \underline{v}_\beta \right) \right\} + \underline{dV}^T * \left\{ \underline{v}_\beta \circ \left(\underline{\nabla_n} \cdot \left(\underline{\nabla^e} \underline{n} \right) \right) \right\} \right] \quad (\text{use eqn. 5.3.6}) \\
\Rightarrow \dot{P}_\beta|_\zeta &= 0 \quad (\text{use eqn. 5.4.14})
\end{aligned}$$

Note that in the last step, identity 5.4.14 has been used, with $\underline{\mathbf{P}}^e = \underline{\nabla^e} \underline{n}$ and $\underline{U} = \underline{v}_\beta$.

The total contribution to energy associated with v_β (where $\beta = r, \phi, z$) from terms associated with density diffusion is

$$\begin{aligned}
\dot{U}_\beta|_\zeta &= \underline{dV}^T * \left\{ \left(\frac{\partial}{\partial t} \left(\frac{1}{2} m_i \underline{n} \circ \underline{v}_\beta^2 \right) \right)_\zeta \right\} \\
&= \underline{dV}^T * \left\{ \frac{1}{2} m_i \underline{\zeta_n} \circ \underline{v}_\beta^2 + \underline{v}_\beta \circ \underline{f}_{\zeta\beta} \right\} \\
&= \underline{dV}^T * \left\{ \frac{1}{2} m_i \zeta \left(\underline{\Delta} \underline{n} \right) \circ \underline{v}_\beta^2 \right. \\
&\quad \left. + \frac{1}{2} m_i \zeta \underline{v}_\beta \circ \left[\underline{\underline{W}_n} * \left(\left(\underline{\nabla^e} \underline{n} \right) \cdot \left(\underline{\nabla^e} \underline{v}_\beta \right) \right) + \underline{\nabla_n} \cdot \left(\underline{v}_\beta^e \circ \left(\underline{\nabla^e} \underline{n} \right) \right) - \underline{v}_\beta \circ \left(\underline{\Delta} \underline{n} \right) \right] \right\} \\
&= \frac{1}{2} m_i \zeta \underline{dV}^T * \left\{ \underline{v}_\beta \circ \left[\underline{\underline{W}_n} * \left(\left(\underline{\nabla^e} \underline{n} \right) \cdot \left(\underline{\nabla^e} \underline{v}_\beta \right) \right) + \underline{\nabla_n} \cdot \left(\underline{v}_\beta^e \circ \left(\underline{\nabla^e} \underline{n} \right) \right) \right] \right\} \\
&= \frac{1}{2} m_i \zeta \left[\underline{dV}^{eT} * \left\{ \underline{v}_\beta^e \circ \left(\left(\underline{\nabla^e} \underline{n} \right) \cdot \left(\underline{\nabla^e} \underline{v}_\beta \right) \right) \right\} \right. \\
&\quad \left. + \underline{dV}^T * \left\{ \underline{v}_\beta \circ \left(\underline{\nabla_n} \cdot \left(\underline{v}_\beta^e \circ \left(\underline{\nabla^e} \underline{n} \right) \right) \right) \right\} \right] \quad (\text{use eqn. 5.3.4}) \\
\Rightarrow \dot{U}_\beta|_\zeta &= 0 \quad (\text{use eqn. 5.4.14})
\end{aligned}$$

In the last step, identity 5.4.14 has been used again, now with $\underline{\mathbf{P}}^e = \underline{v}_\beta^e \circ \left(\underline{\nabla^e} \underline{n} \right)$ and $\underline{U} = \underline{v}_\beta$.

Hence, the modification to total system energy due to density diffusion is canceled with the inclusion of the correction terms using either correction model, thereby ensuring maintenance of global energy conservation. Conservation of angular momentum is maintained using the first model only, but that model is suitable only for simulations that don't involve steep density gradients. Both models compensate for the modifications to radially and axially directed momentum associated with density diffusion.

5.7 Summary

It has been shown how the finite element method has been used to develop first and second order differential matrix operators that mimic some of the properties of their continuous counterparts. Namely, the operators satisfy the discrete forms of the differential product rule and the divergence theorem. Conservation of mass, toroidal flux, angular momentum, and energy for the continuous system of MHD equations has been demonstrated. A discrete counterpart set of equations has been developed, which also satisfy the discrete forms of these conservation laws. A model for anisotropic thermal diffusion has been formulated and implemented to the code. In order to maintain energy conservation, and angular momentum conservation in some scenarios, in the presence of artificial density diffusion, correction terms have been developed and included in the discrete momentum and energy equations.

Chapter 6

Models for CT formation, levitation and magnetic compression, and implementation of simulated diagnostics

In this chapter, the various models developed to simulate CT formation, levitation and magnetic compression, and their implementation to the code, are described. In section 6.1, the boundary conditions used for the different fields that are evolved in time are outlined. Magnetic levitation and compression are modelled through the implementation of boundary conditions for ψ . Appropriate boundary conditions on f lead to toroidal flux conservation, which is a key requirement to successfully reproducing physical properties associated with the experiment. In section 6.2, the method developed to model an insulating region, representing the insulating tube located between the external levitation/compression coils and the CT containment region, is described. The vacuum field solution in the insulating region is coupled to the full MHD solutions in the remainder of the computational domain. In section 6.3, the techniques established to simulate addition of toroidal flux to the domain, representative of either the CT formation process, or, for simulations starting with a Grad-Shafranov equilibrium, the flow of shaft current around the CT containment region, are specified. The strategy developed to maintain toroidal flux conservation when an insulating region is included in the domain is outlined in section 6.4. Section 6.5 consists of an overview of the simulated diagnostics that were implemented to the code. In addition to representations of the experiment's diagnostics, these include methods developed to evaluate, based on various simulated field distributions, the time evolutions of the $q(\psi)$ profile, CT magnetic axis location, volume-averaged β , CT volume and magnetic fluxes, system energy components, and maximum ion and electron temperatures. The chapter concludes with a summary in section

6.1 Boundary conditions

6.1.1 Boundary conditions for density

No boundary condition is explicitly applied to density. As described in section 5.6.2.1, the natural boundary condition

$$(\zeta \nabla_{\perp} n) |_{\Gamma} = 0,$$

is automatically imposed when density diffusion is included in the model. This leads to $(\nabla_{\perp} n) |_{\Gamma} = 0$, if ζ is spatially constant.

6.1.2 Boundary conditions for velocity

For simulations including CT formation and/or magnetic compression, the plasma fluid velocity components are set to zero on the boundary *i.e.*, the no-slip condition for an impermeable boundary:

$$\mathbf{v}|_{\Gamma} = \mathbf{0}$$

Since the plasma viscosity scales with $T^{5/2}$ (Braginskii formulae - equations A.5.14), it might be expected that a *slip* condition would be more suitable because $T \rightarrow 0$ at the boundary, so that there should be negligible viscosity at the wall, and a boundary layer, associated with neutral gas flow at a wall, should be absent. A *slip* condition would involve setting wall-normal velocity components to zero at the wall, and, to ensure unique solutions for the velocity fields, setting the normal derivatives of the wall-tangential components to zero at the wall. On the other hand, physically, friction with cold newly recombined neutral particles at the wall should impede wall-tangential plasma motion at the boundary. In addition, the stuffing field of the Marshall gun is resistively pinned to the vertical electrode walls, and plasma at the walls that is being advected up the gun is partially frozen-into and retarded by the field at the electrode walls, so that the *no – slip* condition, as implemented, may be the more physical choice for the plasma fluid velocity components. For the neutral fluid, the *no slip* condition is also implemented - the suitability of this condition is less ambiguous for

the neutral fluid.

As described in sections 5.6.2.3 and 5.6.3, conservation of system angular momentum requires that no boundary conditions are explicitly applied to v_ϕ , in which case the natural boundary condition $(\nabla_\perp \omega)|_\Gamma = 0$ is automatically imposed. However, angular momentum is conserved only in simulations for which either no density diffusion is included in the model, or the first of the two strategies described in section 5.6.3 for the corrective terms is implemented. These scenarios are suitable for simulations looking at resistive evolution of CTs initially described by a Grad-Shafranov equilibrium, but not for simulations that include CT formation or magnetic compression.

6.1.3 Boundary conditions for temperature

Boundary conditions for pressures follow from equations 5.5.19, with temperatures T_i and T_e set to approximately zero at the boundary:

$$T_i|_\Gamma = T_e|_\Gamma = 0.02 \text{ eV} \approx 20^\circ\text{C}$$

If a neutral fluid is included in the simulation, T_n is also set to 0.02 eV at the boundary. Physically, plasma particles are expected to enter and rattle around in microscopic wall cavities, where they cool and recombine, and are then recycled back into the plasma region as cold neutral particles which can then undergo further ionization.

6.1.4 Boundary conditions for ψ

Toroidal currents in the main, and levitation/compression coils, constitute sources of poloidal flux, which can be included in the model with the application of appropriate boundary conditions for ψ . The locations of the boundary points, that determine the solution domain representing the vacuum region of the magnetic compression machine, along with the insulating areas (air) around the levitation/compression coils, and the ceramic (or quartz) insulating wall surrounding the CT confinement region, were defined in a Matlab code which writes the coordinates of the boundary points to file. For each machine configuration, a LUA script is an output of the code. After assigning the material properties, solution frequencies, and peak coil currents pertaining to either the main stuffing field, the levitation field or the compression field, and running a FEMM [59] model (see example outputs in figures 3.1.1(b) and 3.6.1(b)) for the relevant configuration, the LUA script can be loaded to the various FEMM solutions, and the values of ψ_{main} , ψ_{lev} , and ψ_{comp} at the boundary points listed in

the LUA script are written to file. Field diffusion times in the most electrically conducting parts of the machine are much longer than the timescales associated with the levitation and compression fields. Magnetic boundary conditions are applied at all boundary nodes, but levitation boundary values are significant only on the levitation/compression coil boundaries and on the boundaries of the regions representing the stainless steel above and below the insulating wall, while compression boundary values are significant only on the coil boundaries, and are approximately zero at other boundary regions.

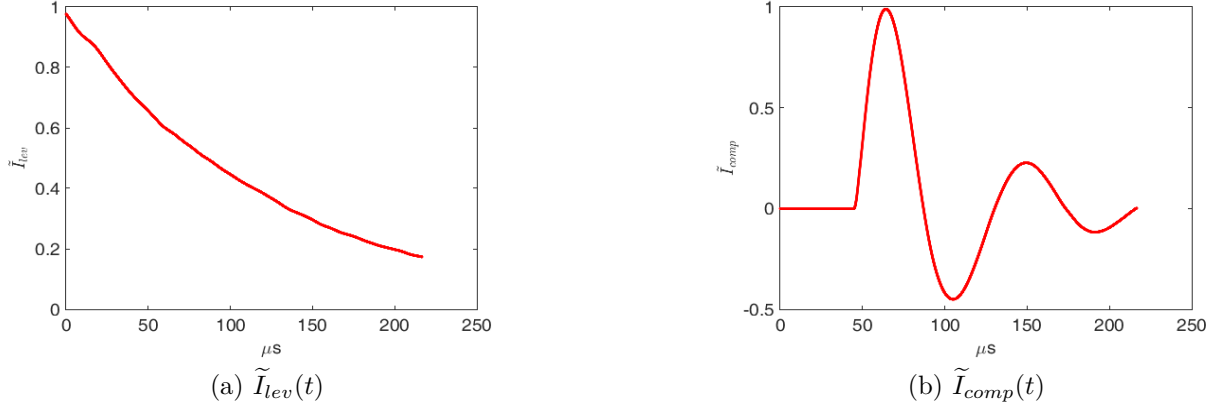


Figure 6.1.1: Normalised levitation and compression current signals

The boundary conditions for $\psi_{main}(\mathbf{r})$ are held constant over time (I_{main} is approximately constant over ~ 3 s before firing the formation banks), while boundary values obtained for $\psi_{lev}(\mathbf{r}, t)$ and $\psi_{comp}(\mathbf{r}, t)$, which pertain to the peak levitation/compression currents, are scaled over time according to the experimentally measured waveforms for $I_{lev}(t)$ and $I_{comp}(t)$:

$$\psi(\mathbf{r}, t)|_{\Gamma} = \psi_{main}(\mathbf{r})|_{\Gamma} + \psi_{lev}(\mathbf{r}, t)|_{\Gamma} + \psi_{comp}(\mathbf{r}, t)|_{\Gamma} \quad (6.1.1)$$

Figure 6.1.1(a) shows $\tilde{I}_{lev}(t)$, the normalised levitation current signal, as measured with Rogowski coils during the experiment; similarly, figure 6.1.1(b) shows $\tilde{I}_{comp}(t)$. For this simulation, $t_{comp} = 45 \mu\text{s}$, and the simulation was run until around $220 \mu\text{s}$. Simulation input parameter R_{cable} was set to 1 for this simulation - *i.e.*, a levitation current profile pertaining to the levitation circuits with the $70 \text{ m}\Omega$ cables in place of the original $2.5 \text{ m}\Omega$ cables was used to control ψ_{lev} (see section 3.6.1). Note that $\tilde{I}_{lev} < 1$ at $t = 0$, because $t_{lev} = -50 \mu\text{s}$ - *i.e.*, in the experiment, the levitation capacitor banks were fired $50 \mu\text{s}$ before the formation banks. With a rise time of $\sim 40 \mu\text{s}$, the levitation current peaks at $t \sim -10 \mu\text{s}$, when $\tilde{I}_{lev} = 1$. The values of $\tilde{I}_{lev}(t)$ and $\tilde{I}_{comp}(t)$ are defined at the times defined by the digitiser sampling time, $dt_{exp} = 50 \text{ ns}$. For evaluation at the simulation times (typically $dt_{sim} \sim 0.01 \text{ ns}$), Matlab function handles are defined in the MHD code, so that $\tilde{I}_{lev}(t)$ and $\tilde{I}_{comp}(t)$ can be obtained at the required simulation times, either by interpolation, or by evaluating a

high-order polynomial fit to the experimental signal.

The MHD code also has the option to set $\psi = 0$ on the entire boundary, representing perfectly conducting walls.

6.1.5 Boundary conditions for f

In general, no boundary conditions are explicitly applied to f on boundary regions representing electrical conductors, and the natural boundary condition

$$(\mathbf{B}_{\theta\perp}\omega + \eta(\nabla_{\perp}f)/r^2)|_{\Gamma} = 0$$

is automatically imposed. In combination with the boundary condition $\mathbf{v}_{\perp}|_{\Gamma} = \mathbf{0}$, this corresponds to having the poloidal component of the electric field perpendicular to the boundary, the condition, in the case of azimuthal symmetry, for a perfectly electrically conducting boundary (see equation 5.5.24). Simulations that include CT formation and compression are run with the boundary conditions $v_{\beta}|_{\Gamma} = 0$ applied explicitly to each velocity component, so that the automatically imposed boundary condition for f , corresponding to the physical case of a perfectly electrically conducting boundary, becomes $(\nabla_{\perp}f)|_{\Gamma} = 0$. Since $f = rB_{\phi} = \mu_0I_{\theta}/2\pi$ (from Ampere's law when $\frac{\partial}{\partial\phi} = 0$), the boundary condition $(\nabla_{\perp}f)|_{\Gamma} = 0$ implies, when $\mathbf{v}|_{\Gamma} = \mathbf{0}$, that any poloidal currents that flow into or out of the wall (*e.g.*, radial intra-electrode formation current or crowbarred shaft current during magnetic compression) flow perpendicular to the wall, *i.e.*, \mathbf{E} has no component parallel to the boundary. Since no currents can flow in insulating regions, f must be spatially constant on the part of the boundary representing the insulating wall surrounding the CT confinement region (see section 6.2 below). As detailed in section 6.4, the value of that constant, consistent with conservation of toroidal flux in the combined domains, is calculated at each timestep and explicitly applied as a boundary condition for f on the interface shared by the plasma and insulating domains.

For formation simulations, sources of toroidal flux include formation current driven through the plasma, and so CT formation can not be modelled by setting boundary conditions. Similarly, during magnetic compression, crowbarred shaft current is diverted through the plasma at the CT edge, as schematically indicated in figure 4.2.1. This implies that for simulations that include magnetic compression, the source of toroidal flux due to crowbarred shaft current can also not be accurately modelled by setting boundary conditions. The methods developed for modelling toroidal flux addition are described in section 6.3.

For simulations starting with a Grad-Shafranov equilibrium, the method of applying boundary conditions on f , in order to model the reduction of toroidal flux over time that

results from decaying crowbarred shaft current, produces reasonable results that compare well with experiment, but only in cases where magnetic compression is not applied. This method can be implemented by setting code input parameter $Shaftbc = 1$. In this case, as outlined in section 6.3.2, experimentally-determined shaft current, taken from a reference non-compression shot, is used to determine boundary conditions for f . The flux conserving natural boundary condition of $(\nabla_{\perp}f)|_{\Gamma} = 0$ is overwritten, so that the system does not conserve toroidal flux. The simulated diagnostic for B_{ϕ} at the chalice magnetic probe locations follows the prescribed crowbarred shaft current profile exactly. When compression is simulated by modifying the boundary conditions for ψ , simulated B_{ϕ} does not deviate from the prescribed profile, so this method is generally not suitable for modelling compression.

The code also has the option to set $f|_{\Gamma} = 0$, representing an electrically insulating boundary through which toroidal flux can leave the system.

6.2 Vacuum field in insulating region

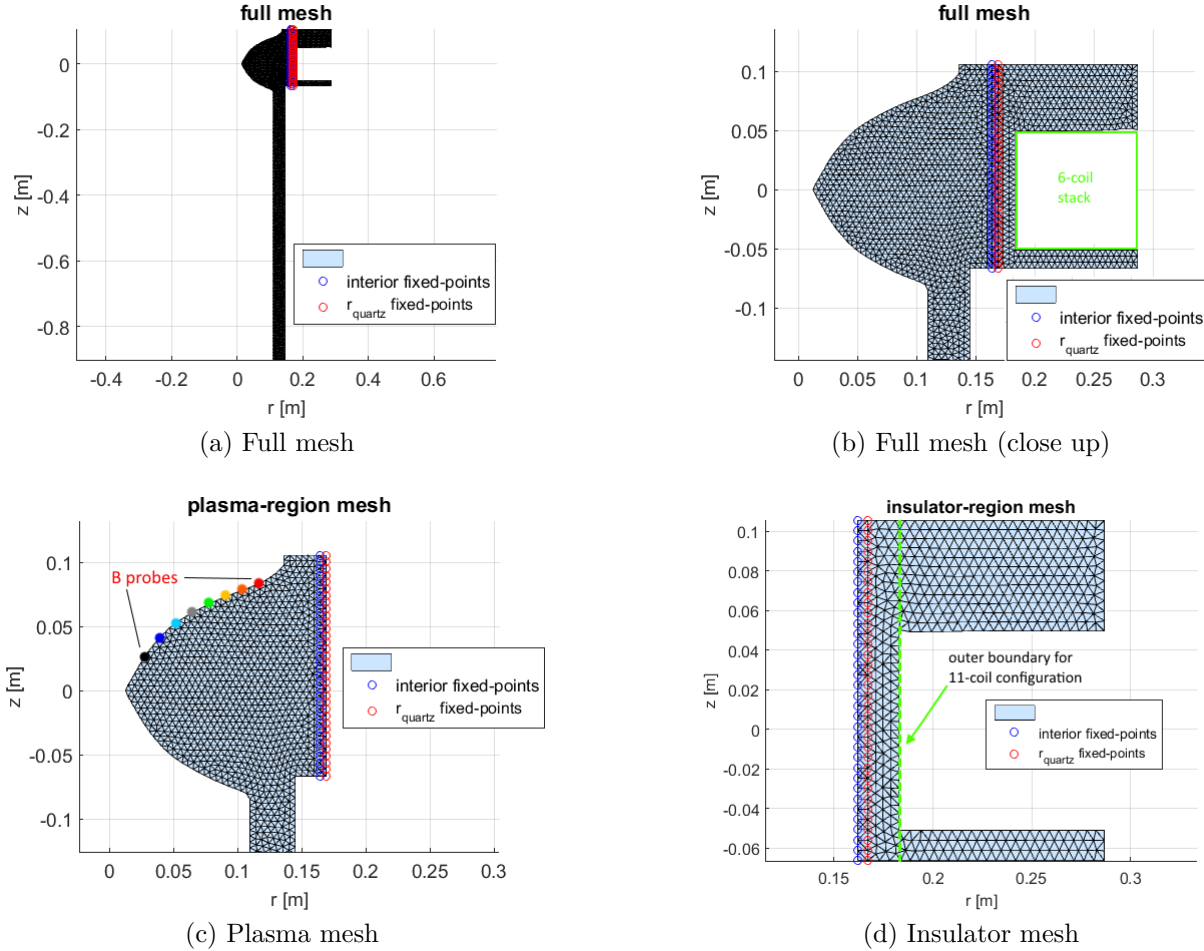


Figure 6.2.1: Computational mesh with insulating region, 6-coil configuration

In order to model the interaction of plasma with the insulating wall during the CT formation process, a vacuum field should be solved for in the insulating area between the inner radius of the insulating outer wall and the levitation/compression coils. The insulating area includes the wall itself as well as the air between the wall and the coil-stack, and the air above and below the coil-stack. If this area is included in the domain in which the plasma fields are solved, then unphysical currents will be allowed to flow in insulating regions. To solve for a vacuum field in the insulating region and couple it to the plasma fields, the computational grid for the combined plasma and insulating domain is split in two, as shown in figure 6.2.1, in which the original six levitation/compression coil configuration is being modelled. The six coil stack representation is specifically indicated in figure 6.2.1(b). For the 11-coil configuration, in which the stack of coils extends along the entire height of the insulating wall, the main

part of the mesh (figure 6.2.1(c)) is unchanged, while the parts of the insulator mesh located above and below the 6-coil stack are deleted, as indicated in figure 6.2.1(d). Note that the magnetic probe locations are indicated in figure 6.2.1(c). To couple between the plasma and vacuum solutions at each timestep, we use the two vertical rows of shared fixed mesh points indicated in the figure to exchange boundary values along the plasma/insulating interface.

No currents can flow in a vacuum, so

$$\Delta^* \psi_v = 0 \quad (6.2.1)$$

where ψ_v represents ψ in a vacuum (or insulator). Defining $\underline{\psi}_v = \underline{\psi}_{v\Gamma} + \underline{\psi}_{vi}$, where $\underline{\psi}_{v\Gamma}$ and $\underline{\psi}_{vi}$ have the values of ψ set to zero at the nodes corresponding to internal / boundary nodes respectively, the discrete form of equation 6.2.1 leads to $\underline{\Delta}^* \underline{\psi}_v = \underline{\Delta}^* \underline{\psi}_{v\Gamma} + \underline{\Delta}_0^* \underline{\psi}_{vi} = \underline{0}$, so that:

$$\underline{\psi}_{vi} = - \left(\underline{\Delta}_0^* \right)^{-1} * \left(\underline{\Delta}^* \underline{\psi}_{v\Gamma} \right) \quad (6.2.2)$$

The discrete operator $\underline{\Delta}_0^*$ is defined in appendix C.4. $\underline{\Delta}^*$ and $\underline{\Delta}_0^*$ operators based on the geometries of the plasma domain and the insulating domain were constructed. With zero initial simulated plasma density everywhere, ψ in the entire domain is initially a vacuum field, so additional $\underline{\Delta}^*$ and $\underline{\Delta}_0^*$ operators based on the geometry of the combined domain are required in order to construct the initial vacuum ψ solution. For formation simulations, initially the time-relevant boundary values for ψ are applied at the boundary points of the combined mesh, according to equation 6.1.1, and the vacuum field in the combined domain is obtained using equation 6.2.2. The sequence of subsequent steps followed at each timestep to couple the solutions is as follows:

1. After evolving ψ_{plasma} at the nodes in the plasma domain according to equations 5.6.1, boundary conditions $\psi(\mathbf{r}, t)|_\Gamma$ are applied separately to the boundary points of the plasma and insulator meshes.
2. The values at the nodes along the left boundary ("interior points" - blue circles in figure 6.2.1(d)) of the insulator mesh are overwritten using the equivalent values from ψ_{plasma} .
3. Equation 6.2.2 is used to calculate ψ_v in the insulating area. Note that the operation $\underline{\Delta}^* \underline{\psi}_{v\Gamma}$ produces inaccurate results at the boundary points, because $\nabla_\perp \psi \neq 0$ at the boundary, while the $\underline{\Delta}^*$ operator requires $\nabla_\perp \psi = 0$ at the boundary for accurate results at the boundary points. Therefore, for plotting purposes only, the ψ_{FEMM} boundary values, and then again the values at the interior points from the plasma-grid solution, are reapplied to the boundary points of the insulator grid.
4. Finally, the values at the outer right boundary of the plasma-grid (red circles in figure

6.2.1(c)) are overwritten using the equivalent values from the insulating region solution ψ_v .

6.3 External sources of toroidal flux

The toroidal flux added to the system as a result of externally-driven poloidal currents must be included in the model. Toroidal flux is added due to formation current and due to crowbarred shaft current. The crowbarred shaft current paths are schematically indicated in figure 4.2.1. Formation current or diverted crowbarred shaft current driven through the plasma can not be modelled by setting boundary conditions. When external sources of toroidal flux are included, the continuous form of the expression for the time-rate of change of f is, referring to equation 5.5.10, modified to:

$$\dot{f}(\mathbf{r}, t) = r^2 \nabla \cdot \left(- \left(\frac{f}{r^2} \mathbf{v} \right) + \omega \mathbf{B} + \frac{\eta}{r^2} \nabla f \right) + \dot{f}_{external}(t) \quad (6.3.1)$$

In practice, the expression for $\dot{f}_{external}$ is added to the existing value for f at the beginning of each timestep, so that the natural toroidal flux conserving boundary condition $((\nabla_{\perp} f)|_{\Gamma} = 0)$ is maintained on electrically conducting boundaries. Conservation of the system's intrinsic toroidal flux implies that the total system flux is equal to the initial flux plus the flux added due to $\dot{f}_{external}(t)$, at each time. For simulations which start with a static plasma and include the formation process, $\dot{f}_{external}(t) = f_{form}(z, t)$, as defined in section 6.3.1. Simulations that start with a Grad-Shafranov equilibrium use $\dot{f}_{external}(t) = F_{shaft}(t)$, where the expression for $F_{shaft}(t)$ is derived in section 6.3.2.

6.3.1 External sources of toroidal flux for formation simulations

Physically, CT formation in a magnetized Marshall gun is achieved as a result of $\mathbf{J}_r \times \mathbf{B}_{\phi}$ forces acting on plasma, where \mathbf{J}_r is the radial formation current density across the plasma between the electrodes, and \mathbf{B}_{ϕ} is the toroidal field due to the axial formation current in the electrodes. Open stuffing magnetic field lines that are resistively pinned to the electrodes, and frozen into the conducting plasma, are advected with the plasma by the $\mathbf{J}_r \times \mathbf{B}_{\phi}$ force, into the containment region, where they reconnect to form CT closed flux surfaces. Simulated formation is initiated with the addition of toroidal flux below the physical locations of the gas puff valves - radial formation current is assumed to occur at the z-coordinate of the valves, where the gas density is initially highest.

Integrating Faraday's law in the poloidal plane over the area defining the formation current path (up the outer gun electrode as far as the region with the initially highest gas concentration at the z-coordinate of the valves, through the plasma across the intra-electrode gap,

and down the inner electrode) we have:

$$\begin{aligned}
\int \nabla \times \mathbf{E}_\theta(\mathbf{r}, t) \cdot d\mathbf{S} &= - \int \dot{\mathbf{B}}_\phi(\mathbf{r}, t) \cdot d\mathbf{S} \\
\Rightarrow \int \mathbf{E}_\theta(\mathbf{r}, t) \cdot d\mathbf{l} &= V(t) = -\dot{\Phi}_{form}(t) \\
\Rightarrow \Phi_{form}(t) &= - \int_0^t V(t') dt' \tag{6.3.2}
\end{aligned}$$

Here,

$$V(t) = V_{gun}(t) + I_{form}(t) R(t) \tag{6.3.3}$$

where $V_{gun}(t)$ is the voltage measured across the formation electrodes and $I_{form}(t) R(t)$ is the resistive voltage drop along the formation current path. $\mathbf{E}_\theta(\mathbf{r}, t)$ is the poloidal electric field that is established through the application of $V_{gun}(t)$, and $\dot{\mathbf{B}}_\phi(\mathbf{r}, t)$ and $\dot{\Phi}_{form}(t)$ are the time-rates of change of the toroidal magnetic field and toroidal flux induced in the area bounded by the path along which formation current driven by $\mathbf{E}_\theta(\mathbf{r}, t)$ flows.

For the simplifying assumption of a fixed formation current path of constant inductance, $-V(t) = \dot{\Phi}_{form}(t) = L\dot{I}_{form}(t)$, where $I_{form}(t)$ is the formation current and L is the inductance of the formation current path. $R(t)$ in equation 6.3.3 is a resistance that depends on the resistivity of the metal along the formation current path, and also on the resistivity of the plasma between the gun electrodes. In addition, it is expected that when plasma, which is advected upwards during the formation process, occupies the gap between the chalice and the inner gun electrode (see figure 2.1.1), that part of the formation current will flow on a path up the outer electrode, through the aluminum bars located outside the insulating wall (see figure 3.1.1(a)), down the chalice, across the plasma in the gap, and down the inner electrode. Physically, $R(t)$ includes the contribution of the resistance of the plasma in the gap shortly after initiation of the formation process. Note that the chalice (*i.e.*, the inner flux conserver indicated in figure 2.2.2) and inner electrode are modelled as a continuous conductor - we do not have sufficient information, for example the voltage measured across the gap, to properly model the effect of the gap. For simplicity, we assume here that R is constant in time. Thus the expression for the voltage measured across the formation electrodes is

$$\begin{aligned}
-V_{gun}(t) &= L\dot{I}_{form}(t) + I_{form}(t)R \\
&= \dot{\Phi}_{form}(t) + \frac{\Phi_{form}(t)}{\tau_{LR}} \tag{6.3.4}
\end{aligned}$$

where $\tau_{LR} = L/R$ is the LR time determining the formation current decay rate. This time constant can be estimated from the e-folding time of the toroidal field that is experimentally

measured at the probes embedded in the chalice. The toroidal field at the probes is a measure of the crow-barred shaft current that flows poloidally around the machine after formation. The value of τ_{LR} varies depending on the formation current path and resistances of the intra-electrode plasma and the plasma in the gap between the chalice and the gun inner electrode, so it can vary from shot to shot depending on plasma conditions. For relatively long-lived magnetically levitated CTs, $\tau_{LR} \sim 90 \mu\text{s}$. Reduced values of τ_{LR} can be chosen as a simulation input when shorter-lived CTs (*e.g.*, for simulations with relatively high thermal diffusion coefficients, or low flux CTs associated with reduced V_{form} and I_{main}) are being modelled. Assuming that $\Phi_{form}(t)$ can be expressed as $\Phi_{form}(t) \sim C(t)e^{-\frac{t}{\tau_{LR}}}$, then with the initial condition $\Phi_{form}(0) = 0 = C(0)$, equation 6.3.4 yields $C(t) = -\int_0^t V_{gun}(t') e^{\frac{t'}{\tau_{LR}}} dt'$, so that

$$\Phi_{form}(t) = -e^{-\frac{t}{\tau_{LR}}} \int_0^t V_{gun}(t') e^{\frac{t'}{\tau_{LR}}} dt' \quad (6.3.5)$$

By definition,

$$\Phi_{form}(t) = \int \frac{f_{form}(z, t)}{r} dr dz \quad (6.3.6)$$

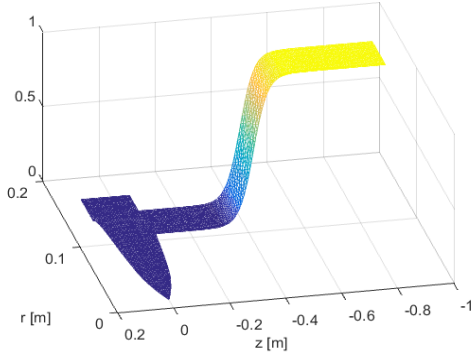
$f_{form}(z, t)$ may be expressed as

$$f_{form}(z, t) = A_{form}(t) g_{form}(z, t) \quad (6.3.7)$$

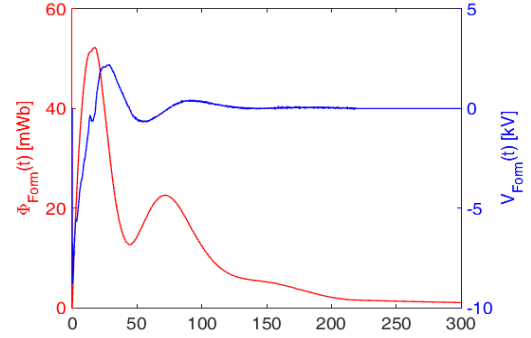
where $A_{form}(t)$ determines the amplitude of $f_{form}(z, t)$, and $g_{form}(z, t)$ is a geometric profile that determines where plasma formation current flows. The smooth logistic profile

$$g_{form}(z, t) = \frac{e^{m z_I(t)}}{e^{m z_I(t)} + e^{m z}} \quad (6.3.8)$$

defines $g_{form}(z, t)$, where $m \sim 40$ defines the profile slope, and $z_I(t)$ is the z coordinate at which the greatest concentration of radial formation current flows between the machine electrodes. For simplicity, we neglect the time dependence in g_{form} by replacing $z_I(t)$ with $z_{gp} = -0.43 \text{ m}$, the z coordinate of the machine's gas puff valves, around which the greatest concentration of radial formation current is expected to flow. Note, $z = 0$ is defined to be at the chalice waist.



(a) $g_{form}(z)$ profile for formation flux input



(b) Measured $V_{gun}(t)$ and calculated $\Phi_{form}(t)$

Figure 6.3.1: Geometric profile for formation flux input and $\Phi_{form}(t)$ scaling

Figure 6.3.1(a) indicates the logistic function formation profile. As outlined in section 6.3.1.1, it is possible to reproduce the measured formation current over the bulk of the simulated formation process, when the time dependence of g_{form} is included. Figure 6.3.1(b) shows the experimentally measured formation voltage signal (right axis) which is numerically integrated over time to evaluate $\Phi_{form}(t)$ (left axis) as defined by equation 6.3.5.

Combining equations 6.3.6 and 6.3.7, we have:

$$\Phi_{form}(t) = A_{form}(t) \int \frac{g_{form}(z)}{r} dr dz \quad (6.3.9)$$

Together with equation 6.3.5, this gives:

$$A_{form}(t) = \frac{-e^{-\frac{t}{\tau_{LR}}} \int_0^t V_{gun}(t') e^{\frac{t'}{\tau_{LR}}} dt'}{\int \frac{g_{form}(z)}{r} dr dz} \quad (6.3.10)$$

Combining equations 6.3.7 and 6.3.10 yields the expression for $f_{form}(z, t)$, which is used in equation 6.3.1 to simulate the formation process:

$$f_{form}(z, t) = \Phi_{form}(t) \kappa_F(z) \quad (6.3.11)$$

where

$$\Phi_{form}(t) = -e^{-\frac{t}{\tau_{LR}}} \int_0^t V_{gun}(t') e^{\frac{t'}{\tau_{LR}}} dt' \quad (6.3.12)$$

and

$$\kappa_F(z) = \frac{g_{form}(z)}{\int \frac{g_{form}(z')}{r} dr dz'} \quad (6.3.13)$$

As outlined in section 6.1.4, the values of experimental measurements are defined at the times

defined by the digitiser sampling time, $dt_{exp} = 50$ ns. Matlab function handles in the MHD code enable assessment of $f_{form}(t)$ at the required simulation times ($dt_{sim} \sim 0.01$ ns), either by interpolation, or by evaluation of a high-order polynomial fit to the experimental signal for $V_{gun}(t)$.

6.3.1.1 Time-dependent formation profile

As indicated in figure 2.1.1, formation current and voltage measurements were recorded. $V_{gun}(t)$ across the electrodes was measured using a voltage divider setup, and $I_{form}(t)$ was measured using a Rogowski coil wrapped around the formation insulator at the bottom of the machine. Prior to firing the formation capacitors, gas is puffed into the vacuum vessel through the eight gas valves located at $z = -0.43$ m. Gas (usually helium) is generally puffed from a gas bottle at ~ 30 psi - the gas valves, which have an opening time of ~ 1 ms, are generally opened ~ 400 μ s before firing the formation banks. The gas can diffuse away from the gas valve locations, but the highest density during the puff is always located around the gas valves. We don't know the axial coordinate ($z_I(t)$) at which radial formation current, $I_{Form-r}(t)$ flows across the gun electrodes and through the plasma, but it is expected to be concentrated where the gas cloud is densest. However the formation current path through the plasma is also determined by energy considerations - the system adjusts so as to have the lowest possible energy, where the inductive contribution to the magnetic energy is proportional to the inductance of the formation current path ($U = \frac{1}{2}LI^2$). To accurately simulate the formation process, it would be convenient to be able to calculate $z_I(t)$. As shown in this section, it is possible to do that using a combination of the $V_{gun}(t)$ and $I_{form}(t)$ measurements, and some simulated parameters, at some, but not all, times during the formation process. Integrating over the region enclosing axially-directed formation current flowing down the inner electrode, in a plane of constant z , at the z coordinate of the Rogowski coil around the lower formation insulator (see figure 6.3.2(a)), and using Ampere's law with toroidal symmetry, we have $\int \nabla \times \mathbf{B}_\phi(r, t) \cdot d\mathbf{S} = \mu_0 \int \mathbf{J}_\theta(r, t) \cdot d\mathbf{S} \Rightarrow rB_\phi = F_{Rog} = \frac{4\pi \times 10^{-7}}{2\pi} I_{form}$ [A], so that:

$$F_{Rog} = 0.2 I_{form} \text{ [MA]} \quad (6.3.14)$$

Here, the formation current is in mega-amps, and F_{Rog} is the total value of rB_ϕ at a fixed location (r_{Rog} , z_{Rog}) just inboard of the Rogowski coil (physically, the Rogowski coil is located just outboard of the simulation domain). We can define:

$$F_{Rog} = 0.2 I_{form} \text{ [MA]} = F_{Form-Rog} + f_{plasma-Rog} \quad (6.3.15)$$

$F_{Form-Rog}$ is the part of F_{Rog} that is present due to the voltage applied between the electrodes, and $f_{plasma-Rog}$ is the part of F_{Rog} that is present due to (poloidal) plasma currents. Since $F_{Form-Rog}$ is the value of $f_{form}(z, t)$ (as defined in equation 6.3.11) at (r_{Rog}, z_{Rog}) , we have:

$$f_{form}(z_{Rog}, t) = \Phi_{form}(t) \kappa_F(z_{Rog}, t) = 0.2 I_{form}[\text{MA}] - f_{plasma-Rog} \quad (6.3.16)$$

Here,

$$\kappa_F(z_{Rog}, t) = \frac{g_{form}(z_{Rog}, t)}{\int \frac{g_{form}(z', t)}{r} dr dz'}$$

and referring to equation 6.3.8,

$$g_{form}(z_{Rog}, t) = \frac{e^{m z_I(t)}}{e^{m z_I(t)} + e^{m z_{Rog}}}$$

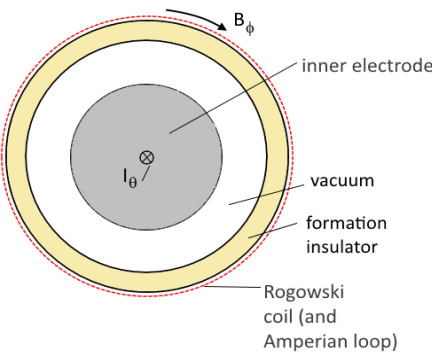
Choosing $z_I(t) < -0.1$ m (the upper coordinate of the straight section of the Marshall gun barrel is at $z \sim -0.085$ m), $\int \frac{g_{Form}(z', t)}{r} dr dz' = h_F \ln(r_{out}/r_{in})$, where r_{in} and r_{out} are the inner and outer radii of the gun electrodes, and $h_F = -z_{min} + z_I = 0.9 + z_I$ is the height of the simulated formation current loop. Here, $z_{min} = -0.9$ m is the z coordinate of the bottom of the barrel of the magnetized Marshall gun. Combining these expressions, we can write:

$$\Phi_{form}(t) g_{form}(z_{Rog}, t) = (0.2 I_{form}(t)[\text{MA}] - f_{plasma-Rog}(t))(0.9 + z_I(t)) \ln(r_{out}/r_{in}) \quad (6.3.17)$$

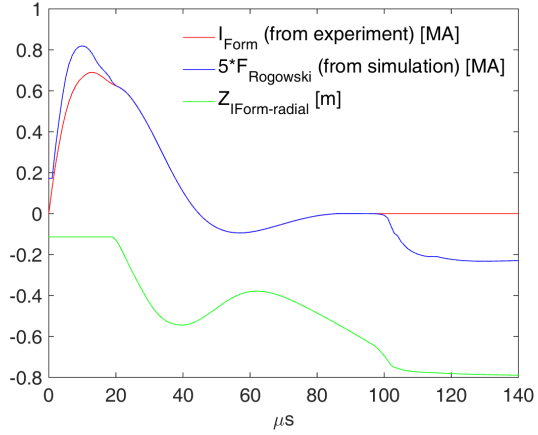
Noting $z_{Rog} \sim -0.8$ m, so that $g_{Form}(z_{Rog}, t) = 1$ (see figure 6.3.1(a)), we arrive at the expression:

$$z_I(t) = \frac{-e^{-\frac{t}{\tau_{LR}}} \int_0^t V_{gun}(t') e^{\frac{t'}{\tau_{LR}}} dt'}{(0.2 I_{form}(t)[\text{MA}] - f_{plasma-Rog}(t)) \ln(r_{out}/r_{in})} - 0.9 \quad (6.3.18)$$

By recording $f_{plasma-Rog}(t)$ (the part of rB_ϕ at (r_{Rog}, z_{Rog}) that is present due to (poloidal) plasma currents) after each timestep (or half/quarter timestep if using Runge-Kutta two/four timestepping), we can use equation 6.3.18 to find the value of $z_I(t)$. In practice, it's necessary to limit $z_I(t)$ to lie between some upper and lower z coordinates. If $z_I(t)$ is too high up the gun, the level of poloidal stuffing flux due to the main coil that will be advected upwards with the accelerating plasma during the formation process will be minimised, resulting in a low-flux CT. On the other hand, $z_I(t)$ can't be too low because the gun has a finite length. To test the effect of varying $z_I(t)$, we imposed upper/lower limits on $z_I(t)$ of -0.11 m and -0.8 m. At each timestep, updated values for $\kappa_F(z_I(t))$ are included in the expression for $f_{external}(t) = f_{form}(t)$ (from equation 6.3.11) in the code's main time loop, with any calculated values of $z_I(t)$ that lie outside the imposed limits being replaced with the nearest limit. By recording $F_{Rog}(t)$ (the total value of rB_ϕ at (r_{Rog}, z_{Rog})), after each timestep, we can use equation 6.3.14 to find the simulated formation current as $I_{form} [\text{MA}] = 5F_{Rog}$.



(a) Geometry definitions



(b) Measured vs. simulated $I_{form}(t)$ (time-dependent z_I , sim. 2225)

Figure 6.3.2: Geometry definitions and measured vs. simulated $I_{form}(t)$

Figure 6.3.2(b) shows a comparison of simulated and measured $I_{form}(t)$, for a case with $z_I(t)$ limited to $-0.11 \text{ m} > z_I(t) > -0.8 \text{ m}$. For the first $20 \mu\text{s}$ of simulation time, $z_I(t)$ was limited to the upper bound $\max(z_I) = -0.11 \text{ m}$. The measured and simulated $I_{form}(t)$ match at times when $z_I(t)$ was free to vary, between $20 \mu\text{s}$ and $\sim 100 \mu\text{s}$. This simulation includes the approximation for the resistive contribution to $\Phi_{form}(t)$ (equation 6.3.12), with $\tau_{RC} = 90 \mu\text{s}$. When the resistive contribution is neglected (*i.e.*, $\Phi_{form}(t) \rightarrow -\int_0^t V_{gun}(t') dt'$), the experimental $I_{form}(t)$ is matched only until $\sim 50 \mu\text{s}$. The high values of $z_I(t)$ over the first $20 \mu\text{s}$, when a large proportion of the total formation current is driven, leads to formation of a CT with lower poloidal flux ($\sim 6 \text{ mWb}$ *cf.* $\sim 10 \text{ mWb}$ for simulations where z_I is fixed at $z_{gp} = -0.43 \text{ m}$), and consequentially low simulated B_θ (maximum $\sim 1.2 \text{ T}$ at bubble-in, recorded at the location of the magnetic probe embedded in the chalice at $r = 26 \text{ mm}$, *cf.* $\sim 2 \text{ T}$ for cases with fixed z_I).

If more information, including a voltage measurement across the gap between the chalice and the inner gun electrode, was available to determine the distribution of formation currents within the machine, an optimised expression for $\Phi_{form}(t)$ may lead to a better match between simulated and measured $I_{form}(t)$. In principle, it should be possible to get a match at all simulated times with a complete model of the formation process, and if physically correct plasma parameters were implemented. For example, classical (Spitzer) resistivity scales with $T_e^{-1.5}$, and T_e is in turn a function of T_i , ν , n , $\chi_{\parallel i}$, $\chi_{\parallel e}$, $\chi_{\perp i}$, $\chi_{\perp e}$. To match experimental I_{form} at all times, we would likely need to include an extended model for transport processes (neoclassical, anomalous resistivity etc). Energy losses due to atomic processes such as impurity line radiation, charge exchange, impact ionization and recombination should also be included. Ultimately, the simulation is 2D and neglects inherently 3D dissipation associated with turbulent transport, this factor is likely another major barrier against seeing perfect

matches between measured and simulated quantities, including the measured and simulated formation current.

6.3.2 External sources of toroidal flux for simulations starting with a Grad-Shafranov equilibrium

For the case where the plasma dynamics are evolved starting from an initial Grad-Shafranov equilibrium, we include experimentally measured crowbarred shaft current, taken from a reference non-compression shot, as an external source for toroidal flux. The decrease in system toroidal flux due to shaft current reduction can be modelled, while conserving the system's intrinsic toroidal flux. Along with the explicitly applied boundary conditions $\mathbf{v}|_{\Gamma} = \mathbf{0}$, the toroidal flux conserving boundary condition $(\nabla_{\perp} f)|_{\Gamma} = 0$ is automatically imposed, and the total system flux at each time is equal to the initial flux plus the flux added due to the shaft current source.

In the experiment, there are at least two crowbarred shaft current paths, as schematically indicated in figure 4.2.1. The magnitude of the crowbarred current in the upper path around the CT confinement region can be calculated using Ampere's law and the toroidal field measured at the magnetic probes embedded in the chalice. There were also a total of twelve probes on the gun shaft, at four toroidal locations, with z coordinates -42 cm, -32 cm and -22 cm (where $z = 0$ is the coordinate of the chalice waist), but those probes were not working reliably at any time, and so the crowbarred current on the lower path can't be determined. In any case, for simulations with an initial Grad-Shafranov equilibrium, the computational mesh used is a shorter one that doesn't include the gun region, so that the lower crowbarred current amplitude is not required.

The measured values of $B_{\phi}(t)$ at the chalice probes, taken from a reference non-compression shot, are averaged over toroidal angle to find $F_{\text{shaft}}(t)$. Ampere's law can be integrated over an Amperian circular loop with $r = r_{\text{probe}}$ in the plane at constant $z = z_{\text{probe}}$, where (for the original chalice configuration) r_{probe} is any of the eight chalice probe radii listed in table 2.2.1, and z_{probe} is the corresponding z coordinate of the relevant probe pair:

$$\begin{aligned} \int \nabla \times \mathbf{B}_{\phi} \cdot d\mathbf{S} &= \mu_0 \int \mathbf{J}_{\theta} \cdot d\mathbf{S} \\ \Rightarrow 2\pi r B_{\phi}(r, t) &= \mu_0 I_{\text{shaft}} \end{aligned} \tag{6.3.19}$$

Note that $B_{\phi}(r, t)$ scales with $\frac{1}{r}$, so that I_{shaft} and F_{shaft} don't have dependence on r :

$$\begin{aligned}
F_{shaft}(t) &= rB_\phi(r, t) = \frac{\mu_0 I_{shaft}(t)[\text{A}]}{2\pi} \\
\Rightarrow F_{shaft}(t) &= 0.2 I_{shaft}(t)[\text{MA}]
\end{aligned} \tag{6.3.20}$$

For equilibrium-evolved simulations, $f_{external}(t) = F_{shaft}(t)$ is generally included as an external source in equation 6.3.1, which describes the evaluation of f in the code's main time loop. As outlined in section 6.1.5, when code input parameter $Shaftbc = 1$, $F_{shaft}(t)$ is used to determine boundary conditions for f , and $f_{external}(t)$ is set to zero. However by default, due to the unsuitability of the boundary condition method for modelling magnetic compression, $Shaftbc = 0$ and no boundary conditions on f are applied except on the interface between the plasma and insulating regions.

As shown in figures 3.6.2(c) and (d), the experimentally measured crowbarred shaft current typically has a peak of around 300 kA and decays to zero at a rate slower than the decay rate of the plasma current, as indicated by the poloidal field decay rate.

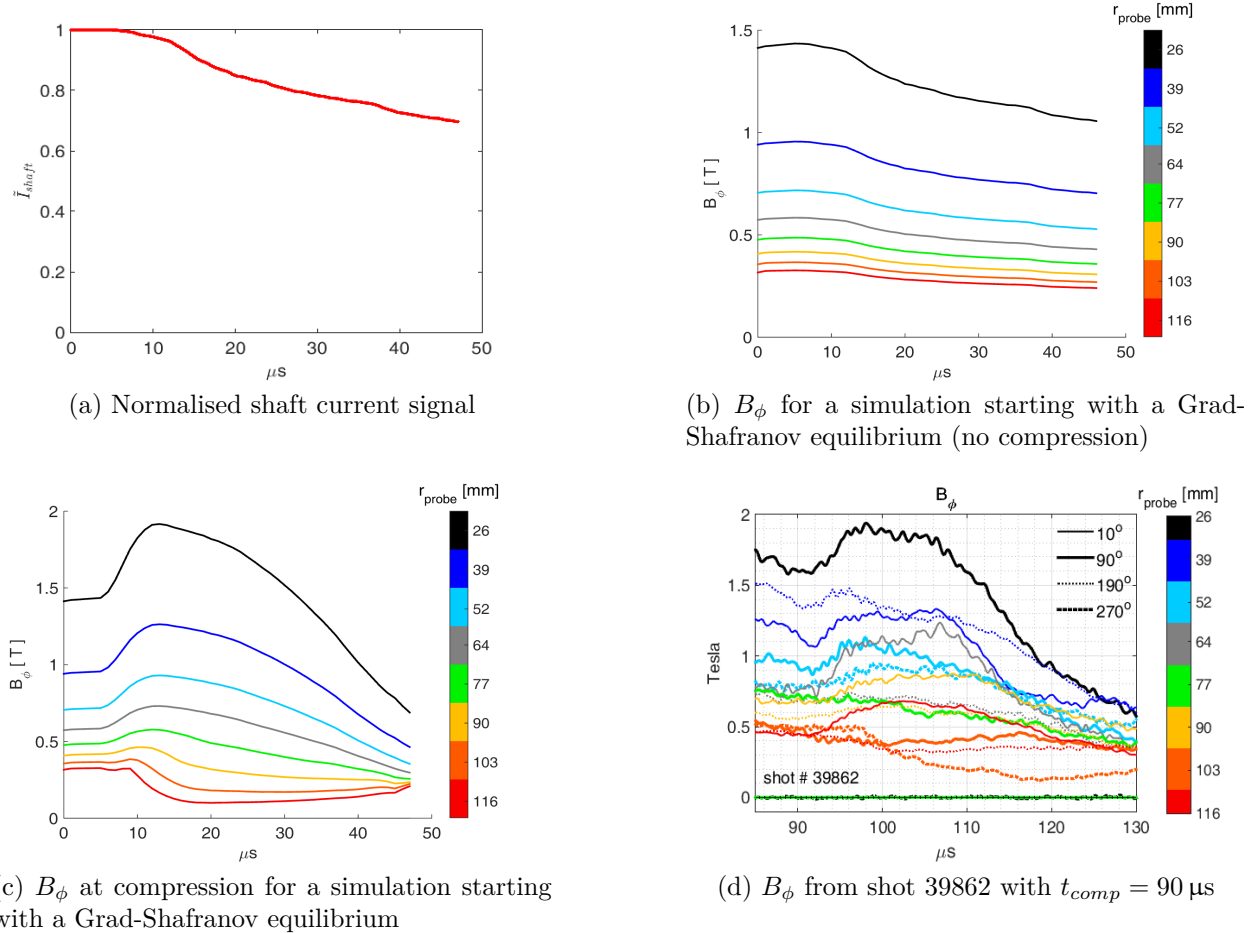


Figure 6.3.3: Comparison of measured and simulated B_ϕ (Grad-Shafranov equilibrium)

By default, simulations starting with a Grad-Shafranov equilibrium use input profiles for $\tilde{I}_{shaft}(t)$ and $\tilde{I}_{lev}(t)$ that have their starting values set to the recorded values at $t = t_{comp}$, where t_{comp} is the code input parameter determining the time of magnetic compression initiation. Figure 6.3.3(a) shows $\tilde{I}_{shaft}(t)$, the crowbarred shaft current, calculated using equation 6.3.19, and normalised with its value at $t = t_{comp}$. This profile, with values at simulation-time interpolated from the digitised B_ϕ signals, which have sampling interval $dt_{exp} = 50$ ns, is used along with the value of I_{shaft} at $t = t_{comp}$, to find $f_{external}(t) = F_{shaft}(t)$ at each timestep. Note that the current is held constant at its maximum value over the first 5 μ s (this simulation example has code input parameter $t_{rise} = 5$ μ s). For equilibrium-evolved simulations, the signal that determines the scaling of the compression ψ boundary conditions (see section 6.1.4) is also held constant (at zero) over the first 5 μ s, and the levitation-relevant signal is ramped up to its starting value over the first 5 μ s. The Grad-Shafranov equilibrium is calculated with the boundary condition $\psi|_\Gamma = 0$ (as described in appendix C.4), and it is required to slowly ramp up the boundary conditions for ψ_{lev} to the starting value, corresponding to ψ_{lev} at $t = t_{comp}$, in order to avoid sharp gradients in pressure that can lead to numerical instability.

For simulations with $Shaftbc = 0$, the simulated diagnostic for B_ϕ at the chalice magnetic probe locations *approximately* follows the experimentally-determined shaft current and toroidal field profile, except at compression. Figure 6.3.3(b) shows B_ϕ at the chalice probe locations from a simulation starting with a Grad-Shafranov equilibrium, without compression and with $Shaftbc = 0$. It can be seen how, for example, individual B_ϕ traces are not exactly constant over the first five microseconds, while the shaft current signal is, as discussed, held constant over that period. Consistent with the naturally imposed boundary condition $(\nabla_\perp f)|_\Gamma = 0$ (when boundary conditions $\mathbf{v}|_\Gamma = \mathbf{0}$ are applied explicitly), this is due to wall-perpendicular currents that act to conserve system toroidal flux. If $Shaftbc$ is set to one, the B_ϕ traces precisely follow the prescribed profile. For compression simulations, with $Shaftbc = 0$, simulated B_ϕ qualitatively follows the experimental measurement signals at compression as shaft current is diverted through the plasma at the CT edge (see section 4.2). Figure 6.3.3(c) shows B_ϕ at the chalice probe locations from a simulation starting with a Grad-Shafranov equilibrium, with magnetic compression. Compression starts at $t_{rise} = 5$ μ s. Figure 6.3.3(d) shows measured B_ϕ for representative shot 39862, which had $t_{comp} = 90$ μ s (note that the B_ϕ probes at $(r, \phi) = (26$ mm, $270^\circ)$ and $(r, \phi) = (77$ mm, $270^\circ)$ were not functioning for this shot). The observed toroidal asymmetry is associated with the compressional instability discussed in section 4.2, and can't be captured in a 2D simulation. Qualitatively, toroidal field increases more at compression at the inner probes, and as also reproduced in the simulation, toroidal field decreases at the outer probes as shaft current is diverted to a path inside the locations of the outer probes.

6.4 Toroidal flux conservation with insulating region

6.4.1 Formation simulations

Integrating toroidal field over the area of the total domain (combined plasma and insulating wall regions) in the poloidal plane, we have:

$$\Phi_{tot}(t) = \underbrace{\int_{\Omega_P} \frac{f_P(\mathbf{r}, t)}{r} dr dz + \int_{\Omega_I} \frac{f_I(t)}{r} dr dz}_{\Phi_{PI}(t)} + \underbrace{\int_{\Omega_P + \Omega_I} \frac{f_{form}(z, t)}{r} dr dz}_{\Phi_{form}(t)} \quad (6.4.1)$$

The subscripts P and I refer to plasma and insulating wall regions. Note that the insulating wall area includes the insulating wall only, and not the insulating (air) regions above and below the coil stack as depicted in figure 6.2.1. Poloidal currents in the aluminum bars located outboard of the insulating wall (depicted in figure 3.1.1(a)) add toroidal flux to the system only in the insulating wall and plasma regions. Since no currents can flow in insulators, f must be spatially constant in the insulating wall inside aluminum bars. The flux-conserving natural boundary condition that is imposed on f_P (which is evolved according to equation 6.3.1) must be overwritten on the interface between the insulating wall and the plasma domain. The second term in equation 6.4.1 can be re-expressed as $\int_{\Omega_I} \frac{f_I(t)}{r} dr dz = f_I(t) h_I \ln(r_{out}/r_{in})$, where h_I is the height of the rectangular cross-section of the insulating wall, and r_{out} and r_{in} are the outer and inner radii of the wall. Initial system toroidal flux is zero, and $\Phi_{PI}(t)$ is to be conserved by design, so the system's only source of toroidal flux is $\Phi_{form}(z, t)$:

$$\begin{aligned} \Phi_{tot}(t) &= \Phi_{form}(t) \Rightarrow \Phi_{PI}(t) = 0 \\ &\Rightarrow \int_{\Omega_P} \frac{f_P(\mathbf{r}, t)}{r} dr dz + \int_{\Omega_I} \frac{f_I(t)}{r} dr dz = 0 \\ &\Rightarrow \sum_{i=1}^{N_n} \left(\frac{f_{P_i}(t) s_i}{3r_i} \right) + f_I(t) (h_I \ln(r_{out}/r_{in})) = 0 \end{aligned} \quad (6.4.2)$$

Here, N_n is the number of nodes in the non-insulating part of the domain (*i.e.*, the plasma domain) in which the MHD equations are solved, $s_i/3$ is the area, and r_i is the radial coordinate, associated with node i . The summation is over all nodes in the plasma domain, which includes the fixed-point nodes along the inner radius of the insulating wall, at which we want to evaluate f_I . Equation 6.4.2 can be solved for the constant f_I if f_{P_i} is temporarily set to zero at the fixed-point nodes along the inner wall of the insulator (see figure 6.2.1), so that

$f_P \rightarrow f_{P0}$. Equation 6.4.2 is modified as:

$$\sum_{i=1}^{N_n} \left(\frac{f_{P0i}(t) s_i}{3r_i} \right) + \left(\sum_{j=1}^{N_{int}} \left(\frac{s_j}{3r_j} \right) + h_I \ln(r_{out}/r_{in}) \right) f_I(t) = 0 \quad (6.4.3)$$

Here, $\sum_{j=1}^{N_{int}}$ implies summation over the interface fixed-point nodes along the inner insulating wall. In equation 6.4.3, $\tilde{L}_{ins} = h_I \ln(r_{out}/r_{in})$ is related to the inductance of the insulating wall's cross-sectional area (recall that the inductance of a co-axial cable is $L_{coaxial} = \frac{\mu_0}{2\pi} l \ln(r_{out}/r_{in})$, where l is the length of the coaxial cable and r_{out}/r_{in} are the cable's outer and inner radii), and $\tilde{L}_{int\Delta} = \sum_{j=1}^{N_{int}} \left(\frac{s_j}{3r_j} \right)$ is related to the inductance of the area of the parts of the triangular elements in the plasma domain that are associated with the interface fixed point nodes. The resulting expression for f_I is:

$$f_I(t) = \frac{-1}{\tilde{L}_{ins} + \tilde{L}_{int\Delta}} \sum_{i=1}^{N_n} \left(\frac{f_{P0i}(t) s_i}{3r_i} \right) \quad (6.4.4)$$

The constant f_I is calculated at each timestep and is applied as a boundary condition for f on the interface shared by the plasma domain and the insulating domain, resulting in conservation of total toroidal flux in the combined domains. Now, with the natural boundary condition $(\nabla_{\perp} f)|_{\Gamma} = 0$ imposed at all boundary points in the plasma domain (in combination with the explicitly applied boundary conditions $\underline{\mathbf{v}}|_{\Gamma} = \mathbf{0}$), and with equation 6.4.4 used to overwrite the values for f_P on the interface, intrinsic toroidal flux conservation is ensured in the combined computational domain.

6.4.2 Simulations starting with a Grad-Shafranov equilibrium

For the case where the plasma dynamics are evolved starting from an initial Grad-Shafranov equilibrium, the expression for $\Phi_{tot}(t)$ (cf. equation 6.4.1) is:

$$\Phi_{tot}(t) = \underbrace{\int_{\Omega_P} \frac{f_P(\mathbf{r}, t)}{r} dr dz + \int_{\Omega_I} \frac{f_I(t)}{r} dr dz}_{\Phi_{PI}} + \underbrace{\int_{\Omega_P + \Omega_I} \frac{F_{shaft}(t)}{r} dr dz}_{\Phi_{shaft}} \quad (6.4.5)$$

Φ_{shaft} is the toroidal flux added to the combined plasma and insulator domains due to crow-barred shaft current that flows in the chalice wall, in the external aluminum bars, and through the ambient plasma surrounding the CT, as depicted in figure 4.2.1. For the equilibrium-evolved simulations, the system's only source of toroidal flux is $\Phi_{shaft}(t)$, and the initial toroidal flux is $\Phi_0 = \int_{\Omega_p} \frac{f_{gs}(\mathbf{r})}{r} dr dz$, where $f_{gs}(\mathbf{r})$ is the $rB_{\phi}(\mathbf{r})$ field associated with the

Grad-Shafranov equilibrium. Using equation 6.4.5, this implies that

$$\begin{aligned}
\Phi_{tot}(t) &= \int_{\Omega_P} \frac{f_{gs}(\mathbf{r})}{r} dr dz + \int_{\Omega_P + \Omega_I} \frac{F_{shaft}(t)}{r} dr dz \\
&= \int_{\Omega_P} \frac{f_P(\mathbf{r}, t)}{r} dr dz + \int_{\Omega_I} \frac{f_I(t)}{r} dr dz + \int_{\Omega_P + \Omega_I} \frac{F_{shaft}(t)}{r} dr dz \\
&\Rightarrow \int_{\Omega_I} \frac{f_I(t)}{r} dr dz = \int_{\Omega_P} \frac{1}{r} (f_{gs}(\mathbf{r}) - f_P(\mathbf{r}, t)) dr dz
\end{aligned}$$

Following from the procedure described in subsection 6.4.1, the constant f_I can be evaluated if f_P and f_{gs} are temporarily set to zero at the fixed-point nodes along the inner wall of the insulator, leading to the expression:

$$f_I(t) = \frac{1}{\tilde{L}_{ins} + \tilde{L}_{int\Delta}} \sum_{i=1}^{N_n} \left(\frac{(f_{gs0_i} - f_{P0_i}(t)) s_i}{3r_i} \right) \quad (6.4.6)$$

6.4.3 Illustration of toroidal flux conservation

The total flux in the system is calculated at each simulation output time using the formula

$$\Phi_{tot}(t) = \sum_{i=1}^{N_n} \left(\frac{f_i(t) s_i}{3r_i} \right) + (h_I \ln(r_{out}/r_{in})) f_I(t) \quad (6.4.7)$$

Note that in equation 6.4.7, $\Phi_{tot}(t)$ refers to the net toroidal flux in the total domain due to (i) the combined effects of internal plasma poloidal currents in the plasma domain, and (ii) flux addition related to $f_{external}(t)$. f_i denotes the value of rB_ϕ at node i due to the combined effects of flux addition due to externally-driven currents as well as internal plasma poloidal currents. In contrast, f_{P_i} in equations 6.4.2 denotes the value of rB_ϕ at node i due to internal plasma poloidal currents only. Φ_{input} at each output time is calculated using the formula:

$$\Phi_{input}(t) = \sum_{i=1}^{N_n} \frac{s_i}{3r_i} (f_{form}(z, t) + F_{shaft}(t)) + F_{shaft}(t) (h_I \ln(r_{out}/r_{in})) \quad (6.4.8)$$

Note that for formation simulations, $F_{shaft}(t)$ is automatically set to zero, while for non-formation simulations, $f_{form}(z, t)$ is automatically set to zero. Note that $f_{form}(z, t) \propto g_{Form}(z)$ (equation 6.3.11), and $g_{Form}(z)$ is not defined in the insulating region, so that $f_{form}(z, t)$ contributes directly to $\Phi_{input}(t)$ in the plasma domain only. The initial toroidal flux in the total domain is

$$\Phi_{initial} = \sum_{i=1}^{N_n} \frac{s_i}{3r_i} f_i(t=0)$$

Note that $f_{(t=0)}$ is zero at all nodes for formation simulations, while $f_{(t=0)} = f_{GS}$ for simulations starting with a Grad-Shafranov equilibrium.

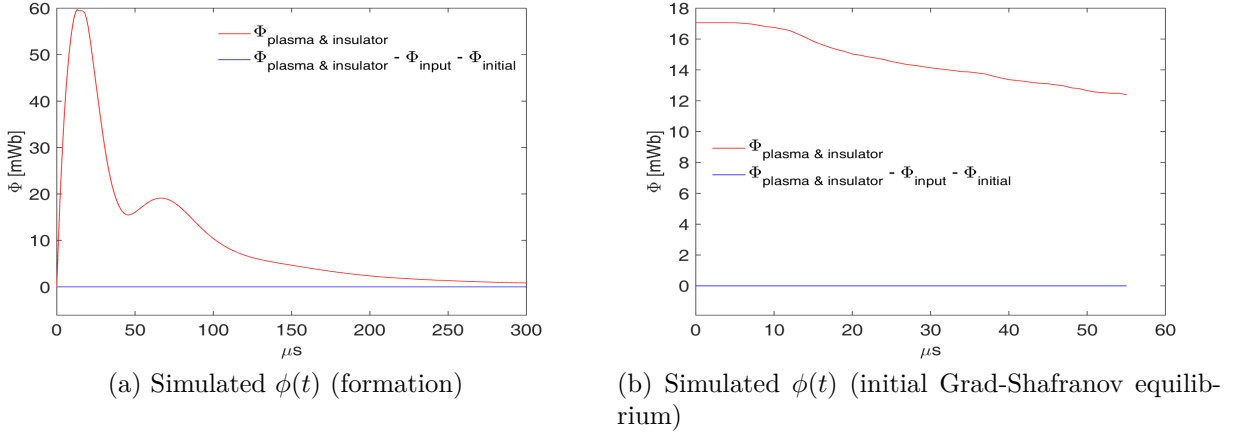


Figure 6.4.1: Illustration of simulated toroidal flux conservation

Now, with the condition $\nabla_{\perp}f = 0$ imposed on all boundary points of the plasma grid (in combination with the explicitly applied boundary conditions $\mathbf{v}|_{\Gamma} = \mathbf{0}$), and with equation 6.4.4 (formation simulations) or 6.4.6 (non-formation simulations) used to overwrite the values for f_{plasma} on the interface, we ensure intrinsic toroidal flux conservation in the computational domain. Figure 6.4.1(a) and (b) indicate toroidal flux conservation over time for formation and non-formation simulations respectively.

6.5 Simulated diagnostics

6.5.1 Simulated diagnostics corresponding to experimental measurements

The experimental diagnostics that can be modelled in simulations are poloidal and toroidal magnetic field at the magnetic probes located in the chalice wall, CT outer separatrix radius (see section 3.7), line averaged electron density along the interferometer chords, and ion temperature along the ion-Doppler chords. The poloidal field experimentally measured at the probe locations is the boundary-tangential component of the field at the probes in the $r - z$ plane. Simulated poloidal field is calculated at the boundary nodes by calculating t_r and t_z , the r and z components of the unit tangents to the computational domain at the

boundary nodes, and using the equation

$$(B_\theta)_{bn} = (\hat{\mathbf{t}} \cdot \mathbf{B}_\theta)_{bn} = (t_r B_r + t_z B_z)_{bn} \quad (6.5.1)$$

Here, the subscript *bn* denotes a particular boundary node. The method using unit tangents allows for consistent evaluation of the sign of the poloidal field, which varies across the separatrix between the CT and levitation/compression field. B_r and B_z are calculated at the boundary nodes using the discrete forms of equation A.7.3: $\underline{B}_r|_\Gamma = (-(\underline{Dz} * \underline{\psi}) \oslash \underline{r})|_\Gamma$ and $\underline{B}_z|_\Gamma = ((\underline{Dr} * \underline{\psi}) \oslash \underline{r})|_\Gamma$. Using equation 6.5.1, the values calculated at the boundary nodes are used to find, by interpolation, the wall-tangential poloidal field at the probe locations. The simulated toroidal field at the magnetic probe locations is also interpolated from the values at the boundary nodes, where $\underline{B}_\phi|_\Gamma = (f \oslash \underline{r})|_\Gamma$.

Simulated CT outer equatorial separatrix radius ($r_s(t)$) is evaluated by finding, at each code output time, the r coordinate, at $z = 0$, of the intersection (where $B_\theta = 0$) between the CT poloidal field and the levitation field.

The simulated diagnostics for n_e and T_i are crude models, simply the line-averaged quantities along the chords indicated in figure 2.2.2.

6.5.2 Additional simulated diagnostics

In addition to the simulated diagnostics that are models of experimental diagnostics, there are several other informative simulated diagnostics that can't be reproduced experimentally due to the absence of experimental measurements in the CT interior. These include time evolutions of the magnetic field across the CT, the CT q profile, CT magnetic axis location, total poloidal flux of the CT, CT volume, and volume-averaged CT beta. Also, the evolution of the system energy components, and maximum ion and electron temperatures in the computational domain can be tracked. The methods for evaluating the q profile, and related CT volume and volume-averaged beta are relatively involved, and will be presented here.

6.5.2.1 q profile

The safety factor, $q(\psi) = \frac{\partial\phi(\psi)}{\partial\psi} = \frac{2\pi}{\iota}$ is defined as the number of toroidal transits a field line makes as it completes one poloidal transit on a closed flux surface. The safety factor is important because magnetically confined plasmas are magnetohydrodynamically unstable if $q \leq 2$ at the last closed flux surface [33]. Here, ι (iota), the rotational transform (or field line pitch angle in radians) is 2π times the number of poloidal transits a

field line makes as it completes one toroidal transit on a closed flux surface. To calculate q , use was made of the contour matrix $cout$ that is returned with the MATLAB command $[cout, hout] = \text{tricontour1}(rz, tri, field, edges, eINT, e2t, ContourLevels)$. Here, $rz [N_n \times 2]$ is a two column vector with N_n rows, the first and second columns contain the r and z coordinates of the computational nodes. $tri [N_e \times 3]$ is a three column vector with N_e rows that contains the indexes of the rows in rz that refer to the three nodes that define each triangular element. $field [N_n \times 1] = \underline{\psi}$, $edges$, $eINT$, and $e2t$ define mesh connectivity data structures, and $ContourLevels$ is a vector defining the values of ψ at which contours are to be drawn. $cout$ is an array with two rows that contains data that defines the contours of ψ . Each $2 \times n$ section (variable n) of $cout$ contains data for a contour defined by $n - 1$ spatial points. The value in the first row of the first column of each section of $cout$ contains the value of ψ on the contour defined by the particular section. The value in the second row of the first column of each section of $cout$ is always an integer that indicates the number of points that define the contour referenced in that section of $cout$. For example, if the first section of $cout$ has dimensions 2×800 , then $cout(1, 1)$ has the value of ψ for the contour defined by the section, $cout(2, 1) = 799$ indicates that 799 points define the contour referenced in the section, while $cout(1, 2 : 800)$ and $cout(2, 2 : 800)$ contain the r and z coordinates of the points that define the contour referenced in the section. By locating the integer values in $cout$, the indexes of columns in $cout$ that are the first columns of the individual sections of $cout$ are found.

q is generally defined only on closed contours. The second and last columns of each section of $cout$ that refers to a *closed* contour are identical and this relationship is used to find the indexes of columns in $cout$ that contain starting point indexes for data defining individual closed contours. For simulations that include the computational domain of the gun, there can be closed ψ contours down the gun (for example, if part of the CT is pinched off during magnetic compression - see figure 2.1.2), and we are not interested in q there. The indexes of columns in $cout$ that contain starting point indexes for data for individual *closed* contours in the *CT confinement region* are found by placing the constraint of a minimum z coordinate on the spatial points that define closed contours.

For each closed poloidal flux contour (index j) in the confinement region, $\underline{I^e}_j [N_e \times 1]$, a logical vector of ones and zeroes defining the rows in $\underline{r^e} [N_e \times 1]$ and $\underline{z^e} [N_e \times 1]$, that refer to triangle centroids lying within the contour, are found. The average value of toroidal magnetic flux $\phi = \int \mathbf{B}_\phi \cdot \mathbf{dS}$ within a particular contour with index j can be found as $\phi_j = S_{in_j} < \underline{f^e}_{in_j} \otimes \underline{r^e}_{in_j} >$. Here S_{in_j} is the area enclosed by contour j , and $< \underline{f^e}_{in_j} \otimes \underline{r^e}_{in_j} >$ is the average of $B_\phi = f/r$ within contour j , where $\underline{f^e}_{in_j} = \underline{f^e}(\underline{I^e}_j)$ and $\underline{r^e}_{in_j} = \underline{r^e}(\underline{I^e}_j)$ contain the values of $\underline{f^e}$ and $\underline{r^e}$ at triangular element centroids that lie within contour j . Note that this averaging method is implemented because it produces smoother results, for moderate mesh

resolution, than the approximately equivalent definition $\phi_j = \underline{s}_{in_j}^{eT} * \left(\underline{f}_{in_j}^e \oslash \underline{r}_{in_j}^e \right)$. Triangle-centered quantities are used instead of nodal quantities because there are more triangles than nodes so averaging is more accurate. With ψ_j and ϕ_j defined for each ψ contour, it is then straightforward to find $q_j = \frac{\partial \phi_j}{\partial \psi_j}$ using the Matlab gradient function. As detailed in section C.5.2, this method yields $q(\psi)$ profiles that are an excellent match to those produced by a well-established equilibrium code.

6.5.2.2 Evaluation of CT volume and volume-averaged β

At each code output time, the data associated with the ψ contour that defines the last closed flux surface (LCFS) can be used to evaluate V_{CT} , the CT volume. Defining $j = 0$ as the index of the poloidal flux contour that defines the LCFS,

$$V_{CT} = 2\pi \underline{r}_{in_0}^{eT} * \underline{s}_{in_0}^e \quad (6.5.2)$$

where $\underline{r}_{in_0}^{eT} = (\underline{r}^e(\underline{I}^e_0))^T$ is the transpose of the vector containing the r coordinates of the triangular element centroids that lie within the LCFS, and vector $\underline{s}_{in_0}^e = \underline{s}^e(\underline{I}^e_0)$ contains the areas of the triangular elements whose centroids lie within the LCFS.

Similarly, at each output time the volume-averaged total, poloidal, and toroidal betas (ratios of fluid pressure to magnetic pressure) can be calculated as

$$\begin{aligned} \langle \beta \rangle &= 2\mu_0 \left(\underline{V}_{in_0}^{eT} * \left(\underline{p}_{i,in_0}^e + \underline{p}_{e,in_0}^e \right) \right) \oslash \left(\underline{V}_{in_0}^{eT} * \left(\left(\underline{B}_{r,in_0}^e \right)^2 + \left(\underline{B}_{\phi,in_0}^e \right)^2 + \left(\underline{B}_{z,in_0}^e \right)^2 \right) \right) \\ \langle \beta_\theta \rangle &= 2\mu_0 \left(\underline{V}_{in_0}^{eT} * \left(\underline{p}_{i,in_0}^e + \underline{p}_{e,in_0}^e \right) \right) \oslash \left(\underline{V}_{in_0}^{eT} * \left(\left(\underline{B}_{r,in_0}^e \right)^2 + \left(\underline{B}_{z,in_0}^e \right)^2 \right) \right) \\ \langle \beta_\phi \rangle &= 2\mu_0 \left(\underline{V}_{in_0}^{eT} * \left(\underline{p}_{i,in_0}^e + \underline{p}_{e,in_0}^e \right) \right) \oslash \left(\underline{V}_{in_0}^{eT} * \left(\underline{B}_{\phi,in_0}^e \right)^2 \right) \end{aligned} \quad (6.5.3)$$

Here, $\underline{V}_{in_0}^{eT} = 2\pi \underline{r}_{in_0}^e \circ \underline{s}_{in_0}^e$ is the transpose of the vector containing the volumes associated with the triangular elements whose centroids lie within the LCFS, and \underline{p}_{i,in_0}^e , \underline{p}_{e,in_0}^e , \underline{B}_{r,in_0}^e , $\underline{B}_{\phi,in_0}^e$ and \underline{B}_{z,in_0}^e contain the values of ion pressure, electron pressure, and the r , ϕ , and z components of the magnetic field at the triangle centroids inside the LCFS.

6.6 Summary

It has been shown how boundary conditions for ψ are evaluated, applied, and varied over time to model the levitation and compression fields, while boundary conditions for ψ corresponding

to the stuffing field are held constant over time. In combination with the boundary conditions $\mathbf{v}|_{\Gamma} = \mathbf{0}$, the natural imposition of the boundary condition $(\nabla f_{\perp})|_{\Gamma} = 0$ is required for conservation of the part of the toroidal flux associated with f_{η} , which enables simulations to reproduce poloidal currents that, in the experiment, are induced to flow primarily in machine walls and across various regions of ambient plasma external to the CT, in order to conserve toroidal flux.

The ability to model part of the domain as an insulating plasma-free material is useful because it expands the code's range of applicability as a problem-solving tool. As shown in chapter 7, this feature has been used to verify that penetration into the insulating wall of poloidal field being advected into the containment region during CT formation was an issue associated with the 6-coil configuration that was alleviated in the 11-coil configuration. It has been shown how particular effort was made to ensure maintenance of toroidal flux conservation when an insulating region is included in the model.

The methods developed to simulate the CT formation process, by adding toroidal flux associated with the measured formation voltage to the domain, have been presented. Even with the simplifying assumption that radial formation current between the electrodes flows at a fixed axial location, the model is able to reproduce experimental measurements to a very acceptable level, as will be shown in chapter 7. Tests to allow variation of the axial location of intra-electrode formation current, with upper and lower bounds, were able to precisely reproduce the experimentally measured formation current signals over the times when the axial location was unrestricted.

Various simulated diagnostics have been implemented to the code. Some of these are counterparts to the available experimental diagnostics. Several other simulated diagnostics have been developed including the time evolutions of the $q(\psi)$ profile, magnetic axis location, β profile, CT volume and magnetic fluxes, system energy components, and maximum ion and electron temperatures. These additional simulated diagnostics are based on various simulated field distributions.

Chapter 7

Simulation input parameters and results

This chapter will begin with descriptions, in section 7.1, of some of the key code input parameters. Some of the principal input parameters for simulation 2353, which includes CT formation into a levitation field, and magnetic compression, will be tabulated. Next, in section 7.2, simulation results which confirm that the level of plasma-wall interaction was reduced by the line-tying effect of increased $|t_{lev}|$, and more significantly, with the switch from the 6-coil to the 11-coil configuration, will be presented. Contour plots depicting the evolution of various fields for simulation 2353 will be shown in section 7.3. Presentation of the evolution of a selection of simulated fields for the case of an extended simulation that includes the effect of the ringing compression field will follow in section 7.4. Proceeding this, in section 7.5, a selection of simulated diagnostics will be presented and compared with the experimental counterparts, for levitation-only shots in the cases with low and high R_{cable} , and for a selection of compression shots. Presentation and discussion of further simulated diagnostics that don't have experimental counterparts, such as simulated q profile, compression scalings, internal magnetic fields, CT volume, β , and magnetic axis location, will follow in section 7.5.3. The chapter will conclude with a summary in section 7.6.

7.1 Simulation input parameters

| simulation # | Plato | do _{formation} | geometry | meshtype | h _e [mm] | do _{insulator} |
|------------------------|---|-----------------------------------|--|--|--|---|
| 2353 | 1 | 1 | 2 | 0 | 2 | 1 |
| vary _H | τ_{LR} [μs] | do _{2temp} | T ₀ [eV] | T _r [eV] | | |
| 0 | 70 | 1 | 0.02 | 0.02 | | |
| RK | dt ₀ [s] | t _{out} [μs] | tsrf | dt _{min} [s] | t _{sim} [μs] | |
| 1 | 8×10^{-11} | 1 | 2 | 1×10^{-12} | 87 | |
| V _{form} [kV] | V _{lev} [kV] | V _{comp} [kV] | I _{main} [A] | t _{lev} [μs] | R _{cable} | t _{comp} [μs] |
| 16 | 16 | 18 | 70 | 60 | 1 | 45 |
| m ₀ | Z _{eff} | n _o [m ⁻³] | σ_n^2 [m ²] | ζ [m ² /s] | ν_{num} [m ² /s] | ν_{phys} [m ² /s] |
| 4 | 1.3 | 9×10^{20} | 0.005 | 50 | 700 | 410 |
| vary _η | η_{max} [m ² /s] | vary _χ | $\chi_{\parallel i}$ [m ² /s] | $\chi_{\parallel e}$ [m ² /s] | $\chi_{\perp i}$ [m ² /s] | $\chi_{\perp e}$ [m ² /s] |
| 1 | 5000 | 0 | 5000 | 16000 | 120 | 240 |

Table 7.1.1: Selection of code input parameters for simulation 2353

In total, there are over one hundred code input parameters. Some of the principal code input parameters for example simulation 2353 results are presented in table 7.1.1. *Plato* = 1 implies that the simulation was run remotely, using a VPN service, on the high performance computing cluster (*Plato*) at the University of Saskatchewan (*Plato* = 0 for cases where the simulation is run directly on a local computer). *do_{formation}* = 1 implies that the simulation started with CT formation, as opposed to starting with a Grad-Shafranov equilibrium (in that case *do_{formation}* would be set equal to zero). *geometry* = 2 implies that the simulation was run in a computational domain representing the geometry for the 11-coil configuration in the full Marshall gun. *meshtype* = 0 and *h_e* = 2 mm implies that a computational grid with uniform triangular elements of size 2 mm was used (see appendix C.1). *do_{insulator}* = 1 implies that an insulating region was included in the simulation (see section 6.2). *vary_H* = 0 implies that the z coordinate of the radial component of formation current between the gun electrodes was held constant at $z = z_{gp} = -0.43$ m, the location of the gas puff valves (see section 6.3.1.1). For a time-dependent formation current profile, *vary_H* would be set equal to one. $\tau_{LR} = 70$ μs defines the timescale associated with the resistive contribution to Φ_{form} (see section 6.3.1). *do_{2temp}* = 1 implies that the single fluid energy equation is split into ion and electron components (equations 5.5.15 and 5.5.16). *T₀* and *T_r* define the initial and

boundary values for the ion and electron temperatures - see section 6.1.3.

The code inputs in the third row of table 7.1.1 pertain to timestepping, see appendix C.2. $RK = 1$ implies that forward Euler timestepping was used. dt_0 defines the initial timestep, t_{out} defines the interval between the instances when the simulation data is saved to file, along with plots of analysed field data. $tsrf$ defines the factor by which the timestep is reduced before continuing the simulation from field data saved to file at the last instance of data output, in the event of a crash caused by having a timestep that is too large. dt_{min} defines the minimum timestep that can be reached before the simulation is terminated. $t_{sim} = 87 \mu\text{s}$ defines the duration of the simulation - this value is chosen here because when compression is started at $t_{comp} = 45 \mu\text{s}$, the peak compression is at around $65 \mu\text{s}$, and compression current falls to zero by around $87 \mu\text{s}$. In this simulation the effect of compression current polarity change (see figure 6.1.1(b)) is not examined. Results from a simulation in which the compression current is allowed to ring are presented in sections 7.4 and 7.5.2.2.

The code inputs in the fourth row of table 7.1.1 are related to the external magnetic conditions. For formation simulations, the formation voltage waveform used to calculate $\Phi_{form}(t)$ in the expression for $f_{external}(z, t) = f_{form}(z, t)$ (section 6.3.1) is taken from an experimental measurement for a typical shot with $V_{form} = 16 \text{ kV}$. This waveform can be linearly scaled according to the formation voltage required as an input parameter for the simulation. As described in section 6.1.4, the boundary conditions for ψ , pertaining to ψ_{main} , ψ_{lev} , and ψ_{comp} are obtained using FEMM models. For the FEMM model used to find ψ_{main} , the dc current in the main coil was set to $I_{main} = 70 \text{ A}$, and the boundary values for ψ_{main} can be linearly scaled according to the value of I_{main} required for the simulation. Similarly, the currents in the levitation and compression coils in the FEMM models, used to obtain boundary conditions for ψ_{lev} and ψ_{comp} , were set to the experimentally measured values corresponding to experimentally recorded $V_{lev} = 16 \text{ kV}$ and $V_{comp} = 18 \text{ kV}$ (voltages to which the levitation and compression capacitors were charged) respectively. Again, the boundary values for ψ_{lev} and ψ_{comp} can be scaled linearly according to the values of V_{lev} and V_{comp} required for the simulation. $|t_{lev}| = 60 \mu\text{s}$ implies that the boundary conditions for ψ_{lev} are taken from a FEMM model with the input current frequency set to a value (4170 Hz) corresponding to having the quarter-period of the levitation current equal to $60 \mu\text{s}$ (see sections 3.1 and 7.2). $R_{cable} = 1$ implies that the levitation current waveform corresponding to inclusion of $70 \text{ m}\Omega$ cables between each levitation coil (or coil-pair) and levitation inductor was used to scale the levitation component of the boundary conditions for ψ over time (see section 3.6.1, note that $R_{cable} = 0$ corresponds to $2.5 \text{ m}\Omega$ cables). $t_{comp} = 45 \mu\text{s}$ means that magnetic compression (*i.e.*, superimposition of the ψ_{comp} boundary conditions, scaled by experimentally recorded

$\tilde{I}_{comp}(t)$, on the ψ_{main} and ψ_{lev} boundary conditions, see section 6.1.4) is started 45 μs into the simulation.

The inputs in the fifth row of table 7.1.1 define some basic plasma parameters and the diffusion coefficients for density and viscosity. $m_0 = 4$ implies that the ion mass is four proton masses ($m_p = 1.67 \times 10^{-27}$ kg), which is relevant for modeling helium plasmas. $Z_{eff} = 1.3$ defines the estimate for the (volume averaged) ion charge, and determines the ratio of electron to ion number density ($n_e = Z_{eff} n_i$). Since the plasma is being modeled as a single fluid, while the energy equation is split into ion and electron components, Z_{eff} determines the ratio between the ion and electron pressures ($p = p_i + p_e = n (T_i [\text{J}] + Z_{eff} T_e [\text{J}])$, where $n \iff n_i$). Z_{eff} also enters into the determination of plasma Spitzer resistivity (equation 5.6.4), the ion-electron heat exchange term Q_{ie} (equation 5.6.5) and, for neutral fluid dynamics (chapter 8), the rate coefficients for ionization and recombination. Fully ionized helium plasma would have $Z_{eff} = 2$, here we assume that a proportion of the helium atoms are only singly ionized. Z_{eff} can be increased to include some of the effects of the inclusion of high Z impurities in the plasma. $n_0 [\text{m}^2/\text{s}]$ determines the plasma number density - note that normalised density $\tilde{n}(\mathbf{r}, t) = \frac{n(\mathbf{r}, t)}{n_0}$ is evolved over time. Along with n_0 , $\sigma_n^2 [\text{m}^2]$ defines the variance of the Gaussian function that determines the initial plasma density distribution, which is centered around $z_{gp} = -0.43$ m, the z coordinate of the physical location of the machine gas puff valves. The initial density profile is given by

$$n_{t0}(z) = n_0 ((n_{high} - n_{low}) \tilde{g}(z) + n_{low}) \quad (7.1.1)$$

where $\tilde{g}(z) = g(z)/\max(g(z))$. Here, $g(z) = \frac{1}{\sqrt{2\pi\sigma_n^2}} \exp\left(\frac{-(z-z_{gp})^2}{2\sigma_n^2}\right)$. n_{high} and n_{low} are typically set to 10 and 0.1 respectively. Note that n_{low} must be finite - density is not allowed to approach too close to zero anywhere in the computational domain. See figure 7.3.5(a) for an example initial density profile. The width of the base of the Gaussian is approximately 0.7 m, 0.45 m, 0.4 m, or 0.2 m for $\sigma_n^2 = 0.01, 0.005, 0.003$, or 0.001 m^2 respectively. The sound speed of a neutral gas is given by $V_s = \sqrt{\frac{\gamma p}{\rho}}$. At room temperature (0.02 eV), for helium gas, this is $V_s \approx \sqrt{\frac{\frac{5}{3}(1.6 \times 10^{-19})(0.02)}{4(1.67 \times 10^{-27})}} \approx 900 \text{ m/s}$. In a typical shot, gas is puffed into the vacuum vessel through the eight gas valves spaced toroidally on the outer electrode, around 400 μs before firing the formation capacitors. A simple estimate of d_n , the maximum spread of the neutral gas around the valves can be estimated using this time and the sound speed, as $d_n = (400 \times 10^{-6})(900) = 0.36$ m, so that choosing $\sigma_n^2 = 0.005 \text{ m}^2$, corresponding to a Gaussian base width of around 0.45 m, is a reasonable estimate for the initial spread. Simulations that don't include a model for interaction between plasma and neutral fluids start with the crude approximation that all the plasma fluid particles are ionized. The

density diffusion coefficient ζ is chosen as $50 \text{ m}^2/\text{s}$, which, as mentioned in appendix C.3, is close to the minimum required value for sufficient density field smoothing for formation simulations. Similarly, at $700 \text{ m}^2/\text{s}$, ν_{num} is close to the minimum value required for sufficient velocity field smoothing, while $\nu_{phys} = 410 \text{ m}^2/\text{s}$, is chosen because it leads to simulated ion temperature close to the levels indicated by the ion-Doppler system (see appendix C.3.2).

The inputs in the sixth row of table 7.1.1 define the resistive and thermal diffusion coefficients. For this simulation, $vary_\eta = 1$ so that the Spitzer formula for plasma resistivity is used to calculate the (isotropic) resistive diffusion coefficient at each timestep according to equation 5.6.4. An upper limit of $\eta_{max} = 5000 \text{ [m}^2/\text{s]}$ is imposed to prevent extremely high values of η in regions where T_e is low, as this would lead to small timesteps, as outlined in appendix C.3. Input parameter $vary_\chi = 0$ for this simulation, so that thermal diffusion is determined by fixed coefficients $\chi_{\parallel i}$, $\chi_{\parallel e}$, $\chi_{\perp i}$ and $\chi_{\perp e}$. The constant thermal diffusion coefficients used in this simulation are $\chi_{\parallel i} = 5000$, $\chi_{\parallel e} = 16000$, $\chi_{\perp i} = 120$ and $\chi_{\perp e} = 240 \text{ [m}^2/\text{s]}$. The high parallel coefficients represent the physical case where particles are free to stream unimpeded along field lines. At early simulation times, all magnetic field lines are open (*i.e.*, field lines do not close on themselves), and connect to the walls of the vacuum vessel, so that parallel thermal diffusion to the walls, where the boundary conditions $T_\Gamma = 0.02 \text{ eV}$ are applied, represents the most significant loss of thermal energy. After CT formation, heat arising from residual formation current down the gun below the CT continues to be lost to the walls through parallel diffusion along open field lines, but perpendicular thermal diffusion is the dominant heat loss mechanism for the plasma constituting the CT itself, because CT field lines are closed so that heat contained within the CT is not lost by parallel diffusion. In the absence of magnetic compression, the constant perpendicular thermal diffusion coefficients chosen for this simulation lead to a CT lifetime that is comparable to experimentally observed lifetimes of levitated CTs in the 11-coil configuration. Note that an explicit model for cooling due to impurity line radiation is not included in the simulation. The relatively high perpendicular thermal diffusion coefficients act as a proxy to include the effects of this cooling mechanism.

Some additional input parameters for simulation 2353 pertain to dynamics of neutral fluid. These parameters, and a selection of simulation results relating to the neutral fluid dynamics, will be presented, along with the model for interaction between the plasma and neutral fluids, in chapter 8.

7.2 Simulated plasma-wall interaction

7.2.1 Effect of increasing levitation field soak-in

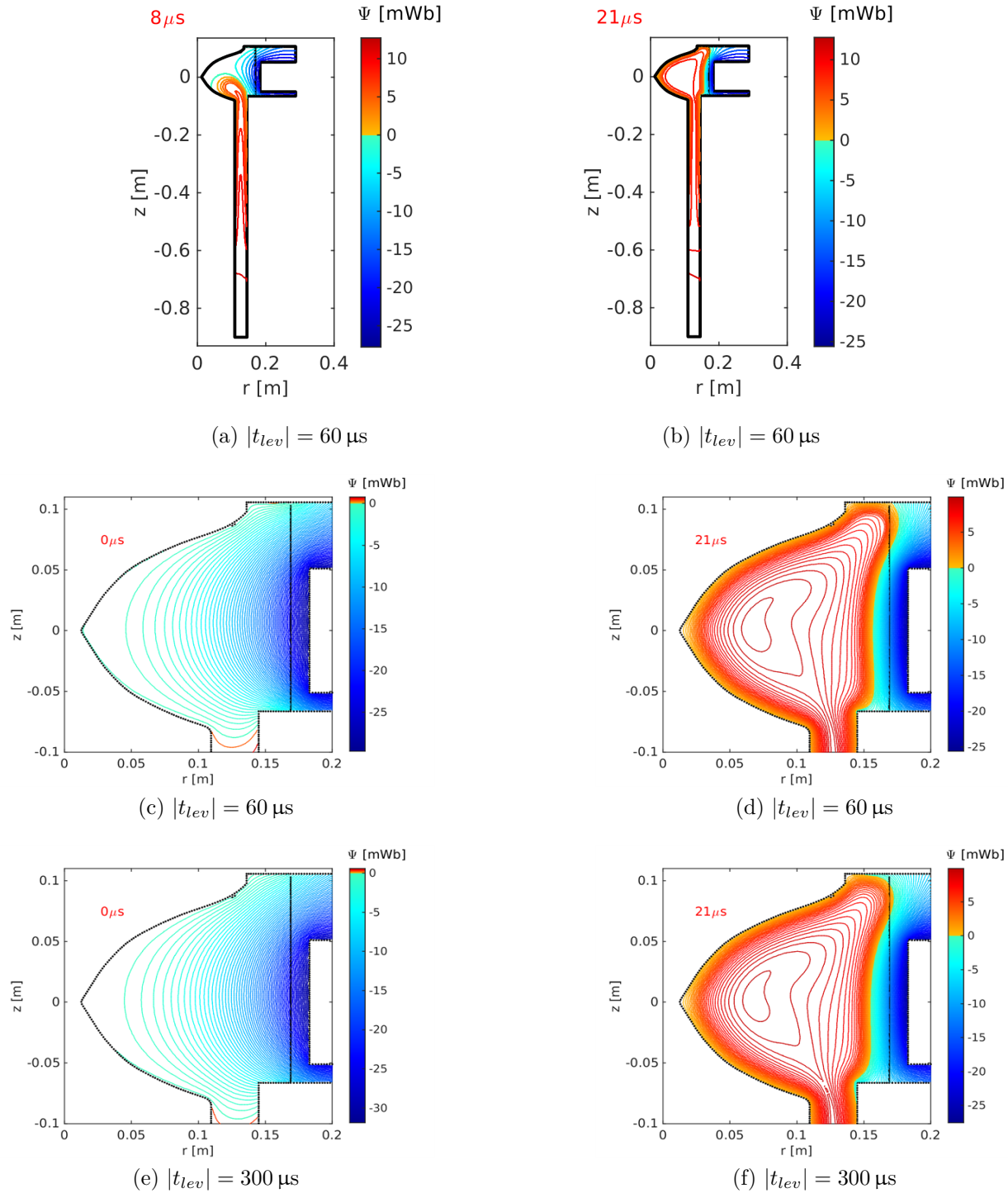


Figure 7.2.1: Poloidal flux contours for 6-coil configuration, effect of t_{lev}

Figure 7.2.1 shows how, for the 6-coil configuration, MHD simulations confirm the reduction of plasma-wall interaction at formation for the cases when the levitation field is allowed to soak into the stainless steel above and below the insulating wall outboard of the CT confinement region. As outlined in section 3.1, magnetic field that is allowed to soak into the steel can only be displaced on the resistive timescale of the steel, which is longer than the time it takes for the CT to bubble-in to the containment region. The resulting line-tying effect is thought to have reduced the level of CT poloidal field that penetrates the insulating wall during the formation process.

Figures 7.2.1(a) and (b) show simulated ψ contours in the entire computational domain during the formation process at $t = 8 \mu\text{s}$ and $t = 21 \mu\text{s}$ for the 6-coil configuration. The simulation input parameters were approximately the same as for simulation 2353, except that parameter *geometry*, which defines the machine configuration, was set to three for this simulation. As depicted explicitly in figure 6.2.1(b), the stack of six coils is partly located in the blank rectangle at the top-right of figures 7.2.1(a) and (b), centered around $z = 0 \text{ mm}$, and extends off further to the right (not shown). The region above, below, and just to the left of the coil-stack represents the air around the stack. The vertical black line at $r = 17 \text{ cm}$ represents the inner radius of the insulating wall, and the outer radius of the insulating wall at $r = 17.7 \text{ cm}$ is not indicated. As described in section 6.2, only ψ , which determines the vacuum poloidal field, is evaluated in the insulating region to the right of the inner radius of the insulating wall. The solution for ψ is coupled to the full MHD solution in the remainder of the domain. To maintain toroidal flux conservation, boundary conditions for f , which has a finite constant value in the insulating wall and is zero outside the current-carrying aluminum bars depicted in figure 3.1.1(a), are evaluated for, and applied to, the part of the boundary representing the inner radius of the insulating wall, as described in section 6.4. In this case (figures 7.2.1(a) and (b)), the boundary conditions for ψ are from a FEMM solution for a case with a current frequency of 4170 Hz, corresponding to a quarter-period of $|t_{lev}| = 60 \mu\text{s}$. Figures 7.2.1(c) and (d) show close ups of the CT confinement region for the same simulation, at $t = 0 \mu\text{s}$, and $t = 21 \mu\text{s}$. It can be seen how, at $t = 21 \mu\text{s}$, the poloidal field at the leading edge of the forming CT intersects the insulating wall above the coil stack. The simulations indicate penetration of CT poloidal field into the insulating wall between $t = 13 \mu\text{s}$, and $t = 33 \mu\text{s}$, with peak penetration at around $t = 21 \mu\text{s}$. Ions gyrorotating around and streaming along poloidal field lines can intersect the wall in the 6-coil configuration and sputter impurities into the plasma, leading to increased energy losses due to line radiation.

For comparison, figures 7.2.1(e) and (f) show the equivalent solutions for a case corresponding to $|t_{lev}| = 300 \mu\text{s}$, with corresponding boundary conditions for ψ from a FEMM solution for a case with a current frequency of 800 Hz. All other code input parameters were identical to those used for the simulation presented in figures 7.2.1(a)→(d). Comparing

figures 7.2.1(c) and 7.2.1(e), it can be seen how, at $t = 0 \mu\text{s}$, the levitation field has soaked further into the steel, particularly below the insulating wall, in the case with increased $|t_{lev}|$. As a consequence of the additional energy required to bend the soaked-in levitation field, poloidal field that has been advected up the gun penetrates less deeply into the insulating wall during formation in the case with $|t_{lev}| = 300 \mu\text{s}$ (figure 7.2.1(d) *cf.* figure 7.2.1(f)). The simulations also indicate that the duration of interaction is reduced with increased $|t_{lev}|$; the initial penetration is delayed from $t = 13 \mu\text{s}$ to $t = 15 \mu\text{s}$, and CT poloidal field stops intersecting the wall sooner, at around $t = 30 \mu\text{s}$ (*cf.* $t = 33 \mu\text{s}$).

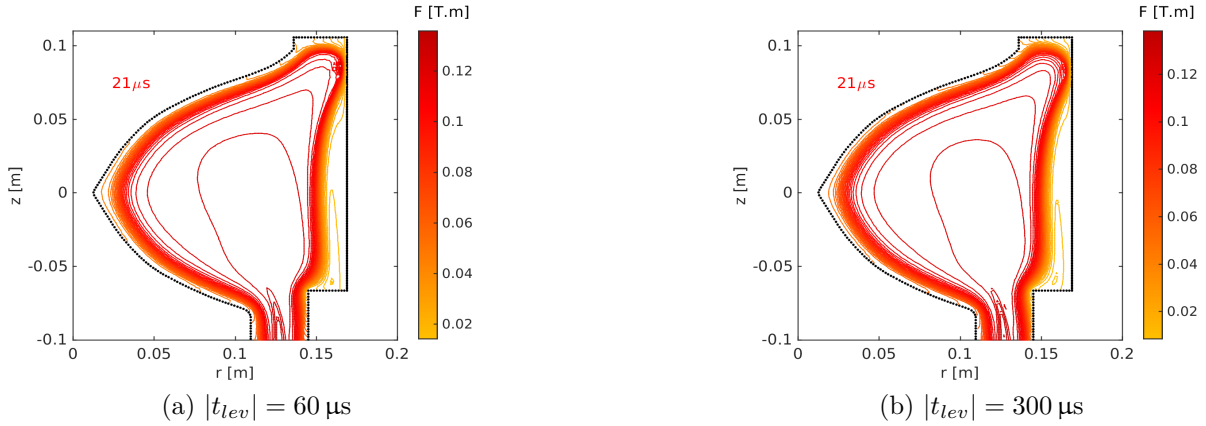


Figure 7.2.2: f contours for 6-coil configuration, effect of t_{lev}

Figure 7.2.2 shows a comparison of contours of f from the same simulations at $t = 21 \mu\text{s}$, the time of peak field penetration. Contours of f represent lines of poloidal current - it can be seen how the contours of f are compressed up against the top of the insulating wall, with less compression in the case with $|t_{lev}| = 300 \mu\text{s}$, indicating a reduced level of poloidal current scraping against the wall.

7.2.2 Effect of levitation field profile (11-coil *cf.* 6-coil configuration)

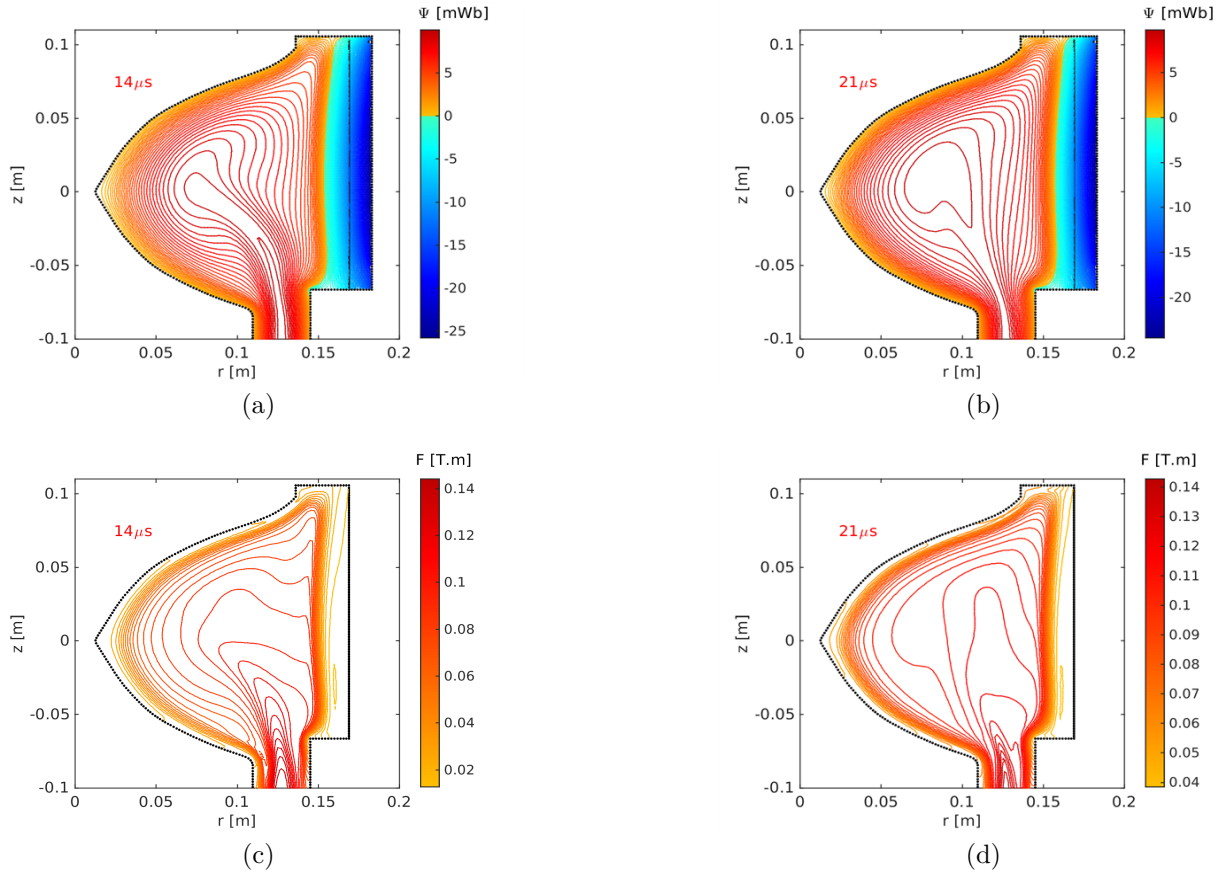


Figure 7.2.3: ψ and f contours for 11-coil configurations ($t_{lev} = 60 \mu\text{s}$)

Figure 7.2.3 shows contours of ψ and f at 14 and 21 μs , during the simulated formation process in the 11-coil configuration, from simulation 2353. In contrast with the case for six coils (figures 7.2.1 and 7.2.2), it can be seen how the leading edge of the forming CT is held off the wall by the levitation field all along the height of the wall for the 11-coil configuration. Note that the simulations presented in figures 7.2.1, 7.2.2, and 7.2.3 all have boundary conditions for ψ_{main} and ψ_{lev} from FEMM models, pertaining to $I_{main} = 70\text{A}$, and with the total levitation current such that ψ_{lev} is approximately the same for each configuration. Formation toroidal flux has been added to the system in each case according to the experimentally measured $V_{gun}(t)$ signal for $V_{form} = 16 \text{ kV}$. The strategy of increasing $|t_{lev}|$ was found to be ineffective for the 25 turn coil and 11-coil configurations. The optimal settings were $|t_{lev}| \sim 150 \mu\text{s}$ and $50 \mu\text{s}$ for the 25 turn coil and 11-coil configurations, approximately the respective rise times of the levitation current (see discussion in section 3.9). Increasing

$|t_{lev}|$ beyond these values led to degraded CT performance in the 25 turn coil and 11-coil configurations. This is thought to be due to the effect of partially blocking plasma entry to the CT containment region, and reduced CT size, with increasing $|t_{lev}|$. Simulations confirm that, as $|t_{lev}|$ is increased, the poloidal field of the CT becomes more distorted during bubble-in, as it is forced to bend around the levitation field that is resistively pinned to the steel at the outboard side of the entrance to the confinement region. The poor recurrence rate of good shots in the 6-coil and 25-turn configurations relative to that in the 11-coil configuration is thought to be related to the high values of $|t_{lev}|$ that were necessarily used with the 25 turn coil configuration, and used for optimal (*i.e.*, occasionally good) performance in the 6-coil configuration. In the 6-coil configuration, the performance degradation associated with increased $|t_{lev}|$ was outweighed by the benefit of reduced plasma-wall interaction associated with increased line-tying, however increasing $|t_{lev}|$ to more than around 300 μs also led to degradation of CT lifetime with the 6-coil configuration.

It is thought that the moderate improvement in CT lifetime seen with increased $|t_{lev}|$ in the 6-coil configuration, and the more significant improvement found with the switch to the levitation field profile associated with the 25 turn coil and 11-coil configurations, are due to the effect of reducing the level of plasma-wall interaction during the CT formation process. Less interaction implies less ion bombardment on the insulating wall, and consequent reductions in impurity concentration and in the level of cooling associated with impurity line radiation. From equation 5.5.3, $\dot{\psi}_\eta \propto \eta$. Since $\eta \propto T_e^{-1.5}$, reduced cooling leads to increased CT lifetimes.

7.3 Evolution of the various fields, simulation 2353

In this section, contours of the evolved fields from simulation 2353, as well as contours of current density, calculated using equation A.7.18, will be presented at a selection of simulation times. The simulations start with CT formation in the magnetized Marshall gun. Plasma starts to bubble-into the containment region at around 8 μs , and closed CT flux surfaces start to form around 25 μs . Magnetic compression is started at $t_{comp} = 45 \mu\text{s}$, with peak compression (*i.e.*, peak compression coil current) occurring at 65 μs . The simulations continues until 87 μs , by which time the primary magnetic compression cycle has completed and compression coil current has dropped back to zero. Full field depictions as well as close-up containment region views will be presented at various output times for ψ and f , while the remaining fields will be presented at various output times in either of the two views.

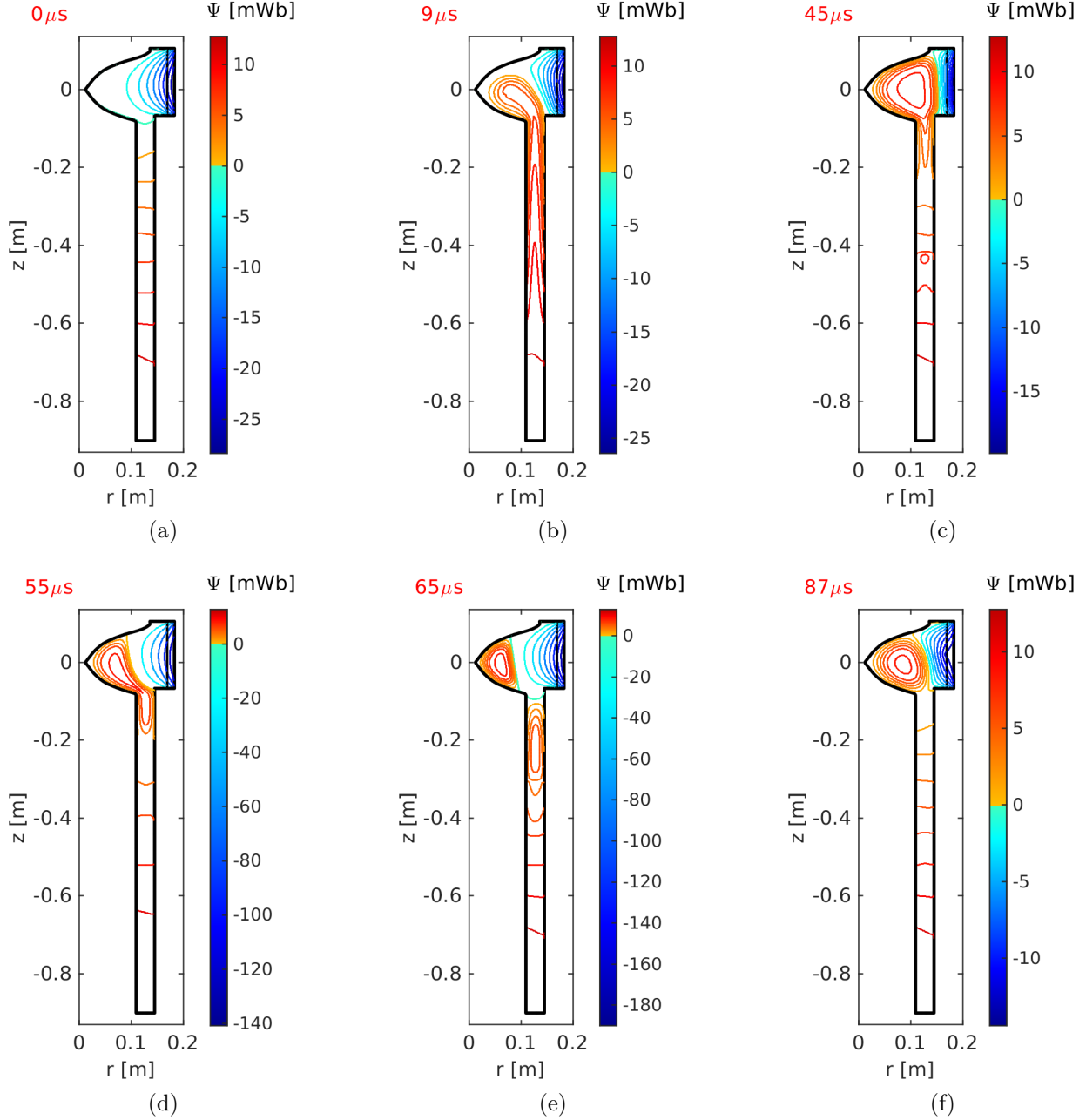


Figure 7.3.1: Poloidal flux contours

Figure 7.3.1 shows ψ contours at various times. Simulation times are notated in red at the top left of the figures. Note that the colorbar scaling changes over time; $\max(\psi)$ decreases slowly over time as the CT decays, while $\min(\psi)$ increases as the levitation current in the external coils decays, and then drops off rapidly as the compression current in the external coils is increased, starting at $t_{comp} = 45 \mu\text{s}$ in this simulation. At time $t = 0$, the stuffing field due to currents in the main coil ($\psi > 0$) fills the vacuum below the containment region, and has soaked well into all materials around the gun, while the levitation field fills the containment region. Open field lines that are resistively pinned to the electrodes, and frozen

into the conducting plasma, have been advected by the $\mathbf{J}_r \times \mathbf{B}_\phi$ force, into the containment region by $t = 9 \mu\text{s}$. By $45 \mu\text{s}$, open field lines have reconnected at the entrance to the containment region, and closed flux surfaces have formed in the containment region. The primary compression cycle starts at $45 \mu\text{s}$ and continues until $65 \mu\text{s}$. Note that at $55 \mu\text{s}$ (figure 7.3.1(d)), magnetic compression causes closed CT poloidal field lines that extend down the gun to be pinched off at the gun entrance, where they reconnect to form a second smaller CT. Field lines that remain open surrounding the main CT are then also reconnectively pinched off, forming additional closed field lines around the main CT, while the newly reconnected open field lines below the main CT act like a slingshot that advects the smaller CT down the gun, as can be seen at $65 \mu\text{s}$. Peak CT compression is at $65 \mu\text{s}$, and the CT re-expands as I_{comp} in the compression coils reduces, reaching maximum expansion at around $87 \mu\text{s}$.

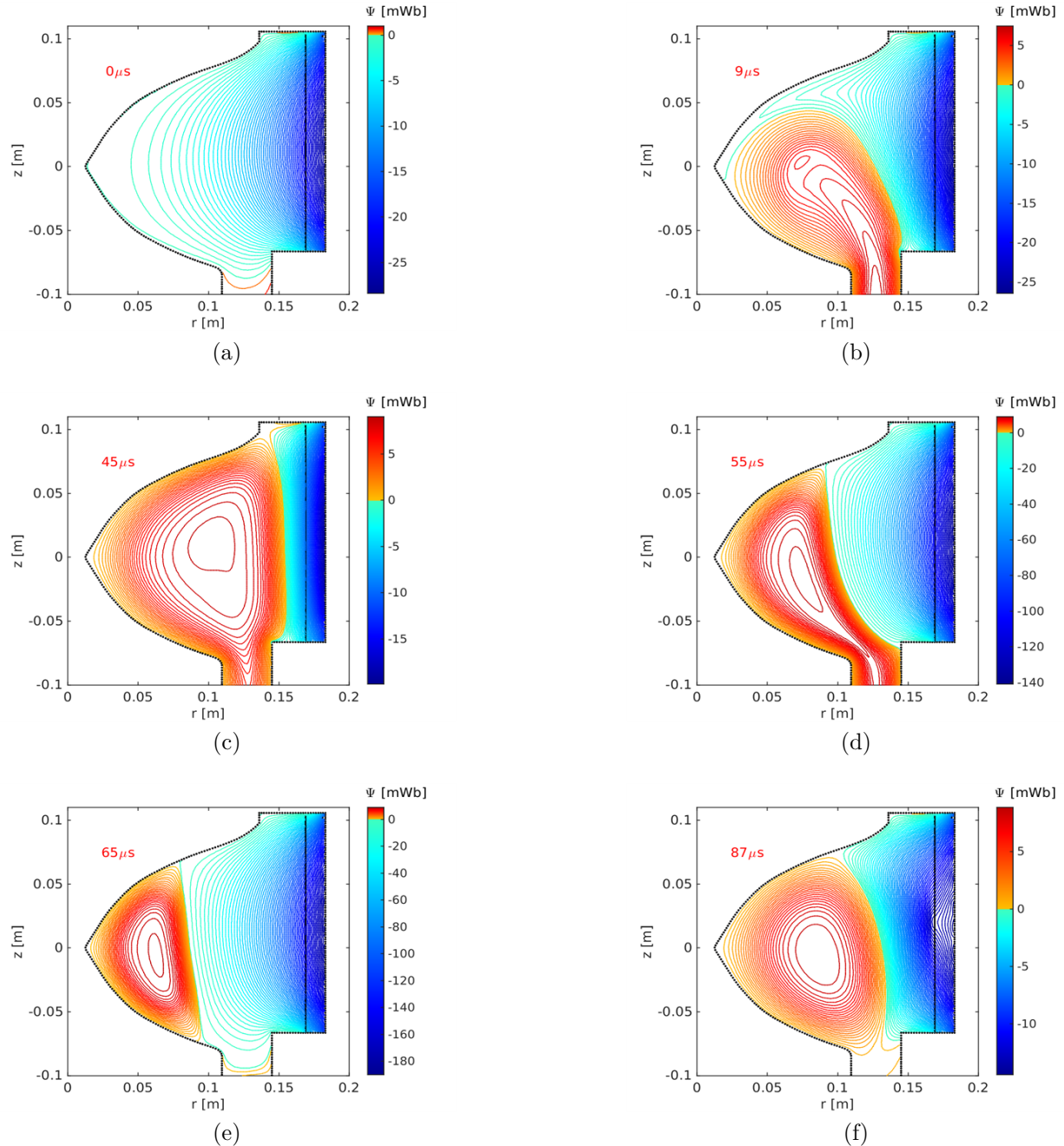


Figure 7.3.2: Poloidal flux contours (confinement region)

Figure 7.3.2 shows close-up views, focused on the CT containment region, of the ψ contours presented in figure 7.3.1.

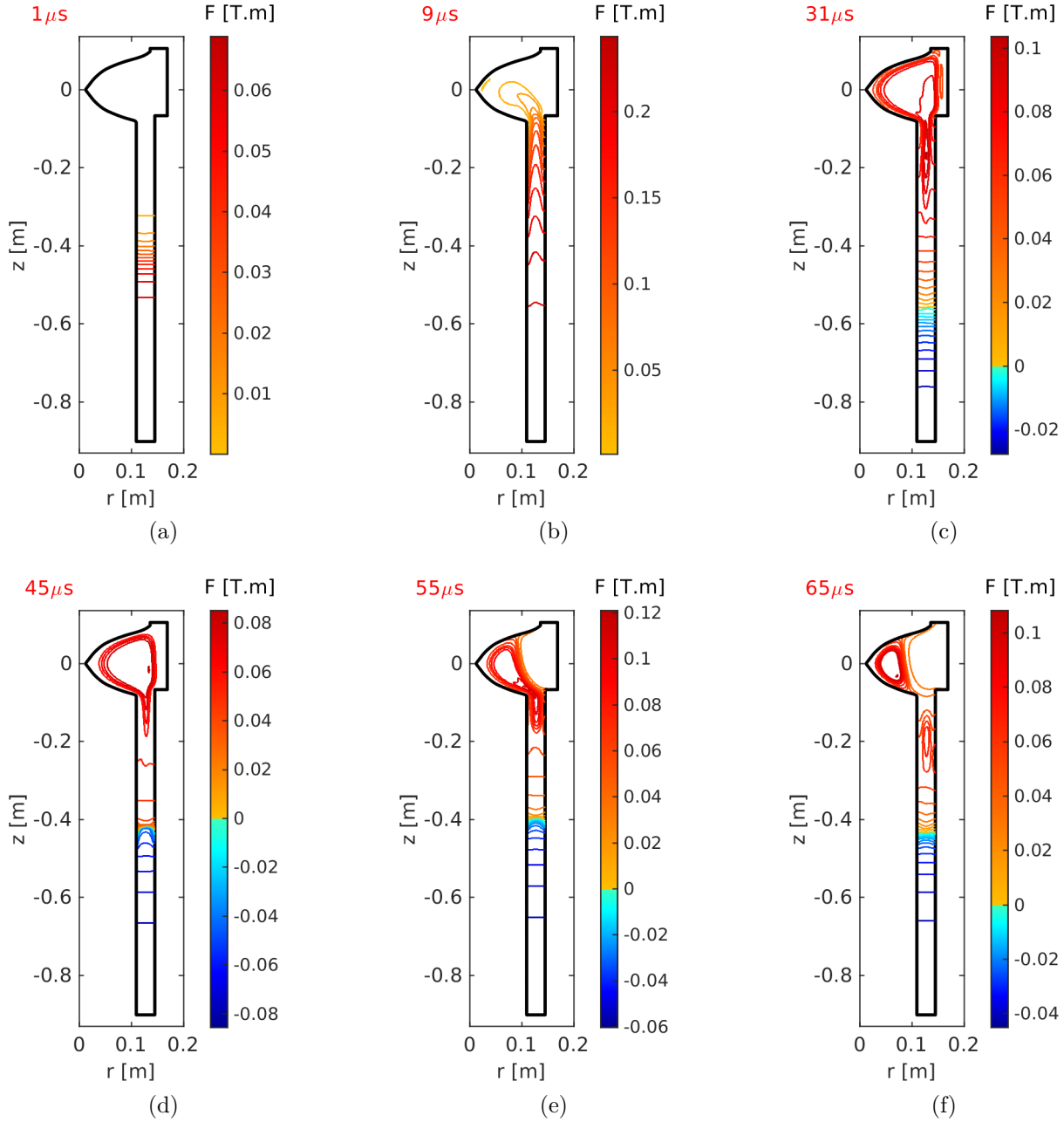


Figure 7.3.3: Lines of poloidal current (f contours)

Figure 7.3.3 shows contours of f at various times from simulation 2353. Recall that contours of $f = rB_\phi$ represent lines of poloidal current. Initially, f is zero at all nodes. At $1\mu\text{s}$, it can be seen how radial formation current between the gun electrodes is concentrated around the gas valve location, at $z = -0.43$ m. Referring to equation A.7.18, it can be seen how radial current corresponds to axial gradients in f . Closely spaced contours indicate regions of high gradients and high poloidal currents. To simulate formation, toroidal flux is being added to the domain according to the geometric profile shown in figure 6.3.1(a). At $1\mu\text{s}$, f is constant, at its highest value in the domain, below the lowermost contour at

$z \sim -0.55$ m representing $f \sim 0.07$ T-m. By 9 μ s, plasma has been advected upwards, and poloidal current is flowing along open poloidal magnetic field lines that remain resistively pinned to the electrodes down the gun. By 31 μ s (figure 7.3.3(c)) poloidal current is flowing along closed and open poloidal magnetic field lines, and most of the toroidal flux in the domain has been advected with the plasma into the containment region. At this time, as the level of toroidal flux added to the domain below the gas valve locations, which is equal to the total toroidal flux in the domain, falls off (see figure 6.4.1(a)), radial currents between the electrodes further down the gun reverse direction, and f becomes negative, as consequences of toroidal flux conservation and upward advection of toroidal flux. As shown in figure 7.3.3(d), (e) and (f), poloidal current flows around the closed poloidal field lines of the main CT as it is being compressed, and around the closed poloidal field lines of the smaller pinched off CT at 65 μ s.

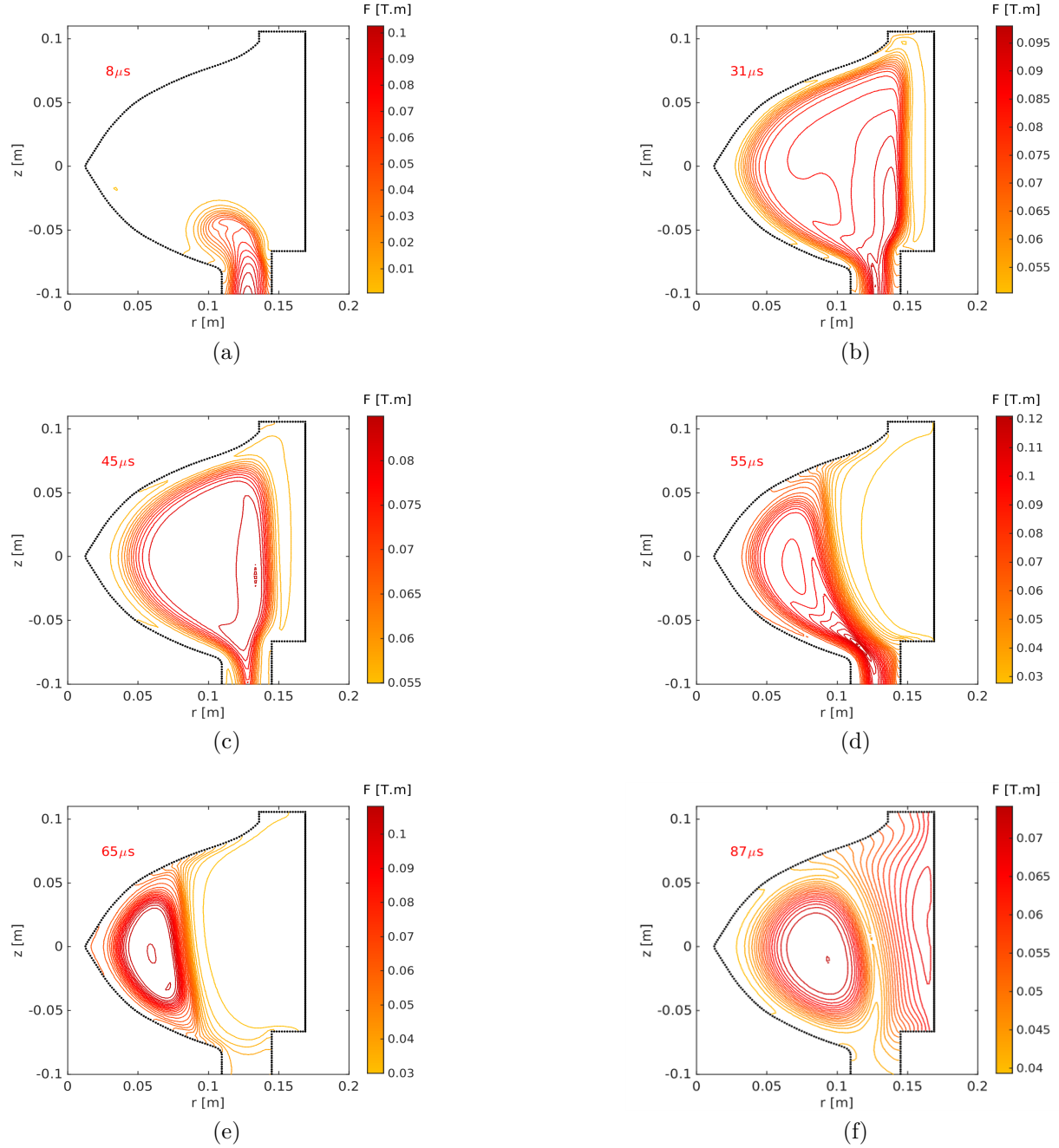


Figure 7.3.4: Lines of poloidal current (f contours), CT confinement region

Figure 7.3.4 shows close-up views of f contours at various times in the CT confinement region. It can be seen how the imposition of toroidal flux conservation leads, at compression, to the induction of poloidal currents flowing from wall-to-wall just external to the outboard boundary of the CT (figures 7.3.4(d) to (f)). This is a partial illustration of the mechanism behind the experimentally observed compressional instability discussed in section 4.2. Note that 2D simulations, which neglect inherently three dimensional turbulent transport and flux conversion, generally overestimate the level of hollowness of the field profiles.

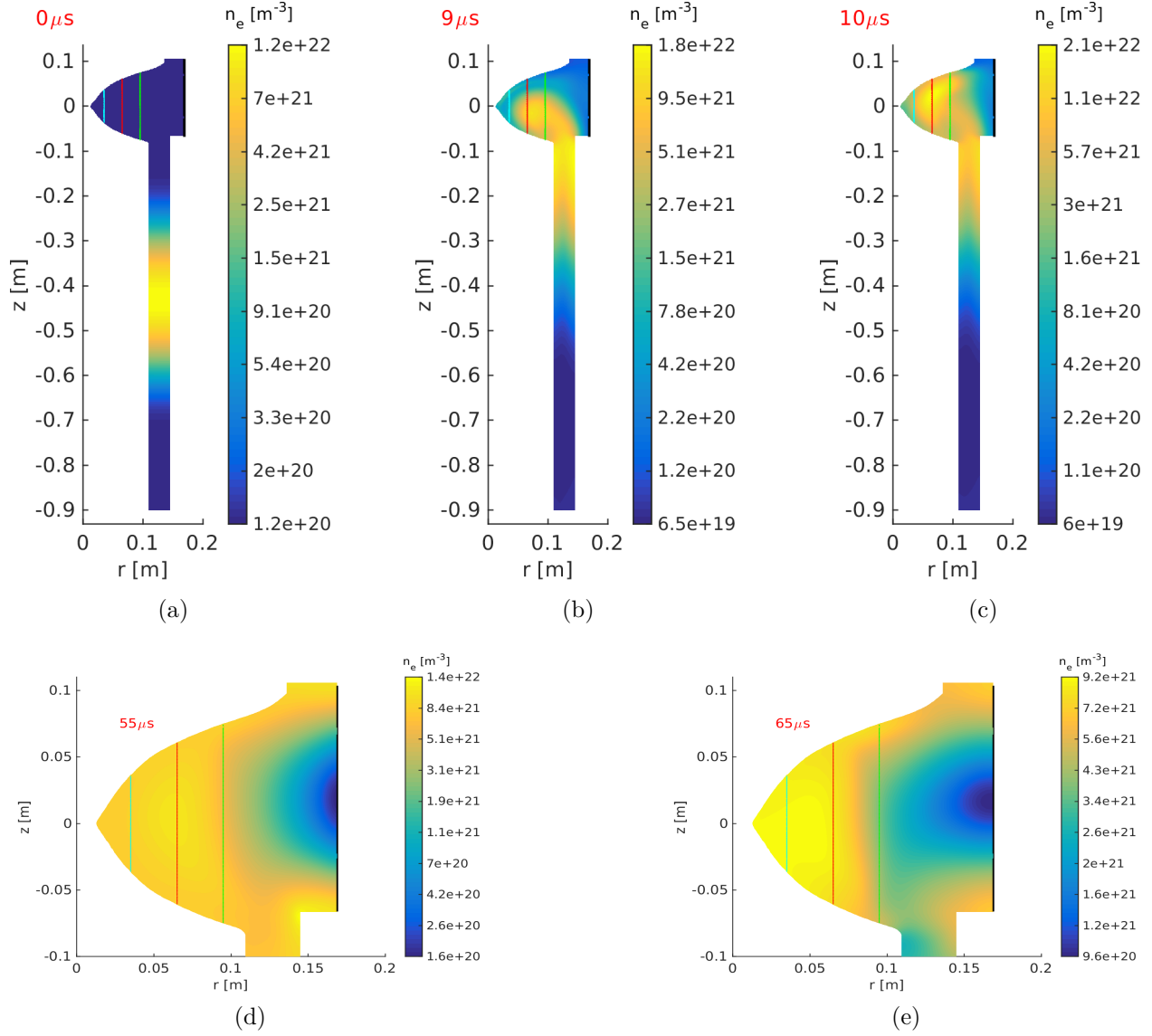


Figure 7.3.5: Electron density profiles

Figure 7.3.5(a) shows the initial profile for the electron density. As described with equation 7.1.1, the initial density profile is defined with a Gaussian profile centered around the axial coordinate of the locations of the gas puff valves. Plasma is advected up the gun during CT formation, and bubbles-in to the containment region, as shown in figures 7.3.5(b) and (c). In figures 7.3.5(d) and (e), it can be seen how density rises over compression around the CT core, and that a region of low density remains outboard of the compressed CT. The vertical blue, red and green chords in the CT containment region in figures 7.3.5(a) to (e) represent the lines of sight of the interferometer measurements (*cf.* figure 2.2.2), along which simulated line averaged-electron density is evaluated for comparison with experimental data.

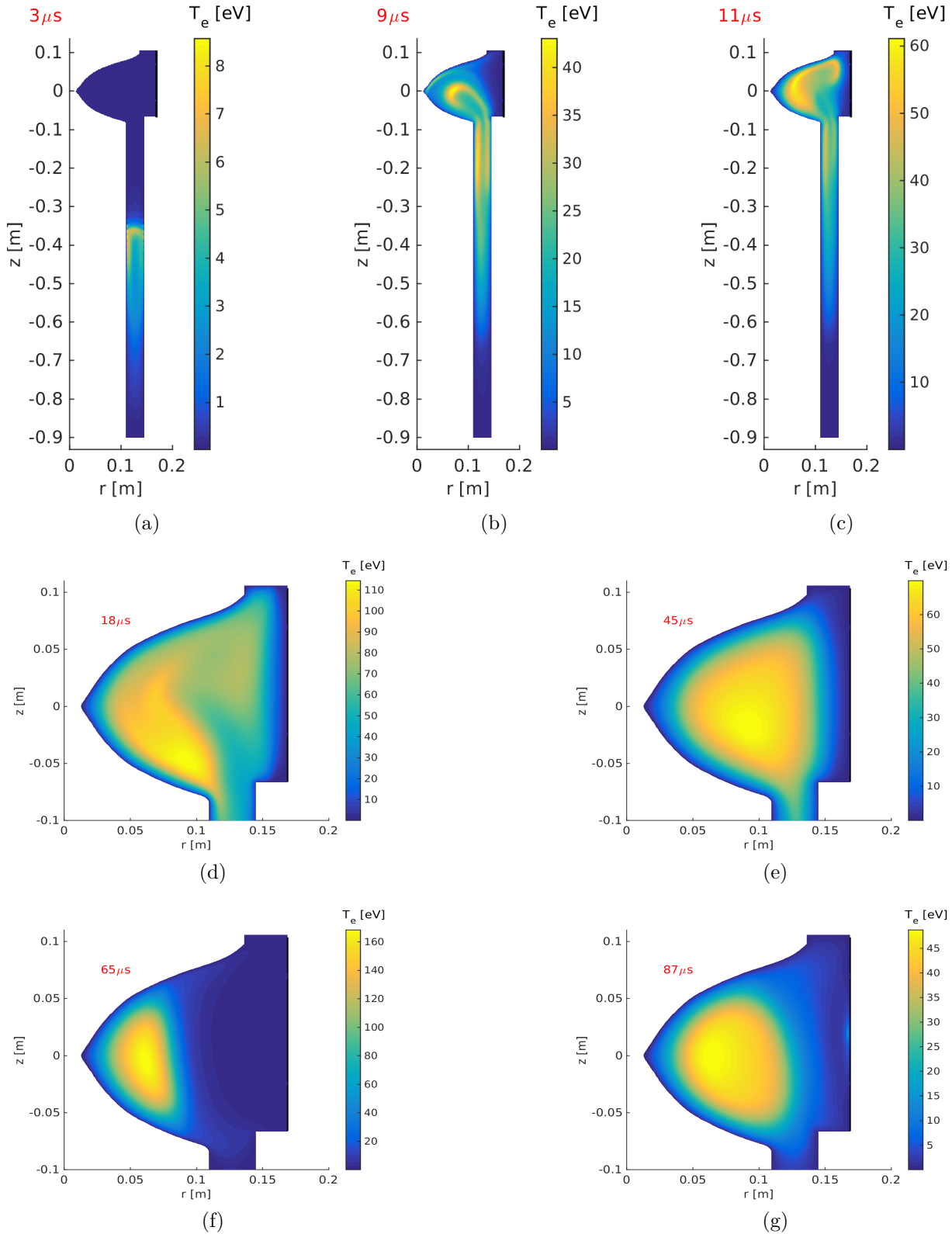


Figure 7.3.6: Electron temperature profiles

Formation current ohmically heats initially cold electrons as plasma is pushed up the gun into the containment region (figures 7.3.6(a) to (c)). The temperature of 115 eV attained by

electrons near the containment region entrance at 18 μ s (figure 7.3.6(d)) is partially due to heat exchange with ions, which, as indicated in figure 7.3.7(d)), have been heated to around 280 eV near the same area at this time due to viscous heating. Thermal diffusion through the boundary causes the electron temperature around the CT core to be reduced to around 70 eV just prior to magnetic compression at 45 μ s. Electron temperature is more than doubled, to 165 eV, at peak magnetic compression at 65 μ s. Comparing with figures 7.3.8 and 7.3.9, it can be seen how ohmic heating is a principal electron heating mechanism. Compressional heating is the main heating mechanism during magnetic compression, and is supplemented by enhanced ohmic heating. When compression time is short compared with the plasma resistive diffusion time, the adiabatic compression relationship of constant pV^γ determines compressional heating, and temperature should scale approximately as $V^{-\frac{2}{3}}$, as in table 1.4.1. As discussed in section 7.5.3.4, electron and ion temperatures at compression increase more, while density increases less, than the predicted increases based on the adiabatic scalings, due to the inclusion of artificial density diffusion. Compression coil current falls to zero by around 87 μ s, by which time the CT has re-expanded, and core electron temperature has fallen to around 50 eV.

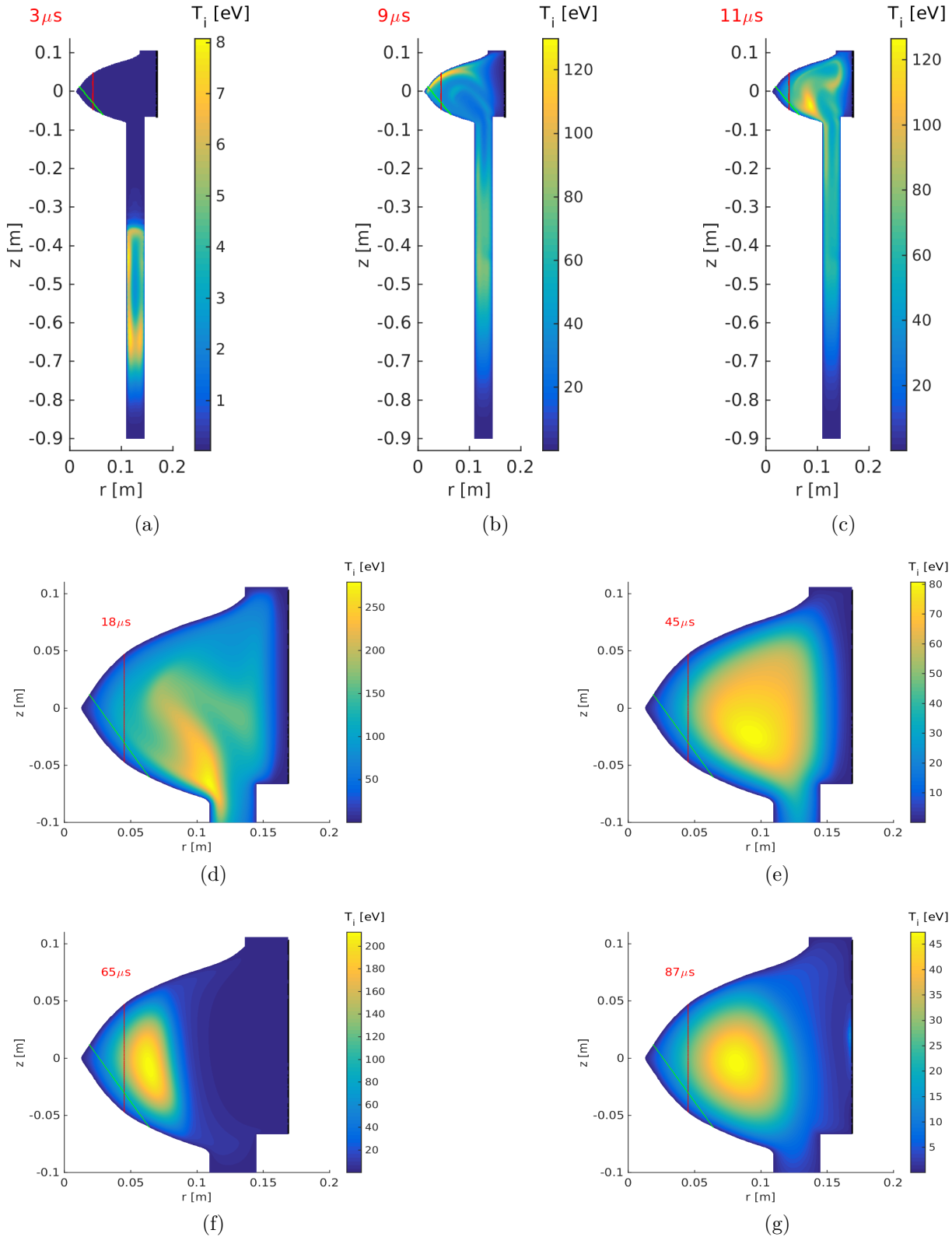


Figure 7.3.7: Ion temperature profiles

Figure 7.3.7 indicates simulated ion temperatures at the same times referred to in figure 7.3.6 for electron temperatures. Over the early stages of the simulation, ion temperature

is significantly higher than electron temperature, due to ion viscous heating during the formation process. Later, ohmic heating of electrons is the main heating source and electron temperature approaches ion temperature. Note that, as a result of compressional heating in combination with heat exchange with the electrons, which are heated ohmically by enhanced currents during compression, ion temperature is more than doubled at peak compression, increasing from around 80 to 210 eV from 45 μ s to 65 μ s. The vertical red chord and diagonal green chord in the CT containment region in figures 7.3.7(a) to (g) represent the lines of sight of the ion-Doppler measurements (*cf.* figure 2.2.2), along which simulated line-averaged ion temperature is evaluated for comparison with experimental data.

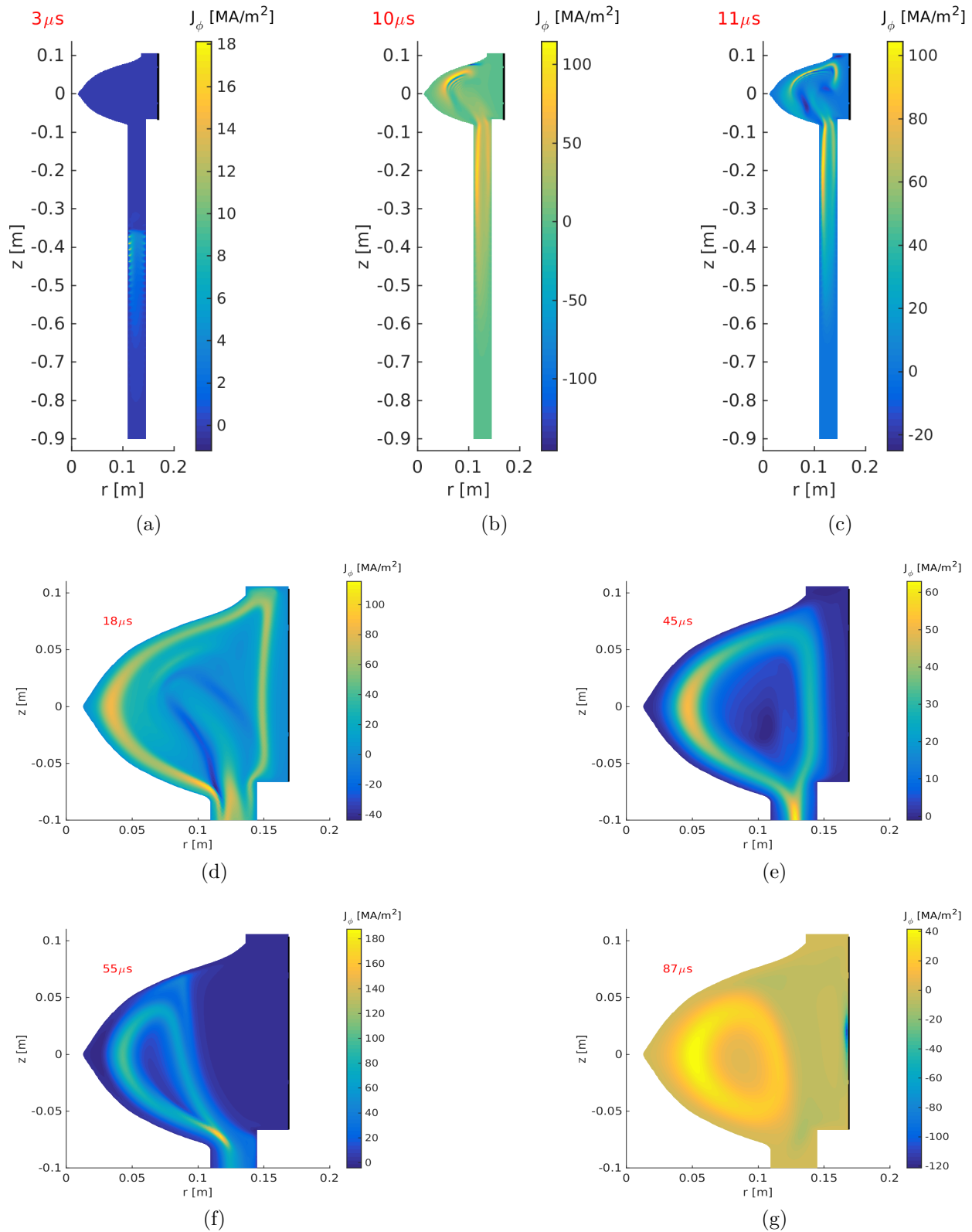


Figure 7.3.8: Toroidal current density profiles

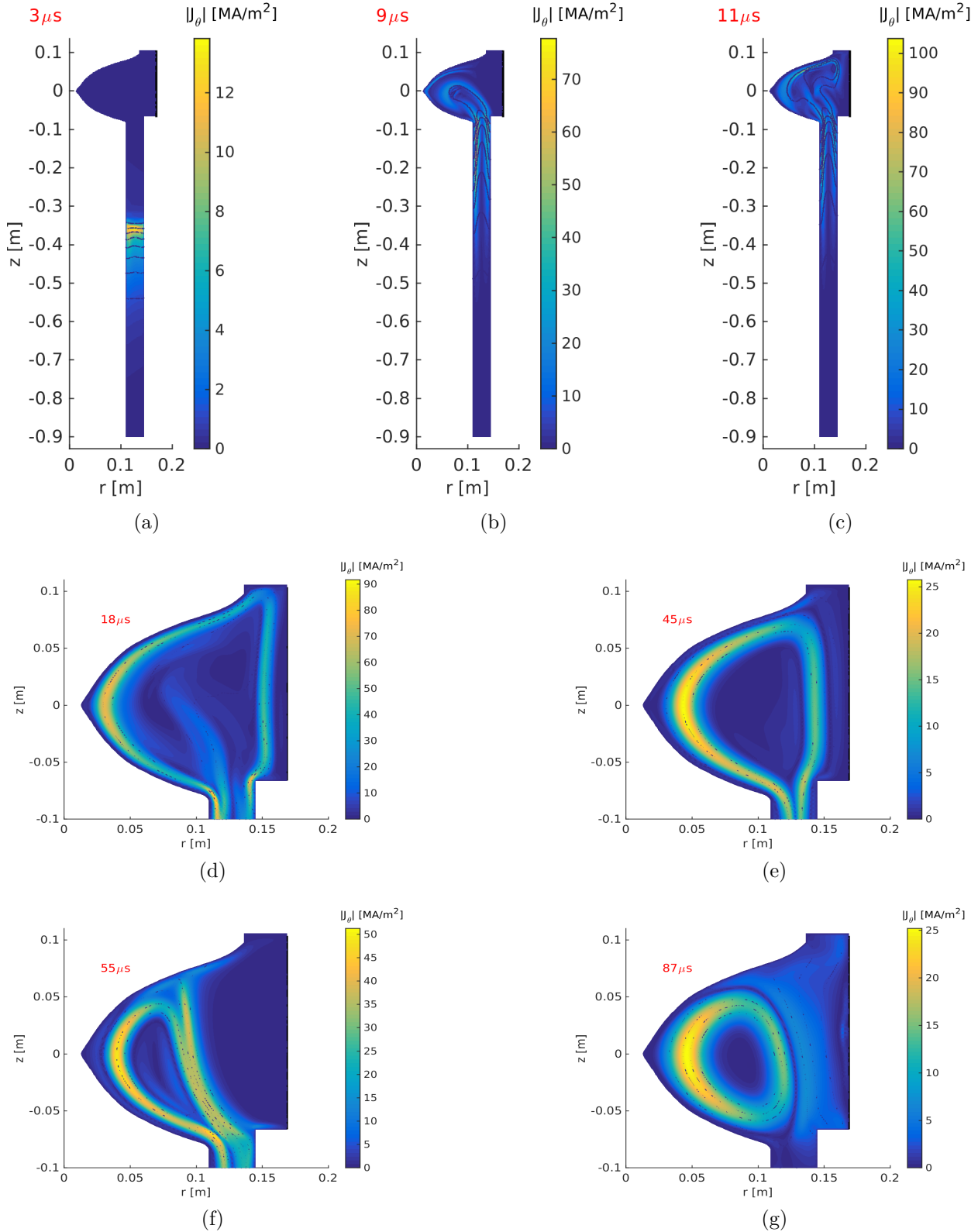


Figure 7.3.9: Poloidal current density profiles

Figures 7.3.8 and 7.3.9 shows simulated toroidal and poloidal current density at various times. The absolute value of poloidal current density, calculated as $|J_\theta| = \sqrt{J_r^2 + J_z^2}$, where

J_r and J_z are found in terms of gradients of f according to equation A.7.18, is plotted under contours of f in figure 7.3.9. Poloidal current is directed from right to left in the gun barrel, and anticlockwise in the CT containment region. Comparing with figure 7.3.6, it can be seen how ohmic heating is a principal electron heating mechanism. Note the high concentration of J_ϕ at 55 μ s (figure 7.3.8(f)), relating to the toroidally directed current sheet present between oppositely directed poloidal field lines during the magnetic reconnection process that occurs as closed CT field lines that extend down the gun, and then open field lines surrounding the CT, are pinched off during magnetic compression. A reconnection-related current sheet is also evident when open poloidal field lines reconnect to form closed CT flux surfaces, for example at 18 μ s (figure 7.3.8(d)). It can be seen how the current density profiles are remarkably hollow; as mentioned previously, 2D simulations generally overestimate the level of hollowness of the field profiles.

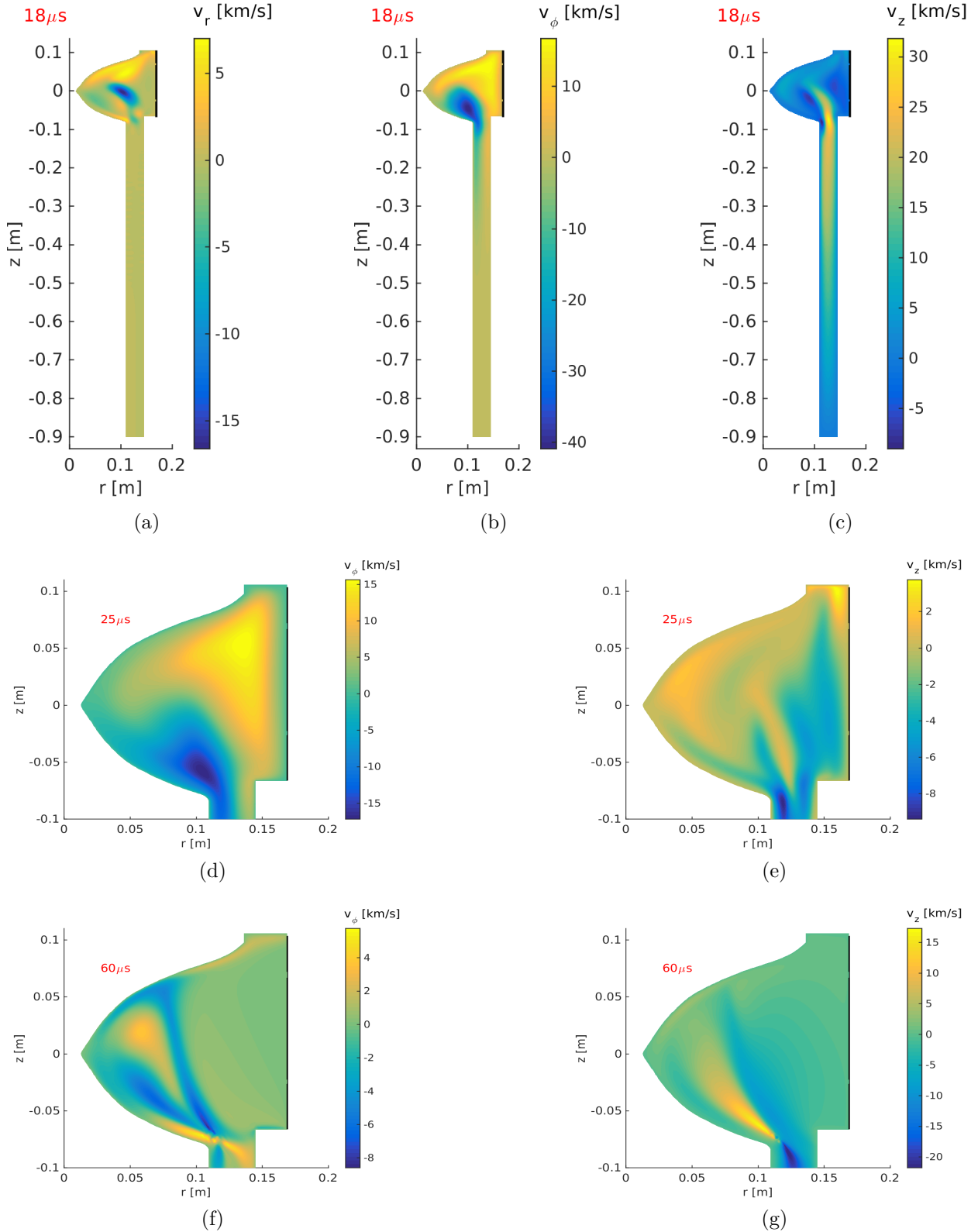


Figure 7.3.10: Profiles of various velocity components

Figure 7.3.10(a) to (c) indicates profiles of v_r , v_ϕ and v_z from simulation 2353 at $18\mu\text{s}$. The dynamics are complicated, but some key features can be noted. Velocities, in particular v_z ,

are especially high around this time during the CT formation process, and lead to enhanced ion viscous heating (see figure 7.3.7(c)). Pre-compression profiles of v_ϕ and v_z are shown at 25 μ s in figures 7.3.10(d) and (e). As discussed in [102], internal flows are naturally associated with plasma in toroidal geometry if the externally imposed magnetic and electric fields are curl-free. When externally imposed magnetic and electric fields are curl-free, the curl of the Lorentz force is finite, so it cannot be balanced by the pressure gradient. When the curl of the Lorentz force is finite, it acts as a source of vorticity. Toroidal vorticity leads to poloidal rotation which interacts with toroidal magnetic field leading to poloidal current density. Poloidal current density and poloidal field lead to toroidal velocities, which are directed according to the relative orientation of the poloidal current density and poloidal magnetic field. The toroidal velocities shown in figure 7.3.10(d), when the CT is approaching an equilibrium state, may result partially from this effect. Simulations run starting with a Grad-Shafranov equilibrium exhibit qualitatively similar toroidal velocity profiles, generally with either a dipolar structure or a quadrupolar structure in v_ϕ . The particularly high downward-directed axial velocity near the entrance to the CT containment region at 25 μ s in figure 7.3.10(e) is related to jets of plasma fluid associated with magnetic reconnection during the formation of closed CT flux surfaces. Velocities are gradually dissipated by viscous effects until $t_{comp} = 45 \mu$ s, when magnetic compression is initiated and velocities rise sharply in reaction to the various dynamics associated with compression. The structures in the profiles of v_ϕ and v_z near the entrance to the CT containment region at 60 μ s (figures 7.3.10(f) and (g)), just after halfway through the main compression cycle, are related to jets of plasma fluid associated with magnetic reconnection when open poloidal field lines surrounding the CT are pinched off.

7.4 Evolution of fields when I_{comp} changes polarity, simulation 2287

As described in chapter 4, when the compression current in the coils changes direction (see figure 2.1.4), the CT poloidal field magnetically reconnects with the compression field, and a new CT with polarity opposite to that of the previous CT is induced in the containment region, compressed, and then allowed to expand. The process repeats itself at each change in polarity of the compression current until either the plasma loses too much heat, or the compression current is sufficiently damped.

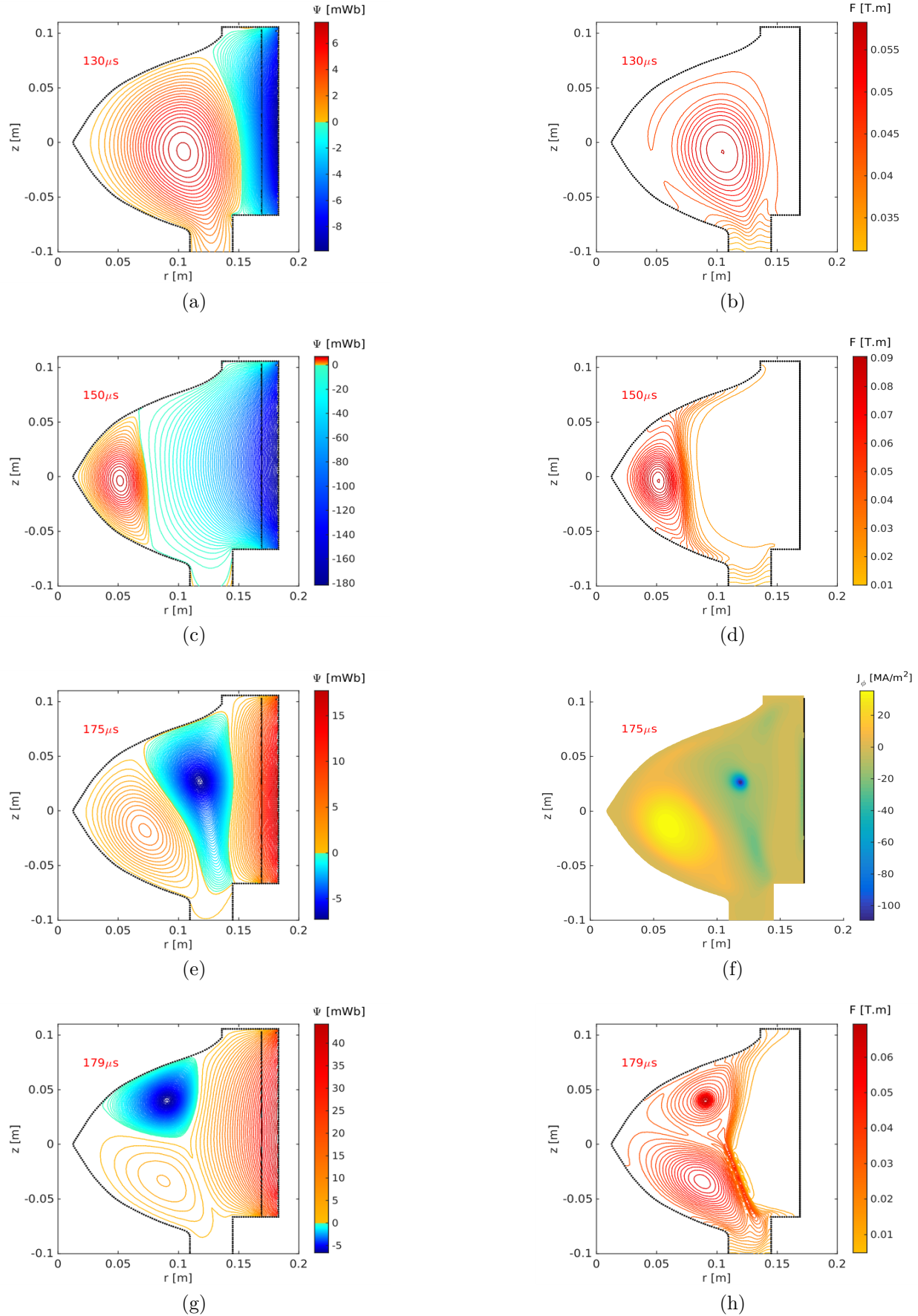


Figure 7.4.1: ψ and f contours, and J_ϕ profiles, for a simulation with compression current reversal

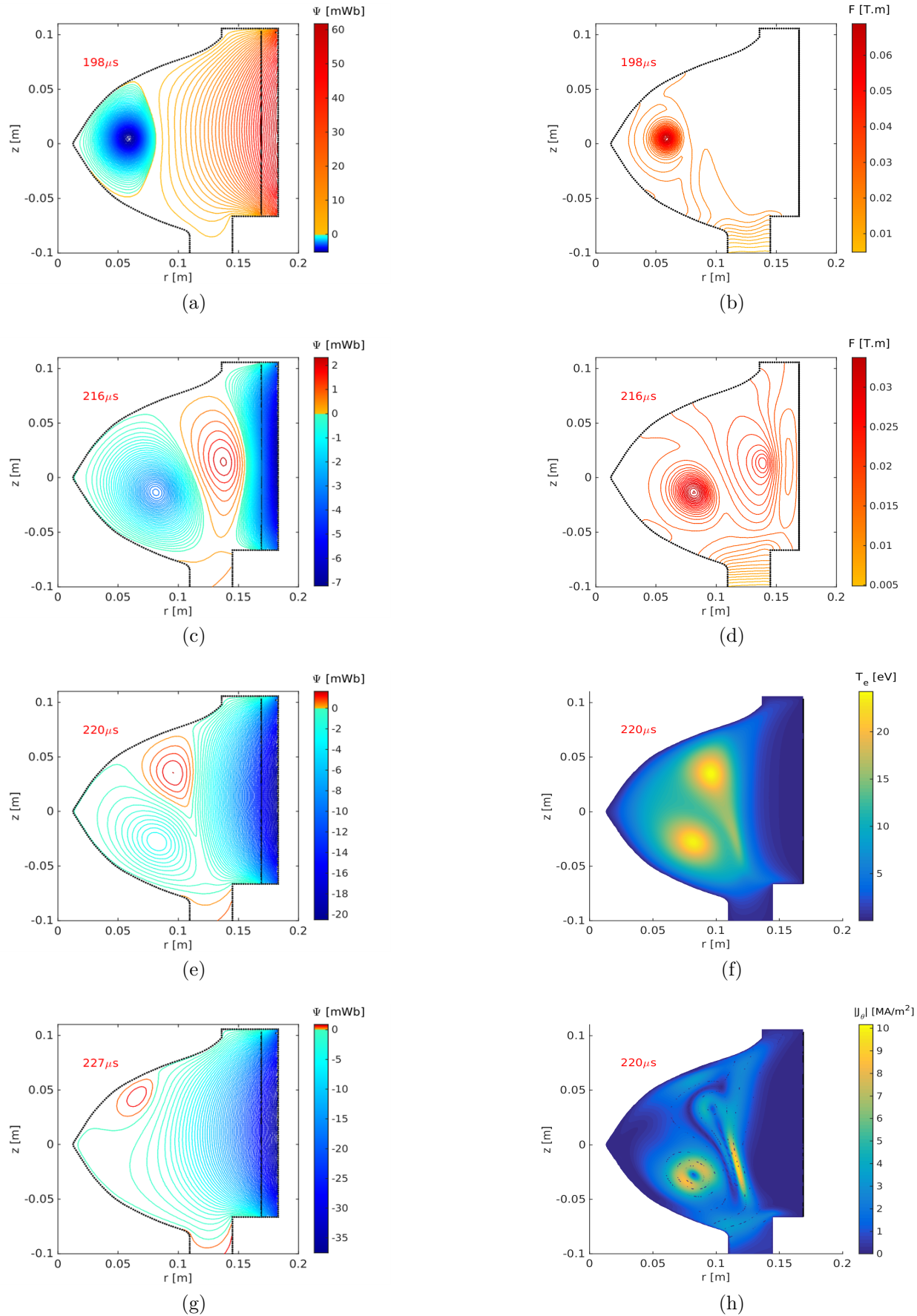


Figure 7.4.2: (sequence continued) ψ and f contours, and T_e and J_θ profiles, for a simulation with compression current reversal 208

Figures 7.4.1 and 7.4.2 show contours of ψ and f , and profiles of J_ϕ , T_e and J_θ from simulation 2287 at various times. Magnetic compression begins at $t = t_{comp} = 130 \mu\text{s}$, and peak compression is at $150 \mu\text{s}$. By $175 \mu\text{s}$, the external compression field has changed polarity. Toroidal currents are induced to flow in the ambient plasma initially located outboard of the original CT, enabling the formation of a new CT (blue closed contours) with polarity opposite to that of the original CT (figures 7.4.1(e) and (f)). The external compression field starts to reconnect with the poloidal field of the original CT at $179 \mu\text{s}$. The new induced CT is magnetically compressed inwards by the increasing reversed polarity compression field, with peak compression at around $198 \mu\text{s}$ (figures 7.4.2(a) and (b)). The compression field polarity rings back to its original state by $216 \mu\text{s}$, and a third CT is induced, with the same polarity as the original CT (figures 7.4.2(c) and (d)). The poloidal field of the second CT starts to reconnect with the compression field at around $220 \mu\text{s}$. Electron temperature and poloidal current density at $220 \mu\text{s}$ for the two co-existing CTs is presented in figures 7.4.2(f) and (h). By $227 \mu\text{s}$, the poloidal flux of the third CT, which is being compressed inwards during the third compression cycle, has almost decayed away (figure 7.4.2(g)). Comparison of simulated diagnostics outputs for simulation 2287 with experimental measurements from the relevant shot will be presented in section 7.5.2.2.

7.5 Simulated diagnostics, and comparison with experimental results

The experimental diagnostics that can be modelled in simulations are poloidal and toroidal magnetic field measured at the magnetic probes locations, the CT outer separatrix radius (see section 3.7), line averaged electron density along the interferometer chords, and ion temperature along the ion-Doppler chords. The methods developed to implement the simulated diagnostics measurements to the code have been described in section 6.5.

7.5.1 Non-compression shots/simulations

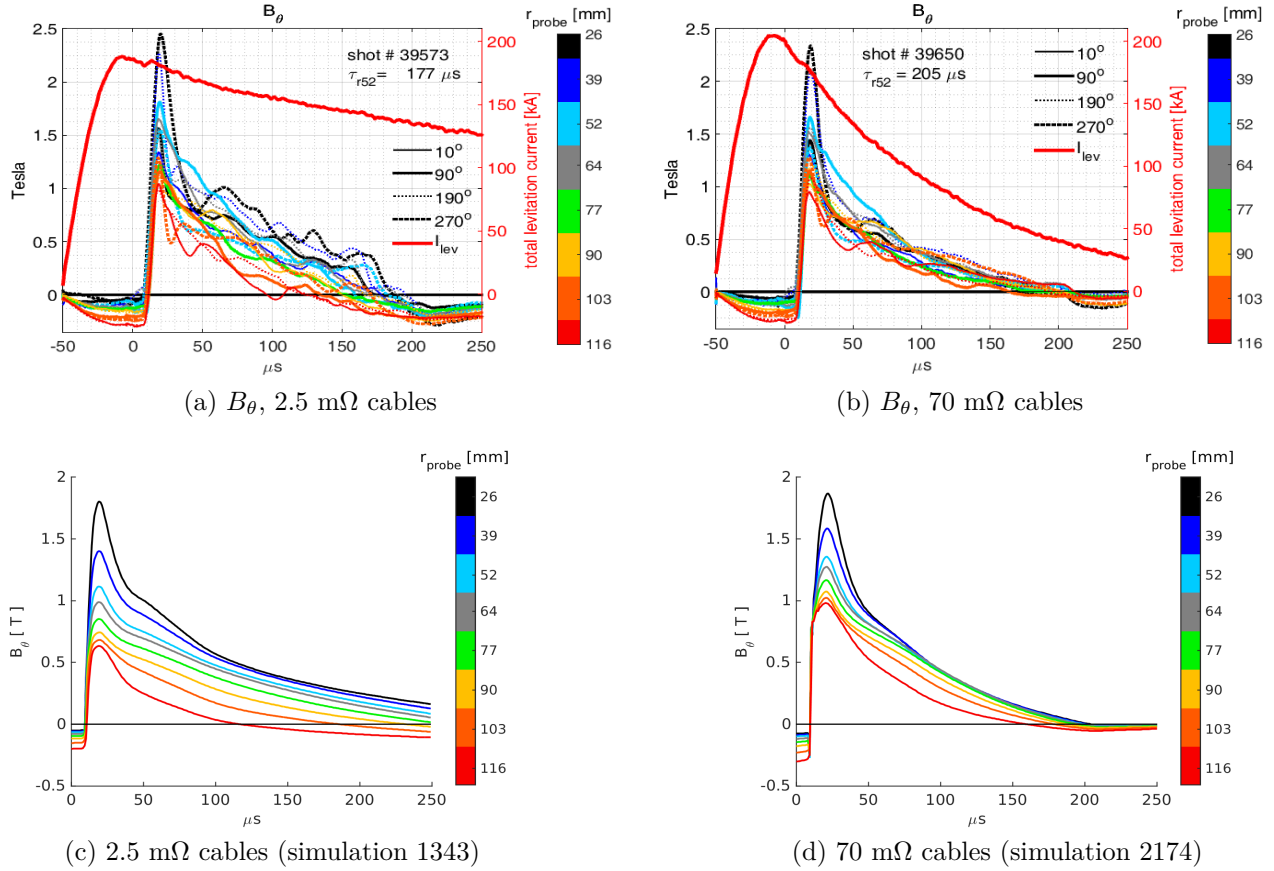


Figure 7.5.1: Comparison of measured and simulated B_θ (levitation - eleven coils)

Figures 7.5.1(a) and (b) show experimentally measured B_θ for two shots with different resistances (R_{cable}) of the cables between the levitation coil (or coil-pair) and main levitation inductor in each of the six levitation circuits (see figure 2.1.3), for the 11-coil configuration (for convenience, figures 3.6.2(a) and (b) have been reproduced here). For comparison, figures 7.5.1(c) and (d) show B_θ recorded at the probe locations for MHD simulations in which the boundary conditions pertaining to the levitation field were evolved over time according to the two different experimentally measured waveforms for I_{lev} , which depend on R_{cable} . The two $I_{lev}(R_{cable}, t)$ waveforms are indicated in figure 7.5.1(a) and (b), right axes. The B_θ traces in figure 7.5.1(c) are from a simulation which had code input parameter R_{cable} set to zero (see section 7.1), while the B_θ traces in figure 7.5.1(d) are from a simulation which had input R_{cable} set to one. Additional code input parameters for these two simulations were approximately the same as for simulation 2353 (table 7.1.1), but with $V_{comp} = 0$ kV.

Comparing the B_θ traces in figures 7.5.1(a) and 7.5.1(c), it can be seen how the comparison

is qualitatively good up until around $170\ \mu\text{s}$, when the compressional instability (discussed in section 4.2), which is not captured by the 2D MHD dynamics, causes the CT to be extinguished rapidly. The comparison in figures 7.5.1(b) and 7.5.1(d) remains good at all times, as the compressional instability did not arise in the case with decay rate matching.

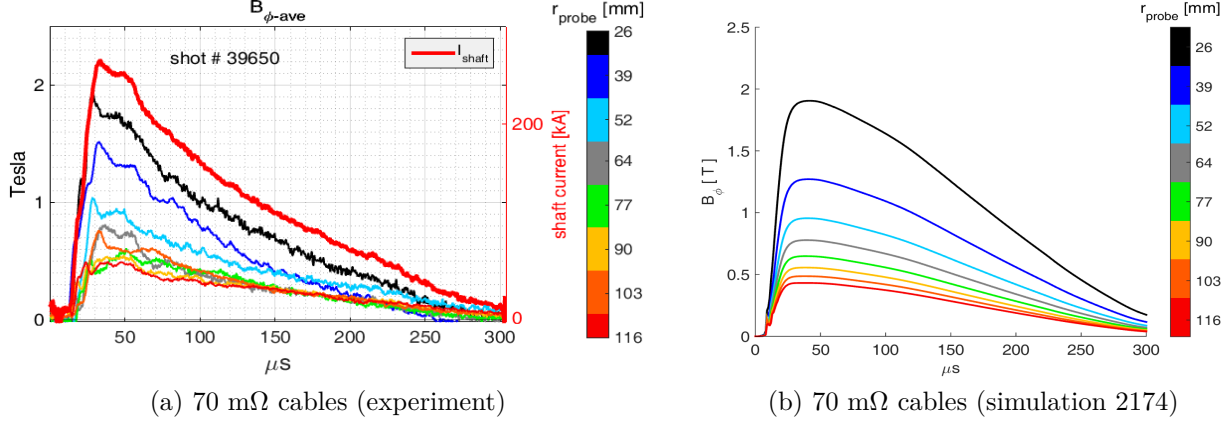


Figure 7.5.2: Comparison of measured and simulated B_ϕ (levitation - eleven coils)

Figure 7.5.2(a) shows experimentally measured B_ϕ for a shot with $70\ \text{m}\Omega$ cable resistance taken with the 11-coil configuration. For ease of comparison, the toroidal averages of the toroidal field traces measured at the two probes 180° apart at each of the eight radii at which the chalice magnetic probes are located (see table 2.2.1) are shown here. With $70\ \text{m}\Omega$ cable resistance, the compressional instability that was routinely observed on levitation-only shots with the $2.5\ \text{m}\Omega$ cable resistance (*e.g.*, see figure 3.6.2(c)) is not manifested on the toroidal field measurements, so the simulated toroidal field is a good match (2D simulations cannot reproduce the compressional instability). Note that this simulation includes the resistive contribution (section 6.3.1) to Φ_{form} ; simulated B_ϕ decreases much more gradually over time after formation, and doesn't match the experimental measurement, if the resistive contribution is neglected.

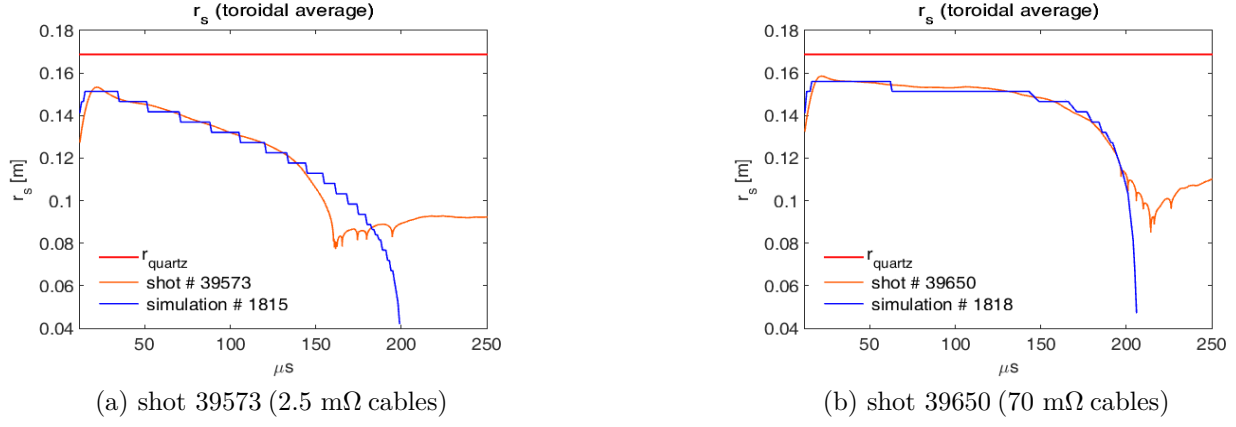


Figure 7.5.3: Comparison of experimentally measured and simulated CT separatrix radius

Figure 7.5.3(a) shows the close match obtained between the toroidally-averaged, experimentally inferred separatrix radius, $r_s(t)$ (from figure 3.7.7(b), see section 3.7), and the separatrix radius determined by MHD simulation. Shot 39573 was taken with the 2.5 mΩ cables in place, and, for comparison, simulation 1815 had code input parameter $R_{\text{cable}} = 0$.

Similarly, figure 7.5.3(b) shows the match obtained between the toroidally-averaged, experimentally inferred separatrix radius (from figure 3.7.4), and the simulated separatrix radius. Shot 39650 was taken with the 70 mΩ cables in place, and simulation 1818 was run with $R_{\text{cable}} = 1$.

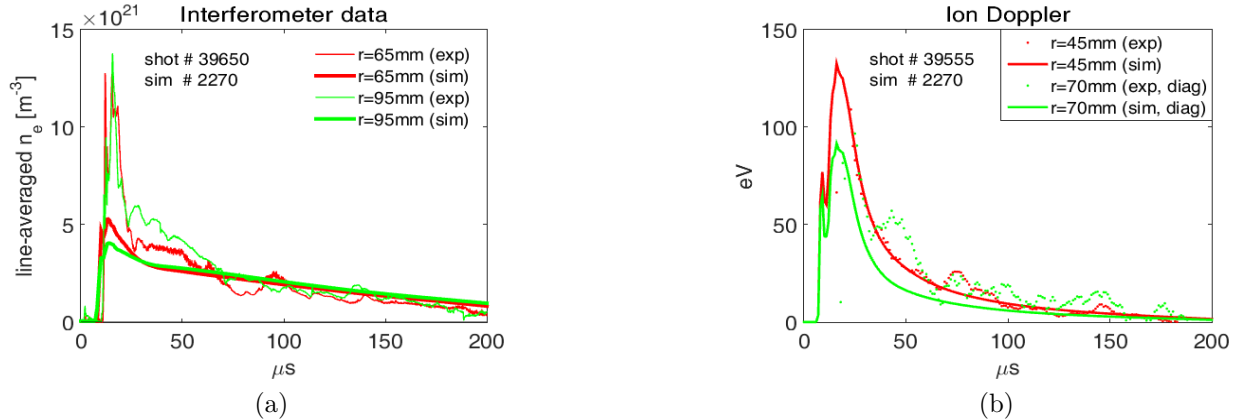


Figure 7.5.4: Comparison of measured and simulated n_e and T_i (levitation only)

Figures 7.5.4(a) and 7.5.4(b) indicate the approximate agreement between experimentally measured and simulated electron density and ion temperature in the case without magnetic compression. The simulated diagnostics for n_e and T_i are simply the line-averaged quantities along the chords indicated in figures 2.2.2, 7.3.5 and 7.3.7. Note that the interferometer looking along the vertical chord at $r = 35$ mm was generally not functioning during the experiment, and so the experimentally measured and simulated line averaged electron density

along that chord hasn't been included in figure 7.5.4(a). In general, compared with the simulated line averaged electron density, the experimentally measured density is higher initially and decays much faster over the first 70 μs or so. This may be related to the rapid recombination of high Z impurity ions that are initially injected to the plasma during the formation process, through the action of sputtering on the electrodes and the insulating outer wall of the CT confinement region. This mechanism would not be captured by the simulation. Another possible explanation is the action of artificial density diffusion, which effectively relocates particles from high density regions to low density regions. This effect is pronounced when the density gradients are more extreme, such as during the formation process.

Code input parameters ν_{phys} and ν_{num} (see section 7.1) were set to 450 m^2/s and 700 m^2/s respectively for simulation 2270, so that ion viscous heating is reduced to an acceptable level, leading to a close match to the experimentally measured ion temperature.

7.5.2 Compression shots/simulations

7.5.2.1 Shots 39475, 39738, and 39510

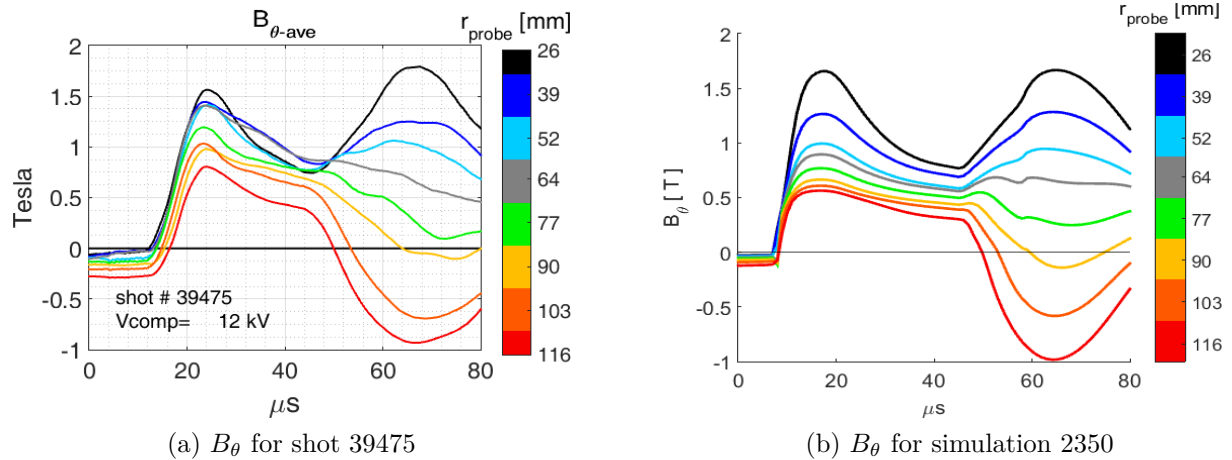


Figure 7.5.5: Comparison of measured and simulated B_θ (compression - eleven coils)

Figure 7.5.5 indicates the comparison between experimentally measured and simulated poloidal field at the magnetic probe locations. For shot 39475 and simulation 2350, $V_{comp} = 12 \text{ kV}$ and $t_{comp} = 45 \mu\text{s}$ (code input parameters for simulation 2350 were the same as for simulation 2353 (table 7.1.1), but with $V_{comp} = 12 \text{ kV}$). For ease of comparison, the toroidal averages of the poloidal field traces measured at the two probes 180° apart at each of the eight radii at which the chalice magnetic probes are located (see table 2.2.1) are shown in figure 7.5.5(a). These

axisymmetric MHD simulations allow for only resistive loss of flux and do not capture inherently three-dimensional plasma instabilities that can lead to poloidal flux loss. Shot 39475 was a flux-conserving shot, and therefore a good match between experimentally measured and MHD-simulated poloidal field is obtained.

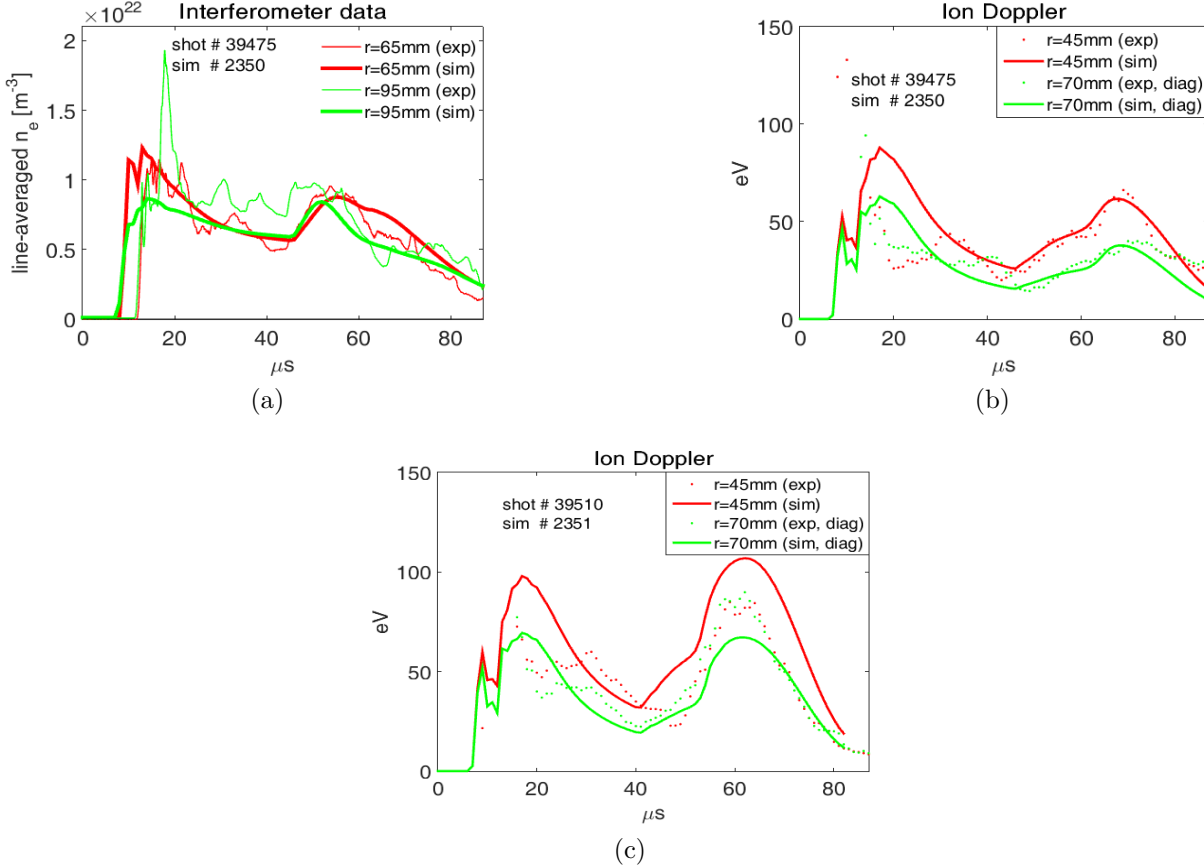


Figure 7.5.6: Comparison of measured and simulated n_e and T_i (compression shots)

Figures 7.5.6(a) and 7.5.6(b) indicate the agreements between experimentally measured and simulated electron density and ion temperature in the case with magnetic compression for shot 39475 and simulation 2350. The simulated line averaged electron density along the interferometer chord at $r = 35$ mm hasn't been included in figure 7.5.6(a) because the experimental data for that chord is not available. It can be seen how the time it takes for plasma to be advected up the gun and enter the CT containment region is underestimated by ~ 5 μ s in this simulation. The electron density and ion temperature magnitudes during CT decay and magnetic compression are approximately reproduced by the simulation. Figure 7.5.6(c) shows the comparison between the experimental and simulated ion-Doppler measurements for shot 39510 and simulation 2351. Like shot 39475, shot 39510 was also a flux conserving shot, but with $t_{comp} = 40$ μ s, and increased compressional energy, with $V_{comp} = 18$ kV. Code input parameters for simulation 2351 were approximately the same as for simulation 2353

(table 7.1.1), but with $t_{comp} = 40 \mu\text{s}$.

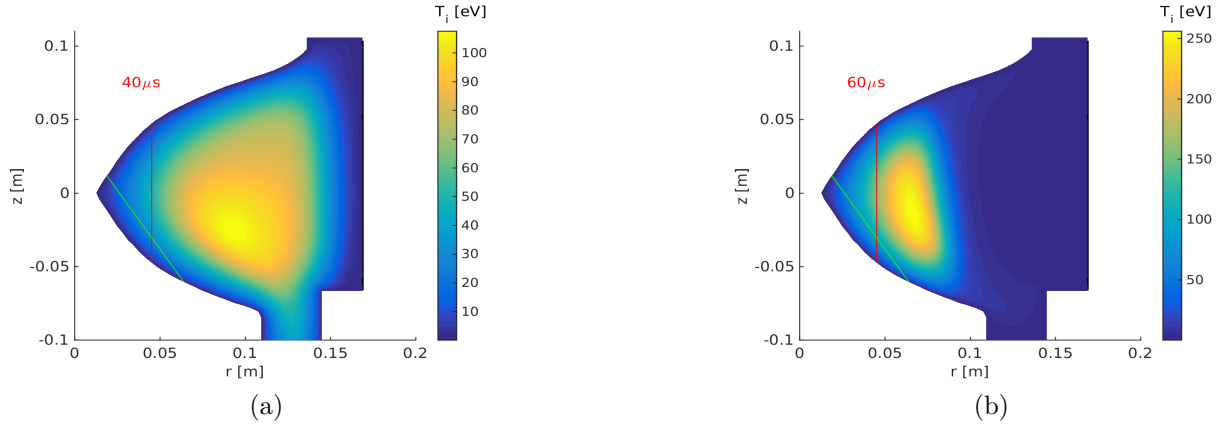


Figure 7.5.7: T_i contours, simulation 2351

When the experimental ion-Doppler measurement is matched by simulations, simulated core ion temperature increases by a factor of around 2.5 over the main compression cycle, as indicated in figure 7.5.7, in which contours of ion temperature, for a simulation of shot 39510, are shown just prior to magnetic compression ($t = 40 \mu\text{s}$) and at around peak compression ($t = 60 \mu\text{s}$). As seen from figure 2.2.2, the ion-Doppler chords are located well away from the CT core.

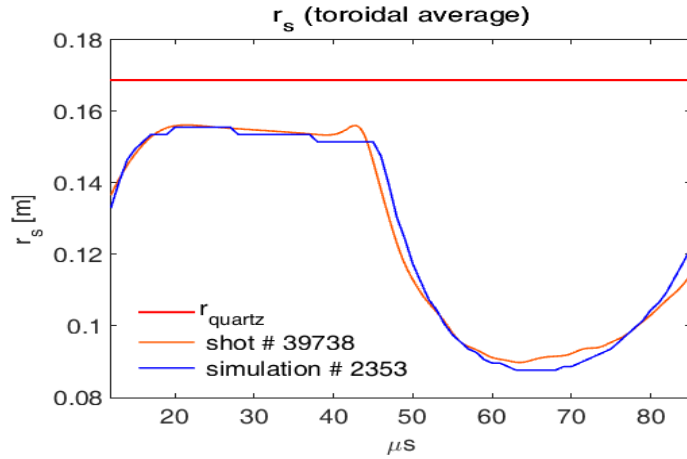


Figure 7.5.8: Comparison of measured and simulated r_s with magnetic compression

Figure 7.5.8 shows the comparison obtained between the toroidally-averaged, experimentally inferred separatrix radius, $r_s(t)$ (from figure 4.4.1(b)), and the separatrix radius evaluated in MHD simulation 2353. Like shot 39475 (for which side probe data, and hence experimental determination of $r_s(t)$ was not available), shot 39738 was a flux-conserving shot, and a good match is found between experimentally determined and simulated r_s . Note that $V_{comp} = 18 \text{ kV}$ for shot 39738 and simulation 2353.

7.5.2.2 Shot 39735

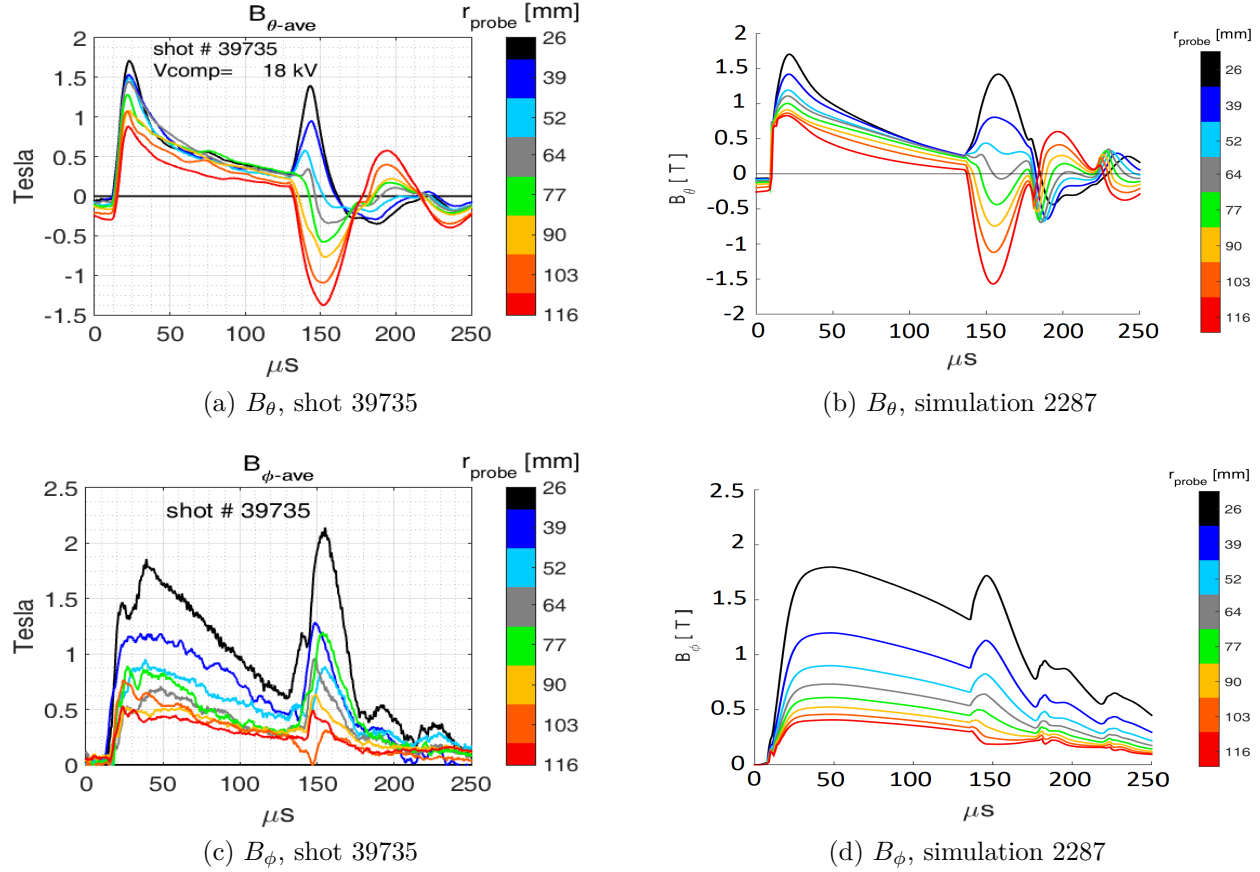


Figure 7.5.9: Comparison of measured and simulated poloidal and toroidal magnetic field at magnetic probe locations ($V_{comp} = 18$ kV, 11-coil configuration)

Figure 7.5.9 shows the comparison between experimentally measured and simulated poloidal and toroidal field, where the experimental measurements have been toroidally averaged for clarity. Shot 39735 presented here (see also figures 4.1.3 and 4.1.4(a)) had $V_{comp} = 18$ kV, and $t_{comp} = 130$ μ s. The simulation was run until $t_{sim} = 250$ μ s, and includes the time when the current in the compression coils changes polarity. Poloidal flux and f contours for this simulation were presented in section 7.4. In shot 39735, the poloidal field measured at the inner probes collapses at ~ 145 μ s, while the compression coil current peaks at ~ 150 μ s. Because of this, as outlined in section 4, shot 39735 had parameter $\tilde{\tau}_c = 0.6$, implying that poloidal flux was not well conserved during compression. Apart from resistive losses, the simulation conserves poloidal flux, so the poloidal field at the inner probes (7.5.9(b)) continues to rise until the compression coil current peaks.

The compressional instability leads to toroidal field measurements that are toroidally very asymmetric, and the axisymmetric code cannot reproduce this. Comparison of figures

7.5.9(c) and 7.5.9(d) shows how the simulated B_ϕ does, in general, rise at the magnetic probes as crowbarred shaft current increases when it is diverted to a lower inductance path (as described in section 4.2). There is at least a qualitative agreement between the simulated B_ϕ and the toroidal-averages of the measured B_ϕ .

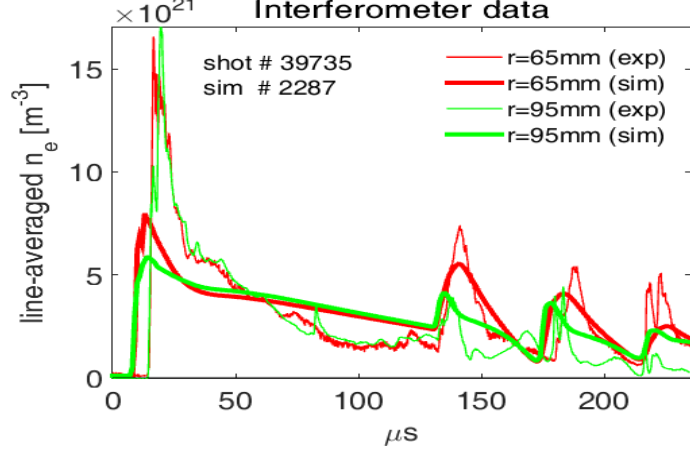


Figure 7.5.10: Comparison of measured and simulated n_e (compression shot 39735)

Figure 7.5.10 indicates the qualitative agreement between experimentally measured and simulated electron density. Note that ion-Doppler and CT outer separatrix measurements were not available for shot 39735.

7.5.2.3 Simulation of compressional flux loss

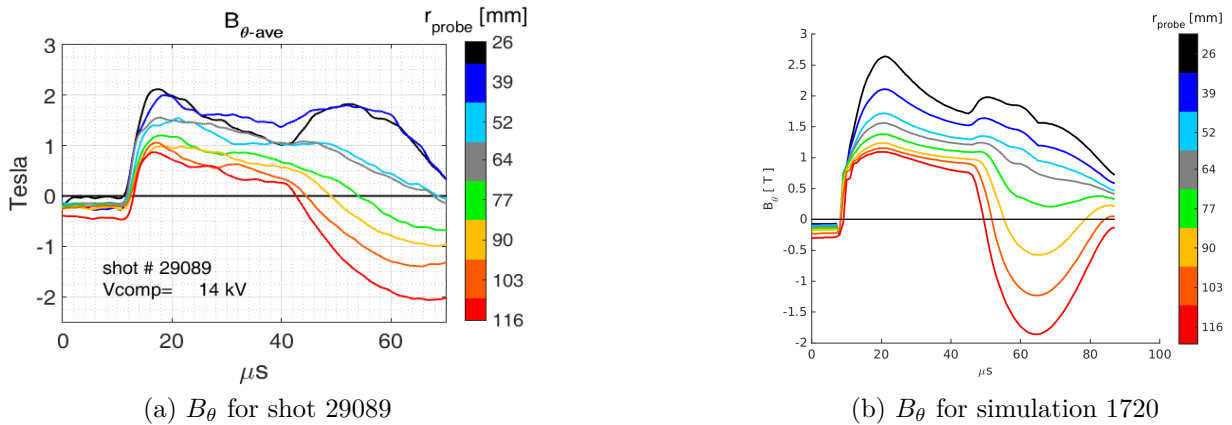


Figure 7.5.11: Measured *cf.* simulated B_θ (compression - 6 coils, with flux loss)

As discussed in section 4.3, it was usual, for shots taken in the 6-coil configuration, for the poloidal field measured at the inner probes to collapse during magnetic compression, leading

to low values of the experimentally determined compressional parameter $\tilde{\tau}_c$. It was assumed that low values of $\tilde{\tau}_c$ implied poor compressional flux conservation. To try and verify this assumption, simulations were run in which CT poloidal flux loss is imposed. Figure 7.5.11(a) shows a typical example of measured poloidal field for a compression shot taken in the 6-coil configuration. Poloidal field at the inner probes initially rises at compression, but then rapidly collapses. For comparison, poloidal CT flux is forced to decrease by 70% over the 20 μs between $t_{comp} = 45 \mu\text{s}$ and peak compression at $\sim 65 \mu\text{s}$ in simulation 1720, and the resultant poloidal field traces in figure 7.5.11(b) are a reasonable match to those in shot 29089, which has compression parameter $\tilde{\tau}_c = 0.5$, helping to confirm the hypothesis.

7.5.3 Results from additional simulated diagnostics

In this section, results from simulated diagnostics that don't have experimental counterparts will be presented and discussed.

7.5.3.1 Simulated diagnostics

for $\psi_{CT}(t)$, $T_{max}(t)$, $r_s(t)$, $r_{axis}(t)$, $V_{CT}(t)$, and $\beta(t)$

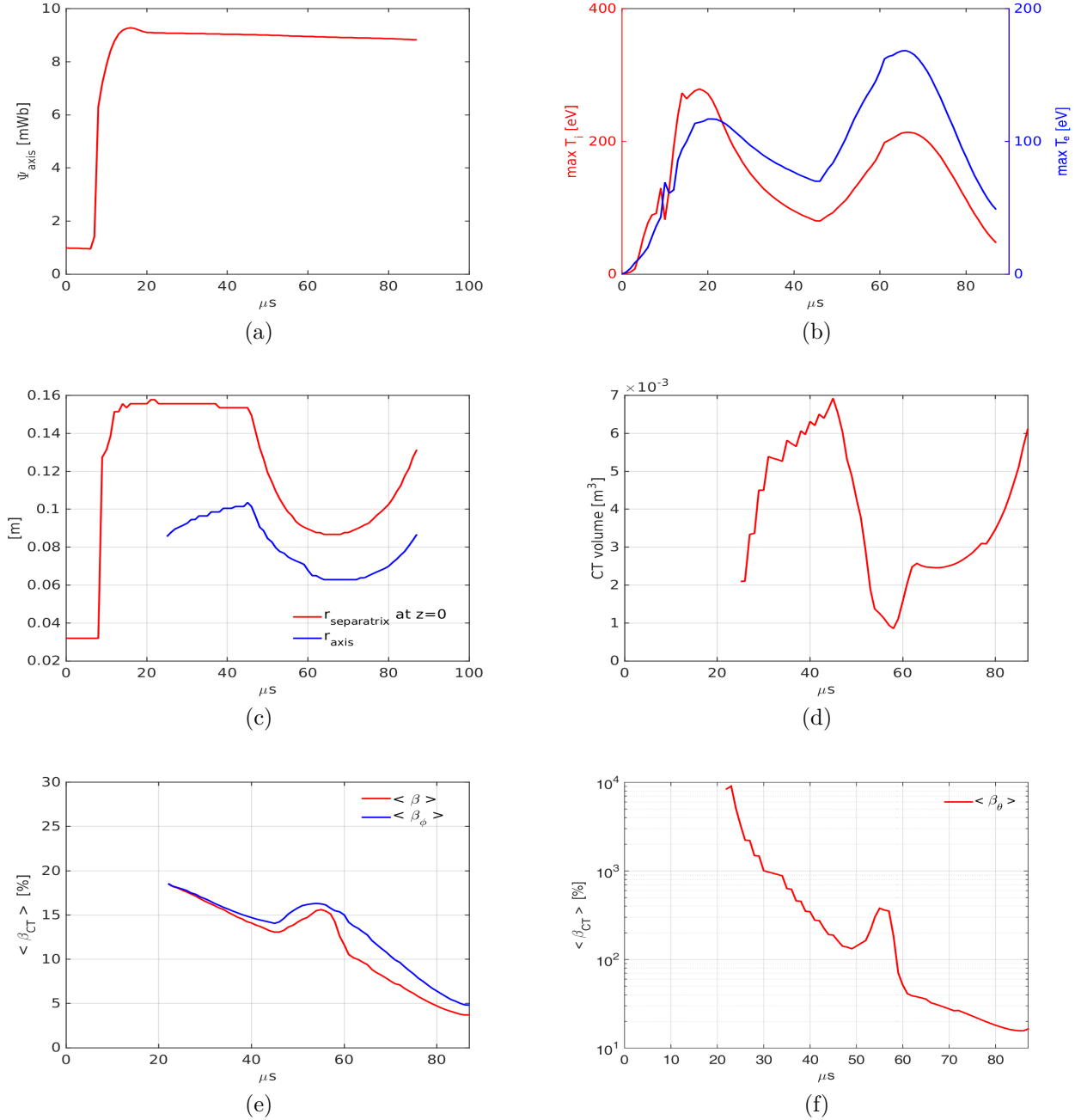


Figure 7.5.12: Selection of additional simulated diagnostics for simulation 2353

Figure 7.5.12 indicates the evolution of various parameters for simulation 2353, which had the code inputs listed in table 7.1.1. Figure 7.5.12(a) indicates the evolution of ψ_{CT} , the value of ψ at the magnetic axis of the CT, and is calculated as the maximum value of ψ in

the part of the simulation domain representing the CT confinement region. Poloidal flux is approximately conserved throughout the simulation, also at compression. The gradual drop in ψ_{CT} over time is due to resistive decay of the CT toroidal current.

Figure 7.5.12(b) shows the maximum ion and electron temperatures in the computational domain. Ions attain their maximum temperature around the entrance to the CT confinement region, due to viscous heating during the formation process, when they are accelerated to extreme velocities by the action of the formation $\mathbf{J}_r \times \mathbf{B}_\phi$ force, and by the jets associated with magnetic reconnection of the poloidal stuffing flux as closed CT flux surfaces are formed (see figure 7.3.7(d)). The electron fluid attains its maximum temperature later around peak compression, in the CT core, due to compressional heating and enhanced ohmic heating.

Simulated CT outer separatrix, $r_s(t)$, also indicated in figure 7.5.8, is plotted in figure 7.5.12(c), along with $r_{axis}(t)$, which the r coordinate of the magnetic axis of the CT. $r_{axis}(t)$ is calculated by finding the r coordinate of the location of ψ_{CT} over time. Note that the CT, and r_{axis} , is defined only after the first closed poloidal flux surface is formed, at around 25 μ s. It can be seen that the simulation indicates that the aspect ratio $(r_s - r_{axis}) / r_{axis}$ is approximately constant over compression.

Figure 7.5.12(d) indicates the evolution of the CT volume, calculated using equation 6.5.2, over time. CT volume decreases by a factor of over three during compression. As shown in figures 7.3.1(d) and (e), simulations indicates that open field lines surround the closed flux surfaces until shortly after halfway through the primary compression cycle. These are pinched off and magnetically reconnect to form additional closed CT flux surfaces at compression, explaining the sharp increase in CT volume at $t \sim 59 \mu$ s. This increase is absent when compression initiation is delayed to a time when there are no open lines surrounding the CT.

Figures 7.5.12(e) and (f) indicate how magnetic energy associated with CT toroidal field is greater than that associated with CT poloidal field. $\langle \beta \rangle$, $\langle \beta_\theta \rangle$, and $\langle \beta_\phi \rangle$ are calculated using equation 6.5.3. The volume-averaged magnetic pressure associated with poloidal field is greater than volume-averaged plasma pressure only after $\sim 57 \mu$ s (figure 7.5.12(f)). At this time, open field lines surrounding the CT are pinched off during magnetic compression, to form additional closed field lines that are then associated with the exterior of the CT. When this occurs, high levels of toroidal current flowing along the originally open field lines results in a sudden increase of poloidal field associated with the CT exterior. Note that because the simulated CT toroidal current profiles are extremely hollow (see figure 7.3.8), the poloidal magnetic field is particularly weak in the CT interior. Simulated volume-averaged total beta increases from $\sim 13\%$ to $\sim 16\%$ over compression.

7.5.3.2 Simulated internal magnetic field

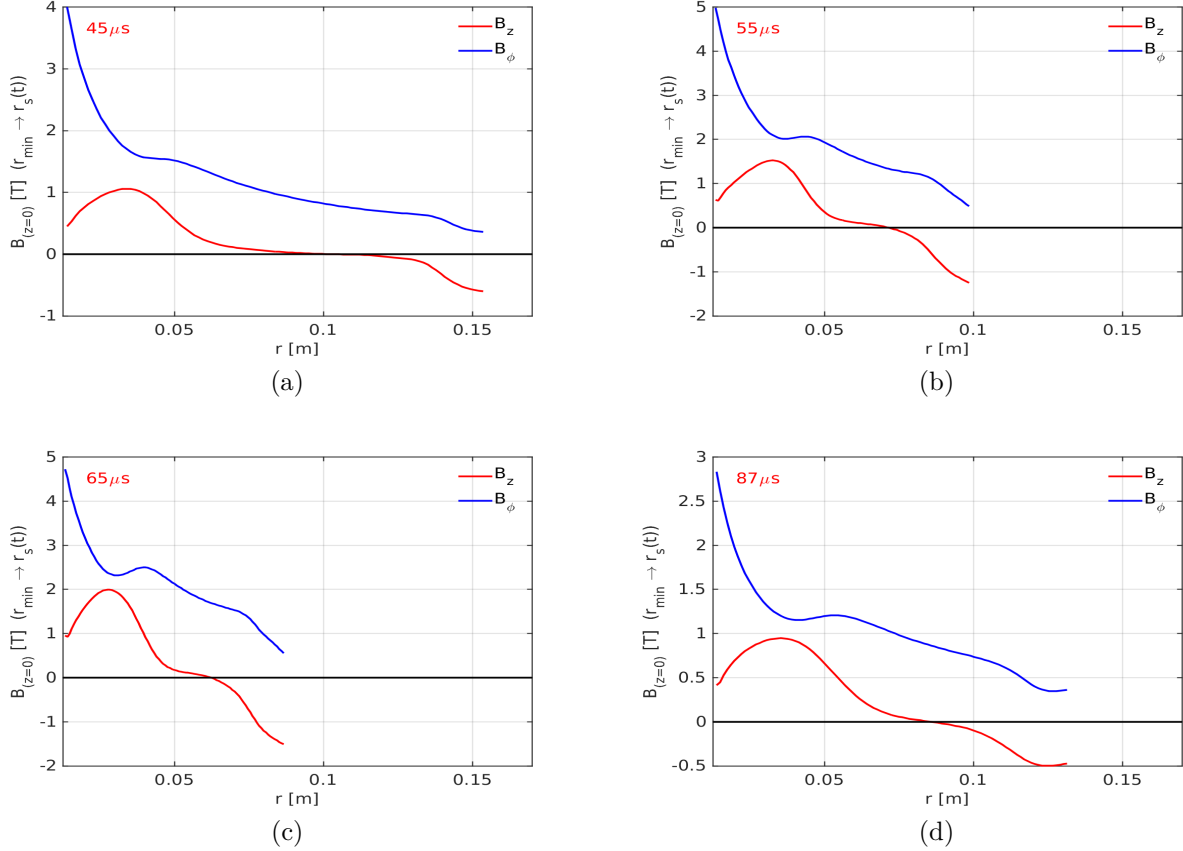


Figure 7.5.13: Internal CT B_z and B_ϕ profiles from simulation 2353

For the same simulation 2353 ($t_{comp} = 45 \mu\text{s}$), figure 7.5.13 indicates the simulated values, at $t = 45, 55, 65$, and $87 \mu\text{s}$, of B_z and B_ϕ along the horizontal line spanning from the chalice waist at $(r, z) = (r_{min} \sim 1.4 \text{ cm}, 0 \text{ cm})$ to the CT outboard equatorial separatrix at $(r, z) = (r_s(t), 0 \text{ cm})$. Although the CT magnetic axis is not located precisely at $z=0$, especially at earlier times, and the closed poloidal field lines are not exactly circular, B_z is still a good approximation for poloidal field at $z=0$. In each of these graphs, the r component of the magnetic axis location, also indicated in figure 7.5.12(c), is the r coordinate at which B_z crosses through zero. Note that the angular shape of the chalice wall, at the waist at $(r, z) = (r_{min} \sim 1.4 \text{ cm}, 0 \text{ cm})$, results in expansion and weakening of the poloidal field in that region from $r_{min} \sim 1.4 \text{ cm}$ to $r \sim 3 \text{ cm}$ at $z = 0 \text{ cm}$, as can be seen in figures 7.5.13(a) to (d), and also in figures 7.3.2(c) to (f). Also evident from 7.5.13(a) to (d) is that the CT toroidal field falls especially rapidly with increasing r in that region, due to the relatively low level of poloidal current there (poloidal currents sustain the externally imposed B_ϕ), as can also be seen in figures 7.3.4(c) to (f), and in figures 7.3.9(c) to (f).

Comparing the profiles with the depiction of the field profiles for the typical tokamak and spheromak configurations in figure 1.3.1, it can be seen how the CT field profile has more in common with that of a tokamak. Crow-barred shaft current flowing around the confinement region produces a tokamak-like toroidal field profile that, in a tokamak, is due to current in the toroidal field coils (figure 1.1.4(a)). However, as shown in section 7.5.3.3, the simulated CT q profile indicates that the shaft current is insufficient to reproduce a typical tokamak q profile.

The magnetic compression experiment did not have internal magnetic measurements that would enable confirmation of these simulated diagnostics for internal field profiles. It is likely that the 2D simulations overestimates the level of hollowness of the current profiles. On the other hand, the magnetic measurements that do exist (magnetic field at the chalice walls) are well matched by the simulated diagnostics, so it seems reasonable to have some level of trust in the simulated field diagnostics.

7.5.3.3 Simulated q profile

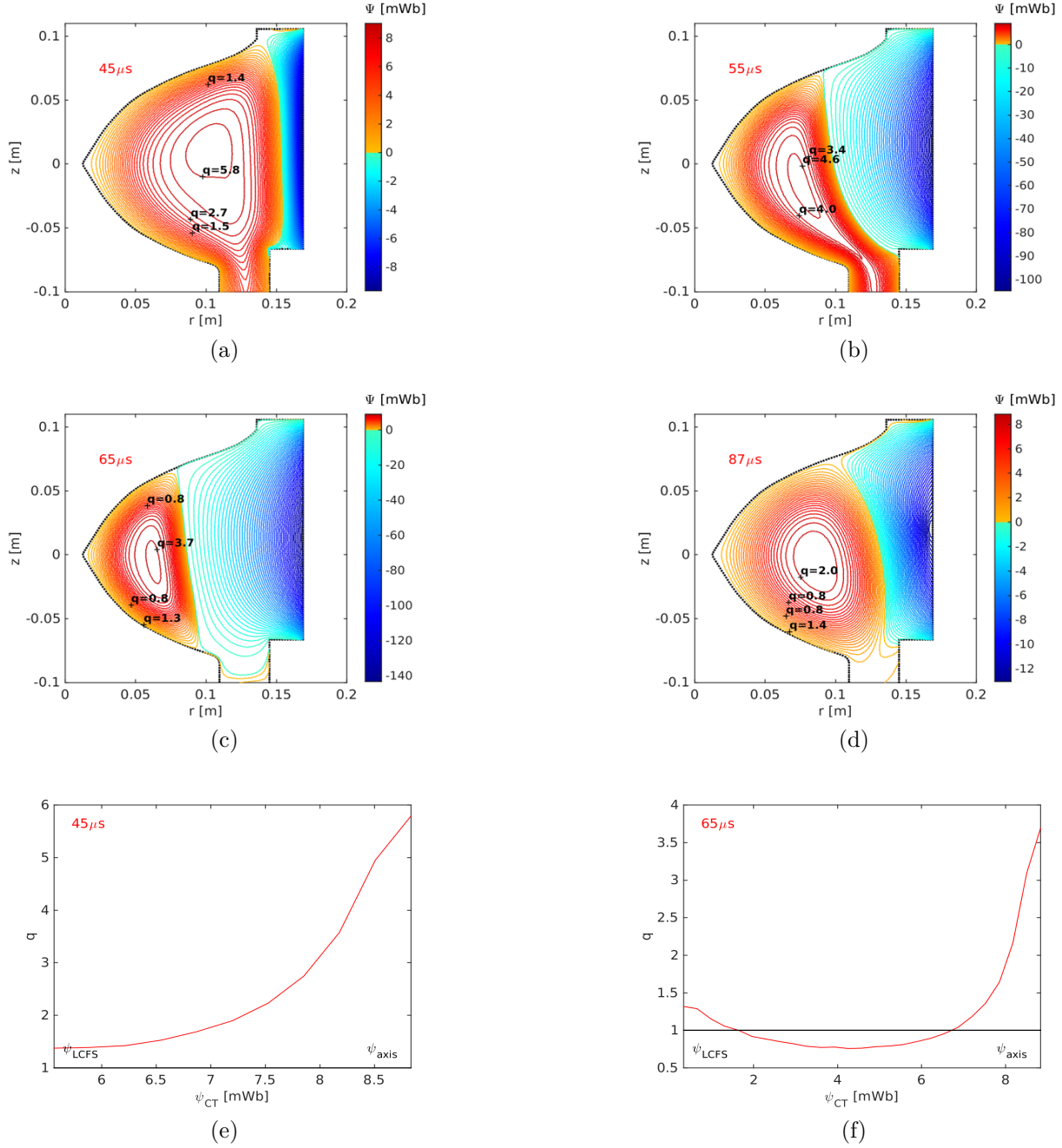


Figure 7.5.14: q profile, simulation 2353

Figure 7.5.14 shows the profile of safety factor $q(\psi)$ for simulation 2353 at various times. The method developed to find the q profile from the simulated magnetic fields has been described in section 6.5.2.1. Simulated $q(\psi)$ shows two trends at compression, depending on the value of t_{comp} . When the compression banks are fired early in the CT's life, for

example at $t_{comp} = 45 \mu\text{s}$ as in simulation 2353, the CT, defined by regions of closed ψ contours, is still, at $t = t_{comp}$, surrounded by open field lines that are pinned to the inner and outer electrodes (figure 7.5.14(a)), and $q(\psi)$ ranges from $q \sim 5.8$ near the magnetic axis (at $\sim 8.75 \text{ mWb}$) to $q \sim 1.4$ at the last closed flux surface (LCFS) at $\sim 5.5 \text{ mWb}$ (figure 7.5.14(e)). At compression, the open field lines surrounding the CT are pinched off, to form additional closed field lines that are then associated with the exterior of the CT, as indicated in figure 7.5.14(c). High levels of toroidal current flowing along the originally open field lines results in these field lines being associated with low q when they are pinched off. At $65 \mu\text{s}$, $q(\psi)$ ranges from $q \sim 3.7$ near the magnetic axis (at $\sim 8.7 \text{ mWb}$) to $q \sim 1.3$ at the LCFS at $\sim 0.3 \text{ mWb}$ (figure 7.5.14(f)), while dipping below $q = 1$ over a large extent between the magnetic axis and the LCFS.

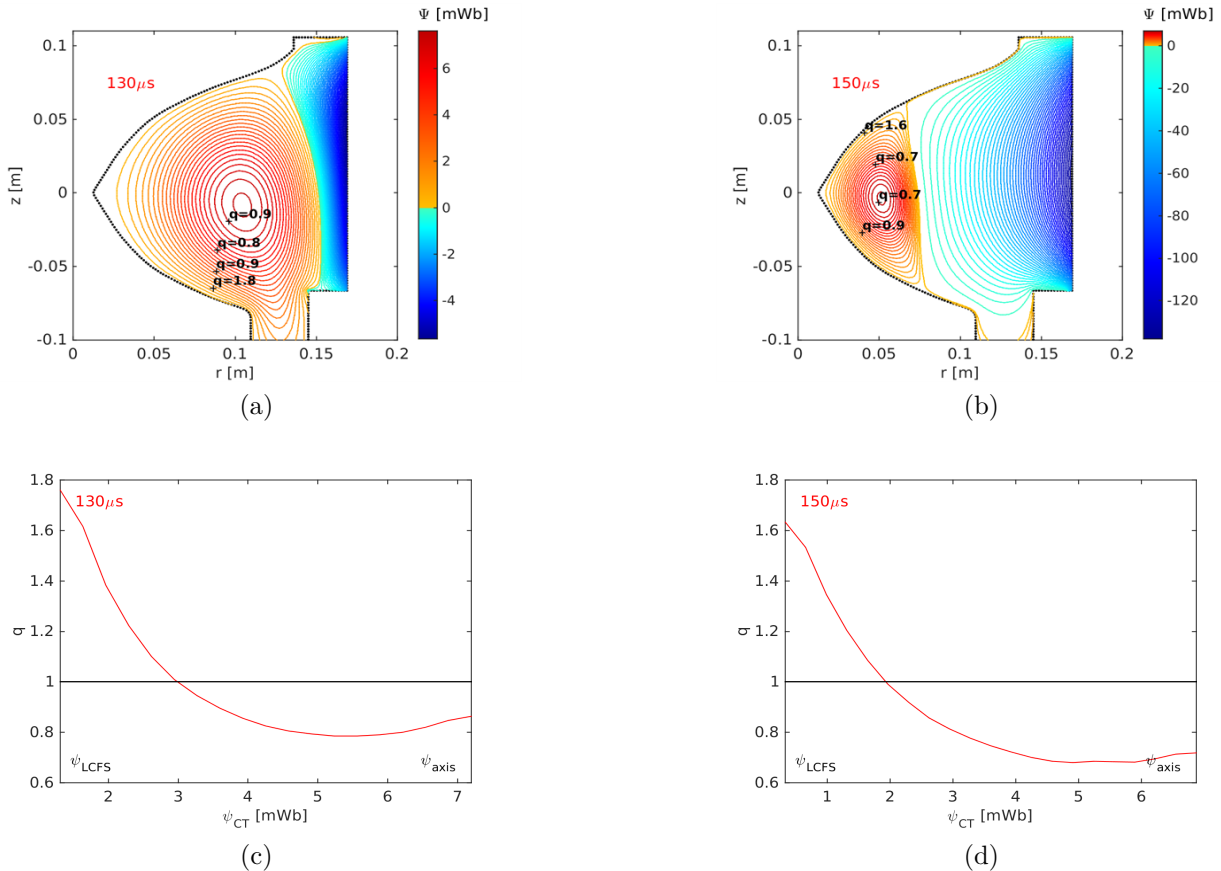


Figure 7.5.15: q profile, simulation 2287

When compression is started late in the CT's life, for example at $t_{comp} = 130 \mu\text{s}$ in simulation 2287, most of the open poloidal field lines that previously surrounded the CT have already reconnected because T_e has dropped and η has increased. Then, MHD simulations typically show $q > 1$ at the LCFS, while the region with $q < 1$ extends all the way to the magnetic axis prior to compression and also at peak compression (figures 7.5.15(a) - (d)).

For both early and late magnetic compression, simulations indicate that the q profile is not contingent to magnetohydrodynamic stability [33], as $q < 2$ at the LCFS in either case. Also, for both early and late compression, q drops below one over extensive spans between the magnetic axis and the LCFS. The 2D simulations, which neglect inherently three dimensional turbulent transport and flux conversion, are likely to overestimate the level of hollowness of the current profiles, and lead to an underestimation of q towards the CT edge, but without further internal experimental diagnostics or 3D simulations, the level of underestimation remains uncertain. The Kruskal-Shafranov limit determines that magnetically confined plasmas are unstable to external kink modes when $q < 1$. This condition for instability doesn't pertain to toroidal sausage modes. As discussed in section 4.2, the external kink or toroidal sausage modes are the most obvious candidates that could lead to the toroidal field behavior that was observed on most compression shots. Both the kink and sausage instabilities can be stabilized with addition toroidal field, so the implementation of additional shaft current should be considered if the magnetic compression experiment was repeated.

7.5.3.4 Adiabatic compression scalings

As discussed in section 1.4, if a magnetically confined plasma is compressed on a time-scale that is short compared with the resistive magnetic decay time and particle confinement time of the plasma, the adiabatic compression scaling laws presented in table 1.4.1 should apply. Diagnostics internal to the CT that would enable assessment of the scalings are not available, but it is possible to estimate them using outputs from simulations that match the available fixed-point external diagnostics for magnetic field, and internal line-averaged diagnostics for density and ion temperature along fixed chords. The CT cross-sectional area in the poloidal plane is irregular, so the scalings in the first row of table 1.4.1 are relevant. $L(t)$ and $S(t)$, the perimeter-length and area of the poloidal CT cross-section, and $V(t)$, the CT volume, can be calculated using the coordinates of the points that define the ψ contour pertaining to the LCFS. As discussed in reference to figures 7.3.1(d) and (e), poloidal field lines that remain open surrounding closed CT poloidal field lines are pinched off during magnetic compression, and reconnect to form additional closed CT field lines. This affects the definition of ψ_{LCFS} , and therefore of the values of the geometric scalings $a_0(t)$, $L(t)$, $S(t)$ and $V(t)$ that are defined by the location of the LCFS and are required to determine the predicted adiabatic scalings. Hence, compression scalings are best assessed from simulations in which compression is initiated relatively late in time when ψ_{LCFS} is close to zero, and few open poloidal field lines surround the CT. In addition, simulations indicate that closed poloidal CT field lines that extend partially down into the gun barrel entrance can be pinched off, and reconnect at compression (figures 7.3.1(d) and (e)), which also affects the

geometric scalings. A solution is to assess the parameters of interest, including the geometric parameters, relevant to a ψ contour, defined by a fixed value of $\psi = \psi^0$, that is internal to the pre-compression LCFS, and doesn't extend partially into the gun barrel, a strategy that naturally does not affect the compression scalings.

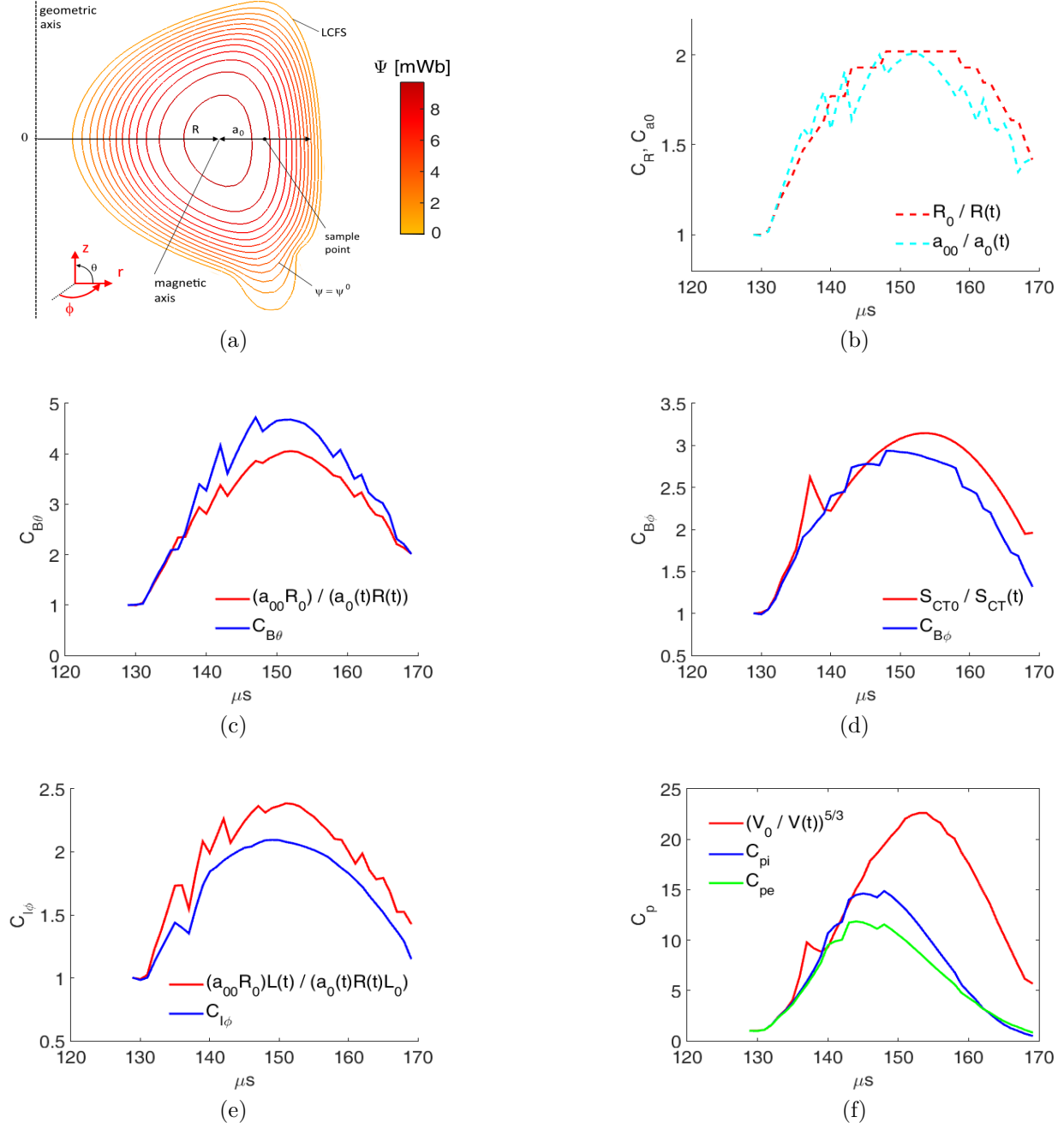


Figure 7.5.16: Compression scalings, simulation 2287

Figure 7.5.16(a) shows pre-compression CT ψ contours from an MHD simulation at relatively late time, when most open poloidal field lines have reconnected to form closed CT field lines, and $\psi_{LCFS} \sim 0$. A flux contour with $\Psi = \Psi^0 = 2$ mWb, that is suitable for

assessing compression scaling parameters, and definitions of $R(t)$ and (modified) $a_0(t)$, are also indicated. Note that $a_0(t)$ has been re-defined as the distance from the CT magnetic axis radially outwards at poloidal angle $\theta = 0$ to the closed flux surface defined by $\Psi = \Psi^0$. Simulated geometric compression scalings for $R(t)$ and $a_0(t)$ from simulation 2287 are shown in figure 7.5.16(b), where the subscript 0 denotes pre-compression values. This indicates approximately constant aspect ratio (in irregular geometry), and that the compression is close to the "Type A" compression regime defined in [19]. With constant aspect ratio, this indicates a geometric compression factor, in terms of equatorial outboard CT separatrix, of $C_s \sim C_R \sim C_{a0} \sim 2$. As described in section 4.4, a geometric compression factor $C_s \sim 1.7$ was determined experimentally, and confirmed by MHD simulation, for shot 39738 ($V_{comp} = 18$ kV and $t_{comp} = 45$ μ s), and that more extreme compression in r_s cannot be experimentally evaluated due to limitations on the technique. More extreme compression would be expected for shots at comparable V_{comp} , with t_{comp} delayed to when pre-compression CT flux has decayed to lower levels. Results from simulation 2287 have also been presented in figures 7.4.1, 7.4.2, and 7.5.9. Simulation 2287 pertains to shot 39735 ($V_{comp} = 18$ kV and $t_{comp} = 130$ μ s), so the increased estimate for C_s is consistent with the shot parameters. Note that, as outlined in chapter 4, with $\tilde{\tau}_c = 0.6$, shot 39735 is not classified as a flux-conserving shot, so the adiabatic compression scalings evaluated here pertain to the shot only up until the time when flux started to be lost, just before peak compression. As outlined above, the technique described here cannot practically be applied to simulations with compression initiated early, and flux-conserving compressed shots were generally taken with $t_{comp} = 45$ μ s. Only a few shots were taken with late compression, none of which conserved flux very well over compression, as determined by the $\tilde{\tau}_c$ metric.

Figure 7.5.16(c) shows how, for simulation 2287, poloidal field scales approximately adiabatically as $B_\theta \rightarrow a_0^{-1} R^{-1}$, where the sample point used to determine the scalings, indicated in figure 7.5.16(a), is located halfway between the magnetic axis and the outboard point where $\psi = \psi^0$ at the same axial coordinate as the magnetic axis. The notation $C_{B\theta}$ denotes the scaling of poloidal field as $C_{B\theta}(t) = \frac{B_\theta(t)}{B_{\theta0}}$ where $B_{\theta0}$ is the pre-compression magnetic field at the sample point. Similarly, figure 7.5.16(d) shows how toroidal field at the same sample point also scales adiabatically, as $B_\phi \rightarrow S^{-1}$. Figure 7.5.16(e) shows how plasma current, calculated as the integral of toroidal current density over the area inside the closed flux surface at $\psi = \psi^0$, evolves approximately according to the adiabatic scaling for plasma current.

As indicated in 7.5.16(f), the scaling for pressure (and hence also for the β scalings) does not follow the adiabatic prediction of $p \rightarrow V^{-\frac{5}{3}}$, due to the presence of artificial density diffusion, which effectively relocates particles from high density to low density regions. For this simulation, density diffusion was $\zeta = 50$ m²/s, which is close to the minimum value

required for numerical stability at moderate timestep and mesh resolution for simulations including magnetic compression, and n_e follows the adiabatic scaling $n_e \rightarrow V^{-1}$ for only the first 5 μs after compression initiation. Ion and electron pressures follow the adiabatic predictions for 15 μs - the extension is due to approximate internal force balance during this portion of the compression cycle, which leads to increased temperature in regions of low density. Temperatures at compression increase more, while density increases less, than the predicted increases based on the adiabatic scalings. When ζ is increased to 150 m^2/s , the duration over which n_e follows the adiabatic scaling is reduced further to around 2 μs .

This simulation, which produces results that closely match the available experimental measurements for shot 39735 over most of the compression cycle, indicates that CT aspect ratio is approximately constant over compression, with $C_s \sim C_R \sim C_{a0} \sim 2$, and that internal CT poloidal and toroidal fields, and CT toroidal current, scale approximately adiabatically, increasing over the main compression cycle by factors of approximately four, three and two respectively.

7.5.3.5 System energy components

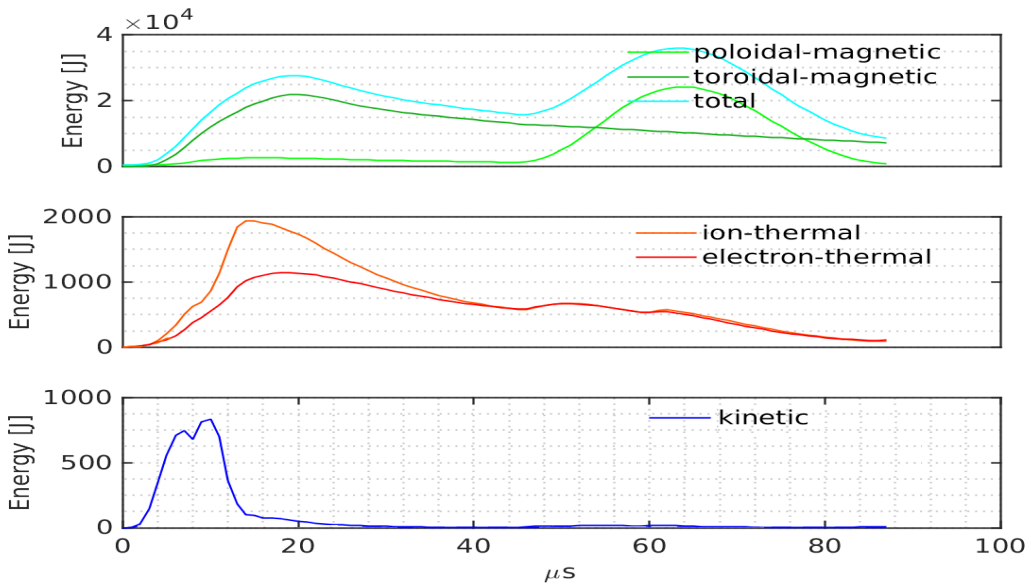


Figure 7.5.17: System energy evolution for simulation 2353

Figure 7.5.17 indicates the evolution of the components of system energy for simulation 2353. Boundary conditions are explicitly applied to the pressure fields to enable thermal losses in accordance with the thermal conduction model, and time-dependent external sources of magnetic energy associated with formation, levitation and compression are imposed. Finite

boundary conditions for ψ enable outward electromagnetic energy losses (Poynting flux). Total system energy is *not* conserved, in contrast to the energy conservation in cases with no thermal diffusion through the boundary and perfectly electrically conducting boundaries, as presented in figure 5.6.2, and in figure 8.6.1 in chapter 8. Figure 7.5.17 shows how total energy and toroidal magnetic energy (*i.e.*, magnetic energy associated with toroidal field) rise at formation until $\sim 20 \mu\text{s}$, as toroidal magnetic flux associated with formation is added to the region below the physical location of the gas valves. The axial gradient in f associated with the formation flux input profile (figure 6.3.1(a)) is associated with radial formation current between the electrodes, which causes ohmic heating of the electrons, and leads to a $\mathbf{J}_r \times \mathbf{B}_\phi$ force which advects the plasma rapidly upwards. This lead to an increase in kinetic energy, and to ion viscous heating, especially over the first $15 \mu\text{s}$ of the simulation. Poloidal magnetic energy also rises until $15 \mu\text{s}$ as toroidal plasma currents are induced to flow, leading to conversion of toroidal flux to poloidal flux during the bubble-in process. As the plasma currents decay resistively, the magnetic energy associated with internal currents decreases and is initially converted to electron thermal energy. Recall that $\dot{U}_{M\theta\eta} = -\dot{U}_{Th\phi\eta}$, equation B.4.10, and $\dot{U}_{M\phi\eta} = -\dot{U}_{Th\theta\eta}$, equation B.4.18. Electrons are ohmically heated and impart energy to ions by collisions (term Q_{ie} , equation 5.6.5). Rapid diffusion of heat through the boundary means that thermal energy is lost faster than it is sourced from magnetic energy after the initial $\sim 20 \mu\text{s}$ period of maximum thermal energy gain, except during the time when the CT is being magnetically compressed. Poloidal magnetic energy associated with the external levitation field decreases as the currents in the levitation coils decay. Further electromagnetic energy is lost from the system due to Poynting flux through the boundary. Note that, as described at the end of section 5.5.3, Poynting flux out of the system is finite unless appropriate boundary conditions, for example $\mathbf{v}|_\Gamma = \mathbf{0}$, $\psi|_\Gamma = 0$ and $(\nabla_\perp f)|_\Gamma = 0$ are imposed. In this simulation with an external source of time-dependent poloidal magnetic energy (*i.e.*, finite $\psi(t)|_\Gamma$), the second condition is not satisfied. The third condition is satisfied only on the parts of the boundary that represent electrically conducting walls; boundary conditions for f consistent with conservation of system toroidal flux are applied explicitly on the part of the boundary that represents an electrical insulator, which breaks the third condition on that part of the boundary.

Ion and electron thermal energy, magnetic energy, kinetic energy and total energy continue to fall until $t_{comp} = 45 \mu\text{s}$, when around 25 kJ of poloidal magnetic energy, due to over 1 MA toroidal current in the levitation/compression coils, is added to the system over around $20 \mu\text{s}$. The rapid inward compression of the CT leads to a slight increase in kinetic energy. Ion and electron thermal energies increase due to compressional heating. Toroidal plasma current increases as the CT is compressed, leading to increased ohmic heating and an additional rise in electron thermal energy. Again, electrons transfer some of this energy to the ion fluid, so

ion thermal energy also rises due to enhanced ohmic heating.

7.6 Summary

The inclusion of a model for the insulating wall enables confirmation that the level of penetration of poloidal field, that is advected into the containment region during CT formation, into the insulating region is reduced in the six coil configuration when $|t_{lev}|$ is increased, and that field penetration is avoided in the eleven coil configuration. Simulated diagnostics from the two dimensional MHD simulations show generally good agreement with experimental measurements. Simulated poloidal and toroidal field at the magnetic probe locations are very close to experimental measurements, for compression and levitation-only shots. Levitation circuit resistance modification was a key strategy developed to improve the performance of levitated CTs and avoid unintentional magnetic compression and the associated instability. The modifications were modelled by varying the rate of change of the amplitudes of boundary conditions for ψ_{lev} in proportion to the corresponding experimentally measured levitation current signals, and the method works well to approximately reproduce the experimentally measured poloidal field in the two principal circuit configurations investigated. The time evolutions of simulated outboard equatorial separatrix radius are a close reproduction of the experimentally measured profiles, for compression shots and levitation-only shots in both levitation circuit configurations.

Simulated ion temperature and electron density are also qualitatively close matches to experimental measurements. The level to which artificial density diffusion affects the simulated density diagnostic, and the evolution of the other fields, should be investigated further. Simulations do not capture the extremely high density that is measured experimentally when plasma first enters the CT containment area, perhaps due to artificial diffusion, or due to the inability of the model to capture the effect of sputtering of high Z ions during formation, and their subsequent recombination as the plasma cools. Ion temperature is measured experimentally using the ion-Doppler diagnostic, while the corresponding simulated diagnostic works by obtaining the line averaged ion temperature along the ion-Doppler chords, which seems reasonable as a crude first approximation. The simulated ion temperature model could be developed further to include additional physics, including density dependence. Qualitatively, the simulated diagnostic for ion temperature approximately reproduces the experimental measurement with the current model, and a suitable choice of ν_{phys} enables scaling to match the experimental measurement.

The poloidal field profiles experimentally measured during magnetic compression routinely indicated loss of CT poloidal flux during compression, suggesting the action of a

disruptive instability. It was found to be possible to approximately reproduce the profiles by forcing CT poloidal flux loss during simulated magnetic compression, thereby verifying that a flux loss mechanism that was involved in the instability.

A range of simulated diagnostics looking at physics internal to the CT were developed. Without experimental counterparts to verify these diagnostics, there is some uncertainty about the validity of the findings. The simulated diagnostics that do have experimental counterparts match experimental measurements very well in general, and this lends some confidence to the internal simulated diagnostics. Simulations confirmed, as also indicated with scintillator and ion-Doppler data, that ion viscous heating is extreme during the formation process, while confirming that electrons are heated more than ions at compression, likely due to enhanced ohmic heating in combination with compressional heating. Plasma jets associated with magnetic reconnection lead to high levels of ion viscous heating, particularly around the entrance to the CT containment region during formation of closed poloidal CT flux surfaces. Simulations show that the pinching off of closed field lines that extend partially down the gun when magnetic compression is initiated early in the life of the CT leads to the formation of a smaller CT located below the entrance to the containment region. Field lines that remain open surrounding the closed CT flux surfaces are then also pinched and reconnect to form additional closed field lines around the main CT. The newly reconnected open field lines below the main CT act like a slingshot that advects the smaller CT down the gun. This effect cannot be verified experimentally, as the magnetic probes located along the gun barrel were not functioning properly at any time. Simulations of magnetic compression indicate that CT volume decreases by a factor of around three over the primary compression cycle - this observation is partially supported in that the time evolution of simulated outboard equatorial separatrix matches the experimental observation. It is shown that the oscillating compression field resulted in the inductive formation, magnetic compression, and subsequent extinguishing (magnetic reconnection of CT poloidal field with the compression field) of a second and third CT. This is supported experimentally in that experimental poloidal field measurements closely match the corresponding simulated diagnostic, and that Xray-phosphor imaging indicates the compressional heating of up to three distinct plasmoids on many compression shots. With extremely high values for poloidal beta, and toroidal beta less than one, it was indicated that magnetic energy associated with CT toroidal field greatly exceeds that associated with CT poloidal field. Simulated volume-averaged total beta increases from $\sim 13\%$ to $\sim 16\%$ over compression. Simulated diagnostics for magnetic field profiles internal to the CT indicate that the CT has a field profile with more in common with a tokamak plasma than a spheromak plasma, but with the amplitude of the toroidal field far lower than that of a tokamak plasma. This is verified by the simulated $q(\psi)$ profile. Tokamaks typically operate at $q \gg 1$ at all points in the plasma, increasing MHD stability.

Simulations indicates that, at early times ($\sim 45 \mu\text{s}$) in the CT life, while $q \sim 6$ around the magnetic axis, it falls to a value not much higher than one towards the LCFS. Over time, as the CT current profile becomes less hollow, q drops to below one at the axis, and rises to around two at the LCFS (figure 7.5.15(c)). It was found that $q < 1$ over extended regions between the magnetic axis and the LCFS at peak magnetic compression, regardless of whether compression was initiated at early or at late times in the CT life. Internal simulated diagnostics were used to compare theoretical adiabatic compression scalings with simulated compression scalings. It was found that while the magnetic fields, and toroidal current at a point located halfway between the magnetic axis and the outboard equatorial separatrix, did rise at compression approximately according to the adiabatic scalings, that the scalings for the other quantities of interest (n_e , T_e , T_i , β_θ and β_ϕ) did not, due to the effect of artificial density diffusion. Approximately constant aspect ratio compression (in irregular geometry) was indicated, so that compression is close to the "Type A" regime defined in [19]. With constant aspect ratio, this indicates a geometric compression factor, in terms of outboard equatorial CT separatrix, of $C_s \sim C_R \sim C_{a0} \sim 2$. As described in section 4.4, an outboard equatorial separatrix radius at peak compression of $r_s \sim 9 \text{ cm}$, and a geometric compression factor $C_s \sim 1.7$, was determined experimentally, and confirmed by MHD simulation, for a shot which was compressed relatively early in time ($V_{comp} = 18 \text{ kV}$ and $t_{comp} = 45 \mu\text{s}$). As noted in section 4.4, when $r_s \lesssim 9 \text{ cm}$, the slope of the functional fit in 3.7.2(b) is too flat to be successfully inverted with good accuracy. For this reason, C_s cannot be experimentally evaluated for shots at comparable V_{comp} if compression is fired relatively late in time, when pre-compression CT flux has decayed to lower levels and compression is more extreme.

The components of system energy evolve as expected with conversions initially from toroidal magnetic energy associated with formation current to thermal energy, kinetic energy and poloidal magnetic energy. Magnetic energy is converted to electron thermal energy via ohmic heating, with kinetic energy being converted to ion thermal energy due to viscous effects. Rapid diffusion of heat through the boundary means that thermal energy is lost faster than it is sourced from magnetic energy after the initial $\sim 20 \mu\text{s}$ period of maximum thermal energy gain, except during the time when the CT is being magnetically compressed. At CT magnetic compression, the principal energy conversion mechanisms are that poloidal magnetic energy does work to compress the CT, leading to compressional heating of ions and electrons. Toroidal plasma current increases as the CT is compressed, leading to increased ohmic heating and an additional rise in electron thermal energy. Again, electrons transfer some of this energy to the ion fluid, so ion thermal energy also rises due to enhanced ohmic heating.

Chapter 8

Model for interaction between plasma and neutral fluids

This chapter focuses on the development and implementation of a model for simulating interaction between plasma fluid and neutral fluid over the process of CT formation into a levitation field and magnetic compression. A paper [52], based on the material presented this chapter, has been submitted for publication.

A primary motivation for including plasma / neutral fluid interaction in the MHD model was to reduce simulated ion temperature to levels corresponding to the ion-Doppler diagnostic measurements while maintaining energy conservation, *i.e.*, while keeping $\nu_{num} = \nu_{phys}$ (see appendix C.3.2). Charge exchange collisions are an important mechanism by which ion temperature is reduced - in a charge exchange reaction, a hot ion takes an electron from a cold neutral particle, resulting in a hot neutral particle and a cold ion. Secondly, it was expected that the presence of a neutral fluid in the gun around the gas valves, which is also a physical phenomenon, would slow down the axially directed plasma during the formation process, leading to reduced viscous heating. In the actual experiment, the formation process is initiated when an electric field is applied across a cloud of cold gas between the inner and outer machine electrodes. The gas cloud is concentrated near the gas-puff valves, at $z = -0.43$ m (see figure 2.1.1). The gas valves are typically opened approximately 400 μ s before the formation voltage is applied across the electrodes, so that a neutral gas cloud has ample time to diffuse away from the valves. The ionization action of the applied formation field results in seed electrons that lead to further impact ionization. The resultant plasma that is advected up the gun by the $\mathbf{J}_r \times \mathbf{B}_\phi$ force is initially surrounded by a relatively static neutral gas cloud that it ionizes or displaces. The neutral cloud slows down the advected plasma through collisions, resulting in a reduction of ion viscous heating as \mathbf{v} and $\nabla \mathbf{v}$ are reduced.

The first attempt at modelling plasma-neutral interactions, in order to reduce simulated

ion temperature while maintaining energy conservation, included charge exchange reactions only. This approach succeeds in reducing simulated ion temperature, but is unphysical because the rate of change of the neutral fluid density, which depends on the rates of ionization and recombination, and therefore on the electron temperature, cannot be determined and is held constant. If the neutral fluid density is kept constant, ion cooling due to charge exchange continues even in situations where the electron temperature is so high that physically the neutral fluid density would be minuscule.

Finally, a plasma-neutral model, in which a single-fluid MHD plasma interacts with a neutral fluid was developed and implemented in the MHD code. The part of the dynamics of both the plasma and neutral fluid that does not depend on inelastic collisions is based on the set of MHD equations presented in section 5.5. For the neutral fluid equations, terms in the MHD equations relating to electromagnetic phenomena are omitted. Thus, total system energy conservation is maintained when the energy lost by electrons due to impact ionization and radiative recombination is accounted for. It turned out that, while the inclusion of a neutral fluid in the CT formation simulations did reduce simulated ion temperature, the cause of the temperature reduction was due to bulk inertial effects, which reduces axial velocities and therefore reduces viscous heating, rather than direct interaction between the fluids. It was found that the same level of ion temperature reduction can be achieved in simulations without a neutral fluid, simply by increasing the initial plasma fluid density until it is equal to the combined neutral and plasma densities for a simulation with the same initial spatial distributions of the neutral and plasma fluids. Due to equilibration between the ion and electron temperatures, ionization rates are high in regions where ions are hot, so that neutral fluid density, and hence the level of charge-exchange related ion cooling, is approximately negligible in those key regions. The model proved to be useful because it helped clarify the mechanisms behind the significant increases in electron density that are routinely observed at $\sim 500 \mu\text{s}$ with CTs formed in the SPECTOR plasma injector (figure 1.2.2(b)). Neutral gas, which remains concentrated below the gas valves after CT formation, diffuses up the gun barrel to the CT containment region where it is ionized, leading to the observed electron density increases.

This chapter is arranged as follows. A model overview is presented in section 8.1. Development of the scattering terms, and the reactive terms pertaining to ionization, recombination and charge exchange collisions, that are included in the plasma and neutral fluid equations, is presented in sections 8.2 and 8.3 respectively. The resultant fluid equations for ions, electrons and neutral particles are derived in section 8.4. The ion and electron MHD equations are reduced to a set of single plasma fluid equations, that include terms pertaining to interaction with the neutral fluid, in section 8.5. A demonstration of total system energy and particle count conservation with inclusion of a neutral fluid in the MHD model is presented and dis-

cussed in section 8.6. Implementation of diffusion terms for the neutral fluid is discussed in section 8.7. A simple model for including effects of charge-exchange reactions only without evolving a neutral fluid is presented in section 8.8. Simulation results are presented and discussed in section 8.9. Section 8.10 concludes the chapter with an overview of the principal findings.

8.1 Model overview

Based on the work presented in [72, 100], the model includes resonant charge exchange, electron impact ionization, and radiative recombination reactions:



Here, i^+ , e^- and n respectively represent singly charged ions and electrons, and neutral particles, h [m²kg/s] is Planck's constant, and ν_p is the wave frequency associated with the photon emitted in the recombination reaction. The charge exchange process is *resonant* because the initial and final states have the same quantum mechanical energy - the exchanged electron's initial and final energy states are the same so that the combined kinetic energy and momentum of the ion and neutral is unchanged [54, 66]. In the following derivations, singly charged ions and a single neutral species will be considered. The plasma is assumed to be optically thin, so that radiation energy $h\nu_p$ associated with radiative recombination is lost from the system. Following from [72, 100], excited states are not tracked in order to simplify the model. Instead, an effective ionization potential, ϕ_{ion} , includes the excitation energy that is expended on average for each ionization event, as well as the electron binding energy.

The Boltzmann equation (A.4.1) is

$$\frac{\partial f_\alpha}{\partial t} + \nabla \cdot (\mathbf{V} f_\alpha) + \nabla_v \cdot \left(\left(\frac{q_\alpha}{m_\alpha} (\mathbf{E}(\mathbf{r}, t) + \mathbf{V} \times \mathbf{B}(\mathbf{r}, t)) \right) f_\alpha \right) = \frac{\partial f_\alpha}{\partial t} |_{collisions} = C_\alpha(f)$$

where $\alpha = i$, e , or n denote ions, electrons, or neutral particles. If $\alpha = n$, then the acceleration term vanishes, because $q_n = 0$.

As mentioned in appendix A.3, the collision operator can be split into parts pertaining to elastic *scattering* collisions and *reacting* collisions: $C_\alpha(f) = C_\alpha^{scatt.}(f) + C_\alpha^{react.}(f)$. Elec-

tron impact ionization, and radiative recombination are inelastic reacting collisions, whereas the resonant charge exchange process is an elastic reacting collision because the initial and final states are degenerate. Moments of $C_{\alpha}^{scatt.}$ were taken in appendix A.3, and used when deriving the two plasma-fluid Braginskii equations in appendix A.4. In section 8.2, moments of the scattering collision operators when a neutral species is included will be considered.

In order to derive the collisional terms in a three-component model (ion, electron and neutral fluids), which will then be reduced to a two-component model (single plasma-fluid and neutral fluid), moments of the part of the collision operator that pertains to reacting collisions can be taken, as is done in [72, 100]. In this work, we show how, for the inelastic reacting collisions of ionization and recombination, the results for the collisional terms in a three-component model that are presented in [72, 100] can be obtained without taking moments. Instead, the sources or sinks that arise in the species continuity equations due to the reacting collisions of ionization and recombination are used directly to determine the consequent terms that arise in the species momentum and energy equations. This approach, described in section 8.3.1, is intuitive and also allows for determination of the terms that must be included in the MHD equations when external particle sources are present. In addition, this approach allows for the determination of terms in the plasma and neutral fluid energy equations that represent thermal energy lost by electrons and transferred to photons and neutral particles in radiative recombination processes. These terms cannot be evaluated using the moment-taking approach and have been neglected in studies based on the model presented in [72].

The terms in the MHD equations that correspond to charge exchange collisions cannot be evaluated using this approach because charge exchange collisions do not give rise to sources or sinks in the species continuity equations. Consequently, the terms in the MHD equations that correspond to reactive charge exchange collisions must be evaluated by taking moments of the part of the collision operator associated with charge-exchange collisions, as is done in [72, 100] - the procedure is briefly outlined in section 8.3.2.

8.2 Scattering collision terms

Scattering collisions have no 0^{th} moment effect, as was indicated in appendix A.3, equation A.3.3. To find the contribution of scattering collisions to the rates of change of momentum of the ions, electrons and neutral particles, the first moments of the operators for scattering collisions can be taken. For convenience, equation A.3.4 is repeated: $\mathbf{R}_{\alpha} = \sum_{\sigma} \mathbf{R}_{\alpha\sigma} = \int m_{\alpha} \sum_{\sigma} C_{\alpha\sigma}^{scatt.} \mathbf{V} d\mathbf{V} = \int m_{\alpha} C_{\alpha}^{scatt.} \mathbf{V} d\mathbf{V}$. Here, \mathbf{R}_{α} is the total friction force acting on species α due to the net effect of the frictional interaction with each of species σ . Note that, using

equations A.2.5, A.2.7 and A.3.3, we can write: $\mathbf{R}_\alpha = \int m_\alpha C_\alpha^{scatt.} \mathbf{c}_\alpha d\mathbf{V}$. In a system with just two species, ions and electrons, \mathbf{R}_α is given by the Chapman-Enskog closures (equation A.5.15). Assuming isotropic resistivity, and ignoring the thermal force terms for simplicity, equation A.5.15 gives $\mathbf{R}_e = -\mathbf{R}_i = \eta' n e \mathbf{J} = \nu_{ei} \rho_e (\mathbf{v}_i - \mathbf{v}_e)$. Recall, from appendix A.3, that $\nu_{ei} = \frac{1}{\tau_{ei}}$ is the electron-ion collision frequency where τ_{ei} (equation A.5.7) is the electron-ion collision time, the time it takes for an electron to be scattered by 90° due to collisions with ions. When there are just two species, then, since $\mathbf{R}_\alpha = \sum_\sigma \mathbf{R}_{\alpha\sigma}$ (equation A.3.4) and $\mathbf{R}_{\sigma\sigma} = 0$ (a fluid does not exert friction on itself), the equivalent notation $\mathbf{R}_e \equiv \mathbf{R}_{ei}$ and $\mathbf{R}_i \equiv \mathbf{R}_{ie}$ can be introduced for the frictional forces due to scattering collisions.

The notation $(X)_{scatt.}$ is introduced to represent the part of X that pertains to scattering collisions. Recall that m_α times the first moment of the first term of the Boltzmann equation is $\frac{\partial(\rho_\alpha \mathbf{v}_\alpha)}{\partial t}$ (appendix A.4). Since $\left(\frac{\partial(\rho_\alpha \mathbf{v}_\alpha)}{\partial t}\right)_{scatt.} = \rho_\alpha \left(\frac{\partial \mathbf{v}_\alpha}{\partial t}\right)_{scatt.} + \mathbf{v}_\alpha \left(\frac{\partial \rho_\alpha}{\partial t}\right)_{scatt.}$, and scattering collisions are not a source of particles ($\Rightarrow \left(\frac{\partial \rho_\alpha}{\partial t}\right)_{scatt.} = 0$), the terms $\rho_\alpha \left(\frac{\partial \mathbf{v}_\alpha}{\partial t}\right)_{scatt.}$ can be expressed as:

$$\rho_\alpha \left(\frac{\partial \mathbf{v}_\alpha}{\partial t}\right)_{scatt.} = \mathbf{R}_\alpha = \sum_\sigma \mathbf{R}_{\alpha\sigma} \quad (8.2.1)$$

With the inclusion of a neutral fluid, this leads to the following relations:

$$\begin{aligned} \rho_i \left(\frac{\partial \mathbf{v}_i}{\partial t}\right)_{scatt.} &= \mathbf{R}_i = \mathbf{R}_{ie} + \mathbf{R}_{in} \\ \rho_e \left(\frac{\partial \mathbf{v}_e}{\partial t}\right)_{scatt.} &= \mathbf{R}_e = \mathbf{R}_{ei} + \mathbf{R}_{en} = -\mathbf{R}_{ie} + \mathbf{R}_{en} \\ \rho_n \left(\frac{\partial \mathbf{v}_n}{\partial t}\right)_{scatt.} &= \mathbf{R}_n = \mathbf{R}_{ni} + \mathbf{R}_{ne} = -\mathbf{R}_{in} - \mathbf{R}_{en} \end{aligned} \quad (8.2.2)$$

where the identities $\mathbf{R}_{\alpha\sigma} = -\mathbf{R}_{\sigma\alpha}$ (implying that the frictional force exerted by species α on species σ is balanced by the frictional force exerted by species σ on species α) have been used. Note that $\mathbf{R}_{ei} = \nu_{ei} \rho_e (\mathbf{v}_i - \mathbf{v}_e)$ and $\mathbf{R}_{ie} = \nu_{ie} \rho_i (\mathbf{v}_e - \mathbf{v}_i)$, where $\nu_{ie} = \sim \frac{m_e}{m_i} \nu_{ei} = \frac{1}{\tau_{ie}}$ is the ion-electron collision frequency and τ_{ie} is the ion-electron collision time, the time it takes for an ion to be scattered 90° due to collisions with electrons. Similarly, the forms for the charged-neutral friction forces are $\mathbf{R}_{in} = \nu_{in} \rho_i (\mathbf{v}_n - \mathbf{v}_i)$ and $\mathbf{R}_{en} = \nu_{en} \rho_e (\mathbf{v}_n - \mathbf{v}_e)$, where $\nu_{\alpha\sigma} \sim \frac{m_\alpha}{m_\sigma} \nu_{\sigma\alpha}$ is the frequency for scattering of particles of species α from particles of species σ [68]. The terms \mathbf{R}_{in} and \mathbf{R}_{en} can be neglected in many cases - in general, neutral-charged particle scattering collisions are unimportant when the plasma is ionized by even a few percent [54, 72].

To find the contribution of scattering collisions to the rates of change of energy of the ions, electrons and neutral particles, the second moments of the operators for scattering collisions can be taken. Since $\mathbf{R}_\alpha = \sum_\sigma \mathbf{R}_{\alpha\sigma}$ and $Q_\alpha = \sum_\sigma Q_{\alpha\sigma}$ (equation A.3.6), equation A.3.7 becomes:

$$\int C_{\alpha}^{scatt.} \left(\frac{1}{2} m_{\alpha} V^2 \right) d\mathbf{V} = Q_{\alpha} + \mathbf{v}_{\alpha} \cdot \mathbf{R}_{\alpha} = \sum_{\sigma} Q_{\alpha\sigma} + \mathbf{v}_{\alpha} \cdot \sum_{\sigma} \mathbf{R}_{\alpha\sigma} \quad (8.2.3)$$

From appendix A.4, the second moment of the first term of the Boltzmann equation is

$$\frac{\partial}{\partial t} \left(\frac{1}{2} \rho_{\alpha} v_{\alpha}^2 + \frac{p_{\alpha}}{\gamma - 1} \right) = \frac{v^2}{2} \frac{\partial \rho_{\alpha}}{\partial t} + \rho_{\alpha} \mathbf{v}_{\alpha} \cdot \frac{\partial \mathbf{v}_{\alpha}}{\partial t} + \frac{1}{\gamma - 1} \frac{\partial p_{\alpha}}{\partial t}$$

where $\gamma = \frac{5}{3}$. Since $\left(\frac{\partial \rho_{\alpha}}{\partial t} \right)_{scatt.} = 0$, this leads to

$$\frac{1}{\gamma - 1} \left(\frac{\partial p_{\alpha}}{\partial t} \right)_{scatt.} = \left(\frac{\partial}{\partial t} \left(\frac{1}{2} \rho_{\alpha} v_{\alpha}^2 + \frac{p_{\alpha}}{\gamma - 1} \right) \right)_{scatt.} - \rho_{\alpha} \mathbf{v}_{\alpha} \cdot \left(\frac{\partial \mathbf{v}_{\alpha}}{\partial t} \right)_{scatt.}$$

Using equations 8.2.3 and 8.2.1, this implies that

$$\begin{aligned} \frac{1}{\gamma - 1} \left(\frac{\partial p_{\alpha}}{\partial t} \right)_{scatt.} &= \sum_{\sigma} Q_{\alpha\sigma} + \cancel{\mathbf{v}_{\alpha} \cdot \sum_{\sigma} \mathbf{R}_{\alpha\sigma}} - \cancel{\mathbf{v}_{\alpha} \cdot \sum_{\sigma} \mathbf{R}_{\alpha\sigma}} \\ &\Rightarrow \frac{1}{\gamma - 1} \left(\frac{\partial p_i}{\partial t} \right)_{scatt.} = Q_{ie} + Q_{in} \\ &\frac{1}{\gamma - 1} \left(\frac{\partial p_e}{\partial t} \right)_{scatt.} = Q_{ei} + Q_{en} \\ &\frac{1}{\gamma - 1} \left(\frac{\partial p_n}{\partial t} \right)_{scatt.} = Q_{ni} + Q_{ne} \end{aligned} \quad (8.2.4)$$

Here, $Q_{\alpha\sigma}$ represents the heat gained by species α due to scattering interactions with species σ . Again, due to the relative unimportance of neutral-charged particle scattering collisions [54, 72], the terms Q_{in} , Q_{en} , Q_{ni} , and Q_{ne} can usually be neglected.

8.3 Reactive collision terms

In this section, the terms in the species (ions, electrons and neutral fluids) mass, momentum and energy conservation equations that pertain to collisions associated with ionization, recombination, and charge exchange reactions will be assessed.

8.3.1 Ionization and recombination

8.3.1.1 Mass Conservation

For electron impact ionization, the collision operator defining the time-rate of change of f_n due to *reacting* collisions between neutral particles and electrons that result in electron impact ionization is [72]:

$$C_n^{ion} = -f_n(\mathbf{r}, \mathbf{V}, t) \int f_e(\mathbf{r}, \mathbf{V}, t) \sigma_{ion}(V_{rel}) V_{rel} d\mathbf{V} \quad (8.3.1)$$

Here, $\sigma_{ion}(V_{rel})$ [m^2] is the cross-section for electron impact ionization, and the relative particle speed for the ionization reaction is $V_{rel} = |\mathbf{V}_e - \mathbf{V}_n|$, where \mathbf{V}_e is the electron particle velocity and \mathbf{V}_n is the neutral particle velocity. To find the source rate for neutral particles due to electron impact ionization, the 0th moment of this operator is taken: $\Gamma_n^{ion} = - \int f_n(\mathbf{r}, \mathbf{V}', t) \left(\int f_e(\mathbf{r}, \mathbf{V}, t) \sigma_{ion}(V_{rel}) V_{rel} d\mathbf{V} \right) d\mathbf{V}'$. Referring to equation A.2.1, the inner integral is $\int f_e \sigma_{ion} V_{rel} d\mathbf{V} = n_e(\mathbf{r}, t) \langle \sigma_{ion} V_{rel} \rangle$, so that, using equation A.2.2, $\Gamma_n^{ion} = -n_n n_e \langle \sigma_{ion} V_{rel} \rangle$. Since the electron mass is much less than the neutral particle mass, it can be assumed that the electron particle (*i.e.*, thermal) velocity is much greater than the neutral particle velocity, so that $V_{rel} \sim V_e$:

$$\Gamma_n^{ion} = \int C_n^{ion} d\mathbf{V} = -n_n n_e \langle \sigma_{ion} V_e \rangle \quad (8.3.2)$$

$\Gamma_n^{ion} [\text{m}^{-3} \text{s}^{-1}]$ (units of particles per metre cubed per second) will appear on the right hand side of the neutral fluid mass continuity equation, constituting a sink of neutral particles due to impact ionization. For each neutral particle lost to ionization, an ion and electron are added to the system. The corresponding collision operators and source rates are

$$C_i^{ion} = C_e^{ion} = -C_n^{ion} \quad (8.3.3)$$

and

$$\Gamma_i^{ion} = \Gamma_e^{ion} = -\Gamma_n^{ion} \quad (8.3.4)$$

Equation 8.3.2 can also be derived with a more intuitive method that doesn't use the collision operator [54]. The mean free path for impact ionization collisions is defined by considering that there is one particle in the volume swept out by the cross-sectional area for impact ionization collisions over one mean free path: $n_n \sigma_{ion}(V_{rel}) \lambda_{mfp}^{ion} = 1 \Rightarrow \lambda_{mfp}^{ion} = \frac{1}{n_n \sigma_{ion}(V_{rel})}$. The frequency for electron impact ionization collisions is defined as an average over all velocities

in the Maxwellian distribution:

$$\nu_{ion} = \langle \frac{V_{rel}}{\lambda_{mfp}^{ion}} \rangle = n_n \langle \sigma_{ion}(V_{rel}) V_{rel} \rangle$$

so that, with $V_e \gg V_n$, and $V_{rel} = |\mathbf{V}_e - \mathbf{V}_n| \approx V_e$, $\nu_{ion} = n_n \langle \sigma_{ion} V_e \rangle$. From this, the rate of increase of ions per unit volume is again $\Gamma_i^{ion} = \Gamma_e^{ion} = -\Gamma_n^{ion} = n_n n_e \langle \sigma_{ion} V_e \rangle$. The velocity integrated quantity $\langle \sigma_{ion} V_e \rangle$ [m³/s] is the *ionization rate parameter* - its value can be found as a function of temperature from the fitting formula given by Voronov [103], as

$$\langle \sigma_{ion} V_e \rangle (\mathbf{r}, t) = \frac{A (1 + P \sqrt{U}) U^K \exp(-U)}{U + X} \quad (8.3.5)$$

where $U(\mathbf{r}, t) = \frac{\phi_{ion}}{T_e(\mathbf{r}, t)}$, with ϕ_{ion} being the effective ionization potential in the same units as T_e . As mentioned previously, an effective ionization potential including the excitation energy that is expended on average for each ionization event, as well as the electron binding energy, is used instead of the regular ionization energy, because, for simplicity, excited states are not tracked. An estimate of the validity of the formula for the ionization rate parameter is given by Voronov for each element. For example, for hydrogen, accuracy is to within 5% for electron temperatures from 1 eV to 20 keV. The MHD code has the option of either hydrogen, deuterium or helium as the neutral gas and plasma source. From [103], the coefficients required for equation 8.3.5 for these options are shown in table 8.3.1. Also included is the atomic diameter (d_{atom}) for each atom, which is used to calculate the viscous and thermal diffusion coefficients for the neutral fluid, using equations A.5.4 and A.5.5, where the mean free path for neutral-neutral collisions is defined in equation A.5.1. The values for effective ionization potentials are taken from [104], the atomic diameters from [100] and [105].

| ion type : | H | D | He |
|-------------------|--|--|--|
| ϕ_{ion} [eV] | 13.6 | 33 | 28 |
| A | 2.91×10^{-14} [m ³ /s] | 2.91×10^{-14} [m ³ /s] | 1.75×10^{-14} [m ³ /s] |
| P | 0 | 0 | 0 |
| K | 0.39 | 0.39 | 0.35 |
| X | 0.232 | 0.232 | 0.18 |
| d_{atom} [m] | 1.06×10^{-10} | 2.4×10^{-10} | 2.8×10^{-10} |

Table 8.3.1: Coefficients for calculating ionization rate parameters

The collision operators defining the time-rates of change of f_α due to reacting collisions

between ions and electrons that result in radiative recombination are [72]:

$$\begin{aligned} C_n^{rec} &= \frac{m_e}{m_n} f_e \int f_i \sigma_{rec}(V_{rel}) V_{rel} d\mathbf{V} + \frac{m_i}{m_n} f_i \int f_e \sigma_{rec}(V_{rel}) V_{rel} d\mathbf{V} \\ C_i^{rec} &= -f_i \int f_e \sigma_{rec}(V_{rel}) V_{rel} d\mathbf{V} \\ C_e^{rec} &= -f_e \int f_i \sigma_{rec}(V_{rel}) V_{rel} d\mathbf{V} \end{aligned} \quad (8.3.6)$$

Here, $V_{rel} = |\mathbf{V}_e - \mathbf{V}_i|$ is the relative particle speed, and $\sigma_{rec}(V_{rel})$ [m²] is the cross-section for radiative recombination. Since $m_e \ll m_n$, and $m_i \approx m_n$, $C_n^{rec} \approx -C_i^{rec}$. With $V_e \gg V_i$, and following the process of the derivation of equation 8.3.2, we arrive at

$$-\Gamma_n^{rec} \approx \Gamma_i^{rec} = \Gamma_e^{rec} = \int C_e^{rec} d\mathbf{V} = -n_i n_e \langle \sigma_{rec} V_e \rangle \quad (8.3.7)$$

As was shown above for the ionization rate parameter, this result can also be obtained, without taking moments of the collision operator, by considering the mean free path and collision frequency associated with recombination [54]. The velocity integrated quantity $\langle \sigma_{rec} V_e \rangle$ [m³/s] is the *recombination rate parameter* - its value can be estimated as a function of electron temperature as [106, 100, 54]

$$\langle \sigma_{rec} V_e \rangle(\mathbf{r}, t) = 2.6 \times 10^{-19} \frac{Z_{eff}^2}{\sqrt{T_e(\mathbf{r}, t) [eV]}} \quad (8.3.8)$$

Here, the recombination rate is for recombination to charge state $Z_{eff} - 1$. Referring to the expressions for two-plasma-fluid mass continuity in the absence of neutral particles and reactive collisions (equation A.4.4), when the particle source rates due to reactive collisions defined in equations 8.3.2, 8.3.4, and 8.3.7 are included, we arrive at the mass continuity equations for the three-fluid system:

$$\begin{aligned} \dot{n}_i &= -\nabla \cdot (n_i \mathbf{v}_i) + \Gamma_i^{ion} - \Gamma_n^{rec} \\ \dot{n}_e &= -\nabla \cdot (n_e \mathbf{v}_e) + \Gamma_i^{ion} - \Gamma_n^{rec} \\ \dot{n}_n &= -\nabla \cdot (n_n \mathbf{v}_n) + \Gamma_n^{rec} - \Gamma_i^{ion} + \Gamma_n^{ext} \end{aligned} \quad (8.3.9)$$

Note that all source terms here, as well as each of n_α and \mathbf{v}_α , are functions of \mathbf{r} and t . In the experiment, the gas puff valves take time to shut, and remain open for several hundred microseconds after the formation banks are fired, so neutral particles are being added to the system near the valves. Additionally, neutral particles are sourced through recycling processes at the vacuum vessel walls, although this recycling effect hasn't yet been implemented in the

code. An additional neutral *external* source term, $\Gamma_n^{ext}(\mathbf{r}, t) [\text{m}^{-3} \text{s}^{-1}]$, has been included on the right side of the expression for \dot{n}_n , in order to be able to simulate neutral particle injection.

8.3.1.2 Momentum Conservation

To find the contributions of ionization and recombination reactions to the rates of change of momentum of the ions, electrons, and neutral particles, the first moments of the reacting collision operators defined in equations 8.3.1, 8.3.3, and 8.3.6 can be taken. This can be done explicitly, as is shown in [72, 100]. However, it is instructive to demonstrate that the formal process of taking first moments (and second moments for the contributions to the rates of change of energy) can be skipped, to arrive at results equivalent to those presented in [72, 100], but with evaluation of the terms which determine the volumetric rate of thermal energy transfer from electrons to photons and neutral particles due to radiative recombination.

Referring to equation 8.3.9, the general form of the expression for the species rates of change of number density that correspond to the reactive collisions of ionization and recombination, and also to any external particle sources, is

$$\left(\frac{\partial n_\alpha}{\partial t} \right)_{ire} = \sum_k S_{\alpha k} \quad (8.3.10)$$

Here, $(X)_{ire}$ denotes the part of X that pertains to the reactive collisions of *ionization* and *recombination*, and to any *external* particle sources. $S_{\alpha k} [\text{m}^{-3} \text{s}^{-1}]$ represents the k^{th} source (in units of particles per metres cubed per second) for particles of type α , as determined from equation 8.3.9. Here, $S_{i1} = S_{e1} = -S_{n2} = \Gamma_i^{ion}$, $S_{i2} = S_{e2} = -S_{n1} = -\Gamma_n^{rec}$, and $S_{n3} = \Gamma_n^{ext}$. Note that particle "sources" with a negative sign such as $S_{i2} = -\Gamma_n^{rec}$ in the expression for \dot{n}_i in equation 8.3.9, are actually particle sinks.

Species momentum conservation is described, in the absence of reactive collisions, by equation A.4.5:

$$\frac{\partial(\rho_\alpha \mathbf{v}_\alpha)}{\partial t} = -\nabla \cdot \underline{\mathbf{p}}_\alpha - \nabla \cdot (\rho_\alpha \mathbf{v}_\alpha \mathbf{v}_\alpha) + q_\alpha n_\alpha (\mathbf{E} + \mathbf{v}_\alpha \times \mathbf{B}) + \mathbf{R}_\alpha$$

To include the terms that correspond to the reactive collisions of ionization and recombination, and to any external particle sources, this can be written as

$\frac{\partial(m_\alpha n_\alpha \mathbf{v}_\alpha)}{\partial t} = \dots + \left(\frac{\partial(m_\alpha n_\alpha \mathbf{v}_\alpha)}{\partial t} \right)_{ire}$, where "..." represents the right side of equation A.4.5. Particles sourced by $S_{\alpha k}$ add, or (for sources with negative sign), remove, species α momentum $\sum_j m_{0jk} \mathbf{v}_{0jk}$, where m_{0jk} and \mathbf{v}_{0jk} are the mass and fluid velocity of the particles of type j which have their momentum introduced or taken away. The summation over sourced parti-

cles of type j is relevant only for $S_{\alpha k} = S_{n1} = \Gamma_n^{rec}$; recombination is a source for total neutral particle momentum, and each neutral particle added to the neutral population through recombination initially has momentum $m_i \mathbf{v}_i + m_e \mathbf{v}_e$. The general form of the expression for the species rates of change of momentum that correspond to the reactive collisions of ionization and recombination, and also to any external particle sources, is

$$\left(\frac{\partial(m_\alpha n_\alpha \mathbf{v}_\alpha)}{\partial t} \right)_{ire} = \sum_k \left(S_{\alpha k} \sum_j (m_{0jk} \mathbf{v}_{0jk}) \right) \quad (8.3.11)$$

This expression must be retained for the neutral recombination source term S_{n1} . However, for all other source terms, $\sum_j (m_{0jk} \mathbf{v}_{0jk}) \rightarrow m_\alpha \mathbf{v}_{0k}$, where \mathbf{v}_{0k} is the "initial" fluid velocity (*i.e.*, the fluid velocity at the time when the ionization or recombination reaction occurs) of the particles of type α which are introduced or taken away due to source $S_{\alpha k}$, and the general expression can be simplified to

$$\left(\frac{\partial(m_\alpha n_\alpha \mathbf{v}_\alpha)}{\partial t} \right)_{ire} = m_\alpha \sum_k (S_{\alpha k} \mathbf{v}_{0k})$$

The corresponding additional terms on the right side of the momentum equations are:

$$\begin{aligned} \left(\frac{\partial(m_i n_i \mathbf{v}_i)}{\partial t} \right)_{ire} &= \Gamma_i^{ion} m_i \mathbf{v}_n - \Gamma_n^{rec} m_i \mathbf{v}_i \\ \left(\frac{\partial(m_e n_e \mathbf{v}_e)}{\partial t} \right)_{ire} &= \Gamma_i^{ion} m_e \mathbf{v}_n - \Gamma_n^{rec} m_e \mathbf{v}_e \\ \left(\frac{\partial(m_n n_n \mathbf{v}_n)}{\partial t} \right)_{ire} &= \Gamma_n^{rec} (m_i \mathbf{v}_i + m_e \mathbf{v}_e) - \Gamma_i^{ion} m_n \mathbf{v}_n + \Gamma_n^{ext} m_n \mathbf{v}_{n0} \end{aligned} \quad (8.3.12)$$

For example, in the expression above for $\left(\frac{\partial(m_i n_i \mathbf{v}_i)}{\partial t} \right)_{ire}$, ions that are sourced from neutral particles through ionization add to the total ion momentum, and newly ionized particles are introduced with velocity \mathbf{v}_n . Meanwhile, ions with velocity \mathbf{v}_i , that are lost to recombination, take away from the total ion momentum. Each neutral particle introduced by recombination initially has momentum $m_i \mathbf{v}_i + m_e \mathbf{v}_e$. Neutral particles introduced by external sources such as gas puffing also add neutral particle momentum - each externally sourced neutral has initial momentum $m_n \mathbf{v}_{n0}$, where \mathbf{v}_{n0} is its initial velocity.

Using equation 8.3.10, equation 8.3.11 can be recast as

$$\begin{aligned}
\left(\frac{\partial(m_\alpha n_\alpha \mathbf{v}_\alpha)}{\partial t} \right)_{ire} &= m_\alpha n_\alpha \left(\frac{\partial \mathbf{v}_\alpha}{\partial t} \right)_{ire} + m_\alpha \mathbf{v}_\alpha \left(\frac{\partial n_\alpha}{\partial t} \right)_{ire} = \sum_k \left(S_{\alpha k} \sum_j (m_{0jk} \mathbf{v}_{0jk}) \right) \\
&= m_\alpha n_\alpha \left(\frac{\partial \mathbf{v}_\alpha}{\partial t} \right)_{ire} + m_\alpha \mathbf{v}_\alpha \left(\sum_k S_{\alpha k} \right) \\
\Rightarrow m_\alpha n_\alpha \left(\frac{\partial \mathbf{v}_\alpha}{\partial t} \right)_{ire} &= \sum_k \left(S_{\alpha k} \sum_j (m_{0jk} \mathbf{v}_{0jk}) \right) - m_\alpha \mathbf{v}_\alpha \left(\sum_k S_{\alpha k} \right)
\end{aligned} \tag{8.3.13}$$

For the ions and electrons (all sources), and for the neutral source terms corresponding to ionization and external sources, where $\sum_j (m_{0jk} \mathbf{v}_{0jk}) \rightarrow m_\alpha \mathbf{v}_{0k}$, this general expression can be simplified to

$$m_\alpha n_\alpha \left(\frac{\partial \mathbf{v}_\alpha}{\partial t} \right)_{ire} = m_\alpha \sum_k (S_{\alpha k} (\mathbf{v}_{0k} - \mathbf{v}_\alpha)) \tag{8.3.14}$$

Equation 8.3.14 and (for neutral recombination only) equation 8.3.13 lead to:

$$\begin{aligned}
\rho_i \left(\frac{\partial \mathbf{v}_i}{\partial t} \right)_{ire} &= \Gamma_i^{ion} m_i (\mathbf{v}_n - \mathbf{v}_i) \\
\rho_e \left(\frac{\partial \mathbf{v}_e}{\partial t} \right)_{ire} &= \Gamma_i^{ion} m_e (\mathbf{v}_n - \mathbf{v}_e) \\
\rho_n \left(\frac{\partial \mathbf{v}_n}{\partial t} \right)_{ire} &= \Gamma_n^{rec} (m_i \mathbf{v}_i + m_e \mathbf{v}_e - m_n \mathbf{v}_n) + \Gamma_n^{ext} m_n (\mathbf{v}_{n0} - \mathbf{v}_n)
\end{aligned} \tag{8.3.15}$$

8.3.1.3 Energy Conservation

Assuming Maxwellian distributions for each of species α , so that $p_\alpha = n_\alpha T_\alpha$, the part of the species energy equation that corresponds to particle sources due to the reactive collisions of ionization and recombination, and to external particle sources, can be written as

$$\left(\frac{\partial}{\partial t} \left(\frac{1}{2} m_\alpha n_\alpha v_\alpha^2 + \frac{p_\alpha}{\gamma - 1} \right) \right)_{ire} = \frac{1}{2} \sum_k \left(S_{\alpha k} \sum_j (m_{0jk} v_{0jk}^2) \right) + \frac{1}{\gamma - 1} \sum_k \left(\xi_{\alpha k} S_{\alpha k} \sum_j T_{0jk} \right) \tag{8.3.16}$$

Here, $\xi_{\alpha k}$ is a particle *mass ratio* that must be considered for the ionization source that introduces ions ($S_{i1} = \Gamma_i^{ion}$) and electrons ($S_{e1} = \Gamma_i^{ion}$), and for the recombination source that introduces neutral particles ($S_{n1} = \Gamma_n^{rec}$). To clarify this for the ionization source, when a neutral particle with thermal energy $\frac{1}{\gamma-1} T_n$ is ionized, the resultant ion and electron have thermal energies $\frac{m_i}{m_n} \frac{1}{\gamma-1} T_n$ and $\frac{m_e}{m_n} \frac{1}{\gamma-1} T_n$ respectively, so that their combined thermal energy is equal to that of the original neutral.

To clarify the relevance of $\xi_{\alpha k}$ for the recombination source, simple analysis of the kine-

matics of the radiative recombination reaction indicates that the bulk of the electron thermal energy, and a fraction of the ion thermal energy, is transferred to the emitted photon. Noting that $m_i \sim m_n \gg m_e$, then, in the rest frame of the neutral particle (post reaction), the ion (prior to the reaction) has negligible kinetic energy (*ie.*, thermal energy, since we are considering single particles with random velocities), the electron has approximately the same energy that it has in the laboratory frame, and the neutral particle has no kinetic energy. Consequently, as an approximation, the bulk of the electron thermal energy (of the order $\sim (m_i/m_n) T_e / (\gamma - 1)$) and a negligible portion of the ion thermal energy ($\sim (m_e/m_n) T_i / (\gamma - 1)$) is transferred to the photon emitted in the radiative recombination reaction, while a negligible portion of the electron thermal energy (of the order $\sim (m_e/m_n) T_e / (\gamma - 1)$) and the bulk of the ion thermal energy ($\sim (m_i/m_n) T_i / (\gamma - 1)$) is transferred to the neutral particle. The combined thermal energy of the neutral particle and photon is equal to the combined thermal energy of the ion and electron. Note that for Γ_n^{ext} , the external neutral particle source, $\xi_{\alpha k} = 1$.

Once again, the summation over j is relevant only for $S_{\alpha k} = S_{n1} = \Gamma_n^{rec}$; recombination is a source for neutral particle energy, and it is assumed that each neutral particle added to the neutral particle population through recombination initially has energy $\frac{1}{2} (m_i v_i^2 + m_e v_e^2) + \frac{1}{\gamma-1} \left(\frac{m_i}{m_n} T_i + \frac{m_e}{m_n} T_e \right)$. Note that for all other sources (apart from recombination) the summation over j in equation 8.3.16 can be neglected; $\sum_j T_{0jk} \rightarrow T_{0k}$, where T_{0k} is the initial temperature of the sourced particle, and $\sum_j (m_{0jk} v_{0jk}^2) \rightarrow m_{\alpha} v_{0k}^2$. We want to obtain an expression for $\left(\frac{\partial p_{\alpha}}{\partial t} \right)_{ire}$, which will be included on the right side of the species energy equations which have the form $\frac{\partial p_{\alpha}}{\partial t} = \dots$. The first step is to use equation 8.3.10 to expand the partial derivative in equation 8.3.16:

$$\begin{aligned} \frac{1}{2} m_{\alpha} v_{\alpha}^2 \left(\frac{\partial n_{\alpha}}{\partial t} \right)_{ire} + m_{\alpha} n_{\alpha} \mathbf{v}_{\alpha} \cdot \left(\frac{\partial \mathbf{v}_{\alpha}}{\partial t} \right)_{ire} + \frac{1}{\gamma-1} \left(\frac{\partial p_{\alpha}}{\partial t} \right)_{ire} &= \frac{1}{2} \sum_k \left(S_{\alpha k} \sum_j (m_{0jk} v_{0jk}^2) \right) + \frac{1}{\gamma-1} \sum_k \left(\xi_{\alpha k} S_{\alpha k} \sum_j T_{0jk} \right) \\ \Rightarrow \frac{1}{\gamma-1} \left(\frac{\partial p_{\alpha}}{\partial t} \right)_{ire} &= \frac{1}{\gamma-1} \sum_k \left(\xi_{\alpha k} S_{\alpha k} \sum_j T_{0jk} \right) + \frac{1}{2} \sum_k \left(S_{\alpha k} \sum_j (m_{0jk} v_{0jk}^2) \right) - \frac{1}{2} m_{\alpha} v_{\alpha}^2 \sum_k (S_{\alpha k}) - m_{\alpha} n_{\alpha} \mathbf{v}_{\alpha} \cdot \left(\frac{\partial \mathbf{v}_{\alpha}}{\partial t} \right)_{ire} \end{aligned}$$

Using equation 8.3.13, this implies that

$$\begin{aligned} \left(\frac{\partial p_{\alpha}}{\partial t} \right)_{ire} &= \sum_k \left(\xi_{\alpha k} S_{\alpha k} \sum_j T_{0jk} \right) + (\gamma-1) \left[\frac{1}{2} \sum_k \left(S_{\alpha k} \sum_j (m_{0jk} v_{0jk}^2) \right) \right. \\ &\quad \left. - \frac{1}{2} m_{\alpha} v_{\alpha}^2 \sum_k (S_{\alpha k}) - \mathbf{v}_{\alpha} \cdot \left(\sum_k \left(S_{\alpha k} \sum_j (m_{0jk} \mathbf{v}_{0jk}) \right) - m_{\alpha} \mathbf{v}_{\alpha} \left(\sum_k S_{\alpha k} \right) \right) \right] \\ \Rightarrow \left(\frac{\partial p_{\alpha}}{\partial t} \right)_{ire} &= \sum_k \left(\xi_{\alpha k} S_{\alpha k} \sum_j T_{0jk} \right) + (\gamma-1) \left(\frac{1}{2} m_{\alpha} v_{\alpha}^2 \sum_k (S_{\alpha k}) + \sum_k \left(S_{\alpha k} \sum_j \left(m_{0jk} \left(\frac{1}{2} v_{0jk}^2 - \mathbf{v}_{\alpha} \cdot \mathbf{v}_{0jk} \right) \right) \right) \right) \\ \Rightarrow \left(\frac{\partial p_{\alpha}}{\partial t} \right)_{ire} &= \sum_k \left(\xi_{\alpha k} S_{\alpha k} \sum_j T_{0jk} \right) + (\gamma-1) \left(\sum_k \left(S_{\alpha k} \left(\frac{1}{2} m_{\alpha} v_{\alpha}^2 + \sum_j \left(m_{0jk} \left(\frac{1}{2} v_{0jk}^2 - \mathbf{v}_{\alpha} \cdot \mathbf{v}_{0jk} \right) \right) \right) \right) \right) \end{aligned} \tag{8.3.17}$$

For the ions and electrons (all sources), and for the neutral source terms corresponding to ionization and external sources, where $\sum_j m_{0jk} \mathbf{v}_{0jk} \rightarrow m_\alpha \mathbf{v}_{0k}$, $\sum_j (m_{0jk} v_{0jk}^2) \rightarrow m_\alpha v_{0k}^2$, and $\sum_j T_{0jk} \rightarrow T_{0k}$, this general expression can be simplified to

$$\begin{aligned} \left(\frac{\partial p_\alpha}{\partial t} \right)_{ire} &= \sum_k (\xi_{\alpha k} S_{\alpha k} T_{0k}) + (\gamma - 1) \left(\frac{1}{2} m_\alpha \sum_k (S_{\alpha k} (v_\alpha^2 - 2\mathbf{v}_\alpha \cdot \mathbf{v}_{0k} + v_{0k}^2)) \right) \\ \Rightarrow \left(\frac{\partial p_\alpha}{\partial t} \right)_{ire} &= \sum_k (\xi_{\alpha k} S_{\alpha k} T_{0k}) + (\gamma - 1) \left(\frac{1}{2} m_\alpha \sum_k (S_{\alpha k} (\mathbf{v}_\alpha - \mathbf{v}_{0k})^2) \right) \end{aligned}$$

However, the more complicated form of equation 8.3.17 must be retained for the recombination neutral source term.

The resultant forms for the individual species are:

$$\begin{aligned} \left(\frac{\partial p_i}{\partial t} \right)_{ire} &= \Gamma_i^{ion} \frac{m_i}{m_n} T_n - \Gamma_n^{rec} T_i + (\gamma - 1) \frac{1}{2} m_i (\Gamma_i^{ion} (\mathbf{v}_i - \mathbf{v}_n)^2) \\ \left(\frac{\partial p_e}{\partial t} \right)_{ire} &= \Gamma_i^{ion} \frac{m_e}{m_n} T_n - \Gamma_n^{rec} T_e + (\gamma - 1) \left(\Gamma_i^{ion} \left(\frac{1}{2} m_e (\mathbf{v}_e - \mathbf{v}_n)^2 - \phi_{ion} \right) \right) \\ \left(\frac{\partial p_n}{\partial t} \right)_{ire} &= \Gamma_n^{rec} \left(\frac{m_i}{m_n} T_i + \frac{m_e}{m_n} T_e \right) - \Gamma_i^{ion} T_n + \Gamma_n^{ext} T_{n0} + (\gamma - 1) \left[\Gamma_n^{rec} \left(\frac{1}{2} m_n v_n^2 + \frac{1}{2} m_i v_i^2 \right. \right. \\ &\quad \left. \left. + \frac{1}{2} m_e v_e^2 - m_i \mathbf{v}_n \cdot \mathbf{v}_i - m_e \mathbf{v}_n \cdot \mathbf{v}_e \right) + \Gamma_n^{ext} \frac{1}{2} m_n (\mathbf{v}_n - \mathbf{v}_{n0})^2 \right] \end{aligned} \quad (8.3.18)$$

Here, T_{n0} is the initial temperature of the externally sourced neutral particles. The effective ionization energy has been included as a sink of electron energy - recalling that $U_{Th} = \frac{p}{\gamma-1}$, for each electron with energy $\left(\frac{1}{\gamma-1} \frac{m_e}{m_n} T_n + \frac{1}{2} m_e (\mathbf{v}_e - \mathbf{v}_n)^2 \right)$ Joules that is sourced by ionization, another electron has expended ϕ_{ion} Joules to initiate the ionization process.

The following definitions are made, representing the thermal energy per unit volume per second transferred between species due to ionization and recombination processes:

$$\begin{aligned} Q_n^{ion} &= \Gamma_i^{ion} \frac{1}{\gamma-1} T_n && \text{(neutral particles} \rightarrow \text{ions and electrons, due to ionization)} \\ Q_i^{rec} &= \Gamma_n^{rec} \frac{1}{\gamma-1} T_i && \text{(ions} \rightarrow \text{neutral particles (and photons), due to recombination)} \\ Q_e^{rec} &= \Gamma_n^{rec} \frac{1}{\gamma-1} T_e && \text{(electrons} \rightarrow \text{photons (and neutral particles), due to recombination)} \end{aligned} \quad (8.3.19)$$

Hence, equation 8.3.18 can be re-expressed as:

$$\begin{aligned}
\left(\frac{\partial p_i}{\partial t} \right)_{ire} &= (\gamma - 1) \left(\frac{m_i}{m_n} Q_n^{ion} - Q_i^{rec} + \frac{1}{2} m_i \left(\Gamma_i^{ion} (\mathbf{v}_i - \mathbf{v}_n)^2 \right) \right) \\
\left(\frac{\partial p_e}{\partial t} \right)_{ire} &= (\gamma - 1) \left(\frac{m_e}{m_n} Q_n^{ion} - Q_e^{rec} + \Gamma_i^{ion} \left(\frac{1}{2} m_e (\mathbf{v}_e - \mathbf{v}_n)^2 - \phi_{ion} \right) \right) \\
\left(\frac{\partial p_n}{\partial t} \right)_{ire} &= (\gamma - 1) \left[\frac{m_i}{m_n} Q_i^{rec} + \frac{m_e}{m_n} Q_e^{rec} - Q_n^{ion} \right. \\
&\quad \left. + \Gamma_n^{rec} \left(\frac{1}{2} m_n v_n^2 + \frac{1}{2} m_i v_i^2 + \frac{1}{2} m_e v_e^2 - m_i \mathbf{v}_n \cdot \mathbf{v}_i - m_e \mathbf{v}_n \cdot \mathbf{v}_e \right) \right. \\
&\quad \left. + \Gamma_n^{ext} \frac{1}{2} m_n (\mathbf{v}_n - \mathbf{v}_{n0})^2 \right] + \Gamma_n^{ext} T_{n0} \tag{8.3.20}
\end{aligned}$$

It is worth noting that in the derivations presented in [72, 100], that Q_e^{rec} (thermal energy transferred from electrons to neutral particles due to recombination, per m^3 per second) is not evaluated because its derivation with the moment-taking method leads to an integral that cannot be solved easily. In particular, the second moment of C_e^{rec} , where C_e^{rec} is defined in equation 8.3.6, is

$$\begin{aligned}
\int \frac{1}{2} m_e V^2 C_e^{rec} d\mathbf{V} &= -\frac{1}{2} m_e \int V'^2 \left(f_e \int f_i \sigma_{rec}(V_{rel}) V_{rel} d\mathbf{V} \right) d\mathbf{V}' \\
&= -\frac{1}{2} m_e n_i \left(v_e^2 \int f_e \sigma_{rec}(V_{rel}) V_{rel} d\mathbf{V} + \int c_e^2 f_e \sigma_{rec}(V_{rel}) V_{rel} d\mathbf{V} \right)
\end{aligned}$$

Here the substitution $\mathbf{V} = \mathbf{c}_e(\mathbf{r}, t) + \mathbf{v}_e(\mathbf{r}, t)$ (equation A.2.5) has been made, and equations A.2.6 and A.2.7 are used. Following the procedure for the example derivation at the beginning of this section (0^{th} moment of C_n^{ion}), the first integral is simply

$-\frac{1}{2} m_e n_i \left(v_e^2 \int f_e \sigma_{rec}(V_{rel}) V_{rel} d\mathbf{V} \right) = -\Gamma_n^{rec} \frac{1}{2} m_e v_e^2$. It is assumed that the electron thermal speed is much greater than the ion thermal speed $V_{the} \gg V_{thi}$, and also much greater than the relative ion-electron fluid speed $V_{the} \gg |\mathbf{v}_i - \mathbf{v}_e|$, so that $V_{rel} \approx c_e$, and the second integral reduces to $-\frac{1}{2} m_e n_i \left(\int c_e^3 f_e \sigma_{rec}(c_e) d\mathbf{V} \right)$. The definition $Q_e^{rec} = \frac{1}{2} m_e n_i \left(\int c_e^3 f_e \sigma_{rec}(c_e) d\mathbf{V} \right)$ is made in [72, 100], but the integral cannot be easily evaluated, and it is suggested that this term can be dropped if the loss of electron thermal energy due to recombination is not expected to play an important role in the energy balance. However, from equation 8.3.19, it can be seen that $Q_e^{rec} = \frac{T_e}{T_i} Q_i^{rec}$, so that in cases where $T_i \sim T_e$, it would be unreasonable to neglect Q_e^{rec} while retaining Q_i^{rec} . The Q_e^{rec} term is included as an undetermined energy sink/source for the electron/neutral fluids respectively in [72, 100], without scaling by the factor m_e/m_n in the neutral fluid energy equation, and is ignored when the equations are implemented to code. When implemented to the DELiTE framework MHD code, it was found that inclusion of the Q_e^{rec} term as an energy source for the neutral fluid (without the

scaling factor m_e/m_n in equation 8.3.20) leads to significant increases in neutral particle temperature, as shown in section 8.9.1.

However, as discussed above, from looking at the kinematics of the radiative recombination reaction, it is more physical to neglect Q_e^{rec} as an energy source for the neutral fluid, but include it as an energy sink for the electron fluid, while Q_i^{rec} may be included as both an energy source for the neutral fluid and an energy sink for the ion fluid. As discussed in section 8.9.1, peak electron temperature falls by around just one percent when the Q_e^{rec} term is included as energy sink for the electron fluid. Overall, in the regimes studied, it turns out that the Q_e^{rec} term can be neglected without significantly affecting electron temperature.

8.3.2 Charge exchange

In order to find the terms in the MHD equations that correspond to the charge exchange reactions, the process of taking moments of the charge exchange collision operators can't be avoided due to, and is complicated by, the degeneracy associated with the charge exchange reaction. In this work, the details of the process won't be reproduced - only the required results that were originally achieved in [107], and then very well detailed in [72, 100], will be presented.

The collision operators defining the time-rates of change of f_n and f_i due to reacting collisions between ions and neutral particles that result in charge exchange are [72]:

$$C_n^{cx} = \frac{m_i}{m_n} f_i \int f_n \sigma_{cx}(V_{rel}) V_{rel} d\mathbf{V} - \frac{m_i}{m_n} f_n \int f_i \sigma_{cx}(V_{rel}) V_{rel} d\mathbf{V}$$

$$C_i^{cx} = f_n \int f_i \sigma_{cx}(V_{rel}) V_{rel} d\mathbf{V} - f_i \int f_n \sigma_{cx}(V_{rel}) V_{rel} d\mathbf{V}$$

$\sigma_{cx}(V_{rel})$ [m²] is the cross-section for charge exchange collisions. In this case, $V_{rel} = |\mathbf{V}_i - \mathbf{V}_n|$, is the relative particle speed for the reaction, where \mathbf{V}_i is the ion particle velocity and \mathbf{V}_n is the neutral particle velocity. The first term in the expression for C_n^{cx} and the second term in the expression for C_i^{cx} represent the conversion of ions to neutral particles, the other two terms represent the conversion of neutral particles to ions.

8.3.2.1 0th moment of the charge exchange collision operator

Charge exchange collisions do not change the number of ions, electrons or neutral particles, but the 0th moment will be taken here to help illustrate some of the details of the charge exchange collision terms. Using the method outlined in [107], and detailed in [100], a good

approximation for C_i^{cx} is

$$C_i^{cx} \approx \sigma_{cx}(V_i^* n_i f_n - V_n^* n_n f_i)$$

where $V_\alpha^* = V_{th\alpha} \sqrt{4/\pi + (|\mathbf{V} - \mathbf{v}_\alpha|/V_{th\alpha})^2}$. The 0th moments of C_i^{cx} and C_n^{cx} can then be evaluated as $\int C_i^{cx} d\mathbf{V} = (\Gamma^{cx} - \Gamma^{cx}) = 0$, and $\int C_n^{cx} d\mathbf{V} = \frac{m_i}{m_n}(\Gamma^{cx} - \Gamma^{cx}) = 0$, where Γ^{cx} [m⁻³s⁻¹] is the source rate of neutral particles, equal to the source rate of ions, for the charge exchange reaction:

$$\Gamma^{cx} = n_i n_n \sigma_{cx}(V_{cx}) V_{cx} \quad (8.3.21)$$

Note σ_{cx} is evaluated at V_{cx} , where V_{cx} is a representative speed for charge exchange collisions [107, 72]:

$$V_{cx} = \sqrt{\frac{4}{\pi} V_{thi}^2 + \frac{4}{\pi} V_{thn}^2 + v_{in}^2} \quad (8.3.22)$$

where $v_{in} = |\mathbf{v}_{in}| = |\mathbf{v}_i - \mathbf{v}_n|$. A formula for $\sigma_{cx}(V_{cx})$ [m²] can be found based on charge exchange data from Barnett [108, 100]. For hydrogen and deuterium the fitting formulae are

$$\begin{aligned} \sigma_{cx-H}(V_{cx}) &= 1.12 \times 10^{-18} - 7.15 \times 10^{-20} \ln(V_{cx}) \\ \sigma_{cx-D}(V_{cx}) &= 1.09 \times 10^{-18} - 7.15 \times 10^{-20} \ln(V_{cx}) \end{aligned} \quad (8.3.23)$$

8.3.2.2 1st moment of the charge exchange collision operator

The first moments of the charge exchange collision operators are [107, 72]:

$$\begin{aligned} \int m_i \mathbf{V} C_i^{cx} d\mathbf{V} &\approx -m_i \mathbf{v}_{in} \Gamma^{cx} - \mathbf{R}_{ni}^{cx} + \mathbf{R}_{in}^{cx} \\ \int m_n \mathbf{V} C_n^{cx} d\mathbf{V} &\approx m_i \mathbf{v}_{in} \Gamma^{cx} + \mathbf{R}_{ni}^{cx} - \mathbf{R}_{in}^{cx} \end{aligned} \quad (8.3.24)$$

where

$$\begin{aligned} \mathbf{R}_{in}^{cx} &\approx -m_i \sigma_{cx}(V_{cx}) n_i n_n \mathbf{v}_{in} V_{thn}^2 \left(4 \left(\frac{4}{\pi} V_{thi}^2 + v_{in}^2 \right) + \frac{9\pi}{4} V_{thn}^2 \right)^{-\frac{1}{2}} \\ \mathbf{R}_{ni}^{cx} &\approx m_i \sigma_{cx}(V_{cx}) n_i n_n \mathbf{v}_{in} V_{thi}^2 \left(4 \left(\frac{4}{\pi} V_{thn}^2 + v_{in}^2 \right) + \frac{9\pi}{4} V_{thi}^2 \right)^{-\frac{1}{2}} \end{aligned} \quad (8.3.25)$$

The term $m_i \mathbf{v}_{in} \Gamma^{cx}$ represents the transfer of momentum due to bulk fluid effects [72, 100]. \mathbf{R}_{ni}^{cx} and \mathbf{R}_{in}^{cx} represent frictional drag forces that arise due to charge exchange, with $\mathbf{v}_{in} = \mathbf{v}_i - \mathbf{v}_n$. Such frictional terms do not arise for the ionization and recombination processes, in which the electron thermal speed is assumed to be far higher than the relative parti-

cle motion [72, 100]. The derivation of the moments of the reacting collision operators assumes that the reacting species are described by Maxwellian distributions. As a result, non-Maxwellian effects due to thermal gradients are neglected and don't appear in the expressions for \mathbf{R}_{ni}^{cx} and \mathbf{R}_{in}^{cx} [72], as they did in the expressions for \mathbf{R}_{ei} and \mathbf{R}_{ie} (equation A.5.15).

The notation $(X)_{cx}$ is introduced to represent the part of X that pertains to charge exchange collisions, in the same way that $(X)_{ire}$ is the part of X relating to ionization, recombination and external sources (section 8.3.1). Recall that m_α times the first moment of the first term of the Boltzmann equation is $\frac{\partial(\rho_\alpha \mathbf{v}_\alpha)}{\partial t}$ (appendix A.4). Since $\left(\frac{\partial(\rho_\alpha \mathbf{v}_\alpha)}{\partial t}\right)_{cx} = \rho_\alpha \left(\frac{\partial \mathbf{v}_\alpha}{\partial t}\right)_{cx} + \mathbf{v}_\alpha \left(\frac{\partial \rho_\alpha}{\partial t}\right)_{cx}$, and charge exchange is not a net source of particles ($\Rightarrow \left(\frac{\partial \rho_\alpha}{\partial t}\right)_{cx} = 0$), the terms $\rho_\alpha \left(\frac{\partial \mathbf{v}_\alpha}{\partial t}\right)_{cx}$ can be expressed, using equation 8.3.24, as:

$$\begin{aligned} \rho_i \left(\frac{\partial \mathbf{v}_i}{\partial t}\right)_{cx} &\approx -m_i \mathbf{v}_{in} \Gamma^{cx} - \mathbf{R}_{ni}^{cx} + \mathbf{R}_{in}^{cx} \\ \rho_n \left(\frac{\partial \mathbf{v}_n}{\partial t}\right)_{cx} &\approx m_i \mathbf{v}_{in} \Gamma^{cx} + \mathbf{R}_{ni}^{cx} - \mathbf{R}_{in}^{cx} \end{aligned} \quad (8.3.26)$$

8.3.2.3 2nd moment of the charge exchange collision operator

The second moments of the charge exchange collision operators are [107, 72]:

$$\begin{aligned} \int \frac{1}{2} m_i V^2 C_i^{cx} d\mathbf{V} &\approx \Gamma^{cx} \frac{1}{2} m_i (v_n^2 - v_i^2) + \mathbf{v}_n \cdot \mathbf{R}_{in}^{cx} - \mathbf{v}_i \cdot \mathbf{R}_{ni}^{cx} + Q_{in}^{cx} - Q_{ni}^{cx} \\ \int \frac{1}{2} m_n V^2 C_n^{cx} d\mathbf{V} &\approx \Gamma^{cx} \frac{1}{2} m_i (v_i^2 - v_n^2) - \mathbf{v}_n \cdot \mathbf{R}_{in}^{cx} + \mathbf{v}_i \cdot \mathbf{R}_{ni}^{cx} - Q_{in}^{cx} + Q_{ni}^{cx} \end{aligned} \quad (8.3.27)$$

where

$$\begin{aligned} Q_{in}^{cx} &\approx m_i \sigma_{cx}(V_{cx}) n_i n_n \frac{3}{4} V_{thn}^2 \sqrt{\frac{4}{\pi} V_{thi}^2 + \frac{64}{9\pi} V_{thn}^2 + v_{in}^2} \\ Q_{ni}^{cx} &\approx m_i \sigma_{cx}(V_{cx}) n_i n_n \frac{3}{4} V_{thi}^2 \sqrt{\frac{4}{\pi} V_{thn}^2 + \frac{64}{9\pi} V_{thi}^2 + v_{in}^2} \end{aligned} \quad (8.3.28)$$

Here, Q_{in}^{cx} and Q_{ni}^{cx} represent the transfer of thermal energy [72, 100] associated with charge exchange reactions. As mentioned above, non-Maxwellian effects due to thermal gradients are neglected; therefore they don't appear in the expressions for Q_{in}^{cx} and Q_{ni}^{cx} [72], as they did in the expressions for Q_{ei} (equation A.5.17).

From appendix A.4, the second moment of the first term of the Boltzmann equation is

$\frac{\partial}{\partial t} \left(\frac{1}{2} \rho_\alpha v_\alpha^2 + \frac{p_\alpha}{\gamma-1} \right) = \rho_\alpha \mathbf{v}_\alpha \cdot \frac{\partial \mathbf{v}_\alpha}{\partial t} + \frac{1}{\gamma-1} \frac{\partial p_\alpha}{\partial t}$ so that:

$$\frac{1}{\gamma-1} \left(\frac{\partial p_\alpha}{\partial t} \right)_{cx} = \left(\frac{\partial}{\partial t} \left(\frac{1}{2} \rho_\alpha v_\alpha^2 + \frac{p_\alpha}{\gamma-1} \right) \right)_{cx} - \rho_\alpha \mathbf{v}_\alpha \cdot \left(\frac{\partial \mathbf{v}_\alpha}{\partial t} \right)_{cx}$$

Using equations 8.3.26 and 8.3.27, this implies that

$$\begin{aligned} \frac{1}{\gamma-1} \left(\frac{\partial p_i}{\partial t} \right)_{cx} &\approx \left(\Gamma^{cx} \frac{1}{2} m_i (v_n^2 - v_i^2) + \mathbf{v}_n \cdot \mathbf{R}_{in}^{cx} - \mathbf{v}_i \cdot \mathbf{R}_{ni}^{cx} + Q_{in}^{cx} - Q_{ni}^{cx} \right) \\ &\quad - \mathbf{v}_i \cdot (-m_i(\mathbf{v}_i - \mathbf{v}_n) \Gamma^{cx} - \mathbf{R}_{ni}^{cx} + \mathbf{R}_{in}^{cx}) \\ &= \Gamma^{cx} m_i \left(\frac{1}{2} v_n^2 - \mathbf{v}_i \cdot \mathbf{v}_n + \frac{1}{2} v_i^2 \right) + (\mathbf{v}_n - \mathbf{v}_i) \cdot \mathbf{R}_{in}^{cx} + Q_{in}^{cx} - Q_{ni}^{cx} \\ \Rightarrow \frac{1}{\gamma-1} \left(\frac{\partial p_i}{\partial t} \right)_{cx} &\approx \Gamma^{cx} \frac{1}{2} m_i (\mathbf{v}_n - \mathbf{v}_i)^2 + (\mathbf{v}_n - \mathbf{v}_i) \cdot \mathbf{R}_{in}^{cx} + Q_{in}^{cx} - Q_{ni}^{cx} \end{aligned} \quad (8.3.29)$$

and

$$\begin{aligned} \frac{1}{\gamma-1} \left(\frac{\partial p_n}{\partial t} \right)_{cx} &\approx \left(\Gamma^{cx} \frac{1}{2} m_i (v_i^2 - v_n^2) - \mathbf{v}_n \cdot \mathbf{R}_{in}^{cx} + \mathbf{v}_i \cdot \mathbf{R}_{ni}^{cx} - Q_{in}^{cx} + Q_{ni}^{cx} \right) \\ &\quad - \mathbf{v}_n \cdot (m_i(\mathbf{v}_i - \mathbf{v}_n) \Gamma^{cx} + \mathbf{R}_{ni}^{cx} - \mathbf{R}_{in}^{cx}) \\ &= \Gamma^{cx} m_i \left(\frac{1}{2} v_i^2 - \mathbf{v}_n \cdot \mathbf{v}_i + \frac{1}{2} v_n^2 \right) + (\mathbf{v}_i - \mathbf{v}_n) \cdot \mathbf{R}_{ni}^{cx} - Q_{in}^{cx} + Q_{ni}^{cx} \\ \Rightarrow \frac{1}{\gamma-1} \left(\frac{\partial p_n}{\partial t} \right)_{cx} &\approx \Gamma^{cx} \frac{1}{2} m_i (\mathbf{v}_i - \mathbf{v}_n)^2 + (\mathbf{v}_i - \mathbf{v}_n) \cdot \mathbf{R}_{ni}^{cx} - Q_{in}^{cx} + Q_{ni}^{cx} \end{aligned} \quad (8.3.30)$$

Note that the term $(\mathbf{v}_n - \mathbf{v}_i) \cdot \mathbf{R}_{in}^{cx} = -\mathbf{v}_{in} \cdot \mathbf{R}_{in}^{cx}$ in the ion energy equation represents the rate of frictional work done by neutral fluid on the ion fluid as a result of charge exchange reactions, and the similar term $\mathbf{v}_{in} \cdot \mathbf{R}_{ni}^{cx}$ in the neutral energy equation represents the rate of frictional work done by \mathbf{R}_{ni}^{cx} , which acts on the neutral fluid with relative velocity \mathbf{v}_{in} .

8.4 3-fluid MHD equations

$(X)_{CE}$, $(X)_{scatt.}$, $(X)_{react.}$, $(X)_{ext.}$, $(X)_{ire}$, and $(X)_{cx}$ are, respectively, the parts of X that pertain to the combination of *collisions* and *external* sources, to *scattering* collisions, to *reacting* collisions, to *external* sources, to the combination of *ionization*, *recombination* and *external* sources, and to *charge exchange* collisions. These quantities are related as

$$(X)_{CE} = (X)_{scatt.} + (X)_{react.} + (X)_{ext.} = (X)_{scatt.} + (X)_{ire} + (X)_{cx}$$

Combining equations 8.2.2, 8.3.15, and 8.3.26, and using the identity $\mathbf{v}_{in} = \mathbf{v}_i - \mathbf{v}_n$, the complete set of terms that arise in the species momentum equations due to scattering and reactive collisions, and an external neutral particle source can be assembled:

$$\begin{aligned} \left(\frac{\partial \mathbf{v}_i}{\partial t} \right)_{CE} &= \frac{1}{\rho_i} \left(\mathbf{R}_{ie} + \mathbf{R}_{in} - \Gamma_i^{ion} m_i \mathbf{v}_{in} - \Gamma^{cx} m_i \mathbf{v}_{in} - \mathbf{R}_{ni}^{cx} + \mathbf{R}_{in}^{cx} \right) \\ \left(\frac{\partial \mathbf{v}_e}{\partial t} \right)_{CE} &= \frac{1}{\rho_e} \left(\mathbf{R}_{ei} + \mathbf{R}_{en} + \Gamma_i^{ion} m_e (\mathbf{v}_n - \mathbf{v}_e) \right) \\ \left(\frac{\partial \mathbf{v}_n}{\partial t} \right)_{CE} &= \frac{1}{\rho_n} \left(\mathbf{R}_{ni} + \mathbf{R}_{ne} + \Gamma_n^{rec} (m_i \mathbf{v}_i + m_e \mathbf{v}_e - m_n \mathbf{v}_n) \right. \\ &\quad \left. + \Gamma_n^{ext} m_n (\mathbf{v}_{n0} - \mathbf{v}_n) + \Gamma^{cx} m_i \mathbf{v}_{in} + \mathbf{R}_{ni}^{cx} - \mathbf{R}_{in}^{cx} \right) \end{aligned} \quad (8.4.1)$$

Similarly, combining equations 8.2.4, 8.3.20, 8.3.29, and 8.3.30, the equivalent set of terms in the species energy equations are:

$$\begin{aligned} \left(\frac{\partial p_i}{\partial t} \right)_{CE} &= (\gamma - 1) \left[Q_{ie} + Q_{in} + \frac{m_i}{m_n} Q_n^{ion} - Q_i^{rec} + \frac{1}{2} m_i (\Gamma_i^{ion} + \Gamma^{cx}) v_{in}^2 \right. \\ &\quad \left. - \mathbf{v}_{in} \cdot \mathbf{R}_{in}^{cx} + Q_{in}^{cx} - Q_{ni}^{cx} \right] \\ \left(\frac{\partial p_e}{\partial t} \right)_{CE} &= (\gamma - 1) \left(Q_{ei} + Q_{en} + \frac{m_e}{m_n} Q_n^{ion} - Q_e^{rec} + \Gamma_i^{ion} \left(\frac{1}{2} m_e (\mathbf{v}_e - \mathbf{v}_n)^2 - \phi_{ion} \right) \right) \\ \left(\frac{\partial p_n}{\partial t} \right)_{CE} &= (\gamma - 1) \left[Q_{ni} + Q_{ne} + \frac{m_i}{m_n} Q_i^{rec} + \frac{m_e}{m_n} Q_e^{rec} - Q_n^{ion} + \Gamma_n^{rec} \left(\frac{1}{2} m_n v_n^2 + \frac{1}{2} m_i v_i^2 + \frac{1}{2} m_e v_e^2 - m_i \mathbf{v}_n \cdot \mathbf{v}_i \right. \right. \\ &\quad \left. \left. - m_e \mathbf{v}_n \cdot \mathbf{v}_e \right) + \Gamma_n^{ext} \frac{1}{2} m_n (\mathbf{v}_n - \mathbf{v}_{n0})^2 + \Gamma^{cx} \frac{1}{2} m_i v_{in}^2 + \mathbf{v}_{in} \cdot \mathbf{R}_{ni}^{cx} - Q_{in}^{cx} + Q_{ni}^{cx} \right] + \Gamma_n^{ext} T_{n0} \end{aligned} \quad (8.4.2)$$

8.4.1 Mass conservation

Mass conservation is expressed by equation 8.3.9:

$$\begin{aligned} \dot{n}_i &= -\nabla \cdot (n_i \mathbf{v}_i) + \Gamma_i^{ion} - \Gamma_n^{rec} \\ \dot{n}_e &= -\nabla \cdot (n_e \mathbf{v}_e) + \Gamma_i^{ion} - \Gamma_n^{rec} \\ \dot{n}_n &= -\nabla \cdot (n_n \mathbf{v}_n) + \Gamma_n^{rec} - \Gamma_i^{ion} + \Gamma_n^{ext} \end{aligned} \quad (8.4.3)$$

8.4.2 Momentum conservation

The expression for species momentum conservation (equation A.4.9) can be combined with equation 8.4.1 for the species momentum equations in the three-fluid system. The term $\frac{1}{\rho_\alpha} \mathbf{R}_\alpha$ in equation A.4.9, which arose by taking the first moment of the collision operator for scattering collisions only, is replaced with the terms in equation 8.4.1 to yield:

$$\begin{aligned}
 \frac{\partial \mathbf{v}_i}{\partial t} &= -(\mathbf{v}_i \cdot \nabla) \mathbf{v}_i + \frac{1}{\rho_i} \left[-\nabla p_i - \nabla \cdot \bar{\boldsymbol{\pi}}_i + q_i n_i (\mathbf{E} + \mathbf{v}_i \times \mathbf{B}) + \mathbf{R}_{ie} + \mathbf{R}_{in} \right. \\
 &\quad \left. - \Gamma_i^{ion} m_i \mathbf{v}_{in} - \Gamma^{cx} m_i \mathbf{v}_{in} - \mathbf{R}_{ni}^{cx} + \mathbf{R}_{in}^{cx} \right] \\
 \frac{\partial \mathbf{v}_e}{\partial t} &= -(\mathbf{v}_e \cdot \nabla) \mathbf{v}_e + \frac{1}{\rho_e} \left[-\nabla p_e - \nabla \cdot \bar{\boldsymbol{\pi}}_e + q_e n_e (\mathbf{E} + \mathbf{v}_e \times \mathbf{B}) + \mathbf{R}_{ei} + \mathbf{R}_{en} \right. \\
 &\quad \left. + \Gamma_i^{ion} m_e (\mathbf{v}_n - \mathbf{v}_e) \right] \\
 \frac{\partial \mathbf{v}_n}{\partial t} &= -(\mathbf{v}_n \cdot \nabla) \mathbf{v}_n + \frac{1}{\rho_n} \left[-\nabla p_n - \nabla \cdot \bar{\boldsymbol{\pi}}_n + \mathbf{R}_{ni} + \mathbf{R}_{ne} + \Gamma_n^{rec} (m_i \mathbf{v}_i + m_e \mathbf{v}_e - m_n \mathbf{v}_n) \right. \\
 &\quad \left. + \Gamma^{cx} m_i \mathbf{v}_{in} + \mathbf{R}_{ni}^{cx} - \mathbf{R}_{in}^{cx} + \Gamma_n^{ext} m_n (\mathbf{v}_{n0} - \mathbf{v}_n) \right]
 \end{aligned} \tag{8.4.4}$$

8.4.3 Energy conservation

The expression for species energy conservation (equation A.4.12) can be combined with equation 8.4.2 for the species energy equations in the three-fluid system. The term $(\gamma - 1) Q_\alpha$ in equation A.4.12, which arose by taking the second moment of the collision operator for scattering collisions only, is replaced with the terms in equation 8.4.2. The resultant species

energy equations for the three-fluid system are:

$$\begin{aligned}
\frac{\partial p_i}{\partial t} &= -\mathbf{v}_i \cdot \nabla p_i - \gamma p_i \nabla \cdot \mathbf{v}_i + (\gamma - 1) \left[-\bar{\boldsymbol{\pi}}_i : \nabla \mathbf{v}_i - \nabla \cdot \mathbf{q}_i + Q_{ie} + Q_{in} + \frac{m_i}{m_n} Q_n^{ion} \right. \\
&\quad \left. - Q_i^{rec} + \frac{1}{2} m_i (\Gamma_i^{ion} + \Gamma^{cx}) v_{in}^2 - \mathbf{v}_{in} \cdot \mathbf{R}_{in}^{cx} + Q_{in}^{cx} - Q_{ni}^{cx} \right] \\
\frac{\partial p_e}{\partial t} &= -\mathbf{v}_e \cdot \nabla p_e - \gamma p_e \nabla \cdot \mathbf{v}_e + (\gamma - 1) \left[-\bar{\boldsymbol{\pi}}_e : \nabla \mathbf{v}_e - \nabla \cdot \mathbf{q}_e + Q_{ei} + Q_{en} \right. \\
&\quad \left. + \frac{m_e}{m_n} Q_n^{ion} - Q_e^{rec} + \Gamma_i^{ion} \left(\frac{1}{2} m_e (\mathbf{v}_e - \mathbf{v}_n)^2 - \phi_{ion} \right) \right] \\
\frac{\partial p_n}{\partial t} &= -\mathbf{v}_n \cdot \nabla p_n - \gamma p_n \nabla \cdot \mathbf{v}_n + (\gamma - 1) \left[-\bar{\boldsymbol{\pi}}_n : \nabla \mathbf{v}_n - \nabla \cdot \mathbf{q}_n + Q_{ni} + Q_{ne} + \frac{m_i}{m_n} Q_i^{rec} + \frac{m_e}{m_n} Q_e^{rec} \right. \\
&\quad \left. - Q_n^{ion} + \Gamma_n^{rec} \left(\frac{1}{2} m_n v_n^2 + \frac{1}{2} m_i v_i^2 + \frac{1}{2} m_e v_e^2 - m_i \mathbf{v}_n \cdot \mathbf{v}_i - m_e \mathbf{v}_n \cdot \mathbf{v}_e \right) + \Gamma^{cx} \frac{1}{2} m_i v_{in}^2 \right. \\
&\quad \left. + \mathbf{v}_{in} \cdot \mathbf{R}_{ni}^{cx} - Q_{in}^{cx} + Q_{ni}^{cx} + \Gamma_n^{ext} \frac{1}{2} m_n (\mathbf{v}_n - \mathbf{v}_{n0})^2 \right] + \Gamma_n^{ext} T_{n0}
\end{aligned}$$

8.5 2-fluid MHD equations

Applying the same procedure described in appendix A.6 for the terms in the 3-fluid MHD equations that don't correspond to interspecies collisions, and summing terms corresponding to interspecies collisions, with the limit $m_e \rightarrow 0$, the ion and electron conservation equations can be reduced to a single plasma-fluid description. In the limit $m_e \rightarrow 0$, the single plasma-fluid velocity is approximately the ion fluid velocity as is clarified by the identities $\mathbf{v} = \frac{1}{\rho} \sum \rho_\alpha \mathbf{v}_\alpha$ and $\rho = \sum_\alpha \rho_\alpha$, so that $\mathbf{v}_{in} \rightarrow (\mathbf{v} - \mathbf{v}_n)$. The charged-neutral particle frictional forces $\mathbf{R}_{in} = -\mathbf{R}_{ni}$ and $\mathbf{R}_{en} = -\mathbf{R}_{ne}$, and heat exchange terms Q_{in} , Q_{en} , Q_{ni} , and Q_{ne} can be neglected, as mentioned in section 8.2. Following from [100], the parameter λ , where $0 \leq \lambda \leq 1$, is introduced. If the mean free paths of the charge-exchanged neutral particles are expected to be large, then λ is set between 0 and 1, so that charge-exchanged neutral particles leave the system without reacting again, taking their energy and momentum with them. If the mean free paths of the charge-exchanged neutral particles are expected to be short, then λ is set to zero. By default, λ is set to zero in MHD simulations, consistent with conservation of energy associated with the neutral fluid. The resulting set of conservation equations, in continuous form, for the two-fluid system, including ionization & recombination and charge exchange terms, as well as neutral source terms, and density diffusion (correction terms \mathbf{f}_ζ / ρ and $\mathbf{f}_{\zeta_n} / \rho_n$ are included to maintain energy and (in some cases) angular momentum conservation, as described in section 5.6.3), is

$$\begin{aligned}
\dot{n} &= -\nabla \cdot (n\mathbf{v}) + \Gamma_i^{ion} - \Gamma_n^{rec} + \nabla \cdot (\zeta \nabla n) \\
\dot{\mathbf{v}} &= -\mathbf{v} \cdot \nabla \mathbf{v} + \frac{1}{\rho} \left(-\nabla p - \nabla \cdot \bar{\boldsymbol{\pi}} + \mathbf{J} \times \mathbf{B} - \Gamma_i^{ion} m_i \mathbf{v}_{in} - \Gamma^{cx} m_i \mathbf{v}_{in} - \mathbf{R}_{ni}^{cx} + \mathbf{R}_{in}^{cx} + \mathbf{f}_\zeta \right) \\
\dot{p} &= -\mathbf{v} \cdot \nabla p - \gamma p \nabla \cdot \mathbf{v} + (\gamma - 1) \left(-\bar{\boldsymbol{\pi}} : \nabla \mathbf{v} - \nabla \cdot \mathbf{q} + \eta' J^2 + \Gamma_i^{ion} \frac{1}{2} m_i v_{in}^2 + Q_n^{ion} - \Gamma_i^{ion} \phi_{ion} \right. \\
&\quad \left. - Q_i^{rec} - Q_e^{rec} - \mathbf{R}_{in}^{cx} \cdot \mathbf{v}_{in} + Q_{in}^{cx} - Q_{ni}^{cx} + \Gamma^{cx} \frac{1}{2} m_i v_{in}^2 \right) \\
\dot{n}_n &= -\nabla \cdot (n_n \mathbf{v}_n) - \lambda \Gamma^{cx} - \Gamma_i^{ion} + \Gamma_n^{rec} + \Gamma_n^{ext} + \nabla \cdot (\zeta_n \nabla n_n) \\
\dot{\mathbf{v}}_n &= -\mathbf{v}_n \cdot \nabla \mathbf{v}_n + \frac{1}{\rho_n} \left(-\nabla p_n - \nabla \cdot \bar{\boldsymbol{\pi}}_n + \Gamma_n^{rec} m_i \mathbf{v}_{in} - \mathbf{R}_{in}^{cx} + (1 - \lambda) (\mathbf{R}_{ni}^{cx} + \Gamma^{cx} m_i \mathbf{v}_{in}) \right. \\
&\quad \left. + \Gamma_n^{ext} m_n (\mathbf{v}_{n0} - \mathbf{v}_n) + \mathbf{f}_{\zeta_n} \right) \\
\dot{p}_n &= -\mathbf{v}_n \cdot \nabla p_n - \gamma p_n \nabla \cdot \mathbf{v}_n + (\gamma - 1) \left(-\bar{\boldsymbol{\pi}}_n : \nabla \mathbf{v}_n - \nabla \cdot \mathbf{q}_n - Q_n^{ion} + \Gamma_n^{rec} \frac{1}{2} m_i v_{in}^2 + Q_i^{rec} \right. \\
&\quad \left. + (1 - \lambda) (\mathbf{R}_{ni}^{cx} \cdot \mathbf{v}_{in} + \Gamma^{cx} \frac{1}{2} m_i v_{in}^2 + Q_{ni}^{cx}) - Q_{in}^{cx} + \Gamma_n^{ext} \frac{1}{2} m_n (\mathbf{v}_n - \mathbf{v}_{n0})^2 \right) + \Gamma_n^{ext} T_{n0}
\end{aligned}$$

As mentioned in appendix A.8, the code has the option to evolve the single plasma-fluid energy equation or to evolve separate energy equations for the ions and electrons. For the latter option, when plasma-neutral interaction is included, the ion and electron energy equations are

$$\begin{aligned}
\dot{p}_i &= -\mathbf{v} \cdot \nabla p_i - \gamma p_i \nabla \cdot \mathbf{v} + (\gamma - 1) \left(-\bar{\boldsymbol{\pi}} : \nabla \mathbf{v} - \nabla \cdot \mathbf{q}_i + Q_{ie} + \Gamma_i^{ion} \frac{1}{2} m_i v_{in}^2 + Q_n^{ion} - Q_i^{rec} \right. \\
&\quad \left. - \mathbf{R}_{in}^{cx} \cdot \mathbf{v}_{in} + Q_{in}^{cx} - Q_{ni}^{cx} + \Gamma^{cx} \frac{1}{2} m_i v_{in}^2 \right) \\
\dot{p}_e &= -\mathbf{v} \cdot \nabla p_e - \gamma p_e \nabla \cdot \mathbf{v} + (\gamma - 1) \left(+\eta' J^2 - \nabla \cdot \mathbf{q}_e - Q_{ie} - \Gamma_i^{ion} \phi_{ion} - Q_e^{rec} \right)
\end{aligned}$$

where Q_{ie} is defined in equation 5.6.5.

8.6 Conservation properties with inclusion of neutral fluid

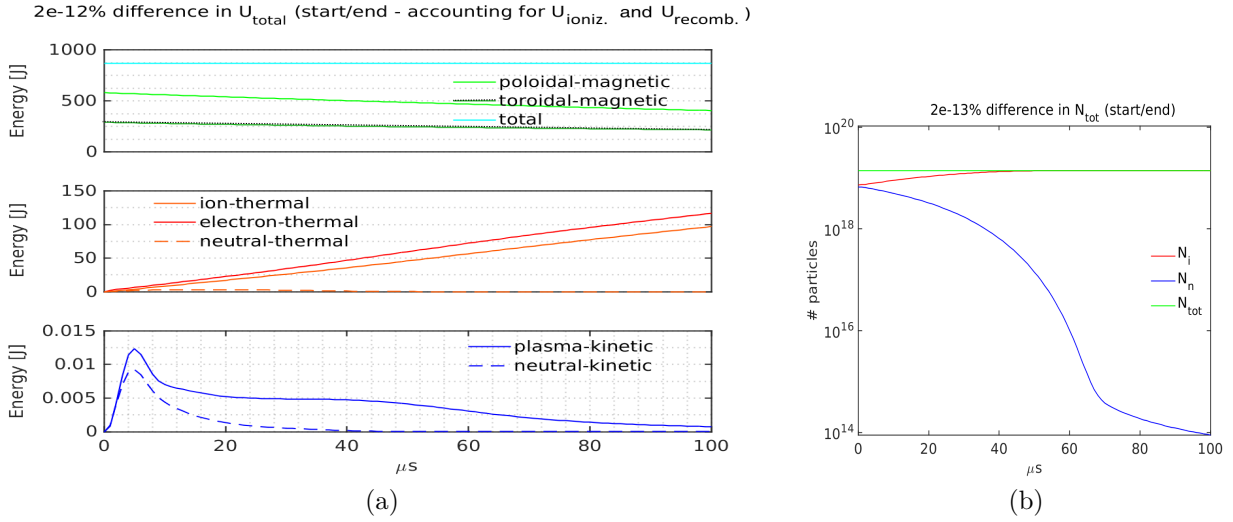


Figure 8.6.1: Illustration of energy and particle conservation for MHD simulation with neutral fluid

Figure 8.6.1(a) indicates the partition of energy, and how total system energy is conserved for a simulation where a neutral fluid is evolved along with the plasma fluid. In this case, the initial neutral fluid number density was approximately equal to the initial plasma fluid number density, with spatially uniform initial distributions. The simulation started from a Grad-Shafranov equilibrium. The only explicitly applied boundary conditions were $v_r|_{\Gamma} = v_z|_{\Gamma} = v_{nr}|_{\Gamma} = v_{nz}|_{\Gamma} = 0$ and $\psi|_{\Gamma} = 0$, so that the thermal and Poynting fluxes are zero through the boundary, as outlined in section 5.6.2. Because the equations for the neutral fluid are analogous, in terms of energy conserving properties, to the equations for the plasma fluid, it is to be expected that energy conservation will be maintained when the evolution of a neutral fluid is simulated along with that of a plasma fluid. When the electron fluid energy lost through the ionization and recombination (the model assumes that in the radiative recombination reaction, the electron thermal energy is lost to the photon emitted, which leaves the optically thin system without further interaction) processes are accounted for, it is evident that total energy is conserved to numerical precision. The partitions of magnetic energy and the thermal and kinetic plasma fluid energies follow the trends outlined in section 5.6.2 for the case without neutral fluid evolution.

Note that the neutral fluid thermal energy is negligible compared with the plasma thermal energy. Initial spatially uniform temperatures were $T_i = T_e = T_n = 0.02$ eV. Due to

ionization, neutral fluid density is low in regions in which electrons are hot. In these regions, ions are also generally hot due to heat exchange with electrons. The hot ions result, through the charge exchange process, in hot neutral particles, so regions with hot neutral particles are regions of relatively low neutral fluid density.

Neutral fluid kinetic energy is small compared with the kinetic energy of the ions and electrons. Charged particle acceleration leads to neutral particle acceleration, largely due to frictional forces between the plasma and neutral fluids associated with charge-exchange reactions, and due to momentum exchange arising from recombination processes. Plasma is accelerated by $\mathbf{J} \times \mathbf{B}$ forces, and is heated in regions where it is accelerated, either by ohmic heating (electrons) or viscous heating (ions). Thus, neutral fluid density tends to be low in regions where neutral fluid is accelerated due to high ionization rates in those regions, so net neutral fluid kinetic energy remains low. Figure 8.6.1(b) shows how total particle count (N_{tot}) is conserved to numerical precision for the same simulation. Initial neutral particle count (N_n) was around equal to the ion inventory (N_i), and by the end of the simulation, neutral particles account for around one in 100,000 of the total number of particles, due to ionization.

Net angular momentum of the plasma and neutral fluids is also conserved to numerical precision. No boundary conditions are explicitly applied to v_ϕ or to $v_{n\phi}$, so the natural boundary conditions $(\nabla_\perp \omega) |_\Gamma = (\nabla_\perp \omega_n) |_\Gamma = 0$ are automatically imposed (see section 5.6.2.3).

8.7 Neutral fluid thermal diffusion

The thermal diffusion coefficient for the neutral fluid, given by the Chapman-Cowling closures (equation A.5.5), can be expressed, with the definition of the neutral-neutral scattering collision frequency, $\nu_{cn} = \frac{V_{thn}}{\lambda_{mfp}}$, as:

$$\chi_n \approx \frac{75\sqrt{\pi}}{64} \frac{V_{thn}^2}{\nu_{cn}} \quad (8.7.1)$$

The expression for χ_n was derived with a Chapman-Enskog expansion using the ratio of the mean free path for scattering collisions to the characteristic system length scale as the small ordering parameter (the principle is outlined in appendix A.5). However, if the charge exchange collision frequency is higher than the frequency for neutral-neutral scattering collisions, neutral thermal conductivity should be reduced. As outlined in [72, 100], an approximation to include the effect of charge exchange collisions on neutral thermal conduction is to replace the term ν_{cn} in the definition for χ_n with $\nu_{cn} + \nu_{cx}$ where $\nu_{cx} = \frac{V_{thn}}{\lambda_{cx}} = V_{thn} \sigma_{cx} n_n$ is the charge exchange frequency, and $\lambda_{cx} \approx \frac{1}{\sigma_{cx} n_n}$ is the mean free path for charge exchange

collisions. In this way, χ_n will be limited by whichever frequency dominates. The resulting expression, which is implemented to the code as an option, is

$$\chi_n \approx \frac{75\sqrt{\pi}}{64} \frac{V_{thn}^2}{\nu_{cn} + \nu_{cx}} = \frac{75\sqrt{\pi}}{64} \frac{V_{thn}}{\frac{1}{\lambda_{mfp}} + \sigma_{cx} n_n} \quad (8.7.2)$$

As described in [100], when charge exchange dominates over scattering, the model compares well with an established model for neutral thermal diffusion [109], which was derived rigorously with a formal Chapman-Enskog-like procedure. A similar modification to the neutral viscous diffusion coefficient (equation A.5.4) could be made but hasn't been experimented with in this work.

8.8 Simple model for charge exchange reactions

If evolving the plasma fluid only, the terms $\frac{1}{\rho} (-\mathbf{R}_{ni}^{cx} - \Gamma^{cx} m_i \mathbf{v}_{in})$ and $(\gamma - 1) (-Q_{ni}^{cx} + \Gamma^{cx} \frac{m_i}{2} v_{in}^2)$ may be retained in the expressions for $\dot{\mathbf{v}}$ and \dot{p}_i . This represents that hot ions that react with cold neutral particles (constant ρ_n) ionize and impart half their energy to the neutral particles and leave the system without reacting again. The simple model is not physically representative because the quantities \mathbf{R}_{ni}^{cx} , Γ^{cx} , Q_{ni}^{cx} and \mathbf{v}_{in} depend on local neutral-fluid-related variables such as $n_n(\mathbf{r}, t)$ and $T_n(\mathbf{r}, t)$ that would need to be estimated, but may be useful to study particular scenarios.

8.9 Simulation results with neutral fluid

| neutralfluid | N_0 [m⁻³] | σ_N^2 [m²] | ζ_n [m²/s] | add_N |
|-----------------------------------|--|---|--|-------------------------------|
| 1 | 4.5×10^{20} | 0.01 | 90 | 1 |
| | | | | |
| vary$_{\chi_N}$ | vary$_{\nu_N}$ | χ_{Nmax} [m²/s] | ν_{Nmax} [m²/s] | χ_{CX} |
| 1 | 1 | 5×10^4 | 1×10^4 | 1 |

Table 8.9.1: Neutral-relevant code input parameters for simulation 2353

The code inputs in table 8.9.1 are related to the neutral fluid dynamics for simulation 2353, for which the principal code input parameters were presented in table 7.1.1. When interaction between the plasma and a neutral fluid is evolved, code input parameter *neutralfluid* is set equal to one. Analogous to the case described in equation 7.1.1 for the initial plasma distribution, the initial static neutral fluid distribution is determined by a Gaussian profile with variance σ_N^2 determining the degree of neutral fluid spread around the gas valves, and neutral number density scaling N_0 . ζ_n [m²/s] is the coefficient of neutral fluid density diffusion. $add_N = 1$ implies that neutral fluid is added to the simulation domain at the location of the gas valves throughout the simulation. Physically, the gas valves remain open for up to around a millisecond after they are first opened. In general, simulations including neutral dynamics have *vary $_{\nu_N}$* and *vary $_{\chi_N}$* set to one, so that the analytical closures given by the Chapman-Enskog formulae (equation A.5.4 and A.5.5) for the neutral fluid viscous and thermal diffusion coefficients are used. However, if code input χ_{CX} is also set to one, as it is for this simulation, the modified expression for χ_N , equation 8.7.2, is used to determine thermal diffusion for the neutral fluid. It is found that this expression results in an increase of maximum T_n of around 10% compared with cases where χ_{CX} is set to zero and *vary $_{\chi_N}$* is set to one, in which case equation A.5.5 is used to determine χ_N . Constant coefficients are used if *vary $_{\nu_N}$* and *vary $_{\chi_N}$* are set to zero. χ_{Nmax} and ν_{Nmax} determine the upper limits applied to the neutral fluid viscous and thermal diffusion coefficients.

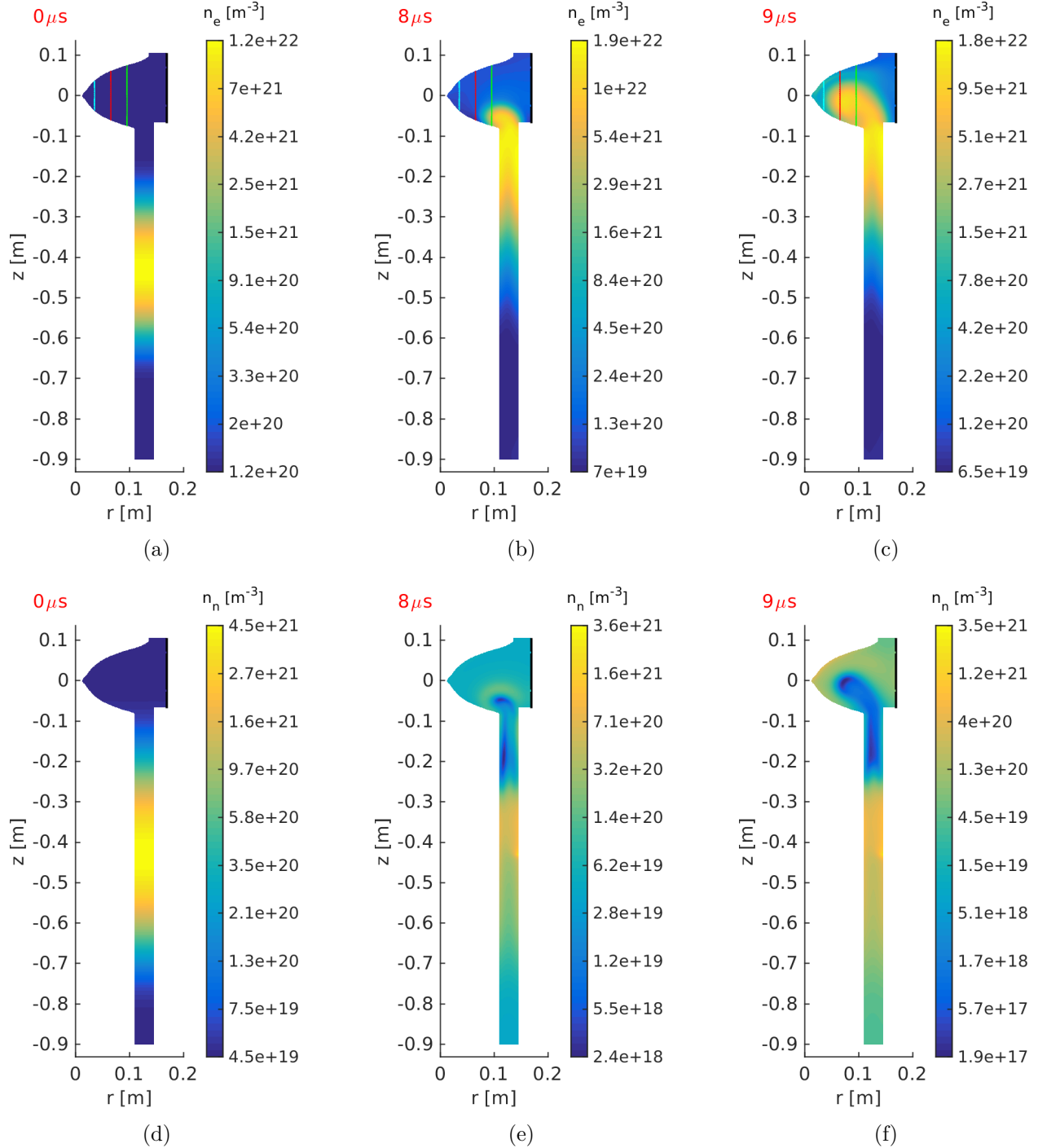


Figure 8.9.1: Neutral fluid dynamics at bubble-in (1)

Figures 8.9.1(a) and (d) show the initial distributions for plasma density, represented by n_e , and neutral fluid density n_n . The initial density distributions are Gaussian profiles, centered around the gas puff locations at $z = -0.43$ m, with a higher variance for the neutral fluid distribution, representing that the neutral gas has diffused around the gas puff valve locations, while the initial plasma distribution, is more localised to the gas puff locations. The

initial neutral particle inventory, determined by σ_N^2 and N_0 , was over half the initial plasma particle inventory for this simulation with $\sigma_n^2 < \sigma_N^2$ and $N_0 = n_0/2$. Note that $n_e = Z_{eff} n_i$, where $Z_{eff} = 1.3$ for simulation 2353. As shown in figures 8.9.1(b) and (c), plasma is starting to enter the CT containment region at 8 μ s and 9 μ s. A front of neutral fluid precedes the plasma as it is advected upwards (figures 8.9.1(e) and (f)). Note that neutral particles are being added at the gas puff valve locations by the outer boundary at $z = -0.43$ m. In the experiment, the gas valves are opened at $t \sim -400$ μ s, and remain open for ~ 1 ms, so that cold neutral gas is being added to the vacuum vessel throughout the simulation, at a rate that can be estimated and assigned to the simulated neutral particle source terms.

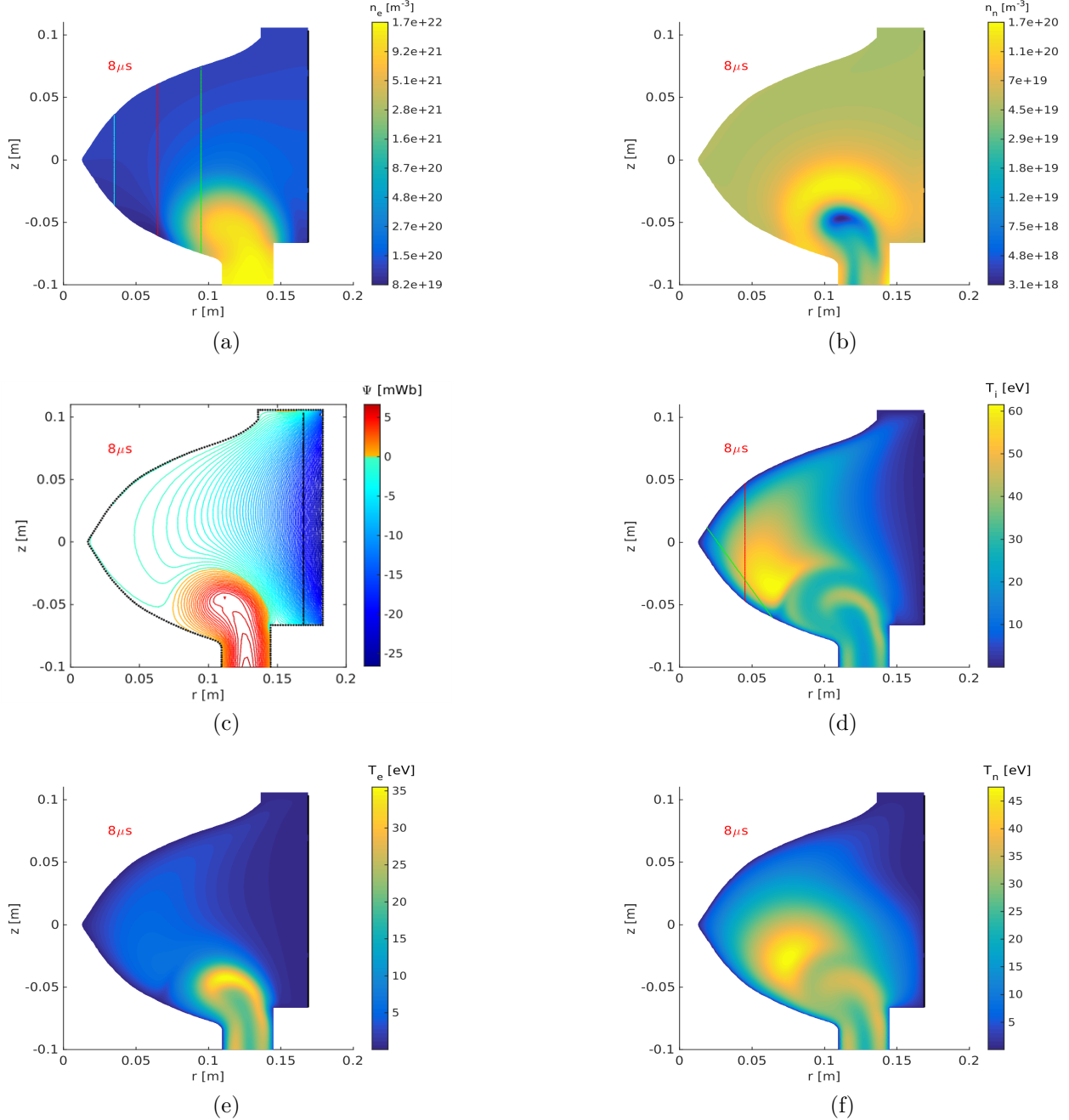


Figure 8.9.2: Neutral fluid dynamics at bubble-in (2)

Figures 8.9.2(a) and (b) show close-up views of n_e and n_n at $8\mu\text{s}$. Figures 8.9.2(c) and (d) show ψ contours and the distribution of T_i at the same time. Ions are hot due to viscous heating. Ohmic heating in combination with heat exchange with ions results in hot electrons (figure 8.9.2(e)). Note that neutral fluid density is low where T_e is high due to ionization (figure 8.9.2(b)). Due to charge exchange reactions, neutral fluid temperature tends to equilibrate with ion temperature (figures 8.9.2 (d) and (f)), and can become hotter than ions if the thermal diffusion for neutral fluid is set to be lower than ion thermal diffusion. In general,

when $\chi_{\parallel i}$ and $\chi_{\parallel e}$ are fixed at moderate experimentally relevant values such as those in table 7.1.1, and χ_N is determined by equation 8.7.1 or 8.7.2, with $\chi_{Nmax} \gtrsim 5 \times 10^4$ [m²/s], as is the case for this simulation, it is found that $T_N < T_i$.

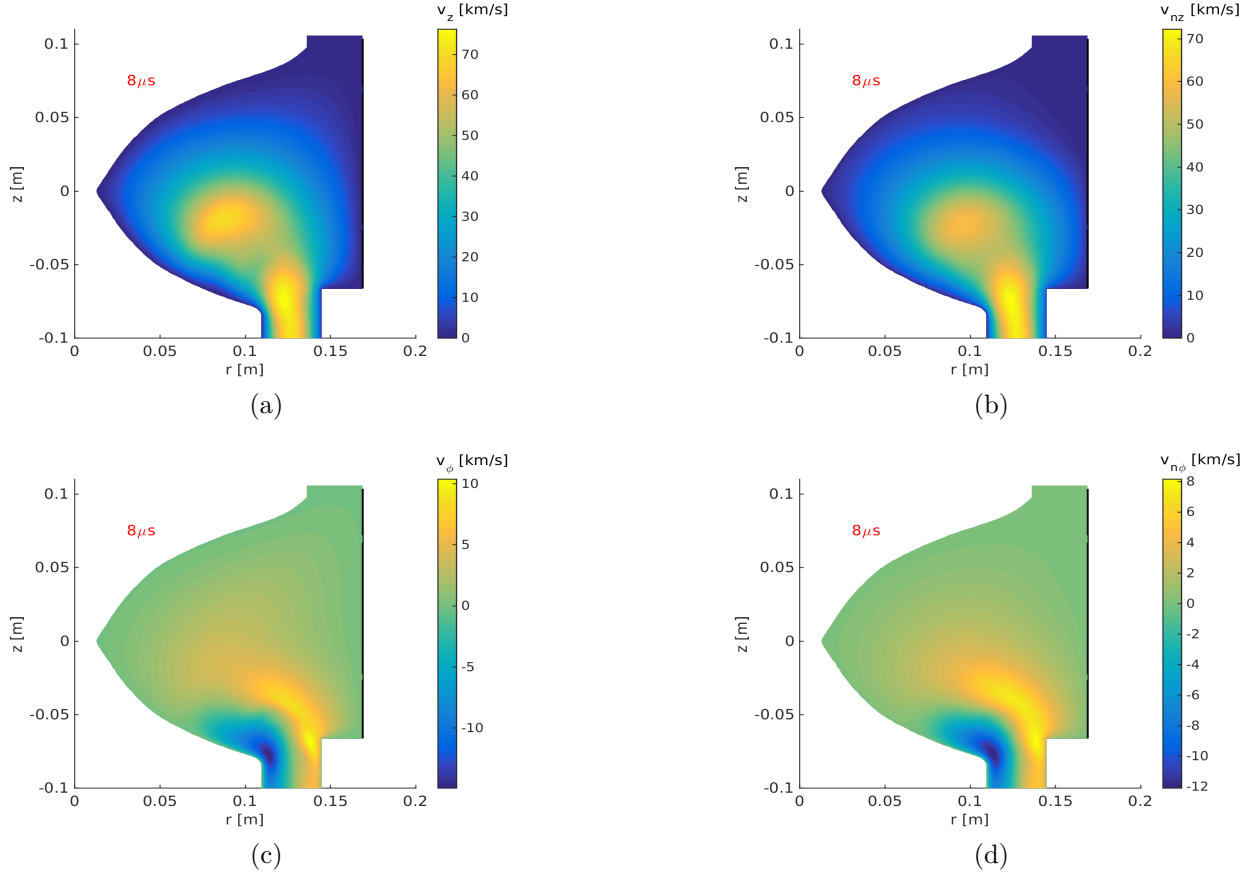


Figure 8.9.3: Neutral fluid dynamics at bubble-in (3)

Figures 8.9.3(a) and (b) shows profiles of axial velocity at 8 μ s for the plasma fluid and neutral fluid respectively, while azimuthal velocity profiles are presented at the same output time in figures 8.9.3(c) and (d). Plasma acceleration leads to neutral fluid acceleration, due to frictional forces associated with charge-exchange reactions, and due to momentum exchange arising from recombination processes. It can be seen how the neutral fluid attains nearly the same velocity magnitudes as the plasma fluid.

8.9.1 Effect of inclusion of the Q_e^{rec} term

Q_e^{rec} [J m⁻³ s⁻¹] determines the volumetric rate of thermal energy transfer from electrons to photons and neutral particles due to radiative recombination. As discussed in section 8.3.1.3, the method described in this chapter to evaluate the terms determining plasma-neutral in-

teractions allows for the evaluation of Q_e^{rec} , which could not be evaluated by the formal moment-taking process described in [72], and has been neglected in studies [100, 110] based on the model. From looking at the kinematics of the radiative recombination reaction (section 8.3.1.3), it is more physical to neglect Q_e^{rec} as an energy source for the neutral fluid (most of the electron thermal energy is transferred to the photon), but include it as an energy sink for the electron fluid. It is interesting however to note the effect of including the term as an energy source for the neutral fluid - in this (unphysical) scenario it is assumed, as presented in [72], that all the electron thermal energy lost during radiative recombination is transferred to the neutral particle.

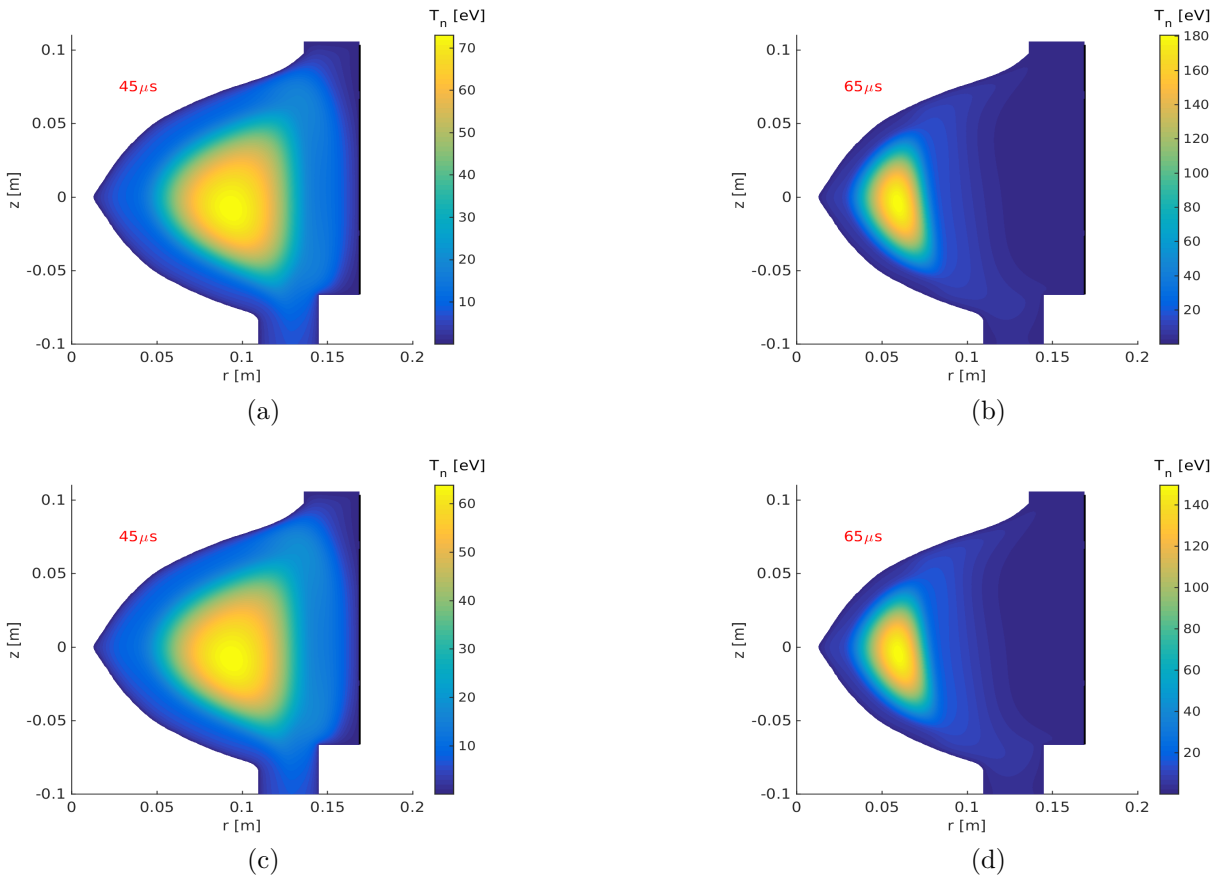


Figure 8.9.4: Effect of inclusion of the Q_e^{rec} term as an energy source for the neutral fluid

Figures 8.9.4(a) and (b) show profiles of T_n from simulation 2353, in which the Q_e^{rec} term is included in the energy equations for the electron and neutral fluids, at 45 μs just prior to magnetic compression, and at peak compression at 65 μs . Note that electron and ion temperature profiles are presented at the same times, from the same simulation, in figures 7.3.6(e) and (f) and in figures 7.3.7(e) and (f). Figures 8.9.4(c) and (d) show T_n profiles at the same times from a simulation that is identical except that the Q_e^{rec} term is not included

in the electron and neutral fluid energy equations. It can be seen how peak T_n increases by around 20% at 45 μs , and by around 30% at 65 μs , when the Q_e^{rec} term is included. Note that if χ_{Nmax} is increased from 5×10^4 [m^2/s] to 1×10^5 [m^2/s], that peak T_n increases by around 30% at 45 μs , and by around 80% at 65 μs when the Q_e^{rec} term is included. From equations 8.3.7, 8.3.8, and 8.3.19, it can be seen that

$$Q_e^{rec} \propto Z_{eff}^3 n_i^2 \sqrt{T_e}$$

Hence, Q_e^{rec} is high in regions where plasma density and electron temperature are high. The increase in T_n when Q_e^{rec} is included is especially large in such regions, for example near the CT core at peak magnetic compression, where the rate of ionization is high and hence n_n , and thermal energy associated with neutral particles, is low.

Not shown here, peak electron temperature falls by around 1% when the Q_e^{rec} term is included in the electron fluid energy equation. Q_e^{rec} appears as a (physical) thermal energy sink in the electron fluid energy equation, but the reduction in T_e when Q_e^{rec} is included is negligible, even in regions where Q_e^{rec} is high, due to the high levels of electron thermal energy in such regions.

8.9.2 Neutral fluid interaction in SPECTOR geometry

A schematic of the SPECTOR machine [111] is presented in figure 1.2.2(b). SPECTOR has a separate circuit to drive up to 1 MA shaft current, as indicated in figure 1.2.2(b), and produces CTs with typical lifetimes of around two milliseconds. It is usual to observe a significant rise in electron density at around 500 μs on the SPECTOR machine, and it was thought that this may be a result of neutral gas, that remains concentrated around the gas valve locations after CT formation, diffusing up the gun. Ionization of the neutral particles would lead to CT fueling and an increase in observed electron density. The model for interaction between plasma and neutral fluids was applied to study the issue.

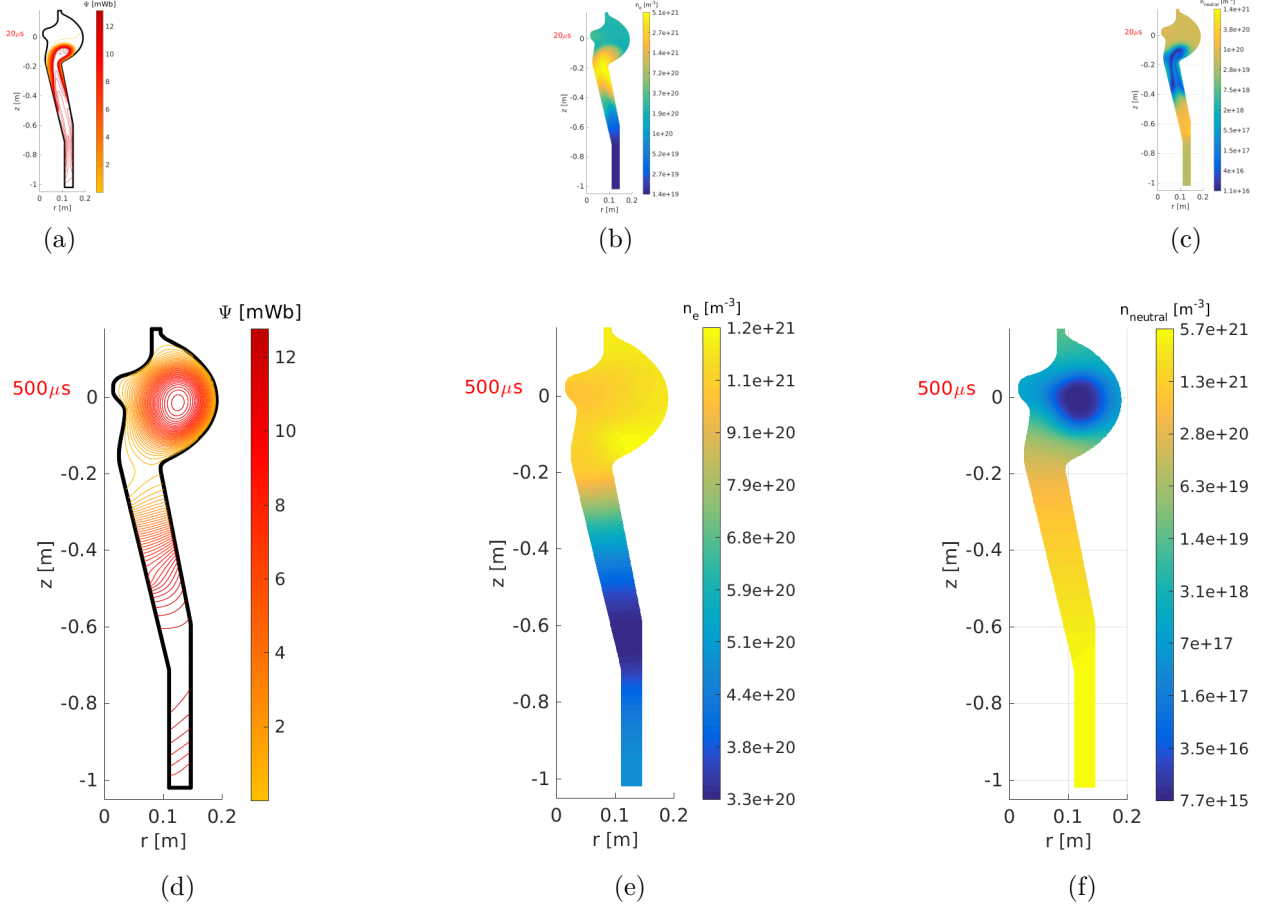


Figure 8.9.5: Poloidal flux contours and profiles of electron and neutral fluid densities in SPECTOR geometry

Figures 8.9.5(a), (b) and (c) show ψ contours and profiles of n_e and n_n at $20 \mu\text{s}$, as plasma enters the CT containment region. Profiles of the same quantities are shown in figures 8.9.5(d), (e) and (f) at $500 \mu\text{s}$, around the time when the density rise is usually observed. It can be seen how neutral fluid density is highest at the bottom of the gun barrel (figure 8.9.5(f)) - any neutral gas advected or diffusing upwards is ionized. A region of particularly high electron density is apparent just above, and outboard of, the entrance to the containment region (figure 8.9.5(e)) - this is due to the fueling effect arising from neutral gas diffusion.

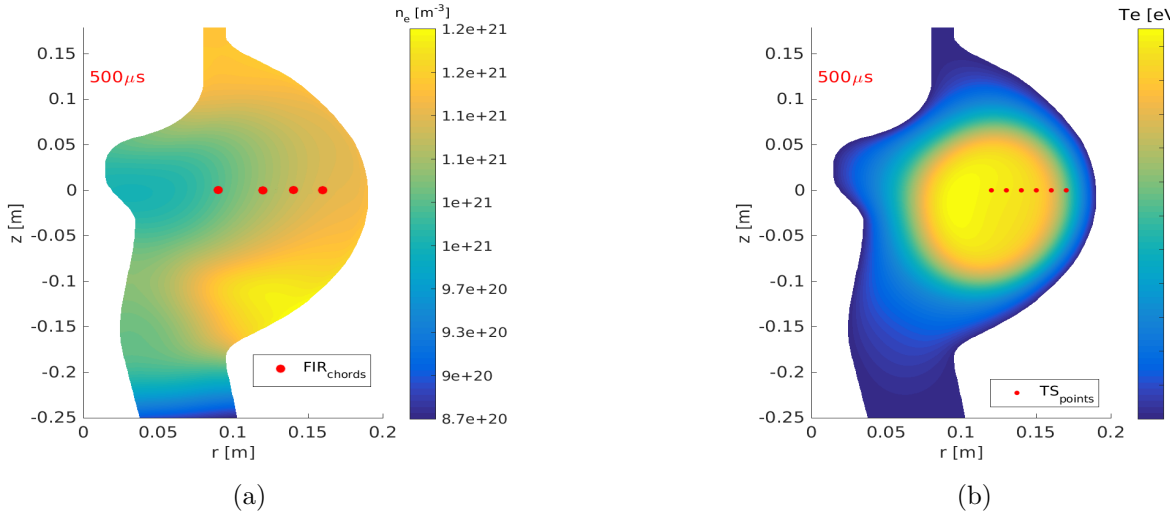


Figure 8.9.6: Profiles of electron density and temperature in SPECTOR geometry

The region of particularly high electron density is more defined in figure 8.9.6(a), in which cross-sections of the horizontal chords representing the lines of sight of the FIR (far-infrared) interferometer [112] are also depicted. The electron temperature profile at $500 \mu\text{s}$ is shown in figure 8.9.6(b). Referring to figure 8.9.5(f), it can be seen how neutral fluid density is low in regions of high T_e as a result of ionization.

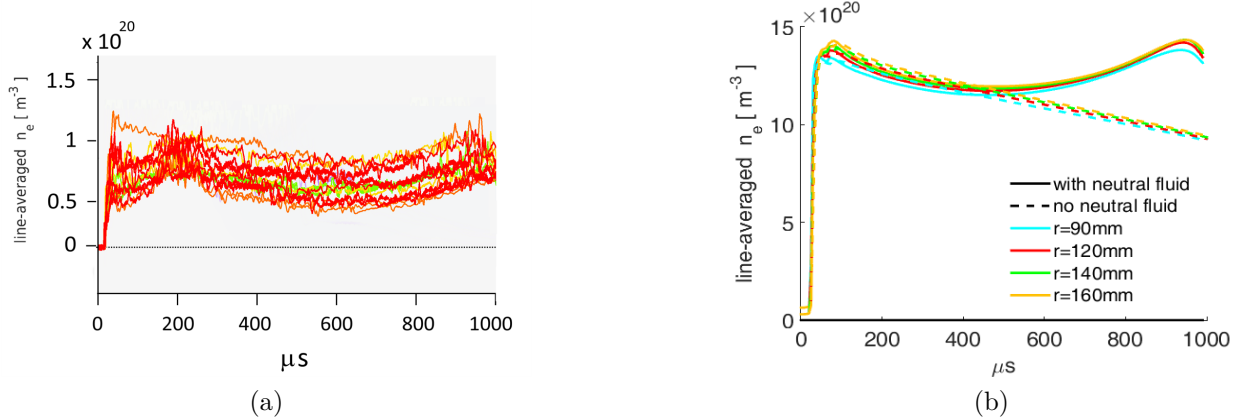


Figure 8.9.7: Effect of neutral fluid dynamics in SPECTOR geometry

Figure 8.9.7(a) shows line-averaged electron density measured along the interferometer chord at $r = 140 \text{ mm}$ from a selection of several shots in SPECTOR. It can be seen how density starts to rise at around 500 to $600 \mu\text{s}$. Figure 8.9.7(b) shows the simulated diagnostic for line-averaged electron density along the chords indicated in figure 8.9.6(a). The density rise is qualitatively reproduced when a neutral fluid is included in the simulation. Similar simulations without the inclusion of neutral fluid do not indicate this density rise (dashed lines in figure 8.9.7(b)). The density rise was not observed in the magnetic compression

experiment because CT lifetimes were shorter than the time it takes for a sufficient amount of neutral gas to diffuse upwards toward the containment region. Note that plasma densities in SPECTOR are far lower than in the magnetic compression device, so that, as discussed in appendix C.2, the timestep must be reduced for simulations with correspondingly low densities. The simulations presented in figure 8.9.7(b) were run with artificially high plasma density in order to allow for an increased timestep and moderately short simulation runtimes. Note that the electron temperatures indicated in figure 8.9.6(b) are underestimations of the actual temperatures due to the overestimation of density in the simulation. The main goal of these simulations was to demonstrate that the inclusion of neutral fluid interaction can qualitatively model the observed electron density increase.

The CT fueling and cooling effect of neutral gas diffusing up the gun is thought to be related to the unusually significant increases in CT lifetime and electron temperature observed when a biased electrode was inserted 11 mm into the CT edge on the SPECTOR plasma injector [53]. Electrode biasing involves the insertion of an electrode, that is biased relative to the vessel wall near the point of insertion, into the edge of a magnetized plasma. This leads to a radially directed electric field between the probe and the wall. The resultant $\mathbf{J}_r \times \mathbf{B}$ force imposed on the plasma at the edge of the plasma confinement region varies with distance between the probe and the wall, because E_r , as well as the magnetic field, vary in that region. The associated torque overcomes viscous forces, spinning up the edge plasma, and results in shearing of the particle velocities between the probe and the wall. The sheared velocity profile is thought to suppress the growth of turbulent eddies that advect hot plasma particles to the wall, thereby reducing this plasma cooling mechanism. In general, high confinement modes induced by probe biasing share features of those initiated by various methods of heating, including a density pedestal near the wall (near the probe radius for probe biasing), diminished levels of recycling as evidenced by reduced H_α emission intensity, and increased particle and energy confinement times. Note the H_α line is located in the deep-red visible spectrum, in the Balmer series (one of the six named series that describe spectral line emission of hydrogen atoms), with a wavelength of $\lambda_{H_\alpha} = 656.28$ nm in air. A photon with energy $E_{H_\alpha} = h\nu_{H_\alpha} = \frac{hc}{\lambda_{H_\alpha}}$ is emitted when an electron in a neutral hydrogen atom falls from its third to second lowest energy level. Here, $h = 6.63 \times 10^{-34}$ [J-s] is Planck's constant, ν_{H_α} [s⁻¹] is the frequency of the photon emitted, and c is the speed of light. Ions and electrons, that diffuse out of the plasma to the vessel walls, cool and recombine at the walls to form neutral atoms, which can then exhibit H_α emission, before being re-ionized and recycled back into the plasma as cold ions and electrons. The presence of a transport barrier reduces the level of H_α emission by reducing the flux of charged particles to the vessel walls.

In contrast to most of the biasing experiments conducted on tokamak plasmas, where electron density is found to increase as a consequence of biasing, electron density was markedly

reduced in the SPECTOR edge biasing experiment. This density reduction is thought to be due to the effect of the transport barrier impeding the CT fueling associated with neutral gas diffusing up the gun. CT lifetimes and temperatures were found to increase by factors of around 2.4 with edge biasing. The scale of the improvements observed is significantly greater than that associated with prior biasing experiments, and it is thought that this result is associated with a reduction of the cooling effect associated with CT fueling. A synopsis of the experiment, based on [53], is presented in appendix D.

8.10 Summary

It has been shown how the terms that determine the source rates of species momentum and energy due to ionization and recombination can be derived from basic principles rather than the more formal and involved process of taking successive moments of the collision operators pertaining to the reactions. The moment-taking method must be used to determine terms relating to charge exchange reactions. Only the simple method enables determination of Q_e^{rec} , which prescribes the volumetric rate of thermal energy transfer from electrons to photons and neutral particles due to radiative recombination. From looking at the kinematics of the radiative recombination reaction, it appears reasonable to neglect Q_e^{rec} as an energy source for the neutral fluid (most of the electron thermal energy is transferred to the photon), but include it as an energy sink for the electron fluid. Inclusion of this term in the electron energy equation leads to an insignificant reduction in electron fluid temperature in the regime examined. The source rate terms have been used to develop the three fluid, and two fluid equations for plasma and neutral gas, which have been implemented to the code.

Energy conservation is maintained with the inclusion of the neutral fluid model if the electron thermal energy expended on ionization and recombination processes is accounted for. The initial motivation for the study of plasma/neutral interaction was that inclusion of a neutral model was expected to lead to net ion cooling; this concept has been disproved. Increased net initial particle inventory results in lower ion temperatures, regardless of whether part of the initial inventory includes neutral particles. Charge exchange reactions lead to ion-neutral heat exchange, but the ion temperature is relatively unchanged by charge exchange reactions in hot-ion regions where electron temperature and ionization rates are also high and neutral fluid density is consequently low. The effect of residual neutral gas, that is concentrated around the gas valves after the formation process, diffusing up the gun to the CT containment area at relatively late times in SPECTOR geometry, leading to increases in measured CT electron density, can be captured by the model. This insight helps account for the exceptionally significant increase in electron temperature, and markedly reduced electron

density, observed during the electrode edge biasing experiment conducted on SPECTOR (see appendix D). The model implementation is a good testbed for further studies and improvements.

PART 3: CONCLUSIONS

Chapter 9

Concluding remarks

In the study of CT formation into a levitation field, interaction between plasma and the insulating wall surrounding the containment region during the CT formation process led to high levels of plasma impurities and consequent radiative cooling. The longest levitated CT lifetimes were up to $\sim 270 \mu\text{s}$ with the 25-turn coil configuration, despite the presence of the quartz wall. This was almost double the maximum of $\sim 150 \mu\text{s}$ lifetimes seen with six coils around quartz wall, but still less than the $\sim 340 \mu\text{s}$ lifetimes observed without levitation with an aluminum flux conserver. The ceramic alumina wall was far less contaminating than the quartz wall. In the six coil configuration, best levitated CT lifetimes decreased significantly when the ceramic wall was replaced with a quartz wall, despite the larger inner radius of the quartz wall, which should have allowed for a 50% increase in lifetime if the material had not also been changed. A revised wall design, such as one implementing a thin-walled tube of pyrolytic boron nitride located inside an alumina tube for vacuum support, would likely be beneficial. Future designs may ideally use levitation/compression coils internal to the vacuum vessel, eliminating the need for an insulating wall, but that would introduce alternative complications.

In the original six-coil configurations, plasma being rapidly advected into the containment region during the formation process was able to displace the levitation field into the large gaps above the coil stack, and come into contact with the insulating wall. Some mitigation of this effect was achieved by firing the levitation banks earlier, allowing the levitation field to soak through and become resistively pinned in the steel above and below the insulating wall. As supported by MHD simulation, this line-tying effect reduced the level of penetration of stuffing field into the insulating wall during CT formation, resulting in up to $20 \mu\text{s}$ increase in CT lifetime. Also supported by MHD simulation, interaction between plasma and the insulating wall during formation was reduced with the modified levitation field profiles of the 25-turn coil and 11-coil configurations, in which current carrying coils extended along the entirety of the outer surface of the insulating wall. These configurations were implemented

towards the end of the experimental phase. Spectrometer data and observations of CT lifetime confirm that the improved design led to reduced levels of plasma impurities and radiative cooling. Consistent with this explanation for the improvement, at the same initial CT poloidal flux, as determined by the voltage on the formation capacitors and the current in the main coil, CT lifetimes were around the same for the six-coil, 25-turn coil, and eleven-coil configurations. However the setups with the 25-turn coil and with eleven coils allowed for the successful formation of higher flux, physically larger, CTs - formation voltage could be increased from 12 to 16 kV and main coil current could be increased from 45 to 70A, corresponding to an increase in Ψ_{gun} from around 8 to 12 mWb. In contrast, the benefit of increased initial CT flux was surpassed by the performance degradation due to increased wall interaction in the six coil setup. Although the recurrence rate of good shots in the 25-turn coil configuration was significantly worse than that in the 11-coil configuration, the longest lived CTs produced in the former configuration endured for noticeably longer than those produced in the latter configuration. The stronger levitation field at the top and bottom of the insulating wall in the 25-turn coil configuration, and consequent reduction in plasma-wall interaction and radiative cooling may partially account for this. In addition, the increased ratio of the levitation coil to levitation circuit holding inductance associated with the 25-turn coil configuration, which led to more levitation flux increase upon plasma entry to the containment region, may have played a role. The longer rise time of the levitation current associated with the 25-turn configuration required an increase in the delay between the firing of levitation and formation banks, which can lead to impediment, through the line-tying effect, of plasma entry to the CT containment region. This is likely to have been the cause of the poor repeatability of good shots in the 25-turn configuration. The benefit of slightly reducing plasma-wall interaction by increasing the delay, and the line-tying effect, outweighed the detrimental effect of impeding plasma entry to the CT containment region in the 6-coil configuration only. Future designs should optimise between the ideals of low coil inductances and high coil to levitation circuit inductance ratios.

Compared with the aluminum flux conserver, the more resistive stainless steel wall led to increased impurity levels and shorter CT lifetimes, likely due to more CT field-diffusion in the material, leading to enhanced impurity sputtering. CT lifetime in the configuration with the stainless steel wall was increased by allowing a levitation field of moderate strength to soak through the wall and partially hold the CT off it. Magnetic perturbations with toroidal mode number $n = 2$ were observed on CTs produced with both stainless steel and aluminum outer flux conservers, and remained even when a moderate levitation field was allowed to soak through the stainless steel wall, but were absent in all configurations tested in which a CT was held off an outer insulating wall by a levitation field. It is known that $n = 2$ fluctuations are a sign of internal MHD activity associated with increased electron temperature. However,

the longest-lived CTs produced with the 25-turn configuration endured for up to 10% longer than, and may therefore be reasonably assumed to be hotter than the CTs produced with the stainless steel outer flux conserver. It is possible that the levitation field acts to damp out helically propagating magnetic fluctuations at the outboard CT edge and that internal MHD activity is relatively unchanged. The $n = 1$ magnetic fluctuations observed when 80 kA additional crowbarred shaft current was applied to the machine in the eleven coil configuration confirmed coherent toroidal CT rotation, and may have been a result of more vigorous MHD activity that remained apparent despite damping.

Indications of an instability, thought to be an external kink, occurred very frequently during magnetic compression and during under-damped magnetic levitation. Levitation circuit modification to match the decay rates of the levitation and plasma currents led to more stable, longer lived plasmas, and a greatly increased the recurrence rate of good shots, by avoiding unintentional magnetic compression during CT levitation. MHD simulation results, which closely match the available experimental measurements, indicate that $q < 1$ over extensive regions between the CT magnetic axis and LCFS. An obvious improvement to the experiment design would be to drive additional shaft current and raise the q profile to MHD stable regimes.

The recurrence rate of shots in which CT poloidal flux was conserved during magnetic compression is an indication of resilience against a disruption-inducing instability during compression, and was increased from around 10% to 70% with the transition to the levitation/compression field profile of the eleven-coil configuration. The improvement is likely to be largely due to the compression field profile itself, which led to more uniform outboard compression, as opposed to the largely equatorial outboard compression associated with the six coil configuration. The effect of having a reduced impurity concentration and increased CT plasma temperature prior to compression initiation, as a consequence of the improved levitation field profile, may also have played a role. Due to improved flux conservation at compression, magnetic compression ratios increased significantly with the eleven coil configuration. Magnetic compression usually did not exhibit good toroidal symmetry.

In the eleven coil configuration, poloidal field at the CT edge, at fixed $r = 26$ mm, increased by a factor of up to six at compression, while line averaged electron density at fixed $r = 65$ mm was observed to increase by a factor of up to four, with the electron density front moving inwards at up to 10 km/s. Ion Doppler measurements, at fixed $r = 45$ mm indicated increases in ion temperature by factors of up to four. Increases in poloidal field, density, and ion temperature at compression were significant only in the eleven coil configuration. The experimental technique developed to measure the CT outboard separatrix confirmed that increasing the damping of the levitation field over time led to CTs that remained physically larger over extended times. Separatrix radii trajectories from MHD simulations matched

those obtained experimentally for various magnetic levitation and compression scenarios, and indicated a radial compression factor, in terms of equatorial outboard CT separatrix, of up to 1.7. MHD simulation results indicate that CT aspect ratio is approximately constant over compression, and that internal CT poloidal and toroidal fields, and CT toroidal current, scale approximately adiabatically. Due to the effect of artificial density diffusion, simulated density and temperature do not scale according to the theoretical adiabatic compression scalings.

Based on a linear finite element method, various differential matrix operators with useful mimetic properties have been developed, and used to ensure conservation of total energy, particle count, toroidal flux, and (in some scenarios) total angular momentum in an axisymmetric numerical scheme that implements the non-linear single fluid, two temperature MHD equations. The principal mimetic qualities of the operators are that they satisfy discrete forms of the differential product rule and the divergence theorem. A novelty of the code is that all discrete spatial differential operators are represented as matrices, and the discretized forms of continuous differential equations may be obtained by simply replacing the original continuous differentiations with the corresponding matrix operators. The resultant DELiTE framework may be applied to solve a wide range of systems of differential equations, and may serve as an educational tool.

A freely available mesh generator has been modified to produce the computational grid. Forward Euler timestepping is found to be adequate for good solution convergence for the short physical timespans associated with the magnetic compression experiment, but the options of the higher order Runge-Kutta 2 and Runge-Kutta 4 timestepping schemes, which have been implemented to the code, may be advantageous for simulations with extended timespans. Methods were developed to vary the simulation timestep according to the time-evolving conditions of the various field solutions, which determine the maximum allowable timestep for stable time-advance, while managing simulation data preservation.

A numerical method to solve for the Grad-Shafranov equilibrium solution has been developed. MHD simulations can begin from an initial equilibrium state, or with the CT formation process. Various simulated diagnostics have been implemented to the code. Some of these are counterparts to the available experimental diagnostics. Several other simulated diagnostics have been developed, including the time evolutions of the $q(\psi)$ profile, magnetic axis location, volume-averaged β , CT volume and magnetic fluxes, system energy components, and maximum ion and electron temperatures. The Grad-Shafranov equilibrium and $q(\psi)$ profile solutions have been benchmarked against solutions from a well-established code, and tests that verified convergence of MHD solutions with increasing mesh resolution were conducted. Two dimensional simulations neglect inherently three dimensional turbulent transport and flux conversion, and are likely to overestimate the level of hollowness of the current pro-

files, and lead to an underestimation of q towards the CT edge, but without further internal experimental diagnostics or 3D simulations, the level of underestimation remains uncertain.

A model for anisotropic thermal diffusion has been formulated and implemented to the code. Viscosity and resistivity are modelled as being isotropic. The Spitzer resistivity formula is implemented for resistive diffusion coefficients. Constant viscous and thermal diffusion coefficients are generally implemented although the code has the options of implementing thermal diffusion coefficients based on the Chapman-Enskog closures, with the option also for Bohm scalings for the perpendicular thermal diffusion coefficients. Thermal diffusion coefficients were set to constant values for the simulations presented in this work, with the high parallel coefficients representing the physical case where particles are free to stream unimpeded along field lines. Perpendicular thermal diffusion coefficients are chosen such that simulated CT lifetimes are comparable to the experimentally observed lifetimes. A model for radiative cooling has not been included - relatively high perpendicular thermal diffusion coefficients act as a proxy to include the effects of this cooling mechanism.

Methods for simulating CT formation, magnetic levitation and magnetic compression to study this novel magnetic compression experiment have been developed. The CT formation process is simulated by adding toroidal flux associated with the measured formation voltage to the domain. Even with the simplifying assumption that radial formation current between the electrodes flows at a fixed axial location, the model is able to reproduce experimental measurements to a very acceptable level. Tests to allow variation of the axial location of intra-electrode formation current, with upper and lower bounds, were able to precisely reproduce the experimentally measured formation current signals over the times when the axial location was unrestricted. Boundary conditions for poloidal flux are evaluated and varied over time to model the levitation and compression fields, and superimposed on boundary conditions for poloidal flux that correspond to the stuffing field, which are held constant over time. In combination with explicitly applied boundary conditions for velocity components, properties of the discrete differential operators lead to the natural imposition of boundary conditions on f , resulting in a model for perfectly electrically conducting boundaries. Boundary conditions for f on the part of the boundary that represents the insulating wall surrounding the CT containment region are overwritten with a constant value, which is updated at each timestep. The value for this constant is evaluated to be consistent with the maintenance of system toroidal flux conservation in accordance with the model in which crow-barred poloidal shaft current flows in the walls of the machine and in the aluminum bars surrounding the insulating wall. Conservation of system toroidal flux enables simulations to reproduce poloidal currents that, in the experiment, are induced to flow between the conducting walls across various regions of ambient plasma external to the CT. In particular, simulations indicate that wall-to-wall currents flow outboard of the CT during magnetic compression. This is thought

to be a representation of real physical phenomenon which led to experimentally measured toroidal field signals that suggested the appearance of an external kink instability at magnetic compression.

Special care has been taken to simulate the poloidal vacuum field in the insulating region between the inner radius of the insulating tube and the levitation/compression coils, and to couple this solution to the evaluation of poloidal flux in the plasma domain, while maintaining toroidal flux conservation. This enables a quantitative model of plasma/wall interaction in various coil configurations.

Simulated diagnostics from the two dimensional MHD simulations show generally good agreement with experimental measurements. Simulations do not capture the extremely high density that is measured experimentally when plasma first enters the CT containment area, perhaps due to artificial diffusion, or due to the inability of the model to capture the effect of sputtering of high Z ions during formation, and their subsequent recombination as the plasma cools. Simulations confirmed, as also indicated with scintillator and ion-Doppler data, that ion viscous heating is extreme during the formation process. The simulated diagnostic for ion temperature works by obtaining the line averaged ion temperature along the ion-Doppler chords, which seems reasonable as a crude first approximation, but could be developed further to include additional physics. Qualitatively, the simulated diagnostic for ion temperature approximately reproduces the experimental measurement with the current model, and a suitable choice for the viscous diffusion coefficient in the ion energy equation enables scaling to match the experimental measurement. Plasma jets associated with magnetic reconnection lead to high levels of ion viscous heating, particularly around the entrance to the CT containment region during formation of closed poloidal CT flux surfaces. Simulations show that the pinching off of closed field lines that extend partially down the gun when magnetic compression is initiated early in the life of the CT leads to the formation of a smaller CT located below the entrance to the containment region. Field lines that remain open surrounding the closed CT flux surfaces are then also pinched and reconnect to form additional closed field lines around the main CT. The newly reconnected open field lines below the main CT act like a slingshot that advects the smaller CT down the gun. This effect cannot be verified experimentally, as the magnetic probes located along the gun barrel were not functioning properly at any time. The poloidal field profiles experimentally measured during magnetic compression routinely indicated loss of CT poloidal flux during compression, particularly in the six coil configuration, suggesting the action of a disruptive instability. It was found to be possible to approximately reproduce the profiles by forcing CT poloidal flux loss during simulated magnetic compression, thereby verifying that a flux loss mechanism was involved in the instability. Simulations of magnetic compression indicate that the oscillating compression field resulted in the inductive formation, magnetic compression,

and subsequent extinguishing (magnetic reconnection of CT poloidal field with the compression field) of a second and third CT. This is supported experimentally in that experimental poloidal field measurements closely match the corresponding simulated diagnostic, and that X-ray-phosphor imaging indicates the compressional heating of up to three distinct plasmoids on many compression shots.

The components of system energy for MHD simulations involving CT formation and magnetic compression evolve as expected, with conversions initially from toroidal magnetic energy associated with formation current to thermal energy, kinetic energy and poloidal magnetic energy. Magnetic energy is converted to electron thermal energy via ohmic heating, with kinetic energy being converted to ion thermal energy due to viscous effects. Rapid diffusion of heat through the boundary means that thermal energy is lost faster than it is sourced from magnetic energy after the initial period of maximum thermal energy gain, except during the time when the CT is being magnetically compressed. At CT magnetic compression, the principal energy conversion mechanisms are that poloidal magnetic energy does work to compress the CT, leading to compressional heating of ions and electrons. Toroidal plasma current increases as the CT is compressed, leading to increased ohmic heating and an additional rise in electron thermal energy. Again, electrons transfer some of this energy to the ion fluid, so ion thermal energy also rises due to enhanced ohmic heating.

A model of plasma/neutral fluid interaction was developed and included in the DELiTE framework. The terms that determine the source rates of species momentum and energy due to ionization and recombination were derived from basic principles rather than applying the involved process of taking successive moments of the collision operators pertaining to the reactions. This method enables determination of the volumetric rate of thermal energy transfer from electrons to photons and neutral particles due to radiative recombination, which has been neglected in other studies. The implementation of the model has enabled clarification of the mechanisms behind the significant increases in CT electron density that are routinely observed on the SPECTOR plasma injector; simulations confirm that neutral gas, which remains concentrated below the gas valves after CT formation, diffuses up the gun barrel to the CT containment region where it is ionized, leading to the observed electron density increases. This understanding helps account for the exceptionally significant increase in electron temperature, and markedly reduced electron density, observed during the electrode edge biasing experiment conducted on SPECTOR. It is thought that edge fueling impedance, a consequence of a biasing-induced transport barrier, is largely responsible for the temperature increase and density decrease. System energy conservation is maintained with the inclusion of the neutral fluid model if the electron thermal energy expended on ionization and recombination processes is accounted for. The initial motivation for the study of plasma/neutral fluid interaction was that inclusion of a neutral fluid model was expected to lead to net

ion cooling. However simulations indicated that ion temperature is relatively unchanged by charge exchange reactions in hot-ion regions, where electron temperature and ionization rates are also high and neutral fluid density is particularly low. The model implementation is a good testbed for further studies and improvements.

Further code development may include a more generally applicable model for density diffusion with correction terms that maintain angular momentum conservation even in simulation scenarios that include CT formation and magnetic compression. The level to which artificial density diffusion affects the simulated density diagnostic, and the evolution of the other fields, should be investigated further. An implicit timestepping scheme may be implemented as this would enable faster simulation times while enabling the use of a greater range of values for the various diffusion coefficients. The ability to model part of the domain as a plasma-free material is useful because it expands the code's range of applicability as a problem-solving tool. For example, the feature can easily be adapted to model the penetration of field associated with magnetically confined plasma into surrounding conductors. Even a much simpler model, such as the isothermal version of the code, can qualitatively reproduce experimental diagnostics for magnetic field and density, and with resistivity simply set artificially high in the regions representing the insulating wall, is able to illustrate intersection of stuffing field with the wall during CT formation, and the mitigation of the effect in the eleven coil configuration. However, the effort invested in developing a conservative scheme with many extended features has resulted in a code framework with a solid foundation for further development and improvement.

The magnetic compression experiment would certainly be worth attempting again. It is unclear if it can work to meet the original goal of supporting the PCS program, as the dynamics of a CT being compressed by a moving metal wall may be too different from those associated with a compressing external magnetic field. However, the goal of achieving levitated CT temperatures and lifetimes comparable to that of CTs formed into a containment region surrounded by a flux conserver appears within reach, if a suitable choice of material is made for the insulating wall, or if compression coils are integrated within the vacuum vessel, and if the levitation circuit parameters are optimised. Furthermore, it has been inferred that CT stability needs to be improved; a first step towards improvement would be to add toroidal field through the action of externally driven shaft current, as is currently done on SPECTOR machines. Having already demonstrated reasonably significant temperature increases at compression, rapid further progress with some design changes based on lessons learned seems likely.

Bibliography

- [1] C. Dunlea, C. Xiao, and A. Hirose, *Operation of a co-axial helicity injector on STOR-M*, submitted to arXiv (2019)
- [2] T. Boyd and J. Sanderson, *Plasma dynamics*, London, Nelson (1969)
- [3] M. Laberge, *An Acoustically Driven Magnetized Target Fusion Reactor*, Journal of Fusion Energy 27:65–68 (2008)
- [4] J. H. Hammer, J. L. Eddleman, C. W. Hartman, H. S. McLean, and A. W. Molvik, *Experimental demonstration of compact torus compression and acceleration*, Physics of Fluids B: Plasma Physics 3, 2236 (1991)
- [5] A. W. Molvik, J. L. Eddleman, J. H. Hammer, C. W. Hartman, and H. S. McLean, *Quasistatic Compression of a Compact Torus*, Physical Review Letters 66 (2), 165 (1991)
- [6] P. Bellan, *Spheromaks*, Imperial College Press, London (2000)
- [7] P. M. Bellan, S. You, and G. S. Yun, *Identification of the Sequence of Steps Intrinsic to Spheromak Formation*, AIP Conf. Proc. 875, 47 (2006)
- [8] P. M. Bellan, *Helicity injection with moving vacuum-plasma boundary with arbitrary flux surfaces*, Phys. Fluids 31, 215 (1988)
- [9] M. Berger, *Introduction to magnetic helicity*, Plasma Phys. Control Fusion 41 B167-B175 (1999)

- [10] J. Taylor, *Relaxation and magnetic reconnection in plasmas*, Reviews of Modern Physics, Vol 58, No. 3 (1986)
- [11] L. Woltjer, *A Theorem on Force-Free Magnetic Fields*, Proceedings of the National Academy of Sciences, 44, 6 (1958)
- [12] M. Schaffer, *Exponential Taylor states in circular cylinders*, Physics of Fluids 30, 160 (1987)
- [13] A. J. Redd, D. J. Battaglia, M. W. Bongard, R. J. Fonck, E. T. Hinson, B. A. Kujak-Ford, B. T. Lewicki, A. C. Sontag, and G. R. Winz, *Point-Source Helicity Injection Current Drive System for the Pegasus Toroidal Experiment*, J. Fusion Energy 28:203-207 (2009)
- [14] M. R. Brown, A. D. Bailey, and P. M. Bellan, *Characterization of a spheromak plasma gun: The effect of refractory electrode coatings*, J. Appl. Phys. 69 (9) (1991)
- [15] M. R. Brown and P. M. Bellan, *Spheromak injection into a tokamak*, Physics of Fluids B: Plasma Physics 2, 1306 (1990)
- [16] T. R. Jarboe, *Review of spheromak research*. Plasma Phys. Control. Fusion 36, 945 (1994)
- [17] R. Dendy, editor, *Plasma Physics: An introductory course*, Cambridge University Press (1993)
- [18] D. D. Meyerhofer, R. A. Hulse, and E. G. Zweibel, *Zero-dimensional study of the compression of low temperature spheromaks*, Nucl. Fusion 26 235 (1986)
- [19] H. P. Furth and S. Yoshikawa, *Adiabatic Compression of Tokamak Discharges*, Physics of Fluids (1958-1988) 13, 2593 (1970)
- [20] P. Carolan and V. Piotrowicz, *The behaviour of impurities out of coronal equilibrium*, Plasma Phys. 25 1065 (1983)
- [21] S. G. Goncharev, V. K. Gusev, and V. A. Ipatov, *Local heat balance and MHD stability in the plasma of Tuman-2A, a tokamak with magnetic compression*, Proceedings of the Plasma Physics and Controlled Nuclear Fusion Research Conference, London (pp. 155-166) (1984)
- [22] M. Yamada, *S-1 Spheromak*, Nucl. Fusion 25 1327 (1985)

- [23] M. Yamada, T. K. Chu, R. A. Ellis Jr., A. C. Janos, F. M. Levinton, R. M. Mayo, R. W. Motley, M. Nagata, Y. Ono, N. Satomi, and Y. Ueda, *Experimental investigation of magnetic compression of a spheromak plasma*, Physics of Fluids B Vol. 2 (12) (1990)
- [24] C. Munson, A. Janos, F. Wysocki, and M. Yamada, *Experimental control of the spheromak tilting instability*, Physics of Fluids 28 (5) (1985)
- [25] S. Woodruff, J. E. Stuber, C. Bowman, P. E. Sieck, P. A. Melnik, C. A. Romero-Talamás, J. B. O'Bryan, and R. L. Miller, *Adiabatic Compression of a Compact Torus*, Fusion Science and Technology, 72:4, 705-712 (2017)
- [26] A. Janos, G. W. Hart, and M. Yamada, *Relaxation of spheromak plasmas toward a minimum-energy state and global magnetic fluctuations*, Phys. Rev. Lett. 55, 2868 (1985)
- [27] A. Janos, G. W. Hart, C. H. Nam, and M. Yamada, *Global magnetic fluctuations in spheromak plasmas and relaxation toward a minimum-energy state*, Physics of Fluids 28, 3667 (1985)
- [28] K. Bol, J. L. Cecchi, C. C. Daughney, F. DeMarco, R. A. Ellis, H. P. Eubank, H. P. Furth, H. Hsuan, E. Mazzucato, and R. R. Smith, *Experiments on the Adiabatic Toroidal Compressor*, Proceedings of the Plasma Physics and Controlled Nuclear Fusion Research Conference, Tokyo (pp. 141-54) (1974)
- [29] K. Bol, R. A. Ellis, H. Eubank, H. P. Furth, R. A. Jacobsen, L. C. Johnson, E. Mazzucato, W. Stodiek, and E. L. Tolnas, *Adiabatic compression of the Tokamak Discharge*, Phys. Rev. Letters 29, 1495 (1972)
- [30] L. Artsimovich, *Tokamak Devices*, Nucl. Fusion 12, 215 (1972)
- [31] N. Inoue, *Ohmic Ignition of Tokamak Plasma via Ultra Low q Discharge Combined with Adiabatic Compression*, J. Nuclear Sci. and Tech. 27 (11) (1990)
- [32] Y. Kamada, T. Fujita, Y. Murakami, T. Ohira, K. Saitoh, Y. Fuke, M. Utsumi, Z. Yoshida, and N. Inoue, *Recent results of ultra low q experiments in TORIUT-6 and REPUTE-1*, Nucl. Fusion 29 713 (1989)
- [33] J. Wesson, *Tokamaks*, 2nd edition., Oxford University Press (1997)
- [34] Z. Yoshida, T. Uchida, and N. Inoue, *Self organization of the reversed field pinch quiescence*, Physics of Fluids 27, 1785 (1984)
- [35] J. Taylor, *Relaxation of Toroidal Plasma and Generation of Reverse Magnetic Fields*, Phys. Rev. Lett. 33, 1139 (1974)

[36] M. Watanabe, *Application of magnetic compression to ultra-low-Q plasmas*, PhD thesis (1994)

[37] I. Hutchinson, *Requirements For Ohmic Ignition*, Journal of Fusion Energy 6, 3 (1987)

[38] M. Watanabe, N. Ikathu, S. Kido, J. Miyazawa, H. Nakanishi, Y. Okamura, P. Richard, T. Sakurai, K. Sasaki, S. Takej, S. Iyengar, J. Morikawa, Y. Ogawa, Z. Yoshida, and N. Inoue, *Reduction of plasma-wall interaction and MHD dynamics of magnetically compressed ULQ plasmas in REPUTE-1*, Jour. nuc. mat, 220, 641 (1995)

[39] M. P. Gryaznevich and A. Sykes, *Merging-compression formation of high temperature tokamak plasma*, Nucl. Fusion 57 072003 (2017)

[40] M. P. Gryaznevich, *Small-aspect-ratio tokamak research at Culham Laboratory*, A Collection of Papers Presented at the IAEA Technical Committee Meeting Research Using Small Tokamaks (Wiirzburg, 28–29 September 1992) (Vienna: IAEA) (1992)

[41] A. Sykes, *Progress on spherical tokamaks*, Plasma Phys. Control. Fusion 36 B93 (1994)

[42] A. Sykes, R. J. Akers, L. C. Appel, E. R. Arendsa, P. G. Carolan, N. J. Conway, G. F. Counsell, G. Cunningham, A. Dnestrovskijb, Yu. N. Dnestrovskijb et al., *First results from MAST*, Nucl. Fusion 41 1423 (2001)

[43] M. Gryaznevich, R. J. Akers, G. F. Counsell, G. Cunningham, A. Dnestrovskij, A. R. Field, T. C. Hender, A. Kirk, B. Lloyd, H. Meyer et al., *Next-step-targeted experiments on the Mega-Amp Spherical Tokamak*, Physics of Plasmas 10, 1803 (2003)

[44] D. J. Rej, D. P. Taggart, M. H. Baron, R. E. Chrien, R. J. Gribble, M. Tuszewski, W. J. Waganaar, and B. L. Wright, *High power magnetic compression heating of field reversed configurations*, Phys. Fluids B 4 1909 (1992)

[45] J. Slough, G. Votroubek, and C. Pihl, *Creation of a high-temperature plasma through merging and compression of supersonic field reversed configuration plasmoids*, Nucl. Fusion 51 053008 (2011)

[46] C. Dunlea, S. Howard, W. Zawalski, K. Epp, A. Mossman, General Fusion Team, C. Xiao, and A. Hirose, *Magnetic Levitation and Compression of Compact Tori*, available at arXiv:1907.10307, submitted to Physics of Plasmas (2019)

[47] C. Dunlea et al., *Magnetic Compression Experiment at General Fusion*, APS DPP San Jose, Oct. 31-Nov. 4, CP10.00105 (2016)

[48] C. Dunlea et al., *Magnetic Compression at General Fusion - Experiment & Simulation*, APS DPP Milwaukee, Oct. 23- 27, UP11.00135 (2017)

[49] C. Dunlea et al., *Magnetic Compression at General Fusion - Experiment & Simulation with neutral fluid*, EPS Prague, July 2- 6 (2018)

[50] C. Dunlea et al., *Magnetic Compression at General Fusion - Experiment & Simulation with a neutral fluid*, ICPP Vancouver, June 4-8 (2018)

[51] C. Dunlea and I. Khalzov, *A globally conservative finite element MHD code and its application to the study of compact torus formation, levitation and magnetic compression*, available at arXiv:1907.13283, submitted to J. Comp. Phys (2019)

[52] C. Dunlea, C. Xiao, and A. Hirose, *A model for plasma-neutral fluid interaction and its application to a study of CT formation in a magnetised Marshall gun*, submitted to arXiv and Physics of Plasmas (2019)

[53] C. Dunlea, General Fusion Team, C. Xiao, and A. Hirose, *First results from plasma edge biasing on SPECTOR*, submitted to arXiv and Physics of Plasmas (2019)

[54] R.J. Goldston and P.H. Rutherford, *Introduction to Plasma Physics*, Institute of Physics Publishing, Bristol UK (1995)

[55] I. Hutchinson, *Principles of Plasma Diagnostics*, Cambridge University Press, New York (1987)

[56] G. Tallents, *Plasma Diagnostic Techniques*, Lecture notes, University of York, UK (2010)

[57] Hans-Joachim Kunze, *Introduction to Plasma Spectroscopy*, Springer-Verlag Berlin Heidelberg (2009)

[58] T.L Pittman and C. Fleurier, *Plasma shifts of the He II, H alpha and P alpha lines*, Phys Rev A, 33(2) 1291-1296 (1986)

[59] D. C. Meeker, Finite Element Method Magnetics (FEMM), Version 4.0.1, <http://www.femm.info>.

[60] R. Causey, *Hydrogen isotope retention and recycling in fusion reactor plasma-facing components*, Journal of Nuclear Materials, 300(2-3), 91–117 (2002)

[61] <http://electronbunker.ca/eb/InductanceCalc.html>

[62] <http://www.66pacific.com/calculators/coil-inductance-calculator.aspx>

[63] S. Fahy, C. Kittel, and S. G. Louie, *Electromagnetic screening by metals*, American Journal of Physics 56, 989-92 (1988)

- [64] http://web.mit.edu/6.013_book/www/chapter10/10.7.html (figure 10.7.5)
- [65] Y. K. Fowler, J. S. Hardwick, and T. R. Jarboe, *Comments Plasma Phys, Control. Fusion* 16, 91(1994)
- [66] R. D. Hazeltine and F. L. Waelbroeck, *The Framework of Plasma Physics*, Westview, Boulder CO (2004)
- [67] <https://farside.ph.utexas.edu/teaching/plasma/Plasma/>
- [68] P. M. Bellan, *Fundamentals of Plasma Physics*, Cambridge University Press, (2008)
- [69] J.A. Bittencourt. *Fundamentals of Plasma Physics*, Third Ed. Springer-Verlag, New York (2004)
- [70] L. Landau and E. Lifshitz, *Physical Kinetics. Course of theoretical physics*, Pergamon Press, Oxford; New York, 3rd edition (1976)
- [71] R. Abhay, *Introductory Plasma Physics*, Lecture notes, MIT (2008)
- [72] E.T. Meier and U. Schumak, *A general nonlinear fluid model for reacting plasma-neutral mixtures*, *Physics of Plasmas* 19, 072508 (2012)
- [73] <http://www.brown.edu/Departments/Engineering/Courses/En221/Notes/Tensors/Tensors.htm>
- [74] G. Degrez, *Transport processes in gas mixtures*.
<http://mecapp42.ulb.ac.be/atm/Members/gdegrez/Lect1-2.pdf>
- [75] S. Chapman and T.G. Cowling. *The mathematical theory of non-uniform gases*, 3rd edition, Cambridge University Press, Cambridge, (1970)
- [76] <http://homepages.cae.wisc.edu/~callen/chap6.pdf>
- [77] R. Schunk and A. Nagy, *Ionospheres: Physics, Plasma Physics, and Chemistry*, Cambridge Atmospheric and Space Science Series, Cambridge University Press, (2009)
- [78] S. O. Knox, C. W. Barnes, G. J. Marklin, T. R. Jarboe, I. Henins, H. W. Hoida, and B. L. Wright, *Observations of spheromak equilibria which differ from the minimum-energy state and have internal kink distortions*, *Phys. Rev. Lett.* 56, 842 (1986)
- [79] J. B. Perot, *Discrete Conservation Properties of Unstructured Mesh Schemes*, *Annual Review of Fluid Mechanics*, Vol.43, p.299-318 (2011)

[80] E. J. Caramana, D. E. Burton, M. J. Shashkov, and P. P. Whalen, *The Construction of Compatible Hydrodynamics Algorithms Utilizing Conservation of Total Energy*, J. Comput. Phys. 146, 227–262 (1998)

[81] L. G. Margolin, M. Shashkov, and P. K. Smolarkiewicz, *A discrete operator calculus for finite difference approximations*, Comput. Methods Appl. Mech. Eng. 187 (2000)

[82] X. Zhang, D. Schmidt, and B. Perot, *Accuracy and Conservation Properties of a Three-Dimensional Unstructured Staggered Mesh Scheme for Fluid Dynamics*, J. Comput. Phys. 175, 764–791 (2002)

[83] D. Derigs, A. R. Winters, G. J. Gassner, and S. Walch, *A novel high-order, entropy stable, 3D AMR MHD solver with guaranteed positive pressure*, J. Comp. Phys. 317, 223–256 (2016)

[84] J. G. Liu and W. C. Wang, *An Energy-Preserving MAC–Yee Scheme for the Incompressible MHD Equation*, 174, 12–37 (2001)

[85] E. Franck, M. Häßl, A. Lessig, and E. Sonnendrucker, *Energy conservation and numerical stability for the reduced MHD models of the non-linear JOREK code*, ESAIM: M2AN 49, 1331 (2015)

[86] T. Hughes, G. Engel, L. Mazzei, and M. G. Larson, *The Continuous Galerkin Method Is Locally Conservative*, J. Comput. Phys. 163, 467–488 (2000)

[87] J. B. Perot, *Conservation properties of unstructured staggered mesh schemes*, J. Comput. Phys. 159, 58 (2000)

[88] M. Shashkov and S. Steinberg, *Support-operator finite-difference algorithms for general elliptic problems*, J. Comput. Phys. 118:131 (1995)

[89] <https://www.particleincell.com/2012/matlab-fem/>

[90] G. Strang, *Computational Science and Engineering*, Wellesley-Cambridge Press (2007)

[91] P. O. Persson and G. Strang, *A Simple Mesh Generator in MATLAB*. SIAM Review, Volume 46 (2), pp. 329-345 (2004)

[92] P. O. Persson, *Mesh Generation for Implicit Geometries*, Ph.D. thesis, Department of Mathematics, MIT, Dec (2004)

[93] <http://persson.berkeley.edu/distmesh/>

[94] L. D. Cloutman, *A Note on Differencing the Viscous Dissipation Terms for a Newtonian Fluid*, Lawrence Livermore National Laboratory Report UCRL-ID-144159 (2001)

[95] [https://en.wikipedia.org/wiki/Tensor_derivative_\(continuum_mechanics\)](https://en.wikipedia.org/wiki/Tensor_derivative_(continuum_mechanics))

[96] S. C. Jardin, *Computational Methods in Plasma Physics*, Taylor and Francis, Boca Raton, (2010)

[97] https://www.uni-muenster.de/imperia/md/content/physik_tp/lectures/ws2016-2017/num_methods_i/heat.pdf

[98] E. B. Hooper, B. I. Cohen, H. S. McLean, R. D. Wood, C. A. Romero-Talamas, and C. R. Sovinec, *NIMROD resistive magnetohydrodynamic simulations of spheromak physics*, Physics of Plasmas 15, 032502 (2008)

[99] Discussion with E. B Hooper

[100] E. T. Meier, *Modeling Plasmas with Strong Anisotropy, Neutral Fluid Effects, and Open Boundaries*, PhD thesis, Univ. Washington (2011)

[101] J. A. Crotninger, L. LoDestro, L. D. Pearlstein, A. Tarditi, T. A. Casper, and E. B. Hooper, *CORSICA: A comprehensive simulation of toroidal magnetic-fusion devices. Final report to the LDRD Program*, LLNL Report UCRL-ID-126284, doi:10.2172/522508 (1997)

[102] J. Morales, W. Bos, K. Schneider, and D. Montgomery, *Magnetohydrodynamically generated velocities in confined plasma*, Phys. of Plasmas, AIP 22 (4) (2015)

[103] G. S. Voronov, *A practical fit formula for ionization rate coefficients of atoms and ions by electron impact: Z=1-28*, Atomic Data Nucl. Data, 65:1 – 35 (1997)

[104] U. Yusupaliev, *Stoletov constant and effective ionization potential of a diatomic gas molecule*, B. Lebedev Phys. Inst., 34:334 – 339 (2007)

[105] https://en.wikipedia.org/wiki/Atomic_radius

[106] R. W. P. McWhirter, *Spectral intensities*, In R. H. Huddlestone and S. L. Leonard, editors, *Plasma Diagnostic Techniques*. Academic Press, New York (1965)

[107] H. L. Pauls, G. P. Zank, and L. L. Williams, *Interaction of the solar wind with the local interstellar medium*, J. Geophys. Research, 100:21,595 – 21,604 (1995)

[108] C. F. Barnett, *Atomic Data for Fusion*, Vol. 1. Oak Ridge National Laboratory (1990)

[109] P. Helander, S. I Krasheninnikov, and P. J. Catto, *Fluid equations for a partially ionized plasma*, Phys. Plasmas, 1:3174 – 3180 (1994)

[110] J. E. Leake, V. S. Lukin, M. G. Linton, and E. T. Meier, *Multi-fluid simulations of chromospheric magnetic reconnection in a weakly ionized reacting plasma*, The Astrophysical Journal, 760:109 (12pp) (2012)

[111] S. Howard, *Experimental results from the SPECTOR device at General Fusion*, oral presentation at 27th IEEE Symposium on Fusion Engineering (2017)

[112] P. Carle, A. Froese, A. Wong, S. Howard, P. O’Shea, and M. Laberge, *Polarimeter for the General Fusion SPECTOR machine*, Rev. Sci. Instrum. 87, 11E104 (2016)

[113] W. C. Young and D. Parfeniuk, *Thomson scattering at general fusion*, Rev. Sci. Instrum. 87, 11E521 (2016)

[114] F. Wagner, G. Becker, K. Behringer, D. Campbell, A. Eberhagen, W. Engelhardt, G. Fussmann, O. Gehre, J. Gernhardt, G. von Gierke et al., *Regime of Improved Confinement and High Beta in Neutral-Beam-Heated Divertor Discharges of the ASDEX Tokamak*, Phys. Rev. Lett. 49 1408 (1982)

[115] R. J. Taylor, M. L. Brown, B. D. Fried, H. Grote, J. R. Liberati, G. J. Morales, and P. Pribyl, *H-Mode Behavior Induced by Cross-Field Currents in a Tokamak*, Phys. Rev. Lett. 63 2365 (1989)

[116] R. Weynants and R. Taylor, *Dynamics of H-mode-like edge transitions brought about by external polarization*, Nucl. Fusion 30 945 (1990)

[117] R. J. Groebner, K. H. Burrell, P. Gohil, and R. P. Seraydarian, *Spectroscopic study of edge poloidal rotation and radial electric fields in the DIII-D tokamak (invited)*, Review of Scientific Instruments 61, 2920 (1990)

[118] F. Zacek, J. Stockel, L. Kryska, K. Jakubka, J. Badalec, and I. Duran, *Preliminary experiments with edge plasma biasing in tokamak CASTOR*, Czech. J. Phys. 48 60 (1998)

[119] G. Van Oost, J. P. Gunn, A. Melnikov, J. Stockel, and M. Tendler, *The role of radial electric fields in the tokamaks TEXTOR-94, CASTOR, and T-10*, Czechoslovak Journal of Physics 51: 957 (2001)

[120] G.S. Kirnev, S.A. Grashin, L.N. Khimchenko, and N.N.Timchenko, *First results of biasing experiments on the T-10 tokamak*, Czechoslovak Journal of Physics 51: 1011 (2001)

- [121] W. Zhang, C. Xiao, and A. Hirose, *Plasma autobiasing during Ohmic H-mode in the STOR-M tokamak*, Physics of Fluids B: Plasma Physics 5, 3961 (1993)
- [122] H. Figueiredo, I. S. Nedzelskiy, C. Silva, C. A. F. Varandas, J. A. C. Cabral, and R. M. O. GalvÃ£o, *Electron emissive electrode for the plasma biasing experiment on tokamak ISTTOK*, Review of Scientific Instruments 75, 4240 (2004)
- [123] S. Jachmich, G. Van Oost, R. R. Weynants, and J. A. Boedo, *Experimental investigations on the role of ExB flow shear in improved confinement*, Plasma Phys. Control. Fusion 40 1105, (1998)
- [124] Y. Sun, Z. P. Chen, T. Z. Zhu, Q. Yu, G. Zhuang, J. Y. Nan, X. Ke, H. Liu, and the J-TEXT Team, *The influence of electrode biasing on plasma confinement in the J-TEXT tokamak*, Plasma Phys. Control. Fusion 56 015001 (2014)
- [125] M. Tendler, *Different scenarios of transitions into improved confinement modes*, Plasma Physics and Controlled Fusion, vol. 39, no. 12, pp. B371–B382 (1997)

PART 4: APPENDICES

Appendix A

Plasma kinetic theory, MHD equations, and equilibrium models

This appendix is largely comprised of background material, assembled mostly from material found in [66, 67, 68, 69, 6]. An overview is presented of the well-established methods used to derive the MHD equations and Grad-Shafranov equation, which are solved for in the code. The overview is included mainly because it lays the groundwork for chapter 8, in which the set of equations that describes co-interacting plasma and neutral fluids are derived, in a process that involves taking moments of collision operators that pertain to the scattering and reactive collisions associated with plasma-neutral interactions. Readers familiar with this material may wish to skip directly to section A.8, where the equations which are solved for in the MHD code (without plasma-neutral interaction) are collected. This appendix begins with a brief overview of plasma kinetic theory in section A.1. In section A.2, it will be shown how various important plasma fluid parameters can be obtained by taking successive moments of the distribution function. For example, the plasma fluid number density, fluid velocity, total stress tensor, and energy flux density are derived by taking the zeroth, first, second and third moments respectively. In section A.3, it will be shown how taking moments of the part of the collision operator pertaining to scattering collisions results in finite terms that will be included in the ion and electron plasma fluid momentum and energy conservation equations. Using the derivations presented in sections A.2 and A.3, the process of taking moments of the Boltzmann equation results in the two-fluid Braginskii MHD equations, as shown in section A.4. A brief overview of the Chapman-Enskog scheme for obtaining fluid closures, which yield expressions for the ion and electron heat flux densities and viscous diffusion coefficients, is presented in section A.5. The process for obtaining the single-fluid MHD equations from the Boltzmann equation and the two-fluid MHD equations is outlined in section A.6. Derivations of the standard form and a simplified form of the Grad-Shafranov equation, which describes the force balance equilibrium in ideal MHD with toroidal symmetry,

are presented in section A.7. The appendix will conclude with section A.8, where the core set of equations implemented to the DELiTE code framework are collected.

A.1 Distribution functions and the Boltzmann equation

We consider a system of point particles with a given charge and mass. The system has two species of particles, electrons and singly charged ions. In six-dimensional phase space (\mathbf{r}, \mathbf{V}) , each particle has its own trajectory - the trajectory of the i^{th} particle is $\mathbf{r}_i(t)$, $\mathbf{V}_i(t)$. Since $\mathbf{V}_i(t) = \dot{\mathbf{r}}_i(t)$, if $\mathbf{r}_i(t)$ and $\mathbf{V}_i(t)$ are known at one time, they are known at all times. The instantaneous dynamic state of each particle is given by a point in phase space that's defined by the six coordinates x, y, z, V_x, V_y, V_z . The microscopic number density [m^{-3}] of particles of species α in phase space is described by the Klimontovich density distribution function [71]:

$$F_\alpha(\mathbf{r}, \mathbf{V}, t) = \sum_{i=1}^{N_0} \delta(\mathbf{r} - \mathbf{r}_i(t)) \delta(\mathbf{V} - \mathbf{V}_i(t)) \quad (\text{A.1.1})$$

where N_0 is the number of particles of each species, and $\delta(x)$ is the Dirac-delta function:

$$\delta(x) = \begin{cases} \infty, & \text{if } x=0 \\ 0, & \text{if } x \neq 0 \end{cases}$$

$$\int_{-\infty}^{\infty} \delta(x) dx = 1$$

Note that for point particles, number density is infinite at singular points where there are particles. F_α is normalised so that its velocity integral is the regular particle number density [66]:

$$\int F_\alpha(\mathbf{r}, \mathbf{V}, t) d\mathbf{V} = n_\alpha(\mathbf{r}, t)$$

The distribution function satisfies the continuity equation in phase space:

$$\frac{dF_\alpha}{dt} = \left(\frac{\partial}{\partial t} + \frac{\partial \mathbf{r}}{\partial t} \cdot \frac{\partial}{\partial \mathbf{r}} + \frac{\partial \mathbf{V}}{\partial t} \cdot \frac{\partial}{\partial \mathbf{V}} \right) F_\alpha = \frac{\partial F_\alpha}{\partial t} + \mathbf{V} \cdot \nabla F_\alpha + \mathbf{a}_\alpha \cdot \nabla_v F_\alpha = 0$$

where $\mathbf{a}_\alpha(\mathbf{r}, t) = \frac{q_\alpha}{m_\alpha}(\mathbf{E}(\mathbf{r}, t) + \mathbf{V}(t) \times \mathbf{B}(\mathbf{r}, t))$ is the species particle acceleration determined by the Lorentz force. The Klimontovich equation is:

$$\frac{\partial F_\alpha}{\partial t} + \mathbf{V} \cdot \nabla F_\alpha + \frac{q_\alpha}{m_\alpha}(\mathbf{E}(\mathbf{r}, t) + \mathbf{V} \times \mathbf{B}(\mathbf{r}, t)) \cdot \nabla_v F_\alpha = 0 \quad (\text{A.1.2})$$

The fields are due to external sources in combination with microscopic fields self-consistently produced by the point particles: $\mathbf{E}(\mathbf{r}, t) = \mathbf{E}_{ext}(\mathbf{r}, t) + \mathbf{E}_m(\mathbf{r}, t)$, and $\mathbf{B}(\mathbf{r}, t) = \mathbf{B}_{ext}(\mathbf{r}, t) + \mathbf{B}_m(\mathbf{r}, t)$. The microscopic fields are determined by Maxwell's equations:

$$\begin{aligned}\nabla \cdot \mathbf{E}_m(\mathbf{r}, t) &= \frac{\rho_{c-m}(\mathbf{r}, t)}{\epsilon_0} \\ \nabla \cdot \mathbf{B}_m(\mathbf{r}, t) &= 0 \\ \nabla \times \mathbf{E}_m(\mathbf{r}, t) &= -\dot{\mathbf{B}}_m(\mathbf{r}, t) \\ \nabla \times \mathbf{B}_m(\mathbf{r}, t) &= \mu_0(\mathbf{J}_m(\mathbf{r}, t) + \epsilon_0 \dot{\mathbf{E}}_m(\mathbf{r}, t))\end{aligned}\tag{A.1.3}$$

The microscopic charge density is

$$\rho_{c-m}(\mathbf{r}, t) = \sum_{\alpha} q_{\alpha} \int F_{\alpha}(\mathbf{r}, \mathbf{V}, t) d\mathbf{V}\tag{A.1.4}$$

and the microscopic current density is

$$\mathbf{J}_m(\mathbf{r}, t) = \sum_{\alpha} q_{\alpha} \int \mathbf{V} F_{\alpha}(\mathbf{r}, \mathbf{V}, t) d\mathbf{V}\tag{A.1.5}$$

It can be said that plasma physics can be viewed formally as a closure of Maxwell's equations by means of constitutive relations - expressions for charge density and current density in terms of the electric and magnetic fields [66]. Given initial fields that are consistent with Maxwell's equations, equations A.1.4 and A.1.5, in combination with equations A.1.1 to A.1.3 make up the desired constitutive relations. The problem is completely deterministic and densities and fields are exactly determined at all times. Although the Klimontovich formalism is exact, it is far too detailed to be of practical use [71]. The fine-grained, spiky distribution function is microscopically exact but does not correspond to the macroscopically smooth quantities observed in experiment. A more useful description is obtained by an averaging process. One method to achieve this is based on the Liouville distribution and the BBGKY hierarchy equations [70, 71]. An equivalent, more straightforward method, is based on taking the ensemble averages of the distribution functions and fields. Splitting the distribution functions and the microscopic parts of the fields into averaged and fluctuating contributions, we define:

$$\begin{aligned}F_{\alpha}(\mathbf{r}, \mathbf{V}, t) &= \ll F_{\alpha}(\mathbf{r}, \mathbf{V}, t) \gg + \delta F_{\alpha}(\mathbf{r}, \mathbf{V}, t) \\ \mathbf{E}(\mathbf{r}, t) &= \mathbf{E}_{ext}(\mathbf{r}, t) + \ll \mathbf{E}_m(\mathbf{r}, t) \gg + \delta \mathbf{E}_m(\mathbf{r}, t) \\ \mathbf{B}(\mathbf{r}, t) &= \mathbf{B}_{ext}(\mathbf{r}, t) + \ll \mathbf{B}_m(\mathbf{r}, t) \gg + \delta \mathbf{B}_m(\mathbf{r}, t)\end{aligned}\tag{A.1.6}$$

where $\ll \dots \gg$ indicates ensemble averaging (e.g., $f_\alpha(\mathbf{r}, \mathbf{V}, t) = \ll F_\alpha(\mathbf{r}, \mathbf{V}, t) \gg$ is a smoothed distribution function for species α that is obtained from a statistical average of the microscopic distribution function), and δ indicates fluctuating contributions. Using the evolution of f_α to characterise the system does not track individual particles (as is done when using F_α) - instead, classes of particles having approximately the same \mathbf{r} and \mathbf{v} are tracked [68]. $f_\alpha(\mathbf{r}, \mathbf{V}, t)$ represents the average of the number density [$\text{m}^{-6} \text{s}^3$] of particles of species α in a 6D volume element in phase space, centered around \mathbf{r}, \mathbf{V} , with dimensions $dx dy dz dV_x dV_y dV_z$, where the average is taken in the 6D volume. Consequently,

$f_\alpha(\mathbf{r}, \mathbf{V}, t) d\mathbf{r} d\mathbf{V} = f_\alpha(\mathbf{r}, \mathbf{V}, t) dx dy dz dV_x dV_y dV_z =$ number of particles of species α in the same 6D volume element.

Using equation A.1.6 in equation A.1.2, and ensemble-averaging, noting that $\ll \delta F_\alpha \gg = \ll \delta \mathbf{E}_m \gg = \ll \delta \mathbf{B}_m \gg = 0$ (statistical average of a random fluctuation is zero), $\ll \ll a \gg \gg = \ll a \gg$, and that $\ll a + b \gg = \ll a \gg + \ll b \gg$, we obtain:

$$\begin{aligned} \frac{\partial f_\alpha}{\partial t} + \mathbf{V} \cdot \nabla f_\alpha + \frac{q_\alpha}{m_\alpha} (\ll \mathbf{E}(\mathbf{r}, t) \gg + \mathbf{V} \times \ll \mathbf{B}(\mathbf{r}, t) \gg) \cdot \nabla_v f_\alpha \\ = -\frac{q_\alpha}{m_\alpha} \ll (\delta \mathbf{E}_m(\mathbf{r}, t) + \mathbf{V} \times \delta \mathbf{B}_m(\mathbf{r}, t)) \cdot \nabla_v \delta F_\alpha \gg \end{aligned} \quad (\text{A.1.7})$$

where $\ll \mathbf{E}(\mathbf{r}, t) \gg = \mathbf{E}_{ext}(\mathbf{r}, t) + \ll \mathbf{E}_m(\mathbf{r}, t) \gg$, and $\ll \mathbf{B}(\mathbf{r}, t) \gg = \mathbf{B}_{ext}(\mathbf{r}, t) + \ll \mathbf{B}_m(\mathbf{r}, t) \gg$. The left side of equation A.1.7 represents collective effects, the right side represents collisional effects. Changing to the standard notations $\ll \mathbf{E}(\mathbf{r}, t) \gg \rightarrow \mathbf{E}(\mathbf{r}, t)$, $\ll \mathbf{B}(\mathbf{r}, t) \gg \rightarrow \mathbf{B}(\mathbf{r}, t)$, and $-\frac{q_\alpha}{m_\alpha} \ll (\delta \mathbf{E}_m(\mathbf{r}, t) + \mathbf{V} \times \delta \mathbf{B}(\mathbf{r}, t)) \cdot \nabla_v \delta F_\alpha \gg \rightarrow \frac{\partial f_\alpha}{\partial t} |_{collisions} = C_\alpha(f)$, we obtain the standard form of the Boltzmann equation:

$$\frac{\partial f_\alpha}{\partial t} + \mathbf{V} \cdot \nabla f_\alpha + \frac{q_\alpha}{m_\alpha} (\mathbf{E}(\mathbf{r}, t) + \mathbf{V} \times \mathbf{B}(\mathbf{r}, t)) \cdot \nabla_v f_\alpha = C_\alpha(f) \quad (\text{A.1.8})$$

Here, $C_\alpha(f)$ is the collision operator, which is not necessarily linear, and generally involves the distribution functions of all the species in the system [66] - for this reason the subscript on the argument of C_α is not included. When collisions are neglected, we have the Vlasov equation:

$$\frac{\partial f_\alpha}{\partial t} + \mathbf{V} \cdot \nabla f_\alpha + \frac{q_\alpha}{m_\alpha} (\mathbf{E}(\mathbf{r}, t) + \mathbf{V} \times \mathbf{B}(\mathbf{r}, t)) \cdot \nabla_v f_\alpha = 0 \quad (\text{A.1.9})$$

A.2 Moments of the distribution function

Each particle in the plasma can be associated with some molecular property $\zeta(\mathbf{r}, \mathbf{V}, t)$, such as the mass, velocity, momentum or energy of the particle. Since $f_\alpha(\mathbf{r}, \mathbf{V}, t) d\mathbf{r} d\mathbf{V}$ is the number of particles of species α in the 6D volume element in phase space, it follows

that the total combined value of ζ for all the particles of type α in the volume element is $\zeta(\mathbf{r}, \mathbf{V}, t) f_\alpha(\mathbf{r}, \mathbf{V}, t) d\mathbf{r} d\mathbf{V}$. Therefore, the total combined value of ζ , irrespective of particle velocity, for all particles of type α in the 3D volume element $d\mathbf{r} = dx dy dz$ in configuration space is $d\mathbf{r} \int \zeta(\mathbf{r}, \mathbf{V}, t) f_\alpha(\mathbf{r}, \mathbf{V}, t) d\mathbf{V}$, where the integral is over all velocity space. The average value of ζ can then be found by dividing this by $n_\alpha(\mathbf{r}, t) d\mathbf{r}$, which is the number of particles of type α in $d\mathbf{r}$ [69]:

$$\langle \zeta(\mathbf{r}, \mathbf{V}, t) \rangle_\alpha = \zeta_{\alpha-\text{ave}}(\mathbf{r}, t) = \frac{1}{n_\alpha(\mathbf{r}, t)} \int \zeta(\mathbf{r}, \mathbf{V}, t) f_\alpha(\mathbf{r}, \mathbf{V}, t) d\mathbf{V} \quad (\text{A.2.1})$$

Considering the cases $\zeta(\mathbf{r}, \mathbf{V}, t) = 1$ and $\zeta(\mathbf{r}, \mathbf{V}, t) = \mathbf{V}$, the first two moments of the distribution function can be defined as follows. The number density [m^{-3}] for species α is defined using the distribution function as

$$n_\alpha(\mathbf{r}, t) = \int f_\alpha(\mathbf{r}, \mathbf{V}, t) d\mathbf{V} \quad (\text{A.2.2})$$

The species fluid velocity is defined as

$$\mathbf{v}_\alpha(\mathbf{r}, t) = \frac{1}{n_\alpha(\mathbf{r}, t)} \int \mathbf{V} f_\alpha d\mathbf{V} \quad (\text{A.2.3})$$

The quantities n_α and $\Gamma_\alpha = n_\alpha \mathbf{v}_\alpha$, are the first two *moments* of the distribution function (0^{th} and 1^{st} order moments). Successive moments are of the form $M_k = \int f \mathbf{V} \mathbf{V} \mathbf{V} \dots \mathbf{V} d\mathbf{V}$, for $k = 2, 3, \dots, \infty$, with k factors of \mathbf{V} - in general, M_k is a tensor of rank k , although it is often contracted to lower rank [66]. For example, the 2^{nd} order moment, describing the flow of momentum in the laboratory frame [67], is the total stress tensor given by

$$\underline{\mathbf{P}}_\alpha(\mathbf{r}, t) = m_\alpha \int \mathbf{V} \mathbf{V} f_\alpha d\mathbf{V} \quad (\text{A.2.4})$$

where m_α is the particle's mass. We define

$$\mathbf{c}_\alpha(\mathbf{r}, t) = \mathbf{V} - \mathbf{v}_\alpha(\mathbf{r}, t) \quad (\text{A.2.5})$$

as the species random particle velocity relative to the species fluid velocity [69]. Note that \mathbf{V} is independent of \mathbf{r} and t . By definition,

$$\int \mathbf{c}_\alpha f_\alpha d\mathbf{V} = \int c_\alpha f_\alpha d\mathbf{V} = 0 \quad (\text{A.2.6})$$

because the statistical average of a random quantity is zero, and, since the average of an averaged value is unchanged:

$$\int \mathbf{v}_\alpha f_\alpha d\mathbf{V} = \mathbf{v}_\alpha \quad (\text{A.2.7})$$

The pressure tensor (2^{nd} order moment in the rest frame of species α) is defined as

$$\underline{\mathbf{p}}_\alpha(\mathbf{r}, t) = m_\alpha \int \mathbf{c}_\alpha \mathbf{c}_\alpha f_\alpha d\mathbf{V} \quad (\text{A.2.8})$$

Scalar pressure is given by the trace of the pressure tensor: $p_\alpha = \frac{1}{3} \text{Tr}(\underline{\mathbf{p}}_\alpha)$. Expressing \mathbf{c}_α in terms of Cartesian coordinates x, y, z as $(c_{\alpha x}, c_{\alpha y}, c_{\alpha z})$, then with the definition $(\underline{\mathbf{p}}_\alpha)_{ij} = m_\alpha \int c_{\alpha i} c_{\alpha j} f_\alpha d\mathbf{V}$, the scalar pressure is:

$$\begin{aligned} p_\alpha &= \frac{1}{3} \left((\underline{\mathbf{p}}_\alpha)_{xx} + (\underline{\mathbf{p}}_\alpha)_{yy} + (\underline{\mathbf{p}}_\alpha)_{zz} \right) = \frac{m_\alpha}{3} \int (c_{\alpha x}^2 + c_{\alpha y}^2 + c_{\alpha z}^2) f_\alpha d\mathbf{V} \\ \Rightarrow p_\alpha &= \frac{m_\alpha}{3} \int c_\alpha^2 f_\alpha d\mathbf{V} \end{aligned} \quad (\text{A.2.9})$$

Substituting equation A.2.5 into equation A.2.4, we have:

$$\begin{aligned} \underline{\mathbf{P}}_\alpha &= m_\alpha \left(\int \mathbf{c}_\alpha \mathbf{c}_\alpha f_\alpha d\mathbf{V} + \int \mathbf{c}_\alpha \mathbf{v}_\alpha f_\alpha d\mathbf{V} + \int \mathbf{v}_\alpha \mathbf{c}_\alpha f_\alpha d\mathbf{V} + \int \mathbf{v}_\alpha \mathbf{v}_\alpha f_\alpha d\mathbf{V} \right) \\ &= m_\alpha \left(\frac{1}{m_\alpha} \underline{\mathbf{p}}_\alpha + \left(\int \mathbf{c}_\alpha f_\alpha d\mathbf{V} \right)^0 \mathbf{v}_\alpha + \mathbf{v}_\alpha \left(\int \mathbf{c}_\alpha f_\alpha d\mathbf{V} \right)^0 + \mathbf{v}_\alpha \mathbf{v}_\alpha n_\alpha \right) \\ &\quad (\text{use eqns. A.2.8, A.2.6, A.2.7, and A.2.2}) \\ \Rightarrow \underline{\mathbf{P}}_\alpha &= \underline{\mathbf{p}}_\alpha + \rho_\alpha \mathbf{v}_\alpha \mathbf{v}_\alpha \end{aligned} \quad (\text{A.2.10})$$

For convenience, $\underline{\mathbf{p}}_\alpha$ can be separated:

$$\underline{\mathbf{p}}_\alpha = p_\alpha \underline{\mathbf{I}} + \bar{\boldsymbol{\pi}}_\alpha \quad (\text{A.2.11})$$

where $\underline{\mathbf{I}}$ is the identity tensor, and $\bar{\boldsymbol{\pi}}$ is the generalised viscosity tensor, which is symmetric and has zero trace [67]. An important contracted 3^{rd} order moment is the energy flux density:

$$\mathbf{Q}'_\alpha(\mathbf{r}, t) = \int \left(\frac{1}{2} m_\alpha V^2 \right) \mathbf{V} f_\alpha d\mathbf{V} \quad (\text{A.2.12})$$

The heat flux density (contracted 3^{rd} order moment in the rest frame of species α), defined as the flux of random (*i.e.*, thermal) energy [69], is:

$$\mathbf{q}_\alpha(\mathbf{r}, t) = \int \left(\frac{1}{2} m_\alpha c_\alpha^2 \right) \mathbf{c}_\alpha f_\alpha d\mathbf{V} \quad (\text{A.2.13})$$

Using equation A.2.5, \mathbf{Q}'_α can be expressed in terms of \mathbf{q}_α :

$$\begin{aligned} \mathbf{Q}'_\alpha &= \frac{1}{2} m_\alpha \int (v_\alpha^2 + 2\mathbf{v}_\alpha \cdot \mathbf{c}_\alpha + c_\alpha^2) (\mathbf{v}_\alpha + \mathbf{c}_\alpha) f_\alpha d\mathbf{V} \\ &= \frac{1}{2} m_\alpha \left(\int v_\alpha^2 \mathbf{v}_\alpha f_\alpha d\mathbf{V} + 2 \int \mathbf{c}_\alpha \cdot (\mathbf{v}_\alpha \mathbf{v}_\alpha) f_\alpha d\mathbf{V} + \int c_\alpha^2 \mathbf{v}_\alpha f_\alpha d\mathbf{V} \right. \\ &\quad \left. + \int v_\alpha^2 \mathbf{c}_\alpha f_\alpha d\mathbf{V} + 2 \int \mathbf{v}_\alpha \cdot (\mathbf{c}_\alpha \mathbf{c}_\alpha) f_\alpha d\mathbf{V} + \int c_\alpha^2 \mathbf{c}_\alpha f_\alpha d\mathbf{V} \right) \\ &= \frac{1}{2} m_\alpha \left[v_\alpha^2 \mathbf{v}_\alpha \left(\int f_\alpha d\mathbf{V} \right) + 2 \left(\int \mathbf{c}_\alpha f_\alpha d\mathbf{V} \right) \cdot \mathbf{v}_\alpha + \left(\int c_\alpha^2 f_\alpha d\mathbf{V} \right) \mathbf{v}_\alpha \right. \\ &\quad \left. + v_\alpha^2 \left(\int \mathbf{c}_\alpha f_\alpha d\mathbf{V} \right) + 2 \mathbf{v}_\alpha \cdot \left(\int \mathbf{c}_\alpha \mathbf{c}_\alpha f_\alpha d\mathbf{V} \right) + \int c_\alpha^2 \mathbf{c}_\alpha f_\alpha d\mathbf{V} \right] \\ &\quad (\text{use eqns. A.2.2, A.2.6, and A.2.7}) \end{aligned}$$

$$\Rightarrow \mathbf{Q}'_\alpha = \frac{1}{2} \rho_\alpha v_\alpha^2 \mathbf{v}_\alpha + \frac{3}{2} p_\alpha \mathbf{v}_\alpha + \mathbf{v}_\alpha \cdot \underline{\mathbf{p}}_\alpha + \mathbf{q}_\alpha \quad (\text{use eqns. A.2.9, A.2.8, \& A.2.13}) \quad (\text{A.2.14})$$

A.3 Moments of the collision operator

At the atomic level, collisions are interactions between the force fields associated with the interacting particles. The collision operator can be split into parts pertaining to elastic *scattering* collisions and *reacting* collisions as $C_\alpha(f) = C_\alpha^{scatt.}(f) + C_\alpha^{react.}(f)$. Electron impact ionization and radiative recombination are examples of inelastic reacting collisions, while resonant charge exchange is an elastic reacting collision [54, 72]. Reacting collisions will be included in a plasma/neutral fluid model in chapter 8. Mass, momentum and energy are conserved and particles are not created or destroyed in elastic scattering collisions.

The Coulomb interaction of charged particles is a long range one characterised by multiple simultaneous interactions. The short range fields (within the electronic shells) of neutral particles result, by contrast, in binary collisions. Because of the long range nature of the Coulomb force, small-angle deflections associated with Coulomb collisions are much more frequent than the large angle deflections associated with binary collisions. The cumulative effect of many small-angle collisions is much larger than that of relatively fewer large-angle collisions [54]. It is possible to deal with multiple collisions by approximating them as a

number of simultaneous binary collisions [69]. Boltzmann's collision operator for neutral gas is:

$$C_{\alpha}^{scatt.}(f) = \sum_{\sigma} C_{\alpha\sigma}^{scatt.}(f_{\alpha}, f_{\sigma}) \quad (\text{A.3.1})$$

Here, $C_{\alpha\sigma}^{scatt.}(f_{\alpha}, f_{\sigma})$, the rate of change of f_{α} due to collisions of species α with species σ , considers only binary collisions and is therefore bilinear because $C_{\alpha\sigma}^{scatt.}$ is a linear function of both its arguments [68, 66]. In plasmas, where long-range Coulomb interactions lead to Debye shielding, a many-body effect, collisions are not strictly binary. However, in a weakly coupled plasma, the departure from bilinearity is logarithmic, and can be neglected to a good approximation since the logarithm is a relatively weakly varying function [67]. The collisional process for the elastic collisions described by $C_{\alpha}^{scatt.}$ conserves particles, momentum and energy at each point [66].

Particle conservation is expressed by:

$$\int C_{\alpha\sigma}^{scatt.} d\mathbf{V} = 0 \quad (\text{A.3.2})$$

In combination with equation A.3.1, this yields

$$\int C_{\alpha}^{scatt.} d\mathbf{V} = 0 \quad (\text{A.3.3})$$

Momentum conservation requires that collisions between different species conserve the total momentum:

$$\int m_{\alpha} C_{\alpha\sigma}^{scatt.} \mathbf{V} d\mathbf{V} = - \int m_{\sigma} C_{\sigma\alpha}^{scatt.} \mathbf{V} d\mathbf{V}$$

The rate of collisional momentum exchange, or the collisional friction force, is defined as

$$\mathbf{R}_{\alpha\sigma} = \int m_{\alpha} C_{\alpha\sigma}^{scatt.} \mathbf{V} d\mathbf{V}$$

so that the total collisional friction force experienced by species α is:

$$\mathbf{R}_{\alpha} = \sum_{\sigma} \mathbf{R}_{\alpha\sigma} = \int m_{\alpha} \sum_{\sigma} C_{\alpha\sigma}^{scatt.} \mathbf{V} d\mathbf{V} = \int m_{\alpha} C_{\alpha}^{scatt.} \mathbf{V} d\mathbf{V} \quad (\text{A.3.4})$$

With these definitions, collisional momentum conservation (the total plasma does not exert a friction on itself) can be re-expressed as [68, 66]:

$$\sum_{\alpha} \mathbf{R}_{\alpha} = 0 \quad (\text{A.3.5})$$

Collisional energy conservation requires that $Q_{L\alpha\sigma} + Q_{L\sigma\alpha} = 0$, where

$Q_{L\alpha\sigma} = \int C_{\alpha\sigma}^{scatt.} \left(\frac{1}{2} m_\alpha V^2 \right) d\mathbf{V}$ is the rate at which species σ transfers energy to species α via collisions. The L subscript is to indicate that the kinetic energy of both species is measured in the same (e.g., Laboratory) frame. $Q_{\alpha\sigma} = \int C_{\alpha\sigma}^{scatt.} \left(\frac{1}{2} m_\alpha c_\alpha^2 \right) d\mathbf{V}$ is the rate at which species σ collisionally transfers energy to species α in the rest frame of species α (the frame moving at \mathbf{v}_α , the fluid velocity of species α) [66, 67]. The total rate of collisional energy transfer to species α in the rest frame of species α is

$$Q_\alpha = \sum_\sigma Q_{\alpha\sigma} \quad (\text{A.3.6})$$

With the relation $\mathbf{c}_\alpha(\mathbf{r}, t) = \mathbf{V} - \mathbf{v}_\alpha(\mathbf{r}, t)$, it can be seen, following the procedure used for the derivation of equations A.2.10 and A.2.14, that

$Q_{L\alpha\sigma} = \int C_{\alpha\sigma}^{scatt.} \left(\frac{1}{2} m_\alpha (\mathbf{c}_\alpha + \mathbf{v}_\alpha)^2 \right) d\mathbf{V} = Q_{\alpha\sigma} + \mathbf{v}_\alpha \cdot \mathbf{R}_{\alpha\sigma}$, so that:

$$\sum_\sigma Q_{L\alpha\sigma} = \int C_\alpha^{scatt.} \left(\frac{1}{2} m_\alpha V^2 \right) d\mathbf{V} = Q_\alpha + \mathbf{v}_\alpha \cdot \mathbf{R}_\alpha \quad (\text{use eqns. A.3.1, A.3.6 and A.3.4}) \quad (\text{A.3.7})$$

With this, collisional energy conservation can be re-expressed as [66]:

$$\begin{aligned} \sum_\sigma (Q_{L\alpha\sigma} + Q_{L\sigma\alpha}) &= 0 \\ \Rightarrow \sum_\alpha (Q_\alpha + \mathbf{v}_\alpha \cdot \mathbf{R}_\alpha) &= 0 \end{aligned} \quad (\text{A.3.8})$$

A.4 Braginskii equations from moments of the Boltzmann equation

Noting that \mathbf{V} is independent of \mathbf{r} (so that $\nabla \cdot (\mathbf{V} f_\alpha) = \mathbf{V} \cdot \nabla f_\alpha$), and that $\mathbf{V} \perp \mathbf{V} \times \mathbf{B}$ (so that $\nabla_v \cdot (\mathbf{V} \times \mathbf{B}(\mathbf{r}, t) f_\alpha) = (\mathbf{V} \times \mathbf{B}(\mathbf{r}, t)) \cdot \nabla_v f_\alpha$), it is convenient to rewrite the Boltzmann equation (equation A.1.8) as:

$$\frac{\partial f_\alpha}{\partial t} + \nabla \cdot (\mathbf{V} f_\alpha) + \nabla_v \cdot \left(\left(\frac{q_\alpha}{m_\alpha} (\mathbf{E}(\mathbf{r}, t) + \mathbf{V} \times \mathbf{B}(\mathbf{r}, t)) \right) f_\alpha \right) = C_\alpha^{scatt.}(f_\alpha) \quad (\text{A.4.1})$$

where only scattering collisions will be considered, *i.e.*, $C_\alpha \rightarrow C_\alpha^{scatt.}$. Taking the 0^{th} , 1^{st} and 2^{nd} moments of the Boltzmann equation we will arrive at the species conservation equations

for mass, momentum and energy. The following identities will be used:

$$\int \nabla_v \cdot \left(\frac{q_\alpha}{m_\alpha} (\mathbf{E}(\mathbf{r}, t) + \mathbf{V} \times \mathbf{B}(\mathbf{r}, t)) f_\alpha \right) d\mathbf{V} = \int \nabla_v \cdot (\mathbf{a}_\alpha f_\alpha) d\mathbf{V} = \int (\mathbf{a}_\alpha f_\alpha) \cdot d\mathbf{S}_v = 0 \quad (\text{A.4.2})$$

(Using Gauss' law, the integral is over a surface in velocity space at $V \rightarrow \infty$.

Since $f_\alpha(\mathbf{r}, \mathbf{V}, t) \rightarrow 0$ as $V \rightarrow \infty$, the integral $\rightarrow 0$)

$$\nabla_v \mathbf{V} = \left(\frac{\partial \mathbf{V}}{\partial \mathbf{V}} \right)_{ij} = \delta_{ij} \quad (\text{A.4.3})$$

A.4.1 0th moment (mass continuity equation)

$$1^{st} \text{ term} : \int \frac{\partial f_\alpha}{\partial t} d\mathbf{V} = \frac{\partial}{\partial t} \left(\int f_\alpha d\mathbf{V} \right) = \frac{\partial n_\alpha}{\partial t} \quad (\text{use eqn. A.2.2})$$

$$2^{nd} \text{ term} : \int \nabla \cdot (\mathbf{V} f_\alpha) d\mathbf{V} = \nabla \cdot \left(\int \mathbf{V} f_\alpha d\mathbf{V} \right) = \nabla \cdot (n_\alpha \mathbf{v}_\alpha) \quad (\text{use eqn. A.2.3})$$

$$3^{rd} \text{ term} : \int \nabla_v \cdot (\mathbf{a}_\alpha f_\alpha) d\mathbf{V} = 0 \quad (\text{use eqn. A.4.2})$$

$$4^{th} \text{ term} : \int C_\alpha^{scatt.} d\mathbf{V} = 0 \quad (\text{use eqn. A.3.3})$$

$$\begin{aligned} & \Rightarrow \frac{\partial n_\alpha(\mathbf{r}, t)}{\partial t} + \nabla \cdot (n_\alpha(\mathbf{r}, t) \mathbf{v}_\alpha(\mathbf{r}, t)) = 0 \\ & \Rightarrow \frac{\partial \rho_\alpha(\mathbf{r}, t)}{\partial t} + \nabla \cdot (\rho_\alpha(\mathbf{r}, t) \mathbf{v}_\alpha(\mathbf{r}, t)) = 0 \quad (\text{use } \rho_\alpha = m_\alpha n_\alpha) \end{aligned} \quad (\text{A.4.4})$$

A.4.2 1st moment (momentum equation)

$$1^{st} \text{ term: } \int \mathbf{V} \frac{\partial f_\alpha}{\partial t} d\mathbf{V} = \frac{\partial}{\partial t} \left(\int \mathbf{V} f_\alpha d\mathbf{V} \right) = \frac{\partial (n_\alpha \mathbf{v}_\alpha)}{\partial t} \quad (\text{using equation A.2.3})$$

2^{nd} term:

$$\int \nabla \cdot (\mathbf{V} f_\alpha) \mathbf{V} d\mathbf{V} = \int \nabla \cdot (\mathbf{V} \mathbf{V} f_\alpha) d\mathbf{V} - \int \mathbf{V} f_\alpha (\nabla \cdot \mathbf{V})^0 d\mathbf{V} = \frac{1}{m_\alpha} \nabla \cdot \underline{\mathbf{P}}_\alpha$$

(note \mathbf{V} is independent of \mathbf{r} , and use equation A.2.4)

3^{rd} term:

$$\begin{aligned} \int \nabla_v \cdot (\mathbf{a}_\alpha f_\alpha) \mathbf{V} d\mathbf{V} &= \int \nabla_v \cdot (\mathbf{a}_\alpha f_\alpha \mathbf{V}) d\mathbf{V} - \int \mathbf{a}_\alpha f_\alpha \cdot (\nabla_v \mathbf{V})^0 d\mathbf{V} \quad (\text{use eqns. A.4.2, A.4.3}) \\ &= -\frac{q_\alpha}{m_\alpha} \left(\mathbf{E} \int f_\alpha d\mathbf{V} + \left(\int \mathbf{V} f_\alpha d\mathbf{V} \right) \times \mathbf{B} \right) \quad (\text{use eqns. A.2.2, A.2.3}) \\ &= -\frac{q_\alpha n_\alpha}{m_\alpha} (\mathbf{E} + \mathbf{v}_\alpha \times \mathbf{B}) \end{aligned}$$

4^{th} term: $\int C_\alpha^{scatt.} \mathbf{V} d\mathbf{V} = \frac{1}{m_\alpha} \mathbf{R}_\alpha$ (using equation A.3.4).

Collecting all four terms, the momentum equation is:

$$\begin{aligned} \frac{\partial(\rho_\alpha \mathbf{v}_\alpha)}{\partial t} + \nabla \cdot \underline{\mathbf{P}}_\alpha - q_\alpha n_\alpha (\mathbf{E} + \mathbf{v}_\alpha \times \mathbf{B}) &= \mathbf{R}_\alpha \\ \Rightarrow \frac{\partial(\rho_\alpha \mathbf{v}_\alpha)}{\partial t} &= -\nabla \cdot \underline{\mathbf{p}}_\alpha - \nabla \cdot (\rho_\alpha \mathbf{v}_\alpha \mathbf{v}_\alpha) + q_\alpha n_\alpha (\mathbf{E} + \mathbf{v}_\alpha \times \mathbf{B}) + \mathbf{R}_\alpha \quad (\text{use eqn. A.2.10}) \end{aligned} \quad (\text{A.4.5})$$

Taking the 2^{nd} term on the right over to the left, the momentum equation can be re-expressed using the following tensor relations:

$$\nabla \cdot (d\underline{\mathbf{T}}) = \nabla d \cdot \underline{\mathbf{T}} + d \nabla \cdot \underline{\mathbf{T}} \quad (\text{A.4.6})$$

$$\nabla \cdot (\mathbf{a} \mathbf{b}) = (\nabla \cdot \mathbf{a}) \mathbf{b} + \mathbf{a} \cdot \nabla \mathbf{b} \quad (\text{A.4.7})$$

$$\begin{aligned}
\frac{\partial(\rho_\alpha \mathbf{v}_\alpha)}{\partial t} + \nabla \cdot (\rho_\alpha \mathbf{v}_\alpha \mathbf{v}_\alpha) &= \rho_\alpha \frac{\partial \mathbf{v}_\alpha}{\partial t} - \mathbf{v}_\alpha \nabla \cdot (\rho_\alpha \mathbf{v}_\alpha) \\
&\quad + \nabla \rho_\alpha \cdot (\mathbf{v}_\alpha \mathbf{v}_\alpha) + \rho_\alpha \nabla \cdot (\mathbf{v}_\alpha \mathbf{v}_\alpha) \quad (\text{use eqns. A.4.4, A.4.6}) \\
&= \rho_\alpha \frac{\partial \mathbf{v}_\alpha}{\partial t} - \cancel{\mathbf{v}_\alpha \rho_\alpha \nabla \cdot \mathbf{v}_\alpha} - \cancel{(\mathbf{v}_\alpha \mathbf{v}_\alpha) \cdot \nabla \rho_\alpha} \\
&\quad + \cancel{\nabla \rho_\alpha \cdot (\mathbf{v}_\alpha \mathbf{v}_\alpha)} + \cancel{\rho_\alpha (\nabla \cdot \mathbf{v}_\alpha) \mathbf{v}_\alpha} + \rho_\alpha (\mathbf{v}_\alpha \cdot \nabla) \mathbf{v}_\alpha \quad (\text{use eqn. A.4.7})
\end{aligned}$$

This is used to re-arrange equation A.4.5 to obtain the final form of the momentum equation:

$$\rho_\alpha \frac{\partial \mathbf{v}_\alpha}{\partial t} + \rho_\alpha (\mathbf{v}_\alpha \cdot \nabla) \mathbf{v}_\alpha = -\nabla \cdot \underline{\mathbf{p}}_\alpha + q_\alpha n_\alpha (\mathbf{E} + \mathbf{v}_\alpha \times \mathbf{B}) + \mathbf{R}_\alpha \quad (\text{A.4.8})$$

$$\Rightarrow \frac{\partial \mathbf{v}_\alpha}{\partial t} = -(\mathbf{v}_\alpha \cdot \nabla) \mathbf{v}_\alpha + \frac{1}{\rho_\alpha} (-\nabla p_\alpha - \nabla \cdot \bar{\mathbf{p}}_\alpha + q_\alpha n_\alpha (\mathbf{E} + \mathbf{v}_\alpha \times \mathbf{B}) + \mathbf{R}_\alpha) \quad (\text{use eqn. A.2.11}) \quad (\text{A.4.9})$$

A.4.3 2nd moment (energy equation)

1st term:

$$\begin{aligned}
\int \left(\frac{1}{2} m_\alpha V^2 \right) \frac{\partial f_\alpha}{\partial t} d\mathbf{V} &= \frac{1}{2} m_\alpha \frac{\partial}{\partial t} \left(\int v_\alpha^2 f_\alpha d\mathbf{V} + 2 \int \mathbf{v}_\alpha \cdot \mathbf{c}_\alpha f_\alpha d\mathbf{V} + \int c_\alpha^2 f_\alpha d\mathbf{V} \right) \quad (\text{use eqn. A.2.5}) \\
&= \frac{1}{2} m_\alpha \frac{\partial}{\partial t} \left(v_\alpha^2 \int f_\alpha d\mathbf{V} + 2 \mathbf{v}_\alpha \cdot \int \mathbf{c}_\alpha f_\alpha d\mathbf{V} + \int c_\alpha^2 f_\alpha d\mathbf{V} \right)^{\frac{3p_\alpha}{m_\alpha}} \\
&\quad (\text{use eqns. A.2.7, A.2.2, A.2.6 and A.2.9}) \\
&= \frac{\partial}{\partial t} \left(\frac{1}{2} \rho_\alpha v_\alpha^2 + \frac{3}{2} p_\alpha \right)
\end{aligned}$$

2nd term:

$$\begin{aligned}
\int \nabla \cdot (\mathbf{V} f_\alpha) \left(\frac{1}{2} m_\alpha V^2 \right) d\mathbf{V} &= \int \nabla \cdot \left(\frac{1}{2} m_\alpha V^2 \mathbf{V} f_\alpha \right) d\mathbf{V} \\
&\quad - \int f_\alpha \mathbf{V} \cdot \nabla \left(\frac{1}{2} m_\alpha V^2 \right) d\mathbf{V} \quad (\mathbf{V} \text{ is independent of } \mathbf{r}) \\
&= \nabla \cdot \int \left(\frac{1}{2} m_\alpha V^2 \mathbf{V} f_\alpha \right) d\mathbf{V} \quad (\mathbf{V} \text{ is independent of } \mathbf{r}) \\
&= \nabla \cdot \mathbf{Q}'_\alpha \quad (\text{use eqn. A.2.12})
\end{aligned}$$

3rd term:

$$\begin{aligned}
\int \nabla_v \cdot (\mathbf{a}_\alpha f_\alpha) \left(\frac{1}{2} m_\alpha V^2 \right) d\mathbf{V} &= \int \nabla_v \cdot \left(\mathbf{a}_\alpha f_\alpha \left(\frac{1}{2} m_\alpha V^2 \right) \right) d\mathbf{V} \quad (\text{use eqn. A.4.2}) \\
&\quad - \int f_\alpha \mathbf{a}_\alpha \cdot \nabla_v \left(\frac{1}{2} m_\alpha V^2 \right) d\mathbf{V} \\
&= - \int f_\alpha \mathbf{a}_\alpha \cdot \frac{\partial}{\partial \mathbf{V}} \left(\frac{1}{2} m_\alpha \mathbf{V} \cdot \mathbf{V} \right) d\mathbf{V} \\
&= - \int f_\alpha \mathbf{a}_\alpha \cdot (m_\alpha \mathbf{I} \cdot \mathbf{V}) d\mathbf{V} \\
&= - q_\alpha \int f_\alpha (\mathbf{E} + \mathbf{V} \times \mathbf{B}) \cdot \mathbf{V} d\mathbf{V} \\
&= - q_\alpha \mathbf{E}(\mathbf{r}, t) \cdot \int f_\alpha \mathbf{V} d\mathbf{V}^{n_\alpha \mathbf{v}_\alpha} \quad (\text{use eqn. A.2.2}) \\
&= - q_\alpha n_\alpha \mathbf{E} \cdot \mathbf{v}_\alpha \quad (\text{A.4.10})
\end{aligned}$$

4th term: $\int C_\alpha^{scatt.} \left(\frac{1}{2} m_\alpha V^2 \right) d\mathbf{V} = Q_\alpha + \mathbf{v}_\alpha \cdot \mathbf{R}_\alpha$ (use equation A.3.7)

$$\begin{aligned}
&\Rightarrow \frac{\partial}{\partial t} \left(\frac{1}{2} \rho_\alpha v_\alpha^2 + \frac{3}{2} p_\alpha \right) + \nabla \cdot \mathbf{Q}'_\alpha - q_\alpha n_\alpha \mathbf{E} \cdot \mathbf{v}_\alpha = Q_\alpha + \mathbf{v}_\alpha \cdot \mathbf{R}_\alpha \\
&\Rightarrow \frac{1}{2} v_\alpha^2 \frac{\partial \rho_\alpha}{\partial t} + \frac{1}{2} \rho_\alpha \frac{\partial (v_\alpha^2)}{\partial t} + \frac{3}{2} \frac{\partial p_\alpha}{\partial t} + \frac{1}{2} \nabla \cdot (\rho_\alpha v_\alpha^2 \mathbf{v}_\alpha) + \frac{3}{2} \nabla \cdot (p_\alpha \mathbf{v}_\alpha) \\
&\quad + \nabla \cdot (\mathbf{v}_\alpha \cdot \underline{\mathbf{p}}_\alpha) + \nabla \cdot \mathbf{q}_\alpha - q_\alpha n_\alpha \mathbf{E} \cdot \mathbf{v}_\alpha = Q_\alpha + \mathbf{v}_\alpha \cdot \mathbf{R}_\alpha \quad (\text{use eqn. A.2.14})
\end{aligned}$$

The first two terms can be rearranged using the mass and momentum conservation equations (A.4.4 & A.4.8):

$$\begin{aligned}
\frac{1}{2}v_\alpha^2 \frac{\partial \rho_\alpha}{\partial t} + \frac{1}{2}\rho_\alpha \frac{\partial(v_\alpha^2)}{\partial t} &= -\frac{1}{2}v_\alpha^2 \nabla \cdot (\rho_\alpha \mathbf{v}_\alpha) + \rho_\alpha v_\alpha \left(\frac{\partial v_\alpha}{\partial t} \right) \\
&= -\frac{1}{2}v_\alpha^2 \nabla \cdot (\rho_\alpha \mathbf{v}_\alpha) + \mathbf{v}_\alpha \cdot \left(\rho_\alpha \frac{\partial \mathbf{v}_\alpha}{\partial t} \right) \\
&= -\frac{1}{2}v_\alpha^2 \nabla \cdot (\rho_\alpha \mathbf{v}_\alpha) + \mathbf{v}_\alpha \cdot \left(-\rho_\alpha (\mathbf{v}_\alpha \cdot \nabla) \mathbf{v}_\alpha - \nabla \cdot \underline{\mathbf{p}}_\alpha \right. \\
&\quad \left. + q_\alpha n_\alpha (\mathbf{E} + \mathbf{v}_\alpha \times \mathbf{B}) + \mathbf{R}_\alpha \right)
\end{aligned}$$

Assemble all four terms:

$$\begin{aligned}
&\Rightarrow -\frac{1}{2}v_\alpha^2 \nabla \cdot (\rho_\alpha \mathbf{v}_\alpha) - \frac{1}{2}\rho_\alpha \mathbf{v}_\alpha \cdot \nabla (v_\alpha^2) - \mathbf{v}_\alpha \cdot (\nabla \cdot \underline{\mathbf{p}}_\alpha) + q_\alpha n_\alpha \mathbf{v}_\alpha \cdot \mathbf{E} + \mathbf{v}_\alpha \cdot \mathbf{R}_\alpha \\
&\quad + \frac{3}{2} \frac{\partial p_\alpha}{\partial t} + \frac{1}{2}v_\alpha^2 \nabla \cdot (\rho_\alpha \mathbf{v}_\alpha) + \frac{1}{2}\rho_\alpha \mathbf{v}_\alpha \cdot \nabla (v_\alpha^2) + \frac{3}{2}p_\alpha \nabla \cdot \mathbf{v}_\alpha + \frac{3}{2}\mathbf{v}_\alpha \cdot \nabla p_\alpha \\
&\quad + \nabla \cdot (\mathbf{v}_\alpha \cdot \underline{\mathbf{p}}_\alpha) + \nabla \cdot \mathbf{q}_\alpha - q_\alpha n_\alpha \mathbf{E} \cdot \mathbf{v}_\alpha = Q_\alpha + \mathbf{v}_\alpha \cdot \mathbf{R}_\alpha
\end{aligned}$$

Using the tensor relationship

$$\nabla \cdot (\mathbf{a} \cdot \underline{\mathbf{T}}) - \mathbf{a} \cdot (\nabla \cdot \underline{\mathbf{T}}) = \underline{\mathbf{T}} : \nabla \mathbf{a} \quad (\text{A.4.11})$$

where the contraction (inner product) of two second order tensors [73] is defined as $\underline{\mathbf{T}} : \underline{\mathbf{U}} = \sum_i \sum_j T_{ij} U_{ij}$ so that $\underline{\mathbf{T}} : \nabla \mathbf{a} = T_{ij} \frac{\partial a_j}{\partial r_i}$, this can be expressed as:

$$\begin{aligned}
&\frac{3}{2} \frac{\partial p_\alpha}{\partial t} + \frac{3}{2} \mathbf{v}_\alpha \cdot \nabla p_\alpha + \frac{3}{2} p_\alpha \nabla \cdot \mathbf{v}_\alpha + \underline{\mathbf{p}}_\alpha : \nabla \mathbf{v}_\alpha + \nabla \cdot \mathbf{q}_\alpha = Q_\alpha \\
&\Rightarrow \frac{3}{2} \frac{\partial p_\alpha}{\partial t} + \frac{3}{2} \mathbf{v}_\alpha \cdot \nabla p_\alpha + \frac{3}{2} p_\alpha \nabla \cdot \mathbf{v}_\alpha + p_\alpha \left(\underline{\mathbf{I}} : \nabla \mathbf{v}_\alpha \right) \nabla \cdot \mathbf{v}_\alpha + \underline{\boldsymbol{\pi}}_\alpha : \nabla \mathbf{v}_\alpha + \nabla \cdot \mathbf{q}_\alpha = Q_\alpha \quad (\text{use eqn. A.2.11}) \\
&\Rightarrow \frac{\partial p_\alpha}{\partial t} = -\mathbf{v}_\alpha \cdot \nabla p_\alpha - \gamma p_\alpha \nabla \cdot \mathbf{v}_\alpha + (\gamma - 1) (-\underline{\boldsymbol{\pi}}_\alpha : \nabla \mathbf{v}_\alpha - \nabla \cdot \mathbf{q}_\alpha + Q_\alpha) \quad (\text{A.4.12})
\end{aligned}$$

Here, $\gamma = \frac{c_p}{c_v}$ is the adiabatic gas constant, where $c_p [\text{J kg}^{-1}\text{K}^{-1}]$ is the specific heat capacity at constant pressure, and $c_v [\text{J kg}^{-1}\text{K}^{-1}]$ is the specific heat capacity at constant volume. $\gamma = \frac{N+2}{N}$, where N is the number of degrees of freedom of the bulk species. For a monatomic gas, $N = 3$, so that $\gamma = \frac{5}{3}$. For a given material, the availability of translational, rotational and intra-molecular exchanges characterise the value of N .

A.5 Chapman-Enskog closures

Lack of closure is an intrinsic property of fluid theory because the evolution equation for each moment involves the next higher order moment, so the system cannot be closed without losing some information. For example, taking the 0^{th} moment of the Boltzmann equation yields the mass conservation equation which involves \mathbf{v}_α , the 1^{st} moment of the distribution function, and taking the 1^{st} moment of the Boltzmann equation yields the momentum conservation equation which requires $\bar{\pi}_\alpha$, the 2^{nd} moment of the distribution function. Truncation closure schemes set higher order moments to zero or describe them in terms of lower order moments, and can be useful to provide insight, but are associated with uncontrolled approximation [67]. Asymptotic schemes work with expansions in terms of some small ordering parameter and have the advantage of providing an estimate of the error associated with the closure, but involve direct interaction with the kinetic equations and so are mathematically demanding [67].

A.5.1 Closures for a neutral gas

The Chapman-Enskog asymptotic closure scheme for a neutral gas dominated by collisions uses the ratio of the mean free path to the characteristic system length scale as the small ordering parameter [67]. The fluid equations for a neutral gas are similar to those derived above for the two-fluid plasma, but without electromagnetic forces as the fluid isn't conducting, and also without friction forces since there is only one species:

$$\begin{aligned}\dot{\rho}_n &= -\nabla \cdot (\rho_n \mathbf{v}_n) \\ \dot{\mathbf{v}}_n &= -\mathbf{v}_n \cdot \nabla \mathbf{v}_n + \frac{1}{\rho_n} (-\nabla p_n - \nabla \cdot \bar{\pi}_n) \\ \dot{p}_n &= -\mathbf{v}_n \cdot \nabla p_n - \gamma p_n \nabla \cdot \mathbf{v}_n + (\gamma - 1) (-\bar{\pi}_n : \nabla \mathbf{v}_n - \nabla \cdot \mathbf{q}_n)\end{aligned}$$

Here, the subscript n implies parameters pertaining to the neutral fluid. The mean free path for a neutral gas is defined by considering that there is, on average, approximately one particle in the volume swept out by another particle over one mean free path:

$$\lambda_{mfp} = \frac{1}{\sqrt{2} n_n \pi d^2} \tag{A.5.1}$$

where d is the particle diameter. Denoting L as the characteristic system length scale, then $\epsilon = \frac{\lambda_{mfp}}{L} \ll 1$, and the distribution function is expanded in orders of ϵ :

$$f(\mathbf{r}, \mathbf{V}, t) = f_0(\mathbf{r}, \mathbf{V}, t) + \epsilon f_1(\mathbf{r}, \mathbf{V}, t) + \epsilon^2 f_2(\mathbf{r}, \mathbf{V}, t) + \dots$$

To zeroth order in ϵ , the Boltzmann equation requires that f_0 is a Maxwellian distribution [67]:

$f_0(\mathbf{r}, \mathbf{V}, t) = n_n(\mathbf{r}, t) \left(\frac{m_n}{2\pi T_n(\mathbf{r}, t)} \right)^{\frac{3}{2}} \exp \left(-\frac{m_n(\mathbf{V} - \mathbf{v}_n(\mathbf{r}, t))^2}{2T_n(\mathbf{r}, t)} \right)$, where T_n [J] is the neutral fluid temperature. In a gas at rest in uniform conditions, the velocity distribution tends towards the Maxwellian distribution. Actually, this would occur very rapidly, in a few collision times [74]. In a flowing gas in a non-uniform state, molecules moving into a neighboring region cause deviations from the Maxwellian distribution. However, if macroscopic gradients are small, it is to be expected that the deviations from the Maxwellian distribution will also be small and that collisions driving the gas towards equilibrium will remain the dominant effect. One interpretation of the principal steps in the Chapman-Enskog method is that the small ordering parameter is introduced into the kinetic equation to give more weight to the collision term, emphasising the strength of the collision-driven drive towards equilibrium [74].

There is no heat flow or viscous stress associated with a Maxwellian distribution function, so \mathbf{q}_n and $\bar{\pi}_n$ depend on the higher order non-Maxwellian corrections to the distribution function [67]. The Boltzmann equation can be linearised (*i.e.*, neglect term of order ϵ^2 and higher) and rearranged into an integral equation for f_1 in terms of f_0 . The equation is integral because the collision operator is an integral one. The equation is solved by expanding f_1 in velocity space using Laguerre (Sonine) polynomials, so that it reduces to an infinite set of simultaneous algebraic equations (which can be truncated) for the coefficients in the expansion. The Laguerre polynomial expansion converges rapidly and it is convenient to keep only the first two terms in the expansion without much loss of accuracy in the solutions for the coefficients that define f_1 [67]. Moments of f_1 are taken to obtain expressions for \mathbf{q}_n and $\bar{\pi}_n$:

$$\mathbf{q}_n = -\kappa_n \nabla T_n \tag{A.5.2}$$

$$(\bar{\pi}_n)_{ij} = -\mu_n \left(\frac{\partial v_{ni}}{\partial r_j} + \frac{\partial v_{nj}}{\partial r_i} - \delta_{ij} \frac{2}{3} \nabla \cdot \mathbf{v}_n \right) \tag{A.5.3}$$

Here, κ_n [$(\text{m}\cdot\text{s})^{-1}$] is the thermal conductivity for the neutral fluid, μ_n [$\text{kg m}^{-1}\text{s}^{-1}$] is the dynamic viscosity, δ_{ij} is the Kronecker delta, and v_{ni} refers to the i^{th} component of \mathbf{v}_n . κ_n and μ_n can be expressed in terms of diffusion coefficients as $\kappa_n = n_n \chi_n$ [m^2/s] and $\mu_n = \rho_n \nu_n$ [m^2/s], where χ_n is the thermal diffusivity and ν_n is the kinematic viscosity. For hard

sphere molecules, these diffusion coefficients, (from Chapman and Cowling [75]) are:

$$\nu_n = \frac{5\sqrt{\pi}}{16} \left(1 + \frac{1}{44} + \dots\right) \nu_{cn} \lambda_{mfp}^2 \approx \frac{5\sqrt{\pi} V_{thn} \lambda_{mfp}}{16} \quad (\text{A.5.4})$$

$$\chi_n = \frac{75\sqrt{\pi}}{64} \left(1 + \frac{3}{202} + \dots\right) \nu_{cn} \lambda_{mfp}^2 \approx \frac{75\sqrt{\pi} V_{thn} \lambda_{mfp}}{64} \quad (\text{A.5.5})$$

Here, the first two terms in the Laguerre polynomial expansion are shown explicitly in the brackets. $\nu_{cn} = \frac{V_{thn}}{\lambda_{mfp}}$ is the neutral-neutral scattering collision frequency where the neutral particle thermal speed is $V_{thn} = \sqrt{\frac{2T_n}{m_n}}$. Viscous and thermal diffusivities for a neutral gas may be interpreted in terms of the random-walk diffusion of molecules with above average momentum and energy, respectively [67]. From classical stochastic theory, if particles move a step length l in a random direction (for ν_n and χ_n , $l = \lambda_{mfp}$, the mean free path for neutral-neutral scattering collisions), with a frequency ν , the motion is associated with a diffusivity of νl^2 . Chapman-Enskog theory enables, for a given force law between molecules, the determination of the constants that precede this classical diffusivity. The constants, as well as the expression for the mean free path, will vary depending on the force law in question [67].

A.5.2 Closures for an unmagnetized collisional plasma

For a plasma, asymptotic closure schemes can be based on one of two possible small parameters. For collisional plasmas, the small parameter has the same form as that for a neutral gas: $\epsilon = \frac{\lambda_{mfp}}{L} \ll 1$, where λ_{mfp} and L are the mean free path and characteristic length scale for the plasma. The ion-ion collision time is

$$\tau_{ii} = \frac{12\pi^{1.5} \epsilon_0^2 \sqrt{m_i} T_i^{1.5}}{\Lambda e^4 n} \quad (\text{A.5.6})$$

and

$$\tau_{ei} = \frac{6\sqrt{2}\pi^{1.5} \epsilon_0^2 \sqrt{m_e} T_e^{1.5}}{\Lambda e^4 n Z_{eff}^2} \quad (\text{A.5.7})$$

is the electron-ion collision time. Collision times are the average times between 90° scattering events. Here, e is the electron charge, Λ is the Coulomb logarithm, ϵ_0 is vacuum permittivity, and T_e , T_i are the electron and ion temperatures in Joules. Note that the collision times increase with temperature - as plasma temperature increases, the cross-section for Coulomb collisions decreases because the distance of closest approach become smaller.

Unmagnetized plasmas are defined by $\omega_{ci}\tau_{ii}$, $\omega_{ce}\tau_{ei} \ll 1$, where $\omega_{c\alpha} = \frac{q_\alpha B}{m_\alpha}$ is the species

cyclotron frequency. The definition implies that, in an unmagnetized plasma, many collisions occur during one gyro-rotation. For collisional, unmagnetized plasma with $Z_{eff} = 1$, the two-Laguerre-polynomial Chapman-Enskog closure scheme gives

$$\mathbf{R}_e = -\mathbf{R}_i = \eta' n e \mathbf{J} - 0.71 n \nabla T_e \quad (\text{A.5.8})$$

$$Q_i = \frac{3m_e}{m_i} \frac{n(T_e - T_i)}{\tau_{ei}} \quad (\text{A.5.9})$$

$$Q_e = -Q_i + \frac{\mathbf{J} \cdot \mathbf{R}_e}{ne} = -Q_i + \eta' J^2 - 0.71 \frac{\mathbf{J} \cdot \nabla T_e}{e} \quad (\text{A.5.10})$$

Here, $\eta' [\Omega - m] = \frac{m_e \nu_{ei}}{1.96 n e^2}$ is the plasma resistivity, where $\nu_{ei} = \frac{1}{\tau_{ei}}$ is the electron-ion collision frequency. Assuming quasineutrality and singly charged ions, (*i.e.*, charge density, $\rho_c = \sum_\alpha n_\alpha q_\alpha = 0$, $q_i = e$, and $q_e = -e$, so that $n_i = n_e = n$), the current density is given by $\mathbf{J} = \sum_\alpha n_\alpha q_\alpha \mathbf{v}_\alpha = ne(\mathbf{v}_i - \mathbf{v}_e)$, so that the first term in the expression for \mathbf{R}_e is $\nu_{ei} \rho_e (\mathbf{v}_i - \mathbf{v}_e)$. In a collision time τ_{ei} , the electrons lose momentum $-m_e(\mathbf{v}_i - \mathbf{v}_e)$ as a result of losing their ordered velocity with respect to that of the ions, so the frictional force on the electrons, which is the rate of change of their momentum due to interaction with the ions, is $\nu_{ei} \rho_e (\mathbf{v}_i - \mathbf{v}_e)$. Since $\eta' \propto \nu_{ei}$ which is inversely proportional to $T_e^{1.5}$, the faster (hotter) electrons in the distribution are the most conductive - current in plasma is carried primarily by fast electrons. This phenomenon gives rise to the thermal force which is the second term in the expression for \mathbf{R}_e [67]. The origin of the thermal force can be clarified as follows. Assuming, for simplicity, that the ion and electron fluids are at rest ($\mathbf{v}_e = \mathbf{v}_i = \mathbf{0}$), then, at any point x_0 (*e.g.*, on the x axis), the flux of electrons directed to the left is balanced by the flux of electrons directed to the right. Due to electron-ion collisions, these fluxes experience frictional forces of order $m_e n V_{the} / \tau_{ei}$, where V_{the} is the electron thermal speed. Since $V_{the} / \tau_{ei} \sim T_e^{-1}$, if electrons coming from the right are hotter on average than those coming from the left, there will be a net force directed to the left, against the electron temperature gradient.

Q_i gives the rate at which energy is imparted from the electrons to the ions due to collisions between the ion and electron fluids. The first term in the expression for Q_e is simply $-Q_i$. The second term on the extreme right is the ohmic heating term, representing the change from ordered electron motion relative to the ions into random motion (heat) due to collisions with the ions. The third term is the work done by the electrons against the thermal force [67].

The closure scheme gives the ion and electron heat flux densities as

$$\begin{aligned}\mathbf{q}_i &= -n\chi_{\parallel i}\nabla T_i \\ \mathbf{q}_e &= -n\chi_{\parallel e}\nabla T_e - 0.71\frac{T_e}{e}\mathbf{J}\end{aligned}\tag{A.5.11}$$

where the ion and electron thermal diffusion coefficients are

$$\begin{aligned}\chi_{\parallel i} &= 3.9\tau_{ii}\frac{T_i}{m_i} \\ \chi_{\parallel e} &= 3.2\tau_{ei}\frac{T_e}{m_e}\end{aligned}\tag{A.5.12}$$

\mathbf{q}_i and the first term in the expression for \mathbf{q}_e are analogous to the corresponding expressions for \mathbf{q}_n (equation A.5.2) (recall $\kappa = n\chi$), while $\chi_{\parallel i}$ and $\chi_{\parallel e}$ can be compared with the neutral conductivity (equation A.5.5). The parallel subscripts on χ_α are included because it turns out that the values of χ_α in the unmagnetized case are the same as the values of $\chi_{\parallel\alpha}$ in the magnetized case (in the magnetized case, the parallel subscripts indicate that the coefficients pertain to thermal diffusion in the direction parallel to \mathbf{B}). As with the closures for a neutral fluid, the ion and electron thermal diffusivities $\chi_{\parallel i}$ and $\chi_{\parallel e}$ represent random-walk heat diffusion, and are given by expressions of the form $\chi = C(\nu l^2) = C(\frac{1}{\nu}V_{th}^2)$, for some constant C , and with $l = \frac{V_{th}}{\nu}$. For example, in equation A.5.12, we have $\chi_{\parallel i} \sim \frac{\tau_{ii}T_i}{m_i} \sim \frac{V_{thi}^2}{\nu_{ii}}$ where $\nu_{ii} = \frac{1}{\tau_{ii}}$ is the ion-ion collision frequency and $V_{thi} = \sqrt{\frac{2T_i}{m_i}}$ is the ion thermal speed. Note that, for $T_i \sim T_e$, that $\frac{\chi_{\parallel e}}{\chi_{\parallel i}} \sim \frac{m_i}{m_e} \frac{\tau_{ei}}{\tau_{ii}} \sim \sqrt{\frac{m_i}{m_e}} \sim 43$, so electron heat diffusivity is much greater than that of the ions in the unmagnetized case, and in the magnetized case, parallel heat diffusivity is much greater for electrons than for ions.

The second term in the expression for \mathbf{q}_e represents additional convection of heat due to relative electron-ion motion. If $\mathbf{v}_{rel} = \mathbf{v}_e - \mathbf{v}_i$, then in the frame moving at \mathbf{v}_e , there are more fast electrons than slow electrons moving in the same direction as \mathbf{v}_{rel} and more slow electrons than fast electrons moving in the opposite direction. Fast electrons carry more energy than slow electrons so additional heat is convected in the direction of \mathbf{v}_{rel} . Since $\mathbf{J} \sim (\mathbf{v}_i - \mathbf{v}_e)$, the additional heat is convected in the direction opposite that of \mathbf{J} .

The ion and electron viscosity tensors have the same form as $\bar{\boldsymbol{\pi}}_n$ (equation A.5.3):

$$(\bar{\boldsymbol{\pi}}_\alpha)_{ij} = -\rho_\alpha\nu_\alpha \left(\frac{\partial v_{\alpha i}}{\partial r_j} + \frac{\partial v_{\alpha j}}{\partial r_i} - \delta_{ij}\frac{2}{3}\nabla \cdot \mathbf{v}_\alpha \right)\tag{A.5.13}$$

where the coefficients of kinematic viscosity (viscous diffusion coefficients) are given as

$$\begin{aligned}\nu_i &= 0.96 \tau_{ii} \frac{T_i}{m_i} \\ \nu_e &= 0.73 \tau_{ei} \frac{T_e}{m_e}\end{aligned}\quad (\text{A.5.14})$$

As with the closure for neutral viscosity, the ion and electron viscous diffusivities ν_i and ν_e represent random-walk diffusion, given by expressions of the form $\nu = C(\nu\lambda^2) = C(\frac{1}{\nu}V_{th}^2)$. It can be seen how, for $T_i \sim T_e$, that $\frac{\mu_i}{\mu_e} = \frac{\rho_i \nu_i}{\rho_e \nu_e} \sim \frac{\tau_{ii}}{\tau_{ei}} \sim \sqrt{\frac{m_i}{m_e}} \sim 43$, so that the viscosity (diffusion of momentum) of a plasma is mostly due to the ions [67].

A.5.3 Closures for a magnetized plasma

Magnetized plasmas are defined by $\omega_{ci}\tau_{ii}, \omega_{ce}\tau_{ei} \gg 1$, which implies that many gyro-rotations occur in one collision time, and that the electron and ion Larmor radii are much smaller than the mean free path [67]. In the magnetized limit, the small ordering parameter is $\epsilon = \frac{r_L}{L} \ll 1$, where $r_L = \frac{V_\perp}{\omega_c}$ is the Larmor radius, where V_\perp is the particle speed perpendicular to \mathbf{B} . The two-Laguerre-polynomial Chapman-Enskog closure scheme gives

$$\mathbf{R}_e = -\mathbf{R}_i = ne(\eta'_\parallel \mathbf{J}_\parallel + \eta'_\perp \mathbf{J}_\perp) - 0.71n\nabla_\parallel T_e - \frac{3n}{2\omega_{ce}\tau_{ei}} \hat{\mathbf{b}} \times \nabla_\perp T_e \quad (\text{A.5.15})$$

$$Q_i = \frac{3m_e}{m_i} \frac{n(T_e - T_i)}{\tau_{ei}} \quad (\text{A.5.16})$$

$$Q_e = -Q_i + \frac{\mathbf{J} \cdot \mathbf{R}_e}{ne} \quad (\text{A.5.17})$$

where $\eta'_\parallel [\Omega - m] = \eta' = \frac{m_e \nu_{ei}}{1.96 ne^2}$ is the plasma resistivity effective parallel to \mathbf{B} , $\eta'_\perp [\Omega - m] = 1.96 \eta'_\parallel$ is the resistivity effective perpendicular to \mathbf{B} , \mathbf{J}_\parallel and \mathbf{J}_\perp are the current densities parallel and perpendicular to \mathbf{B} , and $\hat{\mathbf{b}} = \frac{\mathbf{B}}{B}$. The third and fourth terms in the expression for \mathbf{R}_e constitute the thermal force in the magnetized limit. The MHD model we developed uses the approximation of isotropic resistivity - this was considered a reasonable simplification since $\eta'_\parallel \sim \eta'_\perp$. A further additional simplification is the neglection of last two terms in equation A.5.17, representing work by the electron fluid done against the thermal force. The expressions for the ion and electron viscosity tensors are complicated in the magnetized limit and the details wont be looked here because our MHD model presently also approximates the viscosity as being isotropic.

In the magnetized limit, the ion and electron heat flux densities are given by

$$\mathbf{q}_i = -n\chi_{\parallel i}\nabla_{\parallel}T_i - n\chi_{\perp i}\nabla_{\perp}T_i - (n\chi_{\times i}\hat{\mathbf{b}} \times \nabla_{\perp}T_i) \quad (\text{A.5.18})$$

$$\mathbf{q}_e = -n\chi_{\parallel e}\nabla_{\parallel}T_e - n\chi_{\perp e}\nabla_{\perp}T_e - \left(n\chi_{\times e}\hat{\mathbf{b}} \times \nabla_{\perp}T_e + 0.71\frac{T_e}{e}\mathbf{J}_{\parallel} + \frac{3T_e}{2\omega_{ce}\tau_{ei}e}\hat{\mathbf{b}} \times \mathbf{J}_{\perp}\right) \quad (\text{A.5.19})$$

The 1st and 2nd terms in the expressions for \mathbf{q}_i and \mathbf{q}_e represent diffusive heat transport parallel to and perpendicular to the magnetic field. For simplicity, only these terms are retained in our MHD model. The 3rd terms in the two expressions represent transport that is perpendicular to both the field and to the perpendicular temperature gradients. The 4th and 5th terms in the expression for \mathbf{q}_e correspond to additional convection of heat due to relative electron-ion motion - details can be found in [67]. The Chapman-Enskog scheme gives the ion and electron parallel thermal diffusion coefficients as in equation A.5.12, and the perpendicular thermal diffusion coefficients as

$$\begin{aligned} \chi_{\perp i} &= 2\frac{1}{\tau_{ii}}\frac{T_i}{m_i\omega_{ci}^2} \\ \chi_{\perp e} &= 4.7\frac{1}{\tau_{ei}}\frac{T_e}{m_e\omega_{ce}^2} \end{aligned} \quad (\text{A.5.20})$$

Once again, the perpendicular ion and electron thermal diffusivities $\chi_{\perp i}$ and $\chi_{\perp e}$ represent random-walk heat diffusion, and are given by expressions of the form $\chi = C(\nu l^2)$, for some constant C . Here, the step length l is the Larmor radius: $l_{\alpha} = r_{L\alpha} = \frac{V_{\perp\alpha}}{\omega_{c\alpha}} = \frac{V_{th\alpha}}{\omega_{c\alpha}} = \frac{1}{\omega_{c\alpha}}\sqrt{\frac{2T_{\alpha}}{m_{\alpha}}}$. For example, $\chi_{\perp i} \sim \nu_{ii}r_{Li}^2$, where $\nu_{ii} = \frac{1}{\tau_{ii}}$ is the ion-ion collision frequency and $r_{Li} = \frac{1}{\omega_{ci}}\sqrt{\frac{2T_i}{m_i}}$. Note that, for $T_i \sim T_e$, that $\frac{\chi_{\perp i}}{\chi_{\perp e}} \sim \sqrt{\frac{m_e}{m_i}}\left(\frac{m_i}{m_e}\right)^2\frac{m_e}{m_i} \sim \sqrt{\frac{m_i}{m_e}} \sim 43$, so perpendicular heat diffusivity is much greater for ions than for electrons. Since $\chi \sim \nu l^2 \sim V_{th}l$, the ratios of the parallel to perpendicular thermal diffusion coefficients are given by the ratios of the diffusion random walk step lengths: $\frac{\chi_{\parallel\alpha}}{\chi_{\perp\alpha}} = \frac{\lambda_{mfpa}}{r_{L\alpha}} = \frac{V_{th\alpha}\tau_{\alpha}}{(V_{th\alpha}/\omega_{c\alpha})} = \omega_{c\alpha}\tau_{\alpha}$ (here, $\tau_i \Rightarrow \tau_{ie}$, and $\tau_e \Rightarrow \tau_{ei}$). By definition, plasmas are considered to be magnetized when $\omega_{c\alpha}\tau_{\alpha} \gg 1$, so the parallel thermal diffusion is far higher than perpendicular thermal diffusion. For example, at $T_i = T_e = 100$ eV, $n = 1 \times 10^{20}$ m⁻³, and $B = 1$ T, equations A.5.12 and A.5.20 yield $\chi_{\parallel e} \sim 3 \times 10^8$ m²/s, $\chi_{\parallel i} \sim 6 \times 10^6$ m²/s, $\chi_{\perp i} \sim 1$ m²/s, and $\chi_{\perp e} \sim 0.1$ m²/s.

A.6 Single fluid magnetohydrodynamic equations

The two-fluid equations describe particle motion with the species (ions and electrons) mean velocities \mathbf{v}_{α} , and the pressures $\underline{\mathbf{p}}_{\alpha}$ which describe the random deviation of the particle ve-

locities from the average values [68]. The single fluid MHD equations use single fluid center of mass velocity \mathbf{v} , and current density \mathbf{J} , to describe average motion, where $\mathbf{v} = \frac{1}{\rho} \sum_{\alpha} \rho_{\alpha} \mathbf{v}_{\alpha}$ (with $\rho = \sum_{\alpha} \rho_{\alpha}$), and $\mathbf{J} = \sum_{\alpha} n_{\alpha} q_{\alpha} \mathbf{v}_{\alpha}$.

A.6.1 0th moment (mass continuity equation)

The MHD mass continuity equation can be obtained by summing the two-fluid mass continuity equations (A.4.4) over species:

$$\frac{\partial \rho(\mathbf{r}, t)}{\partial t} + \nabla \cdot (\rho(\mathbf{r}, t) \mathbf{v}(\mathbf{r}, t)) = 0 \quad (\text{A.6.1})$$

A.6.2 1st moment (momentum equation)

Formally, the MHD momentum equation is found by taking the first moment of the Boltzmann equation (A.4.1), multiplying by m_{α} , and summing over species [68]:

$$\sum_{\alpha} \left(m_{\alpha} \int \left[\frac{\partial f_{\alpha}}{\partial t} + \nabla \cdot (\mathbf{V} f_{\alpha}) + \nabla_v \cdot \left(\left(\frac{q_{\alpha}}{m_{\alpha}} (\mathbf{E}(\mathbf{r}, t) + \mathbf{V} \times \mathbf{B}(\mathbf{r}, t)) \right) f_{\alpha} \right) \right] \mathbf{V} d\mathbf{V} \right) = \sum_{\alpha} m_{\alpha} \int C_{\alpha}^{scatt.} \mathbf{V} d\mathbf{V} \quad (\text{A.6.2})$$

The subsequent derivation follows the procedure detailed earlier in the derivation of the expression for two-fluid momentum conservation (equation A.4.9). The 1st term is

$$\sum_{\alpha} \left(m_{\alpha} \int \frac{\partial f_{\alpha}}{\partial t} \mathbf{V} d\mathbf{V} \right) = \frac{\partial}{\partial t} \left(\sum_{\alpha} \left(m_{\alpha} \int f_{\alpha} \mathbf{V} d\mathbf{V} \right) \right) = \frac{\partial}{\partial t} \left(\sum_{\alpha} (m_{\alpha} n_{\alpha} \mathbf{v}_{\alpha}) \right) = \frac{\partial (\rho \mathbf{v})}{\partial t}$$

In particular, the 2nd term is

$$\sum_{\alpha} \left(m_{\alpha} \int \nabla \cdot (\mathbf{V} f_{\alpha}) \mathbf{V} d\mathbf{V} \right) = \sum_{\alpha} \left(m_{\alpha} \nabla \cdot \left(\int \mathbf{V} \mathbf{V} f_{\alpha} d\mathbf{V} \right) - m_{\alpha} \int \mathbf{V} f_{\alpha} \nabla \cdot \mathbf{V} d\mathbf{V} \right) = \nabla \cdot \underline{\mathbf{P}}$$

where $\underline{\mathbf{P}} = \sum_{\alpha} (m_{\alpha} \int \mathbf{V} \mathbf{V} f_{\alpha} d\mathbf{V})$ is the total stress tensor for the single plasma fluid. Instead of defining random particle velocities relative to \mathbf{v}_{α} , as was done in the derivation of the two-fluid momentum equation, random velocities are defined relative to the single fluid velocity

\mathbf{v} :

$$\mathbf{c}_{0\alpha}(\mathbf{r}, t) = \mathbf{V} - \mathbf{v}(\mathbf{r}, t) \quad (\text{A.6.3})$$

Then, through manipulation analogous to that in the derivation of equation A.2.10, $\underline{\mathbf{P}}$ can be expressed as $\underline{\mathbf{P}} = \underline{\mathbf{p}} + \rho \mathbf{v} \mathbf{v}$ [68], where the single fluid pressure tensor is defined as:

$$\underline{\mathbf{p}}(\mathbf{r}, t) = \sum_{\alpha} \left(m_{\alpha} \int \mathbf{c}_{0\alpha} \mathbf{c}_{0\alpha} f_{\alpha} d\mathbf{V} \right)$$

$\underline{\mathbf{p}}$ can be related to $\underline{\mathbf{p}}_{\alpha}$ - firstly the species diffusion velocity is defined as

$$\mathbf{w}_{\alpha}(\mathbf{r}, t) = \mathbf{v}_{\alpha}(\mathbf{r}, t) - \mathbf{v}(\mathbf{r}, t) \quad (\text{A.6.4})$$

Using this definition and equation A.2.5, the species random particle velocities in the frame moving at velocity \mathbf{v} can be expressed as [69]:

$$\mathbf{c}_{0\alpha} = \mathbf{V} - \mathbf{v} = (\mathbf{c}_{\alpha} + \mathbf{v}_{\alpha}) - (\mathbf{v}_{\alpha} - \mathbf{w}_{\alpha}) = \mathbf{c}_{\alpha} + \mathbf{w}_{\alpha} \quad (\text{A.6.5})$$

Note that the average of an averaged value is unchanged:

$$\int \mathbf{w}_{\alpha} f_{\alpha} d\mathbf{V} = \mathbf{w}_{\alpha} \quad (\text{A.6.6})$$

Using these relations, the single fluid pressure tensor can be expressed as:

$$\begin{aligned} \underline{\mathbf{p}}(\mathbf{r}, t) &= \sum_{\alpha} \left(m_{\alpha} \int (\mathbf{c}_{\alpha} + \mathbf{w}_{\alpha})(\mathbf{c}_{\alpha} + \mathbf{w}_{\alpha}) f_{\alpha} d\mathbf{V} \right) && \text{(use eqn. A.6.5)} \\ &= \sum_{\alpha} \left(m_{\alpha} \int (\mathbf{c}_{\alpha} \mathbf{c}_{\alpha} + \mathbf{c}_{\alpha} \mathbf{w}_{\alpha} + \mathbf{w}_{\alpha} \mathbf{c}_{\alpha} + \mathbf{w}_{\alpha} \mathbf{w}_{\alpha}) f_{\alpha} d\mathbf{V} \right) \\ &= \sum_{\alpha} \left(m_{\alpha} \left(\frac{1}{m_{\alpha}} \underline{\mathbf{p}}_{\alpha} + \left(\int \mathbf{c}_{\alpha} f_{\alpha} d\mathbf{V} \right) \mathbf{w}_{\alpha} + \mathbf{w}_{\alpha} \left(\int \mathbf{c}_{\alpha} f_{\alpha} d\mathbf{V} \right) + \mathbf{w}_{\alpha} \mathbf{w}_{\alpha} n_{\alpha} \right) \right) \end{aligned}$$

(use eqns. A.2.8, A.6.6, A.2.6 and A.2.2)

$$\Rightarrow \underline{\mathbf{p}} = \sum_{\alpha} \underline{\mathbf{p}}_{\alpha} + \sum_{\alpha} \rho_{\alpha} \mathbf{w}_{\alpha} \mathbf{w}_{\alpha} \quad (\text{A.6.7})$$

Scalar pressure is given by the trace of the pressure tensor: $p = \frac{1}{3} \text{Tr}(\underline{\mathbf{p}})$ [69]. Expressing $\mathbf{c}_{0\alpha}$ in terms of Cartesian coordinates x, y, z as $(c_{0\alpha x}, c_{0\alpha y}, c_{0\alpha z})$, then with the definition

$(\underline{\mathbf{p}})_{ij} = \sum_{\alpha} \left(m_{\alpha} \int c_{0\alpha i} c_{0\alpha j} f_{\alpha} d\mathbf{V} \right)$, the scalar pressure is:

$$\begin{aligned}
p &= \frac{1}{3} \left((\underline{\mathbf{p}})_{xx} + (\underline{\mathbf{p}})_{yy} + (\underline{\mathbf{p}})_{zz} \right) \\
&= \sum_{\alpha} \left(\frac{m_{\alpha}}{3} \int (c_{0\alpha x}^2 + c_{0\alpha y}^2 + c_{0\alpha z}^2) f_{\alpha} d\mathbf{V} \right) \\
&= \sum_{\alpha} \left(\frac{m_{\alpha}}{3} \int c_{0\alpha}^2 f_{\alpha} d\mathbf{V} \right) \\
&= \sum_{\alpha} \left(\frac{m_{\alpha}}{3} \int (\mathbf{c}_{\alpha} + \mathbf{w}_{\alpha}) \cdot (\mathbf{c}_{\alpha} + \mathbf{w}_{\alpha}) f_{\alpha} d\mathbf{V} \right) \quad (\text{use eqn. A.6.5}) \\
&= \sum_{\alpha} \left(\frac{m_{\alpha}}{3} \int (c_{\alpha}^2 + 2\mathbf{w}_{\alpha} \cdot \mathbf{c}_{\alpha} + w_{\alpha}^2) f_{\alpha} d\mathbf{V} \right) \\
&= \sum_{\alpha} \left(\frac{m_{\alpha}}{3} \left(\int c_{\alpha}^2 f_{\alpha} d\mathbf{V} + 2\mathbf{w}_{\alpha} \cdot \int \mathbf{c}_{\alpha} f_{\alpha} d\mathbf{V} + w_{\alpha}^2 \int f_{\alpha} d\mathbf{V} \right) \right)
\end{aligned}$$

(use eqns. A.2.9, A.6.6, A.2.6 and A.2.2)

$$\Rightarrow p = \sum_{\alpha} p_{\alpha} + \frac{1}{3} \sum_{\alpha} \rho_{\alpha} w_{\alpha}^2 \quad (\text{A.6.8})$$

Analogous to equation A.2.11, we have:

$$\underline{\mathbf{p}}(\mathbf{r}, t) = p(\mathbf{r}, t) \underline{\mathbf{I}} + \bar{\pi}(\mathbf{r}, t) \quad (\text{A.6.9})$$

with $\bar{\pi}$ being the single fluid generalised stress tensor, so starting with equation A.6.7, we can define $\bar{\pi}$ in terms of $\bar{\pi}_{\alpha}$:

$$\begin{aligned}
\underline{\mathbf{p}} &= \sum_{\alpha} \underline{\mathbf{p}}_{\alpha} + \sum_{\alpha} \rho_{\alpha} \mathbf{w}_{\alpha} \mathbf{w}_{\alpha} \\
\Rightarrow p \underline{\mathbf{I}} + \bar{\pi} &= \sum_{\alpha} (p_{\alpha} \underline{\mathbf{I}} + \bar{\pi}_{\alpha} + \rho_{\alpha} \mathbf{w}_{\alpha} \mathbf{w}_{\alpha}) \quad (\text{use eqns. A.6.9 \& A.2.11}) \\
\Rightarrow \sum_{\alpha} p_{\alpha} \underline{\mathbf{I}} + \frac{1}{3} \sum_{\alpha} \rho_{\alpha} w_{\alpha}^2 \underline{\mathbf{I}} + \bar{\pi} &= \sum_{\alpha} (p_{\alpha} \underline{\mathbf{I}} + \bar{\pi}_{\alpha} + \rho_{\alpha} \mathbf{w}_{\alpha} \mathbf{w}_{\alpha}) \quad (\text{use eqn. A.6.8}) \\
\Rightarrow \bar{\pi} &= \sum_{\alpha} \left(\bar{\pi}_{\alpha} + \rho_{\alpha} \left(\mathbf{w}_{\alpha} \mathbf{w}_{\alpha} - \frac{1}{3} w_{\alpha}^2 \underline{\mathbf{I}} \right) \right) \quad (\text{A.6.10})
\end{aligned}$$

The 3rd term in equation A.6.2 is

$$\sum_{\alpha} \left(m_{\alpha} \int \nabla_{\mathbf{v}} \cdot \left(\frac{q_{\alpha}}{m_{\alpha}} (\mathbf{E} + \mathbf{V} \times \mathbf{B}) f_{\alpha} \right) \mathbf{V} d\mathbf{V} \right) = -\sum_{\alpha} (q_{\alpha} n_{\alpha} (\mathbf{E} + \mathbf{v}_{\alpha} \times \mathbf{B})) = -\rho_c \mathbf{E} - \mathbf{J} \times \mathbf{B}$$

where $\rho_c(\mathbf{r}, t) = \sum_{\alpha} q_{\alpha} n_{\alpha}$ is the charge density. The 4th term is

$\sum_{\alpha} \left(m_{\alpha} \int C_{\alpha}^{scatt.} \mathbf{V} d\mathbf{V} \right) = \sum_{\alpha} \mathbf{R}_{\alpha} = 0$ since $\mathbf{R}_i + \mathbf{R}_e = 0$ (equation A.3.5 - the total plasma

does not exert a friction on itself). In the MHD description, the plasma is assumed to be quasineutral because we are interested in plasma behavior at frequencies low compared with the plasma frequency ($\omega \ll \omega_p = \sqrt{\frac{ne^2}{m_e \epsilon_0}}$), and at length scales long compared to the Debye length ($L \gg \lambda_D = \sqrt{\frac{\epsilon_0 k_b T}{ne^2}}$) [76]. Assembling the four terms, in the limit of quasineutrality, the single fluid momentum equation is:

$$\frac{\partial \mathbf{v}}{\partial t} = -(\mathbf{v} \cdot \nabla) \mathbf{v} + \frac{1}{\rho} (-\nabla p - \nabla \cdot \bar{\boldsymbol{\pi}} + \mathbf{J} \times \mathbf{B}) \quad (\text{A.6.11})$$

A.6.3 Ohm's law

The single fluid momentum equation gives one relationship between \mathbf{J} and \mathbf{v} . Another relationship, Ohm's law, can be found starting with the expression for electron momentum conservation (equation A.4.9), which can be written as:

$$\rho_e \frac{d\mathbf{v}_e}{dt} = -\nabla \cdot \underline{\mathbf{p}}_e - e n_e (\mathbf{E} + \mathbf{v}_e \times \mathbf{B}) + \mathbf{R}_e$$

Here, $\frac{d\mathbf{v}_e}{dt} = \frac{\partial \mathbf{v}_e}{\partial t} + \mathbf{v}_e \cdot \nabla \mathbf{v}_e$ is the convective derivative of \mathbf{v}_e , and $e = -q_e$ is the electron charge. Neglecting the thermal force, equation A.5.8 defines the friction force that the ions exert on the electrons as $\mathbf{R}_e = \eta' n e \mathbf{J}$. Along with the assumption of quasineutrality, this implies the electron momentum equation is:

$$m_e \frac{d\mathbf{v}_e}{dt} = -\frac{1}{n} \nabla \cdot \underline{\mathbf{p}}_e - e \mathbf{E} - e \mathbf{v}_e \times \mathbf{B} + \eta' e \mathbf{J}$$

Comparing the magnitudes of the electron inertia and the magnetic force terms, we see that $|m_e \frac{d\mathbf{v}_e}{dt}| / |e \mathbf{v}_e \times \mathbf{B}| = \frac{m_e}{\tau e B} \sim \frac{\omega}{\omega_{ce}}$, where $\omega_{ce} = \frac{eB}{m_e}$ is the electron cyclotron frequency and ω is the frequency of the plasma behaviour that we wish to study. Since MHD is concerned with low frequency phenomena, $\frac{\omega}{\omega_{ce}} \ll 1$, so the electron inertia term can be neglected. It's worth noting that this assumption is good for velocities perpendicular to \mathbf{B} , but not necessarily good for parallel velocities since there are no magnetic forces parallel to \mathbf{B} [68]. The center of mass velocity is $\mathbf{v} = \frac{1}{\rho} \sum_{\alpha} \rho_{\alpha} \mathbf{v}_{\alpha}$, so with $m_e \ll m_i$, $\mathbf{v} \sim \mathbf{v}_i$. Since $\mathbf{J} = n e (\mathbf{v}_i - \mathbf{v}_e)$, this implies that $\mathbf{v}_e \sim -\frac{\mathbf{J}}{n e} + \mathbf{v}$, so the electron momentum equation reduces to:

$$\begin{aligned} 0 &= -\frac{1}{n} \nabla \cdot \underline{\mathbf{p}}_e - e \mathbf{E} - e \left(-\frac{\mathbf{J}}{n e} + \mathbf{v} \right) \times \mathbf{B} + \eta' e \mathbf{J} \\ \Rightarrow 0 &= -\frac{1}{n e} \nabla \cdot \underline{\mathbf{p}}_e - \mathbf{E} + \frac{1}{n e} \mathbf{J} \times \mathbf{B} - \mathbf{v} \times \mathbf{B} + \eta' \mathbf{J} \\ \Rightarrow \mathbf{E} + \mathbf{v} \times \mathbf{B} + \frac{1}{n e} \nabla \cdot \underline{\mathbf{p}}_e - \frac{1}{n e} \mathbf{J} \times \mathbf{B} &= \eta' \mathbf{J} \end{aligned}$$

The term $-\frac{1}{ne}\mathbf{J} \times \mathbf{B}$ is the Hall term. Comparing the magnitudes of the Hall term and the resistive term, we see that $|\frac{1}{ne}\mathbf{J} \times \mathbf{B}| / |\eta'\mathbf{J}| = \frac{eB}{m_e \nu_{ei}} \sim \frac{\omega_{ce}}{\nu_{ei}}$, so the Hall term can be neglected if the electron-ion collision frequency is large compared with the electron cyclotron frequency. Note however, that magnetized plasmas are defined by $\omega_{ci}\tau_{ii}, \omega_{ce}\tau_{ei} \gg 1$. Even when the collision frequency is not large, it is often reasonable to neglect both the Hall term and the pressure tensor term [68, 77], leading to the reduced Ohm's law:

$$\mathbf{E} + \mathbf{v} \times \mathbf{B} = \eta'\mathbf{J} \quad (\text{A.6.12})$$

A.6.4 2nd moment (energy equation)

The MHD energy equation is found by taking the contracted second moment of the Boltzmann equation (A.4.1), and summing over species:

$$\sum_{\alpha} \left(\int \left[\frac{\partial f_{\alpha}}{\partial t} + \nabla \cdot (\mathbf{V} f_{\alpha}) + \nabla_v \cdot \left(\left(\frac{q_{\alpha}}{m_{\alpha}} (\mathbf{E}(\mathbf{r}, t) + \mathbf{V} \times \mathbf{B}(\mathbf{r}, t)) \right) f_{\alpha} \right) \right] \left(\frac{1}{2} m_{\alpha} V^2 \right) d\mathbf{V} \right) = \sum_{\alpha} \int C_{\alpha}^{\text{scatt.}} \frac{1}{2} m_{\alpha} V^2 d\mathbf{V}$$

Again, the subsequent derivation follows the procedure outlined earlier in the derivation of the expression for two-fluid energy conservation (equation A.4.12). However, the 1st term is expanded using random particle velocities relative to \mathbf{v} instead of to \mathbf{v}_{α} , resulting in $\frac{\partial}{\partial t} \left(\frac{1}{2} \rho u^2 + \frac{3}{2} p \right)$, which is then manipulated using the expressions for single fluid mass and momentum conservation (equations A.6.1 and A.6.11), instead of using the two-fluid mass and momentum conservation equations, as was done to derive the two-fluid energy equation. In particular, the 2nd term is

$$\begin{aligned} \sum_{\alpha} \left(\int \nabla \cdot (\mathbf{V} f_{\alpha}) \left(\frac{1}{2} m_{\alpha} V^2 \right) d\mathbf{V} \right) &= \sum_{\alpha} \left(\int \nabla \cdot \left(\frac{1}{2} m_{\alpha} V^2 \mathbf{V} f_{\alpha} \right) d\mathbf{V} - \int f_{\alpha} \mathbf{V} \cdot \nabla \left(\frac{1}{2} m_{\alpha} V^2 \right) d\mathbf{V} \right) \\ &= \nabla \cdot \left(\sum_{\alpha} \int \left(\frac{1}{2} m_{\alpha} V^2 \mathbf{V} f_{\alpha} \right) d\mathbf{V} \right) = \nabla \cdot \mathbf{Q}' \end{aligned}$$

where $\mathbf{Q}'(\mathbf{r}, t) = \sum_{\alpha} \left(\int \left(\frac{1}{2} m_{\alpha} V^2 \right) \mathbf{V} f_{\alpha} d\mathbf{V} \right)$ is the energy flux density for the single plasma fluid. Analogous to equation A.2.14, but using random particle velocities relative to \mathbf{v} instead of to \mathbf{v}_{α} , the energy flux density for the single plasma fluid can be expressed as $\mathbf{Q}' = \frac{1}{2} \rho v^2 \mathbf{v} + \frac{3}{2} p \mathbf{v} + \mathbf{v} \cdot \underline{\mathbf{p}} + \mathbf{q}$, where $\mathbf{q}(\mathbf{r}, t) = \sum_{\alpha} \left(\int \left(\frac{1}{2} m_{\alpha} c_{0\alpha}^2 \right) \mathbf{c}_{0\alpha} f_{\alpha} d\mathbf{V} \right)$ is the heat flux density for the single plasma fluid [69] (flux of random energy, contracted 3rd order moment in the frame moving with the single fluid at velocity \mathbf{v}). Following from equation A.4.10, the 3rd term is $\sum_{\alpha} (-q_{\alpha} n_{\alpha} \mathbf{E} \cdot \mathbf{v}_{\alpha}) = -\mathbf{E} \cdot \mathbf{J}$, since $\mathbf{J} = \sum_{\alpha} (n_{\alpha} q_{\alpha} \mathbf{v}_{\alpha})$. The 4th term vanishes as collisional energy conservation implies that $\sum_{\alpha} \int C_{\alpha}^{\text{scatt.}} \frac{1}{2} m_{\alpha} V^2 d\mathbf{V} = \sum_{\alpha} (Q_{\alpha} + \mathbf{v}_{\alpha} \cdot \mathbf{R}_{\alpha}) = 0$

(equation A.3.8).

Assembling the four terms and simplifying the expression in much the same manner as was done for the derivation of equation A.4.12, the single fluid energy equation is:

$$\frac{\partial p}{\partial t} = -\mathbf{v} \cdot \nabla p - \gamma p \nabla \cdot \mathbf{v} + (\gamma - 1) (-\bar{\pi} : \nabla \mathbf{v} - \nabla \cdot \mathbf{q} + \mathbf{E} \cdot \mathbf{J} - \mathbf{v} \cdot \mathbf{J} \times \mathbf{B})$$

The last two terms can be combined as follows: The reduced Ohm's law (equation A.6.12) gives:

$\mathbf{E} = \eta' \mathbf{J} - \mathbf{v} \times \mathbf{B} \Rightarrow \mathbf{E} \cdot \mathbf{J} = \eta' J^2 - \mathbf{J} \cdot \mathbf{v} \times \mathbf{B} = \eta' J^2 + \mathbf{J} \cdot \mathbf{B} \times \mathbf{v} = \eta' J^2 + \mathbf{v} \cdot \mathbf{J} \times \mathbf{B}$, so that the single fluid energy equation is:

$$\frac{\partial p}{\partial t} = -\mathbf{v} \cdot \nabla p - \gamma p \nabla \cdot \mathbf{v} + (\gamma - 1) (\eta' J^2 - \bar{\pi} : \nabla \mathbf{v} - \nabla \cdot \mathbf{q}) \quad (\text{A.6.13})$$

A.7 Equilibrium models

A.7.1 Grad-Shafranov equation

In cylindrical coordinates with azimuthal symmetry, the divergence of the magnetic field is

$$\nabla \cdot \mathbf{B} = 0 = \frac{1}{r} \frac{\partial (r B_r)}{\partial r} + \frac{\partial B_z}{\partial z} \quad (\text{A.7.1})$$

Poloidal flux through a circular area of radius r in a plane of constant z is defined as $\Psi(r, z)$ [Wb] = $\int_0^r \mathbf{B}_\theta(r, z) \cdot d\mathbf{s}$, where $d\mathbf{s} = ds \hat{\mathbf{z}}$, and $ds = 2\pi r dr$ is an annular elemental area of radius r centered at $(0, z)$. Note that, in cylindrical geometry with azimuthal symmetry, the curl of a toroidal vector has only poloidal components. Hence, using Stokes theorem

$$\Psi(r, z) = \int_0^r \nabla \times \mathbf{A}_\phi(r, z) \cdot d\mathbf{s} = 2\pi r A_\phi(r, z)$$

Defining $\psi = \frac{1}{2\pi} \Psi$ as the poloidal flux per radian in toroidal angle ϕ , this implies that

$$\psi = r A_\phi \quad (\text{A.7.2})$$

The poloidal field is defined as

$$\mathbf{B}_\theta = \nabla \times \mathbf{A}_\phi = -\frac{\partial A_\phi}{\partial z} \hat{\mathbf{r}} + \frac{1}{r} \frac{\partial (r A_\phi)}{\partial r} \hat{\mathbf{z}}$$

Using the definition for ψ , this implies that

$$B_r = -\frac{1}{r} \frac{\partial \psi}{\partial z}, \quad B_z = \frac{1}{r} \frac{\partial \psi}{\partial r} \quad (\text{A.7.3})$$

which satisfies equation A.7.1. In cylindrical coordinates, $\nabla \phi = \hat{\phi}$, so that $\mathbf{B}_\theta = \nabla \times \mathbf{A}_\phi = \nabla \times \frac{\psi}{r} \hat{\phi} = \nabla \times (\psi \nabla \phi) = \nabla \psi \times \nabla \phi$. Using Ampere's law and Stoke's theorem, $\nabla \times \mathbf{B} = \mu_0 \mathbf{J} \Rightarrow 2\pi r B_\phi = \mu_0 I_\theta \Rightarrow B_\phi \hat{\phi} = \frac{\mu_0 I_\theta}{2\pi r} r \nabla \phi$

$$\Rightarrow \mathbf{B}_\phi = \frac{\mu_0 I_\theta}{2\pi} \nabla \phi,$$

where $I_\theta(r, z)$ is the poloidal current linked by a circle of radius r with center on the z -axis at axial location z . Hence, equivalent forms of the general axisymmetric field are:

$$\mathbf{B} = \nabla \psi \times \nabla \phi + f(\psi) \nabla \phi = \frac{1}{2\pi} (\nabla \Psi \times \nabla \phi + \mu_0 I_\theta \nabla \phi), \quad (\text{A.7.4})$$

where

$$f(\psi) = r B_\phi \quad (\text{A.7.5})$$

Here, r is the radius of curvature of \mathbf{B}_ϕ . Note that $\nabla \times \mathbf{B}_\phi = \frac{\mu_0}{2\pi} \nabla \times (I_\theta(r, z) \nabla \phi) = \frac{\mu_0}{2\pi} (\nabla I_\theta \times \nabla \phi)$, a poloidal vector with r and z dependence. Referring to Ampere's law, this implies that

$$\mathbf{J}_\theta = \frac{1}{2\pi} \nabla I_\theta(r, z) \times \nabla \phi \quad (\text{A.7.6})$$

Equivalently, $\mu_0 \mathbf{J}_\theta = \nabla \times \mathbf{B}_\phi = \nabla \times \left(\frac{f(\psi)}{r} \hat{\phi} \right) = \left(-\frac{\partial}{\partial z} \left(\frac{f(\psi)}{r} \right) \right) \hat{r} + \left(\frac{1}{r} \frac{\partial}{\partial r} \left(\frac{r f(\psi)}{r} \right) \right) \hat{z}$, so that

$$J_r = -\frac{1}{\mu_0 r} \frac{\partial f(\psi)}{\partial z}, \quad J_z = \frac{1}{\mu_0 r} \frac{\partial f(\psi)}{\partial r} \quad (\text{A.7.7})$$

The curl of a poloidal vector is toroidal in cylindrical coordinates with azimuthal symmetry, for example $\nabla \times \mathbf{B}_\theta = \hat{\phi} \left(\frac{\partial B_r}{\partial z} - \frac{\partial B_z}{\partial r} \right)$. Together with equation A.7.3, this indicates, as shown in [68], that the magnitude of the curl of the poloidal field is given by a Laplacian-like

operator on ψ .

$$\begin{aligned}
\nabla \times \mathbf{B}_\theta &= |\nabla \times \mathbf{B}_\theta| \hat{\phi} = (\hat{\phi} \cdot \nabla \times \mathbf{B}_\theta) \hat{\phi} \\
&= (r \nabla \phi \cdot \nabla \times \mathbf{B}_\theta) \hat{\phi} \\
&= r \hat{\phi} (\mathbf{B}_\theta \cdot \nabla \times \nabla \phi - \nabla \cdot (\nabla \phi \times \mathbf{B}_\theta)) \\
&= r \hat{\phi} (\nabla \cdot (\mathbf{B}_\theta \times \nabla \phi) = \nabla \cdot ((\nabla \psi \times \nabla \phi) \times \nabla \phi)) \\
&= r \hat{\phi} (\nabla \cdot (-\nabla \psi (\nabla \phi \cdot \nabla \phi) + \nabla \phi (\nabla \phi \cdot \nabla \psi))) \quad (\text{note that } \nabla \phi \perp \nabla \psi) \\
&= -r^2 \nabla \cdot \left(\frac{\nabla \psi}{r^2} \right) \nabla \phi
\end{aligned} \tag{A.7.8}$$

With Ampere's law, this can be expressed as

$$\mathbf{J}_\phi = -\frac{r^2}{\mu_0} \nabla \cdot \left(\frac{\nabla \psi}{r^2} \right) \nabla \phi \tag{A.7.9}$$

The elliptic operator Δ^* is defined as:

$$\begin{aligned}
\Delta^* \psi &= r^2 \nabla \cdot \left(\frac{\nabla \psi(\mathbf{r})}{r^2} \right) = r^2 \left(\nabla \cdot \left(\frac{1}{r^2} \frac{\partial \psi}{\partial r} \hat{\mathbf{r}} + \frac{1}{r^2} \frac{\partial \psi}{\partial z} \hat{\mathbf{z}} \right) \right) \\
&= r^2 \left(\frac{1}{r} \frac{\partial}{\partial r} \left(\frac{1}{r} \frac{\partial \psi}{\partial r} \right) + \frac{\partial}{\partial z} \left(\frac{1}{r^2} \frac{\partial \psi}{\partial z} \right) \right) \\
&= r \frac{\partial}{\partial r} \left(\frac{1}{r} \frac{\partial \psi}{\partial r} \right) + \frac{\partial^2 \psi}{\partial z^2}
\end{aligned} \tag{A.7.10}$$

$$\Rightarrow \mathbf{J}_\phi = -\frac{1}{r \mu_0} \Delta^* \psi \hat{\phi} \tag{A.7.11}$$

In an equilibrium state with no fluid velocity, the expression for single plasma fluid momentum conservation, equation A.6.11, reduces to the force balance equation

$$\mathbf{J} \times \mathbf{B} = \nabla p \tag{A.7.12}$$

which can be expressed as

$$\mathbf{J}_\theta \times \mathbf{B}_\phi + \mathbf{J}_\phi \times \mathbf{B}_\theta + \mathbf{J}_\theta \times \mathbf{B}_\theta = \nabla p \tag{A.7.13}$$

Since poloidal terms can be decomposed to radial and axial terms, $\mathbf{J}_\theta \times \mathbf{B}_\theta$ is toroidally directed and can be finite in non-axisymmetric cases. With axisymmetry, $\frac{\partial p}{\partial \phi} = 0$ so $\mathbf{J}_\theta \times \mathbf{B}_\theta = 0$. Referring to equations A.7.6 and A.7.4, this implies that $\nabla I_\theta \times \nabla \phi \parallel \nabla \psi \times \nabla \phi \Rightarrow \nabla I_\theta \parallel \nabla \psi$. An arbitrary displacement $d\mathbf{r}$ results in changes in current and poloidal flux $dI_\theta = d\mathbf{r} \cdot \nabla I_\theta$ and $d\psi = d\mathbf{r} \cdot \nabla \psi$, so that $\frac{dI_\theta}{d\psi}$ can be expressed as $\frac{dI_\theta}{d\psi} = \frac{d\mathbf{r} \cdot \nabla I_\theta}{d\mathbf{r} \cdot \nabla \psi}$. Since ∇I_θ

is parallel to $\nabla\psi$, the derivative is always defined and can be integrated $\Rightarrow I_\theta = I_\theta(\psi)$, so that $\nabla I_\theta(\psi) = I'_\theta(\psi)\nabla\psi$, where $I'_\theta = \frac{dI_\theta}{d\psi}$ [68]. With this, we can redefine the poloidal current density (equation A.7.6)

$$\mathbf{J}_\theta = \frac{I'_\theta(\psi)}{2\pi} \nabla\psi \times \nabla\phi \quad (\text{A.7.14})$$

Using equations A.7.4, A.7.9 and A.7.14 in equation A.7.13, we obtain

$$\begin{aligned} \nabla p &= \frac{\mu_0 I_\theta I'_\theta(\psi)}{4\pi^2} (\nabla\psi \times \nabla\phi) \times \nabla\phi - \frac{r^2}{\mu_0} \nabla \cdot \left(\frac{\nabla\psi}{r^2} \right) \nabla\phi \times (\nabla\psi \times \nabla\phi) \\ &= ((\nabla\psi \times \nabla\phi) \times \nabla\phi) \left(\frac{\mu_0 I_\theta I'_\theta(\psi)}{4\pi^2} + \frac{r^2}{\mu_0} \nabla \cdot \left(\frac{\nabla\psi}{r^2} \right) \right) \\ &= -\nabla\psi \left(\frac{\mu_0 I_\theta I'_\theta(\psi)}{4\pi^2 r^2} + \frac{1}{\mu_0} \nabla \cdot \left(\frac{\nabla\psi}{r^2} \right) \right) \end{aligned} \quad (\text{A.7.15})$$

Equation A.7.15 shows that $\nabla p \parallel \nabla\psi \Rightarrow p = p(\psi)$ and $\nabla p = p'\nabla\psi$, following the argument above for $I_\theta(\psi)$. With this, the Grad-Shafranov equation can be expressed as

$$\begin{aligned} \nabla \cdot \left(\frac{\nabla\psi}{r^2} \right) + \mu_0^2 \frac{I_\theta I'_\theta(\psi)}{4\pi^2 r^2} + \mu_0 p' &= 0 \\ \Rightarrow \Delta^* \psi &= - \left(\mu_0 r^2 \frac{dp}{d\psi} + \frac{\mu_0^2 I_\theta}{4\pi^2} \frac{dI_\theta}{d\psi} \right) \end{aligned} \quad (\text{A.7.16})$$

Since $I_\theta = \frac{2\pi f(\psi)}{\mu_0}$, $I_\theta I'_\theta = \frac{4\pi^2 f' f}{\mu_0^2}$, leading to the more usual form of the Grad-Shafranov equation:

$$\Delta^* \psi = - \left(\mu_0 r^2 \frac{dp}{d\psi} + f \frac{df}{d\psi} \right) \quad (\text{A.7.17})$$

For convenience, the expressions for the magnetic field and current density components (equations A.7.3, A.7.5 A.7.7, and A.7.11) in the case with toroidal symmetry are reproduced here:

$$\begin{aligned} B_r &= -\frac{1}{r} \frac{\partial\psi}{\partial z} & B_\phi &= \frac{f(\psi)}{r} & B_z &= \frac{1}{r} \frac{\partial\psi}{\partial r} \\ J_r &= -\frac{1}{\mu_0 r} \frac{\partial f(\psi)}{\partial z} & J_\phi &= -\frac{1}{\mu_0 r} \Delta^* \psi & J_z &= \frac{1}{\mu_0 r} \frac{\partial f(\psi)}{\partial r} \end{aligned} \quad (\text{A.7.18})$$

A.7.2 Grad-Shafranov equation for case with linear $\lambda(\psi)$ profile

In equilibrium, when \mathbf{J} is parallel to \mathbf{B} , the magnetic field topology is described by equation 1.3.1: $\nabla \times \mathbf{B} = \lambda \mathbf{B}$. Taking the divergence gives $\mathbf{B} \cdot \nabla\lambda = 0$. Referring to equation A.7.4, this implies that $(\nabla\Psi \times \nabla\phi + \mu_0 I_\theta \nabla\phi) \cdot \nabla\lambda = (\nabla\Psi \times \nabla\phi) \cdot \nabla\lambda + \mu_0 I_\theta \nabla\phi \cdot \nabla\lambda = 0$. All

quantities, including λ , are symmetric in ϕ , so $\nabla\phi \cdot \nabla\lambda = 0$. $\nabla\Psi \times \nabla\phi$ is perpendicular to $\nabla\Psi$, so it is parallel to a flux surface. This implies that $\nabla\lambda$ is perpendicular to flux surfaces, so that $\lambda = \lambda(\psi)$, with the consequence that general axisymmetric force free states must have λ constant on a flux surface. Unlike the Taylor state, in which fields satisfy $\nabla \times \mathbf{B} = \lambda \mathbf{B}$ with constant λ , λ can vary across flux surfaces in general axisymmetric force free states. A simple model for the dependence of λ on ψ is to assume a linear profile [6, 78]:

$$\lambda(\psi) = \lambda_0 + m\psi \quad (\text{A.7.19})$$

where

$$m = \tan \theta = (\lambda(\psi_{max}) - \lambda_0)/\psi_{max} \quad (\text{A.7.20})$$

is the slope of the $\lambda(\psi)$ profile, and λ_0 is the value of λ where $\psi = 0$, as shown in figure A.7.1(c).

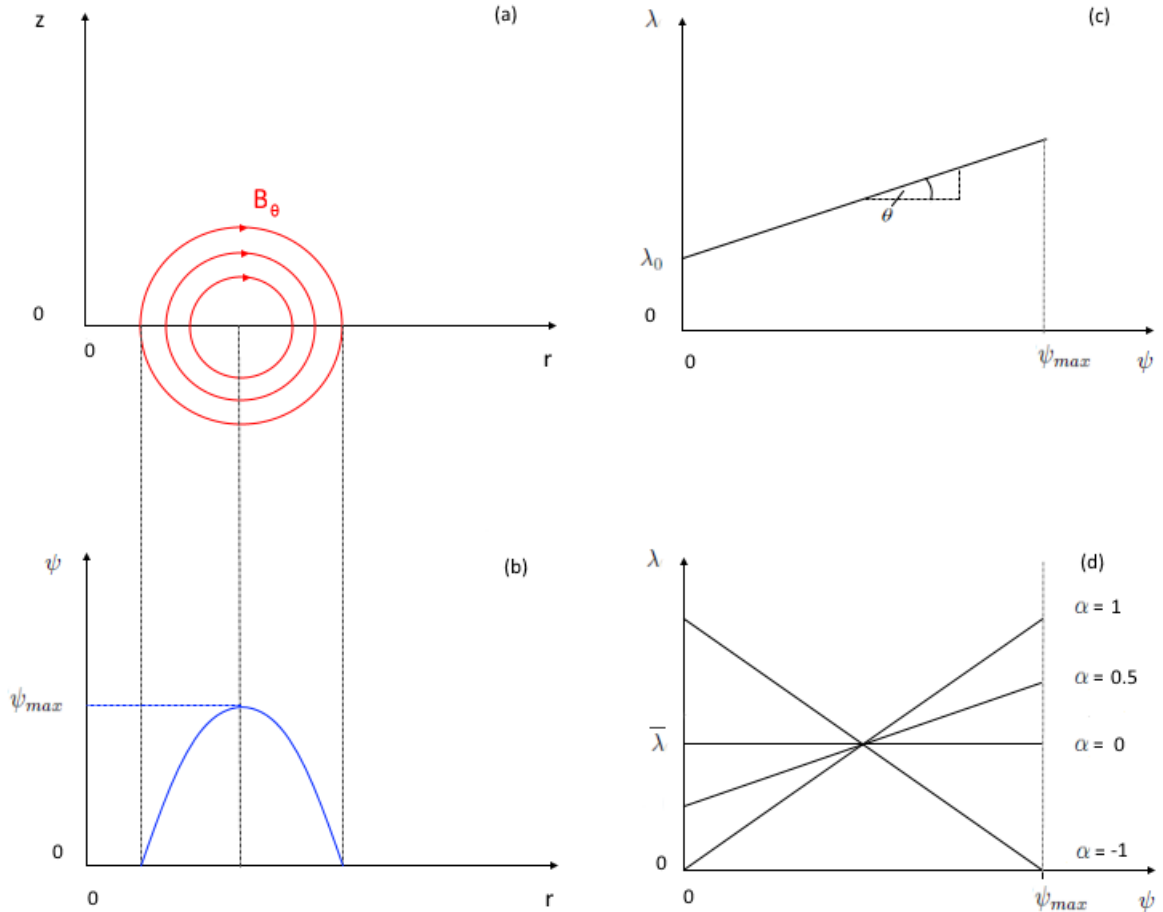


Figure A.7.1: Linear $\lambda(\psi)$ profile

The average value of λ is

$$\bar{\lambda} = \frac{\lambda(\psi_{max}) - \lambda_0}{2} + \lambda_0 \quad (\text{A.7.21})$$

Equations A.7.20 and A.7.21 imply that

$$\bar{\lambda} = \frac{m\psi_{max}}{2} + \lambda_0 \quad (\text{A.7.22})$$

Defining

$$\lambda_0 = \bar{\lambda}(1 - \alpha) \quad (\text{A.7.23})$$

with $-1 \leq \alpha \leq 1$ so that $0 \leq \lambda_0 \leq 2\bar{\lambda}$, equation A.7.22 implies that

$$\bar{\lambda} = \frac{m\psi_{max}}{2} + \bar{\lambda} - \bar{\lambda}\alpha \Rightarrow m = \frac{2\bar{\lambda}\alpha}{\psi_{max}} \quad (\text{A.7.24})$$

Using equations A.7.23 and A.7.24 in equation A.7.19 implies that

$$\begin{aligned} \lambda(\psi) &= \bar{\lambda} - \bar{\lambda}\alpha + 2\bar{\lambda}\alpha\tilde{\psi} \\ \Rightarrow \lambda(\psi) &= \bar{\lambda}(1 + \alpha(2\tilde{\psi} - 1)) \end{aligned} \quad (\text{A.7.25})$$

where ψ has been normalized: $\tilde{\psi} = \frac{\psi}{\psi_{max}}$. From equations A.7.4 and A.7.14 it can be seen that $\frac{J_\theta}{B_\theta} = \frac{1}{2\pi} I'_\theta$. The force free equation $\nabla \times \mathbf{B} = \lambda \mathbf{B} \Rightarrow \mu_0 J_\theta = \lambda B_\theta$, so that:

$$\begin{aligned} \mu_0 \frac{J_\theta}{B_\theta} &= \lambda \\ \Rightarrow \mu_0 \frac{dI_\theta}{d\psi} &= 2\pi \bar{\lambda}(1 + \alpha(2\tilde{\psi} - 1)) \end{aligned} \quad (\text{A.7.26})$$

This can be integrated to give $I_\theta(\psi)$:

$$\begin{aligned} I_\theta &= 2\pi \frac{\bar{\lambda}}{\mu_0} \int (1 + \alpha(2\tilde{\psi} - 1)) d\psi \\ &= 2\pi \frac{\bar{\lambda}}{\mu_0} \left(\psi + \frac{\alpha\psi^2}{\psi_{max}} - \alpha\psi \right) + C \\ \Rightarrow \mu_0 I_\theta(\psi) &= 2\pi \bar{\lambda}\psi(1 + \alpha(\tilde{\psi} - 1)) \end{aligned} \quad (\text{A.7.27})$$

Note that with the boundary condition $I_\theta(\psi = 0) = 0$, C , the constant of integration, is zero. Inserting equations A.7.26 and A.7.27 in equation A.7.16, gives an expression for the Grad-Shafranov equation with a linear dependence of λ on ψ :

$$\Delta^* \psi = - \left(\mu_0 r^2 \frac{dp}{d\psi} + \bar{\lambda}^2 \psi(1 + \alpha(2\tilde{\psi} - 1))(1 + \alpha(\tilde{\psi} - 1)) \right) \quad (\text{A.7.28})$$

As indicated in figure A.7.1(d), the slope of the linear $\lambda(\psi)$ profile is determined by α . Equilibria with $\alpha < 0$ tend to have "hollow" current profiles, where $\lambda \sim J/B$ decreases towards the magnetic axis, so that most of the current flows near the exterior of the magnetically confined plasma, while "peaked" current profiles, where current flows mainly around the center of the plasma, are associated with $\alpha > 0$. In studies of spheromak formation on the CTX magnetized Marshall gun [78], it was found that $\alpha < 0$ during CT formation and $\alpha < 0$ after formation, during the CT decay phase. This is consistent with the concept that helicity flows in the direction of decreasing λ [6]. During formation, helicity is injected into the CT, and when the CT is decaying, helicity flows outwards from the magnetic axis towards the wall.

A.8 Summary

It has been shown how the MHD equations are derived using basic principles of kinetic theory. The techniques outlined, and equations obtained in this chapter, will be referred to in chapter 8, where the set of equations that describes co-interacting plasma and neutral fluids will be developed. The single-fluid MHD equations (equations A.6.1, A.6.11, and A.6.13), and equations defining the time-rates of change of the magnetic field with toroidal symmetry (equations 5.5.3 and 5.5.10), which are solved in the MHD code, are collected here:

$$\dot{\rho} = -\nabla \cdot (\rho \mathbf{v}) \quad (\text{A.8.1})$$

$$\dot{\mathbf{v}} = -\mathbf{v} \cdot \nabla \mathbf{v} + \frac{1}{\rho} (-\nabla p - \nabla \cdot \bar{\boldsymbol{\pi}} + \mathbf{J} \times \mathbf{B}) \quad (\text{A.8.2})$$

$$\dot{p} = -\mathbf{v} \cdot \nabla p - \gamma p \nabla \cdot \mathbf{v} + (\gamma - 1) (\eta' J^2 - \bar{\boldsymbol{\pi}} : \nabla \mathbf{v} - \nabla \cdot \mathbf{q}) \quad (\text{A.8.3})$$

The code has option of evolving separate energy equations for the ion and electron fluids. If this option is chosen, then noting that total plasma fluid pressure is $p = p_i + p_e$, where $p_i = nT_i$, and $p_e = Z_{eff}nT_e$, and that $\mathbf{q} = \mathbf{q}_i + \mathbf{q}_e$, equation A.8.3 is partitioned as

$$\dot{p}_i = -\mathbf{v} \cdot \nabla p_i - \gamma p_i \nabla \cdot \mathbf{v} + (\gamma - 1) (-\bar{\boldsymbol{\pi}} : \nabla \mathbf{v} - \nabla \cdot \mathbf{q}_i + Q_{ie}) \quad (\text{A.8.4})$$

$$\dot{p}_e = -\mathbf{v} \cdot \nabla p_e - \gamma p_e \nabla \cdot \mathbf{v} + (\gamma - 1) (\eta' J^2 - \nabla \cdot \mathbf{q}_e - Q_{ie}) \quad (\text{A.8.5})$$

Consistent with the model simplifications outlined in section A.5.3,

$$\mathbf{q}_\alpha = -n_\alpha \chi_{\parallel\alpha} \nabla_{\parallel} T_\alpha - n_\alpha \chi_{\perp\alpha} \nabla_{\perp} T_\alpha \quad (\text{A.8.6})$$

and

$$Q_{ie} = -Q_{ei} + \eta' J^2 = \frac{3m_e Z_{eff} n(T_e - T_i)}{m_i \tau_{ei}} \quad (\text{A.8.7})$$

Note that the expressions presented in section A.5 were developed with the assumption that $Z_{eff} = 1$. The dependence of \mathbf{q}_α (recall that $n_e = Z_{eff} n$) and Q_{ie} on Z_{eff} has been reintroduced here. Recall that $Q_\alpha = \sum_\sigma Q_{\alpha\sigma}$ (equation A.3.6), and $Q_{\alpha\alpha} = 0$, so that in equations A.5.16 and A.5.17, which are expressed in the context of a two fluid system (ion and electron fluids), $Q_i \equiv Q_{ie}$, and $Q_e \equiv Q_{ei}$. As mentioned, the MHD model we developed neglects the terms in the expression for Q_{ei} (equation A.5.17) that represent work done by the electron fluid against the thermal force. Also, the model approximates resistivity and viscosity as being isotropic - only the anisotropy pertaining to thermal diffusion is included. The viscous heating term has been dropped from the electron energy equation because the magnitudes of species viscous tensor components $(\bar{\pi}_\alpha)_{ij}$ (equation B.3.7) are proportional to $\mu_\alpha = \rho_\alpha \nu_\alpha$. Since $n_i \sim n_e$, $T_i \sim T_e$ (recall ν_α scales with T_α), and $m_e \ll m_i$, it is reasonable to drop this term.

The Grad-Shafranov equation describes MHD equilibrium in the case with toroidal symmetry:

$$\Delta^* \psi = - \left(\mu_0 r^2 \frac{dp}{d\psi} + f \frac{df}{d\psi} \right)$$

As shown in section A.7.2, a simple model assuming a linear dependence of λ on ψ leads to:

$$\Delta^* \psi = - \left(\mu_0 r^2 \frac{dp}{d\psi} + \bar{\lambda}^2 \psi (1 + \alpha(2\tilde{\psi} - 1))(1 + \alpha(\tilde{\psi} - 1)) \right)$$

The numerical method implemented to code to solve the Grad-Shafranov equation, using the discrete form of the Δ^* operator (section 5.4.3), is presented in appendix C.4. Example solutions are presented in appendices C.4 and C.5.2.

Appendix B

Formulation of discretized MHD equations for energy conservation

B.1 Overview

The total energy of any physical system is conserved if there are no sources or sinks of energy into or out of the system. Energy can be distributed between components of the system, and can be converted from one type of energy to another type, but the total energy will remain constant if the system is a completely isolated one. In a plasma system, the energy is composed of kinetic energy, thermal energy and magnetic energy (in this discussion, internal energy due to excited states, electron energy converted to potential energy in ionization processes, and photon energy lost during radiative recombination reactions, is ignored). Moving charged particles constitute kinetic energy, and relative motion between the ion and electron fluids constitute currents, which cause the magnetic fields associated with magnetic energy. The frictional force between ions and electrons leads to resistive (ohmic) heating, and tends to reduce the relative motion between the ion and electron fluids, so that currents are resistively dissipated. The resistive contribution to the reduction of the system's magnetic energy is balanced by the increase in thermal energy due to ohmic heating. Kinetic energy is dissipated by viscous forces between particles of the same species, which leads to viscous heating. The viscous contribution to the reduction of the system's kinetic energy is balanced by an increase in thermal energy due to viscous heating. In general, total energy in a real system, for example a plasma contained within a vacuum vessel, is *not* conserved because heat is lost from the system by thermal conduction through the vessel walls, and there is a radiative flux of electromagnetic energy out of the system. However, energy loss due to thermal and

Poynting fluxes through the system boundary can be eliminated in the physical system if the vessel wall is perfectly thermally insulating and perfectly electrically conducting.

In this appendix, a discrete form of the momentum equation is developed which, on account of the inherent properties of the discrete differential matrix operators, ensures that total energy of the system described by the complete set of discretised MHD equations, in cylindrical geometry with azimuthal symmetry, is conserved with appropriate boundary conditions. In the process of developing the discrete form of the momentum equation, discrete forms of the continuity and energy equations, and expressions defining the evolution of the axisymmetric magnetic field, will be defined. Note that the forms of the element-to-node differential operators (section 5.4.2) were unknown at the time of development of the discrete momentum equation for system energy conservation. At that time, only the node-to-element and node-to-node operators were defined - the process outlined in this section helped to define the element-to-node operators and their properties. The rate of change of total system energy can be expressed in discretized form in terms of the discrete differential operators and the discretised fields quantities. Leaving the discrete forms for \dot{v}_β as the unknowns to be solved for, discretised expressions for $\dot{\rho}$, \dot{p} , $\dot{\psi}$ and \dot{f} will be substituted in the discrete form of equation 5.5.27, which is repeated here for convenience:

$$\dot{U}_{Total} = \dot{U}_K + \dot{U}_{Th} + \dot{U}_M = \int \left[\left(\frac{1}{2} \dot{\rho} v^2 + \rho \mathbf{v} \cdot \dot{\mathbf{v}} \right) + \frac{\dot{p}}{\gamma - 1} + \frac{1}{2\mu_0} \left(\frac{\partial}{\partial t} \left(\left(\frac{\nabla \psi}{r} \right)^2 + \left(\frac{f}{r} \right)^2 \right) \right) \right] dV$$

The thermal diffusion term is temporarily dropped from the expression for \dot{p} , but will be re-included later. It will turn out that we will be able to transmute the terms in the resultant discrete expression for \dot{U}_{Total} as the sum of three collections of terms that are coefficients of the three velocity components. The form of the expression will be:

$$\dot{U}_{Total} = \underline{dV}^T * \left\{ \Sigma_\beta \left(\underline{\rho} \circ \left(\underline{\dot{v}_\beta} + \underline{X_{1\beta}} + \underline{X_{2\beta}} + \dots + \underline{X_{n\beta}} \right) \right) \right\} = 0 \quad (B.1.1)$$

The n quantities $\underline{X_{j\beta}}$ [$N_n \times 1$] are complex expressions involving various physical parameters and mesh-based fields. n will have the same value for the r and z coordinates, but on account of the assumption of axisymmetry, $n\phi < nr = nz$. The identity expressed in equation B.1.1 can hold only if, for each coordinate β , either $\dot{v}_\beta = 0$ at every node (a useless solution), or if $\left(\underline{\rho} \circ \underline{\dot{v}_\beta} + \underline{X_{1\beta}} + \underline{X_{2\beta}} + \dots + \underline{X_{n\beta}} \right) = 0$, for each coordinate β . The latter expressions lead to discrete forms, that ensure total system energy conservation, for the three components of the momentum equation:

$$\underline{\dot{v}_\beta} = - \left(\underline{X_{1\beta}} + \underline{X_{2\beta}} + \dots + \underline{X_{n\beta}} \right) \oslash \underline{\rho} \quad (B.1.2)$$

Naturally, the resultant expressions will be the discrete analogs of the continuous form of the momentum equation components. Various transpose identities, and some of the inherent properties of the discrete differential operators, will be used in the rearrangement of equation

5.5.27 in terms of discrete quantities. Along with the matrix transpose operation defined with equation 5.3.5, note that the following relationships hold for any column vectors \underline{a} , \underline{b} , and \underline{c} , with dimensions $N_n \times 1$, where $\underline{\underline{A}} [N_n \times N_n]$ is a diagonal array with its main diagonal composed of the elements of \underline{a} :

$$\underline{a}^T * (\underline{b} \circ \underline{c}) = \underline{b}^T * \underline{\underline{A}} * \underline{c} = \underline{c}^T * \underline{\underline{A}} * \underline{b} \quad (\text{B.1.3})$$

$$\underline{a}^T * \underline{b} = \underline{c}^T * (\underline{a} \circ \underline{b} \oslash \underline{c}) \quad (\text{B.1.4})$$

This appendix is arranged as follows. A discrete expression for \dot{U}_K , the rate of change of system kinetic energy, is derived in section B.2. A discrete form of the expression for \dot{U}_{Th} , the rate of change of system thermal energy, is derived in section B.3. The focus of section B.3.1 is the part of \dot{U}_{Th} that is due to viscosity, leading to discrete forms of the viscous terms in the energy and momentum equations. A discrete form of the expression for \dot{U}_M , the rate of change of system magnetic energy, is derived in section B.4, along with the discrete form of the ohmic heating term in the energy equation, and discrete forms of the expressions for $\dot{\psi}$ and \dot{f} . The discrete form of \dot{U}_{Total} (*i.e.*, equation B.1.1) is assembled to yield the discrete forms of the components of the momentum equation in section B.5. Finally, the complete set of discretised equations for the axisymmetric MHD model, in a form that ensures conservation of total system energy, are collected in appendix summary B.6.

B.2 Kinetic Energy

The rate of change of system kinetic energy can be expressed as

$$\dot{U}_K = \int \left(\frac{1}{2} \dot{\rho} v^2 + \rho \mathbf{v} \cdot \dot{\mathbf{v}} \right) dV \quad (\text{B.2.1})$$

In discretised form, this is:

$$\dot{U}_K = \underline{dV}^T * \left\{ \frac{1}{2} \dot{\rho} \circ \underline{v}^2 + \underline{\rho} \circ \underline{\frac{v_r}{2}} \circ \dot{\underline{v}_r} + \underline{\rho} \circ \underline{\frac{v_\phi}{3}} \circ \dot{\underline{v}_\phi} + \underline{\rho} \circ \underline{\frac{v_z}{4}} \circ \dot{\underline{v}_z} \right\} \quad (\text{B.2.2})$$

From equation 5.5.13, the discrete form of the mass continuity equation is

$$\dot{\rho} = -\underline{\nabla} \cdot (\underline{\rho} \circ \underline{\mathbf{v}}) \quad (\text{B.2.3})$$

Hence, the first term in equation B.2.2, a scalar expression, is:

$$\dot{U}_K = \underline{dV}^T * \left\{ -\frac{1}{2} \left(\underline{\underline{D}r} * \left(\underline{r} \circ \underline{\rho} \circ \underline{v}_r \right) \right) \circ \underline{v}^2 \otimes \underline{r} - \frac{1}{2} \left(\underline{\underline{D}z} * \left(\underline{r} \circ \underline{\rho} \circ \underline{v}_z \right) \right) \circ \underline{v}^2 \otimes \underline{r} \right\} \quad (\text{B.2.4})$$

The first term here is:

$$\begin{aligned} \dot{U}_K &= \frac{2\pi}{3} (\underline{s} \circ \underline{r})^T * \left\{ -\frac{1}{2} \left(\underline{\underline{D}r} * \left(\underline{r} \circ \underline{\rho} \circ \underline{v}_r \right) \right) \circ \underline{v}^2 \otimes \underline{r} \right\} \\ &= -\frac{\pi}{3} \underline{s}^T * \left\{ \left(\underline{\underline{D}r} * \left(\underline{r} \circ \underline{\rho} \circ \underline{v}_r \right) \right) \circ \underline{v}^2 \right\} \\ &= -\frac{\pi}{3} (\underline{v}^2)^T * \left\{ \underline{\underline{S}} * \underline{\underline{D}r} * \left(\underline{r} \circ \underline{\rho} \circ \underline{v}_r \right) \right\} \quad (\text{use eqn. B.1.3}) \\ &= -\frac{\pi}{3} \left(\underline{r} \circ \underline{\rho} \circ \underline{v}_r \right)^T * \underline{\underline{D}r}^T * \underline{\underline{S}}^T * \underline{v}^2 \quad (\text{transpose the scalar}) \end{aligned}$$

The node-to-node differential operators have the property (equations 5.4.35 and 5.4.36) that

$$(\underline{\underline{S}} * \underline{\underline{D}r} + \underline{\underline{D}r}^T * \underline{\underline{S}})_{int} = (\underline{\underline{S}} * \underline{\underline{D}z} + \underline{\underline{D}z}^T * \underline{\underline{S}})_{int} = 0 \quad (\text{B.2.5})$$

where $\underline{\underline{S}}^T = \underline{\underline{S}}$. Since we will set $v_r = 0$ on the boundary nodes, we can use the property to re-express \dot{U}_K :

$$\begin{aligned} \dot{U}_K &= +\frac{\pi}{3} \left(\underline{r} \circ \underline{\rho} \circ \underline{v}_r \right)^T * \underline{\underline{S}} * \underline{\underline{D}r} * \underline{v}^2 \quad (\text{use eqn. B.2.5}) \\ &= \frac{\pi}{3} \underline{s}^T * \left\{ \left(\underline{r} \circ \underline{\rho} \circ \underline{v}_r \right) \circ \left(\underline{\underline{D}r} * \underline{v}^2 \right) \right\} \quad (\text{use eqn. B.1.3}) \\ &= \frac{2\pi}{3} (\underline{s} \circ \underline{r})^T * \left\{ \left(\underline{\rho} \circ \underline{v}_r \right) \circ \left(\underline{\underline{D}r} * \left(\frac{\underline{v}^2}{2} \right) \right) \right\} \\ &= \underline{dV}^T * \left\{ \underline{v}_r \circ \left(\underline{\rho} \circ \left(\underline{\underline{D}r} * \left(\frac{\underline{v}^2}{2} \right) \right) \right) \right\} \end{aligned}$$

Repeating the process for the second term in equation B.2.4, we arrive at the required form of \dot{U}_K :

$$\dot{U}_K = \underline{dV}^T * \left\{ \underline{v}_r \circ \left(\underline{\rho} \circ \left(\underline{\underline{D}r} * \left(\frac{\underline{v}^2}{2} \right) \right) \right) + \underline{v}_z \circ \left(\underline{\rho} \circ \left(\underline{\underline{D}z} * \left(\frac{\underline{v}^2}{2} \right) \right) \right) + \underline{\rho} \circ \underline{v}_r \circ \dot{v}_r + \underline{\rho} \circ \underline{v}_\phi \circ \dot{v}_\phi + \underline{\rho} \circ \underline{v}_z \circ \dot{v}_z \right\} \quad (\text{B.2.6})$$

We want to reproduce the advective term $-\mathbf{v} \cdot \nabla \mathbf{v}$ in the RHS of the momentum equation. Using the vector identity $\mathbf{A} \times (\nabla \times \mathbf{B}) = (\nabla \mathbf{B}) \cdot \mathbf{A} - (\mathbf{A} \cdot \nabla) \mathbf{B}$, it can be seen that $-(\mathbf{v} \cdot \nabla) \mathbf{v} = \mathbf{v} \times (\nabla \times \mathbf{v}) - \nabla(v^2/2)$. From equation B.2.6, it is evident that the term $-\nabla(v^2/2)$ has arisen naturally in the formulation for a momentum equation, so following from the procedure

outlined above, we need to add the term $\int(-\rho\mathbf{v} \cdot (\nabla \times (\nabla \times \mathbf{v}))) dV$ to \dot{U}_K in order to reproduce the term $-\mathbf{v} \cdot \nabla \mathbf{v}$. This addition will not affect the net value of \dot{U}_K , because $-\rho\mathbf{v} \cdot (\nabla \times (\nabla \times \mathbf{v})) = 0$, since $\mathbf{v} \perp (\nabla \times (\nabla \times \mathbf{v}))$. In cylindrical coordinates with azimuthal symmetry, $\mathbf{v} \times (\nabla \times \mathbf{v})$ may be expanded as:

$$\begin{aligned}\mathbf{v} \times (\nabla \times \mathbf{v}) &= \nabla(v^2/2) - (\mathbf{v} \cdot \nabla)\mathbf{v} \\ &= \hat{\mathbf{r}} \left(\frac{\partial}{\partial r}(v^2/2) - v_r \frac{\partial v_r}{\partial r} - v_z \frac{\partial v_r}{\partial z} + \frac{v_\phi^2}{r} \right) + \hat{\phi} \left(-v_r \frac{\partial v_\phi}{\partial r} - v_z \frac{\partial v_\phi}{\partial z} - \frac{v_\phi v_r}{r} \right) \\ &\quad + \hat{\mathbf{z}} \left(\frac{\partial}{\partial z}(v^2/2) - v_r \frac{\partial v_z}{\partial r} - v_z \frac{\partial v_z}{\partial z} \right)\end{aligned}$$

Noting that $\frac{\partial}{\partial r}(v^2/2) = \mathbf{v} \cdot \frac{\partial \mathbf{v}}{\partial r}$ and $\frac{\partial}{\partial z}(v^2/2) = \mathbf{v} \cdot \frac{\partial \mathbf{v}}{\partial z}$, this can be written as:

$$\begin{aligned}\mathbf{v} \times (\nabla \times \mathbf{v}) &= \hat{\mathbf{r}} \left(v_r \left(\frac{\partial v_r}{\partial r} - \frac{\partial v_r}{\partial r} \right) + v_z \left(\frac{\partial v_z}{\partial r} - \frac{\partial v_r}{\partial z} \right) + v_\phi \left(\frac{\partial v_\phi}{\partial r} + \frac{v_\phi}{r} \right) \right) \\ &\quad + \hat{\phi} \left(-v_r \left(\frac{\partial v_\phi}{\partial r} + \frac{v_\phi}{r} \right) - v_z \frac{\partial v_\phi}{\partial z} \right) + \hat{\mathbf{z}} \left(v_r \left(\frac{\partial v_r}{\partial z} - \frac{\partial v_z}{\partial r} \right) + v_z \left(\frac{\partial v_z}{\partial z} - \frac{\partial v_z}{\partial z} \right) + v_\phi \frac{\partial v_\phi}{\partial z} \right)\end{aligned}$$

Since $\frac{\partial v_\phi}{\partial r} + \frac{v_\phi}{r} = \frac{1}{r} \frac{\partial(rv_\phi)}{\partial r}$ and $\frac{\partial r}{\partial z} = 0$, this becomes

$$\begin{aligned}\mathbf{v} \times (\nabla \times \mathbf{v}) &= \hat{\mathbf{r}} \left(-v_z \left(\frac{\partial v_r}{\partial z} - \frac{\partial v_z}{\partial r} \right) + \frac{v_\phi}{r} \frac{\partial(rv_\phi)}{\partial r} \right) + \hat{\phi} \left(-\frac{v_r}{r} \frac{\partial(rv_\phi)}{\partial r} - \frac{v_z}{r} \frac{\partial(rv_\phi)}{\partial z} \right) \\ &\quad + \hat{\mathbf{z}} \left(v_r \left(\frac{\partial v_r}{\partial z} - \frac{\partial v_z}{\partial r} \right) + \frac{v_\phi}{r} \frac{\partial(rv_\phi)}{\partial z} \right)\end{aligned}\tag{B.2.7}$$

The discretised form of this expression may be used to add $\int(-\rho\mathbf{v} \cdot (\nabla \times (\nabla \times \mathbf{v}))) dV$ to the RHS of equation B.2.6 as follows

$$\begin{aligned}\dot{U}_K &= \underline{dV}^T * \left\{ \underline{v}_r \circ \left(\rho \circ \left(\underline{\underline{Dr}} * \left(\frac{\underline{v}^2}{2} \right) \right) \right) + \underline{v}_z \circ \left(\rho \circ \left(\underline{\underline{Dz}} * \left(\frac{\underline{v}^2}{2} \right) \right) \right) \right. \\ &\quad + \underline{\rho} \circ \underline{v}_r \circ \dot{\underline{v}}_r + \underline{\rho} \circ \underline{v}_\phi \circ \dot{\underline{v}}_\phi + \underline{\rho} \circ \underline{v}_z \circ \dot{\underline{v}}_z \\ &\quad - \underline{\rho} \circ \underline{v}_r \circ \left(-\underline{v}_z \circ \left(\underline{\underline{Dz}} * \underline{v}_r - \underline{\underline{Dr}} * \underline{v}_z \right) + \underline{v}_\phi \circ \left(\underline{\underline{Dr}} * \left(\underline{r} \circ \underline{v}_\phi \right) \right) \right) \otimes \underline{r} \\ &\quad - \underline{\rho} \circ \underline{v}_\phi \circ \left(-\underline{\mathbf{v}} \cdot \left(\underline{\underline{r}} \circ \left(\underline{r} \circ \underline{v}_\phi \right) \right) \right) \otimes \underline{r} \\ &\quad \left. - \underline{\rho} \circ \underline{v}_z \circ \left(\underline{v}_r \circ \left(\underline{\underline{Dz}} * \underline{v}_r - \underline{\underline{Dr}} * \underline{v}_z \right) + \underline{v}_\phi \circ \left(\underline{\underline{Dz}} * \left(\underline{r} \circ \underline{v}_\phi \right) \right) \right) \otimes \underline{r} \right\}\end{aligned}\tag{B.2.8}$$

Equation B.2.8 is the final discretized form for the rate of change of kinetic energy. A similar technique will be applied to the terms in \dot{U}_M and \dot{U}_{Th} , leading to expressions in the form of equations B.1.1 and B.1.2. Note that the 3rd, 4th, and 5th terms in equation B.2.8 will be the only terms containing time-derivatives of the velocity components in the discretised form of \dot{U}_{Total} .

B.3 Thermal Energy

The rate of change of system thermal energy can be expressed as

$$\dot{U}_{Th} = \int \frac{\dot{p}}{\gamma - 1} dV \quad (\text{B.3.1})$$

Ignoring the thermal diffusion term for now, the single fluid energy equation (A.8.3) is $\dot{p} = -\mathbf{v} \cdot \nabla p - \gamma p \nabla \cdot \mathbf{v} + (\gamma - 1) (\eta' J^2 - \bar{\pi} : \nabla \mathbf{v})$. The corresponding discrete form can be expressed as

$$\dot{p} = -\underline{\mathbf{v}} \cdot (\underline{\nabla} \underline{p}) - \gamma \underline{p} \circ (\underline{\nabla} \cdot \underline{\mathbf{v}}) + (\gamma - 1) (\eta' J^2 - \bar{\pi} : \nabla \mathbf{v})_{disc} \quad (\text{B.3.2})$$

where $(\eta' J^2 - \bar{\pi} : \nabla \mathbf{v})_{disc}$ is the discrete form of $\eta' J^2 - \bar{\pi} : \nabla \mathbf{v}$; explicit forms of these terms will be developed. The rate of change of system thermal energy in discrete form is

$$\begin{aligned} \dot{U}_{Th} = dV^T * & \left\{ \frac{1}{\gamma - 1} \left(\underbrace{-\underline{v}_r \circ (\underline{\underline{D}}_r * \underline{p})}_{1} \right. \right. \\ & \left. \left. - \underline{v}_z \circ (\underline{\underline{D}}_z * \underline{p}) \right) \right. \\ & - \gamma \left(\underbrace{\underline{p} \circ (\underline{\underline{D}}_r * (\underline{r} \circ \underline{v}_r)) \otimes \underline{r}}_{3} + \underbrace{\underline{p} \circ (\underline{\underline{D}}_z * (\underline{r} \circ \underline{v}_z)) \otimes \underline{r}}_{4} \right) \left. \right) \left. \right\} \\ & + \dot{U}_{Th\pi} + \dot{U}_{Th\phi\eta} + \dot{U}_{Th\theta\eta} \end{aligned} \quad (\text{B.3.3})$$

Here, $\dot{U}_{Th\pi} = \int (-\bar{\pi} : \nabla \mathbf{v}) dV$ is the rate of change of thermal energy due to viscous heating, $\dot{U}_{Th\phi\eta} = \int \eta' J_\phi^2 dV$ is the rate of change of thermal energy in the volume associated with ohmic heating due to toroidal currents, and $\dot{U}_{Th\theta\eta} = \int \eta' J_\theta^2 dV$ is the rate of change of thermal energy in the volume associated with ohmic heating due to poloidal currents.

The first two terms in equation B.3.3 are already in the required form. The 3rd term can be expressed as follows:

$$\begin{aligned}
\dot{U}_{Th3} &= \frac{\gamma}{\gamma-1} \underline{dV}^T * \left\{ -\underline{p} \circ (\underline{\underline{D}}r * (\underline{r} \circ \underline{v}_r)) \otimes \underline{r} \right\} \\
&= \frac{2\pi\gamma}{3(\gamma-1)} \underline{s}^T * \left\{ -\underline{p} \circ (\underline{\underline{D}}r * (\underline{r} \circ \underline{v}_r)) \right\} \\
&= -\frac{2\pi\gamma}{3(\gamma-1)} \left(\underline{p}^T * \underline{\underline{S}} * (\underline{\underline{D}}r * (\underline{r} \circ \underline{v}_r)) \right) \quad (\text{use eqn. B.1.3}) \\
&= -\frac{2\pi\gamma}{3(\gamma-1)} \left((\underline{r} \circ \underline{v}_r)^T * \underline{\underline{D}}r^T * \underline{\underline{S}} * \underline{p} \right) \quad (\text{transpose the scalar}) \\
&= +\frac{2\pi\gamma}{3(\gamma-1)} \left((\underline{r} \circ \underline{v}_r)^T * \underline{\underline{S}} * \underline{\underline{D}}r * \underline{p} \right) \quad (\text{use eqn. B.2.5}) \\
&= \frac{2\pi\gamma}{3(\gamma-1)} \underline{s}^T * \left((\underline{r} \circ \underline{v}_r) \circ (\underline{\underline{D}}r * \underline{p}) \right) \quad (\text{use eqn. B.1.3}) \\
&= \frac{\gamma}{\gamma-1} \underline{dV}^T * \left\{ \underline{v}_r \circ (\underline{\underline{D}}r * \underline{p}) \right\}
\end{aligned}$$

Similarly, the 4th term in equation B.3.3 can be re-expressed as :

$$\dot{U}_{Th4} = \frac{\gamma}{\gamma-1} \underline{dV}^T * \left(\underline{v}_z \circ (\underline{\underline{D}}z * \underline{p}) \right) \quad (\text{B.3.4})$$

From this, the first four terms in equation B.3.3 can be written as:

$$\dot{U}_{Th1 \rightarrow 4} = \underline{dV}^T * \left\{ \underline{v}_r \circ (\underline{\underline{D}}r * \underline{p}) + \underline{v}_z \circ (\underline{\underline{D}}z * \underline{p}) \right\} \quad (\text{B.3.5})$$

B.3.1 Viscous heating

The 5th term in equation B.3.3 represents the part of the rate of change thermal energy that is due to viscous heating:

$$\dot{U}_{Th\pi} = \int -\bar{\pi} : \nabla \mathbf{v} \, dV \quad (\text{B.3.6})$$

For the viscous terms, we use, for simplicity, the unmagnetised version of the viscous stress tensor in axisymmetric cylindrical coordinates. In cylindrical coordinates, with azimuthal symmetry, the components of the viscosity tensor $\bar{\pi}$ are [94]:

$$\bar{\pi} = -\mu \begin{pmatrix} 2\frac{\partial v_r}{\partial r} - \frac{2}{3}\nabla \cdot \mathbf{v} & r\frac{\partial}{\partial r}\left(\frac{v_\phi}{r}\right) & \frac{\partial v_z}{\partial r} + \frac{\partial v_r}{\partial z} \\ r\frac{\partial}{\partial r}\left(\frac{v_\phi}{r}\right) & 2\frac{v_r}{r} - \frac{2}{3}\nabla \cdot \mathbf{v} & \frac{\partial v_\phi}{\partial z} \\ \frac{\partial v_z}{\partial r} + \frac{\partial v_r}{\partial z} & \frac{\partial v_\phi}{\partial z} & 2\frac{\partial v_z}{\partial z} - \frac{2}{3}\nabla \cdot \mathbf{v} \end{pmatrix} \quad (\text{B.3.7})$$

where μ [$\text{kg m}^{-1}\text{s}^{-1}$] is dynamic viscosity. In the following it is assumed for generality that μ is spatially dependent, $\mu = \mu(\mathbf{r})$. The contraction (inner product) of two second order tensors [73] is defined as $\underline{\underline{T}} : \underline{\underline{U}} = \sum_i \sum_j T_{ij} U_{ij}$, and $\nabla \mathbf{v}$, in cylindrical coordinates with azimuthal symmetry is

$$\nabla \mathbf{v} = \begin{pmatrix} \frac{\partial v_r}{\partial r} & -\frac{v_\phi}{r} & \frac{\partial v_r}{\partial z} \\ \frac{\partial v_\phi}{\partial r} & \frac{v_r}{r} & \frac{\partial v_\phi}{\partial z} \\ \frac{\partial v_z}{\partial r} & 0 & \frac{\partial v_z}{\partial z} \end{pmatrix}$$

$$\Rightarrow \bar{\pi} : \nabla \mathbf{v} = -\mu \left[\underbrace{\left(2 \frac{\partial v_r}{\partial r} - \frac{2}{3} \nabla \cdot \mathbf{v} \right) \frac{\partial v_r}{\partial r}}_1 + \underbrace{\left(r \frac{\partial}{\partial r} \left(\frac{v_\phi}{r} \right) \right) \left(-\frac{v_\phi}{r} \right)}_2 + \underbrace{\left(\frac{\partial v_z}{\partial r} + \frac{\partial v_r}{\partial z} \right) \left(\frac{\partial v_r}{\partial z} \right)}_3 + \underbrace{r \frac{\partial}{\partial r} \left(\frac{v_\phi}{r} \right) \left(\frac{\partial v_\phi}{\partial r} \right)}_4 \right. \\ \left. + \underbrace{\left(2 \frac{v_r}{r} - \frac{2}{3} \nabla \cdot \mathbf{v} \right) \left(\frac{v_r}{r} \right)}_5 + \underbrace{\left(\frac{\partial v_\phi}{\partial z} \right)^2}_6 + \underbrace{\left(\frac{\partial v_z}{\partial r} + \frac{\partial v_r}{\partial z} \right) \left(\frac{\partial v_z}{\partial r} \right)}_7 + \underbrace{\left(2 \frac{\partial v_z}{\partial z} - \frac{2}{3} \nabla \cdot \mathbf{v} \right) \left(\frac{\partial v_z}{\partial z} \right)}_8 \right]$$

The 2nd and 4th terms can be combined: $\bar{\pi} : \nabla \mathbf{v} = -\mu \left(r \frac{\partial}{\partial r} \left(\frac{v_\phi}{r} \right) \right)^2$, as can the 3rd and 7th terms:

$\bar{\pi}_{3+7} : \nabla \mathbf{v} = -\mu \left(\frac{\partial v_z}{\partial r} + \frac{\partial v_r}{\partial z} \right)^2$. The sum of the 1st, 5th and 8th terms is:

$\bar{\pi}_{1+5+8} : \nabla \mathbf{v} = -2\mu \left(\left(\frac{\partial v_r}{\partial r} \right)^2 + \left(\frac{v_r}{r} \right)^2 + \left(\frac{\partial v_z}{\partial z} \right)^2 \right) + \frac{2}{3}\mu \left(\frac{1}{r} \frac{\partial(rv_r)}{\partial r} + \frac{\partial v_z}{\partial z} \right)^2$. Combining terms, and noting that $\frac{\partial r}{\partial z} \rightarrow 0$, and defining the angular speed $\omega = \frac{v_\phi}{r}$, this can be expressed as

$$\bar{\pi} : \nabla \mathbf{v} = -\mu \left[2 \left(\left(\frac{\partial v_r}{\partial r} \right)^2 + \left(\frac{v_r}{r} \right)^2 + \left(\frac{\partial v_z}{\partial z} \right)^2 \right) + (r \nabla \omega)^2 + \left(\frac{\partial v_z}{\partial r} + \frac{\partial v_r}{\partial z} \right)^2 - \frac{2}{3} \left(\frac{1}{r} \frac{\partial(rv_r)}{\partial r} + \frac{1}{r} \frac{\partial(rv_z)}{\partial z} \right)^2 \right] \quad (\text{B.3.8})$$

In cylindrical coordinates, the divergence of a second order tensor [95] is

$$\begin{aligned} \nabla \cdot \bar{\pi} &= \left(\frac{\partial \pi_{rr}}{\partial r} + \frac{1}{r} \left(\frac{\partial \pi_{\phi r}}{\partial \phi} + \pi_{rr} - \pi_{\phi \phi} \right) + \frac{\partial \pi_{zr}}{\partial z} \right) \hat{\mathbf{r}} \\ &+ \left(\frac{\partial \pi_{r\phi}}{\partial r} + \frac{1}{r} \left(\frac{\partial \pi_{\phi\phi}}{\partial \phi} + \pi_{r\phi} + \pi_{\phi r} \right) + \frac{\partial \pi_{z\phi}}{\partial z} \right) \hat{\phi} \\ &+ \left(\frac{\partial \pi_{rz}}{\partial r} + \frac{1}{r} \left(\frac{\partial \pi_{\phi z}}{\partial \phi} + \pi_{rz} \right) + \frac{\partial \pi_{zz}}{\partial z} \right) \hat{\mathbf{z}} \end{aligned}$$

For a symmetric tensor, and with azimuthal symmetry, this becomes

$$\nabla \cdot \bar{\boldsymbol{\pi}} = \left(\frac{1}{r} \frac{\partial}{\partial r} (r\pi_{rr}) - \frac{\pi_{\phi\phi}}{r} + \frac{\partial\pi_{rz}}{\partial z} \right) \hat{\mathbf{r}} + \left(\frac{\partial\pi_{r\phi}}{\partial r} + \frac{2\pi_{r\phi}}{r} + \frac{\partial\pi_{\phi z}}{\partial z} \right) \hat{\boldsymbol{\phi}} + \left(\frac{1}{r} \frac{\partial}{\partial r} (r\pi_{rz}) + \frac{\partial\pi_{zz}}{\partial z} \right) \hat{\mathbf{z}}$$

(B.3.9)

Note that the reduction of the system's kinetic energy due to viscous dissipation is balanced by an increase in thermal energy due to viscous heating. Referring to equations A.8.2 and A.8.3, the rate of change of the energy associated with viscous heating in the system is

$$\begin{aligned} \dot{U}_{vh} &= \int \left(\frac{\dot{p}_{vh}}{\gamma - 1} + \rho \dot{\mathbf{v}}_{vh} \cdot \mathbf{v} \right) dV = - \int (\bar{\boldsymbol{\pi}} : \nabla \mathbf{v} + \mathbf{v} \cdot (\nabla \cdot \bar{\boldsymbol{\pi}})) dV \\ &= - \int \nabla \cdot (\mathbf{v} \cdot \bar{\boldsymbol{\pi}}) dV \quad (\text{use eqn. A.4.11}) \\ &= - \int (\mathbf{v} \cdot \bar{\boldsymbol{\pi}}) \cdot d\Gamma \end{aligned}$$

Thus, these terms balance if $\mathbf{v}_\perp|_\Gamma = 0$. It can be shown that $\dot{U}_{vh\phi}$, the part of \dot{U}_{vh} that contains terms with v_ϕ , can be expressed as the integral over the system's volume of the divergence of a vector that has the quality that each component is a multiple of v_ϕ . With the boundary condition $v_\phi|_\Gamma = 0$, the divergence theorem implies that $\dot{U}_{vh\phi} = 0$. By the same technique, it can be shown that $\dot{U}_{vh_{rz}}$, the part of \dot{U}_{vh} that contains terms with v_r and v_z is zero with boundary conditions $v_r|_\Gamma = v_z|_\Gamma = 0$, so that the kinetic energy loss due to viscous dissipation of toroidal/poloidal fluid motion is balanced by an increase in thermal energy due to viscous heating arising from toroidal/poloidal fluid motion.

With this in mind, the next step is to use the discrete expressions for the viscous contribution to the system's thermal energy to derive discrete expressions for the viscosity term in the momentum equation.

B.3.1.1 Discretisation of $\dot{U}_{Th\pi}$

$\bar{\boldsymbol{\pi}}$ contains terms with squared derivatives, so when we expand the discretized expression for $\dot{U}_{Th\pi} = \int -\bar{\boldsymbol{\pi}} : \nabla \mathbf{v} dV$ to get the parts of the expressions, pertaining to the viscous heating term, that make up the coefficients of the velocity components, in the same way as was done in section B.2, we will obtain terms with 2nd derivatives. For 2nd derivatives, we want to apply consecutive applications of the node-to-element and element-to-node differen-

tial operators for consistency with the three point stencil of the numerical scheme. Therefore, the node-to-element operators will be implemented whenever squared derivatives appear in the following equation development process.

Note that equation B.3.8 leads naturally to the discrete volume-averaged form of $-\bar{\pi} : \nabla \mathbf{v}$, which will be used in the discretised energy equation:

$$(-\bar{\pi} : \nabla \mathbf{v})_{disc} = \underline{Q}_\pi = \underline{W}_n * \left[\underline{\mu}^e \circ \left\{ 2 \left(\underline{\underline{D}}r^e * \underline{v}_r \right)^2 + 2 \left(\underline{\underline{D}}z^e * \underline{v}_z \right)^2 + \left(\underline{r}^e \circ \left(\underline{\underline{\nabla}}^e \omega \right) \right)^2 \right. \right. \\ \left. \left. + \left(\underline{\underline{D}}r^e * \underline{v}_z + \underline{\underline{D}}z^e * \underline{v}_r \right)^2 - \frac{2}{3} \left(\underline{\underline{\nabla}}^e \cdot \mathbf{v} \right)^2 \right\} \right] + 2 \underline{\mu} \circ \left(\underline{v}_r \oslash \underline{r} \right)^2 \quad (\text{B.3.10})$$

where \underline{W}_n is the volume-averaging operator (equations 5.3.2 and 5.3.3). Recalling that the vector of elemental volumes is $dV^e = 2\pi \underline{s}^e \circ \underline{r}^e$, then using equations B.3.6 and B.3.8, the discrete form of the part of the thermal energy that is due to viscous heating is

$$\dot{U}_{Th\pi} = 2\pi (\underline{s}^e \circ \underline{r}^e \circ \underline{\mu}^e)^T * \left\{ \underbrace{2 \left(\underline{\underline{D}}r^e * \underline{v}_r \right)^2}_1 + \underbrace{2 \left(\underline{\underline{D}}z^e * \underline{v}_z \right)^2}_2 \right. \\ \left. + \underbrace{\left(\underline{r}^e \circ \left(\underline{\underline{D}}r^e * \omega \right) \right)^2}_3 + \underbrace{\left(\underline{r}^e \circ \left(\underline{\underline{D}}z^e * \omega \right) \right)^2}_4 + \underbrace{\left(\underline{\underline{D}}r^e * \underline{v}_z \right)^2}_5 + \underbrace{2 \left(\underline{\underline{D}}r^e * \underline{v}_z \right) \circ \left(\underline{\underline{D}}z^e * \underline{v}_r \right)}_6 + \underbrace{\left(\underline{\underline{D}}z^e * \underline{v}_r \right)^2}_7 \right. \\ \left. - \frac{2}{3} \left[\underbrace{\left(\left(\underline{\underline{D}}r^e * \left(\underline{r} \circ \underline{v}_r \right) \right) \oslash \underline{r}^e \right)^2}_8 + \underbrace{2 \left(\left(\underline{\underline{D}}r^e * \left(\underline{r} \circ \underline{v}_r \right) \right) \oslash \underline{r}^e \right) \circ \left(\left(\underline{\underline{D}}z^e * \left(\underline{r} \circ \underline{v}_z \right) \right) \oslash \underline{r}^e \right)}_9 + \underbrace{\left(\left(\underline{\underline{D}}z^e * \left(\underline{r} \circ \underline{v}_z \right) \right) \oslash \underline{r}^e \right)^2}_ {10} \right] \right\} \\ \left. + \underbrace{\frac{2\pi}{3} (\underline{s} \circ \underline{r})^T * \left(2\underline{\mu} \circ \left(\underline{v}_r \oslash \underline{r} \right)^2 \right)}_{11} \right) \quad (\text{B.3.11})$$

Here, $\underline{\mu}^e$ and $\underline{\mu}$ are the vectors of element-based and node-based dynamic viscosities, and are related as $\underline{\mu}^e = \langle \underline{\mu} \rangle^e$ (equation 5.3.1). Note that each term in equation B.3.11 is a scalar. The 11th term, corresponding to the integral over volume of the second term in equation B.3.8, does not involve squared derivatives, so this term can be evaluated using node-based quantities. Recall that we want to express each scalar term in equation B.3.11 in the form: $dV^T * (\underline{s} \circ \underline{X}_{j\beta})$, so that we can use the axiom $\dot{U}_{Total} = 0$ to construct the discretised form of the momentum equation. Only the 3rd and 4th terms contain \underline{v}_ϕ . Defining $\underline{w}_3^e = \underline{\mu}^e \circ \underline{s}^e \circ \underline{r}^e$, the 3rd term in equation B.3.11 can be expressed as:

$$\begin{aligned} \dot{U}_{Th\pi} &= 2\pi \left(\underline{w}_3^e \circ \left(\underline{\underline{D}}r^e * \omega \right) \right)^T * \left(\underline{\underline{D}}r^e * \omega \right) \\ &= 2\pi \underline{\omega}^T * \underline{\underline{D}}r^{eT} * \left(\underline{w}_3^e \circ \left(\underline{\underline{D}}r^e * \omega \right) \right) \quad (\text{transpose the scalar}) \\ &= \frac{2\pi}{3} (\underline{s} \circ \underline{r})^T * \left\{ \underline{\omega} \circ \left(\underline{\underline{D}}r^{eT} * \left(\underline{w}_3^e \circ \left(\underline{\underline{D}}r^e * \omega \right) \right) \right) \oslash (\underline{s} \circ \underline{r}/3) \right\} \quad (\text{use eqn. B.1.4}) \\ &= dV^T * \left\{ \underline{v}_\phi \circ \left(3 \underline{\underline{D}}r^{eT} * \left(\underline{w}_3^e \circ \left(\underline{\underline{D}}r^e * \omega \right) \right) \right) \oslash (\underline{s} \circ \underline{r}^2) \right\} \quad (\text{B.3.12}) \end{aligned}$$

Similarly, the 4th term in equation B.3.11 is

$$\dot{U}_{\frac{4}{4}h\pi} = \underline{dV}^T * \left\{ \underline{v}_\phi \circ \left(3\underline{\underline{Dz}}^{eT} * \left(\underline{w}_3^e \circ \left(\underline{\underline{Dz}}^e * \underline{\omega} \right) \right) \right) \right\} \otimes (\underline{s} \circ \underline{r}^2) \quad (\text{B.3.13})$$

For convenience, we define:

$$\dot{U}_{Th\pi} = \dot{U}_{Th\pi r} + \dot{U}_{Th\pi\phi} + \dot{U}_{Th\pi z} \quad (\text{B.3.14})$$

where $\dot{U}_{Th\pi\beta}$ is the part of $\dot{U}_{Th\pi}$ that contains v_β . Adding equations B.3.12 and B.3.13, we arrive at :

$$\dot{U}_{Th\pi\phi} = \underline{dV}^T * \left\{ \underline{v}_\phi \circ \underline{\Pi}_\phi \right\} \quad (\text{B.3.15})$$

where, with reference to the definitions of the element-to node differential operators (equations 5.4.12 and 5.4.15)

$$\underline{\Pi}_\phi = - \left(\underline{\nabla}_n \cdot \left(\underline{\mu}^e \circ \underline{r}^{e2} \circ \left(\underline{\nabla}^e \underline{\omega} \right) \right) \right) \otimes \underline{r} \quad (\text{B.3.16})$$

This term represents the discrete form of $(\nabla \cdot \bar{\pi})_\phi$, and will appear in the ϕ component of the discretised momentum equation.

The 1st, 6th, 7th, 8th, 9th and 11th terms in equation B.3.11 include r components of velocity and will contribute to $\dot{U}_{Th\pi r}$. Defining $\underline{w}_1^e = \underline{\mu}^e \circ \underline{s}^e \circ \underline{r}^e$, the 1st term can be expressed as

$$\begin{aligned} \dot{U}_{\frac{1}{1}h\pi} &= 4\pi \left(\underline{w}_1^e \circ \left(\underline{\underline{Dr}}^e * \underline{v}_r \right) \right)^T * \left(\underline{\underline{Dr}}^e * \underline{v}_r \right) \\ &= 4\pi \underline{v}_r^T * \underline{\underline{Dr}}^{eT} * \left(\underline{w}_1^e \circ \left(\underline{\underline{Dr}}^e * \underline{v}_r \right) \right) \quad (\text{transpose the scalar}) \\ &= \frac{4\pi}{3} (\underline{s} \circ \underline{r})^T * \left\{ \underline{v}_r \circ \left(3\underline{\underline{Dr}}^{eT} * \left(\underline{w}_1^e \circ \left(\underline{\underline{Dr}}^e * \underline{v}_r \right) \right) \right) \right\} \otimes (\underline{s} \circ \underline{r}) \quad (\text{use eqn. B.1.4}) \\ &= \underline{dV}^T * \left\{ \underline{v}_r \circ \left(6\underline{\underline{Dr}}^{eT} * \left(\underline{w}_1^e \circ \left(\underline{\underline{Dr}}^e * \underline{v}_r \right) \right) \right) \right\} \otimes (\underline{s} \circ \underline{r}) \\ &= \underline{dV}^T * \left\{ \underline{v}_r \circ \left(-2\underline{\underline{Dr}}_n * \left(\underline{\mu}^e \circ \underline{r}^e \circ \left(\underline{\underline{Dr}}^e * \underline{v}_r \right) \right) \right) \right\} \otimes (\underline{s} \circ \underline{r}) \quad (\text{use eqn. 5.4.15}) \end{aligned} \quad (\text{B.3.17})$$

Similarly, the 7th term becomes

$$\dot{U}_{\frac{7}{7}h\pi} = \underline{dV}^T * \left\{ \underline{v}_r \circ \left(-\underline{\underline{Dz}}_n * \left(\underline{\mu}^e \circ \underline{r}^e \circ \left(\underline{\underline{Dz}}^e * \underline{v}_r \right) \right) \right) \right\} \otimes (\underline{s} \circ \underline{r}) \quad (\text{B.3.18})$$

The 6th term in equation B.3.11 is:

$$\begin{aligned}
\dot{U}_{T h \pi} &= 4\pi \left(\underline{w}_1^e \circ \left(\underline{\underline{D}r}^e * \underline{v}_z \right) \right)^T * \left(\underline{\underline{D}z}^e * \underline{v}_r \right) \\
&= 4\pi \underline{v}_r^T * \underline{\underline{D}z}^{eT} * \left(\underline{w}_1^e \circ \left(\underline{\underline{D}r}^e * \underline{v}_z \right) \right) \quad (\text{transpose the scalar}) \\
&= \frac{4\pi}{3} (\underline{s} \circ \underline{r})^T * \left\{ \underline{v}_r \circ \left(3 \underline{\underline{D}z}^{eT} * \left(\underline{w}_1^e \circ \left(\underline{\underline{D}r}^e * \underline{v}_z \right) \right) \right) \right\} \quad (\text{use eqn. B.1.4}) \\
&= \underline{dV}^T * \left\{ \underline{v}_r \circ \left(-2 \underline{\underline{D}z}_n * \left(\underline{\mu}^e \circ \underline{r}^e \circ \left(\underline{\underline{D}r}^e * \underline{v}_z \right) \right) \right) \right\} \quad (\text{use eqn. 5.4.15})
\end{aligned}$$

In the first step above, we could equally have chosen

$$\dot{U}_{T h \pi} = 4\pi \left(\underline{w}_1^e \circ \left(\underline{\underline{D}z}^e * \underline{v}_r \right) \right)^T * \left(\underline{\underline{D}r}^e * \underline{v}_z \right)$$

which would have resulted in the expression

$$\dot{U}_{T h \pi} = \underline{dV}^T * \left\{ \underline{v}_z \circ \left(-2 \underline{\underline{D}r}_n * \left(\underline{\mu}^e \circ \underline{r}^e \circ \left(\underline{\underline{D}z}^e * \underline{v}_r \right) \right) \right) \right\}$$

so it is valid to express the 6th term as:

$$\begin{aligned}
\dot{U}_{T h \pi} &= \underline{dV}^T * \left\{ \underline{v}_r \circ \left(- \underline{\underline{D}z}_n * \left(\underline{\mu}^e \circ \underline{r}^e \circ \left(\underline{\underline{D}r}^e * \underline{v}_z \right) \right) \right) \right\} \otimes \underline{r} \\
&\quad + \underline{v}_z \circ \left(- \underline{\underline{D}r}_n * \left(\underline{\mu}^e \circ \underline{r}^e \circ \left(\underline{\underline{D}z}^e * \underline{v}_r \right) \right) \right) \otimes \underline{r}
\end{aligned} \tag{B.3.19}$$

Defining $\underline{w}_0^e = \underline{\mu}^e \circ \underline{s}^e \otimes \underline{r}^e$, the 8th term in equation B.3.11 is:

$$\begin{aligned}
\dot{U}_{T h \pi} &= -\frac{4}{3}\pi \left(\underline{w}_0^e \circ \left(\underline{\underline{D}r}^e * \left(\underline{r} \circ \underline{v}_r \right) \right) \right)^T * \left(\underline{\underline{D}r}^e * \left(\underline{r} \circ \underline{v}_r \right) \right) \\
&= -\frac{4}{3}\pi \left(\underline{r} \circ \underline{v}_r \right)^T * \underline{\underline{D}r}^{eT} * \left(\underline{w}_0^e \circ \left(\underline{\underline{D}r}^e * \left(\underline{r} \circ \underline{v}_r \right) \right) \right) \quad (\text{transpose the scalar}) \\
&= \underline{dV}^T * \left\{ \left(\underline{r} \circ \underline{v}_r \right) \circ \left(-2 \underline{\underline{D}r}^{eT} * \left(\underline{w}_0^e \circ \left(\underline{\underline{D}r}^e * \left(\underline{r} \circ \underline{v}_r \right) \right) \right) \right) \right\} \otimes (\underline{s} \circ \underline{r}) \quad (\text{use eqn. B.1.4}) \\
&= \underline{dV}^T * \left\{ \underline{v}_r \circ \left(-2 \underline{\underline{D}r}^{eT} * \left(\underline{w}_0^e \circ \left(\underline{\underline{D}r}^e * \left(\underline{r} \circ \underline{v}_r \right) \right) \right) \right) \right\} \otimes \underline{s} \\
&= \underline{dV}^T * \left\{ \underline{v}_r \circ \left(\frac{2}{3} \underline{\underline{D}r}_n * \left(\underline{\mu}^e \circ \left(\underline{\underline{D}r}^e * \left(\underline{r} \circ \underline{v}_r \right) \right) \otimes \underline{r}^e \right) \right) \right\} \quad (\text{use eqn. 5.4.15})
\end{aligned} \tag{B.3.20}$$

Similarly, the 9th term in equation B.3.11 is:

$$\begin{aligned}
\dot{U}_{T_{9}^{h\pi}} &= -\frac{8}{3}\pi \left(\underline{w}_0^e \circ \left(\underline{\underline{D}}r^e * \left(\underline{r} \circ \underline{v}_r \right) \right) \right)^T * \left(\underline{\underline{D}}z^e * \left(\underline{r} \circ \underline{v}_z \right) \right) \\
&= \underline{dV}^T * \left\{ \underline{v}_z \circ \left(-4\underline{\underline{D}}z^{eT} * \left(\underline{w}_0^e \circ \left(\underline{\underline{D}}r^e * \left(\underline{r} \circ \underline{v}_r \right) \right) \right) \right) \oslash \underline{s} \right\} \\
&= \underline{dV}^T * \left\{ \underline{v}_z \circ \left(\frac{4}{3}\underline{\underline{D}}z_n * \left(\underline{\mu}^e \circ \left(\underline{\underline{D}}r^e * \left(\underline{r} \circ \underline{v}_r \right) \right) \oslash \underline{r}^e \right) \right) \right\}
\end{aligned}$$

In the first step above, we could equally have chosen:

$$\dot{U}_{T_{9}^{h\pi}} = -\frac{8}{3}\pi \left(\underline{w}_0^e \circ \left(\underline{\underline{D}}z^e * \left(\underline{r} \circ \underline{v}_z \right) \right) \right)^T * \left(\underline{\underline{D}}r^e * \left(\underline{r} \circ \underline{v}_r \right) \right)$$

which would have resulted in the expression:

$$\dot{U}_{T_{9}^{h\pi}} = \underline{dV}^T * \left\{ \underline{v}_r \circ \left(\frac{4}{3}\underline{\underline{D}}r_n * \left(\underline{\mu}^e \circ \left(\underline{\underline{D}}z^e * \left(\underline{r} \circ \underline{v}_z \right) \right) \oslash \underline{r}^e \right) \right) \right\}$$

so it is valid to express the 9th term as:

$$\begin{aligned}
\dot{U}_{T_{9}^{h\pi}} &= \underline{dV}^T * \left\{ \underline{v}_z \circ \left(\frac{2}{3}\underline{\underline{D}}z_n * \left(\underline{\mu}^e \circ \left(\underline{\underline{D}}r^e * \left(\underline{r} \circ \underline{v}_r \right) \right) \oslash \underline{r}^e \right) \right) \right. \\
&\quad \left. + \underline{v}_r \circ \left(\frac{2}{3}\underline{\underline{D}}r_n * \left(\underline{\mu}^e \circ \left(\underline{\underline{D}}z^e * \left(\underline{r} \circ \underline{v}_z \right) \right) \oslash \underline{r}^e \right) \right) \right\} \tag{B.3.21}
\end{aligned}$$

Transforming the 11th term in equation B.3.11 is straightforward:

$$\dot{U}_{T_{11}^{h\pi}} = \underline{dV}^T * \left\{ 2\underline{\mu} \circ \left(\underline{v}_r \oslash \underline{r} \right)^2 \right\} = \underline{dV}^T * \left\{ \underline{v}_r \circ \left(2\underline{\mu} \circ \underline{v}_r \oslash \underline{r}^2 \right) \right\} \tag{B.3.22}$$

Adding equations B.3.17, B.3.18, B.3.20, B.3.22, and the parts of equations B.3.19 and B.3.21 that pertain to v_r , we arrive at:

$$\dot{U}_{Th\pi r} = \underline{dV}^T * \left\{ \underline{v}_r \circ \underline{\Pi}_r \right\} \tag{B.3.23}$$

where

$$\begin{aligned}
\underline{\Pi}_r &= \left[- \left(2\underline{\underline{D}}r_n * \left(\underline{\mu}^e \circ \underline{r}^e \circ \left(\underline{\underline{D}}r^e * \underline{v}_r \right) \right) \right) \oslash \underline{r} - \left(\underline{\underline{D}}z_n * \left(\underline{\mu}^e \circ \underline{r}^e \circ \left(\underline{\underline{D}}z^e * \underline{v}_r \right) \right) \right) \oslash \underline{r} \right. \\
&\quad - \left(\underline{\underline{D}}z_n * \left(\underline{\mu}^e \circ \underline{r}^e \circ \left(\underline{\underline{D}}r^e * \underline{v}_z \right) \right) \right) \oslash \underline{r} + \frac{2}{3}\underline{\underline{D}}r_n * \left(\underline{\mu}^e \circ \left(\underline{\underline{D}}r^e * \left(\underline{r} \circ \underline{v}_r \right) \right) \oslash \underline{r}^e \right) \\
&\quad \left. + \frac{2}{3}\underline{\underline{D}}r_n * \left(\underline{\mu}^e \circ \left(\underline{\underline{D}}z^e * \left(\underline{r} \circ \underline{v}_z \right) \right) \oslash \underline{r}^e \right) \right] + 2\underline{\mu} \circ \underline{v}_r \oslash \underline{r}^2
\end{aligned}$$

Note that the 2nd and 3rd terms can be combined. With reference to the definition of the node-to-element divergence operation (equation 5.4.2), the 4th and 5th terms can also be combined, leading to the discrete form of $(\nabla \cdot \bar{\boldsymbol{\pi}})_r$:

$$\begin{aligned} \underline{\Pi}_r = & \left[- \left(2\underline{\underline{D}r}_n * \left(\underline{\mu}^e \circ \underline{r}^e \circ \left(\underline{\underline{D}r}^e * \underline{v}_r \right) \right) \right) - \left(\underline{\underline{D}z}_n * \left(\underline{\mu}^e \circ \underline{r}^e \circ \left(\underline{\underline{D}r}^e * \underline{v}_z + \underline{\underline{D}z}^e * \underline{v}_r \right) \right) \right) \right] \oslash \underline{r} \\ & + \frac{2}{3} \underline{\underline{D}r}_n * \left(\underline{\mu}^e \circ \left(\underline{\nabla}^e \cdot \underline{\mathbf{v}} \right) \right) + 2\underline{\mu} \circ \underline{v}_r \oslash \underline{r}^2 \end{aligned} \quad (\text{B.3.24})$$

The 2nd, 5th, 6th, 9th and 10th terms in equation B.3.11 include z components of velocity and will contribute to $\dot{U}_{Th\pi z}$. The re-expression for the 2nd, 5th and 10th terms follow from the re-expressions of the 1st and 8th terms:

$$\dot{U}_{Th\pi} = \underline{\underline{d}V}^T * \left\{ \underline{v}_z \circ \left(-2\underline{\underline{D}z}_n * \left(\underline{\mu}^e \circ \underline{r}^e \circ \left(\underline{\underline{D}z}^e * \underline{v}_z \right) \right) \right) \oslash \underline{r} \right\} \quad (\text{B.3.25})$$

$$\dot{U}_{Th\pi} = \underline{\underline{d}V}^T * \left\{ \underline{v}_z \circ \left(-\underline{\underline{D}r}_n * \left(\underline{\mu}^e \circ \underline{r}^e \circ \left(\underline{\underline{D}r}^e * \underline{v}_z \right) \right) \right) \oslash \underline{r} \right\} \quad (\text{B.3.26})$$

$$\dot{U}_{Th\pi} = \underline{\underline{d}V}^T * \left\{ \underline{v}_z \circ \left(\frac{2}{3} \underline{\underline{D}z}_n * \left(\underline{\mu}^e \circ \left(\underline{\underline{D}z}^e * \left(\underline{r} \circ \underline{v}_z \right) \right) \oslash \underline{r}^e \right) \right) \right\} \quad (\text{B.3.27})$$

Adding equations B.3.25, B.3.26, B.3.27, and the parts of equations B.3.19 and B.3.21 that pertain to v_z , leads to

$$\dot{U}_{Th\pi z} = \underline{\underline{d}V}^T * \left\{ \underline{v}_z \circ \underline{\Pi}_z \right\} \quad (\text{B.3.28})$$

where the discrete form of $(\nabla \cdot \bar{\boldsymbol{\pi}})_z$ is

$$\begin{aligned} \underline{\Pi}_z = & \left[- \left(2\underline{\underline{D}z}_n * \left(\underline{\mu}^e \circ \underline{r}^e \circ \left(\underline{\underline{D}z}^e * \underline{v}_z \right) \right) \right) - \left(\underline{\underline{D}r}_n * \left(\underline{\mu}^e \circ \underline{r}^e \circ \left(\underline{\underline{D}r}^e * \underline{v}_z + \underline{\underline{D}z}^e * \underline{v}_r \right) \right) \right) \right] \oslash \underline{r} \\ & + \frac{2}{3} \underline{\underline{D}z}_n * \left(\underline{\mu}^e \circ \left(\underline{\nabla}^e \cdot \underline{\mathbf{v}} \right) \right) \end{aligned} \quad (\text{B.3.29})$$

B.3.2 Final expression for discretised form of \dot{U}_{Th}

Combining equations B.3.3, B.3.5, B.3.14, B.3.15, B.3.23 and B.3.28, we arrive at the final expression for discretised form of \dot{U}_{Th} :

$$\dot{U}_{Th} = \underbrace{\underline{\underline{d}V}^T * \left\{ \underline{v}_r \circ \left(\underline{\underline{D}r} * \underline{p} + \underline{\Pi}_r \right) + \underline{v}_\phi \circ \underline{\Pi}_\phi + \underline{v}_z \circ \left(\underline{\underline{D}z} * \underline{p} + \underline{\Pi}_z \right) \right\}}_{\dot{U}_{Th\,ideal}} + \dot{U}_{Th\theta\eta} + \dot{U}_{Th\phi\eta} \quad (\text{B.3.30})$$

where $\dot{U}_{Th,ideal}$ refers to the part of the rate of change of system thermal energy that is not related to ohmic heating. The expressions for $\dot{U}_{Th\phi\eta}$ and $\dot{U}_{Th\theta\eta}$, the rates of change of thermal energy in the volume associated with ohmic heating due to toroidal and poloidal currents respectively, will be defined in section B.4.

B.4 Magnetic energy

B.4.1 Discretisation of $\dot{U}_{M\theta}$

Referring to equation 5.5.27, the rate of change of the magnetic energy associated with poloidal magnetic field is:

$$\dot{U}_{M\theta} = \frac{1}{2\mu_0} \int \frac{\partial}{\partial t} \left(\left(\frac{\nabla\psi}{r} \right)^2 \right) dV = \frac{1}{\mu_0} \int \frac{1}{r^2} \left(\frac{\partial\psi}{\partial r} \frac{\partial\dot{\psi}}{\partial r} + \frac{\partial\psi}{\partial z} \frac{\partial\dot{\psi}}{\partial z} \right) dV \quad (\text{B.4.1})$$

As described in section B.3.1.1, we need to use the node-to-element differential operators to expand terms with squared derivatives. In terms of the discrete quantities, equation B.4.1 is

$$\begin{aligned} \dot{U}_{M\theta} &= \frac{1}{\mu_0} \underline{dV}^{eT} * \left\{ \left(\underline{\underline{Dr}}^e * \underline{\psi} \right) \circ \left(\underline{\underline{Dr}}^e * \underline{\dot{\psi}} \right) \otimes \underline{r}^{e2} \right\} + \frac{1}{\mu_0} \underline{dV}^{eT} * \left\{ \left(\underline{\underline{Dz}}^e * \underline{\psi} \right) \circ \left(\underline{\underline{Dz}}^e * \underline{\dot{\psi}} \right) \otimes \underline{r}^{e2} \right\} \\ &= \frac{2\pi}{\mu_0} (\underline{s}^e \circ \underline{r}^e)^T * \left\{ \left(\underline{\underline{Dr}}^e * \underline{\psi} \right) \circ \left(\underline{\underline{Dr}}^e * \underline{\dot{\psi}} \right) \otimes \underline{r}^{e2} \right\} + \frac{2\pi}{\mu_0} (\underline{s}^e \circ \underline{r}^e)^T * \left\{ \left(\underline{\underline{Dz}}^e * \underline{\psi} \right) \circ \left(\underline{\underline{Dz}}^e * \underline{\dot{\psi}} \right) \otimes \underline{r}^{e2} \right\} \\ &= \frac{2\pi}{\mu_0} \left(\underline{s}^e \circ \left(\underline{\underline{Dr}}^e * \underline{\psi} \right) \otimes \underline{r}^e \right)^T * \left(\underline{\underline{Dr}}^e * \underline{\dot{\psi}} \right) + \frac{2\pi}{\mu_0} \left(\underline{s}^e \circ \left(\underline{\underline{Dz}}^e * \underline{\psi} \right) \otimes \underline{r}^e \right)^T * \left(\underline{\underline{Dz}}^e * \underline{\dot{\psi}} \right) \\ &= \frac{2\pi}{\mu_0} \underline{\dot{\psi}}^T * \left(\underline{\underline{Dr}}^{eT} * \left(\underline{s}^e \circ \left(\underline{\underline{Dr}}^e * \underline{\psi} \right) \otimes \underline{r}^e \right) + \underline{\underline{Dz}}^{eT} * \left(\underline{s}^e \circ \left(\underline{\underline{Dz}}^e * \underline{\psi} \right) \otimes \underline{r}^e \right) \right) \\ &= \frac{2\pi}{\mu_0} \underline{\dot{\psi}}^T * \left(\underline{\underline{K}} * \underline{\psi} \right) \end{aligned} \quad (\text{B.4.2})$$

where $\underline{\underline{K}} = \underline{\underline{Dr}}^{eT} * \underline{\widehat{S}} * \underline{\widehat{R}}^{-1} * \underline{\underline{Dr}}^e + \underline{\underline{Dz}}^{eT} * \underline{\widehat{S}} * \underline{\widehat{R}}^{-1} * \underline{\underline{Dz}}^e$. Using identity B.1.4, equation B.4.2 can be re-expressed as

$$\begin{aligned} \dot{U}_{M\theta} &= \frac{2\pi}{3} (\underline{s} \circ \underline{r})^T * \left(\left(3 \dot{\psi} \circ (\underline{\underline{K}} * \underline{\psi}) \right) \otimes (\mu_0 \underline{s} \circ \underline{r}) \right) \\ &= \underline{dV}^T * \left\{ \left(\dot{\psi} \circ \left(3 \underline{\underline{R}} * \underline{\underline{S}}^{-1} * \underline{\underline{K}} \right) * \underline{\psi} \right) \otimes \left(\mu_0 \underline{r}^2 \right) \right\} \\ &= \underline{dV}^T * \left\{ \left(-\dot{\psi} \circ \left(\underline{\underline{\Delta}}^* \underline{\psi} \right) \right) \otimes \left(\mu_0 \underline{r}^2 \right) \right\} \end{aligned} \quad (\text{B.4.3})$$

In the last step, the definition $\underline{\underline{\Delta}}^* = -3\underline{R} * \underline{\underline{S}}^{-1} * \underline{\underline{K}}$ was used (refer to equations 5.4.15 and 5.4.19). Expressed in terms of discrete quantities and operators, equation 5.5.17 is:

$$\dot{\underline{\psi}} = \dot{\underline{\psi}}_{ideal} + \dot{\underline{\psi}}_\eta = -\underline{\mathbf{v}} \circ (\underline{\nabla} \underline{\psi}) + \underline{\eta} \circ (\underline{\underline{\Delta}}^* \underline{\psi}) \quad (\text{B.4.4})$$

The combination of equations B.4.3 and B.4.4 leads to

$$\dot{U}_{M\theta ideal} = \underline{dV}^T * \left\{ \left((v_r \circ (\underline{Dr} * \underline{\psi}) + v_z \circ (\underline{Dz} * \underline{\psi})) \circ (\underline{\underline{\Delta}}^* \underline{\psi}) \right) \otimes (\mu_0 \underline{r}^2) \right\} \quad (\text{B.4.5})$$

and

$$\dot{U}_{M\theta\eta} = \underline{dV}^T * \left\{ \left(-\underline{\eta} \circ (\underline{\underline{\Delta}}^* \underline{\psi})^2 \right) \otimes (\mu_0 \underline{r}^2) \right\} \quad (\text{B.4.6})$$

Here, $\dot{U}_{M\theta ideal}$ and $\dot{U}_{M\theta\eta}$ are the parts of $\dot{U}_{M\theta}$ due to advective and diffusive (*i.e.*, resistive) effects respectively. The two terms that define the coefficients of the velocity components in the expression for $\dot{U}_{M\theta ideal}$ will constitute part of the formulation for the $\mathbf{J} \times \mathbf{B}$ force in the discretised momentum equation. This can be verified as follows:

$$\mathbf{J} \times \mathbf{B} = (J_\phi B_z - J_z B_\phi) \hat{\mathbf{r}} + (J_z B_r - J_r B_z) \hat{\phi} + (J_r B_\phi - J_\phi B_r) \hat{\mathbf{z}} \quad (\text{B.4.7})$$

Equation A.7.18 defines the components of \mathbf{B} and \mathbf{J} :

$$\begin{aligned} B_r &= -\frac{1}{r} \frac{\partial \psi}{\partial z} & B_\phi &= \frac{f(\psi)}{r} & B_z &= \frac{1}{r} \frac{\partial \psi}{\partial r} \\ J_r &= -\frac{1}{\mu_0 r} \frac{\partial f(\psi)}{\partial z} & J_\phi &= -\frac{1}{\mu_0 r} \Delta^* \psi & J_z &= \frac{1}{\mu_0 r} \frac{\partial f(\psi)}{\partial r} \end{aligned} \quad (\text{B.4.8})$$

It can be seen that the terms in equation B.4.5 will contribute to the r and z components of the $\mathbf{J} \times \mathbf{B}$ force in the discretised momentum equation, making up the 1^{st} ($J_\phi B_z = -\frac{1}{\mu_0 r^2} \frac{\partial \psi}{\partial r} \Delta^* \psi$) and 6^{th} ($-J_\phi B_r = -\frac{1}{\mu_0 r^2} \frac{\partial \psi}{\partial z} \Delta^* \psi$) terms in equation B.4.7. The remaining terms in equation B.4.7 will arise from the rearrangement of terms in the expression for the rate of change of the part of magnetic energy associated with toroidal magnetic field.

Since toroidal currents in the plasma decay resistively with time, $\dot{U}_{M\theta\eta} < 0$ (equation B.4.6), as expected. It is also expected that the reduction in the magnetic energy associated with poloidal magnetic field would be balanced by the increase in thermal energy associated with ohmic heating due to toroidal currents. Referring to equation A.8.3, and recalling that $\dot{U}_{Th} = \int \frac{\dot{p}}{\gamma-1} dV$ (equation B.3.1), the expression for $\dot{U}_{Th\phi\eta}$, the part of the rate of change of thermal energy in the volume due to toroidal currents, is $\dot{U}_{Th\phi\eta} = \int \eta' J_\phi^2 dV$. From equation

B.4.8, $J_\phi = -\frac{1}{\mu_0 r} \Delta^* \psi$, and $\eta' = \mu_0 \eta$, so that the discrete form of $\eta' J_\phi^2$, which will appear in the discrete form of the energy equation, is

$$(\eta' J_\phi^2)_{disc} = (\underline{\eta} / \mu_0) \circ ((\underline{\Delta}^* \underline{\psi}) \otimes \underline{r})^2 \quad (\text{B.4.9})$$

Hence, referring to equation **B.4.6**, $\dot{U}_{M\theta\eta} = -\dot{U}_{Th\phi\eta}$, as expected:

$$\dot{U}_{M\theta\eta} = -\dot{U}_{Th\phi\eta} = \underline{dV}^T * \left\{ -\underline{\eta} \circ (\underline{\Delta}^* \underline{\psi})^2 \otimes (\mu_0 \underline{r}^2) \right\} \quad (\text{B.4.10})$$

Finally, from equations **B.4.5** and **B.4.10**, the required expression for $\dot{U}_{M\phi\eta}$ is

$$\begin{aligned} \dot{U}_{M\theta} &= \dot{U}_{M\theta ideal} + \dot{U}_{M\theta\eta} \\ &= \underline{dV}^T * \left\{ \left((\underline{v}_r \circ (\underline{Dr} * \underline{\psi}) + \underline{v}_z \circ (\underline{Dz} * \underline{\psi})) \circ (\underline{\Delta}^* \underline{\psi}) \right) \otimes (\mu_0 \underline{r}^2) \right\} - \dot{U}_{Th\phi\eta} \end{aligned} \quad (\text{B.4.11})$$

B.4.2 Discretisation of $\dot{U}_{M\phi}$

In terms of discrete quantities, the rate of change of the part of magnetic energy associated with toroidal magnetic field is

$$\dot{U}_{M\phi} = \frac{1}{\mu_0} \underline{dV}^T * \left\{ \underline{f} \circ \dot{\underline{f}} \otimes \underline{r}^2 \right\} \quad (\text{B.4.12})$$

Referring to equation **5.5.18**, the discrete form for $\dot{\underline{f}}_{ideal}$ is

$$\dot{\underline{f}}_{ideal} = \underline{r}^2 \circ \left[-\underline{\nabla} \cdot (\underline{f} \circ \underline{\mathbf{v}} \otimes \underline{r}^2) + \underline{\nabla}_n \cdot (\underline{\mathbf{B}}_\theta^e \circ \underline{\omega}^e) \right] \quad (\text{B.4.13})$$

where, with reference to equation **B.4.8**, $\underline{\mathbf{B}}_\theta^e = \left(-(\underline{Dz}^e * \underline{\psi}) \hat{\mathbf{r}} + (\underline{Dr}^e * \underline{\psi}) \hat{\mathbf{z}} \right) \otimes \underline{r}^e$. Note that, with azimuthal symmetry, the toroidal component of \mathbf{B} can be dropped from the second divergence term in the expression for $\dot{\underline{f}}_{ideal}$. Note that, for consistency with the numerical scheme, the second derivatives in the 2^{nd} term in equation **B.4.13** are expressed as successive applications of the node-to-element and element-to-node differential operators. Hence, the discrete form for $\dot{U}_{M\phi ideal}$ is

$$\begin{aligned} \dot{U}_{M\phi ideal} &= \frac{1}{\mu_0} \underline{dV}^T * \left\{ \underline{f} \circ \dot{\underline{f}}_{ideal} \otimes \underline{r}^2 \right\} \\ &= \underline{dV}^T * \left\{ \left[-\underline{f} \circ (\underline{Dr} * (\underline{v}_r \circ \underline{f} \otimes \underline{r})) - \underline{f} \circ (\underline{Dz} * (\underline{v}_z \circ \underline{f} \otimes \underline{r})) \right. \right. \\ &\quad \left. \left. - \underline{f} \circ (\underline{Dr}_n * (\underline{\omega}^e \circ (\underline{Dz}^e * \underline{\psi}))) + \underline{f} \circ (\underline{Dz}_n * (\underline{\omega}^e \circ (\underline{Dr}^e * \underline{\psi}))) \right] \otimes (\mu_0 \underline{r}) \right\} \end{aligned} \quad (\text{B.4.14})$$

Here, the vector of element-based angular speeds is $\underline{\omega}^e = < \underline{v}_\phi \otimes \underline{r} >^e$ (equation 5.3.1). The first term is

$$\begin{aligned}
\dot{U}_{M\phi ideal_1} &= -\frac{2\pi}{3} (\underline{s} \circ \underline{r})^T * \left\{ \underline{f} \circ \left(\underline{\underline{D}}r * \left(\underline{v}_r \circ \underline{f} \otimes \underline{r} \right) \right) \otimes (\mu_0 \underline{r}) \right\} \\
&= -\frac{2\pi}{3\mu_0} \underline{s}^T * \left\{ \underline{f} \circ \left(\underline{\underline{D}}r * \left(\underline{v}_r \circ \underline{f} \otimes \underline{r} \right) \right) \right\} \\
&= -\frac{2\pi}{3\mu_0} \underline{f}^T * \underline{\underline{S}} * \left(\underline{\underline{D}}r * \left(\underline{v}_r \circ \underline{f} \otimes \underline{r} \right) \right) && \text{(use eqn. B.1.3)} \\
&= -\frac{2\pi}{3\mu_0} \left(\underline{v}_r \circ \underline{f} \otimes \underline{r} \right)^T * \underline{\underline{D}}r^T * \underline{\underline{S}} * \underline{f} && \text{(transpose the scalar)} \\
&= +\frac{2\pi}{3\mu_0} \left(\underline{v}_r \circ \underline{f} \otimes \underline{r} \right)^T * \underline{\underline{S}} * \underline{\underline{D}}r * \underline{f} && \text{(use eqn. B.2.5)} \\
&= \frac{2\pi}{3\mu_0} \underline{s}^T * \left(\left(\underline{v}_r \circ \underline{f} \otimes \underline{r} \right) \circ \left(\underline{\underline{D}}r * \underline{f} \right) \right) && \text{(use eqn. B.1.3)} \\
&= \frac{2\pi}{3\mu_0} (\underline{s} \circ \underline{r})^T * \left(\left(\underline{v}_r \circ \underline{f} \otimes \underline{r}^2 \right) \circ \left(\underline{\underline{D}}r * \underline{f} \right) \right) \\
&= \underline{dV}^T * \left\{ \underline{v}_r \circ \left(\underline{f} \circ \left(\underline{\underline{D}}r * \underline{f} \right) \otimes (\mu_0 \underline{r}^2) \right) \right\}
\end{aligned}$$

Note that in the 5th step, the differential operator property defined in equation B.2.5 was used, with the assumption of boundary condition $v_r|_\Gamma = 0$. Similarly, the second term is

$$\dot{U}_{M\phi ideal_2} = \underline{dV}^T * \left\{ \underline{v}_z \circ \left(\underline{f} \circ \left(\underline{\underline{D}}z * \underline{f} \right) \otimes (\mu_0 \underline{r}^2) \right) \right\}$$

The third term is

$$\begin{aligned}
\dot{U}_{M\phi ideal}^3 &= -\frac{2\pi}{3} (\underline{s} \circ \underline{r})^T * \left\{ \underline{f} \circ \left(\underline{\underline{D}r_n} * \left(\underline{\omega^e} \circ \left(\underline{\underline{D}z^e} * \underline{\psi} \right) \right) \right) \otimes (\mu_0 \underline{r}) \right\} \\
&= -\frac{2\pi}{3\mu_0} \underline{s}^T * \left\{ \underline{f} \circ \left(\underline{\underline{D}r_n} * \left(\underline{\omega^e} \circ \left(\underline{\underline{D}z^e} * \underline{\psi} \right) \right) \right) \right\} \\
&= -\frac{2\pi}{3\mu_0} \underline{f}^T * \underline{\underline{S}} * \left(\underline{\underline{D}r_n} * \left(\underline{\omega^e} \circ \left(\underline{\underline{D}z^e} * \underline{\psi} \right) \right) \right) \quad (\text{use eqn. B.1.3}) \\
&= -\frac{2\pi}{3\mu_0} \left(\underline{\omega^e} \circ \left(\underline{\underline{D}z^e} * \underline{\psi} \right) \right)^T * \underline{\underline{D}r_n}^T * \underline{\underline{S}} * \underline{f} \quad (\text{transpose the scalar}) \\
&= -\frac{2\pi}{3\mu_0} \left(\underline{\omega^e} \circ \left(\underline{\underline{D}z^e} * \underline{\psi} \right) \right)^T * \left(-3 \underline{\underline{S}}^{-1} * \left(\underline{\underline{D}r^{eT}} * \underline{\underline{S}} \right) \right)^T * \underline{\underline{S}} * \underline{f} \quad (\text{use eqn. 5.4.15}) \\
&= +\frac{2\pi}{\mu_0} \left(\underline{\omega^e} \circ \left(\underline{\underline{D}z^e} * \underline{\psi} \right) \right)^T * \left(\underline{\underline{S}} * \underline{\underline{D}r^e} * \underline{f} \right) \quad (\text{transpose}) \\
&= \frac{2\pi}{\mu_0} \underline{s}^{eT} * \left\{ \left(\underline{\omega^e} \circ \left(\underline{\underline{D}z^e} * \underline{\psi} \right) \right) \circ \left(\underline{\underline{D}r^e} * \underline{f} \right) \right\} \quad (\text{use eqn. B.1.3}) \\
&= \frac{2\pi}{\mu_0} \left(\underline{s^e} \circ \underline{r^e} \right)^T * \left\{ \left(\underline{\omega^e} \circ \left(\underline{\underline{D}z^e} * \underline{\psi} \right) \right) \otimes \underline{r^e} \right\} \circ \left(\underline{\underline{D}r^e} * \underline{f} \right) \\
&= \underline{dV}^{eT} * \left\{ \underline{\omega^e} \circ \left(\left(\underline{\underline{D}z^e} * \underline{\psi} \right) \circ \left(\underline{\underline{D}r^e} * \underline{f} \right) \right) \otimes \underline{r^e} \right\} / \mu_0 \\
&= \underline{dV}^T * \left\{ \underline{\omega} \circ \left(\underline{W_n} * \left(\left(\underline{\underline{D}z^e} * \underline{\psi} \right) \circ \left(\underline{\underline{D}r^e} * \underline{f} \right) \right) \otimes \underline{r^e} \right) \right\} / \mu_0 \quad (\text{use eqn. 5.3.4}) \\
&= \underline{dV}^T * \left\{ \underline{v_\phi} \circ \left(\underline{W_n} * \left(\left(\underline{\underline{D}z^e} * \underline{\psi} \right) \circ \left(\underline{\underline{D}r^e} * \underline{f} \right) \right) \otimes \underline{r^e} \right) \right\} \otimes (\mu_0 \underline{r})
\end{aligned}$$

Note that in the second last step, the volume-averaging operation, defined by equation 5.3.4, where $\underline{Q^e} = \underline{\omega^e}$ and $\underline{U^e} = \left(\left(\underline{\underline{D}z^e} * \underline{\psi} \right) \circ \left(\underline{\underline{D}r^e} * \underline{f} \right) \right) \otimes \underline{r^e}$, has been implemented. By the same procedure, the 4th term in equation B.4.14 is

$$\dot{U}_{M\phi ideal}^4 = \underline{dV}^T * \left\{ -\underline{v_\phi} \circ \left(\underline{W_n} * \left(\left(\underline{\underline{D}r^e} * \underline{\psi} \right) \circ \left(\underline{\underline{D}z^e} * \underline{f} \right) \right) \otimes \underline{r^e} \right) \right\} \otimes (\mu_0 \underline{r})$$

Collecting terms, the resultant expression for $\dot{U}_{M\phi ideal}$ is

$$\begin{aligned}
\dot{U}_{M\phi ideal} &= \underline{dV}^T * \left\{ \left[\underline{v_r} \circ \left(\underline{f} \circ \left(\underline{\underline{D}r} * \underline{f} \right) \right) + \underline{v_z} \circ \left(\underline{f} \circ \left(\underline{\underline{D}z} * \underline{f} \right) \right) \right. \right. \\
&\quad \left. \left. - \underline{v_\phi} \circ \left(\underline{r} \circ \left(\underline{W_n} * \left(\underline{\underline{B}_\theta^e} \cdot \left(\underline{\nabla^e} \underline{f} \right) \right) \right) \right) \right] \otimes \left(\mu_0 \underline{r}^2 \right) \right\} \quad (\text{B.4.15})
\end{aligned}$$

Recall that the 1st and 6th terms in the expression for the $\mathbf{J} \times \mathbf{B}$ force (equation B.4.7) arose from the rearrangement of terms in the expression for the rate of change of the part of magnetic energy associated with poloidal magnetic field, and will contribute to the r and z components of the $\mathbf{J} \times \mathbf{B}$ force in the discretised momentum equation. Referring to equations B.4.7 and B.4.8, which define the components of the $\mathbf{J} \times \mathbf{B}$ force, it can be seen

that the remaining four terms that will be included in the discretised momentum equation are contained in equation B.4.15.

The discrete form of the part of $\dot{U}_{M\phi}$ pertaining to diffusive effects is

$$\dot{U}_{M\phi\eta} = \frac{1}{\mu_0} \underline{dV}^T * \left\{ \underline{f} \circ \dot{\underline{f}}_\eta \oslash \underline{r}^2 \right\} \quad (\text{B.4.16})$$

We expect that the reduction in the magnetic energy associated with toroidal magnetic field would be balanced by the increase in thermal energy due ohmic heating associated with poloidal currents, *i.e.*, $\dot{U}_{M\phi\eta} = -\dot{U}_{Th\theta\eta}$. The part of the rate of change of thermal energy in the volume due to ohmic heating with toroidal currents, is $\dot{U}_{Th\theta\eta} = \int \eta' J_\theta^2 dV$. Referring to equation B.4.8, the discrete form of $\eta' J_\theta^2 = \eta' \left(\frac{1}{\mu_0 r} \nabla f \right)^2$, is

$$\left(\eta' J_\theta^2 \right)_{disc} = \left(\eta^e / \mu_0 \right) \circ \left(\left(\underline{\nabla}^e f \right) \oslash \underline{r}^e \right)^2$$

Once again, for consistency with the numerical scheme, derivatives squared have been expressed with node-to-element differential operators. $\underline{\eta}^e = \langle \underline{\eta} \rangle^e$ (equation 5.3.1) is the vector of element-based resistive diffusivities. Referring to equation 5.3.3, note that $(\eta' J_\theta^2)_{disc}$ can be expressed as a node-based volume-average, which will appear in the discrete form of the energy equation:

$$\left(\eta' J_\theta^2 \right)_{disc} = \underline{\underline{W}_n} * \left(\left(\underline{\eta}^e / \mu_0 \right) \circ \left(\left(\underline{\nabla}^e f \right) \oslash \underline{r}^e \right)^2 \right) \quad (\text{B.4.17})$$

The identity $\dot{U}_{M\phi\eta} = -\dot{U}_{Th\theta\eta}$ implies that

$$\dot{U}_{M\phi\eta} = -\dot{U}_{Th\theta\eta} = -\frac{1}{\mu_0} \underline{dV}^{eT} * \left\{ \left(\left(\underline{\underline{D}} \underline{r}^e * \underline{f} \right)^2 + \left(\underline{\underline{D}} \underline{z}^e * \underline{f} \right)^2 \right) \circ \underline{\eta}^e \oslash \underline{r}^{e2} \right\} \quad (\text{B.4.18})$$

In order to find the discrete form of $\dot{\underline{f}}_\eta$, we can start by defining

$$\dot{\underline{f}}_\eta = \underline{\underline{D}} * \underline{f} \quad (\text{B.4.19})$$

Equations B.4.16 and B.4.18 imply that

$$\begin{aligned}
& \frac{1}{\mu_0} \underline{dV}^T * \left\{ \underline{f} \circ \dot{\underline{f}}_\eta \otimes \underline{r}^2 \right\} = -\frac{1}{\mu_0} \underline{dV}^{eT} * \left\{ \left((\underline{\underline{D}} * \underline{f})^2 + (\underline{\underline{Dz}}^e * \underline{f})^2 \right) \circ \underline{\eta}^e \otimes \underline{r}^{e2} \right\} \\
& \Rightarrow \frac{1}{3} (\underline{s} \circ \underline{r})^T * \left\{ \underline{f} \circ (\underline{\underline{D}} * \underline{f}) \otimes \underline{r}^2 \right\} = -(\underline{s}^e \circ \underline{r}^e)^T * \left\{ \left((\underline{\underline{Dr}}^e * \underline{f})^2 + (\underline{\underline{Dz}}^e * \underline{f})^2 \right) \circ \underline{\eta}^e \otimes \underline{r}^{e2} \right\} \\
& \Rightarrow \frac{1}{3} \underline{s}^T * \left\{ \underline{f} \circ (\underline{\underline{D}} * \underline{f}) \otimes \underline{r} \right\} = -\underline{s}^e * \left\{ \left((\underline{\underline{Dr}}^e * \underline{f})^2 + (\underline{\underline{Dz}}^e * \underline{f})^2 \right) \circ \underline{\eta}^e \otimes \underline{r}^e \right\} \\
& \Rightarrow \frac{1}{3} (\underline{s} \otimes \underline{r})^T * \left\{ \underline{f} \circ (\underline{\underline{D}} * \underline{f}) \right\} = -(\underline{s}^e \circ \underline{\eta}^e \otimes \underline{r}^e)^T * \left\{ \left((\underline{\underline{Dr}}^e * \underline{f})^2 + (\underline{\underline{Dz}}^e * \underline{f})^2 \right) \circ \underline{\eta}^e \otimes \underline{r}^e \right\} \\
& \Rightarrow \frac{1}{3} \underline{f}^T * \underline{\underline{S}} * \underline{\underline{R}}^{-1} * (\underline{\underline{D}} * \underline{f}) = -(\underline{\underline{Dr}}^e * \underline{f})^T * \underline{\underline{S}} * \underline{\hat{\eta}} * \underline{\underline{R}}^{-1} * (\underline{\underline{Dr}}^e * \underline{f}) \quad (\text{use eqn. B.1.3}) \\
& \quad - (\underline{\underline{Dz}}^e * \underline{f})^T * \underline{\underline{S}} * \underline{\hat{\eta}} * \underline{\underline{R}}^{-1} * (\underline{\underline{Dz}}^e * \underline{f}) \\
& \Rightarrow \frac{1}{3} \underline{f}^T * \underline{\underline{S}} * \underline{\underline{R}}^{-1} * (\underline{\underline{D}} * \underline{f}) = -(\underline{f}^T * \underline{\underline{Dr}}^{eT}) * \underline{\underline{S}} * \underline{\hat{\eta}} * \underline{\underline{R}}^{-1} * (\underline{\underline{Dr}}^e * \underline{f}) \\
& \quad - (\underline{f}^T * \underline{\underline{Dz}}^{eT}) * \underline{\underline{S}} * \underline{\hat{\eta}} * \underline{\underline{R}}^{-1} * (\underline{\underline{Dz}}^e * \underline{f}) \\
& \Rightarrow \frac{1}{3} \underline{f}^T * \underline{\underline{S}} * \underline{\underline{R}}^{-1} * (\underline{\underline{D}} * \underline{f}) = -\underline{f}^T * \underline{\underline{K1}} * \underline{f}
\end{aligned}$$

where $\underline{\hat{\eta}}$ is the diagonal matrix constructed from $\underline{\eta}^e$, and

$$\underline{\underline{K1}} = \underline{\underline{Dr}}^{eT} * \underline{\underline{S}} * \underline{\hat{\eta}} * \underline{\underline{R}}^{-1} * \underline{\underline{Dr}}^e + \underline{\underline{Dz}}^{eT} * \underline{\underline{S}} * \underline{\hat{\eta}} * \underline{\underline{R}}^{-1} * \underline{\underline{Dz}}^e \quad (\text{B.4.20})$$

so that

$$\underline{\underline{D}} = -3 \underline{\underline{R}} * \underline{\underline{S}}^{-1} * \underline{\underline{K1}} \quad (\text{B.4.21})$$

With reference to equations 5.4.12 and 5.4.15, which define the element-to-node divergence operation and differential operators, equations B.4.19 and B.4.21 imply that

$$\begin{aligned}
\dot{\underline{f}}_\eta &= \underline{\underline{D}} * \underline{f} \\
&= \underline{r}^2 \circ \underline{\nabla}_n \cdot (\underline{\eta}^e \circ (\underline{\nabla}^e \underline{f}) \otimes \underline{r}^{e2})
\end{aligned} \quad (\text{B.4.22})$$

Note that the expressions for the element-to-node differential operators were undefined at the time of the development of the discrete momentum equation for system energy conservation. Back then, only the forms of the element-to-node and node-to-node operators were known - the process outlined here to construct an expression for $\dot{\underline{f}}_\eta$ helped to define the element-to-node operators, and confirms that $\dot{U}_{M\phi_\eta} = -\dot{U}_{Th\theta_\eta}$ in discrete form. Now, with the operators and their properties pre-defined, equation B.4.22 is obviously just the discrete form of \dot{f}_η as defined by equation 5.5.18, with continuous differential operators simply replaced with the discrete counterparts.

From equation B.4.16, the required expression for $\dot{U}_{M\phi_\eta}$ is

$$\dot{U}_{M\phi_\eta} = -\dot{U}_{Th\theta\eta} = -\underline{dV}^T * \left\{ \underline{f} \circ \left(\underline{\underline{\nabla}}_n \cdot \left(\underline{\eta}^e \circ \left(\underline{\underline{\nabla}}^e \underline{f} \right) \otimes \underline{r}^{e2} \right) \right) / \mu_0 \right\} \quad (\text{B.4.23})$$

In combination with equation B.4.15, this implies that

$$\begin{aligned} \dot{U}_{M\phi} &= \dot{U}_{M\phi_{ideal}} + \dot{U}_{M\phi_\eta} \\ &= \dot{U}_{M\phi_{ideal}} - \dot{U}_{Th\theta\eta} \\ &= \underline{dV}^T * \left\{ \left[\underline{v}_r \circ \left(\underline{f} \circ \left(\underline{\underline{D}}r * \underline{f} \right) \right) + \underline{v}_z \circ \left(\underline{f} \circ \left(\underline{\underline{D}}z * \underline{f} \right) \right) \right. \right. \\ &\quad \left. \left. - \underline{v}_\phi \circ \left(\underline{r} \circ \left(\underline{\underline{W}}_n * \left(\underline{\mathbf{B}}_\theta^e \cdot \left(\underline{\underline{\nabla}}^e \underline{f} \right) \right) \right) \right) \right] \otimes \left(\mu_0 \underline{r}^2 \right) \right\} - \dot{U}_{Th\theta\eta} \end{aligned} \quad (\text{B.4.24})$$

B.4.3 Final expression for discretised form of \dot{U}_M

Combining equations B.4.11 and B.4.24, we arrive at the final expression for the discretised form of \dot{U}_M :

$$\begin{aligned} \dot{U}_M &= \dot{U}_{M\theta} + \dot{U}_{M\phi} \\ &= \underline{dV}^T * \left\{ \left[\left(\underline{v}_r \circ \left(\underline{\underline{D}}r * \underline{\psi} \right) + \underline{v}_z \circ \left(\underline{\underline{D}}z * \underline{\psi} \right) \right) \circ \left(\underline{\underline{\Delta}}^* \underline{\psi} \right) \right. \right. \\ &\quad \left. \left. + \underline{v}_r \circ \left(\underline{f} \circ \left(\underline{\underline{D}}r * \underline{f} \right) \right) + \underline{v}_z \circ \left(\underline{f} \circ \left(\underline{\underline{D}}z * \underline{f} \right) \right) \right. \right. \\ &\quad \left. \left. - \underline{v}_\phi \circ \left(\underline{r} \circ \left(\underline{\underline{W}}_n * \left(\underline{\mathbf{B}}_\theta^e \cdot \left(\underline{\underline{\nabla}}^e \underline{f} \right) \right) \right) \right) \right] \otimes \left(\mu_0 \underline{r}^2 \right) \right\} \\ &\quad - \dot{U}_{Th\theta\eta} \quad (\dot{U}_{M\theta\eta}) \\ &\quad - \dot{U}_{Th\theta\eta} \quad (\dot{U}_{M\phi\eta}) \end{aligned} \quad (\text{B.4.25})$$

B.5 Assembly of discretised momentum equation

Combining equations B.2.8, B.3.30, and B.4.25, we obtain the final expression for \dot{U}_{Total} :

$$\begin{aligned}
\dot{U}_{Total} &= \dot{U}_K + \dot{U}_{Th} + \dot{U}_M \\
&= \underline{dV}^T * \left\{ \underline{v}_r \circ \left(\underline{\rho} \circ \left(\underline{\underline{D}}r * \left(\frac{\underline{v}^2}{2} \right) \right) \right) + \underline{v}_z \circ \left(\underline{\rho} \circ \left(\underline{\underline{D}}z * \left(\frac{\underline{v}^2}{2} \right) \right) \right) \right. \\
&\quad + \underline{\rho} \circ \underline{v}_r \circ \dot{v}_r + \underline{\rho} \circ \underline{v}_\phi \circ \dot{v}_\phi + \underline{\rho} \circ \underline{v}_z \circ \dot{v}_z \quad (\dot{U}_K) \\
&\quad - \underline{\rho} \circ \underline{v}_r \circ \left(-\underline{v}_z \circ \left(\underline{\underline{D}}z * \underline{v}_r - \underline{\underline{D}}r * \underline{v}_z \right) + \underline{v}_\phi \circ \left(\underline{\underline{D}}r * \left(\underline{r} \circ \underline{v}_\phi \right) \right) \otimes \underline{r} \right) \quad (\dot{U}_K) \\
&\quad - \underline{\rho} \circ \underline{v}_\phi \circ \left(-\underline{\mathbf{v}} \cdot \left(\underline{\nabla} \left(\underline{r} \circ \underline{v}_\phi \right) \right) \otimes \underline{r} \right) \quad (\dot{U}_K) \\
&\quad - \underline{\rho} \circ \underline{v}_z \circ \left(\underline{v}_r \circ \left(\underline{\underline{D}}z * \underline{v}_r - \underline{\underline{D}}r * \underline{v}_z \right) + \underline{v}_\phi \circ \left(\underline{\underline{D}}z * \left(\underline{r} \circ \underline{v}_\phi \right) \right) \otimes \underline{r} \right) \quad (\dot{U}_K) \\
&\quad + \underline{v}_r \circ \left(\underline{\underline{D}}r * \underline{p} + \underline{\Pi}_r \right) + \underline{v}_\phi \circ \underline{\Pi}_\phi + \underline{v}_z \circ \left(\underline{\underline{D}}z * \underline{p} + \underline{\Pi}_z \right) \quad (\dot{U}_{Th\,ideal}) \\
&\quad \left. + \underline{\dot{U}}_{Th\phi\eta} \right. \quad (\dot{U}_{Th\phi\eta}) \\
&\quad \left. + \underline{\dot{U}}_{Th\theta\eta} \right. \quad (\dot{U}_{Th\theta\eta}) \\
&\quad + \left[\left(\underline{v}_r \circ \left(\underline{\underline{D}}r * \underline{\psi} \right) + \underline{v}_z \circ \left(\underline{\underline{D}}z * \underline{\psi} \right) \right) \circ \left(\underline{\Delta}^* \underline{\psi} \right) \right. \quad (\dot{U}_{M\theta\,ideal}) \\
&\quad + \underline{v}_r \circ \left(\underline{f} \circ \left(\underline{\underline{D}}r * \underline{f} \right) \right) + \underline{v}_z \circ \left(\underline{f} \circ \left(\underline{\underline{D}}z * \underline{f} \right) \right) \quad (\dot{U}_{M\phi\,ideal}) \\
&\quad \left. - \underline{v}_\phi \circ \left(\underline{r} \circ \left(\underline{\underline{W}}_n * \left(\underline{\mathbf{B}}_\theta^e \cdot \left(\underline{\nabla}^e \underline{f} \right) \right) \right) \right) \right] \otimes \left(\mu_0 \underline{r}^2 \right) \quad (\dot{U}_{M\phi\,ideal}) \\
&\quad \left. - \underline{\dot{U}}_{Th\phi\eta} \right. \quad (\dot{U}_{M\theta\eta}) \\
&\quad \left. - \underline{\dot{U}}_{Th\theta\eta} \right. \quad (\dot{U}_{M\phi\eta})
\end{aligned}$$

Collecting the terms that make up the coefficients of each velocity component, we obtain:

$$\begin{aligned}
\dot{U}_{Total} &= \underline{dV}^T * \left\{ \underline{v}_r \circ \left[\underline{\rho} \circ \dot{v}_r + \underline{\rho} \circ \left(\underline{\underline{D}}r * \left(\frac{\underline{v}^2}{2} \right) \right) \right. \right. \\
&\quad - \underline{\rho} \circ \left(-\underline{v}_z \circ \left(\underline{\underline{D}}z * \underline{v}_r - \underline{\underline{D}}r * \underline{v}_z \right) + \underline{v}_\phi \circ \left(\underline{\underline{D}}r * \left(\underline{r} \circ \underline{v}_\phi \right) \right) \otimes \underline{r} \right) \\
&\quad + \underline{\underline{D}}r * \underline{p} + \underline{\Pi}_r + \left[\left(\underline{\underline{D}}r * \underline{\psi} \right) \circ \left(\underline{\Delta}^* \underline{\psi} \right) + \left(\underline{f} \circ \left(\underline{\underline{D}}r * \underline{f} \right) \right) \right] \otimes \left(\mu_0 \underline{r}^2 \right) \left. \right] \\
&\quad + \underline{v}_\phi \circ \left[\underline{\rho} \circ \dot{v}_\phi - \underline{\rho} \circ \left(-\underline{\mathbf{v}} \cdot \left(\underline{\nabla} \left(\underline{r} \circ \underline{v}_\phi \right) \right) \otimes \underline{r} \right) \right. \\
&\quad + \underline{\Pi}_\phi - \left(\underline{\underline{W}}_n * \left(\underline{\mathbf{B}}_\theta^e \cdot \left(\underline{\nabla}^e \underline{f} \right) \right) \right) \otimes \left(\mu_0 \underline{r} \right) \left. \right] \\
&\quad + \underline{v}_z \circ \left[\underline{\rho} \circ \dot{v}_z + \underline{\rho} \circ \left(\underline{\underline{D}}z * \left(\frac{\underline{v}^2}{2} \right) \right) \right. \\
&\quad - \underline{\rho} \circ \left(\underline{v}_r \circ \left(\underline{\underline{D}}z * \underline{v}_r - \underline{\underline{D}}r * \underline{v}_z \right) + \underline{v}_\phi \circ \left(\underline{\underline{D}}z * \left(\underline{r} \circ \underline{v}_\phi \right) \right) \otimes \underline{r} \right) \\
&\quad + \underline{\underline{D}}z * \underline{p} + \underline{\Pi}_z + \left[\left(\underline{\underline{D}}z * \underline{\psi} \right) \circ \left(\underline{\Delta}^* \underline{\psi} \right) + \underline{f} \circ \left(\underline{\underline{D}}z * \underline{f} \right) \right] \otimes \left(\mu_0 \underline{r}^2 \right) \left. \right] \left. \right\} \quad (B.5.1)
\end{aligned}$$

Now, the only way to achieve $\dot{U}_{Total} = 0$, apart from having all velocity components equal to zero everywhere, is to set the expressions that make up the coefficients of the velocity components individually to zero, leading to the components of the discretised momentum equation, which are presented along with the discrete forms of the continuity and energy equations, and discretised expressions for $\dot{\psi}$ and \dot{f} , in the following appendix summary.

B.6 Summary

Here, the complete set of discretised equations for the axisymmetric MHD model, in a form that ensures conservation of total system energy, are collected. The discrete form of the expression for mass conservation is given by equation B.2.3:

$$\dot{n} = -\underline{\nabla} \cdot (\underline{n} \circ \underline{\mathbf{v}})$$

From equation B.5.1, the discrete forms of the components of the momentum conservation equation are

$$\begin{aligned} \dot{v}_r &= \underbrace{-\underline{Dr} * \left(\frac{v^2}{2}\right) - \underline{v}_z \circ (\underline{Dz} * \underline{v}_r - \underline{Dr} * \underline{v}_z) + \underline{v}_\phi \circ (\underline{Dr} * (\underline{r} \circ \underline{v}_\phi)) \oslash \underline{r}}_{-(\mathbf{v} \cdot \nabla \mathbf{v})_r = (-\nabla(v^2/2) + \mathbf{v} \times (\nabla \times \mathbf{v}))_r} - \underbrace{(\underline{Dr} * \underline{p}) \oslash \underline{\rho}}_{-\frac{1}{\rho}(\nabla p)_r} \\ &\quad - \underbrace{\underline{\Pi}_r \oslash \underline{\rho}}_{-\frac{1}{\rho}(\nabla \cdot \bar{\pi})_r} + \underbrace{(-(\underline{Dr} * \underline{\psi}) \circ (\underline{\Delta}^* \underline{\psi}) - (\underline{f} \circ (\underline{Dr} * \underline{f}))) \oslash (\mu_0 \underline{r}^2 \circ \underline{\rho})}_{\frac{1}{\rho}(\mathbf{J} \times \mathbf{B})_r} \\ \dot{v}_\phi &= \underbrace{-\underline{\mathbf{v}} \cdot (\underline{\nabla} (\underline{r} \circ \underline{v}_\phi)) \oslash \underline{r}}_{-(\mathbf{v} \cdot \nabla \mathbf{v})_\phi = (-\nabla(v^2/2) + \mathbf{v} \times (\nabla \times \mathbf{v}))_\phi} - \underbrace{\underline{\Pi}_\phi \oslash \underline{\rho}}_{-\frac{1}{\rho}(\nabla \cdot \bar{\pi})_\phi} + \underbrace{(\underline{W}_n * (\underline{\mathbf{B}}_\theta^e \cdot (\underline{\nabla}^e \underline{f}))) \oslash (\mu_0 \underline{r} \circ \underline{\rho})}_{\frac{1}{\rho}(\mathbf{J} \times \mathbf{B})_\phi} \\ \dot{v}_z &= \underbrace{-\underline{Dz} * \left(\frac{v^2}{2}\right) + \underline{v}_r \circ (\underline{Dz} * \underline{v}_r - \underline{Dr} * \underline{v}_z) + \underline{v}_\phi \circ (\underline{Dz} * (\underline{r} \circ \underline{v}_\phi)) \oslash \underline{r}}_{-(\mathbf{v} \cdot \nabla \mathbf{v})_z = (-\nabla(v^2/2) + \mathbf{v} \times (\nabla \times \mathbf{v}))_z} - \underbrace{(\underline{Dz} * \underline{p}) \oslash \underline{\rho}}_{-\frac{1}{\rho}(\nabla p)_z} \\ &\quad - \underbrace{\underline{\Pi}_z \oslash \underline{\rho}}_{-\frac{1}{\rho}(\nabla \cdot \bar{\pi})_z} + \underbrace{(-(\underline{Dz} * \underline{\psi}) \circ (\underline{\Delta}^* \underline{\psi}) - \underline{f} \circ (\underline{Dz} * \underline{f})) \oslash (\mu_0 \underline{r}^2 \circ \underline{\rho})}_{\frac{1}{\rho}(\mathbf{J} \times \mathbf{B})_z} \end{aligned}$$

Here, the components of $\underline{\Pi}$ represent the discrete forms of the components of $\nabla \cdot \underline{\pi}$, and are defined by equations B.3.16, B.3.24 and B.3.29:

$$\begin{aligned}\underline{\Pi}_r &= \left[-2\underline{Dr}_n * \left(\underline{\mu}^e \circ \underline{r}^e \circ \left(\underline{Dr}^e * \underline{v}_r \right) \right) - \underline{Dz}_n * \left(\underline{\mu}^e \circ \underline{r}^e \circ \left(\underline{Dr}^e * \underline{v}_z + \underline{Dz}^e * \underline{v}_r \right) \right) \right] \oslash \underline{r} \\ &\quad + \frac{2}{3} \left(\underline{\underline{Dr}}_n * \left(\underline{\mu}^e \circ \left(\underline{\nabla}^e \cdot \underline{\mathbf{v}} \right) \right) \right) + 2 \underline{\mu} \circ \underline{v}_r \oslash \underline{r}^2 \\ \underline{\Pi}_\phi &= - \left(\underline{\nabla}_n \cdot \left(\underline{\mu}^e \circ \underline{r}^{e2} \circ \left(\underline{\nabla}^e \omega \right) \right) \right) \oslash \underline{r} \\ \underline{\Pi}_z &= \left[-2\underline{Dz}_n * \left(\underline{\mu}^e \circ \underline{r}^e \circ \left(\underline{Dz}^e * \underline{v}_z \right) \right) - \underline{\underline{Dr}}_n * \left(\underline{\mu}^e \circ \underline{r}^e \circ \left(\underline{Dr}^e * \underline{v}_z + \underline{Dz}^e * \underline{v}_r \right) \right) \right] \oslash \underline{r} \\ &\quad + \frac{2}{3} \left(\underline{\underline{Dz}}_n * \left(\underline{\mu}^e \circ \left(\underline{\nabla}^e \cdot \underline{\mathbf{v}} \right) \right) \right)\end{aligned}\tag{B.6.1}$$

The discrete form of the single fluid energy equation, where thermal diffusion is temporarily neglected, is given by the combination of equations B.3.2, B.3.10, B.4.9, and B.4.17:

$$\begin{aligned}\dot{\underline{p}} &= -\underline{\mathbf{v}} \cdot \left(\underline{\nabla} \underline{p} \right) - \gamma \underline{p} \circ \left(\underline{\nabla} \cdot \underline{\mathbf{v}} \right) + (\gamma - 1) \left[\underbrace{\underline{Q}_\pi}_{-\underline{\pi} : \nabla \mathbf{v}} + \underbrace{\left(\underline{\eta} / \mu_0 \right) \circ \left(\left(\underline{\Delta}^* \underline{\psi} \right) \oslash \underline{r} \right)^2}_{\eta' J_\phi^2} \right. \\ &\quad \left. + \underbrace{\underline{W}_n * \left(\left(\underline{\eta}^e / \mu_0 \right) \circ \left(\left(\underline{\nabla}^e \underline{f} \right) \oslash \underline{r}^e \right)^2 \right)}_{\eta' J_\theta^2} \right]\end{aligned}\tag{B.6.2}$$

Here, \underline{Q}_π , the discrete form of $-\underline{\pi} : \nabla \mathbf{v}$, is given by equation B.3.10:

$$\begin{aligned}\underline{Q}_\pi &= \underline{\underline{W}}_n * \left[\underline{\mu}^e \circ \left\{ 2 \left(\underline{Dr}^e * \underline{v}_r \right)^2 + 2 \left(\underline{Dz}^e * \underline{v}_z \right)^2 + \left(\underline{r}^e \circ \left(\underline{\nabla}^e \omega \right) \right)^2 \right. \right. \\ &\quad \left. \left. + \left(\underline{Dr}^e * \underline{v}_z + \underline{Dz}^e * \underline{v}_r \right)^2 - \frac{2}{3} \left(\underline{\nabla}^e \cdot \underline{\mathbf{v}} \right)^2 \right\} \right] + 2 \underline{\mu} \circ \left(\underline{v}_r \oslash \underline{r} \right)^2\end{aligned}\tag{B.6.3}$$

The discretised single fluid energy equation can be partitioned into parts pertaining to the ions and electrons, as shown in section 5.6.1. Discretised expressions for $\dot{\underline{\psi}}$ and $\dot{\underline{f}}$ are given by equations B.4.4, and the combination of equations B.4.13 and B.4.22:

$$\begin{aligned}\dot{\underline{\psi}} &= -\underline{\mathbf{v}} \cdot \left(\underline{\nabla} \underline{\psi} \right) + \underline{\eta} \circ \left(\underline{\Delta}^* \underline{\psi} \right) \\ \dot{\underline{f}} &= \underline{r}^2 \circ \left[-\underline{\nabla} \cdot \left(\underline{f} \circ \underline{\mathbf{v}} \oslash \underline{r}^2 \right) + \underline{\nabla}_n \cdot \left(\underline{\mathbf{B}}_\theta^e \circ \underline{\omega}^e \right) + \underline{\nabla}_n \cdot \left(\underline{\eta}^e \circ \left(\underline{\nabla}^e \underline{f} \right) \oslash \underline{r}^{e2} \right) \right]\end{aligned}$$

Appendix C

General code setup

In this appendix, general aspects of the code setup will be discussed. Section C.1 describes the computation mesh, and the methods developed to repair damaged meshes and introduce non-uniform cell size. Section C.2 outlines the options implemented for timestepping, and describes the protocols implemented for timestep correction and data preservation. Section C.3 presents a general discussion of diffusion coefficients, and how they are implemented to the code. The numerical methods developed to solve the Grad-Shafranov equation are presented in section C.4. Section C.5 describes the analysis used to verify and validate the code. This appendix concludes with a summary in section C.6.

C.1 Computational grid

We adapted the freely-available DistMesh MATLAB mesh generator algorithms described in [91, 92, 93] to provide the computational grid. DistMesh generates unstructured triangular and tetrahedral meshes, and employs Delaunay triangulation to optimize node locations with a force-based smoothing procedure, regularly updating the topology with the Delaunay routine. The boundary points are restrained and can only move tangentially to the boundary. The r and z coordinates of points that denote the boundary of the computational domain are required as inputs to the meshing program. These points, which should have an interspacing that is sufficiently small for definition of any curved features, can be extracted from Solidworks models of the machine geometry. The points at the corners of the computational domain are assigned as fixed nodes that remain fixed in space during the mesh generation. For simulations where the MHD solutions are coupled to the levitation/compression vacuum field solution (see section 6.2) in electrically insulating areas, fixed nodes are also assigned along the interface between the insulating region and the plasma-domain.

The mesh generator code was found to be not entirely robust, and some repairs had to

be implemented in order to obtain usable meshes.

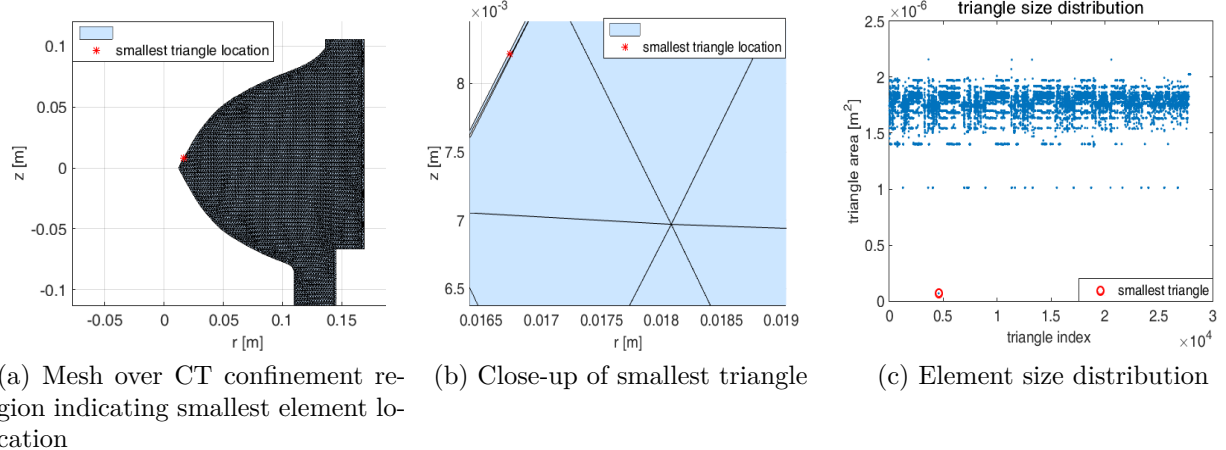


Figure C.1.1: Mesh repairs

In particular, meshes produced with DistMesh would often include exceptionally small elongated triangle elements, usually located near curved boundaries, as indicated in figure C.1.1. Figures C.1.1(a) and (b) show the part of a mesh that represents the CT confinement region, with the smallest triangle highlighted. The figures here are from a Matlab program that was made to diagnose and repair the meshes produced by DistMesh. The mesh shown here is intended to have approximately uniform triangle sizes, $h_e = 2 \text{ mm}$. Figure C.1.1(c) indicates the triangle size distribution.

Arrays \mathbb{P} and \mathbb{T} are the outputs of the DistMesh program. \mathbb{P} has dimensions $[N_n \times 2]$, where N_n is the number of nodes in the mesh; each row contains the r and z coordinates of an individual node. \mathbb{T} has dimensions $[N_e \times 3]$, where N_e is the number of triangles in the mesh, and each row in \mathbb{T} contains the indexes of the nodes that define the vertices of an individual triangle. The node index is defined as the number of the node-corresponding row in \mathbb{P} .

To allow the MHD code to run, any erroneously small triangles must be removed, by deleting the row(s) corresponding to the small triangle(s) in array \mathbb{T} . In cases where the exceptionally small triangle is located exterior to the nominal boundary, for example, as indicated in figures C.1.1(a) and (b), this repair is sufficient. When several tiny triangles are included in the original mesh, removing the corresponding rows from \mathbb{T} may result in mapping errors, leading to holes (missing triangles) in the mesh. This can be addressed by adding new row(s) to \mathbb{T} that include the indexes of the nodes that make up the vertices of the missing element(s).

The MHD code has the option of running with a mesh with uniformly sized triangular elements, or with a mesh with increased resolution near the boundaries. To implement the variable resolution option, the *dpoly* function, that is part of the DistMesh package, is used

calculate the distances from mesh-interior points to the nearest boundary, so that triangle size can be scaled inversely to the distance from the nearest boundary. The principle mesh options for MHD code, characterised by code-parameter *meshtype*, are:

- meshtype* = 0 Uniform triangles of size h_e
- meshtype* = 1 Triangles have size h_e at boundaries, and gradually get bigger towards the interior, to maximum size h_{max} . Triangles in the insulating areas have size h_{max} .
- meshtype* = 2 Triangles have size h_e at boundaries, and gradually get bigger towards the interior, to maximum size h_{max} wherever $d \geq d_{electrode}$ (i.e., distance to nearest boundary is greater or equal to the distance between the inner and outer formation electrodes).

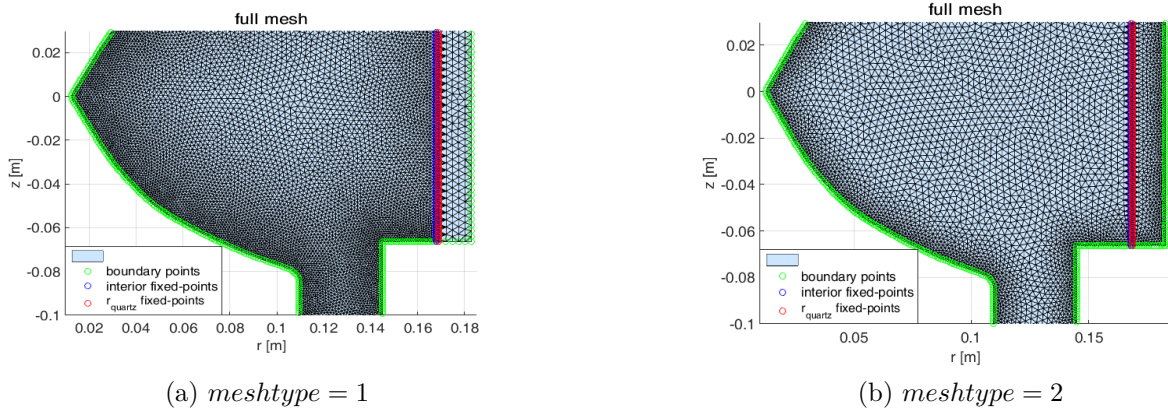


Figure C.1.2: Variable-resolution meshes

Figures C.1.2(a) and (b) indicate sections of meshes produced for cases with *meshtype* = 1 and *meshtype* = 2. The functionality of the indicated interior and r_{quartz} fixed points, which are required to solve different sets of equations in different parts of the domain, is described in section 6.2. In general, as shown in section C.5.1, a good degree of solution accuracy can be obtained with meshes with resolution, defined by h_e , of around 5 mm. Mesh resolution should be increased, to $h_e \sim 2$ mm, for high quality contour plots of output fields. The main benefit of increasing resolution near the boundaries is that simulation times can be reduced (fewer elements) while maintaining resolution at boundaries, where the imposition of temperature and velocity boundary conditions in particular is more likely to lead to solution overshooting with coarser meshes.

C.2 Timestepping methods

The code has the option of using either the forward Euler, Runge-Kutta 2, or Runge-Kutta 4 timestepping scheme. The forward Euler method is adequate for the short physical timespans ($\lesssim 300 \mu\text{s}$) required to model the magnetic compression experiments. For these short simulations, the Runge-Kutta schemes don't produce different results but increase simulation runtimes by a factor of approximately two (Runge-Kutta 2) or four (Runge-Kutta 4). The error associated with the forward Euler scheme scales with $N dt$, where dt is the timestep and N is the number of iterations, and so it increases with the physical timespan associated with the simulation. For extended simulations, the Runge-Kutta schemes, where error scales with $N dt^2$ (Runge-Kutta 2) or $N dt^4$ (Runge-Kutta 4) are more suitable. With the forward Euler method, the field $X(t)$ being evolved is updated at each timestep using the value at the previous timestep according to:

$$X(t + dt) = X(t) + dt \dot{X} \quad (\text{C.2.1})$$

C.2.1 Timestep correction and data preservation

The code saves the evolved fields to file every t_{out} seconds of simulation time, where t_{out} is a code input parameter, typically set to $t_{out} = 1 \mu\text{s}$. If code input parameter *Saveplots* is set to one, plots of various interesting quantities against simulation time are saved to file each time the evolved fields are saved to file. For example, time-evolution of simulated diagnostics such as B_θ and B_ϕ at the magnetic probe locations, and line-averaged electron density and ion temperature along the interferometer and ion-Doppler chords are produced. In addition, graphs are saved to record the time-evolution of ψ_{CT} , total system toroidal flux, CT $q(\psi)$ (safety factor) profile, maximum ion and electron temperatures in the system, system energy components, CT volume, CT outer separatrix, and magnetic field components at the locations of the magnetic probes on the Marshall gun wall below the containment region. If the code input parameter *Savecontourplots* is also set to one, contour plots of the evolved fields (ψ , f , n_e , p_i , p_e , v_r , v_ϕ and v_z , as well as T_i , T_e , J_r , J_ϕ and J_z) are saved to file every $t_{out} \mu\text{s}$. When code input parameter *neutralfluid* is set equal to one, and a neutral fluid is also being evolved (see chapter 8), contour plots of n_n , p_n , T_n , v_{nr} , $v_{n\phi}$ and v_{nz} (the neutral fluid number density, pressure, temperature and velocity components) are also saved to file when *Savecontourplots* is also set to one.

If the simulation timestep exceeds the minimum required for numerical stability, unphysical field values, such as negative densities or pressures, can be calculated. These errors

ultimately lead to imaginary values in all the evolved fields. Throughout the simulations, after each timestep, a check is performed to see if any of the values of the ψ field (which is coupled to the other field solutions) are imaginary. If so, the timestep is reduced by a factor of $tsrf \sim 2$ (the "timestep reduction factor", a code input parameter is typically set to ~ 2). When this occurs, the simulation time and evolved fields are overwritten with the last saved values, and the simulation continues with the reduced timestep.

Although extremely low or high diffusion coefficient values can be used while maintaining numerical stability if the timestep is reduced, lower and upper limits need to be imposed on diffusion coefficients in order to achieve numerical stability in combination with acceptably short simulation runtimes. This is consistent with the standard stability criteria [96] that timestep is limited by the constraints $dt \lesssim D_{min}/V_{max}^2$ and $dt \lesssim h_e^2/D_{max}$, where D_{min} and D_{max} [m²/s] are the minimum and maximum diffusion coefficients, and V_{max} is the maximum speed associated with the system.

The code can also calculate, at each timestep, the maximum allowed timestep for the subsequent timestep, based on the mesh resolution, the ion sound speed and Alfvén speed, and the diffusion coefficients. The limit applied on the maximum allowed timestep by the Alfvén speed, $V_A = \frac{B}{\sqrt{\mu_0 \rho}}$, is $dt_{V_A} = \frac{h_e}{V_A}$, where h_e is the dimension associated with the smallest triangle element in the mesh. Similarly, the ion acoustic speed $c_s = \sqrt{\frac{T_i[J] + T_e[J]}{m_i}}$ imposes a limit of $dt_{c_s} = \frac{h_e}{c_s}$. The limit imposed by the diffusion coefficients is $dt_D \sim \frac{h_e^2}{4D_{max}}$. Here, D_{max} [m²/s] is the maximum of all the active diffusion coefficients, $D_{max} = \max(\chi_{\parallel i}, \chi_{\parallel e}, \chi_{\perp i}, \chi_{\perp e}, \eta, \nu, \zeta)$. Note that all these diffusion coefficients may vary, depending on other code input parameters, from node to node as a function of plasma parameters. The factor of four in the expression for dt_D arises when the system is two-dimensional [97]. It was found that, for reasonably high D_{max} (e.g., $D_{max} = \chi_{\parallel e} \sim 16000$ m²/s), that dt_D places the limit on the maximum allowed timestep over the early part of the simulation, but that later on in the simulation $dt_{v_A} < dt_D$, and so dt_{v_A} imposes the limit as the magnetic field strength increases after the bubble-in process. At typical magnetic compression settings, dt_{v_A} decreases further near peak magnetic compression, and then increases again after peak compression.

In practice, it was found that no significant reduction in overall simulation time was found with the more sophisticated method - the simpler timestep adjustment method using the timestep reduction factor seems quite adequate. It is worth noting that artificially increasing the ion mass m_i , allows for an increased timestep, as it reduces the Alfvén and thermal speeds, but also leads to increased plasma fluid inertia, with a consequently delayed and weakened formation process for simulations that include CT formation. Reducing Alfvén speed by increasing μ_0 also enables increased timestep, but leads to weakened formation and compression, as it reduces advective $\mathbf{J} \times \mathbf{B}$ forces. Overall, these methods are not practical when simulating CT formation as they alter the physics, but can be useful for code testing.

C.3 General discussion of diffusion coefficients

Care must be taken when choosing the values of the various diffusion coefficients, which are inputs to the code. The primary diffusion coefficients, ν , η , and χ , which determine viscosity, electrical resistivity, and thermal conduction respectively, are physical quantities that depend on inter-particle collisions on the microscopic level, and determination of the physically correct values is not trivial.

On the other hand, minimum levels of diffusion are required for numerical stability. Excessive spatial gradients in the various fields being evolved can result, at the timestep update, in overshooting of the field solutions, leading to spurious results at the regions of steep gradients. For example, viscosity, which appears in the momentum equation, acts to smooth out the velocity field. Resistivity appears in the expressions for $\dot{\psi}$ and \dot{f} , and smooths out gradients in the magnetic field, and thermal conduction in the species energy equations acts to smooth the pressure fields. In addition, density diffusion, which is artificial, is required to smooth out the density field, and also contributes to smoothing of the pressure fields. Excessive smoothing can blur the physics. Ideally, the "physically correct" diffusion coefficients would be higher than the coefficients required for stability, but this may not be the case. Increasing mesh resolution in regions of high gradients, and reducing the timestep, can reduce the minimum required levels of diffusion, but increasing resolution or reducing the timestep indefinitely is computationally impractical as it leads to excessive simulation run-times.

C.3.1 Thermal diffusion

Code input parameter $vary_\chi$ determines whether constant values, or values that vary with plasma parameters according to established relationships, are used as thermal diffusion coefficients. If $vary_\chi$ is set equal to one, then the thermal diffusion coefficients $\chi_{\parallel e}(T_e(\mathbf{r}, t), n(\mathbf{r}, t))$, $\chi_{\parallel i}(T_i(\mathbf{r}, t), n(\mathbf{r}, t))$, $\chi_{\perp e}(T_e(\mathbf{r}, t), n(\mathbf{r}, t), B(\mathbf{r}, t))$, and $\chi_{\perp i}(T_i(\mathbf{r}, t), n(\mathbf{r}, t), B(\mathbf{r}, t))$ are updated at each timestep according to the Braginskii expressions given in equations A.5.12 and A.5.20.

As outlined in section C.2, the maximum acceptable timestep for explicit timestepping schemes can be limited by the maximum diffusion coefficient, so inconveniently small timesteps are required for very large diffusion coefficients. In addition, in order to have sufficient smoothing of temperature gradients, mesh resolution needs to be increased, or time-step reduced, as diffusion coefficients are reduced to extremely small values. As an example, at $T_i = T_e = 100$ eV, $n = 1 \times 10^{20} \text{ m}^{-3}$, $Z_{eff} = 1$, $m_i = 4m_p$, where m_p is the proton mass, and $B = 1$ Tesla, the Braginskii coefficients give $\chi_{\parallel e} \sim 2 \times 10^7$, $\chi_{\parallel i} \sim 4 \times 10^5$, $\chi_{\perp e} \sim$

0.01, and $\chi_{\perp i} \sim 0.05$ [m²/s]. Hence, if the Braginskii expressions for the thermal diffusion coefficients are used, it is necessary to place upper and lower limits on the coefficients in order to have a conveniently large timestep (*e.g.*, $dt \geq 1 \times 10^{-11}$ s), moderate mesh resolution (*e.g.*, $h_e \geq 2$ mm), and consequently moderate simulation run times (*e.g.*, ~1-2 days for a 90 μ s simulation with $h_e = 2$ mm). For these practical values of h_e and dt , it was found that, for formation simulations, that the thermal diffusion coefficients should lie between around 25 m²/s and 20000 m²/s. Implementation of an implicit timestepping scheme would extend the range of acceptable thermal diffusion coefficients. In any case, the Braginskii formulae for diffusion coefficients are based on a model that doesn't include turbulence and other anomalous effects, and wouldn't be expected to be completely suitable, especially for CT formation simulations which involve extreme accelerations and turbulence.

If $vary_\chi$ is set equal to two, the empirical Bohm scaling [69], expressed as

$$\chi_{\perp\alpha}(\mathbf{r}, t) = (T_\alpha(\mathbf{r}, t) [\text{eV}]) / (16 B(\mathbf{r}, t) [\text{T}])$$

is used to update the perpendicular thermal diffusion coefficients, again constrained by upper and lower bounds, at each timestep, and constant values are chosen for the field-parallel coefficients.

In general, it is found that moderate run times and a good agreement to experimental magnetic compression data can be had by keeping $vary_\chi = 0$, and using constant values for $\chi_{\parallel\alpha}$ and $\chi_{\perp\alpha}$.

C.3.2 Viscous diffusion

The Braginskii formulae give expressions for species kinematic viscosity:

ν_α [m²/s] = μ_α [kg/m-s]/ ρ_α [kg/m³] in an unmagnetized, turbulence-free plasma. When single fluid MHD is implemented, only the ion viscosity is relevant. For a magnetized plasma, the Braginskii formulae give expressions for $\nu_{\parallel\alpha}$ and $\nu_{\perp\alpha}$, but again these expressions are only relevant for cases without turbulence. Hence, the physically correct values are basically undetermined. Equation A.5.14 gives the expression for the parallel ion viscosity as $\nu_{\parallel i} = 0.96 \tau_{ii} T_i$ [J]/ m_i , while perpendicular ion viscosity is given by $\nu_{\perp i} = 3 T_i$ [J]/ $10 \omega_{ci}^2 m_i \tau_{ii}$ [67], where τ_{ii} is the ion-ion collision time is given by equation A.5.6, and ω_{ci} is the ion cyclotron frequency. For $n = 1 \times 10^{20}$ [m⁻³], $T_i = 100$ eV, $B = 1$ T, and $m_i = 4m_p$, this gives the parallel and perpendicular components of the ion viscosity as $\nu_{\parallel i} \sim 1 \times 10^5$ [m²/s], and $\nu_{\perp i} \sim 0.03$ [m²/s]. As mentioned in appendix A.8, electron viscous heating is neglected in the two-temperature, single fluid MHD model. Including anisotropic viscosity would add complexity to the expression for the viscous tensor [67], so isotropic viscosity is implemented

in the code for simplicity.

In practice, for formation simulations using a moderate timestep, and with a mesh of practical resolution ($h_e \sim 2$ mm), it is found that we need to use a value of $\nu_{num} \gtrsim 500$ m²/s to maintain sufficiently smooth velocity fields for numerical stability. This level appears excessively high, as it leads to excessive viscous heating of the ions, especially for simulations with low density, when plasma velocity is high, such as during CT formation. Increased number density reduces the maximum observed ion temperature. Some researchers [98, 99] remove the viscous heating term entirely from the ion energy equation, but this is not considered to be a good choice when CT formation is being modelled, when the high ion speeds do in fact lead to extreme viscous heating. When deuterium is used for gas-fill, fusion neutrons are routinely detected during CT formation on GF plasma injectors, and have also been detected during formation on the magnetic compression experiment on the last night before the experiment was disassembled, when scintillators were installed on the machine (see section 4.5). Viscous heating is thought to be the mechanism behind this ion heating. We want to reduce viscous heating to acceptable levels, but do not want to eliminate it entirely.

To reduce ion viscous heating for low density simulations, so that simulated ion temperature is close to the levels indicated by the ion-Doppler diagnostic, ν_{num} is used in the viscous tensor in the expression for $-\nabla \cdot \bar{\pi}$ in the momentum equation, and a reduced value, a crude estimate of the "physically correct" value, $\nu_{phys} < \nu_{num}$ may be used in the expression for $-\bar{\pi} : \nabla \mathbf{v}$ in the ion energy equation. Other codes, *e.g.*, HiFi [100] also adopt this approach. In practice, determining ν_{phys} is not straightforward, ν_{phys} is always an approximation at best. For the relatively high densities associated with the magnetic compression experiment, it is possible to set $\nu_{phys} \sim \nu_{num}$, or even equal to ν_{num} , and still achieve reasonable simulated ion temperatures. However, it was necessary to increase numerical viscosity to $\nu_{num} > \sim 1500$ m²/s, and to set $\nu_{phys} \sim \nu_{num}/3$, for numerical stability and reasonable simulated ion temperatures when simulating CT formation in SPECTOR (see section 8.9.2) geometry. SPECTOR CTs have densities around five to ten times lower than those associated with the magnetic compression experiment. Ideally, the strategy of having different values for ν_{num} and ν_{phys} would be avoided because it breaks the conservation of system energy pertaining to the viscous terms (the terms in the last set of square brackets in equation 5.6.8). However, it was found that the discrepancy does not, apart from a reduction in ion viscous heating, significantly alter these particular simulation results, and appears at this stage to be an acceptable method for reducing ion heating in simulation scenarios with low density and high plasma velocities.

C.3.3 Resistive diffusion

Code input parameter $vary_\eta$ determines whether fixed values, or values that vary in space and time according to the Spitzer formula, are used for the isotropic plasma resistive diffusion coefficient. If $vary_\eta = 1$, equation 5.6.4 is used to calculate the resistive diffusion coefficient at each timestep. To limit the timestep to acceptably high values, an upper limit is placed on η , typically $\eta_{max} = 5000$ [m²/s], corresponding to constant $\eta = \eta_{max}$ at nodes where $T_e \lesssim 0.5$ eV. It would be reasonably straightforward to implement anisotropic resistivity (much simpler than implementing anisotropic viscosity), but since the parallel and perpendicular coefficients are of the same order ($\eta_{\parallel} \sim \frac{1}{2}\eta_{\perp}$ [67]), isotropic resistivity was considered to be a good approximation of the physical situation.

C.3.4 Density diffusion

An artificial density diffusion term $\underline{\nabla}_n \cdot (\zeta \circ \underline{\nabla}^e n)$ is included in the mass continuity equation (see equation 5.6.1). A certain minimum level of density diffusion is required for numerical stability, as density diffusion acts to smooth out gradients in the density field. Increasing mesh resolution in regions of high gradients can reduce the minimum required level of density diffusion, but this is often computationally impractical. The code input parameter ζ gives the coefficient of density diffusion, and, for simulations including magnetic compression, is typically required to be at least around 30 m²/s for numerical stability in combination with an acceptably high timestep and consequently short runtimes. As shown in section 5.6.3, correction terms have been developed and included in the discrete momentum and energy equations in order to maintain energy conservation, and angular momentum conservation in some scenarios, when density diffusion is included in the model.

C.4 Numerical solution of the Grad-Shafranov equation

The MHD code has the option of using an equilibrium described by the Grad-Shafranov equation (section A.7) as starting point from which the dynamical solutions to the various fields are evolved. The Grad-Shafranov equation (equation A.7.17) can be written as:

$$\Delta^* \psi + w(\psi) = 0 \quad (\text{C.4.1})$$

where $w(\psi) = \mu_0 r^2 \frac{dp(\psi)}{d\psi} + f(\psi) \frac{df(\psi)}{d\psi}$. In general, $w(\psi)$ has non-linear dependence on ψ , while $\Delta^* \psi$ has linear dependence on ψ .

An iterative pseudo time-stepping scheme method was developed to solve equation C.4.1. Over artificial time \tilde{t} , an initial guess for the solution ψ converges to the correct value that satisfies equation C.4.1. Using the forward Euler method, with pseudo timestep $\Delta\tilde{t}$, the scheme is

$$\begin{aligned} \frac{\psi^{n+1} - \psi^n}{\Delta\tilde{t}} &= \Delta^* \psi^n + w(\psi^n) \\ \Rightarrow \psi^{n+1} &= \Delta\tilde{t}(\Delta^* \psi^n + w(\psi^n)) + \psi^n \end{aligned} \quad (\text{C.4.2})$$

This explicit scheme results in unstable solutions for ψ without a suitably small timestep. A better approach for faster convergence is to use an implicit scheme for the iterations. We keep $w(\psi^n)$, the non-linear part of equation C.4.1, as an explicit term, and solve implicitly for the linear term $\Delta^* \psi$:

$$\begin{aligned} \frac{\psi^{n+1} - \psi^n}{\Delta\tilde{t}} &= \Delta^* \psi^{n+1} + w(\psi^n) \\ \Rightarrow \psi^{n+1} &= \Delta\tilde{t}(\Delta^* \psi^{n+1} + w(\psi^n)) + \psi^n \\ &= \Delta\tilde{t}(\Delta^* \psi^{n+1} + w(\psi^n)) + \psi^n + \Delta\tilde{t}(\Delta^* \psi^n - \Delta^* \psi^n) \\ &= \Delta\tilde{t} \Delta^* \psi^{n+1} + \Delta\tilde{t}(\Delta^* \psi^n + w(\psi^n)) + \psi^n - \Delta\tilde{t} \Delta^* \psi^n \\ \Rightarrow (1 - \Delta\tilde{t} \Delta^*) \psi^{n+1} &= \Delta\tilde{t}(\Delta^* \psi^n + w(\psi^n)) + (1 - \Delta\tilde{t} \Delta^*) \psi^n \\ \Rightarrow (1 - \Delta\tilde{t} \Delta^*)(\psi^{n+1} - \psi_n) &= \Delta\tilde{t}(\Delta^* \psi^n + w(\psi^n)) \\ \Rightarrow \psi^{n+1} &= (1 - \Delta\tilde{t} \Delta^*)^{-1} \times (\Delta\tilde{t}(\Delta^* \psi^n + w(\psi^n))) + \psi_n \end{aligned} \quad (\text{C.4.3})$$

To find the discrete expression for equation C.4.3, note that $(\nabla_\perp \psi)|_\Gamma \neq 0$, while the differential matrix operator $\underline{\underline{\Delta}}^*$, described in section 5.4.3, produces accurate results at the boundary nodes only when the boundary-normal component of the gradient of the operand field is zero at the boundary.

Defining $\underline{\psi} = \underline{\psi}_\Gamma + \underline{\psi}_{int}$, where $\underline{\psi}$ is the vector containing the values of ψ for the Grad-Shafranov solution at the nodes, while $\underline{\psi}_\Gamma$ and $\underline{\psi}_{int}$ have the values of ψ set to zero at internal / boundary nodes respectively, the discrete form of $\Delta^* \psi$ is

$$\underline{\underline{\Delta}}^* \underline{\psi} = \underline{\underline{\Delta}}^* \underline{\psi}_\Gamma + \underline{\underline{\Delta}}_0^* \underline{\psi}_{int} \quad (\text{C.4.4})$$

The operator $\underline{\underline{\Delta}}_0^*$ is designed to produce the same results as $\underline{\underline{\Delta}}^*$ at internal nodes if the boundary values of the operand field are set to zero. The boundary values of \underline{a} are preserved in the operation $\underline{c} = \underline{\underline{\Delta}}_0^* \underline{a}$, and do not contribute to the values calculated for elements corresponding to internal nodes in \underline{c} . Defining $\underline{b} [N_n \times 1]$ as the logical vector defining the

indexes of the boundary nodes (*i.e.*, $\underline{b}(i) = 1$ if node i is a boundary node, otherwise $\underline{b}(i) = 0$), $\underline{\underline{\Delta}}_0^*$ is defined as $\underline{\underline{\Delta}}_0^* = \underline{\underline{\Delta}}^*$, with $\underline{\underline{\Delta}}_0^*(\underline{b}, :) = \underline{\underline{\Delta}}_0^*(; \underline{b}) = 0$, and $\underline{\underline{\Delta}}_0^*(\underline{b}, \underline{b}) = 1$. The Grad-Shafranov solution for ψ is defined as having values of zero at the boundary nodes, *i.e.*, $\psi_\Gamma = \underline{0}$, so that

$$\underline{\underline{\Delta}}^* \underline{\psi} = \underline{\underline{\Delta}}_0^* \underline{\psi}_{int}$$

Hence, referring to equation C.4.3, the Grad-Shafranov solution for ψ can be evaluated at internal nodes, as

$$\underline{\psi}_{int}^{n+1} = (\underline{\underline{I}} - \Delta \tilde{t} \underline{\underline{\Delta}}_0^*)^{-1} * \Delta \tilde{t} \underline{\Lambda}_{int}^n + \underline{\psi}_{int}^n$$

where $\underline{\underline{I}}$ is the identity matrix with dimensions $N_n \times N_n$. For the explicit scheme (equation C.4.2), the Grad-Shafranov solution can be evaluated at internal nodes as

$$\underline{\psi}_{int}^{n+1} = \Delta \tilde{t} \underline{\Lambda}_{int}^n + \underline{\psi}_{int}^n$$

Introducing the $\underline{\underline{\Delta}}_0^*$ operator and solving equation C.4.3 at internal nodes eliminates, for the implicit scheme, the requirements for boundary values associated with the regular $\underline{\underline{\Delta}}^*$ operator. $\underline{\Lambda}_{int}^n = (\underline{\underline{\Delta}}^* \underline{\psi} + \underline{f} \circ \underline{f}' + \mu_0 \underline{r}^2 \circ \underline{p}')_{int}^n$ is the discrete form of the left side of equation C.4.1, where the values at the boundary nodes have been set to zero, and is the term that converges to zero. At each iteration, the expression for $\underline{\Lambda}^n$ is found and then the boundary values of $\underline{\Lambda}^n$ are set to zero. The L_2 norm of $\underline{\Lambda}_{int}^n$ is then determined as $d\Lambda^n = (\underline{\Lambda}_{int}^n)^T * (\underline{\Lambda}_{int}^n)$; if $d\Lambda^n < \epsilon \ll 1$, the solution $\underline{\psi}$ is considered to have converged. Otherwise, the boundary values of $\underline{\psi}^{n+1}$ are set to zero for the next iteration (in which $\underline{\psi}^{n+1} \rightarrow \underline{\psi}^n$). At convergence, the solution fields are evaluated as $\underline{\psi} = \underline{\psi}^n$, with $\underline{\psi}(\underline{b}) = 0$, $\underline{f} = \underline{f}(\underline{\psi})$, and $\underline{p} = \underline{p}(\underline{\psi})$.

$\underline{f}(\underline{\psi})$, $\underline{f}'(\underline{\psi})$, $\underline{p}(\underline{\psi})$ and $\underline{p}'(\underline{\psi})$ are the discretised functional forms of $f(\psi)$, $\frac{\partial f(\psi)}{\partial \psi}$, $p(\psi)$ and $\frac{\partial p(\psi)}{\partial \psi}$, and are defined as code inputs. As described in appendix A.7.2, possible functional forms for $f(\psi)$ and $f'(\psi)$ are $f(\psi) = \bar{\lambda}\psi(1 + \alpha(\tilde{\psi} - 1))$ and $f'(\psi) = \bar{\lambda}(1 + \alpha(2\tilde{\psi} - 1))$, but any functional form can be chosen. When external shaft current is included in this particular model, the expression for f is modified to $f(\psi) = f_{external} + \bar{\lambda}\psi(1 + \alpha(\tilde{\psi} - 1))$, where $f_{external} = \frac{\mu_0 I_{external}}{2\pi} = 0.2 I_{shaft}$ [MA]. For pressure, a reasonable choice of input functional form is the parabolic profile $p(\psi(\mathbf{r})) = p_\Gamma + p_{axis}(\psi(\mathbf{r})/\psi_{axis})$, so that $p' = p_{axis}/\psi_{axis}$. Here, p_Γ is the choice of boundary condition for pressure, p_{axis} is the prescribed peak pressure at the magnetic axis, and ψ_{axis} is the value of ψ at the magnetic axis. Setting $p = 0$ and $p' = 0$ is also possible - in general, finite pressure has little effect on the Grad-Shafranov equilibrium, apart from a slight outward translation of the magnetic axis (known as the "Shafranov shift"), and some upward scaling of ψ_{axis} . Of course, pressure should be finite for equilibria that are used as an initial condition for MHD simulations.

With an initial guess of uniform $\underline{\psi}^0 = 1 \times 10^{-3} * \underline{1}$, with $\underline{\psi}^0(b) = 0$, and mesh resolution $h_e = 5$ mm, the number of iterations required for convergence to $\epsilon = 5 \times 10^{-22}$ with the implicit scheme varies non-linearly with $\Delta\tilde{t}$. Optimal $\Delta\tilde{t}$ is around 1×10^{-3} , for convergence within $N_{iter} = 200$ iterations. N_{iter} increases as $\Delta\tilde{t}$ is increased or reduced around the optimal value. In contrast, with the explicit scheme, the number of iterations required for convergence varies linearly (*i.e.*, constant product $\Delta\tilde{t} \times N_{iter}$) with N_{iter} , but only within a particular range. The optimal point for the explicit scheme is $\Delta\tilde{t} \sim 4 \times 10^{-6}$, for convergence after $\sim 13,000$ iterations. The solution for the explicit scheme doesn't converge with $\Delta\tilde{t} \gtrsim 4 \times 10^{-6}$, and the range over which the number of iterations required for convergence varies linearly with $\Delta\tilde{t}$ extends from $\Delta\tilde{t} \sim 4 \times 10^{-6}$ to $\Delta\tilde{t} \sim 2 \times 10^{-7}$.

The explicit scheme is not very sensitive to the initial estimate for ψ^0 . The number of iterations for convergence ranges from $\sim 20,000$ at $\psi^0 = 1 \times 10^{10}$, to $\sim 13,000$ at $\psi^0 = 1 \times 10^{-3}$ and $\sim 16,000$ at $\psi^0 = 1 \times 10^{-10}$. The implicit scheme is even less sensitive to the initial estimate - the number of iterations for convergence ranges from ~ 190 at $\psi^0 = 1 \times 10^{-3}$, to ~ 210 at $\psi^0 = 1 \times 10^{\pm 10}$.

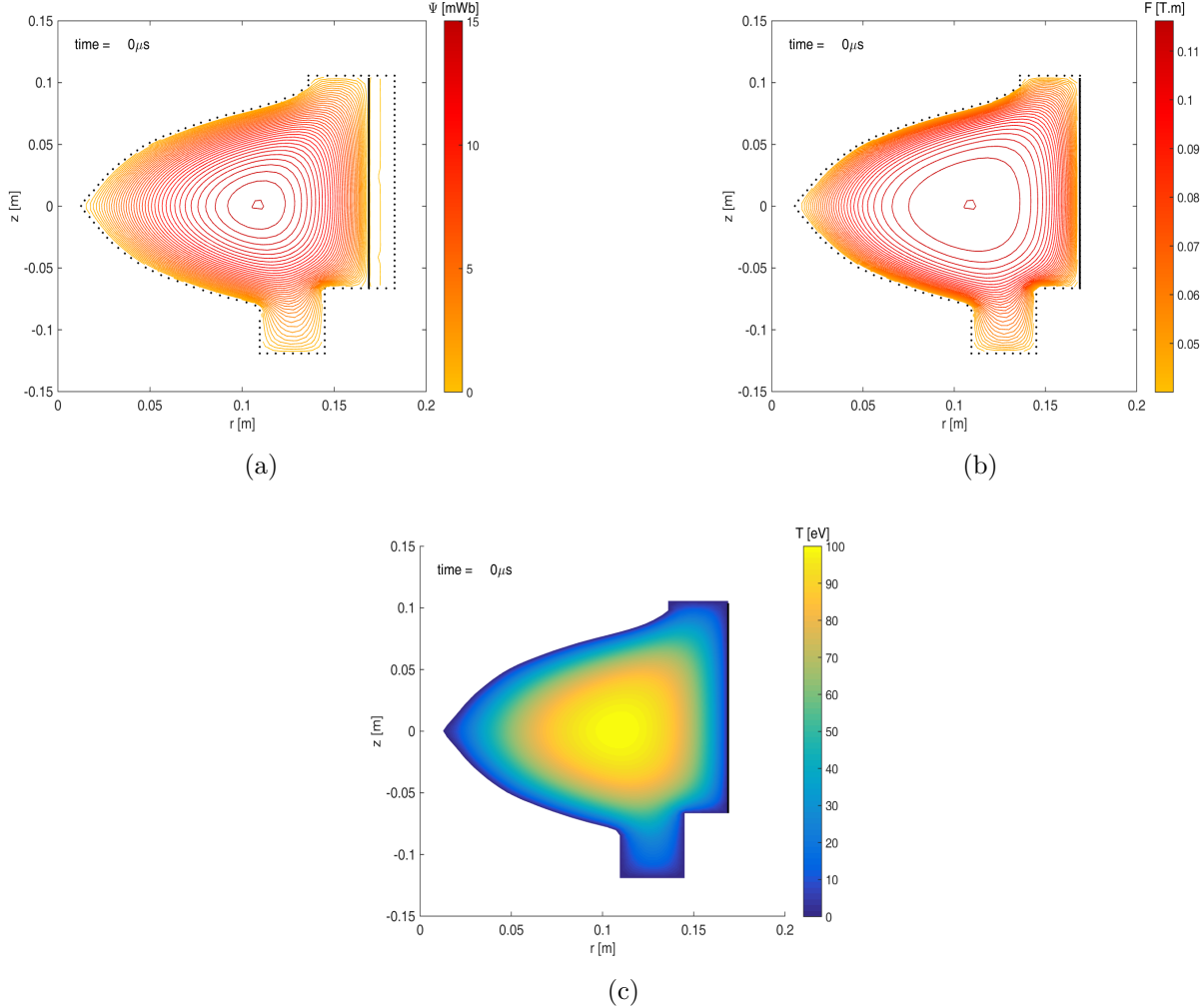


Figure C.4.1: Grad-Shafranov equilibrium solution example

Figure C.4.1 shows contours of ψ , f , and T for a Grad-Shafranov solution run using the model for $f(\psi)$ described in appendix A.7.2, with code input parameters $\bar{\lambda} = 31.85 \text{ [m}^{-1}\text{]}$, $\alpha = -0.8$, $I_{shaft} = 200 \text{ kA}$, $n_0 = 5 \times 10^{20} \text{ m}^{-3}$, $Z_{eff} = 1$, peak temperature $T_0 = 100 \text{ eV}$, and $T|_{\Gamma} = 0.02 \text{ eV}$. These input parameters determine the value of ψ_{axis} , 15 mWb in this case. The pressure profile is described by $p(\psi(\mathbf{r})) = p_{\Gamma} + p_{axis}(\psi(\mathbf{r})/\psi_{axis})$, where $p = n_0 T \text{ [J]}(1 + Z_{eff})$. As discussed in appendix A.7.2, having negative α for this prescription for f results in "hollow" current profiles where the magnetic field and current is concentrated towards the CT exterior. A solution with a less hollow profile is presented, and compared with the solution from a well-established equilibrium code, in section C.5. The MHD simulation results presented in chapter 7 are generally from simulations that include CT formation. Evolution of simulated CT toroidal field, and comparison with experiment, is presented for an MHD simulation that started with a Grad-Shafranov equilibrium in section 6.3.2.

C.5 Code verification and validation

C.5.1 Convergence studies (verification)

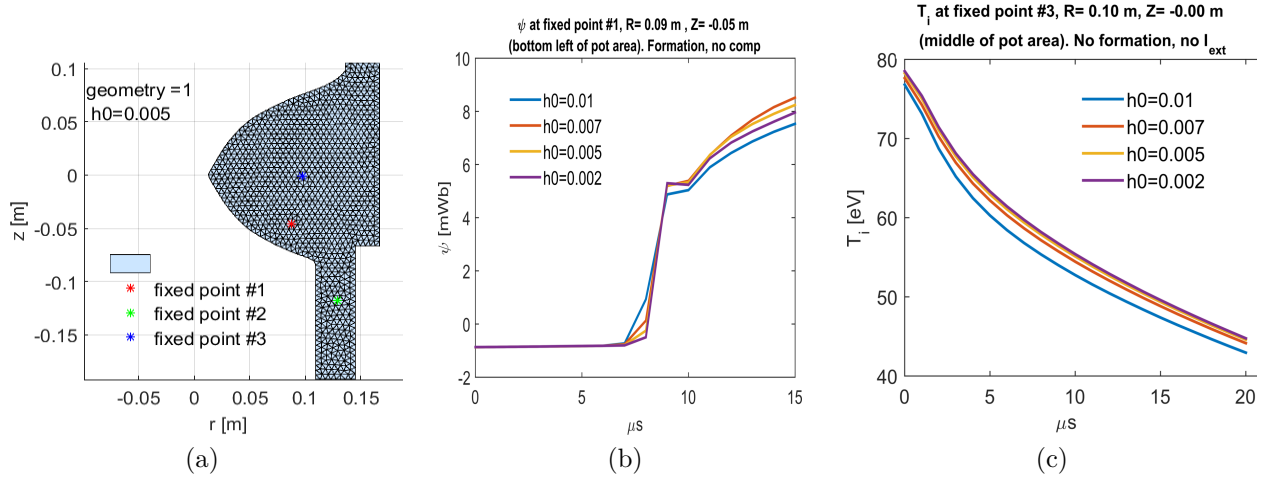


Figure C.5.1: Example convergence studies with varying h_e (triangular element size [m])

To study and verify the convergence of the equilibrium and MHD solutions with increasing mesh resolution, we ran a series of tests to record the values of various solution fields at some fixed points in the domain for various values of h_e , which quantifies triangular element size. Figure C.5.1(a) indicates the fixed point locations for a mesh with $h_e = 5$ mm - the mesh generator was forced to include a solution node at the fixed points for the test meshes with $h_e = 2, 5, 7$ and 10 mm. The truncated mesh shown here was used for non-formation tests - a mesh with the full extent of the gun included was used for tests that included simulated CT formation, and has additional fixed points down the gun. Convergence with increasing mesh resolution was verified for all solution fields at the various fixed points. Example convergence study results for ψ and T_i are shown in figures C.5.1(b) (formation simulation, with levitation, without compression) and (c) (no formation, no levitation or compression - the dynamics of this simulation started from a Grad-Shafranov equilibrium, with $\psi = 0$ maintained on the boundaries).

C.5.2 Equilibrium solution comparison with Corsica solution (validation)

The code's Grad-Shafranov solution was benchmarked against a solution obtained using the well-developed Corsica code [101]. The simple model [78] that assumes a linear dependence of $\lambda(\psi)$ on ψ was used to define $f(\psi)$ (see appendix A.7.2). Corsica's Grad-Shafranov solution is solved using a finite difference method on a structured grid.

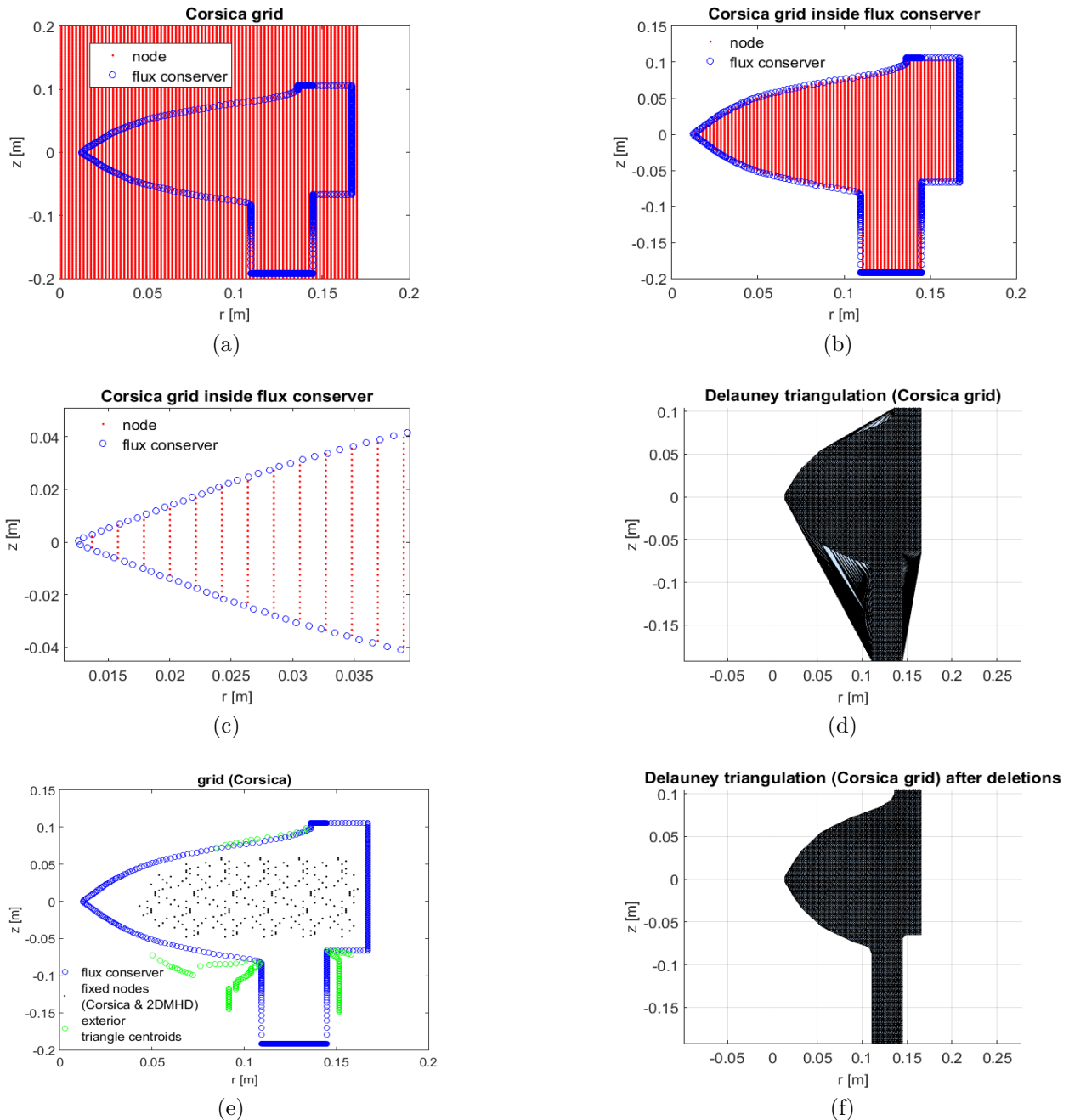


Figure C.5.2: Corsica grid with triangulation

Figure C.5.2(a) indicates the locations of the computational nodes, and the positions that define the flux conserver for the full Corsica grid. Figures C.5.2(b) and (c) indicate the locations of the nodes inside the flux conserver. As shown in figure C.5.2(d), the vectors defining the r and z coordinates of these interior nodes were used to produce a grid of triangular elements using Matlab's Delaunay triangulation function, for plotting contours of ψ from the Corsica solution. Figure C.5.2(e) shows the locations of the (~ 300) nodes in the Corsica grid that are assigned as fixed nodes in the grid for our code, so that a direct (no interpolation) comparison of solutions for ψ at these nodes can be made. Also shown in figure C.5.2(e) are the locations of the centroids of triangles that lie outside the flux conserver - these triangles were deleted from the mesh.

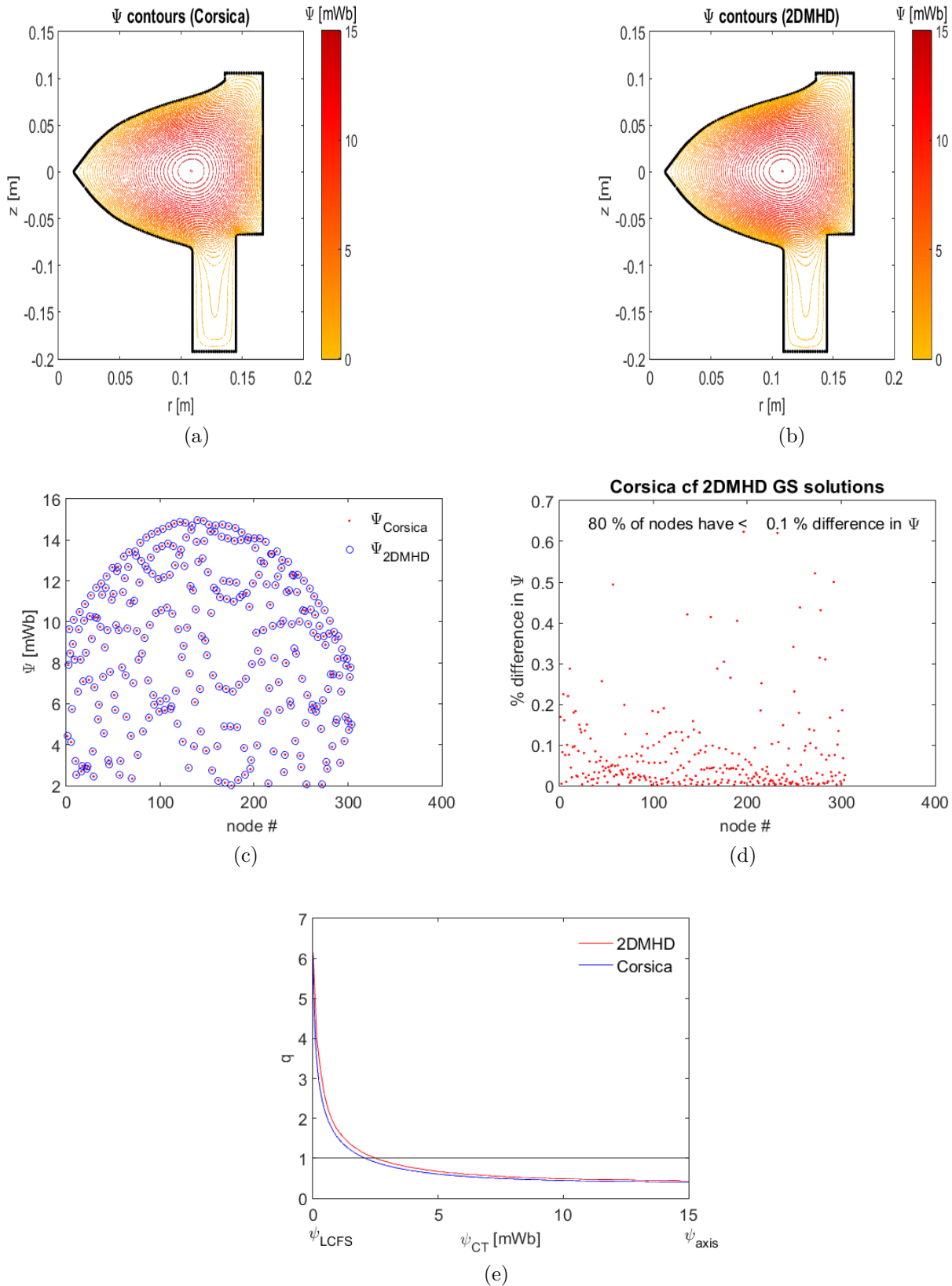


Figure C.5.3: Equilibrium solution comparison

Figures C.5.3(a) and (b) show ψ contours from the Corsica and DELiTE MHD code

respectively, for solutions with comparable grid resolutions, and with $\bar{\lambda} = 23.18$ [m⁻¹], $I_{shaft} = 200$ kA, $p = 0$, and $\alpha = -0.2$. The calculated values of ψ at the fixed nodes are shown in figure C.5.3(c). As indicated in figure C.5.3(d), the difference between the two solutions, expressed as a percentage of $\psi_{corsica}$, is less than 0.1% at 80% of the fixed nodes, and less than $\sim 0.5\%$ at all fixed nodes. Figure C.5.3(e) indicates the excellent match between the profiles of $q(\psi) = \frac{\partial\phi(\psi)}{\partial\psi}$ for the two codes. Note that ψ_{axis} and ψ_{LCFS} denote ψ at the magnetic axis and at the last closed flux surface. See section 6.5.2.1 for details of the method developed to evaluate the CT q profile. Additional tests were done that indicate similar levels of agreement between the calculated q and ψ profiles for the codes with various inputs parameters $\bar{\lambda}$, I_{shaft} , p , and α .

To date, no benchmark code comparison tests have been done to validate the MHD part of the code. As presented in chapter 7, the code reproduces many features of the experimental observations - this is a form of validation of the MHD model.

C.6 Summary

A freely available mesh generator has been modified to produce the computational grid. Forward Euler timestepping is found to be adequate for good solution convergence for the short physical timespans associated with the magnetic compression experiment, but the options of the higher order Runge-Kutta 2 and Runge-Kutta 4 timestepping schemes, which have been implemented to the code, may be advantageous for simulations with extended timespans. Methods were developed to vary the simulation timestep according to the time-evolving conditions of the various field solutions, which determine the maximum allowable timestep for stable time-advance, while managing simulation data preservation. Many approximations and simplifications are made when determining the various diffusion coefficients, which are generally representations of their physical counterparts, but are also required for numerical stability. Density diffusion is an artificial term that is required purely for numerical stability. For turbulent plasmas, there is no widely applicable formula that can be applied for determination of the thermal and viscous diffusion coefficients. When setting the viscous diffusion coefficient, care must be taken, especially when simulating CT formation, which involves regions of high velocity and low density, to have adequate viscous diffusion for numerical stability, while avoiding excessive ion viscous heating. The timestepping scheme is explicit, leading to restrictions imposed by the minimum acceptable timestep on the values of the diffusion coefficients. A numerical method to solve for the Grad-Shafranov equilibrium solution has been developed. The Grad-Shafranov equilibrium and $q(\psi)$ profile solutions have been benchmarked against solutions from a well-established code, and demonstrate an excellent

match. Ideally, tests would be conducted to validate the MHD solutions against a recognised code, this has not yet been done. Tests that verified convergence of code solutions with increasing mesh resolution were successfully conducted. As shown in chapter 7, experimental diagnostics are closely matched by the counterpart simulated diagnostics; this is also a form of code validation.

Appendix D

First results from plasma edge biasing on SPECTOR

D.1 Introduction

In this appendix, a description of an edge-biasing experiment conducted on the SPECTOR plasma injector [53], and initial results, are presented. The insertion of a disc-shaped molybdenum electrode (probe), biased at up to +100V, into the edge of the CT resulted in up to 1 kA radial current being drawn. Core electron temperature, as measured with a Thomson-scattering diagnostic, was found to increase by a factor of up to 2.4 in the optimal configuration tested. H_α intensity was observed to decrease, and CT lifetimes increased by a factor of up to 2.3. A significant reduction in electron density was observed; this is thought to be due to the effect of a transport barrier impeding CT fueling, where, as described in section 8.9.2, the fueling source is neutral gas that remains concentrated around the gas valves after CT formation.

High confinement mode (H-mode) has been implemented by various means (*e.g.*, edge biasing, neutral beams, ion or electron cyclotron heating, lower hybrid heating, and ohmic heating) on a range of magnetic confinement configurations including tokamaks, reversed field pinches, stellarators, and mirror machines. The first H-mode was produced in the ASDEX tokamak by neutral beam injection in 1982 [114]. In 1989, H-mode was first produced by electrode edge biasing on the CCT tokamak [115, 116]. In 1990, it was observed that edge impurity ion poloidal speed is modified abruptly during transitions from low to high confinement modes on the DIII-D tokamak [117]. H-mode has subsequently been produced routinely on many toroidal magnetic-fusion experiments, including practically all the large tokamaks including JET, TFTR, and JT-60. Since the initial electrode-biasing experiments on CCT, H-mode has been produced by edge biasing on many tokamaks, for example CAS-

TOR [118, 119], T-10 [119, 120], STOR-M [121], ISTTOK [122], TEXTOR [119, 123], and J-TEXT [124].

Electrode biasing involves the insertion of an electrode, that is biased relative to the vessel wall near the point of insertion, into the edge of a magnetized plasma. This leads to a radially directed electric field between the probe and the wall. The resultant $\mathbf{J}_r \times \mathbf{B}$ force imposed on the plasma at the edge of the plasma confinement region varies with distance between the probe and the wall, because E_r , as well as the magnetic field, vary in that region. The associated torque overcomes viscous forces, spinning up the edge plasma, and results in shearing of the particle velocities between the probe and the wall. The sheared velocity profile is thought to suppress the growth of turbulent eddies that advect hot plasma particles to the wall, thereby reducing this plasma cooling mechanism. In general, H-modes induced by probe biasing share features of those initiated by various methods of heating, including a density pedestal near the wall (near the probe radius for probe biasing), diminished levels of recycling as evidenced by reduced H_α emission intensity, and increased particle and energy confinement times. For example, increases in energy confinement times by factors of 1.5, 1.5, 1.2, and 1.8 were reported for CCT, STOR-M, TEXTOR and T-10 respectively. Core electron density increased by a factor of four on CCT, while line-averaged electron density increased by factors of 2, 2, 1.5, and 1.8 on STOR-M, TEXTOR, T-10, and CASTOR respectively. Of these five examples, a biasing-induced temperature increase was noted only for the T-10 experiment, with an increase in core ion temperature by a factor of 1.4 reported, while reduced H_α emission intensity was recorded in each case.

Positive as well as negative electrode biasing works well on some machines; in other instances only one biasing polarity has the desired effect. Most biasing experiments have used passive electrodes, while some have implemented electron-emitting electrodes. Emissive electrodes have, in addition to a circuit to bias the electrode relative to the vacuum vessel, a separate heating circuit, and are heated until they emit electrons. Materials traditionally used for emissive electrodes include lanthanum hexaboride (LaB6) and tungsten (W). Generally speaking, emissive electrodes add complexity to an experiment, but may be beneficial when the edge plasma electron density is so low that dangerously high voltages (which could initiate a current arc that could damage the electrode and vessel) would be required in order to draw an edge current sufficiently high enough for the $\mathbf{J}_r \times \mathbf{B}$ force to overcome inertial effects (viscosity, friction) and drive edge rotation. In the CCT tokamak [115], LaB6 cathodes heated by carbon rods drew edge current up to 40 A when the voltage measured between the electrode (probe) and vessel wall was $V_{probe} \sim -250$ V. On CCT, for negative bias, it was found that both electron-emissive electrodes and passive graphite electrodes produced similar results, as long as the electrode was large enough to draw sufficient current (~ 20 A), and small enough not to form a limiter [115]. For negative biasing on ISTTOK, it was not possible

to draw more than 2 to 3 A with a passive electrode, *cf.* ~ 20 A with an emissive electrode, while the current drawn with positive biasing was the same for emissive and non-emissive electrode ($I_{probe} \sim 28$ A at $V_{probe} \sim +130$ V).

Pre-biasing conditions of radial electric field and an extensive range of plasma parameters play roles in determining the beneficial polarity and the level of bias-induced plasma confinement improvement [125]. A reduction of radial transport at the edge would be beneficial for confinement not only because of reduced outward thermal transport, but also due to reduced inward transport of cold wall-recycled particles to the core. This latter effect is especially relevant on small machines for which the surface area to volume ratio of the magnetically confined plasma is large, particularly in the absence of a limiter or divertor, where the recycling process is more important. It may be partly due to this effect, in combination with the effect of a transport barrier impeding the CT fueling process that arises due to neutral particles diffusing up the gun after the CT formation process (section 8.9.2), that the improvements in confinement times and electron temperatures observed with the initial edge biasing tests on SPECTOR ($R \sim 11$ cm, $a \sim 8$ cm, no limiter or divertor) appear especially significant.

An overview of the experiment setup with a description of the biasing electrode assembly is presented in section D.2. Circuit analysis, leading to an estimate for the resistance of the plasma between the electrode and flux conserver, which was useful for optimising the circuit, is the focus of section D.3. Main results are presented in section D.4. The appendix ends with a discussion of principal findings, conclusions and possible further improvements to the experiment in section D.5

D.2 Experiment setup

A schematic of the SPECTOR [111] plasma injector is depicted in figure 1.2.2(b), where the red dots represent the locations of magnetic probes. SPECTOR is a magnetized Marshall gun that produces compact tori (CTs). It has, in addition to the formation circuit that drives up to 0.8 MA formation current over around 80 μ s, a separate circuit to produce an approximately constant shaft current of up to 0.5 MA, which flows up the outer walls of the machine and down the central shaft, increasing CT toroidal field and making the CT more robust against MHD instability. Shaft current duration is extended to around 3 ms with a crowbar inductor/diode circuit, which is indicated schematically in figure 1.2.2(b). Toroidal field at the CT core is typically around 0.5 T. The high CT aspect ratio, and the q profile, define the CTs as spherical tokamaks. Coaxial helicity injection produces plasma currents in the range 300 – 800 kA. A selection of Thomson-scattering (TS) system-produced electron temperature and electron density measurements [113] (both taken at 300 μ s after CT

formation), electron density measurements obtained with a far-infrared (FIR) interferometer [112], spectral data, and magnetic probe data, will be presented in the following.

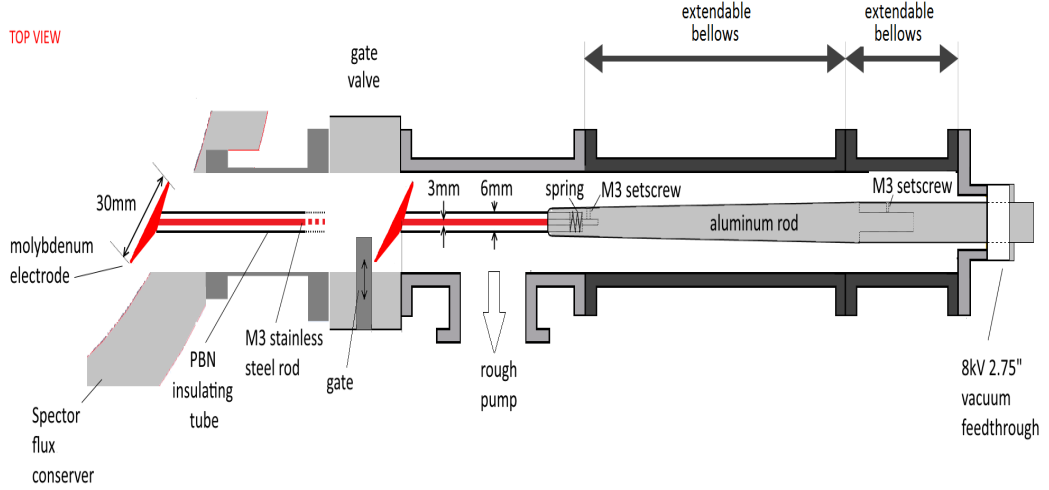


Figure D.2.1: Biasing probe assembly

Figure D.2.1 indicates a top-view of the electrode (probe) assembly with extendable vacuum bellows. The biasing electrode can be retracted behind the gate valve and isolated from the machine vacuum. The approximately disc-shaped electrode is machined from molybdenum and has a 30 mm diameter. Molybdenum was chosen for its high work function against sputtering, high melting point, and its resilience against the corrosive action of lithium, which is used as a gettering agent on SPECTOR. A pyrolytic boron nitride (PBN) tube is used as a plasma-compatible insulator around the M3 stainless steel rod that connects the electrode to a tapered aluminum rod, which is in turn connected to the 0.5" diameter copper rod that forms part of the 8 kV 2.75" CF vacuum feedthrough. The electrode can be inserted up to 45 mm into the vacuum vessel; insertion depth was 11 mm for the results presented here.

D.3 Circuit analysis

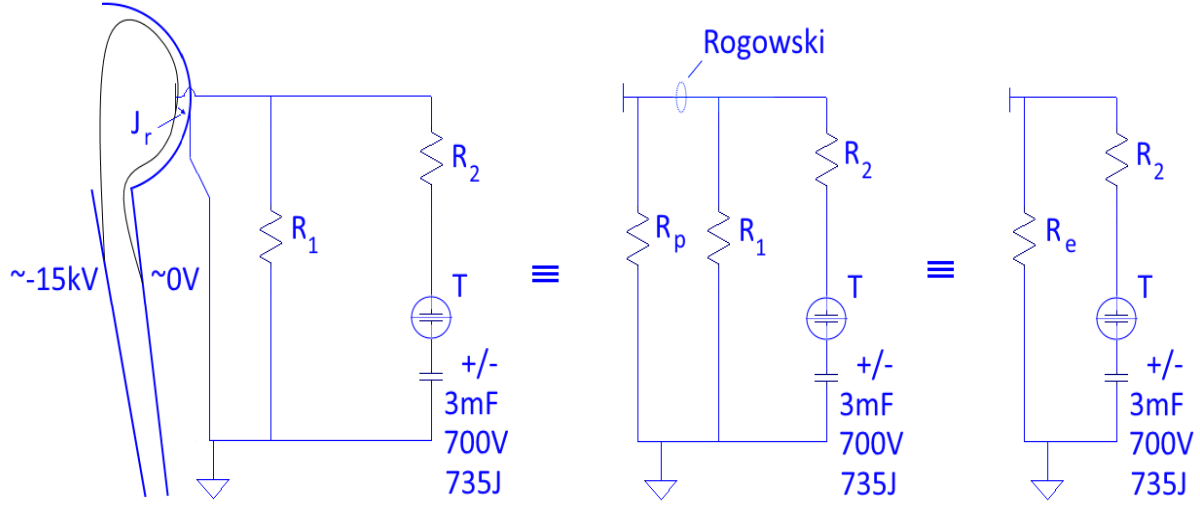


Figure D.3.1: Biasing probe circuit diagram

Figure D.3.1 indicates the most optimal of the biasing probe circuit configurations tested. The biasing circuit was kept open-circuited until well after CT formation, in order to protect biasing circuit components. A thyratron switch (indicated in the figure) is robust against large amplitude negative voltage spikes that can appear on the probe during CT formation when initially open stuffing-field lines, that are resistively pinned to the injector inner and outer electrodes, intersect the probe (see left subfigure). These thyratron switches are designed to operate at several kilovolts, and usually require several kiloamps of current to remain closed, but careful setting of switch temperature enabled operation at moderate voltages and currents. The biasing capacitor voltage setting V_{bc0} , parallel and series resistors R_1 and R_2 , and R_p , the plasma resistance between the electrode (*i.e.*, probe) and flux conserving electrode, determine V_{probe} , the voltage measured between the probe and flux conserving electrode, and I_{probe} , the radial current drawn through the plasma edge. The radial current leads, in the classical edge biasing scenario, to $\mathbf{J}_r \times \mathbf{B}$ driven edge velocity shearing and consequential decorrelation of turbulence cells and confinement improvement. For the circuit with the 3 mF capacitor depicted in figure D.3.1, optimal circuit resistances were found to be $R_1 \sim 0.2 \Omega$, and $R_2 \sim 0.5 \Omega$. Negative electrode biasing was briefly tested; the results presented here were obtained with positive biasing. The effective resistance R_e , comprised of R_p and R_1 in parallel (see figure D.3.1, right subfigure), is given by

$$R_e(t) = \frac{R_p(t) R_1}{R_p(t) + R_1} \quad (\text{D.3.1})$$

The voltage applied by the capacitor on the probe is

$$V_{applied}(t) = V_{bc}(t) \left(\frac{R_e(t)}{R_e(t) + R_2} \right) \quad (\text{D.3.2})$$

where $V_{bc}(t)$ is the voltage across the biasing capacitor. Equations D.3.1 and D.3.2 can be combined to provide an expression for R_p :

$$R_p(t) = \frac{R_1 R_2 V_{applied}(t)}{R_1(V_{bc}(t) - V_{applied}(t)) - V_{applied}(t) R_2} \quad (\text{D.3.3})$$

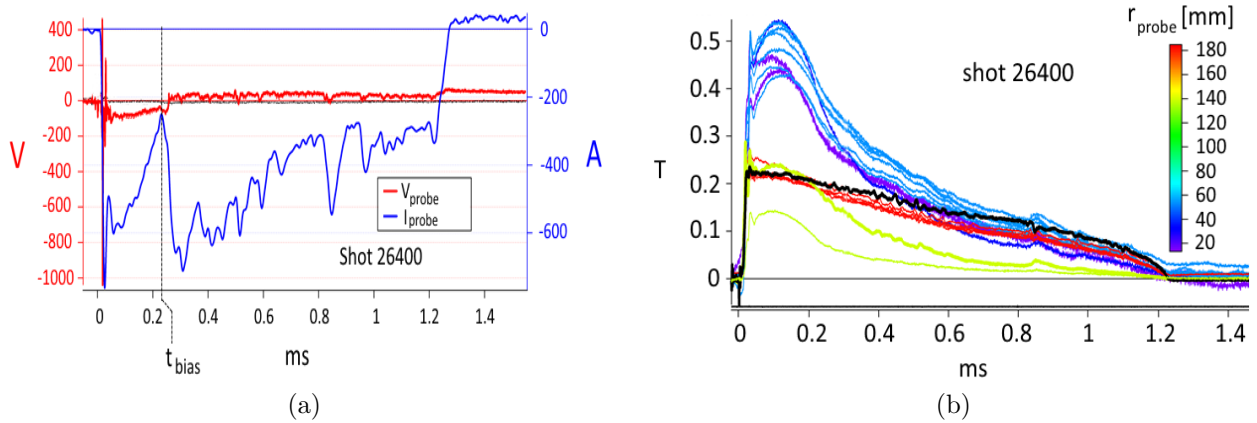


Figure D.3.2: Measured bias probe voltage and current (a), and poloidal field (b) for shot 26400, which had $V_{bc0} = 700$ V (3 mF capacitor)

Figure D.3.2(a) shows the voltage measured between the probe and the vacuum vessel, and the current drawn through the plasma edge, as measured with the Rogowski coil indicated in figure D.3.1, for shot 26400. At the biasing capacitor voltage found to be most optimal for CT lifetime and electron temperature (as obtained with the TS system), the voltage measured between the probe and vacuum vessel was typically $V_{probe} \sim +50$ V to $+80$ V, and the maximum radial current drawn to the probe from the wall was $I_{probe} \sim 700$ A to ~ 1 kA shortly after firing the biasing capacitor(s). For shot 26400, the electrode was inserted 11 mm into the edge plasma, and biased at $t_{bias} = 230$ μ s after firing the formation capacitor banks, as indicated in figure D.3.2(a). Note that current is already flowing through the plasma edge, and through resistor R_1 , before t_{bias} , as a result of the plasma-imposed potential on the electrode, which typically led to a measurement of $V_{probe} \sim -100$ V when magnetized plasma first enters the CT confinement area at around 20 μ s. V_{probe} and I_{probe} decrease over time at a rate that depends on plasma and circuit parameters. Figure D.3.2(b) indicates, for shot 26400, the poloidal field measured at the magnetic probes indicated as red dots in figure 1.2.2(b). It is interesting that the fluctuations in B_θ , which are thought to be associated

with internal reconnection events, are also manifested on the biasing voltage and current measurements, *e.g.*, at $\sim 845 \mu\text{s}$ in figures D.3.2(a) and (b). This observation is enabled by the presence of the small parallel R_1 . As edge plasma impedance varies, as determined by internal MHD events, the system can divert varying proportions of capacitor driven current through R_1 . In future studies, it may be possible to influence the behaviour of the internal modes that cause the B_θ fluctuations, by driving an edge current that is resonant with the fluctuations.

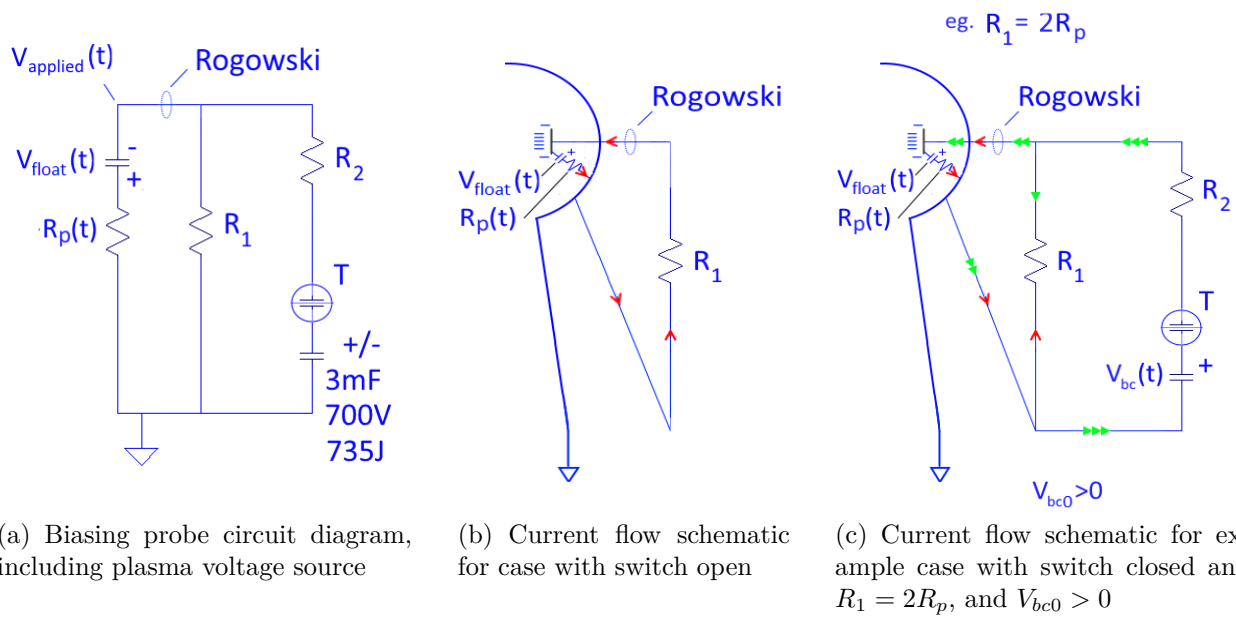


Figure D.3.3: Biasing probe circuit diagram, including plasma voltage source, with current flow schematics

When the plasma is considered as a time-dependent voltage source, which biases the probe to floating potential $V_{float}(t)$, a more complete circuit diagram is as depicted in figure D.3.3(a). The inclusion of R_1 , a small external resistance in parallel with R_p (the plasma resistance between the probe and wall), allows current driven by the floating potential to flow in the circuit in the case where the thyatron switch is open (see figure D.3.3(b)). When the switch is closed, a proportion of the biasing capacitor-driven current may divert to flow through R_1 , see figure D.3.3(c). This proportion increases as R_p increases with reducing electron temperature as the CT decays, thereby allowing I_{probe} to decrease at a rate roughly in proportion to the rate of decrease of the main CT plasma currents. The presence of an appropriately sized R_1 also prevents development of a sustained arc, which could damage the wall and probe, through the ambient plasma that remains between the probe and wall after the CT has extinguished. In previous edge biasing studies on tokamaks, the standard is to maintain approximately constant $V_{applied}$ and I_{probe} for an extended time which is a segment

of the duration over which the approximately constant externally driven toroidal plasma current flows. On SPECTOR plasmas, the plasma currents are not driven and are allowed to decay naturally after formation, so a circuit configuration that establishes constant $V_{applied}$ and I_{probe} would not be compatible.

The differential voltage measured between the probe and flux conserver is

$$V_{probe}(t) = V_{applied}(t) + V_{float}(t) \quad (\text{D.3.4})$$

If the bias capacitor is not fired, and R_1 is removed from the circuit, then in the open circuit condition $V_{probe}(t) = V_{float}(t)$. Note that V_{float} is not measured directly on each shot, however, looking at the V_{probe} measurements taken during several open circuit, probe-in shots, the floating potential can be approximated as an RC rise of the form

$$V_{float}(t) = V_{f0} e^{-\frac{t}{\tau_{RCf}}} \quad (\text{D.3.5})$$

with $V_{f0} \sim -80$ V, and, (depending on CT lifetime) $\tau_{RCf} \sim 1$ ms. $V_{float}(t)$ rises from ~ -80 V at the time when plasma enters the CT confinement region, to 0 V when the CT has decayed away. With this, an approximation for $V_{applied}$ can be made using equation D.3.4. $V_{bc}(t)$, the voltage across the biasing capacitor, was not measured directly in the experiment, but can be estimated as

$$V_{bc}(t) = V_{bc0} e^{-\frac{t}{\tau_{RCb}}} \quad (\text{D.3.6})$$

where, for shot 26400, $V_{bc0} = 700$ V and $\tau_{RCb} = 0.5 \Omega * 3 \text{ mF} = 1.5$ ms (resistance $R_2 = 0.5 \Omega \gg R_e$). With these approximations for $V_{applied}(t)$ and $V_{bc}(t)$, an estimate of the plasma resistance along a path that has a principal component along the helical magnetic field between the probe (with insertion depth 11 mm) and flux conserver is evaluated, between $t_{bias} = 250 \mu\text{s}$ until the time when the CT has decayed, using equation D.3.3:

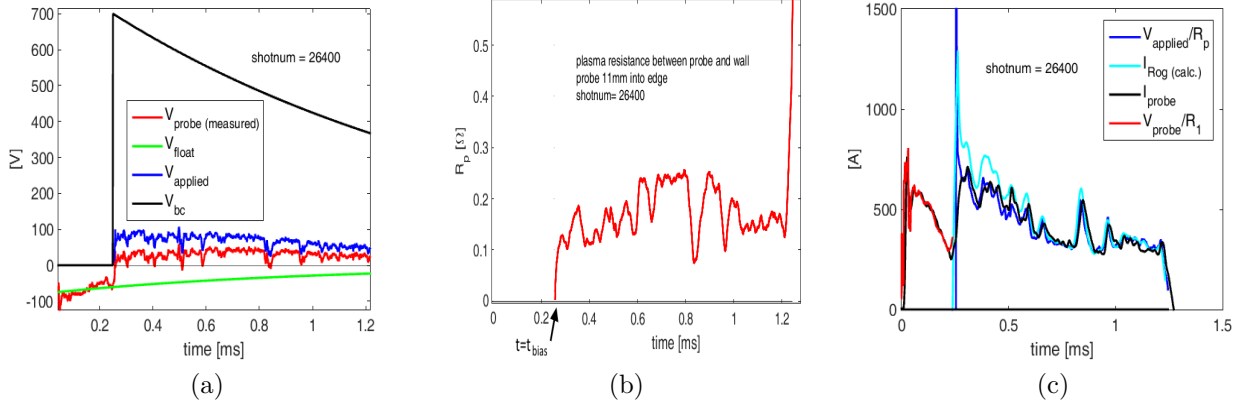


Figure D.3.4: Calculated / measured probe voltages, edge plasma resistance and bias currents for shot 26400

The approximations (from equations D.3.4, D.3.5, and D.3.6) for $V_{\text{applied}}(t)$, $V_{\text{float}}(t)$, and $V_{\text{bc}}(t)$, and measured $V_{\text{probe}}(t)$, for shot 26400, are shown in figure D.3.4(a). Figure D.3.4(b) shows the estimation, from equation D.3.3, for $R_p(t)$. $R_p(t) \sim 0.15 \Omega$ to 0.2Ω , and rises as T_e decreases (η_{plasma} increases) over CT decay, then drops as the edge current path length L (recall $R(t) = \eta(t)L(t)/A(t)$) decreases. Path length decreases because B_θ decreases faster than B_ϕ (CT toroidal field is maintained at a relatively constant level by the crow-barred external shaft current) as the CT decays, *i.e.*, q increases - there are fewer poloidal transits for each toroidal transit along the path which defines R_p . The sharp dip in R_p at $t \sim 845 \mu\text{s}$ coincides with the fluctuations in $I_{\text{probe}}(t)$ and B_θ seen in figures D.3.2(a) and (b). Note that the current through the path enclosed by the Rogowski coil depicted in figures D.3.1 and D.3.3 can be calculated using basic circuit theory as:

$$I_{\text{rog}(\text{calc.})} = \frac{1}{R_p(t)} \left[\frac{R_2 (V_{\text{bc}}(t) R_1 + V_{\text{float}}(t) R_1 + V_{\text{bc}}(t) R_p(t))}{R_1 R_2 + R_2 R_p(t) + R_p(t) R_1} - V_{\text{bc}}(t) - V_{\text{float}}(t) \right] \quad (\text{D.3.7})$$

Figure D.3.4(c) compares measured $I_{\text{probe}}(t)$ (black trace) with calculated parameters, to verify the calculation of $R_p(t)$. Referring to figure D.3.3(c), it is seen that $V_{\text{applied}}(t)/R_p(t)$ should, as is confirmed in figure D.3.4(c) (dark blue trace), give the measured $I_{\text{probe}}(t)$ current when the switch is closed after $t = t_{\text{bias}}$. Referring to figure D.3.3(b), $V_{\text{probe}}(t)/R_1 \sim I_{\text{probe}}(t)$ when the switch is open before $t = t_{\text{bias}}$ (red trace in D.3.4(c)). A good match to measured $I_{\text{probe}}(t)$ is found by using calculated $R_p(t)$ and the estimated profile of $V_{\text{float}}(t)$ in equation D.3.7 (after $t = t_{\text{bias}}$, cyan trace). A good estimate of $R_p(t)$ is useful for optimizing external circuit resistances.

D.4 Main results

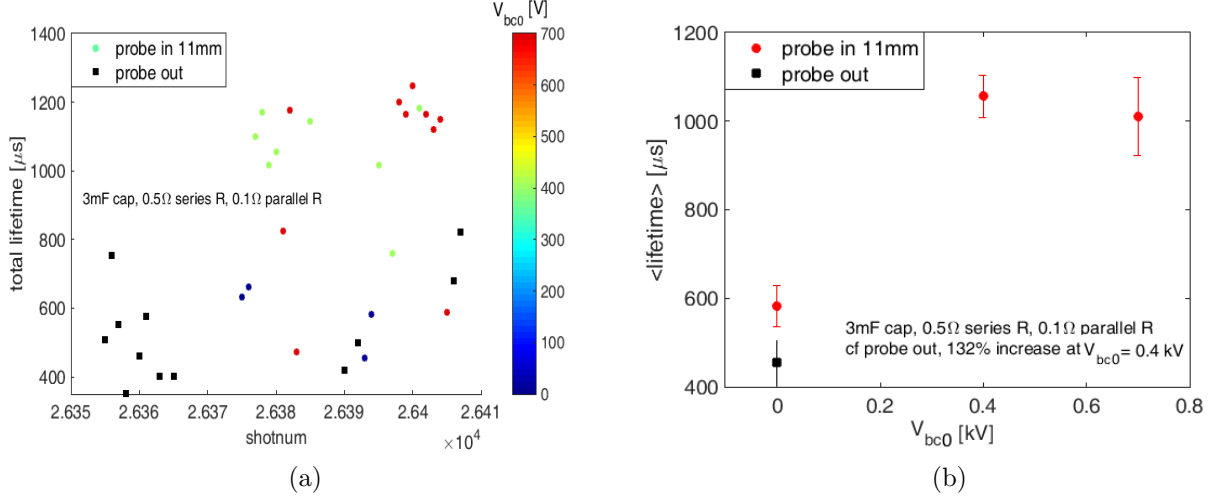


Figure D.4.1: 3 mF capacitor: total CT lifetimes *cf.* V_{bc0} (bias capacitor voltage setting)

Figure D.4.1(a) indicates how CT lifetimes varied with V_{bc0} (coloured circles) for shots taken with the biasing probe inserted 11 mm into the plasma edge in the configuration using the 3 mF biasing capacitor circuit, with $R_1 = 0.1\Omega$ and $R_2 = 0.5\Omega$, compared with shots taken with the probe removed (black squares). Figure D.4.1(b) indicates the average of CT lifetimes for the probe-out configuration (black squares), and the averages for the probe-in configuration (red circles) for the setpoints $V_{bc0} = 0$ V, 400 V, and 700 V. It is indicated that CT lifetime increased from around 450 to 600 eV, even when the biasing capacitor was not fired - in that case, the presence of the resistor (R_1) in parallel with the biasing capacitor enables current, driven by the potential applied by the plasma, to flow from the electrode to the wall. At $V_{bc0} = 400$ V, CT lifetime increased by a factor of around 2.3, from $\sim 460\ \mu\text{s}$ to $\sim 1070\ \mu\text{s}$. Note that TS data is not available for the configuration with the 3 mF capacitor in the biasing circuit.

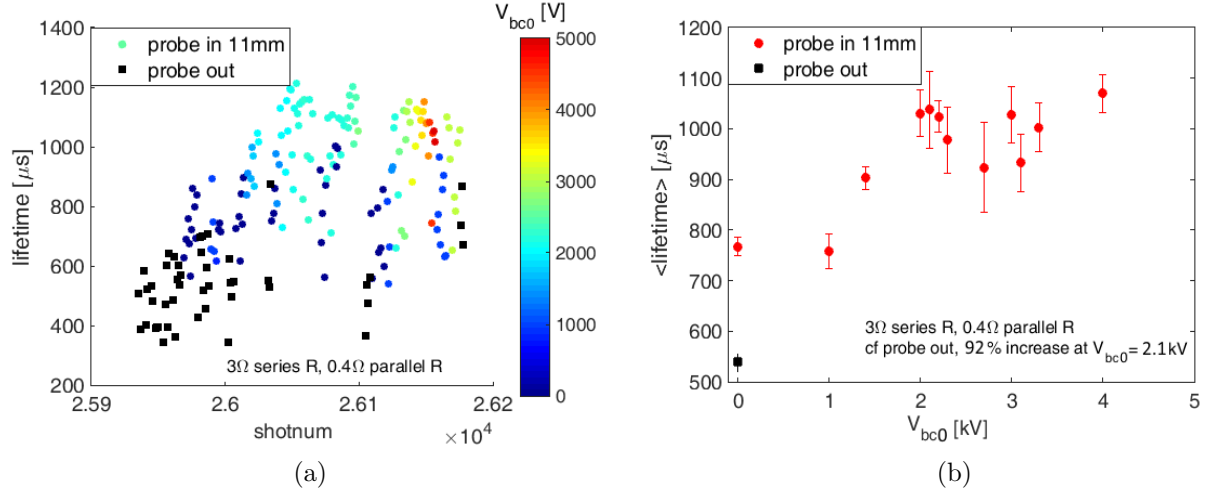


Figure D.4.2: 100 μF capacitor: CT lifetimes *cf.* V_{bc0}

Figure D.4.2 shows equivalent information for shots taken with a 100 μF , 5 kV capacitor in the biasing circuit, with $R_1 = 0.4\Omega$ and $R_2 = 3\Omega$ (TS data is available for this configuration). CT lifetimes were approximately doubled in this configuration, with an optimal biasing capacitor setpoint of $V_{bc0} \sim 2$ kV.

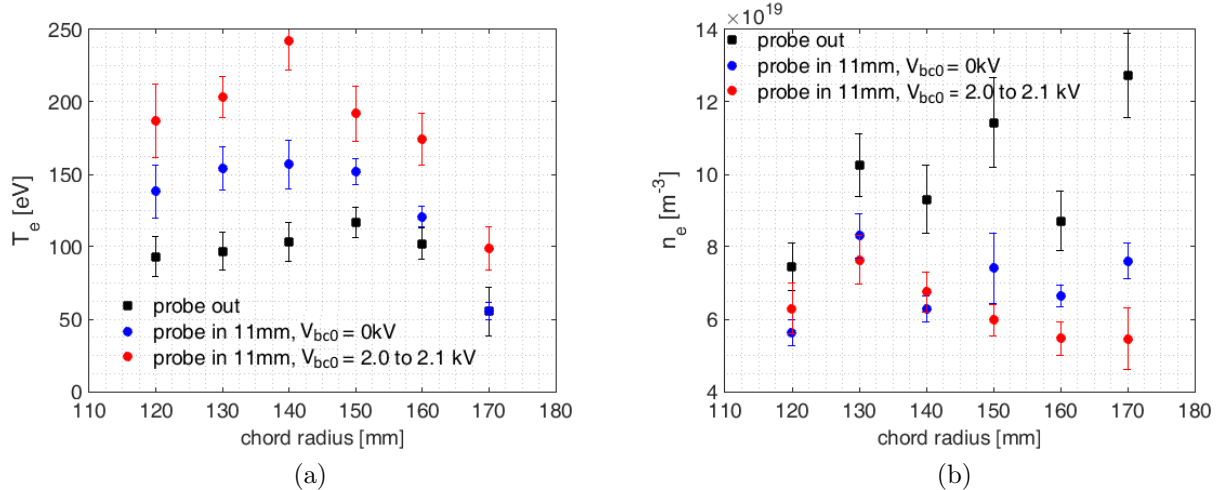


Figure D.4.3: 100 μF capacitor: electron temperature and density profiles at 300 μs , for $V_{bc0} \sim 2$ kV

Figure D.4.3 shows shot data indicating the temperature and density profiles obtained with the TS system at 300 μs after firing the formation capacitor banks, for the configuration with the 100 μF , 5 kV biasing capacitor. Note that the TS sampling points are indicated in figure 8.9.6(b). With $V_{bc0} \sim 2$ kV, the measurements indicate that temperature is more than doubled at the inner sampling points, increasing by a factor of around 2.4 at the sampling point at $r = 140$ mm, (black squares *cf.* red circles) and the proportional increase in tem-

perature falls off towards the CT edge. Note that current drawn through the CT edge leads to a temperature increase even when no voltage is externally applied to the electrode (black squares *cf.* blue circles). Referring to figure D.4.3(b), electron density is markedly reduced when the electrode is inserted and the reduction is enhanced when the electrode is externally biased. The proportional decrease in density is greater towards the CT edge, consistent with the theory that edge fueling impediment due to an edge transport barrier is largely responsible for the density reduction. The diagnostic indicates an electron density reduction by factors of approximately 1.5 and 2.3 at $r = 130$ mm and $r = 170$ mm respectively.

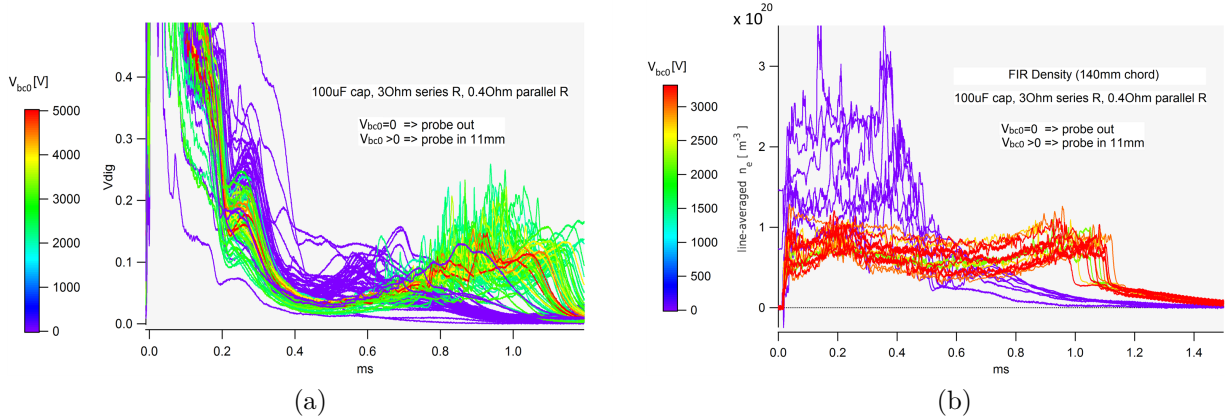


Figure D.4.4: $100 \mu\text{F}$ capacitor: (a) H_{α} intensity, (b) electron density (FIR interferometer)

Figure D.4.4(a) indicates how H_{α} intensity, along a vertical chord located at $r = 88$ mm, is reduced when the electrode is inserted and biased. H_{α} intensity reduction is a sign of reduced recombination at the vessel walls, and is associated with improved confinement. The purple traces are from shots with the electrode removed from the vacuum vessel. As shown in figure D.4.4(b), time-resolved FIR interferometer data from the chord at 140 mm (FIR chord locations are indicated in figure 8.9.6(a)) confirms the reduction in electron density when the biased probe is inserted into the plasma edge. Again, the purple traces are from shots taken with the electrode retracted. This density reduction is thought to be due to the effect of the transport barrier impeding the level of CT fueling associated with neutral gas diffusing up the gun, as discussed in section 8.9.2. Note that the fueling effect is not entirely eliminated by the biasing effect - density starts to increase at around 500 to 600 μs (*cf.* figure 8.9.7(b)). Note that H_{α} intensity increases dramatically at around the same time (figure D.4.4(a)). The CTs associated with the purple traces in figure D.4.4(a) and (b) do not last for long enough to enable observation of the density and H_{α} intensity increases at that time.

D.5 Summary

Significant increases in CT lifetime and electron temperature, and reductions in electron density and H_α intensity, were observed when the electrode was inserted into the plasma edge, even when the biasing capacitor was not fired. In that case, the presence of the resistor (R_1) in parallel with the biasing capacitor enables current, driven by the potential applied by the plasma, to flow from the electrode to the wall. Note that in cases where the biasing capacitor was not fired, the enhanced performance was eliminated when R_1 was removed from the circuit. In terms of enhanced CT lifetime, which was observed to increase by a factor of up to 2.3, the optimal biasing circuit tested was with the 3 mF capacitor in place, but TS data was not available in that configuration. CT lifetimes and electron temperatures were observed to increase by factors of around 2 and 2.4 (temperature near the CT core) respectively in the configuration with the 100 μ F capacitor charged to 2.1 kV, while density decreased by a factor of around 2.3 near the CT edge. This density reduction is thought to be due to the effect of the transport barrier impeding level of CT fueling associated with neutral gas diffusing up the gun. The consequent reduction of cool particle influx to the CT is thought to partially responsible for the particularly significant increases in observed temperature, as compared with prior edge biasing experiments. Up to ~ 1200 A was drawn 11 mm through the edge plasma, while improving CT lifetime and temperature.

Note that the biasing experiment was conducted without a fresh lithium coating on the inside of the SPECTOR flux conserver. With a fresh coating, CT lifetimes are typically around 2 ms. The biasing experiment may be run again with a fresh coating. The experiment was conducted over a short period (less than two weeks). As the majority of the probe-out shots were taken at the beginning of each day, there is likely some data skew due to cleaning effects. The improvement shown with biasing may be extended with further circuit optimization. Negative biasing was tested briefly - a slight increase of electron temperature and a peaking of the electron temperature profile was observed, but there was no evidence of lifetime increase. It may be that the ion-sputtering of the probe associated with negative biasing lead to performance degradation associated with plasma impurities that offset the improvement associated with the establishment of a transport barrier. Perhaps more cleaning shots are required to see a significant improvement with negative biasing - the efficacy of negative biasing hasn't been confirmed. An IV curve was produced with the electrode biased to a range of positive and negative voltages on a shot to shot basis. Langmuir analysis indicated $T_e \sim 130$ eV and $n_e \sim 10^{19}$ [m $^{-3}$] at the probe location at 300 μ s, and $T_e \sim 85$ eV and $n_e \sim 5 \times 10^{18}$ [m $^{-3}$] at 600 μ s. Compared with TS data, the electron temperature estimates in particular appear too high. The fact that probe biasing affects electron temperature and electron density makes the Langmuir analysis results dubious at best, but it may be possible

to correct for this effect.

It would be worth repeating the experiment with a fresh lithium coating on the inner flux conserver. Circuit parameters, probe insertion depth, and machine operation settings should be optimized further. The effects of biasing on edge conditions should be characterised using Langmuir and Mach probes, and ion Doppler diagnostics. Negative biasing may be tested more rigorously. It would be interesting to look at the effects of driving edge current resonant to the MHD behaviour that manifests itself in the form of fluctuations on measurements including CT poloidal field.

The biasing experiment was especially noteworthy because it has generally been found that insertion of foreign objects, such as thin alumina tubes containing magnetic probes, into SPECTOR and MRT CTs, leads to performance degradation associated with plasma impurities. After the extensive problems encountered relating to plasma/material interaction and impurities during the magnetic compression experiment, special care was taken to choose a plasma-compatible material for the biasing electrode assembly. The pyrolytic boron nitride tube and molybdenum electrode combination seems to have been a good choice - at least the benefit due to drawing a current through the CT edge outweighed any performance degradation that may have been associated with impurities introduced to the system.